RICE UNIVERSITY

Space Weather Event Modeling of Plasma Injection Into the Inner Magnetosphere with the Rice Convection Model

by

Yang Song

A Thesis Submitted
in Partial Fulfillment of the
Requirements for the Degree

Doctor of Philosophy

Approved, Thesis Committee:

Stanislav Sazykin, Chair
Senior Faculty Fellow of Physics and Astronomy

Richard A. Wolf
Emeritus Professor of Physics and Astronomy

Frank Jones
Noah Harding Professor of Mathematics

Houston, Texas

May, 2010

ABSTRACT

Space Weather Event Modeling of Plasma Injection Into the Inner Magnetosphere with the Rice Convection Model

by

Yang Song

The inner magnetosphere modeling is an important component of the magnetosphere simulation frameworks with significant implications for space weather and a principle methodology to understand the magnetospheric response to changes in the solar wind. The thesis shows our efforts in constructing and validating the contemporary Rice Convection Model (RCM) code and its interface as a next-generation code to predict electric fields, field-aligned currents, and energetic particle fluxes in the inner magnetosphere and subauroral ionosphere during geomagnetic disturbed times. The RCM was used to simulate the geomagnetic storms with fixed boundary conditions of time-dependent Tsyganenko-Mukai boundary conditions. This work shows the results of two extremely strong storm events with significant interchange motion. The ring current injection predicted by the RCM is shown to be overestimated, consistent with the previous results of overestimating particle fluxes by the RCM. This effect is magnified here since the southward component of interplanetary magnetic field is very strong reaching about 50 nT. Time-dependent Borovsky's boundary condition is implemented and used to alleviate the huge pressure and get better tendency of ring current energy calculated by the Dessler-Parker-Sckopke relation. This work also describes a new module of generalized Knight's relation to compute the parallel po-

tential drops from the calculated field-aligned currents through Vasyliunas equation. It gives different ionospheric conductance and plasma drift signatures particularly around the midnight. The inclusion of parallel electric fields will replace the treatments of energy flux in the substorm simulations since that the Hardy normalization cannot perform the desired function during the substorm expansion phase and the energy flux floor gives arbitrary enhanced the precipitating energy flux and ionospheric conductances at high latitude especially for the westward electrojet around the midnight. Since the original Knight's relation gives too large field-aligned potential drop, the modified Knight's relation is applied and implemented successfully into the RCM. Therefore, the RCM is capable of real time event simulation including strong geomagnetic storms and magnetospheric substorms, although full validation of model predictions with typical observations remains to be done.

Acknowledgements

I would like to express my sincere gratitude to my thesis advisor Dr. Stanislav Sazykin for his support and guidance during my studies in the Space Physics program at Rice. He gave me an abundance of advice and encouragement throughout this work.

I am also grateful to Dr. Richard A. Wolf and Dr. Frank Jones for serving on my committee and for making many useful suggestions. Special thanks to Dr. Robert Hardt for his time being my committee member although the time conflict prevents him from attending my oral defense.

I would also like to acknowledge the help from Dr. Robert W. Spiro, Dr. Frank R. Toffoletto, Dr. Paul Ontiveros, Dr. Jian Yang, Dr. Jichun Zhang on coding and numerical implementation and from Bei Hu, Liheng Zhang for useful discussions and assistances.

At last, I thank my parents, my sister and my wife Rong Zhang for their consistent supporting and encouraging on my Ph.D. study.

Work at Rice University was supported by NSF Space Weather grant ATM-0720309, NASA Sun-Earth-Connection theory program grant NNG05GH93G, the NASA living with a star targeted research and technology (LWS TR&T) grant NNX06AC03G, NASA heliophysics theory grant NNX08AI55G.

.

Contents

Illustrations

Tables

Chapter 1

Introduction

Space weather refers to conditions on the Sun and in the space environment that can influence the performance and reliability of space-borne and ground-based technological systems, and can endanger human life or health. Adverse conditions in the space environment can cause disruption of satellite operations, communications, navigation, and electric power distribution grids, leading to a variety of socioeconomic losses[24]. A fundamental need of the National Space Weather Program (NSWP) is that of promoting the research to advance the understanding of fundamental processes, numerical modeling, data processing and analysis, and the integration of this understanding into physics-based first-principle models capable of predicting space weather. Numerical models do exist for the regions where space weather originates, develops, and interacts with the Earth, but the models cannot include all the physical processes involved. The Rice Convection Model (RCM) has proven to be useful in explicating much of what is known about the physics of the inner magnetosphere. This paper describes both the scientific goal of understanding plasma transport between the plasma sheet and inner magnetosphere during magnetic storms, substorms, and related phenomena and the practical aim of the NSWP by development of a code capable of much-improved specification and forecast of inner magnetospheric conditions.

1.1 Solar Wind and Interplanetary Magnetic Field

The Sun of our solar system is a typical star of intermediate size and luminosity. It's radius is about 7×10^5 km, and it rotates with a period that increases with latitude from 25 days at the equator to 36 days at poles. Its mass is about 2×10^{30} kg, consisting mainly of 90% hydrogen and 10% helium. The Sun emits radio waves, X-rays, and energetic particles in addition to visible light. Figure 1.1 shows the structure layers of the Sun. In the core of the Sun a continuous nuclear fusion is converting hydrogen into helium. The energy of nuclear reaction is radiated from the core into the layers above. Above 3/4 of solar radii heat is mainly transported by convection rather than radiation. The visible solar surface over the convective zone with a temperature of about 6000 K is called the photosphere. As a result, the sun is most luminous in visible light[25]. The free energy that drives space weather is created in the convective zone with the generation and convective distortion of magnetic fields[26].

Above the photosphere are two transparent layers. The chromosphere, visible during eclipses, extends 10000 km above the photosphere and has a temperature in the order 10^4 K. The corona at temperature of 10^6 K is observable beyond chromosphere for more than 10^6 km without an apparent termination. The solar corona is very hot that the hydrogen and helium can escape gravitational attraction and form a steadily streaming outflow of material called the solar wind. The solar wind is fully ionized plasma and supersonic above a few solar radii because of the heating, compression, and subsequent expansion. The term plasma is used as a synonym for ionized gas containing about equal numbers of ions and electrons[27]. The solar wind plasma consist of primarily of hot electrons and protons with a minor fraction of He^{2+} ions and some other heavier ions, typically at high charge states. Although the solar wind

moves out almost radially from the Sun, the rotation of the Sun gives the magnetic field a spiral form. At the orbit of the Earth the angle between the field lines and the radial is about 45°.

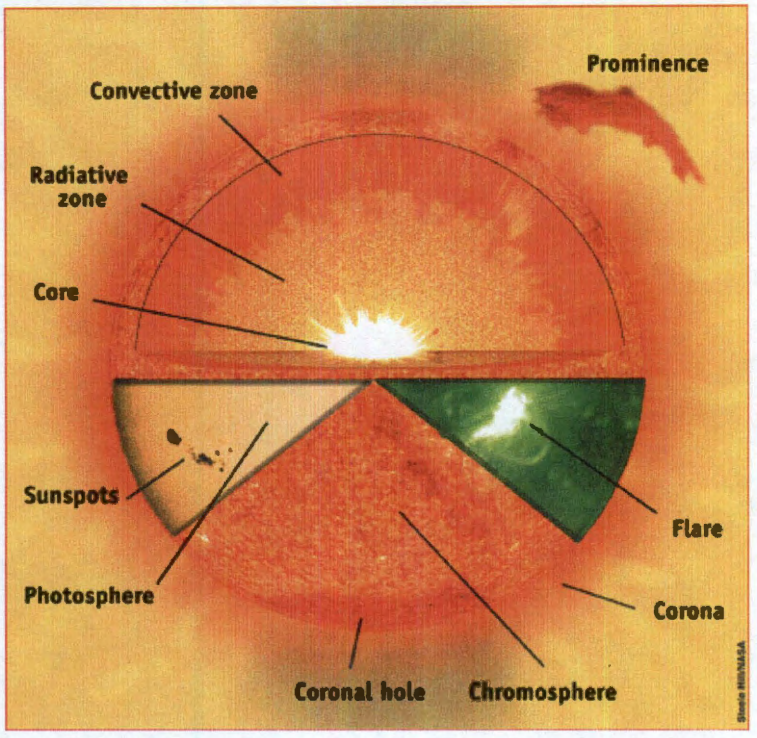

Figure 1.1 : Structure layers of the Sun. Photo courtesy of the Solar and Heliospheric Observatory (SOHO) consortium.

The solar wind carries the solar magnetic field into space, forming the interplanetary magnetic field (IMF) and defining the heliosphere. The magnetic field of the Sun is extremely complicated. However, most of the complications don't extend very far from the surface, and the magnetic field of the outer corona can often be described by a dipole or quadrupole.

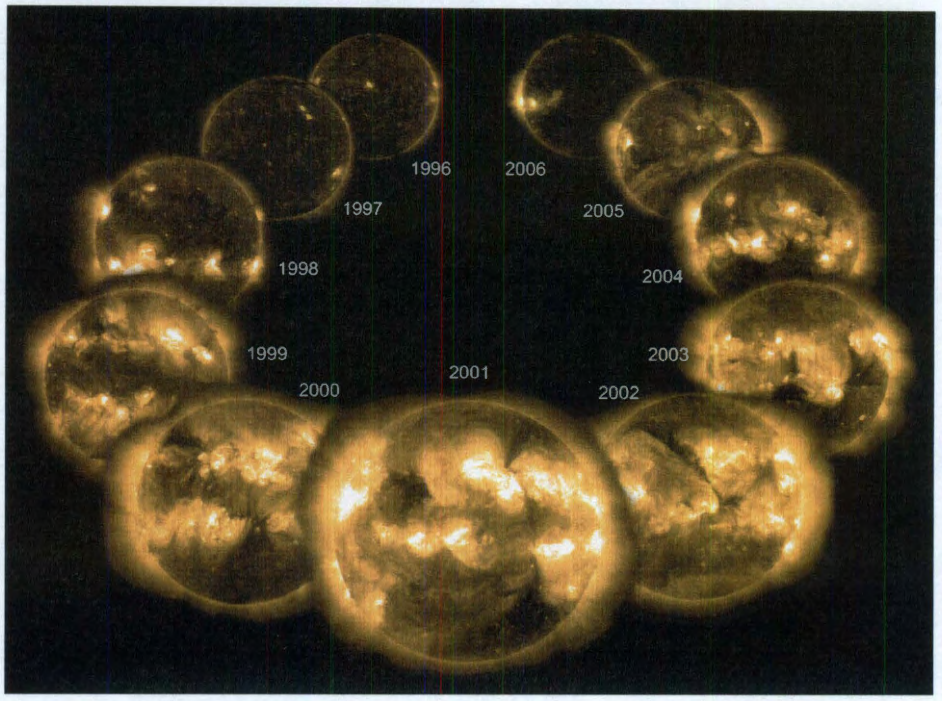

Figure 1.2 : SOHO observation of the 23rd solar cycle. Photo courtesy of SOHO EIT consortium.

Additional complications arise from the variability of the field, which is also reflected in the Sun's activity. The destruction and recreation of the internal magnetic dipole structure occurs during a 11-year solar cycle, as shown in Figure 1.2, or actually 22-year considering the dipole orientation. All solar cycles are not equally intense, and it is possible that longer period modulations are operating.

Sunspots are manifestations of magnetically disturbed conditions at the Sun's visible surface as shown in Figure 1.3. They are about 4000 K, cooler than their surroundings on the photosphere. Because of the temperature difference and their size, about 10^3 to 10^5 km in diameter, sunspots can be observed visually from the Earth.

Figure 1.3 : An image shows sunspots during the active time of the Sun leading to a geomagnetic process. Figure courtesy of NASA.

Sun emits radio energy with a slowly varying intensity. This radio flux, originating from atmospheric layers high in the Sun's chromosphere and low in its corona, changes daily with the sunspot number, and thus also follows the solar cycle as shown in Figure 1.4. The F10.7 flux, which has a frequency of 2800 MHz or a wavelength of 10.7 cm, affects the Earth's atmosphere.

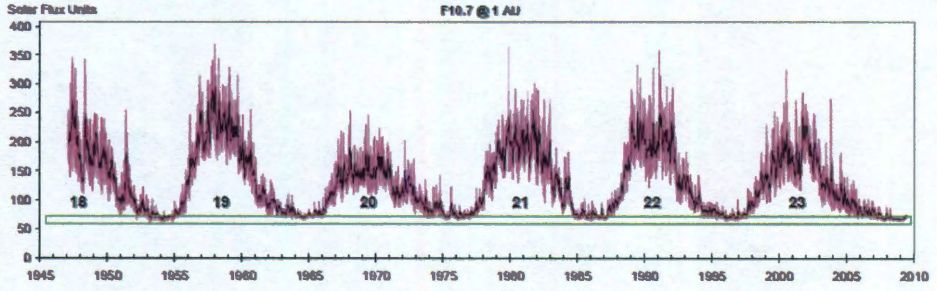

Figure 1.4 : The entire record up of F10.7 flux May 14, 2009 with daily noon values (pink) and a 27-day mean (black). The green box implies that the flux at every minimum is very nearly the same[1].

1.2 Earth's Magnetosphere

All planets in the Solar System are surrounded by the hot, magnetized, supersonic collisionless solar wind plasma capable of conducting electrical current and carrying a large amount of kinetic and electrical energy. There is controversy as to whether the distribution of solar wind particles can be treated as a Maxwellian or not, and even whether fluid theory can be applied[25]. The Earth is the third in distance from the Sun in the Solar System and the fifth largest in diameter. The mean distance of the Earth from the Sun is 1.5×10^8 km, and radius varies from 6378 km in the equator to 6356 km in polar direction. Earth is one of the planets that have a strong internal magnetic field. In the absence of any external drivers, the geomagnetic field can be approximated by a dipole field with an axis tilted about 11° from the spin axis. The solar wind reaches the Earth at about 400 km/s. Due to the supersonic nature of the solar wind, shock waves are formed in front of the planets. The bow shock deflects the supersonic solar wind and shelters the surface of the planet from the high energy particles of the solar wind, creating a cavity called the magnetosphere as shown in Figure 1.5. Some of the solar wind energy finds its way into the Earth's magnetosphere, ionosphere and atmosphere, and creates geomagnetic activity and drives the magnetospheric convection system. Earth's magnetosphere is determined by the Earth's magnetic field, solar wind, and interplanetary magnetic field (IMF). The volume of the Earth's magnetosphere is difficult to define and highly variable, but is usually on the order of several tens of thousands of Earth volumes[28]. The outer boundary of the magnetosphere is called the magnetopause which is a direct consequence of solar wind interaction with magnetized planets. Solar wind and the magnetic field it carries along modify the form of the magnetosphere, by pushing it in in the dayside and creating a long magnetotail in the nightside. On the northern

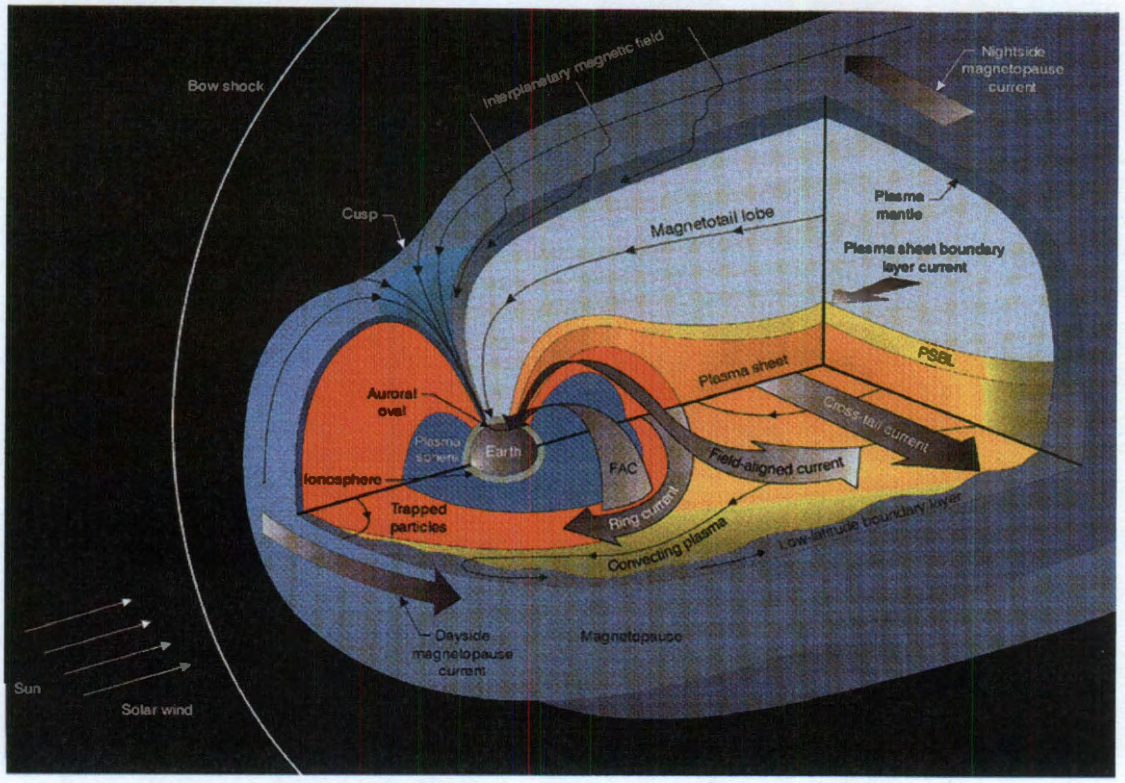

Figure 1.5 : Earth's magnetosphere and current system. Figure courtesy of NASA.

and southern boundaries, it falls on open magnetic field lines and is called as plasma mantle. On the western and eastern boundaries, it falls on closed field lines and is called as low latitude boundary layer (LLBL). The region between the bow shock and the magnetopause is the magnetosheath. In the center of the magnetosphere, the region of closed field lines in the equatorial magnetotail is called plasma sheet, which is divided into central plasma sheet and plasma sheet boundary layer (PSBL), the latter being at higher latitudes adjacent to the tail lobes which is a region devoid of plasma. At low-altitude limit, magnetosphere ends at the ionosphere. The magnetosphere is filled with plasma that originates both from the ionosphere and the

solar wind. However, the relative importance of these two sources is unclear. The plasmasphere can provide part of the plasma in plasma sheet. Although it originates from ionosphere, the transport mechanism is quite different than in direct ionospheric outflow.

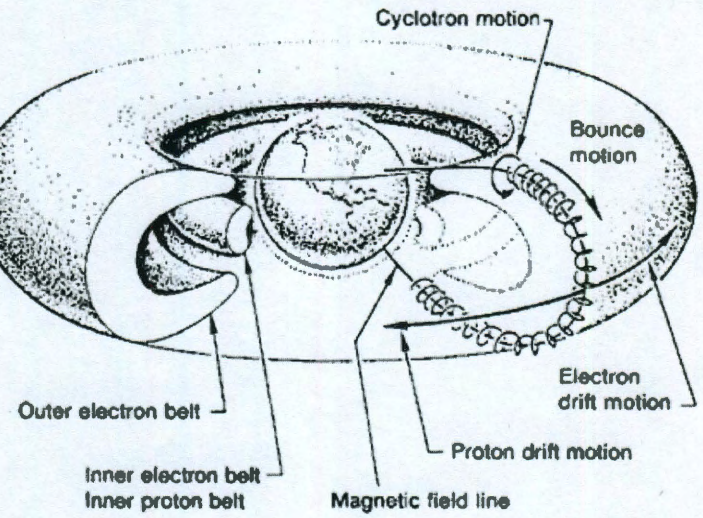

Figure 1.6 : Plasma motion and Van Allen radiation belts. The radiation of the Van Allen belt is composed of protons and electrons temporarily trapped in the Earth's magnetic field. The intensity of radiation varies with the distance from the Earth. Spacecraft and their occupants orbiting within this belt os passing through it must be protected against this radiation[2].

The trapping regions of high-energy charged particles surrounding the Earth are called radiation (or Van Allen) belts[29, 30]. The radiation belts are of importance primarily because of the harmful effects of high energy particle radiation for man and electronics. Figure 1.6 shows the structure of radiation belts. The inner one located between about 1.1 to 3.3 R_E in the equatorial plane, contains primarily protons with energies exceeding 10 MeV. This is a fairly stable population but it is subject to occasional perturbations due to geomagnetic storms, and it varies with 11-year solar

cycle. The outer belt contains mainly electrons with energies up to 10 MeV. It is produced by injection and energization events following geomagnetic storms, which makes it much more dynamic than the inner belt. It has an equatorial distance of about 3 to 9 R_E, with maximum for electrons above 1 MeV occurring at about 4 R_E. Recently a new belt has been found within the inner belt. It contains heavy nuclei, mainly oxygen, with energies below 50 MeV.

In the first order approximation, magnetopause is formed at a distance where the solar wind dynamic pressure equals the magnetic pressure of Earth's field. At this location, typically around 8 to 11 R_E away on the Earth-Sun line, a large scale duskward current, also called as Chapman-Ferraro current, develops in the dayside magnetopause to cancel the Earth's field outside. The thickness of the current layer is typically from several hundred to a thousand kilometers, which corresponds to several ion gyroradii[31]. Similar current flows around the magnetotail, with reverse direction in order to cancel the field outside. This current is closed via the cross-tail current which flows across the tail from the dawn magnetopause to the dusk magnetopause. The current is carried by plasma sheet particles. It is also called "neutral sheet current" because the magnetic field in its center is much weaker than the magnetic field outside it. Near the Earth, the positive charged ions and negative charged electrons have different motion and create a westward ring current around the Earth at a radial distance between 2 and 7 R_E, overlapping the radiation belt region. It creates a southward magnetic field perturbation which is usually measured by Dst index as the perturbation of horizontal magnetic field strength. The ring current consists of geomagnetically trapped ions (mainly H^+, He^+, and O^+) with energy from 10 to 200 keV and electrons that drift azimuthally around the Earth. The term "partial ring current" is used to describe inner- and middle-magnetospheric currents

that neither flow in closed loops near the equatorial plane nor flow into or out of the magnetopause. They connect two sets of field-aligned currents (FACs), or Birkeland currents, that flow up from or down to the conducting ionosphere. The poleward set is called region-1 FAC, which flow into the ionosphere in the dawn side and out of the ionosphere in the dusk side. They connect far out in the magnetosphere to the boundary layers or distant plasma sheet. They drive the convection electric field and currents in the high-latitude ionosphere. The equatorward set is called region-2 FAC, which flow into the ionosphere in the dusk side and out of the ionosphere in the dawn side. They shield the low-latitude ionosphere from convection electric fields.

Plasma sheet is a very important region for auroral physics, since the nighttime auroral oval maps to it. The diffuse aurora originates from a region closer to Earth than the discrete aurora. Plasma sheet particles are hot, having energies in the keV range. Plasma density is a slowly varying function of time and also solar wind density, with average value being about 0.4 to 2 cm^{-3}. This and the fact that H^+ dominates during low geomagnetic activity indicates that solar wind is providing most of the plasma. Ion temperature is about 7 times the electron temperature[32].

Because of the magnetospheric, large scale convection electric field, plasma is moving continuously both toward Earth and toward the central cross-tail current region from tail lobes. At the inner plasma sheet boundary electrons and ions are on different convection paths. The paths of electrons turns dawnward and the paths of ions turns duskward[33]. The plasma sheet is then separated into electron plasma sheet and ion plasma sheet near the Earth. The electron plasma sheet does not always quite reach the geosynchronous orbit[33].

The lowest part of the Earth's atmosphere, the troposphere extends to about 10 km. Above 10 km is the stratosphere, followed by the mesosphere. In the stratosphere

incoming solar radiation creates the ozone layer. At heights of above 80 km in the thermosphere, the number of free electrons is sufficient to affect radio propagation. This partly ionized portion of the atmosphere is referred to the ionosphere. This region, ranging from 70 to 1500 km, is coupled to both the magnetosphere and the neutral atmosphere. Ionization appears at a number of atmospheric levels, producing layers or regions which may be identified by their interaction with radio waves. These layers are known as the D, E, and F layers. The E layer is used by radio operators as a surface from which signals can be reflected to distant stations. The F layer also reflects radio waves. However, the D layer principally absorbs radio waves due to the high ion-neutral collision frequencies. The electron density of different layers in the ionosphere is quite different and shown in Figure 1.7.

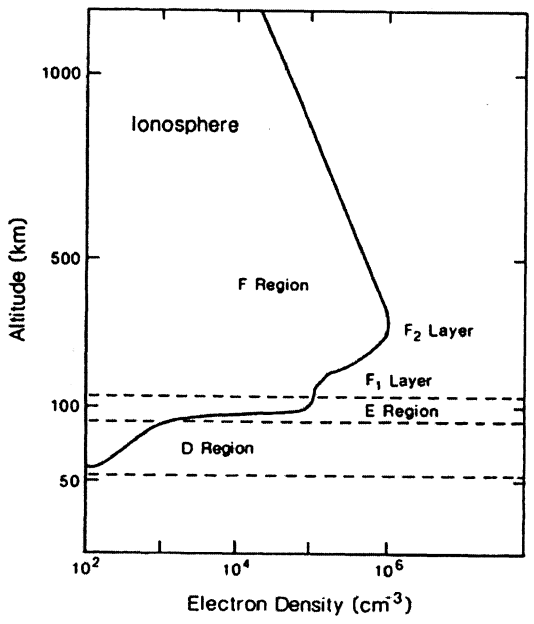

Figure 1.7 : Electron density of the Earth's ionosphere[3].

The ionosphere and magnetosphere are connected through the magnetic field lines

and FACs. The regions where field-aligned currents flow down into the ionosphere charge up positively, whereas the regions where field-aligned currents flow up from the ionosphere charge up negatively, creating the ionospheric electric field pattern. As the downward and upward parts of the current systems are typically separated, horizontal current systems must be formed within the conducting ionosphere. The auroral electrojet relates to the formation of substorm current wedge. Ionospheric currents close the current loops together with partial ring currents and field-aligned currents. The ionospheric currents flow in response to the electric field, consisting of a Pedersen current which flows parallel to the electric field, and a Hall current that flows in the direction of $-\mathbf{E} \times \mathbf{B}$.

The plasma convection pattern leads to ionospheric Hall currents, and along the auroral oval so-called convection electrojets are formed at about 100 km altitude, eastward electrojet on the duskside and westward on the dawnside. The Harang discontinuity is one of the ionospheric features related to the plasma convection pattern. The Harang discontinuity is a region of sharp reversal in the evening sector (around 2200-2400 MLT) of ionospheric convection electric field from the poleward field on the equatorward side of the auroral oval to an equatorward field on the poleward side of the oval. The Harang discontinuity corresponds to the shear zone where the eastward electrojet, equatorward of the shear, the westward electrojet, poleward of the shear, meet together. The Harang discontinuity locates in the nightside region 1 current system[34], which may be a result of a dawn-dusk pressure gradient in the central plasma sheet[35]. The longitudinal position of the Harang discontinuity is controlled by IMF B_Y component: increasing positive (negative) values displace it towards earlier (later) local times within the evening sector[36].

The plasma in the inner magnetosphere co-rotates with the Earth. As a conse-

quence, the ionospheric plasma at mid-latitudes can expand upward along the magnetic field lines and fill them until the plasma gas pressure is equalized along the entire field line. The plasma region above the ionosphere on such closed magnetic field lines is called the plasmasphere. In fact, the plasmasphere can be considered as an extension of the ionosphere since they both have very dense but cold plasma and there is no clear distinction between them. The outer boundary of the plasmasphere is called the plasmapause. The plasmasphere is normally earthward of the plasma sheet and overlaps with the ring current.

1.3 Magnetospheric Dynamics

1.3.1 Plasma Motion

The charged particle motion in an electric and magnetic field is controlled by the Lorentz force:

$$\mathbf{F} = q(\mathbf{E} + \mathbf{v} \times \mathbf{B}) \tag{1.1}$$

The magnetic force is perpendicular to $\mathbf{v}$, and leads to a circular motion in the plane perpendicular to the magnetic field. The instantaneous center of the circular motion is referred to as the center of gyration. So the motion is called gyro motion, and the radius

$$r = \frac{mv_\perp}{|q|B} \tag{1.2}$$

is called the gyro radius, cyclotron radius or Larmor radius. Correspondingly, the cyclotron frequency or the gyro frequency is defined as

$$\Omega = \frac{|q|B}{m} \tag{1.3}$$

The distribution of perpendicular kinetic energy and parallel kinetic energy would change along the magnetic field lines due to the change of magnetic field strength.

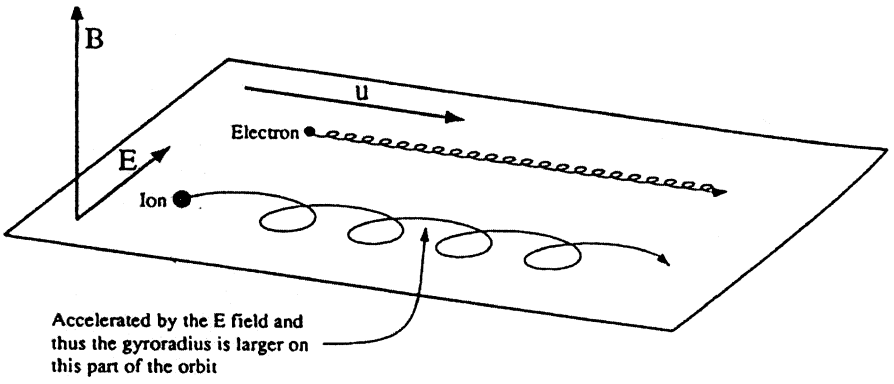

Figure 1.8 : Schematic showing the motions of ions and electrons in a uniform magnetic field $\mathbf{B}$ in the presence of an electric field $\mathbf{E} \perp \mathbf{B}$[4].

The parallel motion of the particle could change its direction where all kinetic energy is normal to the field line where the magnetic field strength reaches a local maximum. This kind of motion is called bounce motion. The response of the charged particles to the perpendicular component of electric field is quite different than the acceleration or deceleration by the parallel component. Figure 1.8 shows how positively and negatively charged particles move in a uniform magnetic field if an electric field is perpendicular to the magnetic field. Although both particles gyrate in a circle, the direction of motion around the circle depends on the sign of the particle's charge. The gyro radius would vary with the particle's mass so that an ion has larger gyro radius than an electron. The electric force accelerates the particle during part of each orbit and decelerates it during the remaining part of the orbit which give a distorted circle. So the particle moves in a circle, in a reference frame moving with velocity

$$\mathbf{v}_E = \frac{\mathbf{E} \times \mathbf{B}}{B^2} \tag{1.4}$$

The $\mathbf{E} \times \mathbf{B}$ drift is the most important drift motion. It does not depend on the magnitude and sign of their charges. Particles at certain location all drift at the same velocity.

In a uniform magnetic field, the magnetic force would always point toward the particle's guiding center. In a nonuniform magnetic field, the particle could experience different forces at every position along its helical path[37]. In the case of a magnetic field with a gradient perpendicular to the field, the particle's guiding center will undergo a perpendicular drift, since the gyroradius is shorter in the region of stronger magnetic field. The rate of this drift due to the perpendicular gradient is

$$\mathbf{v}_G = \frac{K_\perp \mathbf{B} \times \nabla B}{qB^3} \tag{1.5}$$

where $K_\perp$ is the kinetic energy of the particle due to its velocity perpendicular to the magnetic field. When such a perpendicular gradient exists in a dipole field, particles will drift in circular orbits about the dipole.

If the magnetic field has a gradient parallel to the field, the particle guiding center will experience acceleration along the direction of the magnetic field. The force on the particle has a component that is parallel to the magnetic field vector that exists at the location of the guiding center. The particle's guiding center will bounce back and forth along the magnetic field which called the bounce motion. Particle kinetic energy is conserved in this process, with energy transferred between the velocity components parallel and perpendicular to the magnetic field.

However, as particles bounce back and forth, they must have an additional force applied to them that constrains their motion to follow the curved field lines. This force gives rise to a drift perpendicular to both the curvature force and the magnetic

field.

$$\mathbf{v}_C = \frac{2K_{\|}\mathbf{B} \times \kappa}{qB^2} \tag{1.6}$$

where

$$\kappa = \frac{(\mathbf{B} \cdot \nabla)\mathbf{B}}{B^2} \tag{1.7}$$

is the curvature vector for the magnetic field and $K_{\|}$ is the parallel kinetic energy.

Since the gradient drift depends on perpendicular kinetic energy and the curvature drift depends on parallel kinetic energy, they are often written together after bounce-average as

$$\mathbf{v}_{GC} = \frac{\mathbf{B} \times \nabla K}{qB^2} \tag{1.8}$$

By playing with Eular potentials, the quantity $\lambda = KV^{2/3}$ is proved to be conserved as the flux tube filled with an isotropic distribution of particles drifts along. λ is usually called energy invariant.

The particle in the Earth's magnetosphere undergoes three kind of motions as shown in Figure 1.9: the gyro motion around the magnetic field line, the bounce motion along the magnetic field line between the north and the south hemisphere, and the drift motion with the guiding center perpendicular to the magnetic field lines.

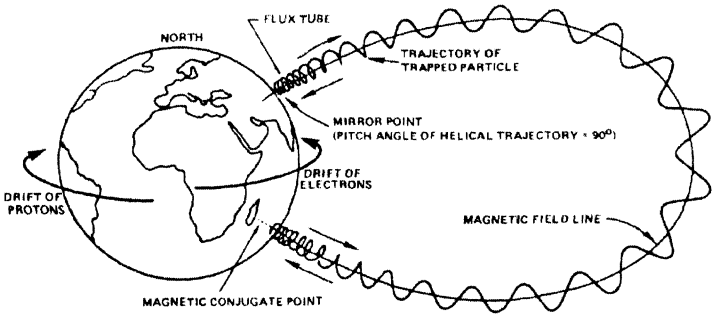

Figure 1.9 : The three specific motion of particles in the Earth's magnetosphere[5].

A remarkable feature of the motion of the charged particles in collisionless plasma is that even though the energy changes, there is a quantity that will remain constant if the field changes slowly enough[4]. It requires that the field changes encountered by the particle within a single gyration orbit are small compared with the initial field[4]. Therefore, adiabatic behavior occurs when electromagnetic field varies on a length scale that is long compared to the gyro radius and a timescale long compared to a cyclotron period. So the temporal or spatial changes in the electromagnetic field from one cyclical orbit to the next are sufficiently gradual to be effectively continuous and differentiable[27]. Fist adiabatic invariant is the magnetic moment

$$\mu = \frac{p_\perp^2}{2mB} \tag{1.9}$$

where $p_\perp$ is the perpendicular momentum so that $\mu = K_\perp/B$ remains constant for gyro motion. The second invariant is defined as

$$J = \oint m u_\parallel ds \tag{1.10}$$

where the velocity $u_\parallel$ and the path element ds now refer to the longitudinal motion of the guiding center. It's an adiabatic invariant corresponding to the bounce motion. When the guiding center is situated off the axis of a rotationally symmetric mirror field, the radial gradient of the magnetic field causes a drift around this axis in addition to the oscillatory motion along the lines of force. In the absence of electric fields and other disturbances the guiding center traces out a rotational surface, the longitudinal invariant surface. The magnetic flux enclosed by this surface is the third adiabatic invariant[38].

The magnetohydrodynamics (MHD) equations are a relatively straightforward means of simulating large-scale plasma physics, and are frequently used to model the global magnetosphere. The plasma is supposed to be strongly collisional so that the

time scale of collisions is shorter than the other characteristic times in the system, and the particle distributions are thus close to Maxwellian. MHD usually treats the plasma as a single fluid, even though particles of different energies exhibit different motions. The simplest form of MHD, ideal MHD, assumes that the fluid has so little resistivity that it can be treated as a perfect conductor. In particular, the typical magnetic diffusion times over any scale length presented in the system must be longer than any time scale of interest. We are interested in length scales much longer than the ion skin depth and Larmor radius perpendicular to the field, as well as the length scald of Landau damping which describes the energy loss of longitudinal waves due to wave-particle interaction, and time scales much longer than the ion gyration time. Lenz's law dictates that the fluid is in a sense tied to the magnetic field lines. This difficulty in reconnecting magnetic field lines makes it possible to store energy by moving the fluid or the source of the magnetic field. The energy can then become available if the conditions for ideal MHD break down, allowing magnetic reconnection that releases the stored energy from the magnetic field.

Plasma theory gives equations of ideal MHD as

$$\begin{aligned}
\frac{\partial \rho}{\partial t} + \nabla \cdot (\rho \mathbf{v}) &= 0 \\
\rho \frac{d\mathbf{v}}{dt} &= \mathbf{J} \times \mathbf{B} - \nabla p \\
\frac{d}{dt}\left(\frac{p}{\rho^{\gamma}}\right) &= 0 \\
\mathbf{E} + \mathbf{v} \times \mathbf{B} &= 0 \\
\nabla \times \mathbf{E} &= -\frac{\partial \mathbf{B}}{\partial t} \\
\nabla \times \mathbf{B} &= \mu_0 \mathbf{J} \\
\nabla \cdot \mathbf{B} &= 0
\end{aligned} \tag{1.11}$$

Here the first three equations are continuity equation, momentum equation, and

energy equation in magnetohydrodynamics. The fourth equation is the assumption of perfect conduction. The latter three equations come from Maxwell equation set. The displacement current in the Ampère law is neglected.

There are many other MHD formula. Resistive MHD describes magnetized fluids with finite electron diffusivity which leads to a breaking in the magnetic topology. Extended MHD describes a class of phenomena in plasmas that are higher order than resistive MHD, but which can adequately be treated with a single fluid description, including the effects of Hall physics, electron pressure gradients, finite Larmor Radii in the particle gyro motion, and electron inertia. Two-fluid MHD describes plasmas that include a non-negligible Hall electric field so that the electron and ion momenta must be treated separately. Hall MHD takes the Hall term in the Ohm's law into account so that in the absence of field line breaking, the magnetic field is tied to the electrons and not to the bulk fluid. Collisionless MHD is used for collisionless plasmas and derived from the Vlasov equation.

The magnetospheric interchange instability is a particular type of Rayleigh-Taylor instability in a MHD fluid in magnetosphere. The Rayleigh-Taylor instability occurs whenever an adiabatic interchange of fluid parcels results in a reduction of stored energy[39].

1.3.2 Solar-Terrestrial Interaction

The solar wind is the ultimate power source for virtually all dynamic processes in Earth's magnetosphere. The important types of large-scale magnetospheric plasma motion are: gradient/curvature drift, which is dominant for the trapped radiation belts; co-rotation with the Earth, which dominates in the plasmasphere; sunward convection, which is dominant in the inner plasma sheet; turbulent motion, which is

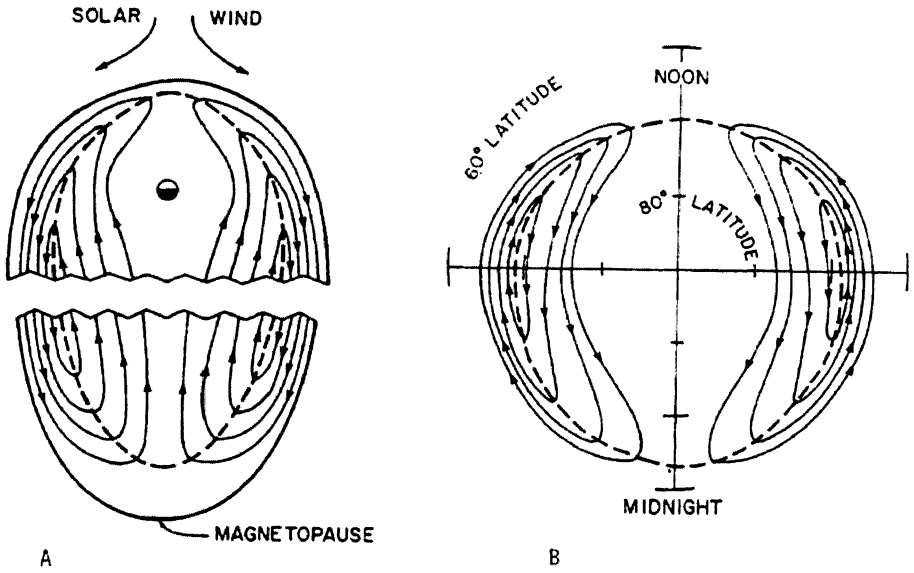

Figure 1.10 : Streamlines of the Axford-Hines convection patter, (a) in the magnetospheric equatorial plane, and (b) on the polar-cap ionosphere[6].

a major effect throughout the plasma sheet[40]. The essential role of the IMF was stressed by Axford (1962)[41]. The solar-wind magnetosphere coupling produces "convection" in the magnetosphere and in the magnetically-connect ionosphere. Plasma in the outermost layers of the magnetosphere, and in the magnetically-connected high-latitude ionosphere flows away from the sun as if propelled by frictional contact with the adjacent post-shock solar wind. Plasma in the inner magnetosphere, and the magnetically connected lower-latitude ionosphere flows sunward to complete the circulation pattern[6]. This magnetospheric convection system is the essence of the solar-wind magnetosphere interaction. The dynamical coupling between the solar wind and the magnetosphere is described in general terms within the context of two antipodal coupling models[6]. One is the Axford-Hines model[42], as shown in Figure 1.10. Solar-wind momentum is transmitted to the magnetosphere in a vis-

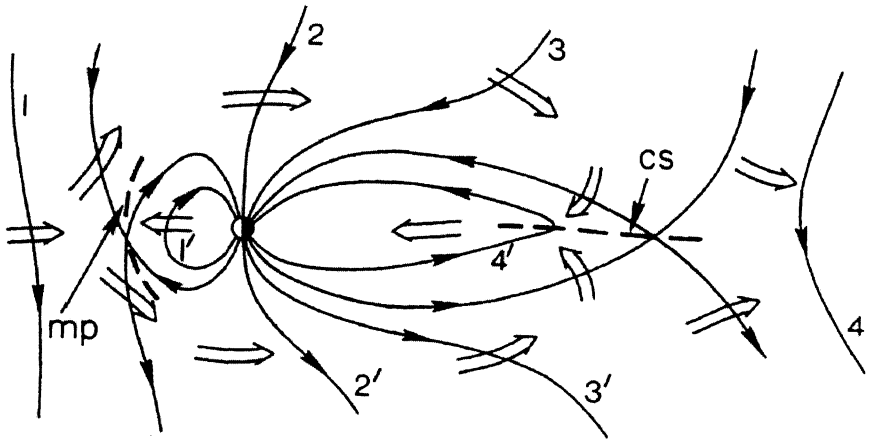

Figure 1.11 : The Dungey magnetosphere model in noon-midnight meridian plane during southward IMF[6].

cous boundary layer just inside the magnetopause, producing the required antisunward high latitude flow and the implied low latitude return flow. The corresponding "convection electric field" has a dawn-to-dusk orientation in the "polar cap". The Axford-Hines model provides a coherent phenomenological description of the basic solar-wind magnetosphere coupling but it can't explain the correlation between the coupling efficiency and the IMF direction[43] and what a mechanism could produce sufficient effective viscosity. Dungey (1961) proposed that the required momentum transfer could be attributed to magnetic rather than viscous coupling if high-latitude geomagnetic field lines are allowed to extend into interplanetary space[44], i.e. "interconnect" with IMF, as shown in Figure 1.11. A portion of the magnetic field of the Earth is connected to the IMF, forming "open" field lines that have one end connected to the solar wind and the other end to the high latitude ionosphere of the Earth, the polar cap[45]. The magnetic tension transfers solar-wind momentum to the magnetosphere and ionosphere. There is very little energy transfer occurring

during times of northward IMF.

Because the solar wind is essentially a perfectly conducting plasma, it drags the solar magnetic field along with it as it expands from the Sun. The magnetic flux is "frozen in" to the plasma as described by

$$\mathbf{E} + \mathbf{v} \times \mathbf{B} = 0 \tag{1.12}$$

The frozen-in-flux theorem is violated in the open model at two places: once at the dayside magnetopause where interplanetary and geomagnetic flux tubes become interconnected, and in the magnetotail current sheet where they become disconnected[6]. The process within a thin current sheet is called "magnetic reconnection". Reconnection is thought to be the main process that transports mass, momentum, and energy from the solar wind into the magnetosphere, and it drives the large scale magnetospheric convection. Magnetic reconnection is a non-ideal instability where the plasma is effectively ideal everywhere except at a very thin boundary layer where the ideal MHD frozen-in assumption fails so magnetic fields can leak across the plasma and change their topology. The merging process requires an electric-field component tangent to the current in the boundary[46]. This electric field allows a transfer of energy and momentum orders-of-magnitude larger than that provided by collisional viscosity.

The Dungey model is usually called the "open model" because it requires the existence of open, interconnected, field lines. The Axford-Hines model is called the "closed model" because it does not. The IMF-dependence of the flow pattern provides a strong indication that magnetic coupling is an important factor in powering magnetospheric convection.

Wave-particle interaction and Kelvin-Helmholtz wave instability also have been suggested to inject solar-wind plasma into the magnetosphere[6]. In the case of the

Kelvin-Helmholtz instability, the coupling still depends somewhat on the relative orientations of the internal and external fields, but the results are symmetric with regard to the fields' being parallel or antiparallel[47]. It is uncertain whether such a mechanism could provide sufficient energy to drive convection within the magnetosphere.

Apart from magnetic merging, there are two mechanisms that violate the frozen-in-flux theorem and can thereby transport magnetosheath particles onto closed geomagnetic field lines: classical magnetic (gradient and curvature) drift, and anomalous (non-collisional) cross-field diffusion[6]. But their effects on the global scale are expected to be small[48].

1.3.3 Magnetosphere and Ionosphere Coupling

Both the Dungey model and the Axford-Hines model require a magnetic transfer of antisunward momentum from the outer magnetosphere to the ionosphere by an electric current circuit[6]. The Birkeland current system is determined by the flow pattern imposed on the ionosphere and by the distribution of ionospheric conductivity. On the dawn and dusk sides of the ionosphere, the two rings of Birkeland currents feed the ionospheric Pedersen currents, which flow equatorward on the dawn side, poleward on the dusk side. Near local noon and local midnight, a major part of the Birkeland currents compensate for the divergence of the eastward and westward electrojets, which are Hall currents following antiparallel to the $\mathbf{E} \times \mathbf{B}$ drift.

Ionosphere and magnetosphere are closely linked together via magnetic field lines. Magnetospheric electric fields map down to the ionosphere, creating plasma convection, frictional heating and plasma instabilities. Auroral particle precipitation ionizes the high latitude atmosphere during nighttime, and heat can be conducted from the magnetosphere down to the ionosphere. In addition, some of the atmospheric con-

stituents are excited to higher energy levels: this can lead to emission of auroral light. Most of this activity occurs within auroral oval. The regions that are left inside the ovals are called the polar caps. Collisions between the convecting ionospheric plasma and the neutral atmosphere lead to generation of neutral winds and Joule heating of the neutral gas. Neutral gas can be further heated by plasma instabilities that arise due to the ionospheric currents. On the other hand, some of the cold ionospheric electrons and ions evaporate into the plasmasphere, plasma sheet and tail lobes. The changed magnetospheric ion composition, especially increased O^+, can have large effects on some important magnetospheric processes.

The auroral precipitation is concentrated in an auroral band that is typically about 5 degrees in latitudinal width. While the nightside auroras reflect the dynamics of the magnetotail, dayside precipitation relates more directly to solar wind parameters. Primary auroral particles have energies between few tens eV and few hundred keV, being higher on the nightside than on dayside. Some of them are accelerated in the field-aligned direction, indicating the presence of a special auroral acceleration region.

The auroras are often classified into discrete and diffuse precipitation. Diffuse aurora are found on the equatorward part of auroral oval, in the region of the so-called central plasma sheet (CPS) precipitation most likely mapping to inner plasma sheet, where magnetic field is almost dipolar. The Auroral Boundary Index, ABI, is the latitude of the equatorward edge of the diffuse aurora at midnight. It is routinely determined with about 30 min resolution from Defense Meteorological Satellite Program (DMSP) electron precipitating data. This boundary maps to the inner edge of the plasma sheet so that it moves to lower latitudes with increasing magnetic activity. The precipitating particles are drifting around Earth, electrons to the east and protons to the west. The strongest diffuse auroras are found on the post-midnight

sector produced mainly by electrons. Proton precipitation is important especially in the pre-midnight sector. Discrete auroras are the most intense auroral types where field-aligned acceleration play an important role, forming the so-called inverted-V precipitation in the precipitating spectrum of logarithm scale. Discrete auroral types include: quiet auroral arcs; spirals, curls, and folds; auroral bulge; omega bands. All these are nighttime, auroral oval, arc related phenomena. They are more pronounced pre-midnight than post-midnight, and reflect the dynamics of the Earth's magneto-tail. They are located on the poleward part of the auroral oval, in the region of the so-called boundary plasma sheet (BPS) precipitation mapping to plasma sheet and its boundary layer (PSBL).

The diameter of the ovals depends on the amount of the open flux in the polar cap: during active periods, especially during major geomagnetic storms, the ovals expand to lower latitudes. The size of the polar caps can be regarded as an indication of the amount of open magnetic flux in the magnetosphere. The polar cap potential drop is a convenient measure of the total rate of magnetospheric convection. It is defined as $\int \mathbf{E} \cdot dl$. It could be measured by a spacecraft (i.e. DMSP) moving across the polar cap above the ionosphere. The cross polar cap potential drop is one of the parameters that are strongly affected by the direction of IMF[49]. This potential drop exceeds 100 kV for active times with strongly southward IMF, but is less than 40 kV for quiet times with strongly northward IMF. Polar-cap plasma flow is normally predominantly antisunward, which corresponds to the classical picture of magnetospheric convection. However, in periods of sustained, strongly northward IMF, plasma is frequently observed to flow sunward in a region near the center of the polar cap.

1.3.4 Geomagnetic Storm and Substorm

The Earth is hit by a hot, magnetized, supersonic collisionless plasma carrying a large amount of kinetic and electrical energy. Some of this energy finds its way into our magnetosphere creating geomagnetic activity which consists of geomagnetic storms, substorms, and aurora. The solar wind electric field, determined by the solar wind velocity and the IMF north-south component, and the turbulence amplitude are the most important trigger of the geomagnetic activities, as shown in Figure 1.12. The geomagnetic storm happens with strong solar wind driver and turbulence, while the substorm activity is more complicated because of the temporal storing of energy in the magnetotail. It is not necessary to have a storm in order to have a substorm. Some auroras, extending to low latitudes, are storm-time features and some others, the most active ones, relate to substorms, the oval does not disappear even during the more quiet magnetospheric periods.

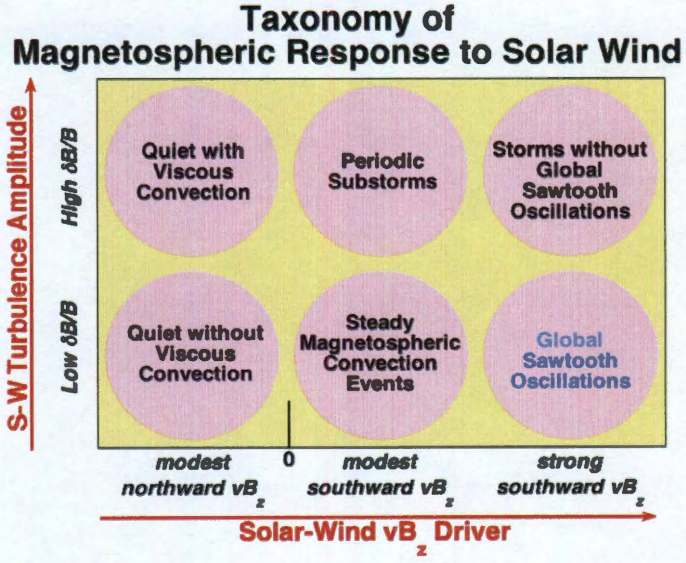

Figure 1.12 : Taxonomy of magnetospheric response to solar wind. Figure courtesy of J. Borovsky (LANL).

Storms, the main contributors to space weather, are initiated when enhanced energy transfer from the solar wind and IMF into the magnetosphere leads into intensification of ring current. The ring current development can be monitored with the Dst index. The horizontal intensity of the magnetic field is observed to decrease and subsequently recover during geomagnetic storms[50]. During a storm, auroral ovals become greatly disturbed, broadening and expanding equatorward, particularly on the nightside. This brings the aurora to the skies of middle and low latitudes. The largest storms are often related to coronal mass ejections from the Sun. In these cases, the related enhancements of solar wind velocity accompanied by southward IMF direction result into Sudden Storm Commencements (SSC). These storms are typically nonrecurrent or transient. Moderate storms are often recurrent, which refers to disturbances that repeat with the 27-day rotation period of the Sun. CME-driven storms refers to storms driven by all or some of the various components: shock, CME sheath, ejecta, and magnetic cloud. Recurrent sources are usually attributed to high speed solar wind streams emanating from coronal holes. However, compression at the leading edge of the stream as it runs into the higher-density slow flow surrounding the heliospheric current sheet leads to a co-rotating interaction region (CIR)[51]. Either the CIR or the high-speed stream or both can be drivers of storms[52].

Storms are typically divided into three distinct phases according to the signatures in ring current or Dst index: initial phase which lasting from minutes to hours with increasing Dst up to a few or tens of nT and compressed dayside magnetopause; main phase which lasting from half an hour to several hours with a minimum Dst of negative tens or hundreds of nT and building of strong ring current; recovery phase which lasting from tens of hours to a week with gradually return of Dst to the normal level and lost of ring current ions. The events with minimum Dst less than -60 nT

are referred as storm. A storm where Dst drops to a few negative hundreds nT is usually called a major storm. The main feature of a storm is shown in Figure 1.13.

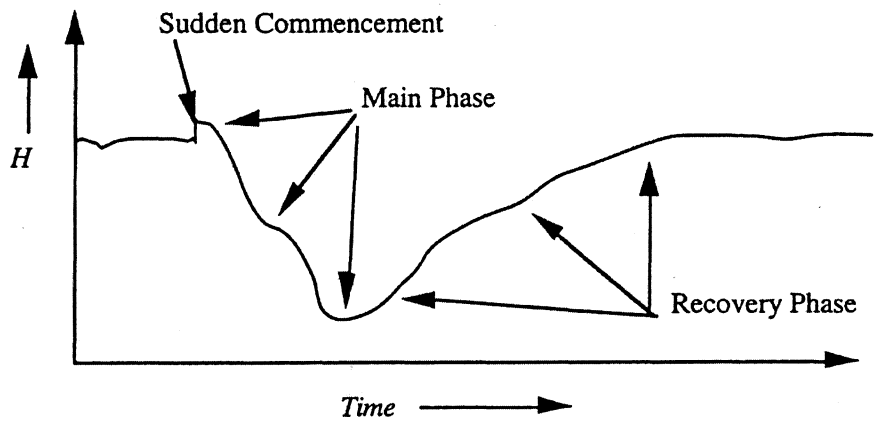

Figure 1.13 : Low-latitude ground magnetogram for an idealized magnetic storm. The total strength of the horizontal (H) component is shown[7].

The initial phase begins with a sudden increase in Dst that can be attributed to a rapid compression of the magnetosphere that strengthens that northward magnetic field near the equator[28]. This so-called sudden storm commencement (SSC) is understood to be caused by the increased solar wind ram pressure.

The essential characteristic of a magnetic storm is a large negative deviation in the Dst index indicating the injection of plasma particles in to the ring current. It needs a period of sustained strong southward IMF. The strong convection in the magnetosphere is usually accompanied by repeated substorms. Particles are transported form the magnetotail region into the nightside inner magnetosphere where they can azimuthally drift in the strong magnetic field and form a westward current. The ring current is initially asymmetric which has more currents on the nightside than on the dayside. This asymmetric ring current is often referred to as a partial ring

current. The mechanism responsible for ring current injections is one of the fundamental problems in the study of magnetospheric dynamics. The electric fields could be characterized by potential electric fields due to convection, large-scale induction electric fields due to substorm dipolarization, and small-scale wave-generated electric fields. The convection potential can reach well over 100 kV. But it is plausible that the convection potential could energize plasma sheet ions from approximately 10 keV to 200 keV. The substorm dipolarizations lead to an induced westwards electric field that supplements the convection electric field. However, substorm-induced electric fields are able to inject particles into the geosynchronous orbit range. They cannot inject particles deep enough to account for the storm-time ring current. The ring current is not enhanced during the substorm expansion phase. Storm-time ring current is built up be repeated substorm-injection of particles from the hot plasma sheet.

The recovery phase of a storm occurs when the solar wind driving conditions return to quiet levels, and plasma injection into the inner magnetosphere ceases. The convection electric field is reduced, and azimuthal drift therefore becomes the dominant drift mechanism for particles in the inner magnetosphere. The ring current becomes symmetric as plasma from the nightside ring current is able to drift in closed orbits. While magnetospheric loss process slowly reduce the ion density over a period of days or more. The primary process responsible for ring current decay is believed to be charge exchange loss[53]. Charge exchange processes between energetic ions and cold neutral atoms in the exosphere produce energetic neutral atoms and cold ions. Since cold ions drift too slowly to carry a significant current, charge exchange effectively removes ions from the ring current.

Substorms represent an inherently non-steady process in the magnetosphere. They are less intense, shorter-lived, and more frequent phenomena[54]. They are triggered

by a reconfiguration of the tail magnetic field. They are also divided into three phases: growth phase, expansion phase, and recovery phase. At the onset of a substorm, a stable, east-west oriented, southward moving auroral arc "explodes" and forms the so-called auroral bulge. In addition to these optical signatures, auroral substorms can be seen in the ground-based magnetometer recordings due to created ionospheric currents. The substorm process has its origin in the Earth's magnetosphere and is often referred as magnetospheric substorm. Some substorms that never "breakup" into full strength are called pseudobreakups. They can occur as substorm precursors, isolated events during quiet times, or isolated events during Steady Magnetospheric Convection (SMC) times. Pseudobreakups have most of the signatures found in real substorms, like injections, dipolarization, current disruption, thin current sheet, ground-based magnetic disturbances up to several hundred nT, weak Pi2 pulsations, quasi-neutral current sheet, reconnection. However, only substorms are associated with a significant poleward expansion of auroras and currents in the ionosphere. On the other hand, the strongest substorms tend to occur during longer periods of enhanced activity, i.e., magnetic storms. This corresponds to the case with a southward IMF lasting for several hours. If the IMF is northward except for a brief period, then it is an isolated substorm.

The growth phase starts the substorm process and lasts about 1 hour. It starts with southward turning of the IMF, which enhances the convection electric field as the solar wind energy transferred to the magnetosphere via reconnection between interplanetary and magnetospheric field lines. The tail lobe field strength increases implying the compression of the near-Earth plasma sheet. The cross-tail current increases, leading to a tailward stretching of field lines in the near-Earth tail. The current sheet becomes very thin just tailward of the dipole-like field lines. Concen-

tration of O^+ increases in the magnetosphere, most likely due to nightside auroral activity related to the upcoming substorm. Electrojets strengthen slightly.

The substorm growth phase is followed by the substorm onset, which starts the substorm expansion phase. It starts the active part of the substorm process and lasts typically around 30 minutes, varying from 10 minutes to 2 hours. The substorm onset together with the breakup of auroral is usually triggered externally by changes in the IMF and solar wind characteristics. It is related to the unloading of energy stored during the growth phase. In the magnetosphere, earthward high speed plasma flows are observed within the near-Earth plasma sheet, and plasmoids are detected in the far tail. During a magnetospheric substorm the cross-tail current is disrupted. A current system called the substorm current wedge (SCW) is formed as this current is diverted through a circuit consisting of earthward (downward) field-aligned currents (FACs) on the eastern side of the wedge, a westward auroral electrojet in the ionosphere, and tailward (upward) FACs on the western side of the wedge. The current disruption leading to SCW formation is acting on current sheet that has been enhanced and propagated closer to Earth during the proceeding substorm growth phase. The magnetic field returns to a more dipolar configuration within the wedge. Particles are injected and accelerated close to the geosynchronous orbit. Near the local midnight, enhanced fluxes of particles with a wide range of energies arrive suddenly and almost simultaneously. Aurora suddenly brightens and expand in the nightside, starting from the southernmost arc near the poleward edge of the diffuse aurora. An auroral bulge with a westward travelling surge (WTS) on the poleward boundary of the auroral zone near local midnight forms. Expansion phase continues until the aurora has reached its most poleward location corresponding to the SCW propagation tailward and usually a northward turning of IMF.

The recovery phase lasts about 1 hour, with plasma sheet recovering and magnetosphere returning into the pre-substorm state or preparing for the next substorm. Subauroral electric field events occur and double oval structure forms. If the IMF remains southward, then no clear recovery phase exists. Particle injection ceases with fluxes gradually diminishing due to precipitation and charge exchange.

During increased geomagnetic activity, O^+ ion dominates in the inner magnetosphere. This is evident both in storms time ring current and substorm time plasma sheet. Since these ions come from the ionosphere, ionosphere may be able to control the evolution of dynamic geospace processes via transient and localized dominance. The major substorm phenomena, including magnetic field dipolarization and particle injections, occur within the inner plasma sheet. Another substorm related phenomena are the high speed flows observed both in the central and boundary layer plasma sheet. It has also been suggested that the periods of superdense plasma sheet may be an important precondition for geomagnetic storms[55]. The southward component of the IMF has strong and positive correlation with different phenomena, such as the polar cap potential drop, the strength of region-1 FACs, the auroral electrojets and the occurrence of substorms, the development of the ring current, the total power in auroral precipitation, the size of the polar cap and auroral zone[7].

1.3.5 Geomagnetic Indices

Geomagnetic indices are used to specify the state of the magnetosphere. They are measurements of magnetic field variations on the surface of the Earth.

The global strength of the ring current can be monitored by ground-based magnetometers at middle or equatorial latitudes because it decreases the intensity of the Earth's magnetic field. The hourly Dst index is obtained from magnetometer sta-

tions near the equator but deviating from it to avoid the region with the magnetic perturbations dominated by the equatorial electrojet. At such latitudes the horizontal, H, component is mainly northward component of the magnetic perturbation and it is strongly affected by the intensity of the magnetospheric ring current, together with contribution from upper atmospheric neutral winds and the Chapman-Ferraro currents. The Dst index is a direct measure of the hourly average of this perturbation. Large negative perturbations are indicative of an increase in the intensity of the ring current and typically appear on time scales of about an hour. The decrease of intensity may takes much longer for several hours or even days. The entire period is called a storm. This index can be used to monitor the development of geomagnetic storm, as the main signature of the storm main phase is the build-up of an enhanced ring current. The Dst index calculated from the observations gives an estimate of the total energy content of the particles forming the ring current. The main enhancement of the storm-time ring current occurs at distances $L < 4$, due to either substorm particle injections or transport and energization of plasma sheet particles by enhanced convection electric field. The current view is that the latter process is more capable of delivering particles as deep as $L < 4$, especially if the electric field fluctuates [56].

AE index is an auroral electrojet index obtained from a number, typically 12, of stations distributed in local time in the latitude region that is typical of the northern hemisphere auroral zone. A superposition of the north-south magnetic perturbation H from all the stations enables a lower bound or maximum negative excursion of the H component to be determined which is called the AL index. Similarly, an upper bound or maximum positive excursion in H is determined which is called the AU index. AE index is the difference between these two indices, $AU - AL$. Negative H perturbations occur when stations are under an westward-flowing current. Thus the

indices AU and AL give some measure of the individual strengths of eastward and westward electrojets, while AE provides a measure of the overall horizontal current strength. AE index is the most commonly used indicator of substorm activity when a westward electrojet is measured with field-aligned currents in the dawn side and the dusk side. However, they are not a perfect measurement of electrojet strengths. The chain of stations used frequently gives inadequate longitudinal coverage and very few stations under southern hemisphere auroral zone. The fact that the auroral zone varies in latitude makes those stations miss the intense regions for very active or very quiet conditions[7].

The Kp index is obtained from a number of magnetometer stations at mid-latitudes where the stations are not greatly influenced by the auroral electrojet currents. If the auroral zone expands equatorward, these stations can record the effects of the auroral electrojet current system and of the magnetospheric ring current and field-aligned currents. This occurs during magnetically disturbed periods. The mid-latitude stations are rarely directly under an intense horizontal current system and thus magnetic perturbations can be dominant in either the H or D component, where the D component is the angle between geographic north and the horizontal vector. The Kp index utilizes both these perturbations by taking the logarithm of the largest excursion in H or D over a 3-hour period and placing it on a scale from 0 to 9. The ap-index is a three-hour world-wide index that is very similar to Kp but on a linear scale. The Ap-index is a daily average of ap[7].

1.4 Motivation of Space Weather Modeling

Space weather is the concept of changing environmental conditions in near-Earth space. The Earth's magnetic field presents a barrier to the solar wind and creates

a cavity between the solar wind and the Earth called the magnetosphere[48]. Space weather often implicitly means the conditions in near-Earth space within the magnetosphere. The major goal of magnetospheric physics is to understand the dynamical processes that occur in the Earth's magnetosphere to its interaction with the solar wind plasma[37].

Many technologies must include considerations of the solar-terrestrial environment in their designs and operations. The systems are grouped into broad categories that have similar physical origins. Figure 1.14 schematically illustrates these effects.

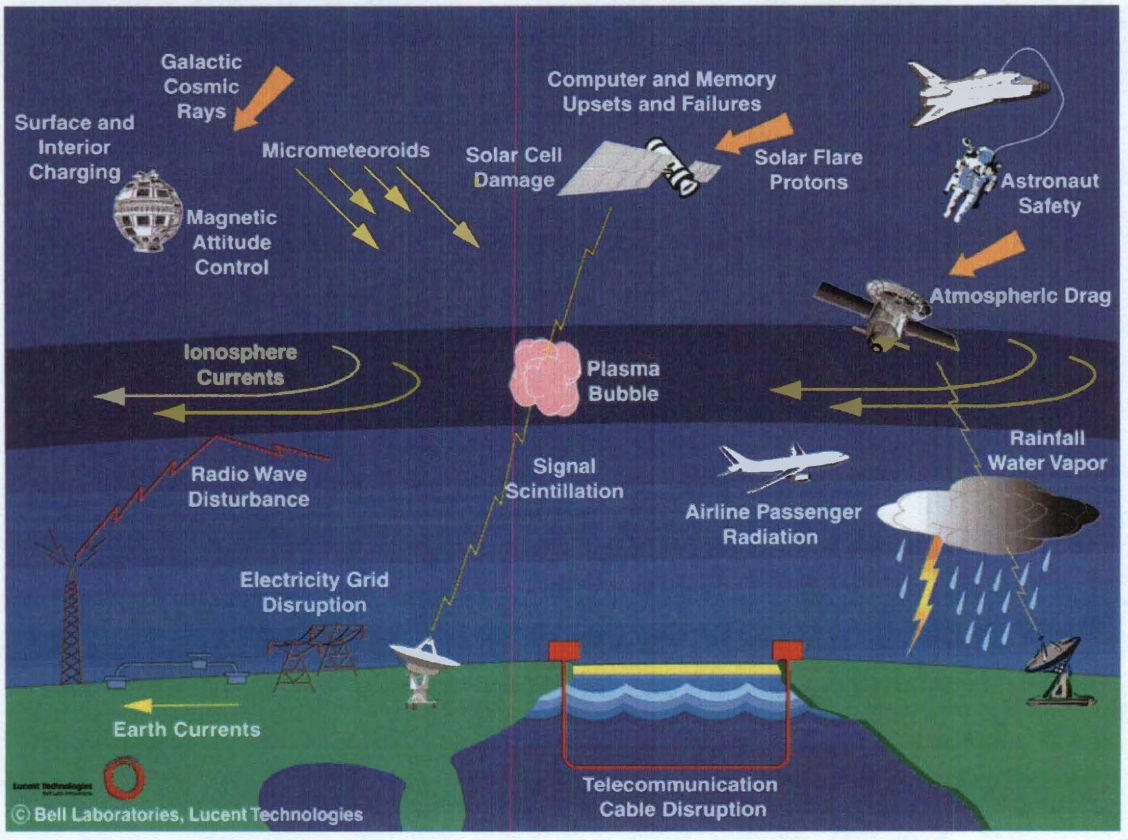

Figure 1.14 : Some of the effects of space weather on technical systems that are deployed on the Earth's surface and in space. Adapted from Lanzerotti [2001][8].

A variety of physical phenomena are associated with space weather, including geomagnetic storms and substorms, energization of the Van Allen radiation belts, ionospheric disturbances and scintillation, aurora and geomagnetically induced currents at Earth's surface. The beautiful auroral observed in the nighttime sky at high latitudes is one of the major effects of space weather, caused predominately by electrons from the space environment that stream along the Earth's magnetic field lines and collide with the upper atmosphere[37].

The National Space Weather Program (NSWP) is an interagency initiative to speed improvement of space weather services. It emerged in 1994 from the efforts of several U.S. government agencies to deal with technological vulnerabilities associated with the space environment. The overarching goal of the NSWP is to achieve an active, synergistic, interagency system to provide timely, accurate, and reliable space weather warnings, observations, specifications, and forecasts. The program includes contributions from the user community, operational forecasters, researchers, modelers, and experts in instruments, communications, and data processing and analysis. Several agencies have been participated in this program, including Department of Commerce (DOC), National Aeronautics and Space Administration (NASA), Department of Defense (DOD), National Science Foundation (NSF), Department of the Interior (DOI), Department of Energy (DOE), and Department of Transportation (DOT). The NSWP is an excellent example of interagency cooperation toward the achievement of both scientific and societal goals[57].

A working group on the space environment, consisting of the Air Force Space Command (AFSPC), the National Aeronautics and Space Administration (NASA), and the The National Oceanic and Atmospheric Administration (NOAA), examined the status of space weather modeling in 1997. The group recommended to develop

a modeling center responsible for the testing and validation of research codes. Both DOD and NOAA were attempting to set up Rapid Prototyping Centers (RPCs) that would receive validated research models and mold them into software that could run efficiently on operational platforms. However, it was clear the RPCs could not handle the process of validation and testing of research models[57]. The AFSPC/NASA partnership eventually inspired the creation of the Community Coordinated Modeling Center (CCMC).

The CCMC is built around the successful transitioning of the Magnetospheric Specification Model (MSM) and the Magnetospheric Specification and Forecast Model (MSFM) undertaken by the Air Force during the 1980s[57]. Magnetospheric Specification Model (MSM) is an operational space environment model of the inner and middle magnetosphere designed to specify charged particle fluxes up to 100 keV. It was designed for the Air Weather Service branch of the Air Force and used as a diagnostic tool for spacecraft charging and other spacecraft anomalies in post-event analysis[58]. It is essentially a derivative of the Rice Convection Model (RCM)[59, 60, 61, 62]. However, because the MSM is an operational model, it is required to be computationally fast, highly automated, and the code must be easily transportable. As the design goal, the MSM had to meet the following criteria[63]: (1) be responsive to changes in geophysical conditions on time scales of 15-30 minutes; (2) contain as much of the essential physics and cover as much of the physical system as possible; (3) make maximum use of the extensive near-real-time data stream available to the Air Force; (4) run faster than real time on computers available at the time. The Magnetospheric Specification and Forecast Model (MSFM) is similar to the MSM but was designed and tested for greater accuracy over a wider range of geocentric distances[63]. It is the second generation of the MSM with improvements to many of the original MSM

algorithms, including electron loss algorithm, the initial condition, and the ability to provide short-term forecasts of the magnetospheric particle fluxes[58].

Forecasts of geomagnetic storms, the equatorial radiation environment, and geomagnetic activity indices have all been aided by the availability of observations from satellite, and new numerical models[64]. Before rockets and satellites, remote observations from the ground were the only available means to study process outside the atmosphere, and are still used extensively[28]. Ground-based magnetometers provide observations of magnetic field perturbations caused by currents in the ionosphere and beyond. All-sky cameras are used to image the whole sky in auroral regions. Radar measurements of the upper atmosphere give a complementary picture of ionospheric activity. Rockets eventually allowed scientists to take brief measurements above the atmosphere. Satellites and other spacecraft provided the revolutionary capability of long term in situ measurements.

Since 1995, the joint NASA-ESA Solar and Heliospheric Observatory (SOHO) spacecraft is the main source of near-real time solar data for space weather prediction. It was joined in 1998 by the NASA Advanced Composition Explorer (ACE), which carries a space weather beacon for continuous transmission of relevant in situ space environment data. SOHO and ACE are located near the L1 Lagrangian point of the earth-sun distance, upstream of the earth where it measures solar wind plasma and magnetic field approximately one hour before it reaches the earth. Most recently, the launch of the NASA-ESA Solar-Terrestrial Relations Observatory (STEREO) added an additional space weather data stream that covers the region between the sun and the earth with stereoscopic imagery.

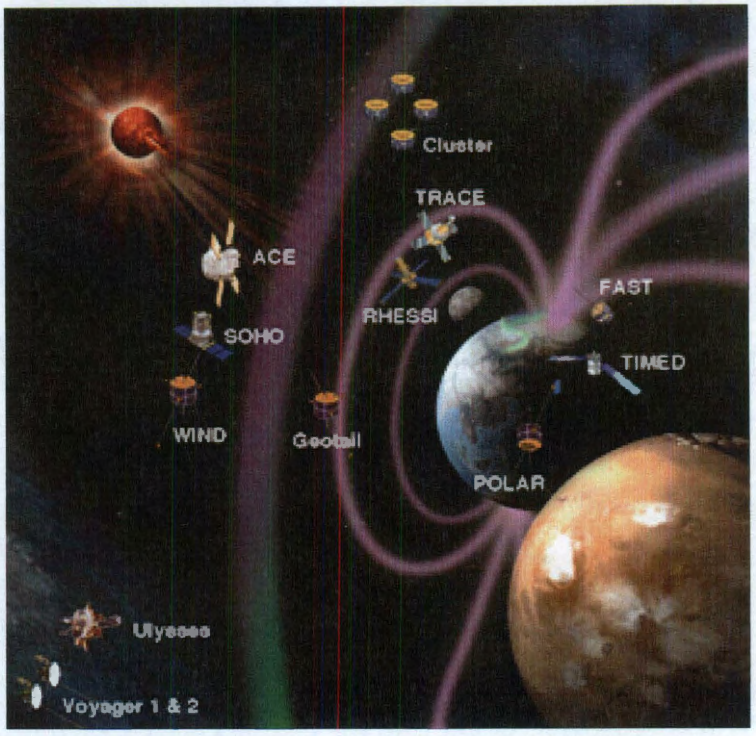

Figure 1.15 : A fleet of spacecraft observe phenomena that emerge from the Sun and cause space weather to improve space weather modeling. Courtesy of NASA.

Many space research missions of NASA and its international partners have been used to monitor and detect the space environment. Several of them are shown in Figure 1.15. The relevant solar missions are Yohkoh (Yohkoh solar observatory), SOHO (Solar and Heliospheric Observatory), TRACE (Transition Region and Coronal Explorer), RHESSI (Ramaty High Energy Solar Spectroscopic Imager)[65]. The relevant heliospheric missions are: IMP-8 (Interplanetary Monitoring Platform), Ulysses ("Odysseus"), ACE (Advanced Composition Explorer). The relevant geospace missions are: Geotail, SAMPEX (Solar Anomalous and Magnetospheric Particle Explorer), WIND (Global Geospace Science WIND), POLAR (Global Geospace Science Polar), FAST (Fast Auroral SnapshoT Explorer), IMAGE (Imager for Magnetopause-

to-Aurora Global Exploration), Cluster, TIMED (Thermosphere Ionosphere Mesosphere Energetics and Dynamics), TWINS (Two Wide-angle Imaging Neutral-atom Spectrometers), DMSP (Defense Meteorological Satellite Program), THEMIS (Time History of Events and Macroscale Interactions during Substorms). The GOES (Geostationary Operational Environmental Satellite) series of NOAA operational missions and Los Almos National Laboratory (LANL) series are the major source of data at geostationary orbit. GOES-1 to GOES-9 have been decommissioned, while GOES-10 to GOES-13 are still in use. The LANL series include 1967-059, 1977-007, 1979-053, 1981-025, 1982-019, 1984-037, 1984-129, 1987-097, 1989-046, 1990-095, 1991-080, 1994-084, LANL-97A, LANL-01A, LANL-02A satellites. Some other satellites are observing other planets in the Solar System, such as Voyager, Pioneer, Casini.

Major modeling efforts to simulate from the Sun to the Earth and beyond using three-dimensional magnetohydrodynamics frameworks have been undertaken since the 1990s. In the United States, the two major centers are the Michigan Center for Space Environment Modeling (CSEM) and the Center for Integrated Space weather Modeling (CISM). These frameworks could work as a scientific tool for increased understanding of the complex space environment, a specification and forecast tool for space weather prediction, and an educational tool for teaching about the space environment.

CSEM uses the Space Weather Modeling Framework (SWMF) to study and ultimately predict the space weather. The included physics modules are Eruptive Event Generator Model, Magnetogram Driven Solar Corona Model, Inner Heliophysics Model, Solar Energetic Particle Model, Earth Global Magnetosphere Model, Earth Radiation Belt Model, Earth Inner Magnetosphere Drift Physics Model, Earth Upper Atmosphere and Ionosphere Model, Earth Ionospheric Electrodynamics Model.

The Earth Global Magnetosphere Model in SWMF is Block Adaptive Tree Solar-wind Roe Upwind Scheme (BATS-R-US)[66, 67, 68]. The RCM participants as the Earth Inner Magnetosphere Drift Physics Model.

The CISM comprehensive model is built from existing state-of-the-art codes. The MAS (Magnetohydrodynamics outside A Sphere) is used to model the region of space from the solar surface to 20-50 solar radii. The ENLIL 3-D MHD Heliospheric Code is a numerical model for simulations of the ambient corotating solar wind as well as transient disturbances throughout the inner and mid heliosphere. Lyon-Fedder-Mobarry Global (LFM) MHD code is an integrated simulation model for the global magnetosphere-ionosphere system. The Thermosphere Ionosphere Nested Grid (TING) Model is a first-principles physical model of the thermosphere-ionosphere system. The Rice Convection Model (RCM) is an established physical model of the inner and middle magnetosphere that includes the coupling to the ionosphere.

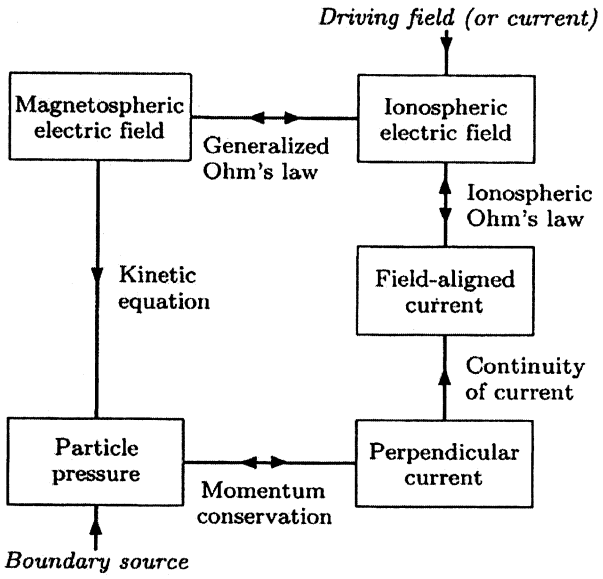

Figure 1.16 : Schematic diagram of magnetosphere-ionosphere coupling calculatoins[9].

The RCM follows from a long line of analytic and numerical models describing the electrodynamics of plasma convection in the Earth's inner and middle magnetosphere[23], as shown in Figure 1.16. The first general formulation of the convection-model idea was given by Vasyliunas[69]. The RCM started at about the same time[59] and have been described many times[60, 61, 62, 35, 23, 45]. The model works in the closed field line region which extends to middle plasma sheet. The RCM is an inner magnetosphere model that computes potential electric fields, electric currents, and magnetospheric particle distributions including the effects of magnetosphere-ionosphere coupling and the transport of magnetospheric particles by gradient/curvature drift[45]. It also includes the effects of magnetospheric shielding, subauroral ion drifts, the physics of ring current asymmetries[63]. A variety of work focussed on coupling the RCM to global MHD codes has been doing as a major part of space weather modeling. Both scientific and practical extension is further discussed in the thesis. Using numerical modeling to simulate magnetospheric dynamics will allow us to better forecast space weather and minimize the economic and social impact of space weather[28].

My thesis research work focuses on recent development of the RCM and the effects of these modifications through event modeling. This first chapter introduced the physics background in the solar-terrestrial interaction system. Chapter 2 will give a brief idea about the relationship between fluid description and kinetic description of magnetospheric convection in the inner magnetosphere and the necessity of kinetic formalism in this region. The consistency of three models involved and the difference between fluid-type equation and kinetic equation are illustrated by analytical analysis and numeric tests. Specific description of the RCM is given in chapter 3. The assumptions and basic equations in the RCM will be reemphasized. The logical loop for the RCM is carefully designed to illustrate the calculation sequence of the code.

The chapter is organized by the running procedure of the RCM to give an overall impression of the model. Although the RCM is a well-established physics model, it still needs timely update of existing models and implementation of newer models since more physics has been understood in this region. The validity of the code is essential in computational physics to obtain reasonable results from the existing physics. Therefore, several changes have been made to the modules of magnetic field, plasma boundary condition, and ionospheric conductances. Some recent improvements and developments made for practical purpose are discussed in chapter 4. The two dimensional grid has been unwrapped in the azimuthal direction to be consistent with other numerical codes. The code is optimized and parallelized to be capable of routine event simulations that run faster than real time. A prototype web page to request RCM runs inputs selection, module selection, RCM outputs selection, and desirable comparisons with observational data from satellites or ground based radars and magnetograms is also shown in the chapter. Chapter 5 shows simulation results of two extremely strong storms by the RCM with special interest in different high-latitude plasma boundary conditions. A time-dependent boundary condition should be applied for realistic event modeling. Statistical plasma sheet model could overestimate the plasma density and temperature from tailward boundary during extreme conditions. The ring current injection and interchange motion are also observed in the simulations as always. Chapter 6 describes the parallel electric fields and the steps we had to implement a module including the generalized Knight's relation to calculate the parallel potential drop from the field-aligned currents. The enhancement of plasma deposition by the parallel electric field is essential in substorm expansion phase when the upward field-aligned currents appear at the west edge of the substorm current wedge. Chapter 7 goes through the sources and sinks of plasma content. Besides

solar wind plasma moving earthward from the magnetotail, particle precipitation, charge exchange, and ionospheric outflows are included in the continuity equations. The electron precipitation is modified and the ion precipitation is implemented. Simple ion outflow module is also added into the code. The effect of two corrections to the precipitating energy flux is examined in chapter 8 by the simulation results of an isolated substorm. These corrections are widely used in storm simulations with the RCM, but first compared here in substorm simulations. The Hardy normalization can not perform the desired function during the substorm expansion phase. An arbitrary energy flux floor could be used to enhance the precipitating energy flux and ionospheric conductances at high latitude. Another way to give realistic conductance is to include the acceleration from the parallel electric fields. The original Knight's relation overestimates the parallel potential drop in the way we used together with Vasyliunas's equation. The modified Knights relation gives reasonable parallel electric fields and strong enhancement of conductances on the west edge of the plasma bubble. The role of parallel electric fields is illustrated in the comparisons of the runs without and with the parallel electric fields in chapter 9. The last chapter gives a brief summary that by developing old modules, such as magnetic field and plasma sheet parameters, and implementing new modules, such as field-aligned potential drop, particle precipitation, and ion outflow, the RCM is capable of real time event simulation including strong geomagnetic storms and magnetospheric substorms.

Chapter 2

Descriptions of Magnetospheric Convection

In the inner magnetosphere, the plasma flows are mostly slow compared to thermal or Alfvén speeds, but the convection is far away from the ideal magnetohydrodynamic since the gradient/curvature drifts become significant closer to the Earth. Several formalisms have been used to describe plasma dynamics, but it is not fully understood how they relate to each other. In this chapter, we explore the relations among kinetic, fluid and an "average" model in an attempt to find the simplest yet realistic way to describe the convection[10]. We will first give some background information of inner magnetosphere modeling. Then the assumptions and the equations of the three formalisms will be discussed. We will show that the average model, unclosed in its published form, immediately follows from the RCM formalism. Next, we prove analytically that the average model, when closed with the assumption of a Maxwellian distribution, is equivalent to the fluid model and kinetic model with a Maxwellian distribution. To give better understanding of those formulas, we analyze the transport of both one-dimensional and two-dimensional Gaussian-shaped blob of hot plasma. For the kinetic case, it is known that the time evolution of such a blob is gradual spreading in time. For the fluid case, the blob separates into two drifting at different speeds for one-dimensional case[70]. We present a fully-nonlinear solution of this case confirming this behavior but demonstrating what appears to be a shock-like steepening of the faster drifting secondary blob. A new, more realistic two-dimensional example using the dipole geometry with a uniform electric field confirms the one-dimensional

solutions[10]. Some discussions are given at the end of this chapter to demonstrate that the kinetic form seems to be a necessary approach in the inner magnetospheric modeling.

2.1 Background

Fundamental theoretical investigations of magnetospheric physical processes require solving a closed set of equations to model specific physical processes[10]. At high latitudes, anti-sunward convection is driven by the interaction of the solar wind with the geomagnetic field, commonly resulting in the so-called two-cell pattern. Numerical solutions of global three-dimensional ideal magnetohydrodynamics (MHD) equations have been used with a great success in explaining patterns of anti-sunward flow in the magnetospheric boundary layers, or over the polar cap in the ionosphere, and a required "return" sunward flow in the central plasma sheet, or in the auroral oval in the ionosphere[71, 72, 66]. The ideal MHD equations represent the simplest possible formalism describing bulk plasma flows and electrodynamics in a self-consistent way.

The inner magnetosphere is one of the regions where this approximation becomes progressively inadequate as the plasma becomes heated and subject to non-negligible energy-dependent gradient/curvature drifts besides earthward motion due to the cross-tail electric field[10]. Flows can no longer be approximated by a single-fluid type plasma with the "frozen-in" flux condition. A more appropriate form of the equations is required to include some of the kinetic drift physics and electrodynamic effects of drift currents on the plasma. In this chapter, we analyze three such formulations that can be written down in a closed form and that have been solved for realistic magnetospheric configurations.

Since the timescales of magnetic field changes in the inner magnetosphere are

much longer than the typical periods of particle's gyro and bounce motion and the plasma is slow-flowing compared to the thermal speed, under many circumstances the transport equations are based on adiabatic guiding center drift theory. While different assumptions have been added into the procedure to simplify and complete the chain of equations, there are only two different formalisms that combine plasma transport, based on adiabatic drift theory, and the electrodynamic coupling to the ionosphere, that lead to a set of closed equations and yield realistic solutions.

A special form of the kinetic approach to the systematic calculation of magnetospheric convection underlies the well-known Rice Convection Model (RCM) numerical code[69, 59, 60, 61, 40] developed more than 40 years at Rice University. We will refer to it as the "RCM formalism", "RCM model", or "kinetic model", for brevity purposes. The approach invokes an equation of current conservation and includes field-aligned currents resulting from pressure-gradients of hot magnetospheric plasma with transport equations for the distribution function assuming an isotropic pitch-angle distribution of particles. Due to energy dependence of drift velocities, a suitable discretization of the distribution function is used, resulting in a large number of transport equations.

The two-fluid description[73, 74, 75] was established in nearly the same spatial region as the RCM. While the electrodynamic equation for the electric field is the same, the equations replacing the drift RCM equations are just four partial differential equations for mass density and energy for each of the two species. Instead of the actual drift velocity, the formalism requires use of the diamagnetic velocity[75]. Heinemann[76] pointed out the need for an additional term accounting for the heat flux term in the energy equation, which is perpendicular to both magnetic field and the temperature gradient. With the addition of the heat flux term[77] under the assump-

tion of the Maxwellian distribution function, the model of Peymirat and Fontaine [1994] is the same as that of Heinemann [1999], and will be referred to as the "fluid" model in this chapter.

The relationship between the two formalisms was analyzed initially by Heinemann and Wolf[70], who showed that if the RCM model includes an additional assumption that the distribution function locally comes to thermal equilibrium faster than the characteristic drift times, the two sets of equations become equivalent. Without assuming Maxwellian distribution, one-dimensional solutions of a test case indicated physically different evolutions of a density and pressure perturbation. Specifically, for the situation of an initially Gaussian-shaped blob of plasma in the uniform background, they showed that the kinetic model predicts a gradual spreading of the blob with time due to energy-dependent gradient/curvature drifts of particles in the distribution function, while in the fluid case, the blob evolved into two distinct blobs separating from each other with time[70].

Liu published a model that is based on the RCM-like adiabatic drift theory but is a single-fluid model[78], assuming ions carrying all of the particle pressure and electrons to be cold, with a heat-flux term. With a clever choice of a Cartesian coordinate system and by employing the concept of time reversal mapping, Liu [2006] presents two partial differential equations describing the evolution of density and energy that supposedly include the RCM drift physics formalism in an average way. Thus, this model would appear to have the best of the RCM and fluid descriptions published before and be referred as the "ensemble-averaged", or simply "average" model in this chapter.

Our first reason for this work is an attempt to further understand what minimum amount of physics is necessary in order to treat the electrodynamics of the inner

magnetosphere in a realistic manner[10]. While the fluid model of Heinemann [1999] displays properties in stark contrast to those of the RCM formalism, at least in the simple case published by Heinemann and Wolf [2001], the model of Liu [2006] is supposed to include the full RCM drift physics but in only two partial differential equations. Thus, it would be imperative to understand how this model is related to the previously published two formalisms.

Another reason for our analysis is that for practical purposes, a one- or two-fluid model is simpler and faster to evolve numerically, although the full details of the distribution function must be sacrificed. A kinetic model is constructed from the guiding center drift theory and would appear to be closer to the real world, but solving equations numerically is more difficult and computationally slower.

A third less obvious but no less important reason is related to a recent line of work building "coupled" numerical models of the magnetosphere where some form of the inner magnetospheric representation is installed, in a modular way, into a global MHD code[79, 45, 80]. In this approach, drift physics of the inner magnetospheric "hot" particle population is tracked in a kinetic model, and the results are used in a global MHD code by computing the appropriate plasma moments. The MHD code provides a time dependent magnetic field model for the inner magnetospheric model and continuously updated boundary conditions for the electric potential and plasma. The inner magnetospheric model computes the distribution functions of particles in the inner magnetosphere and passes the calculated inner magnetospheric pressures to the MHD model. A combined global MHD model and an inner magnetospheric model could yield more information in understanding the dynamics and provide a more physical and realistic model than using either model alone, especially in the inner magnetosphere[10].

Following this idea, De Zeeuw et al.[79] incorporated the RCM into the Block Adaptive Tree Solar-wind Roe-type Upwind Scheme (BATS-R-US). The MHD code generates the magnetic field model and updated boundary conditions for electric potential and plasma distribution as RCM inputs. The RCM computes the distribution functions of inner magnetospheric particles and passes pressures back to MHD. The coupled RCM/BATS-R-US code predicts formation of the ring current and region-2 FACs in a way that is significantly better than the MHD code itself. Similarly, Toffoletto et al.[45] are working to integrate RCM in the Lyon-Fedder-Mobarry (LFM) global MHD model. The RCM uses magnetic and electric fields, ionospheric conductance and plasma distribution from LFM calculation. When the pressure in the ring current and the density of field-aligned currents obtained with the coupled model are compared with those of the ideal MHD alone, the coupled model seems to show more realistic solutions[45, 81]. Another major global MHD code, open Geospace General Circulation Model (OpenGGCM), is trying to couple to the RCM as well. Hu et al.[80] use the OpenGGCM magnetic field, plasma information to supply inputs and boundary conditions for the RCM. The OpenGGCM ionospheric potential is used to drive the RCM. Given the complexity and technical difficulties in constructing these models, an adequate fluid description of the inner magnetosphere could be used to eliminate some of this computational complexity.

2.2 Assumptions

In this chapter, we will emphasize the major assumptions of models in the inner magnetosphere region. Since they all take account of the magnetospheric convection pattern, the similar physics makes all three descriptions have nearly the same assumptions[10]: pitch angle distribution is isotropic; flow speed is much less than the

thermal speed; timescales of magnetic field change are slow compared to the bounce motion so that the adiabatic condition is satisfied. In addition, a few assumptions are made particular for this chapter. There are no parallel electric fields, and for simplicity we are going to assume that there are no losses or local sources of particles. All formalisms are applicable in the region of closed magnetic field lines and away from boundary layers.

2.3 Kinetic Formula

As mentioned in the first chapter, the kinetic model is based on the Vasyliunas' logical loop and the theory of Wolf [1970, 1983], Harel et al. [1981], and Vasyliunas [1970, 1972][59, 40, 61, 69, 82]. The major assumption is that plasma in the inner magnetosphere remains isotropic in pitch-angle along magnetic field lines. For plasma sheet ions, such an isotropizing mechanism is most likely chaotic motion near the neutral sheet[83], while for the electrons wave-particle interactions are probably the dominant mechanism. Then the parameter $\lambda = KV^{2/3}$ is conserved along drift paths[40, 84] considering slow-flow particles filling isotropic flux tubes and averaging the total drift velocity due to $\mathbf{E} \times \mathbf{B}$ and gradient/curvature drifts. Here K is particle's kinetic energy, V is the flux-tube volume, $\mathbf{E}$ and $\mathbf{B}$ are electric and magnetic fields. This and all subsequent integrals are from one hemisphere of the ionosphere to the other along the flux tube on closed field line region. Since λ is an invariant along trajectories, it can be used as a variable labeling the distribution function in the velocity space $f = f(\lambda, \mathbf{x}, t)$.

The drift velocity averaged along a flux tube can be shown to be[84]:

$$\mathbf{v}_D(\lambda, \mathbf{x}, t) = \frac{\mathbf{E} \times \mathbf{B}}{B^2} + \frac{\lambda \mathbf{B} \times \nabla V^{-2/3}}{qB^2} \tag{2.1}$$

This velocity is the familiar $\mathbf{E}\times\mathbf{B}$ and gradient/curvature drift velocity averaged along a flux tube under the assumption of pitch-angle isotropy and expressed in terms of invariant energy λ. Without sources or losses, the quantity

$$\eta = \int \frac{nds}{B} = nV \tag{2.2}$$

where n is number density, ds is the displacement along the field line, and η is essentially the number of particles per unit magnetic flux, turns out to be conserved along the drift path.

$$\left(\frac{\partial}{\partial t} + \mathbf{v}_D \cdot \nabla\right) \eta(\lambda, \mathbf{x}, t) = 0 \tag{2.3}$$

Equations (2.1) and (2.3) have the species indices omitted; for simplicity, in this chapter we will assume that positive ions of one type carry all the pressure and that the electrons are cold and don't carry pressure. No assumptions regarding the shape of the distribution function beside the pitch-angle isotropy are made.

The electric field in equation (2.1) depends on the spatial distribution of plasma and must be solved for separately. It can be obtained by assuming that $\mathbf{E}$ is a potential field in the ionosphere and considering current conservation between the magnetosphere and the ionosphere. The result is a two-dimensional elliptic partial differential equation for the electrostatic potential that has gradients of total plasma pressure p. Since this equation is exactly the same for all three models we consider, we don't discuss it any further in this chapter.

For our purposes, the most important fact is that (2.1) and (2.3) depend on λ. When (2.1) is substituted into (2.3), the result is a hyperbolic partial differential equation of the advection type that can be solved given appropriate initial and boundary conditions. Dependence on λ then means representing the distribution function $f = f(\lambda, \mathbf{x}, t)$ on the boundary, and then solving (2.3) for these "energy levels". In

reality, this results in a set of 100-200 equations of type (2.3) simultaneously since they are only coupled via the electric field. Having to solve a large number of equations (2.3) is a computational burden of this RCM approach but allows an accurate representation of the inner magnetospheric plasma transport.

2.4 Fluid Formula

Heinemann [1999] showed that the three-dimensional equations of conservation of mass, momentum, and energy of fully collisionless inner magnetospheric plasma can be written as[76]:

$$\begin{aligned} \frac{\partial n}{\partial t} + \nabla \cdot (n\mathbf{v}) &= 0 \\ \nabla p - qn\left(\mathbf{E} + \mathbf{v} \times \mathbf{B}\right) &= 0 \\ \frac{3}{2} n \left(\frac{\partial}{\partial t} + \mathbf{v} \cdot \nabla\right) T + p \nabla \cdot \mathbf{v} + \nabla \cdot \mathbf{h} &= 0 \end{aligned} \tag{2.4}$$

where temperature T, equivalent to p/n, is in energy units, and $\mathbf{h}$ is the perpendicular heat flux having a form in the rest frame as

$$\mathbf{h} = \frac{5p}{2qB^2} \mathbf{B} \times \nabla T \tag{2.5}$$

The above equation set is reduced to two coupled partial differential equations after bounce averaging along a flux tube

$$\left(\frac{\partial}{\partial t} + \mathbf{v} \cdot \nabla\right) \eta + \frac{\eta}{qB^2} \mathbf{B} \times \nabla T \cdot \nabla s = 0 \tag{2.6}$$

$$\left(\frac{\partial}{\partial t} + \mathbf{v} \cdot \nabla\right) s + \frac{5}{2qB^2} \mathbf{B} \cdot \nabla T \times \nabla \ln \eta = 0 \tag{2.7}$$

where η is defined by (2.2) and s is entropy per unit mass expressed through pressure p and number density n as

$$s = \frac{3}{2} \ln \left(\frac{p}{n^{5/3}}\right) \tag{2.8}$$

The equations (2.6) and (2.7) are written in the magnetospheric equatorial plane. A strong assumption in this approach is that the distribution function is Maxwellian locally, which implies energy transfer in the velocity space. The drift velocity v, coming from momentum equation in equation set (2.4), is analogous to (2.1) in the RCM approach:

$$\mathbf{v} = \frac{\mathbf{E} \times \mathbf{B}}{B^2} + \frac{\mathbf{B} \times \nabla p}{nqB^2} \tag{2.9}$$

but the second term in the right hand side is not an actual gradient/curvature drift velocity but a "diamagnetic drift velocity" instead. The diamagnetic drift is not a guiding center drift. A pressure gradient does not cause any single particle to drift, but results in more particles moving in one direction than in the other. The heat flux term in the fluid case appears to have a "collisional" form which is proportional to the density gradient. Sets of fluid transport equations can probably be derived that are more complicated and involve more physics than the ones we use here, i.e. including Landau damping[85]. However, we have chosen to limit ourselves just to terms that are needed to represent the effects of adiabatic-drifts[10].

2.5 Average Formula

2.5.1 Description

In order to show the heat flux term explicitly, Liu [2006] modified the basic RCM convection equation to obtain a model that is described by only two partial differential equations per species, similar to the two-fluid case above[10]. A Cartesian coordinate system is cleverly chosen so that the y-direction is locally tangent to the contour of flux tube volume V. So that the gradient/curvature drift velocity is locally always in the y-direction, and the drift velocity in the x-direction is thus energy independent.

By the concept of time reversal mapping[78], the particle sources of those particles in position x at time t are distributed on a flux tube volume contour at a very recent past. The reference source point, which is the time reversal along average drift velocity $\mathbf{u} = \langle \mathbf{v}_D \rangle$, is obtained by ensemble average of drift velocity over different kinetic energies. The expressions for density n and pressure p are expanded around the reference source point. After some mathematical manipulations, the mass and energy transport equations are written as

$$\left(\frac{\partial}{\partial t} + \mathbf{u} \cdot \nabla\right) \eta = \frac{n}{qB^2} (\nabla V \times \nabla T) \cdot \mathbf{B} \tag{2.10}$$

$$\left(\frac{\partial}{\partial t} + \mathbf{u} \cdot \nabla\right) \Xi = \frac{4V^{2/3}}{9qB^2} \nabla V \times \left(\nabla S + \frac{9}{4} p \nabla T\right) \cdot \mathbf{B} \tag{2.11}$$

where the quantity S is related to phase space density $F(K)$ as:

$$S = \int F(K)(K - \langle K \rangle) K^{3/2} dK \tag{2.12}$$

The quantity $\Xi = pV^{\gamma}$, or entropy, is an adiabatic invariant that is conserved in the RCM approach for a given "energy level" λ as

$$\Xi = \frac{2}{3} \eta \lambda \tag{2.13}$$

since $\gamma = 5/3$. But its summation over all energies is in general not conserved. The phase space density F is proportional to the distribution function f in such a way that $n = \int F(K) \sqrt{K} dK$, so that

$$F(K, \mathbf{x}, t) = \frac{4\pi\sqrt{2}}{m^{3/2}} f(\lambda, \mathbf{x}, t) \tag{2.14}$$

The "ensemble average" drift velocity $\mathbf{u}$ is defined as

$$\mathbf{u} = \frac{\mathbf{E} \times \mathbf{B}}{B^2} - \frac{T}{qB^2} \mathbf{B} \times \nabla \ln V \tag{2.15}$$

Formally, this looks similar to the fluid model but includes the RCM drift physics.

2.5.2 Comments

Regarding the approach of Liu [2006], we first note that the phase space density is a function of time, and so is the quantity S. Therefore, the equation set (2.10,2.11) is not closed without a model for the evolution of the distribution function, knowledge of which is needed to evaluate S. Expression (2.12) can be evaluated in a closed form for a kappa distribution function, yielding[78]

$$S = \frac{3\kappa n T^2}{2\kappa - 5}$$

However, it is easy to see that assuming a kappa distribution function in general would be inconsistent with the adiabatic drift laws assumed in the average model. Thus, it appears that this model suffered from the well-known problem of the closure of moment equations[86].

One possible way to close the equation set (2.10,2.11) is to assume that the distribution function is Maxwellian. Then, since the Maxwellian is obtained from the kappa distribution function in the limit of $\kappa \to \infty$,

$$S = \frac{3}{2} n T^2 \tag{2.16}$$

If this is the case, we now show that equation set (2.10,2.11) directly follow from the RCM equations (2.3) and (2.1). Indeed, we can write the RCM transport equation (2.3) as

$$\left(\frac{\partial}{\partial t} + \mathbf{v}_D \cdot \nabla \right) n_\lambda V = 0$$

Furthermore, since λ is constant along drift trajectories, (2.3) can be written as

$$\left(\frac{\partial}{\partial t} + \mathbf{v}_D \cdot \nabla \right) \frac{2}{3} \eta_\lambda \lambda = 0$$

Here, we add the subscript λ to emphasize the energy dependence. The drift velocity (2.1) can be written in a different form by re-writing the gradient/curvature drift

term:

$$\mathbf{v}_D = \frac{\mathbf{E}\times\mathbf{B}}{B^2} - \frac{2K}{3qB^2}\mathbf{B}\times\nabla\ln V \tag{2.17}$$

and when averaging over energy, one obtains the same "ensemble-averaged" drift velocity of equation (2) in Liu [2006] since $\langle K\rangle = 3T/2$.

If we recall that the number of particles for energy interval [K,K+dK] is

$$n(K)dK = F(K,\mathbf{x},t)\sqrt{K}dK \tag{2.18}$$

The density equation (2.10) follows from the RCM conservation law (2.3)

$$\begin{aligned}
&\left(\frac{\partial}{\partial t}+\mathbf{u}\cdot\nabla\right)\eta \\
=\;& \sum_\lambda\left(\frac{\partial}{\partial t}+\mathbf{u}\cdot\nabla\right)n_\lambda V \\
=\;& \sum_\lambda\left(\frac{\partial}{\partial t}+\mathbf{v}_D\cdot\nabla\right)n_\lambda V + \sum_\lambda\left[(\mathbf{u}-\mathbf{v}_D)\cdot\nabla\right]n_\lambda V \\
=\;& \sum_\lambda\left[\frac{2\left(K_\lambda-\langle K_\lambda\rangle\right)}{3qB^2}\mathbf{B}\times\nabla\ln V\right]\cdot\nabla\left(n_\lambda V\right) \\
=\;& \int\frac{2\left(K_\lambda-\langle K_\lambda\rangle\right)}{3qB^2}\left[\nabla V\times\nabla F(K)\cdot\mathbf{B}\right]\sqrt{K}dK \\
=\;& \frac{2}{3qB^2}\nabla V\times\left[\nabla\int\left(K-\langle K\rangle\right)F(K)\sqrt{K}dK + \nabla\langle K\rangle\int F(K)\sqrt{K}dK\right]\cdot\mathbf{B} \\
=\;& \frac{n}{qB^2}\left(\nabla V\times\nabla T\right)\cdot\mathbf{B}
\end{aligned} \tag{2.19}$$

and we used the fact that the pressure p is $\gamma-1=2/3$ of the energy density

$$p = \int(\gamma-1)F(K)K\sqrt{K}dK = \frac{2}{3}\int F(K)K^{3/2}dK$$

then we can derive equation (2.11) from the RCM formalism in a similar way

$$\begin{aligned}
&\left(\frac{\partial}{\partial t}+\mathbf{u}\cdot\nabla\right)\Xi \\
=&\sum_{\lambda}\left(\frac{\partial}{\partial t}+\mathbf{u}\cdot\nabla\right)\frac{2}{3}\eta_{\lambda}\lambda \\
=&\sum_{\lambda}\left(\frac{\partial}{\partial t}+\mathbf{v}_D\cdot\nabla\right)\frac{2}{3}\eta_{\lambda}\lambda+\sum_{\lambda}\left[(\mathbf{u}-\mathbf{v}_D)\cdot\nabla\right]\frac{2}{3}\eta_{\lambda}\lambda \\
=&\sum_{\lambda}\left[\frac{2\left(K_{\lambda}-\langle K_{\lambda}\rangle\right)}{3qB^2}\mathbf{B}\times\nabla\ln V\right]\cdot\nabla\left(\frac{2}{3}n_{\lambda}K_{\lambda}V^{5/3}\right) \\
=&\int\frac{4\left(K_{\lambda}-\langle K_{\lambda}\rangle\right)}{9qB^2}V^{2/3}\left[\nabla V\times\nabla F(K)\cdot\mathbf{B}\right]K^{3/2}dK \\
=&\frac{4V^{3/2}}{9qB^2}\nabla V\times\left[\nabla\int\left(K-\langle K\rangle\right)F(K)K^{3/2}dK+\nabla\langle K\rangle\int F(K)K^{3/2}dK\right]\cdot\mathbf{B} \\
=&\frac{4V^{3/2}}{9qB^2}\nabla V\left(\nabla S+\frac{9}{4}p\nabla T\right)\cdot\mathbf{B}
\end{aligned}\tag{2.20}$$

as stated in equation (2.12)

$$\begin{aligned}
S &= \int F(K)\left(K-\langle K\rangle\right)K^{3/2}dK \\
&= \int F(K)\left(K-\langle K\rangle\right)^2\sqrt{K}dK \\
&= n\langle\Delta K^2\rangle
\end{aligned}\tag{2.21}$$

This shows that the average model directly follows from the RCM kinetic model stated above.

2.6 Relation

Since the RCM and fluid equations are equivalent if the RCM case includes the additional assumption the distribution function is maintained Maxwellian[70], our result from the previous section means that the average model is equivalent to the fluid model of [Heinemann, 1999] under that assumption. The kinetic model, such as the

RCM formalism, does not make any assumptions about the shape of the distribution function except for the pitch-angle isotropy[10]. To verify it, we found an elegant way to show this, by reducing all three formalisms to the same common set of equations, which is presented in this section. Let's assume that the distribution function is Maxwellian in the average model and in the RCM model. It was explicitly assumed to be Maxwellian in the case of the fluid model, of course. Then we show that the mass equation and energy equation in these three models are equivalent. Specifically, we show that the three mass equations can be transformed to

$$\frac{\partial \eta}{\partial t} + \left(\frac{\mathbf{E} \times \mathbf{B}}{B^2} \cdot \nabla \right) \eta + \frac{1}{qB^2} \nabla p \times \nabla V \cdot \mathbf{B} = 0 \tag{2.22}$$

The energy equations from the three models can be transformed to the common form

$$\frac{\partial \Xi}{\partial t} + \left(\frac{\mathbf{E} \times \mathbf{B}}{B^2} \cdot \nabla \right) \Xi + \frac{1}{qB^2} \nabla \frac{p^2}{n} \times \nabla V^{5/3} \cdot \mathbf{B} = 0 \tag{2.23}$$

2.6.1 Mass Equation

We start with the fluid model. Taking gradients of the ideal gas law $p = nT$ and the definition of entropy per unit mass (2.8) yields: $dp = ndT + Tdn$ and $ds = 3dp/2p - 5dn/2n$. Then we start from the density equation (2.6) of the fluid model and use gradients of p and s to obtain:

$$\begin{aligned}
& 0 \\
= & \left(\frac{\partial}{\partial t} + \mathbf{v} \cdot \nabla \right) \eta + \frac{\eta}{qB^2} \mathbf{B} \times \nabla T \cdot \nabla s \\
= & \frac{\partial \eta}{\partial t} + \left(\frac{\mathbf{E} \times \mathbf{B}}{B^2} \cdot \nabla \right) \eta + \left(\frac{\mathbf{B} \times \nabla p}{nqB^2} \cdot \nabla \right) \eta + \frac{nV}{qB^2} \left(\frac{\nabla p}{n} - \frac{p}{n^2} \nabla n \right) \times \left(\frac{3}{2p} \nabla p - \frac{5}{2n} \nabla n \right) \cdot \mathbf{B} \\
= & \frac{\partial \eta}{\partial t} + \left(\frac{\mathbf{E} \times \mathbf{B}}{B^2} \cdot \nabla \right) \eta + \frac{\mathbf{B} \times \nabla p}{nqB^2} \cdot (n \nabla V + V \nabla n) - \frac{V}{nqB^2} \nabla p \times \nabla n \cdot \mathbf{B} \\
= & \frac{\partial \eta}{\partial t} + \left(\frac{\mathbf{E} \times \mathbf{B}}{B^2} \cdot \nabla \right) \eta + \frac{1}{qB^2} \nabla p \times \nabla V \cdot \mathbf{B}
\end{aligned} \tag{2.24}$$

which is exactly of the form (2.22).

Second, we show that (2.22) follows from the RCM equations, in a way similar to that of Heinemann and Wolf [2001]. First, we note that K is proportional to the distribution function f, which is easy to see if one writes the number of particles per unit magnetic flux within energy invariants interval $[\lambda,\ \lambda + \Delta\lambda]$ in terms of η and in terms of f:

$$\eta(\lambda, \mathbf{x}, t)\Delta\lambda = V 4\pi v^2 \Delta v f(\lambda, \mathbf{x}, t) = \frac{4\pi\sqrt{2}}{m^{3/2}}\sqrt{\lambda} f(\lambda, \mathbf{x}, t)\Delta\lambda \tag{2.25}$$

Equation (2.25) implies that the RCM transport equation (2.3) can be written as:

$$\left[\frac{\partial}{\partial t} + \mathbf{v}_D(\lambda, \mathbf{x}, t) \cdot \nabla\right] f(\lambda, \mathbf{x}, t) = 0 \tag{2.26}$$

In addition, integrating (2.25) over all values of λ yields a useful relation:

$$\frac{4\pi\sqrt{2}}{m^{3/2}} \int_0^\infty d\lambda \sqrt{\lambda} f(\lambda, \mathbf{x}, t) = nV \tag{2.27}$$

For a Maxwellian distribution

$$f(\lambda, \mathbf{x}, t) = n\left(\frac{m}{2\pi T}\right)^{3/2} e^{-\frac{\lambda}{TV^{2/3}}} \tag{2.28}$$

(2.27) can be integrated by parts to yield:

$$\begin{aligned}
\frac{4\pi\sqrt{2}}{m^{3/2}} \int_0^\infty d\lambda \lambda^{3/2} f(\lambda, \mathbf{x}, t) &= \frac{3}{2} nTV^{5/3} \\
\frac{4\pi\sqrt{2}}{m^{3/2}} \int_0^\infty d\lambda \lambda^{5/2} f(\lambda, \mathbf{x}, t) &= \frac{15}{4} nTV^{5/3} \\
\frac{4\pi\sqrt{2}}{m^{3/2}} \int_0^\infty d\lambda \lambda^{7/2} f(\lambda, \mathbf{x}, t) &= \frac{105}{8} nTV^{5/3}
\end{aligned} \tag{2.29}$$

We also need these partial derivatives:

$$\begin{aligned}
\frac{\partial f}{\partial n} &= f\frac{1}{n} \\
\frac{\partial f}{\partial V} &= f\frac{2\lambda V^{-5/3}}{3T} \\
\frac{\partial f}{\partial T} &= f\left(\frac{\lambda V^{-2/3}}{T^2} - \frac{3}{2T}\right)
\end{aligned} \tag{2.30}$$

We will need to take two moments of (2.26):

$$\begin{aligned}\int_0^\infty d\lambda\lambda^{1/2}\left[\frac{\partial}{\partial t}+\mathbf{v}_D(\lambda,\mathbf{x},t)\cdot\nabla\right]f(\lambda,\mathbf{x},t) &= 0\\ \int_0^\infty d\lambda\lambda^{3/2}\left[\frac{\partial}{\partial t}+\mathbf{v}_D(\lambda,\mathbf{x},t)\cdot\nabla\right]f(\lambda,\mathbf{x},t) &= 0\end{aligned} \tag{2.31}$$

We start from the first of the moment equations (2.31) by using (2.27),(2.29),(2.30), and the expression for the drift velocity (2.1), as well as these identities

$$\begin{aligned}\frac{V^{-2/3}}{T^2}\frac{3}{2}nTV^{5/3} &= \frac{3}{2T}nV\\ \frac{V^{-2/3}}{T^2}\frac{15}{4}nT^2V^{7/3} &= \frac{5}{3}\frac{3}{2T}\frac{3}{2}nTV^{5/3}\\ \frac{V^{-2/3}}{T^2}\frac{105}{8}nT^3V^3 &= \frac{7}{3}\frac{3}{2T}\frac{15}{4}nT^2V^{7/3}\end{aligned} \tag{2.32}$$

to simplify the derivatives

$$\begin{aligned}&0\\ =&\int_0^\infty d\lambda\lambda^{1/2}\left[\frac{\partial}{\partial t}+\mathbf{v}_D\cdot\nabla\right]f\\ =&\int_0^\infty d\lambda\lambda^{1/2}\left(\frac{\partial}{\partial t}+\frac{\mathbf{E}\times\mathbf{B}}{B^2}\cdot\nabla+\frac{\lambda\mathbf{B}\times\nabla V^{-2/3}}{qB^2}\cdot\nabla\right)f\\ =&\int_0^\infty d\lambda\lambda^{1/2}f\left[\frac{1}{n}\left(\frac{\partial}{\partial t}+\frac{\mathbf{E}\times\mathbf{B}}{B^2}\cdot\nabla\right)n+\frac{\lambda\mathbf{B}\times\nabla V^{-2/3}\cdot\nabla n}{nqB^2}\right.\\ &+\frac{2\lambda V^{-5/3}}{3T}\left(\frac{\partial}{\partial t}+\frac{\mathbf{E}\times\mathbf{B}}{B^2}\cdot\nabla\right)V\\ &\left.+\left(\frac{\lambda V^{-2/3}}{T^2}-\frac{3}{2T}\right)\left(\frac{\partial}{\partial t}+\frac{\mathbf{E}\times\mathbf{B}}{B^2}\cdot\nabla\right)T+\lambda\left(\frac{\lambda V^{-2/3}}{T^2}-\frac{3}{2T}\right)\frac{\mathbf{B}\times\nabla V^{-2/3}\cdot\nabla T}{qB^2}\right]\\ =&\int_0^\infty d\lambda\lambda^{1/2}f\left[\frac{1}{n}\left(\frac{\partial}{\partial t}+\frac{\mathbf{E}\times\mathbf{B}}{B^2}\cdot\nabla\right)n+\frac{1}{V}\left(\frac{\partial}{\partial t}+\frac{\mathbf{E}\times\mathbf{B}}{B^2}\cdot\nabla\right)V\right.\\ &\left.+\frac{\lambda\mathbf{B}\times\nabla V^{-2/3}}{qB^2}\cdot\left(\frac{\nabla n}{n}+\frac{\nabla T}{T}\right)\right]\\ =&\left(\frac{\partial}{\partial t}+\frac{\mathbf{E}\times\mathbf{B}}{B^2}\cdot\nabla\right)(nV)+\frac{\nabla V^{-2/3}\times\nabla p\cdot\mathbf{B}}{pqB^2}\frac{3}{2}nTV^{5/3}\\ =&\frac{\partial\eta}{\partial t}+\frac{\mathbf{E}\times\mathbf{B}}{B^2}\cdot\nabla\eta+\frac{1}{qB^2}\nabla p\times\nabla V\cdot\mathbf{B}\end{aligned} \tag{2.33}$$

which is identical to (2.22).

The mass equation in the average model is transformed as:

$$\begin{aligned}
& 0 \\
= & \left(\frac{\partial}{\partial t}+\mathbf{u}\cdot\nabla\right)\eta-\frac{n}{qB^2}\left(\nabla V\times\nabla T\right)\cdot\mathbf{B} \\
= & \frac{\partial\eta}{\partial t}+\left(\frac{\mathbf{E}\times\mathbf{B}}{B^2}\cdot\nabla\right)\eta-\frac{T}{qB^2}\mathbf{B}\times\nabla\ln V\cdot\nabla\eta-\frac{n}{qB^2}\left(\nabla V\times\nabla T\right)\cdot\mathbf{B} \\
= & \frac{\partial\eta}{\partial t}+\left(\frac{\mathbf{E}\times\mathbf{B}}{B^2}\cdot\nabla\right)\eta-\frac{T}{qB^2}\left(\nabla V\times\nabla n\right)\cdot\mathbf{B}-\frac{n}{qB^2}\left(\nabla V\times\nabla T\right)\cdot\mathbf{B} \\
= & \frac{\partial\eta}{\partial t}+\left(\frac{\mathbf{E}\times\mathbf{B}}{B^2}\cdot\nabla\right)\eta+\frac{1}{qB^2}\nabla p\times\nabla V\cdot\mathbf{B} \qquad (2.34)
\end{aligned}$$

Thus, equation (16) in [Liu, 2006] has been shown to be equivalent to (2.22).

2.6.2 Energy Equation

Using similar techniques as in previous part, we can transform the energy equations to the same form (2.23) for all three models. The transformations become algebraically complicated due to the need to include the mass equation into them, but we attempt to spell out all the major steps so that the interested reader can reproduce our results.

First, for the fluid model we start with (2.7) and proceed as follows:

$$\begin{aligned}
& 0 \\
= & \left(\frac{\partial}{\partial t}+\mathbf{v}\cdot\nabla\right)s+\frac{5}{2qB^2}\mathbf{B}\cdot\nabla T\times\nabla\ln\eta \\
= & \frac{3}{2p}\left(\frac{\partial}{\partial t}+\frac{\mathbf{E}\times\mathbf{B}}{B^2}\cdot\nabla+\frac{\mathbf{B}\times\nabla p}{nqB^2}\cdot\nabla\right)p-\frac{5}{2n}\left(\frac{\partial}{\partial t}+\frac{\mathbf{E}\times\mathbf{B}}{B^2}\cdot\nabla+\frac{\mathbf{B}\times\nabla p}{nqB^2}\cdot\nabla\right)n \\
& +0\left(\frac{\partial}{\partial t}+\frac{\mathbf{E}\times\mathbf{B}}{B^2}\cdot\nabla+\frac{\mathbf{B}\times\nabla p}{nqB^2}\cdot\nabla\right)V+\frac{5}{2nqB^2V}\left(n\nabla T\times\nabla V+\frac{V}{n}\nabla p\times\nabla n\right)\cdot\mathbf{B} \\
= & -\frac{5}{2n}\left(\frac{\partial}{\partial t}+\frac{\mathbf{E}\times\mathbf{B}}{B^2}\cdot\nabla\right)n-\frac{5}{2V}\left(\frac{\partial}{\partial t}+\frac{\mathbf{E}\times\mathbf{B}}{B^2}\cdot\nabla\right)V-\frac{5}{2nqB^2V}\nabla p\times\nabla V\cdot\mathbf{B} \\
& +\frac{3}{2p}\left(\frac{\partial}{\partial t}+\frac{\mathbf{E}\times\mathbf{B}}{B^2}\cdot\nabla\right)p+\frac{5}{2V}\left(\frac{\partial}{\partial t}+\frac{\mathbf{E}\times\mathbf{B}}{B^2}\cdot\nabla\right)V+\frac{5}{2nqB^2V}\left(\nabla p+n\nabla T\right)\times\nabla V\cdot\mathbf{B} \\
= & \frac{3}{2pV^{5/3}}\left[\frac{\partial}{\partial t}\left(pV^{5/3}\right)+\left(\frac{\mathbf{E}\times\mathbf{B}}{B^2}\cdot\nabla\right)\left(pV^{5/3}\right)+\frac{1}{qB^2}\nabla\frac{p^2}{n}\times\nabla V^{5/3}\cdot\mathbf{B}\right] \qquad (2.35)
\end{aligned}$$

By multiplying $2pV^{5/3}/3$, we recover (2.23). Thus (2.7) has been shown equivalent to (2.7).

Moving on to the RCM, we start from the second moment equation in (2.31):

$$
\begin{aligned}
& 0 \\
= & \int_0^\infty d\lambda \lambda^{3/2} \left(\frac{\partial}{\partial t} + \mathbf{v}_D \cdot \nabla \right) f \\
= & \int_0^\infty d\lambda \lambda^{3/2} \left(\frac{\partial}{\partial t} + \frac{\mathbf{E} \times \mathbf{B}}{B^2} \cdot \nabla + \frac{\lambda \mathbf{B} \times \nabla V^{-2/3}}{qB^2} \cdot \nabla \right) f \\
= & \int_0^\infty d\lambda \lambda^{3/2} f \left[\frac{1}{n} \left(\frac{\partial}{\partial t} + \frac{\mathbf{E} \times \mathbf{B}}{B^2} \cdot \nabla \right) n + \frac{\lambda \mathbf{B} \times \nabla V^{-2/3} \cdot \nabla n}{nqB^2} \right. \\
& + \frac{2\lambda V^{-5/3}}{3T} \left(\frac{\partial}{\partial t} + \frac{\mathbf{E} \times \mathbf{B}}{B^2} \cdot \nabla \right) V \\
& \left. + \left(\frac{\lambda V^{-2/3}}{T^2} - \frac{3}{2T} \right) \left(\frac{\partial}{\partial t} + \frac{\mathbf{E} \times \mathbf{B}}{B^2} \cdot \nabla \right) T + \lambda \left(\frac{\lambda V^{-2/3}}{T^2} - \frac{3}{2T} \right) \frac{\mathbf{B} \times \nabla V^{-2/3} \cdot \nabla T}{qB^2} \right] \\
= & \int_0^\infty d\lambda \lambda^{3/2} f \left[\frac{1}{p} \left(\frac{\partial}{\partial t} + \frac{\mathbf{E} \times \mathbf{B}}{B^2} \cdot \nabla \right) p + \frac{5}{3V} \left(\frac{\partial}{\partial t} + \frac{\mathbf{E} \times \mathbf{B}}{B^2} \cdot \nabla \right) V \right. \\
& \left. + \frac{\lambda \mathbf{B} \times \nabla V^{-2/3}}{qB^2} \cdot \left(\frac{\nabla n}{n} + 2 \frac{\nabla T}{T} \right) \right] \\
= & \frac{1}{pV^{5/3}} \left(\frac{\partial}{\partial t} + \frac{\mathbf{E} \times \mathbf{B}}{B^2} \cdot \nabla \right) \left(pV^{5/3} \right) \left(\frac{3}{2} nTV^{5/3} \right) \\
& + \frac{1}{nT^2 qB^2} \nabla V^{-2/3} \times \nabla \left(nT^2 \right) \cdot \mathbf{B} \left(\frac{15}{4} nT^2 V^{7/3} \right) \\
= & \frac{3}{2} \frac{\partial \left(pV^{5/3} \right)}{\partial t} + \frac{3}{2} \left(\frac{\mathbf{E} \times \mathbf{B}}{B^2} \cdot \nabla \right) \left(pV^{5/3} \right) + \frac{3}{2qB^2} \nabla \frac{p^2}{n} \times \nabla V^{5/3} \cdot \mathbf{B}
\end{aligned}
\tag{2.36}
$$

which is the same as (2.23) except for the factor of 3/2.

In the average model, if f is a Maxwellian, then $S = 3nT^2/2$, and the energy transport equation (2.11) becomes:

$$
\begin{aligned}
0 & \\
= & \left(\frac{\partial}{\partial t}+\mathbf{u}\cdot\nabla\right)\Xi-\frac{4V^{2/3}}{9qB^2}\nabla V\times\left(\nabla S+\frac{9}{4}p\nabla T\right)\cdot\mathbf{B} \\
= & \frac{\partial\Xi}{\partial t}+\left(\frac{\mathbf{E}\times\mathbf{B}}{B^2}\cdot\nabla\right)\Xi-\frac{T}{qB^2}\mathbf{B}\times\nabla\ln V\cdot\nabla\left(pV^{5/3}\right) \\
& -\frac{4V^{2/3}}{9qB^2}\nabla V\times\left[\nabla\left(\frac{3}{2}nT^2\right)+\frac{9}{4}p\nabla T\right]\cdot\mathbf{B} \\
= & \frac{\partial\Xi}{\partial t}+\left(\frac{\mathbf{E}\times\mathbf{B}}{B^2}\cdot\nabla\right)\Xi-\frac{TV^{2/3}}{qB^2}\nabla V\times\nabla p\cdot\mathbf{B}-\frac{4V^{2/3}}{9qB^2}\nabla V\times\left(\frac{3T}{2}\nabla p+\frac{15p}{4}\nabla T\right)\cdot\mathbf{B} \\
= & \frac{\partial\Xi}{\partial t}+\left(\frac{\mathbf{E}\times\mathbf{B}}{B^2}\cdot\nabla\right)\Xi+\frac{5V^{2/3}}{3qB^2}T\nabla p\times\nabla V\cdot\mathbf{B}+\frac{5V^{2/3}}{3qB^2}p\nabla T\times\nabla V\cdot\mathbf{B} \\
= & \frac{\partial\Xi}{\partial t}+\left(\frac{\mathbf{E}\times\mathbf{B}}{B^2}\cdot\nabla\right)\Xi+\frac{1}{qB^2}\nabla\frac{p^2}{n}\times\nabla V^{5/3}\cdot\mathbf{B}
\end{aligned}
\tag{2.37}
$$

which is the same as (2.23).

2.7 Comparison of Fluid and Kinetic Approaches

We now proceed to look at the differences that these three formalisms imply for convection in the inner magnetosphere. Since the average model, when closed with the assumption of a Maxwellian, is equivalent to the fluid approach of Heinemann [1999], we will only consider the RCM and fluid approaches. Unfortunately, analytical solutions of equations (2.1), (2.3), (2.6), (2.7) seem difficult to construct. Previously, Heinemann and Wolf considered a one-dimensional case to contrast solutions of the RCM and fluid equations[70], and obtained approximate solutions in the fluid case. In this section, we first revisit that case but generalize the solution, and consider both an analytic linearized solution as in [Heinemann and Wolf, 2001] as well as a numerical case. We then present a somewhat more realistic two-dimensional example[10].

2.7.1 One-dimensional drift picture

For the one-dimensional test case[70], no electric field is present, so that transport is considered due to gradient/curvature drifts only. The magnetic field $\mathbf{B}$ is normal to the equatorial plane, and its magnitude is a function of x only: $\mathbf{B} = [0, 0, B(x)]$. Particles are assumed to mirror between two "plates" at $z = 0$ and $z = L$, so that the flux tube volume is L/B, and L is a constant distance. If the magnetic field is chosen as

$$B = \frac{a}{(x_m - x)^3} \tag{2.38}$$

then the drift velocity (2.1) for the RCM approach is:

$$\begin{aligned} \mathbf{v}_D &= \frac{\lambda \mathbf{B} \times \nabla V^{-2/3}}{qB^2} \\ &= \frac{\lambda}{qBL^{2/3}} \frac{d(B^{2/3})}{dx} \hat{y} \\ &= \frac{2\lambda}{qL^{2/3}a^{1/3}} \hat{y} \\ &= C_1 \lambda \hat{y} \end{aligned} \tag{2.39}$$

where

$$\begin{aligned} C_1 &= \frac{1}{qB} \frac{dV^{-2/3}}{dx} \\ &= \frac{2}{qa^{1/3}L^{2/3}} \end{aligned} \tag{2.40}$$

The plasma is assumed to consist of constant background density and pressure and a perturbation term that is initially of Gaussian shape:

$$\begin{aligned} n(y, t = 0) &= 1 + Ae^{-\frac{y^2}{\sigma^2}} \\ p(y, t = 0) &= 1 + Ae^{-\frac{y^2}{\sigma^2}} \end{aligned} \tag{2.41}$$

where A is the magnitude ratio of perturbation to background, σ is half-width of the initial Gaussian, and we assumed normalization $T(t = 0) = 1$. The distribution

function of the plasma is assumed to be Maxwellian initially:

$$f(\lambda, y, t = 0) = f_0(y)e^{-\lambda/\Lambda} \tag{2.42}$$

where $\Lambda = TV^{2/3}$ and $f_0(y)$ is given by (2.41).

The perturbations of density and pressure can be expressed as[70]:

$$\begin{aligned} \frac{\delta n}{n} &= A\frac{\int_0^\infty d\lambda\lambda^{1/2}e^{-\lambda/\Lambda}e^{-(y-\lambda C_1 t)^2/\sigma^2}}{\int_0^\infty d\lambda\lambda^{1/2}e^{-\lambda/\Lambda}} \\ \frac{\delta p}{p} &= A\frac{\int_0^\infty d\lambda\lambda^{3/2}e^{-\lambda/\Lambda}e^{-(y-\lambda C_1 t)^2/\sigma^2}}{\int_0^\infty d\lambda\lambda^{3/2}e^{-\lambda/\Lambda}} \end{aligned} \tag{2.43}$$

Given a choice of A,C_1,Λ, and σ, the integrals in (2.43) can be evaluated numerically as functions of time.

We now switch to finding the solution in the fluid case. Since there is no electric field and flux tube volume is independent of time, the mass and energy equations (2.22) and (2.23), written in terms of n and p, become:

$$\begin{aligned} \frac{\partial n}{\partial t} + \frac{1}{qB^2V}\nabla p \times \nabla V \cdot \mathbf{B} &= 0 \\ \frac{\partial p}{\partial t} + \frac{5}{3qB^2V}\nabla\frac{p^2}{n} \times \nabla V \cdot \mathbf{B} &= 0 \end{aligned} \tag{2.44}$$

To uncouple these two partial differential equations, we transform (2.44) to two equations such that each one has only one unknown function to solve which looks like $p^\alpha n^\beta$, by setting

$$\begin{aligned} \alpha &= 1 \\ \beta_\pm &= \frac{-5 \pm \sqrt{10}}{3} \\ k_\pm &= pn^{\beta_\pm} \end{aligned} \tag{2.45}$$

Then (2.44) can be written as:

$$\frac{\partial k_\pm}{\partial t} + \beta_\mp \frac{T}{qB^2V}\frac{dV}{dx}\frac{\partial k_\pm}{\partial y} = 0 \tag{2.46}$$

Define

$$\begin{aligned} C_2 &= \frac{T}{qBV}\frac{dV}{dx} \\ &= \frac{T}{qL}\left(-\frac{L}{B^2}\right)\frac{dB}{dx} \\ &= -\frac{3}{2}\frac{2}{qa^{1/3}L^{2/3}}TV^{2/3} \\ &= -\frac{3}{2}C_1\Lambda \end{aligned} \tag{2.47}$$

and "velocities" $v_\pm$ as

$$\begin{aligned} v_\pm &= \beta_\mp C_2 \\ &= \frac{-5\mp\sqrt{10}}{3}\frac{-3}{2}C_1\Lambda \\ &= \frac{5}{2}\left(1\pm\sqrt{\frac{2}{5}}\right)C_1\Lambda \end{aligned} \tag{2.48}$$

If the perturbation is small ($A \ll 1$), (2.46) can be linearized to yield the equations for the perturbations $\delta k_\pm$:

$$\left(\frac{\partial}{\partial t} + v_\pm\frac{\partial}{\partial y}\right)\delta k_\pm = 0 \tag{2.49}$$

The general solution of (2.49) is an arbitrary function of $y - v_\pm t$. Since the initial condition in our case are:

$$\begin{aligned} \left(\frac{\delta k_\pm}{k_\pm}\right)_0 &= \frac{-5\pm\sqrt{10}}{3}\left(\frac{\delta n}{n}\right)_0 + \left(\frac{\delta p}{p}\right)_0 \\ &= \frac{-2\pm\sqrt{10}}{3}\left(\frac{\delta n}{n}\right)_0 \\ &= \frac{-2\pm\sqrt{10}}{3}Ae^{-\frac{y^2}{\sigma^2}} \end{aligned} \tag{2.50}$$

We can write solutions for $\delta k_\pm$:

$$\begin{aligned} \frac{\delta k_\pm}{k_\pm} &= \frac{-2\pm\sqrt{10}}{3}Ae^{-\frac{(y-v_\pm t)^2}{\sigma^2}} \\ &= \frac{-2\pm\sqrt{10}}{3}A_\pm \end{aligned} \tag{2.51}$$

where $A_{\pm} \equiv Ae^{-\frac{(y-v_{\pm}t)^2}{\sigma^2}}$ are two moving Gaussian peaks. Therefore, the solutions for number density and pressure can be obtained from:

$$\begin{aligned} \frac{\delta n}{n} &= \frac{3}{2\sqrt{10}}\left(\frac{\delta k_+}{k_+} - \frac{\delta k_-}{k_-}\right) \\ \frac{\delta p}{p} &= \frac{\sqrt{5}+\sqrt{2}}{2\sqrt{2}}\frac{\delta n}{n}\frac{\delta k_+}{k_+} - \frac{\sqrt{5}-\sqrt{2}}{2\sqrt{2}}\frac{\delta k_-}{k_-} \end{aligned} \tag{2.52}$$

which is equivalent to previous results[70]. The nature of the solutions (2.52) becomes clear if we write solutions as functions of $A_{\pm}$. The initial perturbations of density and pressure decompose with time into two Gaussian-shaped peaks drifting with different speeds:

$$\begin{aligned} \frac{\delta n}{n} &= \frac{\sqrt{5}-\sqrt{2}}{2\sqrt{5}}A_+ + \frac{\sqrt{5}+\sqrt{2}}{2\sqrt{5}}A_- \\ \frac{\delta p}{p} &= \frac{1}{2}A_+ + \frac{1}{2}A_- \end{aligned} \tag{2.53}$$

The temperature perturbation and entropy follow as:

$$\begin{aligned} \frac{\delta T}{T} &= \frac{\delta p}{p} - \frac{\delta n}{n} \\ &= \frac{1}{\sqrt{10}}A_+ - \frac{1}{\sqrt{10}}A_- \\ \delta s &= \frac{3}{2}\frac{\delta p}{p} - \frac{5}{2}\frac{\delta n}{n} \\ &= \frac{-2+\sqrt{5}}{2\sqrt{2}}A_+ - \frac{2+\sqrt{5}}{2\sqrt{2}}A_- \end{aligned} \tag{2.54}$$

In principle, linearization is necessary to obtain analytical solutions (2.52) only. To verify our approximation, and also to generalize the analytical case, we solve (2.44) numerically without assuming $A \ll 1$. The three sets of solutions (RCM, analytic solution for the fluid case with linearization, and numerical solution for the fluid case), are presented in figures 2.1-2.3. For simplicity, we chose $C_1 = \sigma = 1$. In analytical case, we also have $\Lambda = 1$,$C_2 = -3/2$. We first take up the case of a small perturbation

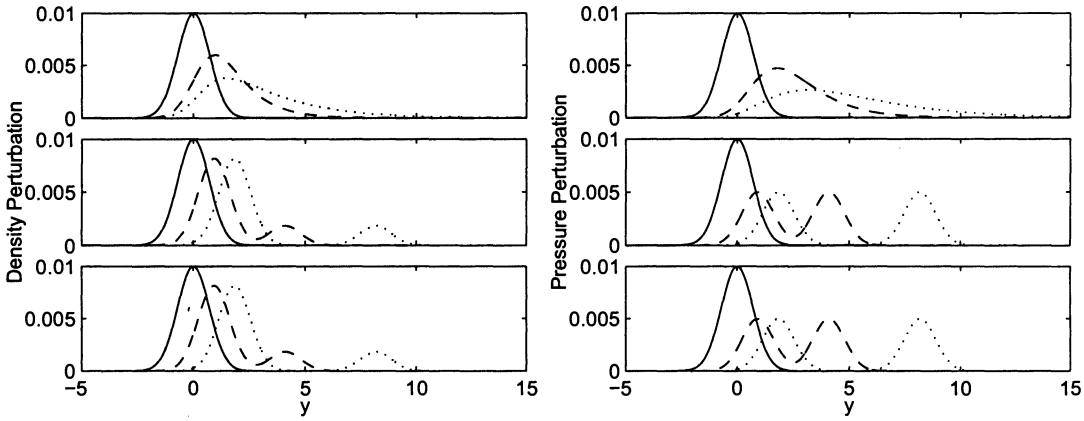

Figure 2.1 : Solutions for density (left) and pressure (right) perturbations for times $t = 0$ (solid), 1 (dashed), and 2 (dotted) plotted for the 1-D case in the RCM model (top), the fluid model obtained analytically (middle), and the fluid model (bottom) obtained numerically. $A = 0.01$. Figure from [10].

($A = 0.01$). Comparison between the middle and bottom panels of Figure 2.1 shows no discernable differences between the analytical solution and the numerical solution in the fluid case. The behavior of the fluid case solution and the RCM solution (top panels of Figure 2.1) are exactly the same as those published by Heinemann and Wolf [2001]. The fluid and kinetic solutions behave very differently, of course: the RCM solution shows a spread of the initially Gaussian-shaped perturbation. Physically, the spread is straightforward to understand: faster particles drift faster, while slower ones lag behind, resulting in a gradual spreading in time.

The time dependence of the fluid solution, displayed in the second and third rows in Figure 2.1 and restated in Figure 2.2, is remarkably different: an initial Gaussian-shaped perturbation separates into two Gaussian-shaped peaks drifting at different speeds. This difference, pointed out by Heinemann and Wolf [2001], is what led us to re-derive analytical solutions in the fluid case[10]. For $A = 0.01$, we find

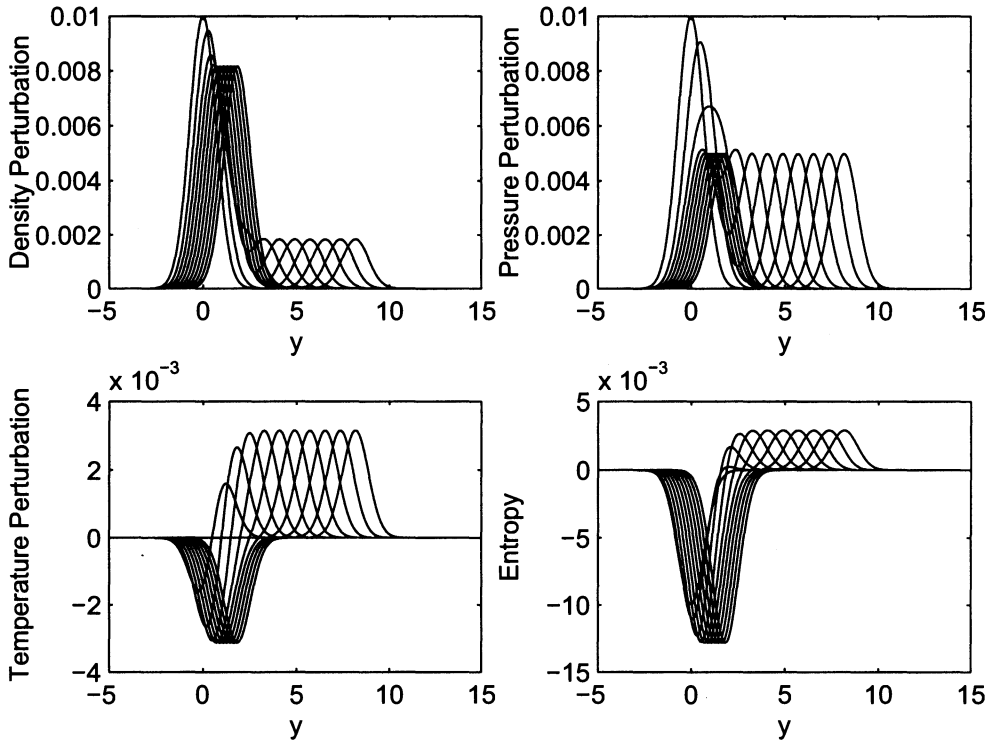

Figure 2.2 : Numerical solutions for the fluid 1-D case are shown for density perturbation (top left), pressure perturbation (top right), temperature perturbation (bottom left), and entropy (bottom right) as functions of time from $t = 0$ to $t = 2$ with a time step of 0.2. $A = 0.01$. Figure from [10].

exactly the same behavior, thus providing an independent verification of previous result[70]. Figure 2.2 plots time dependence of temperature which deviates from the initial background value but in the opposite sense for the two peaks. The magnitudes are small (10^{-3}) and consistent with our first-order perturbation theory for the analytical solution. Temperature plots indicate that the faster drifting peak is hotter compared to the initial perturbation, while the slower peak is colder.

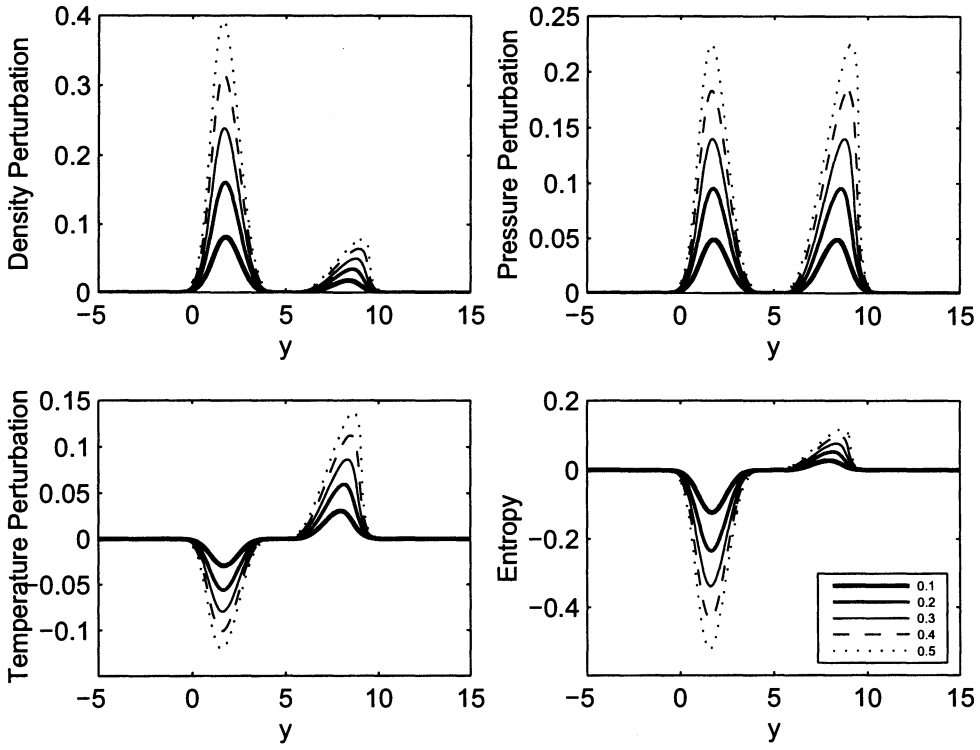

Figure 2.3 : Numerical solutions for the 1-D fluid case at $t = 2$ for increasingly large levels of the perturbation amplitude A (0.1, 0.2, 0.3, 0.4, and 0.5). Quantities shown are perturbations of density (top left), pressure (top right), temperature (bottom left), and entropy (bottom right). Figure from [10].

Figure 2.3 shows how the four quantities (2.53),(2.54) change with increasing A, at a later time $t = 2$. Two new prominent features of the numerical solution are disappearance in the symmetry of the peaks, and a gradual steepening on the faster-moving peak that results in formation of what appears to be a shock front. Temperature perturbations are no longer small.

2.7.2 Two-dimensional drift picture

The behavior of the solution of the fluid model in the one-dimensional case found by [Heinemann and Wolf, 2001], generalized and confirmed in this work, is far from intuitive. One possibility is that it might be an artifact of the simplifications leading to a one-dimensional "made-up" magnetosphere. We thus construct a more general and slightly more realistic-looking two-dimensional example solution[10]. We assume that the magnetic field has dipolar geometry, is in the z-direction in the equatorial plane, and is given by:

$$B = \frac{B_0}{L^3} \tag{2.55}$$

and also that the flux-tube volume varies as (assuming $L \gg 1$):

$$V = V_0 L^4 \tag{2.56}$$

where $L = \sqrt{x^2 + y^2}$, scaled by Earth's radius, R_E. Now L is L-shell value but not a constant distance as in the one-dimensional case. Assume that the electric field is no longer zero but is uniform and is in the y-direction. We solve both the fluid and the RCM equations in the x-y coordinate system intended to represent the magnetospheric equatorial plane in the GSM coordinate system. The region of interest is $(x, y) \in (-22, -2; -10, 10)$, where we use a rectangular uniform grid with steps $\Delta x = \Delta y = 0.1$, to numerically solve the equations. Due to the equivalence shown in previous section, we solve equations (2.22)-(2.23) for the fluid case.

The parameters are chosen as similar as possible to the one-dimensional case. In this case, we prescribe the problem not in terms of p and n but in terms of η and Ξ. We assume that initially there is a background plasma population with uniform $\eta_0 = 1$, $\Xi_0 = 1$. Since we treat this problem numerically, we go ahead and assume there is a uniform electric field in the y-direction $E = 10$, particle charge $q = 0.04$,

$R_E = 1$, $B_0 = 10^4$, and $V_0 = 10^{-4}$. The initial condition is the background plus a Gaussian-shaped blob of plasma centered at $(x_0, y_0) = (-10, 0)$ with half-width $\sigma = 1$:

$$\begin{aligned} \eta(x, y, t = 0) &= 1 + Ae^{-(x-x_0)^2-(y-y_0)^2} \\ \Xi(x, y, t = 0) &= 1 + Ae^{-(x-x_0)^2-(y-y_0)^2} \end{aligned} \tag{2.57}$$

Given the initial conditions (2.57) and the dipole-type magnetic field (2.55)-(2.56), we numerically integrate the fluid equations (2.22)-(2.23) forward in time using the standard 4th-order Runge-Kutta method.

Our results for the fluid case are summarized in figures 2.4-2.7. Figure 2.4 displays time evolution of density and pressure perturbations for the case of small $A = 0.01$. The solution behaves in essentially the same manner as the one-dimensional case we considered previously: the initial peak separates into two peaks with different moving speed. Both peaks maintain their separate shapes while drifting apart. The magnitudes of the peaks are comparable in terms of pressure but the faster-drifting density peak is much lower than the slower-drifting density peak. Contrast this with Figure 2.5, which shows the same solutions for the case of large $A = 0.5$. While the initial peak separates into two as in the two-dimensional case of $A = 0.01$, the peaks no longer remain symmetric. In fact, the faster-drifting peak has its "front" steepening with time and forming what might appear as a shock front.

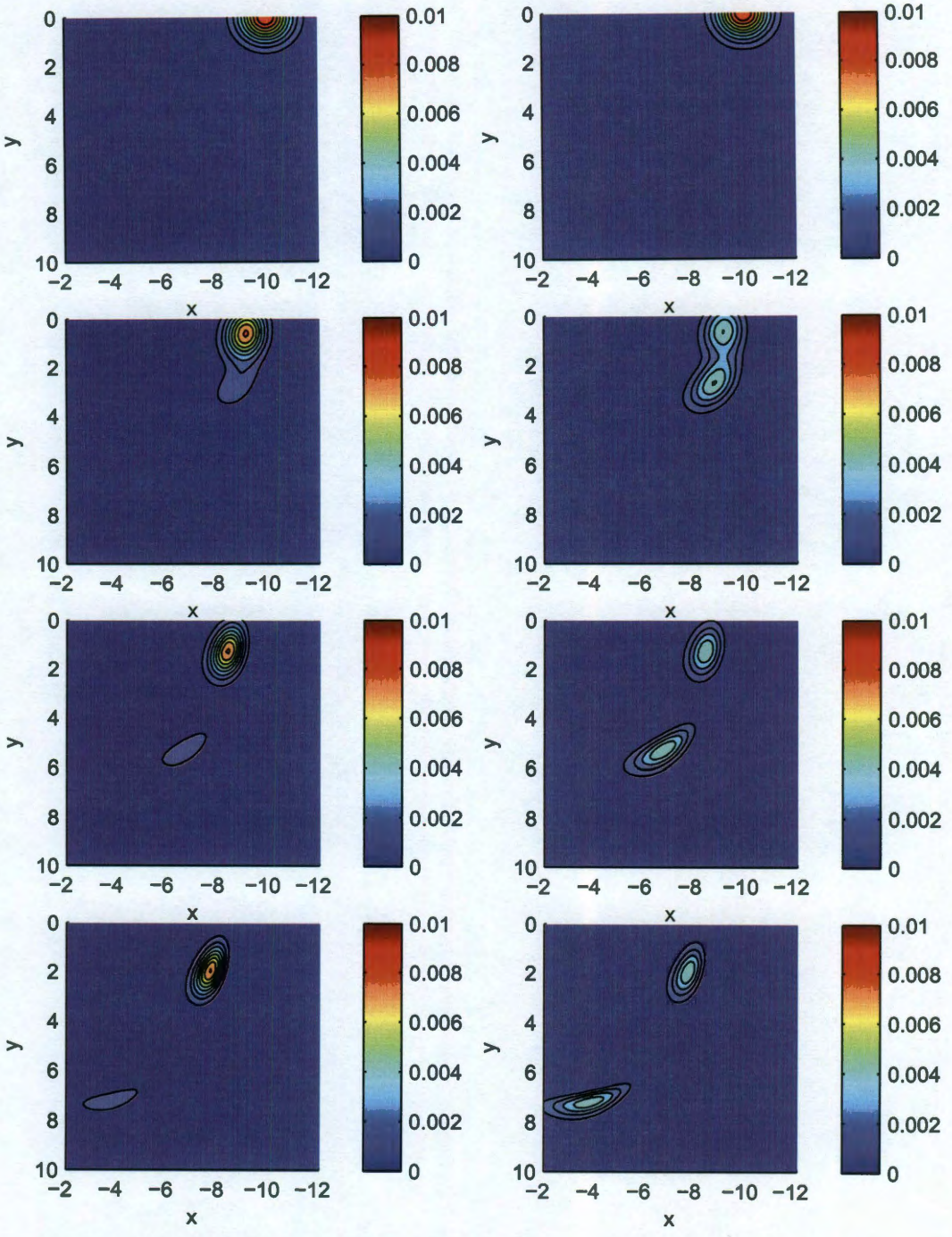

Figure 2.4 : Fluid solutions for the 2-D case of density (left column) and pressure (right column) perturbations for the case of a small initial perturbation amplitude $A = 0.01$. Time increases top to bottom as $t = 0, 1, 2[10]$.

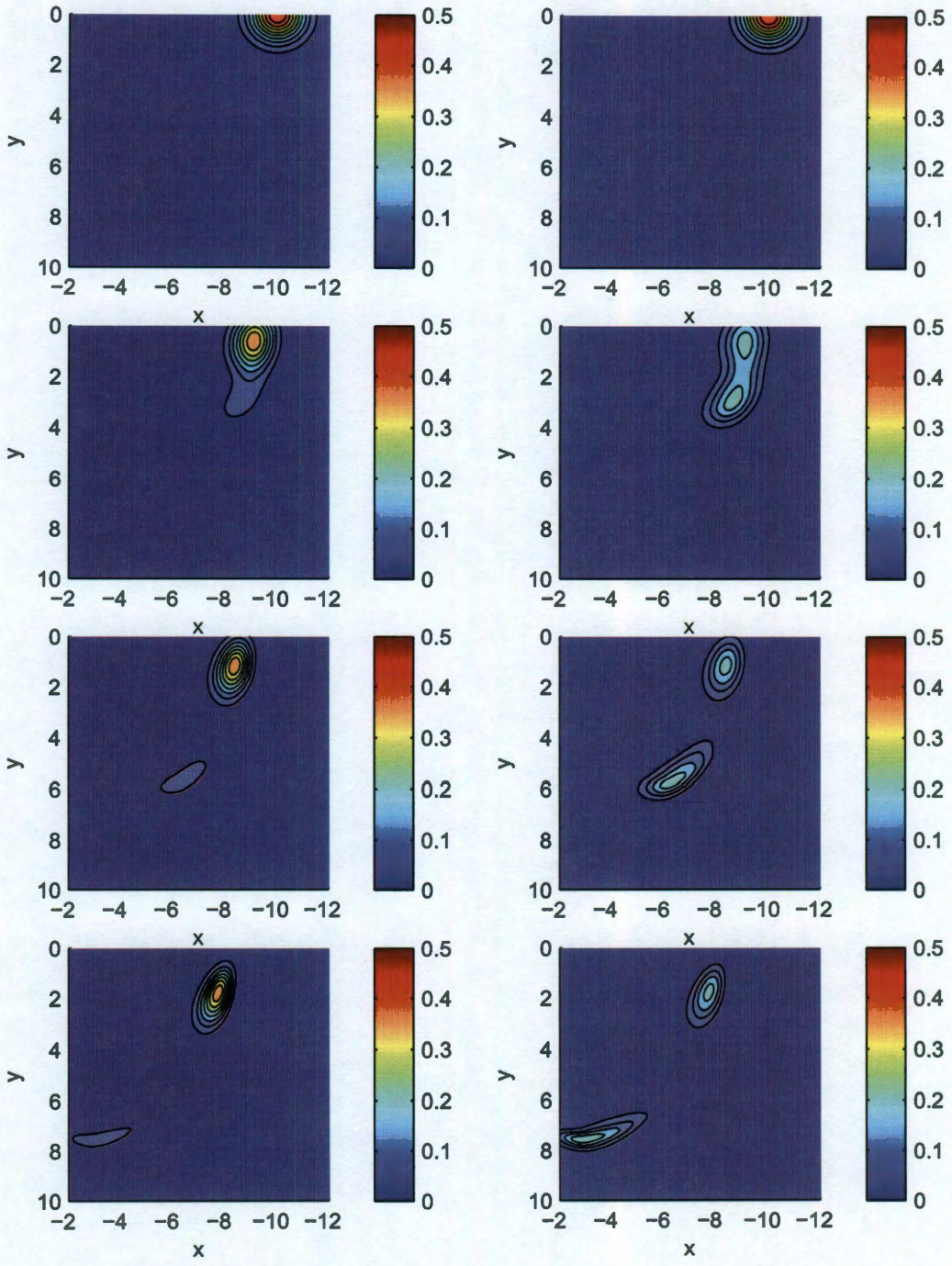

Figure 2.5 : Fluid solutions for the 2-D case of density (left column) and pressure (right column) perturbations for the case of a small initial perturbation amplitude $A = 0.5$. Time increases top to bottom as $t = 0, 1, 2$.[10]

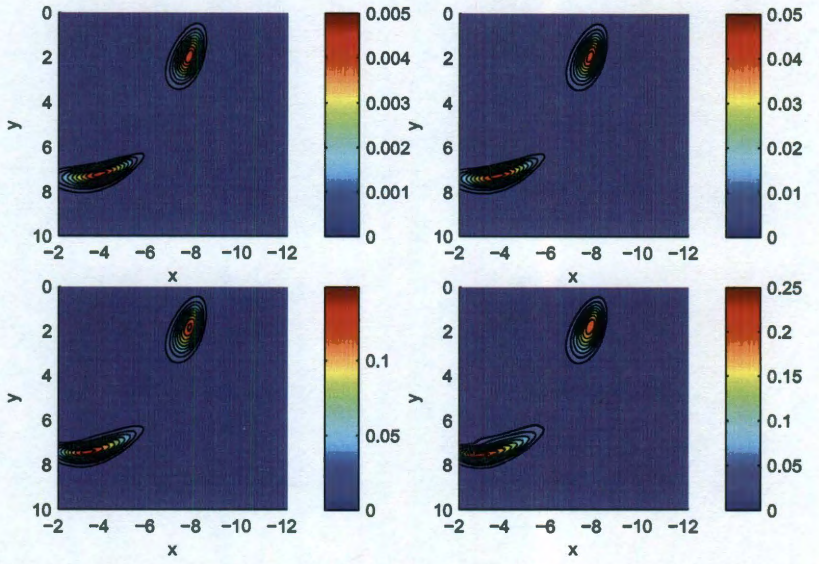

Figure 2.6 : Fluid 2-D solutions for pressure perturbations at $t = 3$ for different values of $A = 0.01$ (top left), 0.1 (top right), 0.3 (bottom left), and 0.5 (bottom right)[10].

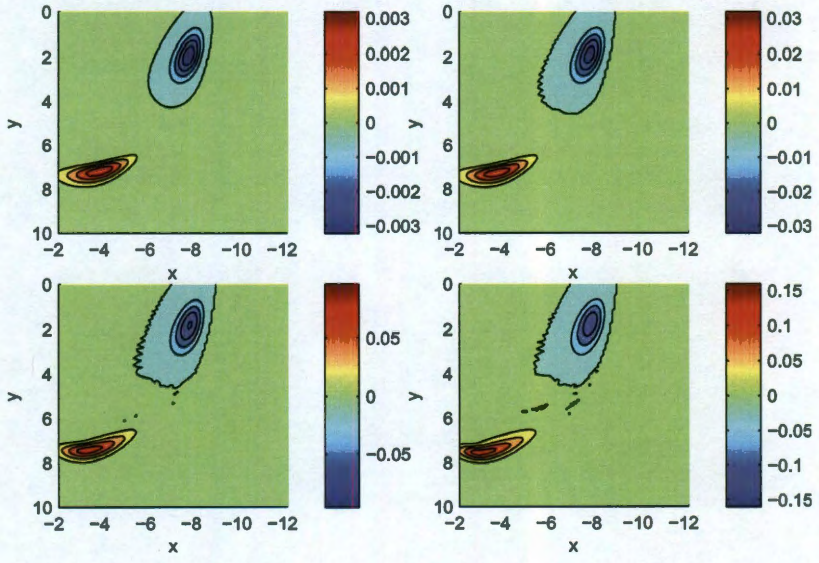

Figure 2.7 : Fluid 2-D solutions for temperature perturbations at $t = 3$ for different values of $A = 0.01$ (top left), 0.1 (top right), 0.3 (bottom left), and 0.5 (bottom right)[10].

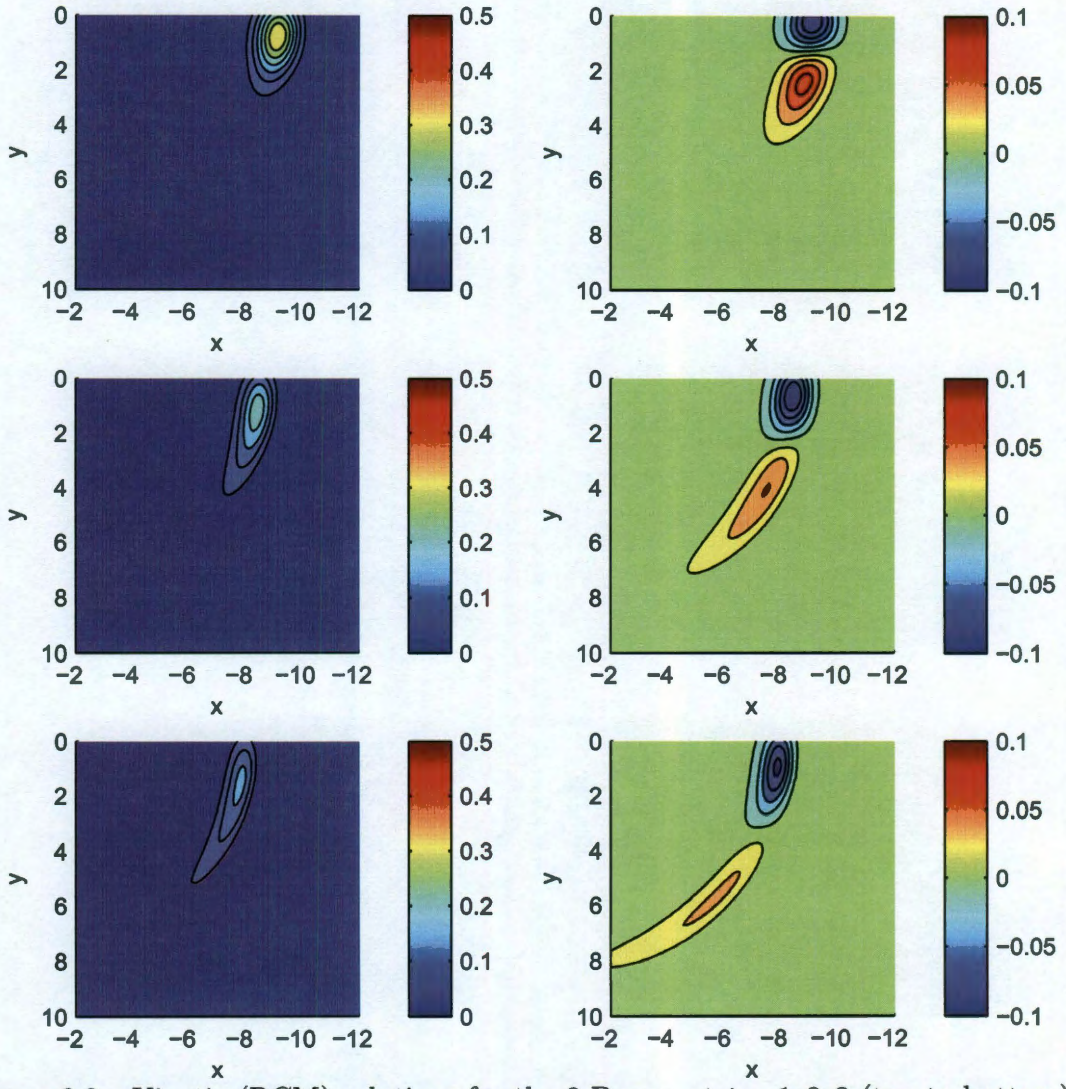

Figure 2.8 : Kinetic (RCM) solutions for the 2-D case at $t = 1, 2, 3$ (top to bottom). Left column is density perturbations, right column is temperature perturbations[10].

This highly non-linear effect becomes more obvious in Figure 2.6 showing the "fully-developed" ($t = 3$) solutions for pressure perturbations, for four increasing values of A. As the two peaks drift, the leading peak becomes steeper and steeper on its "front" and also somewhat "thinner" in the radial direction partly due to the

electric field. Parameters are chosen so that the gradient/curvature drift velocity dominates the $\mathbf{E} \times \mathbf{B}$ drift velocity as in the inner magnetosphere. Adding a constant electric field to the numerical solution indicates that the character of the solutions do not depend on the assumption of no electric field.

Figure 2.7 is a plot of the temperature perturbation in the same format, and should be compared with the appropriate curves for the one-dimensional case presented earlier. Again, we observe that the faster-drifting peak is hotter and the lagging peak is colder. As A increases, the steepening of the leading peak on its leading edge increases[10].

As in the one-dimensional case, we contrast these fluid solutions with those obtained for the RCM theory. Obtaining solutions in the kinetic case is completely analogous to the one-dimensional case in that the distribution function f at an arbitrary time t can be mapped to f at $t = 0$ along drift trajectories. We choose to solve the case with $A = 0.5$. The distribution function was discretized in terms of λ and 201 levels were used. Values of density and pressure perturbations were obtained by taking the appropriate moments of the distribution function. Density and temperature perturbations are presented for three times 1, 2, and 3 in Figure 2.8 in the left column and right column, respectively. The initial conditions are the same as in the fluid case. The properties of these solutions are physically easy to understand. Just like in the one-dimensional case, the initial Gaussian-shaped blob of plasma will gradient/curvature drift roughly in the azimuthal direction around the Earth, gradually spreading, with higher-energy particles leading and the lower-energy particles trailing. The double-peaked structure of the temperature perturbation is due to our specification of the initial conditions and the dipole geometry, with slower drifting particles being colder and faster drifting ones hotter.

2.8 Discussion

Inspired by a new theoretical model[78] for describing hot plasma convection in the inner magnetosphere of the Earth, we presented our analysis of this and the other two such previously-published models, kinetic and two-fluid. For the case of a Maxwellian distribution function, we proved that the three models:

1. Maxwellianized RCM, which assumes that some collisional or wave-particle interactions not only keep the distribution function isotropic (as in ordinary RCM) but also maintain local thermodynamic equilibrium,

2. Peymirat and Fontaine's fluid equations with the Braginskii heat flux added

3. Liu's energy and mass conservation equations for the case of a Maxwellian distribution

are equivalent.

The equivalence of 1 and 3, together with our comments regarding proper closure of average model, serves as proof that it is not really a new model but is simply a version of 2, at least for the case of a Maxwellian distribution function. One might argue that if the average model were closed with the assumption of, say, kappa-shaped distribution function, it would be in better agreement with the kinetic model. However, when we repeated our one-dimensional case for the two models and the kappa-shaped ($\kappa = 6$) distribution functions, we found essentially the same results.

By verifying equivalence of 1 and 2, we performed a verification of the Heinemann and Wolf calculations. We also verified the conclusions of the specific one-dimensional example given by Heinemann and Wolf, and we extended it to the non-linear case. To better understand the implications of that one-dimensional case, we constructed

solutions of a new and more realistic two-dimensional case in the dipolar magnetic field geometry.

The development of the shock wave in both one- and two-dimensional cases is an interesting new and unexpected feature. Physically, one might interpret this phenomenon in a way similar to formation of shock waves in gases. Indeed, for the one-dimensional case, the speed of the blob is proportional to temperature (equation 2.48). Since the temperature is enhanced in the center of the leading blob, in the nonlinear regime it is possible for the center to travel faster than the leading edge, forming the predicted steepening. The decrease in temperature in the trailing blob, in the same way, should cause a slowing of the center of the trailing blob. The implication of it is that a fluid code that describes the inner magnetosphere can be expected to form shock waves. The calculations should serve as a caution to fluid modelers who might wish to include gradient/curvature drift effects in the inner magnetosphere by adding appropriate terms (equation 2.4) to fluid equations: the fluid solutions for a drifting blob of plasma look completely different from the solutions obtained using RCM-type drift equations.

There is an implicitly requirement for the Maxwellization of the RCM in this chapter. Since the distribution function in kinetic models is usually more complex than a simple expression, the time scale of the Maxwellization must be shorter than the typical bounce period so that the plasma with different energy arriving at certain flux tube would redistributed to a Maxwellian. To show the implication of the Maxwellization, we defined a function as

$$u(k) = \frac{4\pi\sqrt{2}}{m^{3/2}} \int_0^\infty d\lambda \lambda^{k+1/2} f(\lambda, x, t) \tag{2.58}$$

where

$$f(\lambda, \mathbf{x}, t) = n\left(\frac{m}{2\pi T}\right)^{3/2} e^{-\frac{\lambda}{TV^{3/2}}} \tag{2.59}$$

We obtain a property

$$u(k) = \left(k + \frac{1}{2}\right) TV^{2/3} u(k-1) \tag{2.60}$$

from integration by part. Then the first several values of this function are

$$\begin{aligned} u(0) &= nV \\ u(1) &= \frac{3}{2} nTV^{5/3} \\ u(2) &= \frac{15}{4} nT^2 V^{7/3} \\ u(3) &= \frac{105}{8} nT^3 V^3 \end{aligned} \tag{2.61}$$

Notice that the derivatives of f could be expressed as

$$\frac{\partial f}{\partial n} = f\frac{1}{n} \tag{2.62}$$

$$\frac{\partial f}{\partial V} = f\frac{2\lambda V^{-5/3}}{3T} \tag{2.63}$$

$$\frac{\partial f}{\partial T} = f\left(\frac{\lambda V^{-2/3}}{T^2} - \frac{3}{2T}\right) \tag{2.64}$$

Since the continuity equation gives

$$0 = \left(\frac{\partial}{\partial t} + \mathbf{v}_D \cdot \nabla\right) f = \left(\frac{\partial}{\partial t} + \mathbf{v}_E \cdot \nabla\right) f + \frac{\lambda \mathbf{B} \times \nabla V^{-2/3}}{qB^2} \cdot \nabla f \tag{2.65}$$

so the two terms in the right hand side have the same magnitude but different sign. Then a general form of transport equation looks like

$$\begin{aligned}
&\left(\frac{\partial}{\partial t}+\mathbf{v}_E\cdot\nabla\right)u(k)\\
=&\left(\frac{\partial}{\partial t}+\mathbf{v}_E\cdot\nabla\right)\frac{4\pi\sqrt{2}}{m^{3/2}}\int_0^\infty d\lambda\lambda^{k+1/2}f\\
=&\frac{4\pi\sqrt{2}}{m^{3/2}}\int_0^\infty d\lambda\lambda^{k+1/2}\left(\frac{\partial}{\partial t}+\mathbf{v}_E\cdot\nabla\right)f\\
=&-\frac{4\pi\sqrt{2}}{m^{3/2}}\int_0^\infty d\lambda\lambda^{k+3/2}\frac{\mathbf{B}\times\nabla V^{-2/3}}{qB^2}\cdot\nabla f\\
=&\frac{4\pi\sqrt{2}}{m^{3/2}}\int_0^\infty d\lambda\lambda^{k+3/2}\frac{1}{qB^2}\nabla f\times\nabla V^{-2/3}\cdot\mathbf{B}\\
=&\frac{1}{qB^2}\nabla u(k+1)\times\nabla V^{-2/3}\cdot\mathbf{B}
\end{aligned}\tag{2.66}$$

for $k=0$ and $k=1$, these equation comes to the mass and energy equations of those fluid models. Comparing the two sides of the equation, we get

$$\begin{aligned}
0=&\left(\frac{\partial}{\partial t}+\mathbf{v}_E\cdot\nabla\right)u(k)-\frac{1}{qB^2}\nabla u(k+1)\times\nabla V^{-2/3}\cdot\mathbf{B}\\
=&\left(\frac{\partial}{\partial t}+\mathbf{v}_E\cdot\nabla\right)u(k)-\frac{1}{qB^2}\left(k+\frac{3}{2}\right)\nabla\left[TV^{2/3}u(k)\right]\times\nabla V^{-2/3}\cdot\mathbf{B}\\
=&\frac{4\pi\sqrt{2}}{m^{3/2}}\int_0^\infty d\lambda\lambda^{k+1/2}\left[\left(\frac{\partial}{\partial t}+\mathbf{v}_E\cdot\nabla\right)f+\left(\frac{2}{3}k+1\right)\frac{1}{qB^2V}\nabla\left(Tf\right)\times\nabla V\cdot\mathbf{B}\right]\\
=&\frac{4\pi\sqrt{2}}{m^{3/2}}\int_0^\infty d\lambda\lambda^{k+1/2}f\left\{\frac{1}{n}\left(\frac{\partial}{\partial t}+\mathbf{v}_E\cdot\nabla\right)n+\frac{2\lambda}{3TV^{5/3}}\left(\frac{\partial}{\partial t}+\mathbf{v}_E\cdot\nabla\right)V\right.\\
&+\left(\frac{\lambda}{T^2V^{2/3}}-\frac{3}{2T}\right)\left(\frac{\partial}{\partial t}+\mathbf{v}_E\cdot\nabla\right)T\\
&\left.\left(\frac{2}{3}k+1\right)\frac{1}{qB^2V}\left[\nabla T+T\frac{\nabla n}{n}+T\left(\frac{\lambda}{T^2V^{2/3}}-\frac{3}{2T}\right)\nabla T\right]\times\nabla V\cdot\mathbf{B}\right\}\\
=&u(k)\left[\frac{1}{n}\left(\frac{\partial}{\partial t}+\mathbf{v}_E\cdot\nabla\right)n+\left(\frac{2}{3}k+1\right)\frac{1}{V}\left(\frac{\partial}{\partial t}+\mathbf{v}_E\cdot\nabla\right)V+\frac{k}{T}\left(\frac{\partial}{\partial t}+\mathbf{v}_E\cdot\nabla\right)T\right.\\
&\left.+\left(\frac{2}{3}k+1\right)\frac{1}{qB^2V}\frac{T}{n}\nabla n\times\nabla V\cdot\mathbf{B}+\left(\frac{2}{3}k+1\right)\frac{1}{qB^2V}\left(k+1\right)\nabla T\times\nabla V\cdot\mathbf{B}\right]
\end{aligned}$$

The summation of the terms in the bracket should be zero. Since k is an arbitrary non-negative integer, only the last term contains nonlinear term and thus should

vanish.

$$\nabla T \times \nabla V \cdot \mathbf{B} = 0 \tag{2.67}$$

Because the gradient of flux tube volume is always normal to the magnetic field, so the temperature gradient is in the plane determined by flux tube volume gradient and the magnetic field. On the other hand, if the density and pressure keep the same along the magnetic field lines, then so does the temperature. The temperature gradient must be normal to the magnetic field line as well. So it implies that the temperature gradient and flux tube volume gradient are parallel, or antiparallel with each other. If the magnetic field is dipolar, then the flux tube volume gradient is in radial direction. The temperature contour would be concentric circles. Since this is generally the case, there is an extra term in the bracket when $k = 1$, which implies that the Maxwellization violates the energy transport equation. When the temperature gradient is westward, the particle gains energy and becomes faster which is consistent with the shock waves observed in our numerical tests.

If the relation 2.67 holds, we can put it back to energy equation and get a diamagnetic drift term in that fluid type equation.

$$\begin{aligned} 0 &= \frac{\partial \Xi}{\partial t} + \frac{\mathbf{E} \times \mathbf{B}}{B^2} \cdot \nabla \Xi + \frac{1}{qB^2} \nabla \frac{p^2}{n} \times \nabla V^{5/3} \cdot \mathbf{B} \\ &= \frac{\partial \Xi}{\partial t} + \frac{\mathbf{E} \times \mathbf{B}}{B^2} \cdot \nabla \Xi + \frac{T}{qB^2} \nabla p \times \nabla V^{5/3} \cdot \mathbf{B} \\ &= \frac{\partial \Xi}{\partial t} + \frac{\mathbf{E} \times \mathbf{B}}{B^2} \cdot \nabla \Xi + \frac{1}{nqB^2} \nabla p \times \nabla \left(p V^{5/3} \right) \cdot \mathbf{B} \\ &= \frac{\partial \Xi}{\partial t} + \frac{\mathbf{E} \times \mathbf{B}}{B^2} \cdot \nabla \Xi + \frac{\mathbf{B} \times \nabla p}{nqB^2} \cdot \nabla \Xi \end{aligned} \tag{2.68}$$

So the entropy parameter, $pV^{5/3}$ is conserved along the drift path and no heat flux term is enrolled.

Chapter 3

Rice Convection Model

A broad goal of magnetospheric physics is to understand the dynamical processes that occur in the Earth's magnetosphere. The RCM, developed over 40 years, is one of the best theoretical tools of exploring the physics in inner magnetosphere region. The RCM is a multi-fluid physical model for the reason that different particle populations of the inner magnetosphere cannot be treated as a single fluid because of the spread of energy, and its electromagnetic coupling to the ionosphere. The RCM self-consistently computes particle drifts, field-aligned currents and electric fields. It treats the three dimensional coupling problem as a pair of two dimensional problems, one in the equatorial plane and the other in the ionosphere. These two regions are connected by the magnetic field mapping. This chapter will discuss the model in detail including the assumptions, equations, and the structure of the code following the running procedure.

3.1 Assumptions

The RCM deals with the Earth's inner and middle magnetosphere. With regard to the dayside of the magnetosphere, it considers the region earthward and equatorward of the magnetopause and its associated boundary layers[40]. With regard to the nightside, it considers the inner part of the plasma sheet. Theoretical considerations determine the limits of the modeling region. The boundaries of the modeling region

are all magnetic-field aligned since the theory treats each magnetic field line and the particles on it as a discrete entity[40].

The theory and idea of the RCM is based on the assumption that the inertial term

$$\rho\frac{d\mathbf{v}}{dt} = (\frac{\partial}{\partial t} + \mathbf{v}\cdot\nabla)\mathbf{v} \tag{3.1}$$

in the MHD momentum equation can be neglected. This limit is applicable to subsonic, slow-flow region of the magnetosphere. It allows us to separate the problem of magnetospheric convection from the problem of the propagation of MHD waves in the magnetosphere. It greatly simplifies the basic equation of magnetosphere-ionosphere electrical coupling and it reduces the instability problems involved in numerical solution of the equations. The slow-flow part of the plasma sheet corresponds to middle magnetosphere. The inner magnetosphere refers to trapped-radiation belts and plasmasphere. The same region contains a high density of low-energy plasmaspheric particles that co-rotate with the Earth, and also a much lower density of energetic Van-Allen belt particles which mainly gradient/curvature drift around the Earth. The assumption implies that there is no wave-particle interaction involved and the magnetic field is force balanced.

For particles in the 100 eV to 100 keV range, three types of motion occur on three different time scales. The gyro motion around the magnetic field line is the fastest which is the advantage of using guiding center drift model instead of purely kinetic model. In the slow-flow region, where the drift velocity is defined to be small compared to the fast-mode speed, or the magnetosonic speed, the bounce period is much smaller than the drift period for any particle whose thermal velocity is greater than, or comparable to, the fast-mode speed.

The fortunate wide separation of the gyro, bounce, and drift time scales allows the convenient use of simple adiabatic invariant. After taking the bounce average

drift velocity, it could shown that η, the number of particles per unit magnetic flux, remains constant along the drift path of a particle.

Another convenient approximation is the isotropic pitch angle distribution. It is a very elegant approximation, because it makes the distribution function describing particles on a given field line as a function only of energy and not of either pitch angle or location on the field lines[40].

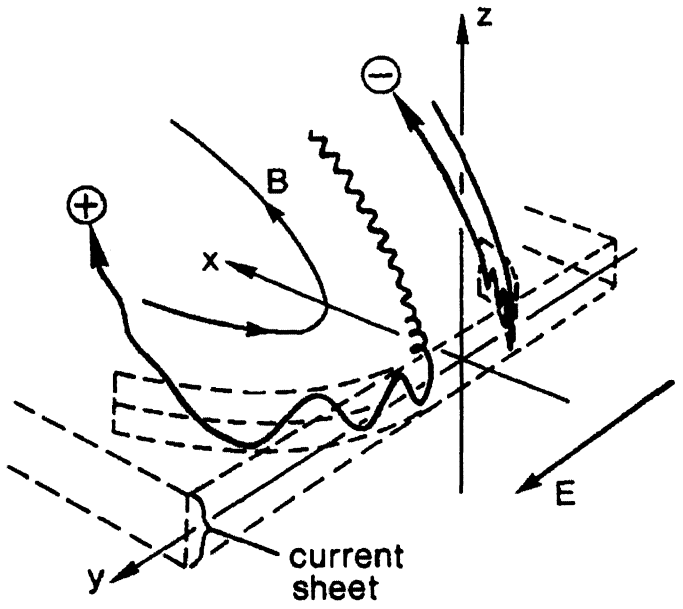

Figure 3.1 : Schematic illustration of electrons' and ions' orbits near the center of the tail current sheet whiere the curvature of the field line is comparable to the ion gyroradius[11].

Some wave-particle interactions could elastically scatter electron pitch angle on a time scale short compared to a drift time. Chaotic behavior is probably the main mechanism for plasma sheet ions. As shown in Figure 3.1, the ion gyro radius in the equatorial plane is larger than the thickness of the current sheet. Neither the first nor the second adiabatic invariant is conserved[7]. The chaotic motion keeps the ion

distribution isotropic. This approximation is reasonable for the plasma sheet and consistent with observations there. If no loss of heat and particles is considered, then λ, is constant along a drift path. The validity of bounce-averaged gradient/curvature drift relies on a slowly varying magnetic-field configuration, as well as time-independent magnetic fields. The change of electric field must be slow as well so that the electric field on the ionosphere could be represented by a scalar potential according to the Faraday's law.

3.2 Logic Diagram

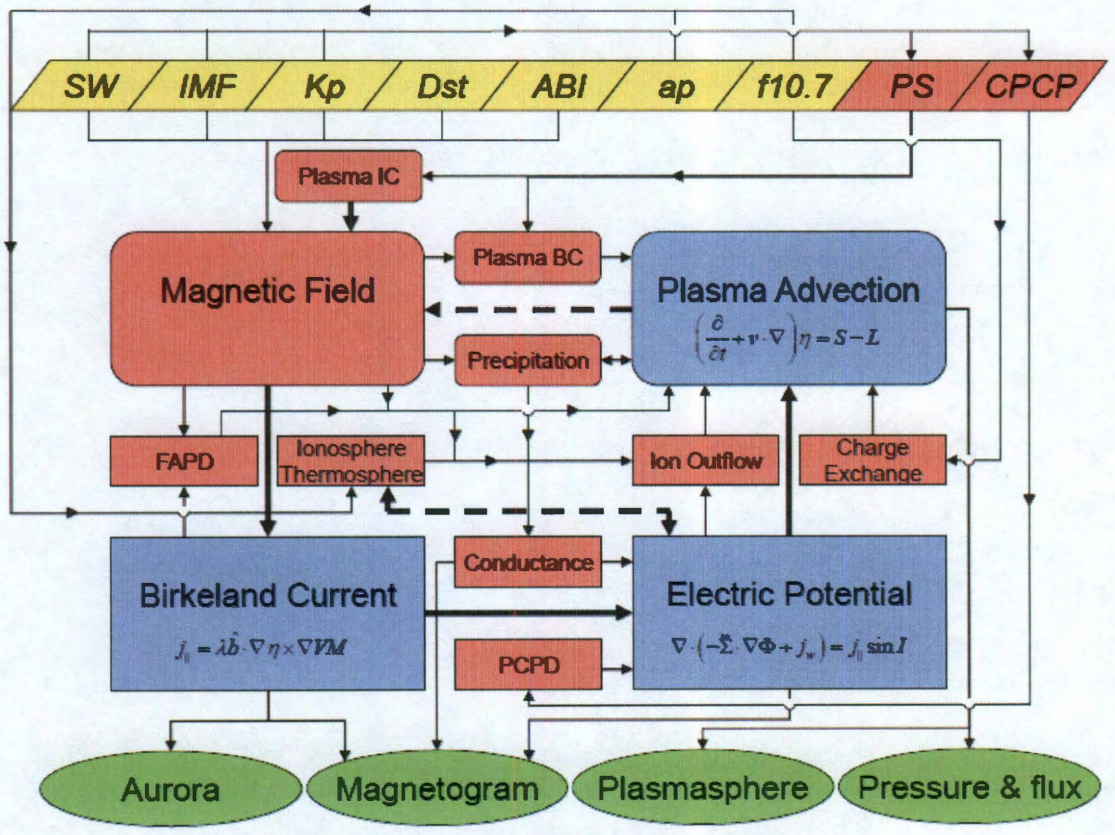

Figure 3.2 : RCM calculation diagram.

RCM equations and numerical methods have been chosen for accurate treatment of the inner magnetosphere, including the flow of electric currents along magnetic field lines to and from the conducting ionosphere. The RCM computes plasma distribution, Birkeland currents and associated electric fields self-consistently, assuming perfectly conducting field lines and employing pre-computed time-dependent magnetic field information and associated induction electric fields. Other efforts has been made to self-consistently compute the magnetic field in force-balance with RCM-computed pressure distributions[63].

```
  89 145.3 256.3 192.0 170.0 169.6  22.0  12.0  12.0   7.0  12.0  17.9  47.9
# DATE    TIME  IBTIME  N_SW  V_SW Na/Np   PCP  Phase    Dst   ABI   Kp  IMF_BX IMF_BY IMF_BZ
20010330 180000 000000  9.73  402.1 0.95  31.72 -1.00    2.50 62.20 2.83  -1.22  -1.59  -0.62
20010330 180500 000300  9.36  403.9 0.95  37.60 -1.00    3.00 62.34 2.84  -0.39  -1.72  -1.09
20010330 181000 000600 11.37  399.9 0.95  30.29 -1.00    3.50 62.48 2.85  -0.83  -2.10  -0.27
20010330 181500 000900 10.69  407.5 0.95  40.70 -1.00    8.00 62.62 2.86   0.59  -2.53  -1.08
20010330 182000 001200 12.62  410.2 0.95  28.18 -1.00   15.50 62.76 2.87   0.30  -2.54   0.47
20010330 182500 001500 14.22  410.1 0.95  20.46 -1.00   23.00 62.90 2.88   0.00  -1.79   1.84
20010330 183000 001800 11.26  406.1 0.95  22.00 -1.00   22.00 63.04 2.89   0.46  -2.69   2.28
20010330 183500 002100 10.06  402.7 0.96  20.98 -1.00   16.50 63.03 2.90   0.23  -2.60   2.56
20010330 184000 002400 11.05  403.7 0.96  19.35 -1.00   14.50 62.91 2.91  -0.44  -1.94   2.70
20010330 184500 002700 10.45  401.3 0.96  18.25 -1.00   11.50 62.80 2.92  -0.91  -1.39   2.85
20010330 185000 003000  8.88  403.3 0.96  20.30 -1.00    6.00 62.68 2.93  -0.57  -2.18   2.34
20010330 185500 003300  7.75  403.5 0.96  22.21 -1.00    3.00 62.56 2.94  -0.71  -2.25   1.54
20010330 190000 003600  6.17  396.8 0.96  27.91 -1.00   -1.50 62.44 2.94  -0.49  -3.99   1.87
```

Figure 3.3 : Initial part of the inputs.dat file for the March 31, 2001 storm event.

Figure 3.2 shows the calculation diagram of the RCM. Inputs parameters are listed on the top of the diagram, including solar wind density, solar wind velocity, Kp index, Dst index, ABI index, ap index and F10.7 flux. These inputs parameters are stored in the file "inputs.dat" (Figure 3.3) which gives observational parameters during the interested time interval. In the first line of the file, it saves the sun spot number, the F10.7 flux right before the event, monthly averaged, 81-day averaged, and yearly averaged F10.7 flux, and a series of ap index. The sun spot number could be calculated by the F10.7 flux since they have a very good linear relation $F10.7 = 60.19 + 0.907 \times sun\_spot\_number$. The file then lists some input parameters,

including solar wind density, solar wind velocity, the ion component ratio, the polar cap potential drop, the Dst, ABI, kp indices, and the IMF conditions, for each time between the starting time and ending time.

The ion composition ratio of $[O]^+/[H]^+$ is usually given as[87]

$$\frac{[O]^+}{[H]^+} = 0.045 \times e^{0.17 \times kp_{in} + 0.010 \times F10.7_{in}} \tag{3.2}$$

which use Kp and F10.7 as parameters.

The interpretation and parameterization of the polar cap potential drop as a function of solar wind conditions have been studied extensively both theoretically and empirically[88, 49, 89]. Boyle developed s statistical relation[90]

$$PCP = (1.01 \pm 0.11)10^{-4} v_{SW}^2 + 11.7(\pm 0.70)|B| \sin^3 \frac{\theta}{2} \tag{3.3}$$

where PCP is in kV, v is the solar wind velocity in km/s, B is the magnitude of the interplanetary magnetic field in nT, θ is the angle that $\cos\theta = B_Z/B$. It has been predicted that once the induced electric field from the solar wind reached a certain magnitude the ionospheric potential would stop increasing and saturate[88, 91].

What known as the Hill-Siscoe formulation of the transpolar potential is based on the idea that the strength of the region 1 current system is limited in such a way that it cannot produce significant changes in the magnetic field strength at the low-latitude magnetopause[88, 89]. The final form used in RCM looks like

$$PCP = 10^{-4} v_{SW}^2 + \frac{57.6 p_{SW}^{1/3} E_{SW}}{p_{SW}^{1/2} + 0.43 E_{SW}} \tag{3.4}$$

where p_{SW} is the solar wind pressure and and E_{SW} is the interplanetary electric field in mV/m defined as

$$E_{SW} = v_{SW} \sin^3 \frac{\theta'}{2} B \sin\theta \tag{3.5}$$

and

$$\tan\theta' = \frac{B_Y}{B_Z} \tag{3.6}$$

The density and temperature of the plasma at the RCM's boundary, and cross polar cap potential drop are also inputs into the RCM, but they are currently calculated by statistical models using other parameters. The plasma sheet density and temperature can be obtained by satellite measurement, including geosynchronous satellites, Geotail and THEMIS satellites. A geosynchronous orbit is an orbit around a planet, mostly the Earth, with an orbital period that matches the planets rotation period. A geostationary orbit is a geosynchronous orbit directly above the Earth's equator, with a period equal to the Earth's rotational period and an orbital eccentricity of approximately zero. Geostationary orbits are useful because they cause a satellite to appear stationary with respect to a fixed point on the rotating Earth. The geosynchronous plane is about 35,800 km above the Earth. NOAA GOES and LANL satellites provide continuous monitoring for intensive data analysis. However, the RCM has its nightside boundary further out in the tail, the geosynchronous measurements can not be used as boundary condition in the RCM. The Geotail is a mission developed by Japanese Institute of Space and Astronautical Science (ISAS) and NASA to study the structure and dynamics of the tail region of the magnetosphere with a comprehensive set of scientific instruments. Its orbit has been designed to cover the magnetotail over a wide range of distances: 8 to 210 R_E from the Earth. The present orbit is $9R_E \times 30R_E$ with inclination of $-7°$ to the ecliptic plane. The five THEMIS spacecraft are placed in highly elliptical orbits where the spacecraft will line up at apogee every four days. The satellites have different orbits in their 13 phases up to now. During their tail science phases, they could give measurements at nightside approximately in the range from 10 R_E to 30 R_E. The Geotail or THEMIS observation could be

used as boundary condition for short events. However, it can not provide the plasma sheet information throughout a long storm. For the cross polar cap potential drop, although the DMSP satellite, in a sun-synchronous, low altitude polar orbit, could give an estimation based on measured ion velocity and calculated magnetic field strength through frozen-in flux equation, the time resolution of the estimation could be larger than the time scale of the change. Therefore, these satellite data are usually not used as a direct input to the model.

The plasma distribution and the polar cap potential distribution are derived from the calculated plasma sheet density, plasma sheet temperature, and cross polar cap potential drop. They serve as the high-latitude boundary conditions to solve the plasma distribution and ionospheric electric field, which are two of the main calculations in the RCM. As shown in the center of the diagram, the major component in the RCM calculation includes the plasma distribution, the field-aligned currents, and the electric field. The stand alone RCM doesn't calculate the magnetic field in a self-consistent manner. To the contrary, the magnetic field model is an input module to the RCM calculation. But it is calculated in an equilibrium version. Given the magnetic field and the initial condition of the plasma sheet, we could estimate the Birkeland currents by the pressure gradient using Vasyliunas equation. The current density on the ionosphere gives the term in the right hand side of the fundamental equation of magnetosphere-ionosphere coupling. With the thermal wind from the ionosphere/thermosphere model and ionospheric conductances consisting solar radiation and particle precipitation, we could solve the ionospheric electric potential. Knowing the ionospheric electric field and as well as the parallel electric field along the magnetic field line, we could get the plasma drift velocity. With the ion outflow as the source term, particle precipitation and charge exchange as loss terms, we could

then solve for the plasma advection and finish the logical loop.

```
 15900                                  ! itimei: start time (s)
 18000                                  ! itimef: stop  time (s)
   199                                  ! irdr: record # to read from
   199                                  ! irdw: record # to begin writing at
     2     1                            ! idt: basic time step (s); idt_reduce_factor
    10                                  ! idt1: time step to change disk write record
   600                                  ! idt2: time step for formatted output to log
    60                                  ! idt3: time step for invoking edge cleaning
 1        10.0                         ! ibnd: equatorial_boundary (4)
 1 F F          1.0 1.0 0.1 0.1        ! icond; sum; gash; th; ph; dth; dph
   F T T F                    1.0E+4 ! sm_birk; vpar=0; floor; correct; vparmax
16 2 0      0.0 1.0 1.0     10.0       ! ipcp; pcp; iwind; BHLB (11); hw; xi; K (16)
 4 1                500 500 1.0E-5 ! ipot; iswitch; jkrylmax; itermax; tol (4)
 1 F 2 0    0.9                1.0E-8 ! ivoptn; vel; lim; verbosity; cfl; eta_floor
   F 0.25   1.5 3.1 0.5 0.1 1.0E-4 ! edge; dlim; dmin; dmax; rhomax; vmfact; eps
   F F F F                          ! spiro; plasma_moments; maxwellianize; qr
            3   1   1               ! i_auroral_prec_type
            1   1   1               ! i_iono_outflow_type
            1   2   2               ! i_charge_exchange
            6.0 6.0 6.0             ! kappa
 3   16.0 119.5 -0.02   1.5 3.0     ! grid; i_pc; i_pp; dthdi_min; dthdi_max; di
 9 T T T 220.0 1  1600 0.0 3.1E+4 ! bf; imfby=0; scw; 3db; cw; ni; nf; tilt; dm
 4 T F F 2 7.8 2  1.0 0.63 2.3E+3 ! tps; tid; tcut; kcut; el; ti/te; ic; kp; ps
  6375.0    6475.0    24.0 1.0     ! R_planet; R_iono; dth; signbe
```

Figure 3.4 : Example of the rcm.params file for the July 22, 1998 substorm event.

A file named "rcm.params" (Figure 3.4) is used to specify the modules and options in the RCM run. The first information provided by this file is the starting time and the ending time of the simulation. These times are relative times, or elapsed times, from the beginning of the event. So the starting time must be set to zero at the time to run the event. The file then specify the record index and the time steps. These time steps include the running time step in the simulation, the time step to write the record file, the time step to write the log file, and the time step to clean up the plasma edge information. We then need to specify the modeling region either in the ionosphere based on latitude or in the equatorial plane based on the distance to the Earth relative to the stand off distance. Some conductance parameters, polar cap distribution parameters, threshold parameters are also listed in the file. The file next writes the choices of particle precipitation, ion outflow, charge exchange. Debugging parameters could be switched on and off to match the requirements of the run. The

grid resolution, magnetic field parameters, and plasma sheet parameters are included at the end of the file. As shown by the small boxes in the loop diagram, in general, RCM needs the following inputs modules

- 3D Magnetic Field
- Plasma Initial Condition
- Plasma Distribution Function at High-latitude Boundary
- Potential at High-latitude Boundary
- Ionospheric Conductances
- Electron Precipitation
- Thermospheric Winds
- Field-aligned Potential Drop
- Ion outflow including polar wind, auroral wind, etc.
- Ion Precipitation and Charge Exchange

The first 5 terms must be presented to run the simulation, while the latter 5 terms are kind of optional in numerical sense, which means it's fine to run without turning them on, but also essential on the plasma convection pattern. You could choose certain method for each module by giving an integer number or logical parameter in "rcm.params".

After you have these two files ready, you could perform the RCM run. First, you need to set up the grid points on the ionosphere according to specified grid resolution. It will read an index of grid resolution, calculate the colatitude and local time of each grid point. Then you need to set up the magnetic field. The RCM traces the magnetic field lines from the ionosphere foot points to the equatorial plane and records the coordinates of the cross point in the equatorial plane, the minimum magnetic field there, and integrates for the flux tube volume. In the standard RCM, these information is calculated before the main code so that we could examine the

magnetic field before the running of the main code since it might be time-consuming to set up complicated magnetic field. We then need to set up high latitude plasma boundary condition and solar radiation contribution to the ionospheric conductances. Since the solar radiation doesn't change much especially during an interval of several hours or a few days, only the contribution at the initial time would be calculated. We can then run the main code afterwards.

```
T T T T T T F T F F F F ! ax,bf,ef,cd,pm,fs,cs,ps,qr,m3,v3,u3
  0 F F F   0           ! k_selected,time,combine,overlay,k_edge_selected
 F T T T T T F F F F F F ! pf,gs,gl,bc,ft,te,sc,dst,ae,ena,euv,fuv
RCMRUN                  ! run_id_string
   1  999    1          ! rec_1,rec_2,rec_s
```

Figure 3.5 : Example of the tecplot.params file for post-processing of RCM results.

The output and post processing choices are specified in the file currently named as "tecplot.params" (Figure 3.5) since the tecplot is the main processing tool. The results could be compared with observation data from both satellite or ground based instruments, i.e. magnetometers, radars or images. The output from RCM includes but not limited to:

- Ionospheric Electric Field
- Field-Aligned Currents (FAC)
- Magnetospheric Electric Field
- Particle Fluxes in Magnetosphere
- Auroral Structure
- Plasmasphere and Plasmapause
- Ground Magnetic Fluctuation or Magnetic Indices

The examples of RCM outputs are shown at the bottom of the diagram. The field-aligned currents or the precipitating energy flux could be converted the auroral signature in the ionosphere. A magnetogram code[17] calculating the magnetic field all

around the Earth could be used to derive Dst or AL/AU indices. The first channel in the RCM represents the plasmasphere. So we could track the shape of the plasmapause. Pressure or fluxes could be calculated by taking different moments of energy invariant λ.

3.3 Computing Grid

The RCM boundary could be set either in the magnetic equatorial plane or in the ionosphere. The basic calculation in RCM is done on a two dimensional grid on a spherical surface, uniform in longitudinal direction, that represents the ionosphere. However, quantities are often plotted in the equatorial plane to spread out the displaying area. All magnetospheric quantities are mapped from the ionosphere to the magnetosphere according to magnetic field line tracing.

If magnetic field changes in the ionosphere is neglected, as the case of fixed grid points in the ionosphere in the RCM, then the electric field there can be represented as the gradient of a potential, $\mathbf{E} = -\nabla\phi$. However, the mapping of ionospheric electric field to the equatorial plane does not represent the electric field there due to the changes of magnetic field cross point. The magnetic field is represented by $\mathbf{B} = \nabla\alpha \times \nabla\beta$, where α and β are Euler potentials specifying a point on the ionosphere[92, 93] and constant along magnetic field line. The induction electric field is estimated to be

$$\mathbf{E}_{induction} = -\left(\frac{\partial \mathbf{x}_e}{\partial t}\right)_{\alpha,\beta} \times \mathbf{B}_e \tag{3.7}$$

where $(\partial \mathbf{x}_e/\partial t)_{\alpha,\beta}$ is the velocity of the equatorial map of the grid point corresponding to α and β. In the RCM for the case where there is no electric field parallel to the magnetic field, we use a gauge in which the scalar potential Φ is constant along a magnetic field line[21]. Even in the version with the field-aligned potential drop, the

electric potential is still treated as constant except for the thin acceleration region right above the ionosphere. The Hamiltonian then needs to include the field-aligned potential drop to represent the plasma motion above the acceleration area. It also requires the acceleration region to be thin enough to treat the magnetic field there time-independently.

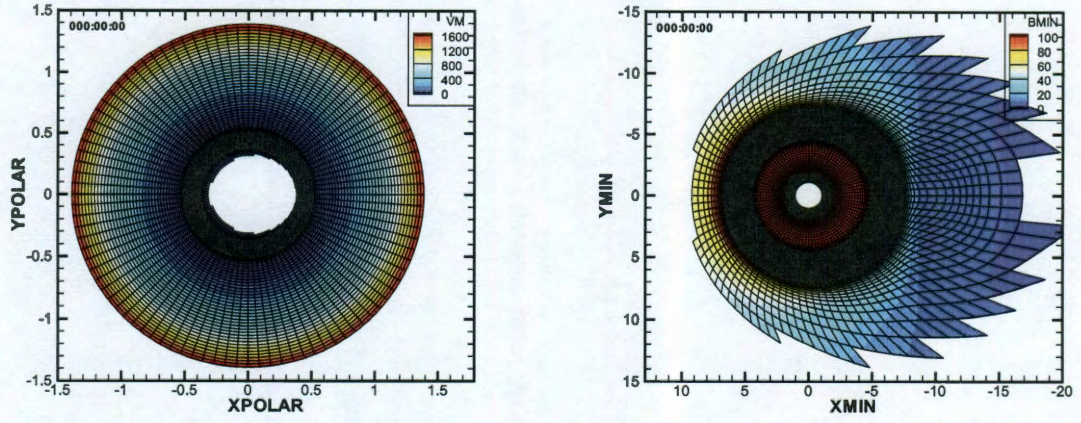

Figure 3.6 : The RCM standard grid in the ionosphere (left) and its mapping to the magnetosphere (right). The color shows the $V^{-2/3}$ and minimum B_Z. The magnetic field is modified Tsyganenko 89 model as described later in the chapter. The blank area in the center of ionosphere corresponds to the open field line region. The grid resolution is modified to concentrate in ring current area.

The boundary is usually placed in the equatorial plane instead of on the ionosphere. A major parameter in determining the modeling region is the standoff distance, which is the distance of the dayside magnetopause form the Earth. In general, the standoff distance is squeezed during times of strong solar wind dynamic pressure when solar wind pushes the dayside magnetopause. The RCM boundary is basically an ellipse with about 2 times of standoff distance at midnight, 0.95 times of standoff distance at noon, and 1.5 times of standoff distance at dawn or dusk. For magnetic

quite times, it's about 20 R_E at midnight and up to 10 R_E at dawn or dusk.

Since there is north-south symmetry assumed in RCM, the grid only covers the northern hemisphere. The grid is uniformly distributed in local time with a wrap of 3, which means the last longitude grid line is the same as the third longitude grid line both of them are pointing to the Sun from the Earth. Therefore, the first and second longitude grid lines are in pre-noon sectors and coincide with the third last and the second last longitude directions. This wrap has been removed for clarity reason and coupling intention in current version as describe in next chapter.

The RCM has 4 standard grid resolutions right now. The coarsest solution is an inheritance from MSM grid, as 62 by 51 with wrapping. There are 48 scales in longitude direction and 62 scales in latitude direction. So the divergence of each two adjacent azimuthal directions are 7.5° longitude. And the latitude coverage is from 0° colatitude to about 50° colatitude. The second grid is 78 by 51 with wrapping, which also has 48 scales in longitude direction but has 78 scales in latitude direction with more points equatorward. So it covers up to about 80° colatitude. The most commonly used grid solution is 155 by 99 with wrapping, which is basically doubled in both directions compared to the second grid. This grid has 96 scales in longitude direction, which means 4 scales per hour in local time direction or 3.75° longitude. The finest resolution is 309 by 195 with wrapping, which again doubled in both directions compared to the third grid. Other grid resolutions could be used if parameters are set up correctly. Although high grid resolution always gives fine structure in the simulation, numerical instability requires shorter time step which makes the computation time much longer. The time to run the code must be quicker than real time evolution for space weather prediction. Therefore, a suitable grid resolution needs to be selected to include essential phenomena without sacrificing computation

time. Figure 3.6 shows a modified grid based on the third grid of RCM both in the ionosphere and also its mapping to the equatorial plane in the magnetosphere. The colors are a parameter, VM which related to the flux tube volume as $VM = V^{-2/3}$ and the minimum magnetic field B_Z which is the magnetic field in the equatorial plane. The flux tube volume V is generally larger far from the Earth, so VM, on the opposite, is smaller far from the Earth. Since the high-latitude grid points are mapping further out, the grid points close to the north pole has smaller VM. The B_z component of the magnetic field is northward in the equatorial plane. It is stronger closer to the Earth and weaker away from the Earth. The grid resolution is modified to concentrate in ring current area and facilitate its use for a substorm simulation.

In the RCM, we use i as the index of latitudinal grids and j as the index of longitudinal grids. Then $i = 1$ represents the grid points closest to the pole, having highest latitude and lowest co-latitude and mapping far in the magnetotail. When the index i reaches its maximum, isize, it presents the equatorwardmost grid points, which usually set to about 10° latitude unless the coarsest grid resolution is used. With jsize is defined as the maximum of the index j, colat or θ is the co-latitude of the grid point, aloct is the local time of the grid point from 0 at noon to π at night, and

$$\begin{aligned} d\lambda &= \frac{1}{isize - 1} \\ d\psi &= \frac{2\pi}{jsize} \\ \alpha &= \frac{\frac{d\theta}{di}}{d\lambda} \\ \beta &= \sin\theta \end{aligned} \tag{3.8}$$

so that the area per grid point is given by $R_I^2 \alpha\beta d\lambda d\psi$, where R_I is radius of the ionosphere. Equatorial grid points are established by mapping ionospheric grid points

to the equatorial plane. But the grid is not orthogonal in the equatorial plane and would change with time.

3.4 Magnetic Field Model

Magnetic field models are first quantitative models of the interior of the magnetosphere. They have formed a basis for the investigation of the detailed physics of the magnetospheric interior. The Earth's magnetosphere is a very dynamical system, whose configuration depends on many internal and external factors, including the orientation of the Earth's magnetic axis with respect to the direction of the incoming solar wind flow, the state of the solar wind, e.g. the orientation and strength of the interplanetary magnetic field. The Earth's magnetic field model consists of its internal main field and external fields due to effects of currents system. So it generally has five components: the internal field, the magnetopause, the ring current, the tail, and Birkeland currents[94].

3.4.1 Earth's Inner Magnetic Field

For the purpose of representing the magnetic field out in the magnetosphere, one usually just considers the dipole term since the quadrupole, octupole, etc., terms die out rapidly with distance from the Earth, and magnetospheric-physics is basically not a high-precision subject. However, people might need to use the full expansion to get an accurate idea of where a given magnetospheric field lines intersects the current-carrying layers of the ionosphere.

Another way to specify the main field is the "International Geomagnetic Reference Field", a standard mathematical description of the Earth's main magnetic field by a series of mathematical models. It models the magnetic field above the Earth's

surface that is generated by currents inside the Earth as the negative gradient of a scalar potential which can be represented by a truncated series expansion.

The magnetic field from external sources, e.g. currents in the magnetospheric plasma, rapidly outweighs the main field with growing distance from the Earth. The external field is not current-free and it is no longer possible to conveniently represent it by a scalar potential. Tremendous effort has been devoted to predict the magnetic field that should be expected at any point in the magnetosphere. There are two basic approaches which represent the extremes in large scale modeling of the Earth's magnetosphere[95]. One is the physical approach of MHD models which self-consistently include plasma physical processes and the other is the purely empirical approach which relies on the synthesis of observational data. These models systematically utilize the growing database of magnetospheric magnetic-field measurements and solve two equations $\nabla \cdot \mathbf{B} = 0$ and $\nabla \times \mathbf{B} = \mu_0 \mathbf{J}$. The latter doesn't really constrain the model much because the usual way to measure current in the magnetosphere is to measure the magnetic field and estimate its curl.

3.4.2 Tsyganenko Magnetic Field Models

Unlike the main geomagnetic field on the Earth's surface, the distant magnetic field varies constantly due to changing condition in the solar wind and internal magnetospheric instabilities[96]. Quantitative models should be able to replicate essential features of the response of the magnetospheric configuration to the variable external input. In general, the approach is to represent the external field by a sum of modules, each representing an individual source, with its own geometry and its own response to external factors and the Earth's dipole tilt.

The present leader in semi-empirical field models is Nicolai Tsyganenko. Tsy-

ganenko's basic approach has been to develop a very complicated analytic formula for the contribution for the magnetospheric magnetic field including a large number of adjustable coefficients[97]. The empirical approach to the modeling not only makes it possible to quantitatively represent the variable magnetosphere, but helps derive from data valuable information on its response to variations in interplanetary conditions[96].

Tsyganenko and Usmanov [1982] and Tsyganenko [1987] proposed a simple and flexible model of the Earth's magnetospheric tail current sheet with a finite thickness constructed as a continuous distribution of infinitely long straight current filaments[98, 99]. A search for a better representation of the near-tail magnetic field resulted in analytical models based on disklike equatorial current sheets[100]. The analytical vector potentials derived in this T89 model were used for modeling the magnetic field produced by the ring current and the tail current sheet. An advantage of using vector potentials is that none of these modifications violate the condition $\nabla \cdot \mathbf{B} = 0$. However, the T89 model has several deficiencies. First, it failed to properly reproduce a step profile of the electric current density in the vicinity of the inner edge of the current sheet[101]. It also lacked the eastward ring current that exists in the inner L shells[102]. The model uses an oversimplified method for representing the field from the magnetopause currents. Another limitation is related to the parameterizing of the model, which implies that the models need a better method for quantifying the magnetospheric conditions[13].

A newer approach had been developed [13, 103] with (1) a realistic shape and size of the magnetopause based on fits to a large number of observed crossings, (2) fully controlled shielding of the magnetic field produced by all magnetospheric current systems, (3) new flexible representations for the tail and ring currents, and (4) a new

directional criterion for fitting the model field to spacecraft data, providing improved accuracy for field line mapping. This T96 model was developed with continuous dependence on the solar wind pressure, IMF, and Dst index, replacing earlier binning into several Kp index intervals[104].

However, because of an oversimplified approximation for the ring current, the model field in the inner magnetosphere was found generally overstretched[96], especially during strongly disturbed conditions[104]. Another deficiency of the data-based models was their inability to replicate the strong dawn-dusk asymmetry of the inner magnetosphere during stormy periods. A new model based on a completely revised mathematical framework, a new set of spacecraft data, and an improved method of parameterizing the external field sources was presented[104, 105]. The external field includes the effects from Chapman-Ferraro currents, ring current, cross-tail current sheet, large-scale field-aligned currents, and a partial penetration of the IMF inside the model magnetosphere. The model is for the near and inner magnetosphere within about 15 R_E.

The T01 model is then applied to storm time inner magnetosphere by adding a duskside partial ring current with variable amplitude and scale size[106]. Strong geomagnetic storms are relatively rare events. The data set included about 143000 records with 5-min average B-vectors covering 37 major disturbances in 1996-2000 with $Dst \leq -65nT$[106]. Most of the data came from GOES-8, GOES-9, GOES-10, Polar, and Geotail spacecraft. Interplanetary medium data were mainly provided by Wind and ACE. The modeling revealed an enormous distortion and dawn-dusk asymmetry of the inner magnetosphere during the peak of the storm main phase, caused by the combined effect of the symmetric and partial ring currents, cross-tail

current, and Birkeland currents[106]. Unlike using

$$G_1 = \left\langle V \frac{B_{\perp/40}^2}{1 + B_{\perp/40}} \sin^3 \frac{\theta}{2} \right\rangle \tag{3.9}$$

and

$$G_2 = \frac{1}{200} \langle V B_s \rangle \tag{3.10}$$

in the T01 model, the T01S (TSK03) model uses G2 and

$$G_3 = \frac{1}{2000} \langle N V B_s \rangle \tag{3.11}$$

to parameterize the strengths of the cross-tail current, the partial ring current, and the field-aligned currents. N, V, $B_\perp$, θ are the solar wind density, solar wind speed, the IMF transverse component, and its clock angle. During quiet times, both G_1 and G_2 are close to zero; for moderately disturbed periods with IMF $B_Z \approx -5nT$, they reach values between 30 and 60; during great space storms, they can exceed 200[106]. The time averaging smoothed out fast and abrupt variations of the external input and resulted in a more gradual variation of the model field[107]. Such simple averaging ignored the fact that different sources of the geomagnetic field have widely different response and decay times.

To try more general combinations other than G_2 and G_3, the external driving factors were written as

$$S = a N^\lambda V^\beta B_s^\gamma \tag{3.12}$$

where the coefficients a and the power indices λ, β, γ are unknown parameters. The external model field is approximated by a linear combination of seven vectors: (1) the Chapman-Ferraro field $\mathbf{B}_{CF}$, confining the Earth's internal field within the magnetopause, (2) the tail field $\mathbf{B}_T$, (3) the field $\mathbf{B}_{SRC}$ of a symmetrical ring current, (4) the field of a partial ring current $\mathbf{B}_{PRC}$, (5) region-1 Birkeland current $\mathbf{B}_{R1}$, (6)

region-2 Birkeland current $\mathbf{B}_{R2}$, (7) a penetrated component of the IMF given by an "interconnection" term $\mathbf{B}_{int} = \varepsilon \mathbf{B}_{\perp}^{IMF}$. The total field of the magnetospheric sources has the form

$$\mathbf{B} = \mathbf{B}_{CF} + t_1\mathbf{B}_{T1} + t_2\mathbf{B}_{T2} + s\mathbf{B}_{SRC} + p\mathbf{B}_{PRC} + b_1\mathbf{B}_{R1} + b2\mathbf{B}_{R2} + \varepsilon\mathbf{B}_{\perp}^{IMF} \quad (3.13)$$

Assuming a uniform penetrated field and no modulation by the IMF clock angle θ, the best fit value of the penetration coefficients was found equal to $\varepsilon = 0.46$, in close agreement with the earlier estimate $\varepsilon = 0.42$ of TSK03[107]. Other 6 coefficients are represented by 6 variables.

More recently, a high resolution data-based magnetic field model was established[108]. The field is expanded into a sum of orthogonal basis functions of different scales, capable to reproduce arbitrary radial and azimuthal variations of the geomagnetic field, including its noon-midnight and dawn-dusk asymmetries. The new model has been fitted to various subsets of data from Geotail, Polar, Cluster, IMP-8, and GOES-8, GOES-9, GOES-10, and GOES-12 spacecrafts. The model reveals the following features[108]: (1) compressed field on the dayside, growing in magnitude with increasing solar wind pressure; (2) strong erosion of the field in the subsolar region during the times of large southward IMF, driving the storm main phase; (3) depression of the inner magnetospheric field, whose depth and dawn-dusk asymmetry dramatically grow during stormy periods; (4) extended region of weak equatorial field in the near tail, increasing toward the tails flan, especially for strong northward IMF conditions; (5) strong correlation of the "penetrating" δB_z with the concurrent IMF B_Z; (6) strong increase of the current in the postmidnight and evening sectors at the storm main phase, accompanied by its dramatic reduction in the entire pre-noon sector and resulting in a hooklike shape of the overall pattern of the storm-time equatorial current; (7) fairly broad and virtually axisymmetric equatorial current for the storm

recovery phase without any significant distinction between the ring and tail current systems.

3.4.3 Voigt Magnetic Field Models

The first three dimensional model with predescribed magnetopause was provided by Voigt[109]. It only includes the Earth's dipole field and tail current field. The tail current is an infinitely thin sheet current in the tail equatorial plane with a constant current density. It was abandoned later through stretching the confined dipole field to represent the magnetic effect of the tail current[110]. The tilt effect of Earth's dipole and related tail current sheet warping were included implicitly with a nice warping of the plasma sheet. It became the basis for the Hilmer-Voigt inner magnetosphere model and for the Toffoletto-Hill open magnetosphere model[111].

A tilt-dependent magnetic field model of the Earth's magnetosphere with variable magnetopause standoff distance was constructed[95] with flexible analytic representations for the ring and cross-tail currents, each composed of elements derived from the Tsyganenko and Usmanov (1982) model[98], and the fully shielded vacuum dipole configuration[110]. Field-aligned currents are not explicitly represented. While the dipole's contribution to the magnetic field component normal to the magnetopause is fully shielded using the method of Voigt [1981], the ring and cross-tail currents remain unshielded and limit the model's range of validity to the lower-latitude regions of the inner magnetosphere[95].

The model depends on four independent external parameters: (1) the dipole tilt angle, (2) the magnetopause standoff distance, (3) the midnight equatorward boundary of the diffuse aurora, and (4) the geomagnetic index Dst. The first two are used to determine the magnetopause currents shielding, the dipole and the inner edge of the

current sheet is constrained to map to the midnight ionospheric boundary. The model field must reproduce Dst and associated ΔB patterns specified in the noon-midnight meridian.

The Hilmer-Voigt model has been successfully used in the Rice Convection Model (RCM) and in the Magnetosphere Specification and Forecast Model (MSFM). While the Hilmer-Voigt model represents the inner portion of the magnetosphere fairly well, points close to the magnetopause are less well represented[111].

3.4.4 Force Balanced Magnetic Field

A magnetic field model is classified as "theoretical" if it also satisfies the momentum equation as

$$\rho\left(\frac{\partial}{\partial t}+\mathbf{v}\cdot\nabla\right)\mathbf{v}=-\nabla p+\mathbf{j}\times\mathbf{B} \tag{3.14}$$

The quasi-static or slow-flow approximation to ideal MHD consists of neglecting the inertial term so that

$$\nabla p=\mathbf{j}\times\mathbf{B} \tag{3.15}$$

To neglect the $\rho(\mathbf{v}\cdot\nabla)\mathbf{v}$ term in the momentum equation relative to the ∇p term and the $\mathbf{j}\times\mathbf{B}$ term is valid if $v^2 \ll c_s^2$ and $v^2 \ll c_A^2$, where c_s is the sound speed and c_A is the Alfvén speed. The quasi-static approximation to ideal MHD is usually valid if the flow is highly subsonic and the time scales considered are very long compared to MHD-wave travel times.

In contract to traditional ring current models[112, 113, 114, 115], which used a prescribed time-dependent convection electric field distribution and a prescribed magnetic model, convection models like the Rice Convection Model (RCM)[63], Comprehensive Ring Current Model (CRCM)[116], and the Michigan Ring Current-Atmosphere Interaction Model (RAM)[117] calculate the inner magnetospheric potential electric

field self-consistently, proceeding from a prescribed potential on the outer boundary[28]. As discipline, magnetospheric modeling faces a fortunate situation in having two model types that nearly ideally complement each other[118]. The inability of MHD to model gradient and curvature drifts leads to an inaccurate representation of this region[119]. These inner magnetospheric drift physics play an important part of the frameworks of space weather prediction. A typical way of "coupled" work is to install inner magnetospheric representation as a module to a global MHD code[79, 45, 80]. Global MHD codes take solar wind conditions as input and provide electric and magnetic fields everywhere within the magnetosphere as output[118]. The drift physics model tracks the particle population and gives fluid parameters to a global MHD code by computing the appropriate plasma moments. The Rice Convection Model-Equilibrium (RCM-E) is a version of the RCM with its own MHD solver: the MagnetoFriction (MF) code which calculates force balanced magnetic field based on the plasma distribution in the magnetosphere[120, 121, 63, 37]. The MF code uses the standard MHD equations, except that the momentum equation includes artificial friction (α) and viscosity (ν) terms to iterate towards a solution to the force balance equation.

$$\begin{aligned}
\frac{\partial \rho}{\partial t} + \nabla \cdot (\rho \mathbf{v}) &= 0 \\
\frac{\partial \rho \mathbf{v}}{\partial t} &= \mathbf{j} \times \mathbf{B} - \nabla \cdot (p\overleftrightarrow{I} + \rho \mathbf{v}\mathbf{v}) - \alpha \rho \mathbf{v} + \nu \nabla^2 \mathbf{v} \\
\frac{\partial p}{\partial t} &= -\nabla \cdot (\mathbf{v} p) - (\gamma - 1) p \nabla \cdot \mathbf{v} \\
\frac{\partial \mathbf{B}}{\partial t} &= \nabla \times (\mathbf{v} \times \mathbf{B}) \\
\nabla \times \mathbf{B} &= \mu_0 \mathbf{j}
\end{aligned} \tag{3.16}$$

3.4.5 Substorm Current Wedge

A wedge-shaped current linking the nightside ionosphere and the plasma sheet is believed to be the principal cause of a major reconfiguration of the magnetospheric field on the nightside[12]. The concept of the substorm current wedge (SCW) was suggested based on an extensive evidence from space- and ground-based magnetic field observations during the expansion phase of magnetospheric disturbances[122]. An essential feature of a substorm was a sudden disruption of a part of the cross-tail current and its redirection along geomagnetic field lines with downward and upward Birkeland currents concentrated on the dawn and dusk sides of the disturbance sector[123]. The rapid disruption of the cross-tail current in a localized region on the nightside and its diversion via field-aligned currents to low altitudes is equivalent to a buildup of a three-dimensional wedge-shaped circuit with a limited longitudinal extent as schematically shown in Figure 3.7.

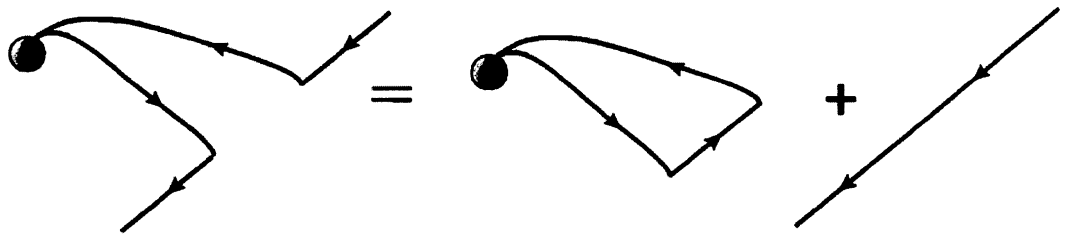

Figure 3.7 : A sketch illustrating the concept of a substorm current wedge (SCW), confined within a limited interval of longitude[12].

Hilmer and Voigt [1995] suggested modeling the magnetic effects of the SCW by adding to the background magnetic field model a disturbance field from an eastward current sheet with a limited extension in the dawn-dusk and tailward-sunward

directions[95]. Although they were able to reproduce the observed dipolarization of the nightside field, the equatorial current in their model extended out into the tail lobes, instead of closing in the ionosphere via localized Birkeland currents. That limitation did not allow a strong $\mathbf{B}_y$ disturbance to arise, which is typically observed on the nightside during the substorm expansion phase.

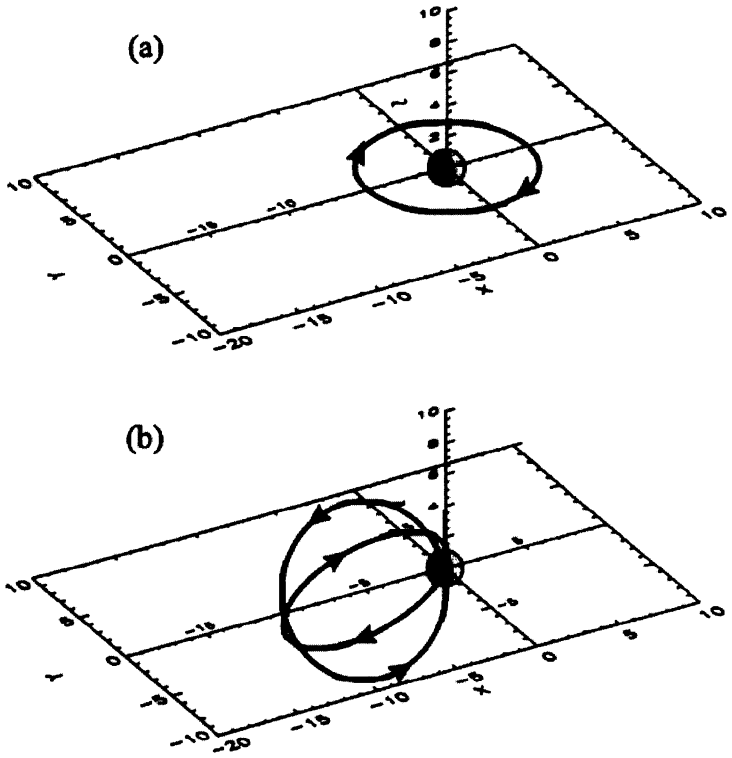

Figure 3.8 : Three-dimensional views illustrating the method of constructing the simple SCW model: (a) a single loop in the equatorial plane; (b) a combination of two circular current loops, providing the prototype magnetic field for the SCW model[12].

A simple and flexible analytical model is proposed for the magnetic field of substorm current wedge[12]. The key element of the mathematical treatment is the vector potential of the field produced by a pair of current loops (Figure 3.8). The basic idea

is to combine two identical loops, symmetrically tilted with respect to the midnight meridian plane, shift them tailward, so that the currents flow nearly along the dipolar field lines at close geocentric distances, and introduce a variable finite thickness of the current loops by a simple modification of the vector potential.

Applying appropriate shift, rotation, and a minor stretching deformation makes it possible to reproduce the desired geometry of the entire system, including field-aligned currents. The current wedge has a variable longitudinal width and warping effects due to the tilt of Earth's dipole.

3.5 Plasma and Convection

The different particle populations of the inner magnetosphere cannot be treated as a single fluid because of the large range of energies present. Even within the ring-current population the differential drift of particles with different energies can be critical for the electrodynamics. The Rice Convection Model (RCM) was specifically designed to treat this unique and complicated system[63].

The RCM represents the plasma population in terms of multiple fluids, typically 200 so far. It contains 3 chemical species: electron (e^-), proton (H^+), and oxygen ion (O^+), although other species could be implemented quite easily. The oxygen ion is extremely important during magnetic active times. For each species, the distribution function is specified on tens of fluid elements with different energy invariant $\lambda = KV^{2/3}$. The quantity of plasma is not presented by number density but a plasma content in a unit magnetic flux, η_s. It relates to the distribution function as

$$\eta_s = \frac{4\pi\sqrt{2}}{m_s^{3/2}} \int_{\lambda_{min}}^{\lambda_{max}} \sqrt{|\lambda_s|} f_s(\lambda_s) d\lambda \tag{3.17}$$

where channel s represents invariant energies between λ_{min} and λ_{max}. The reason

that we are using the magnitude of λ is that λ here is actually λ/q. So it's positive for ions but negative for electrons.

Since the number density in constant along a field line, the number density could be calculated as η_s/V. The total pressure is computed from

$$p = \frac{2}{3}\sum_s (\eta_s|\lambda_s|)V^{-5/3} \tag{3.18}$$

In the inner magnetosphere, the plasma drift velocity mainly consists of three parts: the electric field drift, the gradient drift, and the curvature drift.

$$\mathbf{v}_E = \frac{\mathbf{E}\times\mathbf{B}}{B^2} \tag{3.19}$$

$$\mathbf{v}_G = \frac{1}{2}mv_\perp^2\frac{\mathbf{B}\times\nabla B}{qB^2} \tag{3.20}$$

$$\mathbf{v}_C = mv_\parallel^2\frac{\mathbf{B}\times\left[\left(\hat{\mathbf{b}}\cdot\nabla\right)\hat{\mathbf{b}}\right]}{qB^2} \tag{3.21}$$

The relative importance of gradient and curvature drifts depends on the particle pitch angle, the angle between the magnetic field and the particle velocity[37]. Equatorial particles with 90° pitch angles have no parallel velocity component, and therefore do not undergo curvature drift; particles with 0° pitch angles have no perpendicular velocity component, and do not undergo gradient drift. An accurate accounting of the particle drifts therefore requires us to calculate the individual drifts of particles with different pitch angles. The RCM simplifies things by assuming that the plasma particles are constantly isotropizing their pitch angles without changing their energies. Since this assumption is reasonable for much of the magnetosphere, the RCM is capable of reproducing the physics of magnetospheric particle motion.

By reducing the particle dynamics to a description of the bounce-averaged guiding center drift motion, the net motion of the particle is now only perpendicular to the magnetic field[37]. The motion can be described on any two-dimensional surface that

intersects the magnetic field lines, such as the equatorial plane or the ionosphere. The location of a particle is characterized by the field line that guiding center point is located on, but not where the particle is located along that field line.

Based on adiabatic drift theory for a plasma with isotropic pitch angles, the RCM equations for evolution of the plasma distribution are

$$\left(\frac{\partial}{\partial t} + \mathbf{v}_s \cdot \nabla\right) \eta_s = S(\eta_s) - L(\eta_s) \tag{3.22}$$

where S and L are source term and loss term, the drift velocity is

$$\mathbf{v}_s = \frac{\lambda_s}{q_s B^2} \mathbf{B} \times \nabla V^{-2/3} + \frac{\mathbf{E} \times \mathbf{B}}{B^2} \tag{3.23}$$

The source term here is ion outflow. The current RCM doesn't include plasma coming from plasmasphere. The solar wind plasma coming from magnetotail is considered as the plasma boundary condition when solving for the plasma distribution as described in next section. The lost term includes plasma precipitation for all particles and charge exchange for ions.

3.6 Plasma Sheet and Boundary Condition

Quantitative models of ring current injection require specification of the electric and magnetic fields as well as initial and boundary conditions on the particle distribution function[124]. The RCM generally places the nightside boundary far away from the geosynchronous orbit and reaching about 12 to 20 R_E to include most of the region-2 Birkeland currents.

The plasma sheet is the most dynamic component of the magnetosphere. It plays an important role in dynamic processes in the magnetotail and energy transfer from the solar wind to the Earth. The plasma sheet is suggested to feed the inner magnetosphere and the ring current and partial ring current systems with the plasma

convected from the far tail region[15]. It is also the particle source of the auroral particle precipitation.

Adiabatic drift theory leads to the conclusion that nV and $pV^{5/3}$ are conserved along the drift path with isotropic pitch angle distribution in $\mathbf{E} \times \mathbf{B}$ drift[40]. The corresponding quantities $n_s V$ and $p_s V^{5/3}$ are conserved along the drift path where gradient and curvature drifts are important, where n_s and p_s are the partial number density and partial pressure of particles characterized by charge q_s and isotropic invariant λ_s.

Several studies have been done to estimate $pV^{5/3}$ as a function of position in the equatorial plasma sheet[125, 126, 127, 128, 129, 130, 131]. There is an increase of more than an order of magnitude in $pV^{5/3}$ from $-10R_E$ to $-25R_E$. This is contradict to the expectation of roughly uniform $pV^{5/3}$ throughout the plasma sheet. This has been called as "pressure balance inconsistency", "pressure crisis", and "entropy inconsistency"[132]. A large potential drop across the tail would lead to magnetic field configurations much more stretched than statistical models which is the essence of the pressure balance inconsistency[132]. A significant fraction of electrons may be lost from the inner plasma sheet, especially in the upward field-aligned electric field regions. But electrons carry only about one seventh of the plasma sheet pressure[32]. The ion precipitation rate, even in strong pitch angle scattering, is usually longer than the convection time without widespread large downward field-aligned electric fields. Ion outflows from the ionosphere should tend to make entropy increase earthward in the plasma sheet and thus compensate for loss by precipitation.

It seems likely that a combination of the gradient/curvature drift and bubble effects are adequate to explain the observed systematic increase of average entropy with distance down the tail[132]. The observed ions in the inner plasma sheet

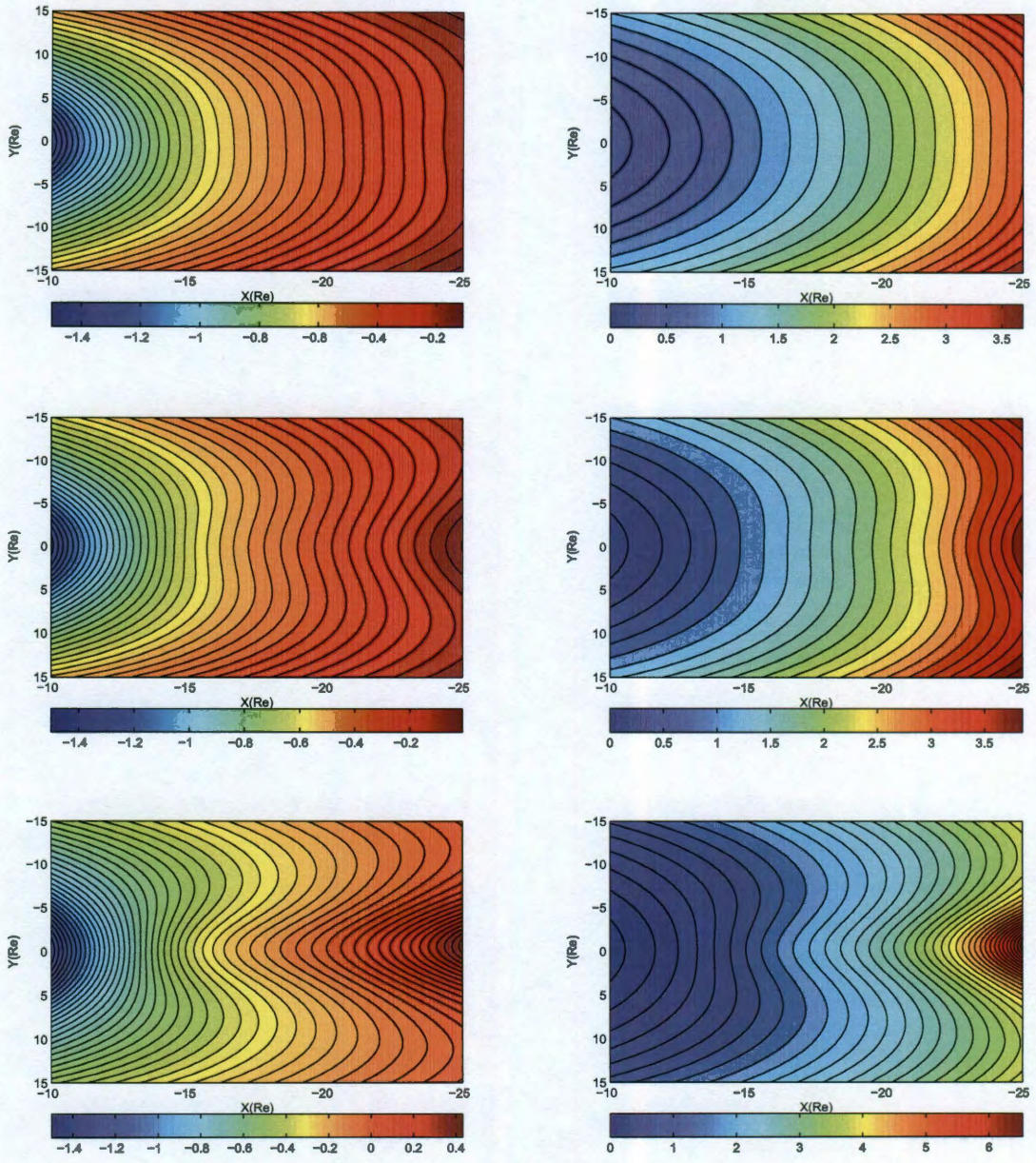

Figure 3.9 : Distribution of $\log_{10}(pV^{5/3})$ in $\log_{10}(nPa(R_E/nT)^{5/3})$ (left) and V in R_E/nT (right) in the equatorial plasma sheet, based on a T96 magnetic field model[13] and a Tsyganenko and Mukai [2003] model of the plasma sheet[14], for average solar wind conditions, i.e. $n = 5cm^{-3}$, $v = 400km/s$, $B_x = B_y = 5nT$, and $B_z = -5nT$ (top), $B_z = 0$ (middle), $B_z = 5nT$ (bottom). Adapted from Xing [2008][15].

come from the near-Earth low-latitude boundary layer (LLBL) instead of the distant magnetotail so that the gradient and curvature drift mechanism is getting lower $pV^{5/3}$[127, 133, 134, 135, 136, 131]. Model results indicate that the LLBL might be a significant source of near-tail central plasma sheet plasma during periods of weak convection[134]. Defined as a set of flux tubes with significantly lower entropy $pV^{5/3}$ than their neighbors[137, 138, 139], bubbles would move systematically earthward through the plasma sheet, creating a current wedge with downward field-aligned current on the east side of the bubble, westward ionospheric current across the bubble, and upward current on the west side of the bubble[132]. Transport by bubbles tends to enhance the effectiveness of the gradient and curvature mechanism, while its efficiency is determined by the relative magnitudes of $\mathbf{E} \times \mathbf{B}$ and gradient/curvature drifts[132].

The phenomena of plasma sheet bubbles is related to flow channels[140], bursty bulk flows (BBFs)[141, 142, 143], poleward boundary intensification, and substorm expansions[132]. In the quite time conditions where the magnetic activity is low, the plasma confined in the plasma sheet region undergos a slow steady earthward flow[143]. The flow velocity is usually around 50 km/s[32], which is much lower than the sound speed (400 km/s) in the central plasma sheet region. But this kind of steady adiabatic earthward convection cannot supply the pressure balance in the plasma sheet because the near-Earth magnetic flux tubes contains less plasma than the far tail field[125]. So there has to be time-dependent non-adiabatic substorms to release the low-content plasma confined in the flux tubes to the inner magnetosphere[15].

Since particles from the model boundary, after drifting into the model region, form the main population of the plasma sheet, an appropriate description of their distributions is crucial to successfully modeling the plasma sheet[144]. Unlike substorm,

geomagnetic storms are long-lasting and strong disturbed conditions. Since the inner magnetospheric models usually have their boundary beyond geosynchronous orbit, the satellite observations can not provide continuous nightside plasma sheet conditions. Therefore, the RCM particle flux boundary conditions are estimated using statistical plasma sheet models particularly for storm events.

The current version of the RCM has 4 time-dependent boundary conditions and 3 time-independent boundary conditions. The time-dependent boundary conditions are statistical model, while the time-independent boundary condition is given by user through inputting numbers. The RCM currently accept 3 ways of specify time-independent plasma sheet conditions, which is the density and temperature of plasma sheet at $-13R_E$, the density and temperature of plasma sheet at -9 R_E which is about the place of Geotail spacecraft, and the $pV^{5/3}$ and $TV^{2/3}$ at -13 R_E, which then converted to the plasma sheet density and temperature in the code. The difference between time-dependent and time-independent plasma sheet is kind of artificial. Any time-dependent boundary conditions could be considered as time-independent, if the initial conditions are used through the simulation. If time-independent boundary conditions are provided at each time step, then they are time-dependent. Following this rule, we have modified several time-independent statistical boundary conditions into time-dependent boundary conditions.

To estimate plasma sheet properties statistically, we need to be clear that the properties of the plasma sheet are highly correlated with the properties of the solar wind[33]

1. the density of the plasma sheet is strongly correlated with the density of the solar wind
2. the temperature of the plasma sheet is strongly correlated with the velocity of

the solar wind

3. the particle pressure and total pressure of the plasma sheet are strongly correlated with the ram pressure of the solar wind
4. B_y in the plasma sheet is strongly correlated with the B_y in the solar wind
5. B_z in the plasma sheet is weakly correlated with B_z in the solar wind
6. E_y in the plasma sheet is weakly correlated with the E_y in the solar wind
7. plasma sheet earthward-tailward flow velocity is weakly anticorrelated with the solar wind velocity

The first time-dependent boundary condition is a Kp-based formula as a heritage from the MSM era. The density and temperature of the plasma sheet is expressed as

$$\begin{aligned} n_{ps} &= 0.25 \times [0.4 \times (Kp-1) + 0.5 \times (5-Kp)] \\ t_{ps} &= \frac{4}{3} \times \frac{2}{3} \times t_{ratio} \times [0.2885 \times (Kp-1) + 0.15625 \times (5-Kp)] \end{aligned} \quad (3.24)$$

where the number density n is in cm^{-3}, and the temperature t is in keV, t_{ratio} is the temperature ratio between ions and electrons, which is about 7.8[32]. The factor 4/3 is used to convert E_0 in kappa distribution to kT with the assumption that $\kappa = 6$. The factor 2/3 is a correction term due to their initial mistake. Then t_{ratio} is used to convert the plasma sheet electron temperature to plasma sheet ion temperature.

The second time-dependent boundary condition is a 2-dimension distribution of the central plasma sheet ion temperature, density, and pressure, as functions of the incoming solar wind and interplanetary magnetic field parameters[14]. The region is along and across the Earth's magnetotail, at distances between 10 and 50 R_E. The models are based on a large set of data of the Low-Energy Particle (LEP) and Magnetic Field (MGF) instruments, taken by Geotail spacecraft between 1994 and 1998. The solar wind and IMF data were provided by the Wind and IMP 8 spacecraft.

The spatial distribution of parameters are presented in polar coordinates $\{\rho, \phi\}$, where $\rho = (X_{GSM}^2 + Y_{GSM}^2)^{1/2}$ is the distance from the Z_{GSM} axis and $\tan\phi = -Y_{GSM}/X_{GSM}$ is the azimuthal angle measured from the midnight meridian and positive in the dusk sector. The IMF B_Z has been separated into two terms containing its northward term B_N, 0 during southward IMF, and southward term B_S, 0 during northward IMF.

The adopted form for the central plasma sheet temperature was

$$\begin{aligned} T &= A_1 V_{SW}^* + A_2 B_N^* + A_3 B_S^* + A_4 e^{-\left(A_9 V_{SW}^{*A_{15}} + A_{10} B_N^* + A_{11} B_S^*\right)(\rho^* - 1)} \\ &\quad + \left[A_5 V_{SW}^* + A_6 B_N^* + A_7 B_S^* + A_8 e^{-\left(A_{12} V_{SW}^{*A_{16}} + A_{13} B_N^* + A_{14} B_S^*\right)(\rho^* - 1)}\right] \sin^2\phi \end{aligned} \tag{3.25}$$

where $\rho^* = \rho/10R_E$, $V_{SW}^* = V_{SW}/500kms^{-1}$, $B_N^* = B_N/5nT$, and $B_S^* = B_S/5nT$, As are free parameters to fit the observational data. The central plasma sheet density is

$$N = (A_1 + A_2 N_{SW}^{*A_{10}} + A_3 B_N^* + A_4 V_{SW}^* B_S^*)\rho^{*A_8} + (A_5 N_{SW}^{*A_{11}} + A_6 B_N^* + A_7 V_{SW}^* B_S^*)\rho^{*A_9} \sin^2\phi \tag{3.26}$$

where $N_{SW}^* = N_{SW}/10cm^{-3}$. The adopted form of pressure is

$$P = A_1 \rho^{*A_6} + A_2 P_{SW}^{*A_{11}} \rho^{*A_7} + A_3 F^{*A_{12}} \rho^{*A_8} + \left[A_4 P_{SW}^{*A_{13}} e^{-A_9\rho^*} + A_5 F^{*A_{14}} e^{-A_{10}\rho^*}\right] \sin^2\phi \tag{3.27}$$

where $P_{SW}^* = P_{SW}/3nPa$, and $F^* = F/5nT$. The function F is given by

$$F = B_\perp \sqrt{\sin\frac{\theta}{2}} \tag{3.28}$$

where $B_\perp$ is the perpendicular component of the IMF.

Information that can be derived from data-based models is naturally limited by the spatial extent of the data used in the derivation of model parameters[14]. The distributions of the values of the solar wind and IMF parameter used for this model

is shown in Figure 3.10. This data set provides a fair coverage of the average conditions, but contains very few data with unusually fast and dense solar wind, and/or strongly southward/northward IMF. The third time-dependent plasma sheet condition is based on solar wind condition. The entry of matter and fields from the solar wind is statistically examined by looking at data from pairs of satellites: one satellite in the solar wind and one satellite in the plasma sheet. To examine the connection between the solar wind and different regions of the plasma sheet, different pairs of satellites are used[33]. One pair deals with the connection of the solar wind to the magnetotail plasma sheet and other pairs deal with the connection of the solar wind to the near-Earth plasma sheet.

The gradient and curvature drift effects act differently on the electrons and ions, causing the two populations to move on different trajectories. So the near the Earth, the plasma sheet separates into an electron plasma sheet and an ion plasma sheet. The flux tubes that contain the plasma sheet electrons eventually empty out of electrons via precipitating into the loss cone. While only about 10% of the plasma sheet ions are lost to atmosphere to produce proton aurora[145]. The first pair is ISEE-2 in the plasma sheet and ISEE-3 in the solar wind. The other pairs of satellites are the four geosynchronous-orbit satellites 1989-046, 1990-095, 1991-080, and 1994-084 in the near-Earth plasma sheet and either IMP-8 or WIND in the solar wind.

The transport time from the solar wind at the Earth to the mid-tail plasma sheet can be of the order of 1 hour, and the transport time from the solar wind to the near-Earth nightside plasma sheet can be of the order of a few hours. With the 2-hour time shift implemented, "simultaneous" comparisons can be made of the plasma sheet and solar wind properties.

The central plasma sheet density is related to the solar wind density by a power

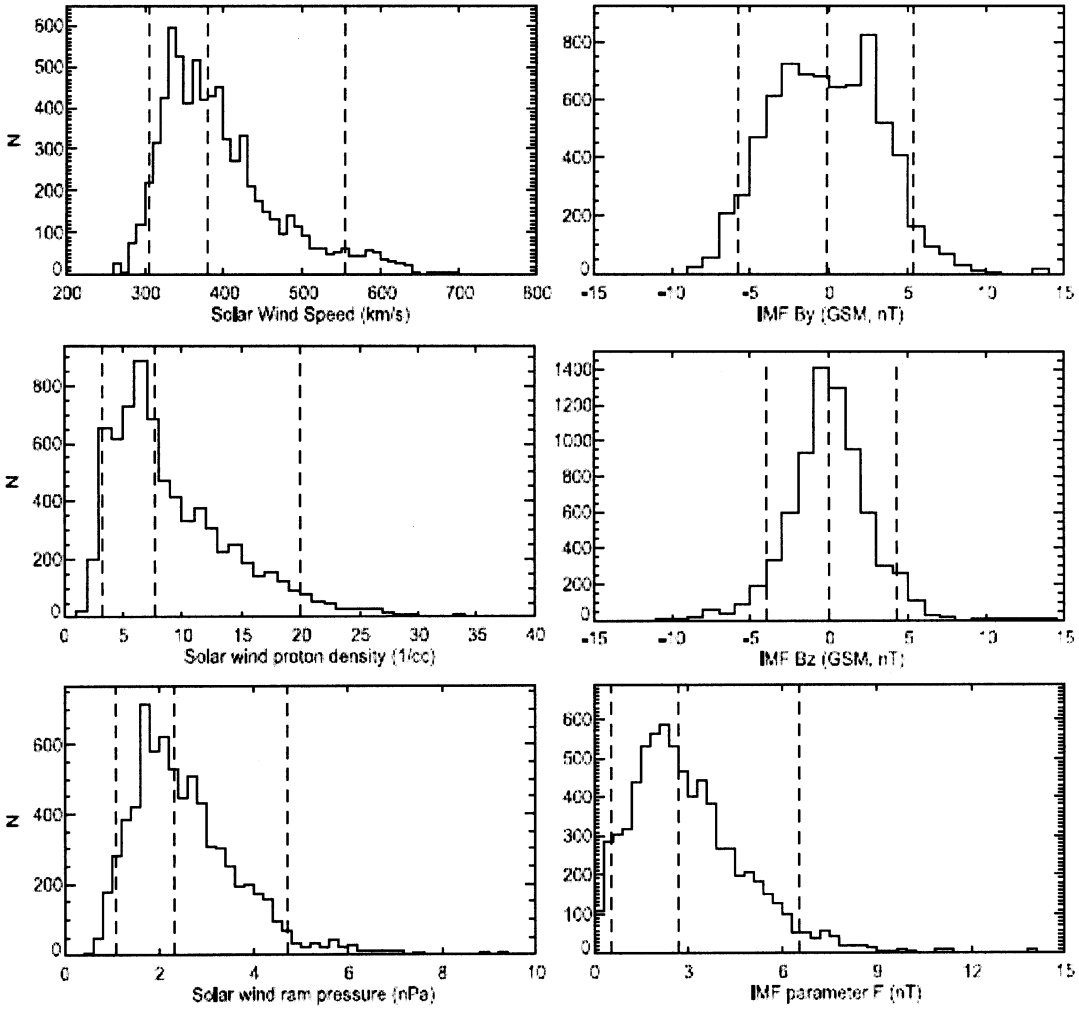

Figure 3.10 : Histogram illustrating the coverage by the data of the parametric space of the solar-wind and IMF-related variables.

of 0.062.

$$n_{ps} = 0.0785 n_{sw}^{0.062} \tag{3.29}$$

where the units for n_{sw} and n_{ps} are cm^{-3}. The temperature has a linear relation with the solar wind velocity.

$$T_{ps} = -3.65 + 0.0190 v_{sw} \tag{3.30}$$

where the unit of T_{ps} is keV and v_{sw} is in km/s.

To facilitate the comparison work between the RCM and the CRCM, another plasma sheet condition is implemented to use Borovsky's plasma sheet temperature with Ebihara's plasma sheet density[146]. It examined the relation between the solar wind density and the plasma sheet density at geocentric distance $9 \sim 11 R_E$, which is appropriate for the boundary condition of a ring current model. The number density and the temperature of ions in the plasma sheet are provided by LEP in the Geotail satellite. The solar wind and IMF data sets are provided by Solar Wind Experiment (SWE) and Magnetic Fields Investigation (MFI). The time lag from WIND to the earth is adjusted by assuming that the solar wind velocity is fixed to be 400 km/s. However, the delay of the penetration of the solar wind medium into the plasma sheet is not adjusted[146].

$$n_{ps} = 0.395 + 0.025 n_{sw} \tag{3.31}$$

where the units for n_{sw} and n_{ps} are cm^{-3}.

3.7 Birkeland Currents and Ionospheric Conductance

In the Earth's magnetosphere, the currents flowing on the magnetopause are called Chapman-Ferraro currents, a westward current through the center of the tail near the equatorial plane is called tail current, the currents flowing around the Earth is called

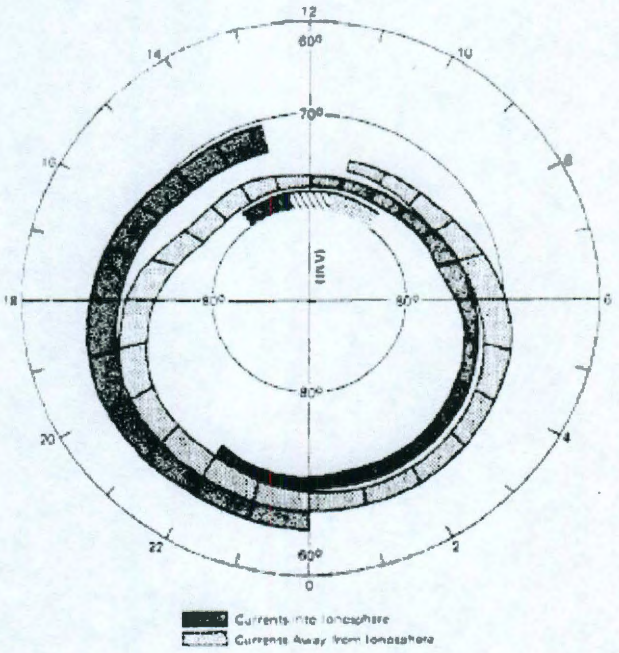

Figure 3.11 : The observational Birkeland currents footprints in the polar region. The inner half circles correspond to high latitude Region 1 currents. The outer half circles are Region 2 currents at lower latitude. Adopted from to Xing [2008] and Iijima and Potemra [1976][15, 16].

ring currents. Between cross-tail currents and ring currents, partial ring currents exist and connect to Birkeland currents to form loops together with horizontal conduction currents in the ionosphere.

The Birkeland currents flow along the magnetic field lines to and from the ionosphere, so it's also called field-aligned currents, shown in Figure 3.11. The current density in region-1 FAC is statistically larger than that of region-2 in quiet time except that the region-2 currents density can exceed region-1 in midnight to morning local time sector[15]. The current density is usually in the order of $10^{-6}A/m^2$, but the average total current is typically in the order of $10^6 A$. Assuming force balance in magnetosphere, so the plasma pressure gradient is approximately balancing the

magnetic forces on the plasma as $\nabla P = \mathbf{j} \times \mathbf{B}$, or

$$\mathbf{J}_{\perp} = \frac{\mathbf{B} \times \nabla p}{B^2} \tag{3.32}$$

By applying the current conservation law $\nabla \cdot \mathbf{J} = 0$, the Birkeland current is calculated by the Vasyliunas' equation

$$\frac{J_{\parallel in}}{B_{in}} - \frac{J_{\parallel is}}{B_{is}} = \frac{\hat{\mathbf{b}}}{B} \cdot \nabla V \times \nabla p \tag{3.33}$$

where $J_{\parallel in}$ is the density of Birkeland current flowing into the northern ionosphere, and B_{in} is the magnetic field strength there; $J_{\parallel is}$ is the density of Birkeland current flowing out of the southern ionosphere, and B_{is} is the magnetic field strength there. The right side can be evaluated at any point along the field line.

The Vasyliunas equation is only applicable in the slow-flow region of the magnetosphere, where plasma flow velocities are small compared to the magnetohydrodynamic wave speeds and the time scales are long relative to the wave travel times[37]. In RCM, it is easier to obtain entropy $pV^{5/3}$ rather than pressure p, so the above equation could be transformed to

$$\frac{J_{\parallel in}}{B_{in}} - \frac{J_{\parallel is}}{B_{is}} = \frac{\hat{\mathbf{b}}}{BV^{5/3}} \cdot \nabla V \times \nabla \left(pV^{5/3}\right) \tag{3.34}$$

Then the right hand side quantity could be easily evaluated on the ionosphere.

Gradient and curvature drift drives Birkeland currents along field lines until they reach the collisional region of the Earth's upper atmosphere: the ionosphere. Unlike occupied by fully ionized collisionless plasma in magnetosphere, the ionosphere is only partly ionized and is strongly affected by collisions. A principal difference between the ionospheric collisional plasma and the magnetospheric collisionless plasma is that a substantial component of the current is proportional to and following the electric

field in the ionosphere. Therefore, the currents in the ionosphere are largely driven by the electric field rather than the magnetic and electric drift.

The current required to produce the force that drags the charged particles through the neutrals is the conduction current. Energy is taken from the process that drives magnetospheric convection and is transferred to the neutral atmosphere in two forms: kinetic energy and Joule heating. The conductivity parallel to the magnetic field lines is called direct conductivity. Each electron tends to move initially antiparallel to the direction of $\mathbf{E}$ after each collision, but each ion tends to move initially parallel to the direction of $\mathbf{E}$. The result is a current in the direction of $\mathbf{E}$. This conductivity is called Pedersen conductivity. The third conductivity is called Hall conductivity. In a collisionless plasma, the response of both ions and electrons is to $\mathbf{E} \times \mathbf{B}$ drift, but they produce no current. But for collisional plasma, the collisions tend to slow the drifts for both particles. The electrons, being more tightly bound to the field lines, are less affected by collisions and therefore come closer to $\mathbf{E} \times \mathbf{B}$ drift which resulting in a current in the direction of $-\mathbf{E} \times \mathbf{B}$. The specific conductivity, another name of direct conductivity, is much larger than either the Pedersen or the Hall conductivity. It's therefore possible to picture magnetic field lines as being perfect conductors within the main conducting regions of the ionosphere, although substantial field-aligned potential drops do occur at altitudes of thousands of kilometers. In the E-region, the Pedersen and Hall conductivities are of the same order of magnitude. While in the F-region, the Pedersen conductivity is dominating since it doesn't change much with the altitude.

The electric current in the rest frame of the Earth could be written as

$$\mathbf{J} = \sigma_0 \left(\mathbf{E} + \mathbf{v}_n \times \mathbf{B}\right)_{\parallel} \hat{\mathbf{e}}_B + \sigma_1 \left(\mathbf{E} + \mathbf{v}_n \times \mathbf{B}\right)_{\perp} + \sigma_2 \hat{\mathbf{e}}_B \times \left(\mathbf{E} + \mathbf{v}_n \times \mathbf{B}\right)_{\perp} \qquad (3.35)$$

where $\mathbf{v}_n$ is the neutral particle velocity, $\hat{\mathbf{e}}_B$ is the unit vector along magnetic field

direction, σ_0 is the "direct conductivity", σ_1 is the Pedersen conductivity, σ_2 is the Hall conductivity. So, the first term is the current directly due to the electric field applied to the plasma; the second term is the Pedersen current perpendicular to the magnetic field but parallel to some component of electric field; the third therm is the Hall current in the $-\mathbf{E} \times \mathbf{B}$ direction.

The ionosphere is treated as a conducting shell which is characterized by conductance instead of conductivity. The conductivity is used to relate current density to electric field. But the conductance is used to relate surface current density to electric field. The conductances are calculated by height integration along magnetic field lines.

$$\Sigma_P = \int \sigma_1 dh \tag{3.36}$$

$$\Sigma_H = \int \sigma_2 dh \tag{3.37}$$

The dominant ionization sources included in global models are the solar-EUV radiation and the auroral electron precipitation at high latitudes. Even though energetic protons are not a dominant energy source in the high-latitude region overall, their contribution to the total auroral energy flux represents on the average about 15% that of electrons[147]. The background radiation, cosmic radiation, scattered EUV sunlight, and the lower latitudes weak precipitation from the radiation belts represent minor ionization sources[148].

For two conductances from two different process, if the sources were strictly separated in altitude, one could simply add the conductances; if the source altitude distributions were identical, the ionization rates would add in the same proportion at every altitude, and the electron density at each altitude would scale by a constant factor as the square root of the summed production rates. For combining solar-EUV-produced

and particle-produced conductances, this estimate of the root-sum-square is far more accurate than a simple sum. It seems reasonable also to apply the root-sum-square approximation to combine conductances from electron and proton sources[149].

The International Reference Ionosphere (IRI) is used in the RCM to provide monthly averages of electron density, electron temperature, ion temperature, and ion composition in the altitude range from 50 km to 2000 km. Additionally parameters given by IRI include the total electron content, the occurrence probability for Spread-F and also the F1-region, and the equatorial vertical ion drift.

A statistical model could be used to estimate auroral electron and ion precipitation[150, 147, 151]. It uses the data from the Defense Meterological Satellite Program (DMSP) data. It determines the average characteristics of auroral precipitation as a function of magnetic local time, magnetic latitude, and geomagnetic activity either measured by Kp[150, 147] or categorized as solar wind velocity and IMF B_Z[151].

In the RCM, Σ_P and Σ_H are computed from precipitating energy flux and the average energy of the precipitating particles. The electron contribution to the Hall and Pedersen conductances is given by[152]

$$\begin{aligned} \Sigma_P &= \frac{40\bar{E}}{16+\bar{E}^2}\Phi_E^{0.5} \\ \Sigma_H &= \frac{18\bar{E}^{1.85}}{16+\bar{E}^2}\Phi_E^{0.5} \end{aligned} \tag{3.38}$$

where Pedersen conductance Σ_P and Hall conductance Σ_H are in the unit of S, Φ_E is the energy flux in mW/m^2s or $ergs/cm^2s$, $\bar{E}$ is the average energy in keV, both for electrons with energy between $500eV$ and $20keV$. And the ratio between Hall conductances and Pedersen conductances is $0.45\bar{E}^{0.85}$. The Pedersen and Hall

conductances produced by an incident proton beam are computed as[149]

$$\begin{aligned} \Sigma_P &= 5.7\Phi_E^{0.5}\left(\frac{B}{B_0}\right)^{-1.45} \\ \Sigma_H &= 2.6\Phi_E^{0.5}\left(\frac{B}{B_0}\right)^{-1.90}\bar{E}^{0.3} \end{aligned} \tag{3.39}$$

where $B_0 = 54\mu T$, energy flux and average energy are for protons with energy between $2keV$ and $40keV$. The conductances produced by electrons are relatively insensitive to the shape of the energy spectrum[152]. The conductances produced by protons should be even less sensitive to the shape of thee energy spectrum[149].

We could also use the Naval Research Laboratory (NRL) SAMI3 code to compute the field-line integrated conductances in the RCM[153]. This model is based on the two dimensional model SAMI2[154, 155] and contains chemical evolution of 7 ion species (H^+, He^+, N^+, O^+, NO^{+2}, O^{+2}) in the altitude range 85 km to 20000 km. The complete ion temperature equation is solved for three ion species (H^+, He^+, and O^+) as well as the electron temperature equation. Ion inertia is included in the ion momentum equation for motion along the geomagnetic field. The plasma is modeled in the low- to mid-latitude ionosphere up to $\pm 55°$ magnetic latitude. SAMI3 and the RCM are self-consistently coupled electrodynamically through the potential equation.

The current flowing across the field lines driven by the electrostatic potential Φ can be written as

$$\mathbf{J} = -\overleftrightarrow{\Sigma} \cdot \nabla\phi \tag{3.40}$$

The conductance tensor is defined as

$$\overleftrightarrow{\Sigma} = \begin{pmatrix} \Sigma_{\theta\theta} & \Sigma_{\theta\phi} \\ \Sigma_{\phi\theta} & \Sigma_{\phi\phi} \end{pmatrix} \tag{3.41}$$

where

$$\Sigma_{\phi\phi} = \Sigma_{\theta\theta} \sin^2(I) \approx 2\Sigma_P \tag{3.42}$$

$$\Sigma_{\theta\phi} = -\Sigma_{\phi\theta} \approx \frac{2\Sigma_H}{\sin(I)} \tag{3.43}$$

And I is the inclination angle of the magnetic field relative to the ionosphere:

$$\sin(I) = \frac{2\cos\theta}{\sqrt{1+3\cos^2\theta}} \tag{3.44}$$

and θ is the colatitude angle, the latitude angle measured with respect to the pole.

The electric field on the ionosphere is assumed to be a gradient of a scalar potential. The condition of conservation of current $\nabla \cdot \mathbf{J} = 0$ is expressed as

$$\nabla_h \cdot \left(-\overleftrightarrow{\Sigma} \cdot \nabla_h \phi + \mathbf{j}_w \right) = (J_{\parallel in} - J_{\parallel is}) \sin(I) \tag{3.45}$$

where the subscript "h" represents a 2 dimensional vector operator on the hemispherical reference surface. The left side of the equation represents the divergence of ionospheric conduction current, with the southern ionosphere mapped to the northern hemisphere. The right side consists of the Birkeland current per unit ionospheric area from both hemispheres.

The RCM uses the neutral atmosphere empirical model–MSISE90 and the Horizontal wind model–HWM93 to calculate the contribution of neutral wind. The MSISE (Mass Spectrometer - Incoherent Scatter) model describes the neutral temperature and densities in Earth's atmosphere from ground to thermospheric heights[156]. Below 72.5 km the model is primarily based on the MAP Handbook[157] tabulation of zonal average temperature and pressure, which was also used for the CIRA-86 (COSPAR International Reference Atmosphere), a model provides empirical models of atmospheric temperatures and densities as recommended by the Committee on Space Research (COSPAR). Above 72.5 km MSISE-90 is essentially a revised MSIS-86

model taking into account data derived from space shuttle flights and newer incoherent scatter results. The HWM93 (Horizontal Wind Model) is an empirical model of the horizontal neutral wind in the upper thermosphere[158, 159]. It is a subsequent version of HWM87[160] and HWM90[161]. It provides zonal and meridional winds for specified latitude, longitude, time, and Ap index. Mid- and low-latitude data are reproduced quite well by the model.

SAMI3 could also estimate contributions from the neutral wind term $\mathbf{j}_w$ to the electric potential for quiet-time conditions using the Scherliess and Fejer [1999] empirical model[162]. Another way to estimate $\mathbf{j}_w$ is the Coupled Thermosphere Ionosphere Plasmasphere Electrodynamic (CTIPe) model. It is a global, there-dimensional, time-dependent, non-linear code. It is a union of three physical components: a global, non-linear, time-dependent neutral thermosphere code[163, 164], a mid- and high-latitude ionosphere convection model[165], a plasmasphere and low-latitude ionosphere[166]. The first two components were initially coupled self-consistently and are known as the Coupled Thermosphere-Ionosphere Model (CTIM)[167]. CTIM was further extended by adding the third component to form the CTIP. Later the electrodynamics was solved self-consistently with the neutral dynamics and plasma components. The thermospheric code simulates the time-dependent structure of the wind vector, temperature and density of the neutral thermosphere by numerically solving the non-linear, first-principles, equations of continuity, momentum, and energy.

In the RCM, after plugging the Vasyliunas equation to the right hand side, it gives

$$\nabla_h \cdot \left(-\overleftrightarrow{\Sigma} \cdot \nabla_h \phi + \mathbf{j}_w \right) = \sin(I) B_i \left(\frac{\hat{\mathbf{b}}}{B} \cdot \nabla V \times \nabla p \right) \tag{3.46}$$

which is called the Fundamental Equation of Ionosphere-Magnetosphere Coupling. We solve this equation with polar cap potential distribution to get the electric field potential in the ionosphere.

Chapter 4

Implementation of the RCM

The space physics modeling projects have significant utilities in both scientific study and practical forecasting. The inner magnetosphere drifting models should be able to achieve their physics goals in a timely manner and easily implemented into the whole framework of space weather prediction. This chapter describes several improvement of the RCM for practical use.

4.1 Unwrapping

The RCM has two dimensional grids in the ionosphere. The one in the azimuthal direction is uniform and periodic. A wrapping in this direction was used in the RCM so that we can take the second order spatial derivative at any time without checking the local time direction. However, such wrapping technique is not widely used. It leads to some confusion and difficulties when comparing with or coupling to other codes. For example, three dimensional magnetspheric grids used in MHD codes don't have to be orthogonal or uniform (Figure 4.1) so that there is no periodic direction and thus no wrapping involved. A version of the RCM is created to unwrap the azimuthal direction. Then the first grid in the azimuthal direction in at local noon and the last grid is at the dawn side of the noon. Whenever the values across the noon are needed for computing, they are achieved from the beginning or ending part of the arrays.

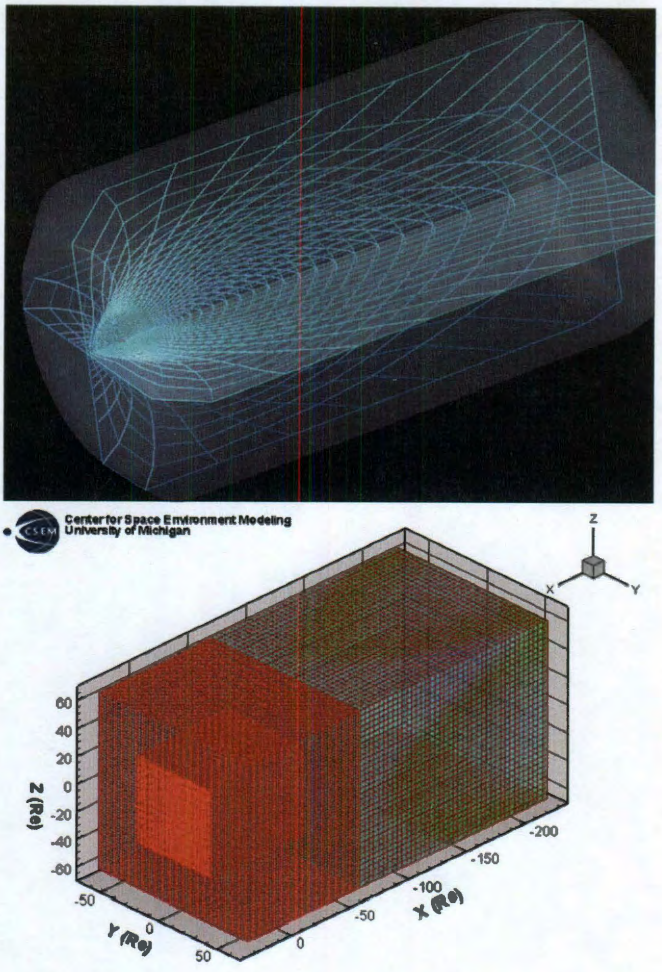

Figure 4.1 : Top: Lyon-Fedder-Mobarry (LFM) model uses a distorted spherical grid with azimuthal symmetry about the polar axis (pointing in the x-direction of the SM coordinate system, roughly sunward). The MHD grid usually covers the domain from about 30 R_E upwind to 300 R_E downwind of the Earth and roughly 100 R_E out to the sides. The complementary ionospheric grid is a mapping of the inner surface of the MHD (magnetospheric) domain to the two polar ionospheres. This typically covers the region from the pole to $45 - 60°$ latitude. Figure courtesy of CCMC. Bottom: Center for Space Environment Modeling (CSEM) uses a nonuniform orthogonal grid with finer grid around the Earth for about 0.25 R_E and coarser grid down to the magnetotail for about 4 R_E. The computational domain occupies the volume from 224 R_E in the nightside to 32 R_E in the dayside, 64 R_E in dawn and dusk directions as well as north and south directions. Figure courtesy of CSEM.

4.2 Parallelization

Since the RCM converts the three dimension magnetosphere calculation into two dimension ionosphere calculation, the computation time in the RCM is usually very quick. However, as a prediction tool, we still need the code to run faster. The parallelization of RCM will not only improve the time efficiency but also make the RCM easier to couple with global MHD codes since they are all parallel versions.

The RCM describes the plasma dynamics in the inner magnetosphere and the electrodynamics of the magnetosphere-ionosphere coupling. The RCM calculates the plasma distribution, field-aligned currents, and the ionospheric electric field potential self-consistently. Those three parts are also the most time-consuming subroutines in the code: the Gmresm subroutine is used to solve potential matrix; the Clawpack subroutine is used to compute the plasma convection; the get_jbirk subroutine is used to integrate the Birkeland currents. Since the grid is two dimensional in the ionosphere, we use partial differential equations in two dimensions. Another subroutine that takes a lot computing time is the subroutine move_plasma_grid, which computes the drift velocity in the ionosphere, the source and lost terms, and then put this information in the calls of the subroutine CLAWPACK.

The RCM has orthogonal grids in the ionosphere. The i direction latitudinal direction. The j direction is the azimuthal direction. We decide to separate the j direction into different processes. Therefore, all one dimensional arrays are kept in each process. All two dimensional or three dimensional arrays are saved in different processes by their direction. Some arrays that were one dimensional arrays but could be separated into processes are modified to two dimensional arrays.

Each processor should have more or less the same burden. Therefore, each processor deals with almost the same number of js. Assume jsize is the size of the grid

points in azimuthal direction, N is the total number of processors, and n is the processor identification number from 0 to N-1. Also, $jsize = pN + q$, where p and q are both integers and $0 \leq q < N$. Then there are $N - q$ processors working on p of j's, and there are q processors working on $p + 1$ of j's. The beginning and ending j's for each process are calculated by

$$j_{beg} = jsize \times n/N + 1 \tag{4.1}$$

$$j_{end} = jsize \times (n + 1)/N \tag{4.2}$$

where the right hand side uses integer division during the calculations.

The parallelization of the subroutines get_jbirk and move_plasma_grid are quite straightforward. Both subroutines loop over both i direction and j direction and also the energy dimension k. So each process now just deals with the azimuthal direction in certain range. Communication might be necessary if values from adjacent process are needed in the calculation.

CLAWPACK (Conservation LAWs PACKage) is a software package designed to compute numerical solutions to hyperbolic partial differential equations using a wave propagation approach. Most of the one-dimensional and two-dimensional CLAWPACK routines were written by Randall J. LeVeque, from Department of Applied Mathematics at University of Washington at Seattle.

CLAWPACK is a package of Fortran subroutines for solving time-dependent hyperbolic systems of partial differential equations in 1, 2, and 3 space dimensions, including nonlinear systems of conservation laws. The software can also be used to solve nonconservative hyperbolic systems and systems with variable coefficients, as well as systems including source terms. The package includes an MPI version in which the domain can be distributed among multiple processors, and adaptive mesh

refinement versions (AMRCLAW) in two and three space dimensions.

The methods used in CLAWPACK are based on solving Riemann problems for the wave structure and then introducing a fluctuation splitting technique that generalizes the notion of flux-difference splitting from conservation laws. The left-going and right-going fluctuations capture the net effect of all left-going and right-going waves, and these fluctuations are then split in the transverse direction in the generalization to more space dimensions[168].

The Godunov scheme involves three distinct steps to obtain the solution at $t = (n+1)\Delta t$ from the known solution at $t = n\Delta t$, as follows:

1. Define piecewise constant approximation of the solution at $t = (n+1)\Delta t$, which is an average of the solution over the cell of size, corresponding to a finite volume method representation whereby the discrete values represent averages of the state variables over the cells. Exact relations for the averaged cell values can be obtained from the integral conservation laws.

2. Obtain the solution for the local Riemann problem at the cell interfaces. The discontinuities at the interfaces are resolved in a superposition of waves satisfying locally the conservation equations. The original Godunov method is based upon the exact solution of the Riemann problems. However, approximate solutions can be applied as an alternative.

3. Average the state variables after a time interval Δt. The state variables obtained after Step 2 are averaged over each cell defining a new piecewise constant approximation resulting from the wave propagation during the time interval Δt. To be consistent, the time interval Δt should be limited such that the waves emanating from an interface do not interact with waves created at the adja-

cent interfaces. Otherwise the situation inside a cell would be influenced by interacting Riemann problems.

In most cases the easiest way to apply CLAWPACK to a problem of interest is to find an existing application to a similar problem, copy the relevant files to your own computer, and adapt them to your problem.

Although there is MPI version of CLAWPACK which could be downloaded from the webside, we modify the code from the serial version. For the CLAWPACK, each process could solve their own equation set according to the coefficients calculated in the subroutine move_plasma_grid. The boundary condition is still using periodic boundary condition. Each process needs the values for $j = j_{beg} - 2$ and $j = j_{beg} - 1$ from one side and the values from $j = j_{end} + 1$ and $j = j_{end} + 2$ from the other side. The major change in the CLAWPACK is that now the CFL condition needs to be satisfied in all processes instead of only one process. The time step should keep the same as well.

The Gmres(m) method is used to solve the ionospheric electric potential distribution by the Fundamental Equation of Ionosphere-Magnetosphere Coupling. The derivatives of some conductance at grid point (i,j) in the left hand side depends on the values at grid points (i-1,j), (i+1,j), (i,j-1), (i,j+1). The weight coefficients form the matrix A. The right hand side is basically the Birkeland current, which is stored in a vector b. The vector to be solved is the electric potential, x. The size of latitudinal direction is $isize$ and the size of azimuthal direction is $jsize$. The subroutine would estimate the potential in the closed field line region with boundary conditions given in the open field line region. Set i_{min} as the minimum i so that for any j, the magnetic field line connecting to the ionospheric grid point (i,j) is a closed field line. Then we define $nij \equiv (isize - i_{min} + 1) \times jsize$. So the matrix A is an $nij \times nij$ array

and stored in compressed row method. The vectors b and x are of size nij. The goal is to solve equations $Ax = b$, where A is a matrix, x and b are two vertical vectors.

To solve this matrix equation, iterative methods are used to repeatedly improving an approximate solution until it is accurate enough. Jacobi and Gauss-Seidel methods are the most popular two. Other methods are also in use, such as Successive Over-Relaxation (SOR), Symmetric Successive Over-Relaxation (SSOR), Conjugate Gradient (CG), Minimal Residual (MINRES), and so on. The Jacobi, Gauss-Seidel, SOR and SSOR methods are stationary which are simpler to understand and implement but usually not very effective. CG, MINRES, and many other nonstationary methods are harder to understand but highly effective.

The Generalized Minimal Residual (GMRES) method is an extension of Minimal Residual (MINRES), which is only applicable to symmetric systems. Like MINRES, it generates a sequence of orthogonal vectors. All previously computed vectors in the orthogonal sequence have to be retained since the absence of symmetry makes the procedure no longer be done with short recurrences. The pseudo code of GMRES method looks like

$x^{(0)}$ is an initial guess

while j=1,2,...,max iteration

Solve r from $Mr = b - Ax^{(0)}$

$v^{(1)} = r/\|r\|_2$

$s = \|r\|_2 e_1$ where e_1 is the unit vector $e_1 \equiv (1, 0, 0, \cdots, 0)^T$

for i=1,2,...,m

Solve w from $Mw = Av^{(i)}$

for k=1,...,i

$h_{k,i} = (w, v^{(k)})$

$w = w - h_{k,i}v^{(k)}$

end for

$h_{i+1,i} = \|w\|_2$

$v^{i+1} = w/h^{i+1,i}$

apply rotation matrix $J_1, \cdots, J_{i-1}$ on $(h_{1,i}, \cdots, h_{i+1,i})$

construct J_i such that (i+1)th component of $J_i h_{.,i}$ is 0

$s := J_i s$

if s(i+1) is small enough then UPDATE($\tilde{x}$,i) and return

end for

UPDATE($\tilde{x}$,m)

end while

In the scheme UPDATE($\tilde{x}$,m) replaces the following computations:

Compute y as the solution of $Hy = \tilde{s}$

$H_{i,j} = h_{i,j}$ in the upper $i \times i$ triangular part

$\tilde{s}$ represents the first i component of s

$\tilde{x} = x^{(0)} + y_1 v^{(1)} + y_2 v^{(2)} + \cdots + y_i v^{(i)}$

$s^{(i+1)} = \|b - A\tilde{x}\|_2$

if $\tilde{x}$ is an accurate enough approximation then return

else $x^{(0)} = \tilde{x}$

We start from inputting the matrix A, the vector b, and the initial guess $x^{(0)}$ which is the solution from the previous step in the RCM. Then continue by computing the initial residual, r, based on the initial input. The goal is to minimize this residual through the algorithm. $\|r\|_2$ is the 2-norm of the residual, s is the residual vector, and $v^{(1)}$ is the normalized residual vector. This is the vector from which we build the Krylov subspace.

Using the normalized vector, $v^{(i)}$, we construct the a subspace by multiplying it by A, then orthogonalize it to all previous $v^{(i)}$, and then normalizing to get $v^{(i+1)}$. The vectors $v^{(1)}$, $v^{(2)}$, $\cdots$, $v^{(m)}$ then form the orthonormal m-th Krylov subspace. We use a modified Gram-Schmidt orthogonalization called the "Arnoldi method". At the same time we construct the upper Hessenberg $(m+1)\times m$ matrix by saving the inner product of new residual w and vector $v^{(k)}$. The new solution is given by

$$x^{(i)} = x^{(0)} + y_1 v^{(1)} + y_2 v^{(2)} + \cdots + y_i v^{(i)} \tag{4.3}$$

where the coefficients y_k have been chosen to minimize the residual norm $\|b - Ax^{(i)}\|_2$. The GMRES algorithm has the property that this residual norm can be computed without the iterate having been formed. Thus, the expensive action of forming the iterate can be postponed until the residual norm is deemed small enough.

If no restarts are used, GMRES will converge in no more than n steps (assuming exact arithmetic), where n is the size of the vectors, like any orthogonalized Krylov-subspace method. The major drawback to GMRES is that the amount of work and storage required per iteration increases linearly with the iteration count. Unless, we could obtain extremely fast convergence, the cost will rapidly become prohibitive. For this reason, "restarted" versions of the method are used. After a chosen number m of iterations, the accumulated data are cleared and the intermediate results are used as the initial guess for the next m iterations. This procedure is repeated until

convergence is achieved. Indeed, the crucial element for successful application of GMRES(m) revolves around the decision of when to restart; that is, the choice of m. If m is too small, it might be so slow to converge or fail to converge entirely. If m is too large, it would cost excessive work and storage.

The algorithm for the subroutine Gmresm is the most complicated. However, such kind of parallelization has been widely discussed. In the package of Gmresm, there are three pieces of code to be changed. The first one is the preconditioner calculation. The convergence rate of iterative methods depends on spectral properties of the coefficient matrix. So we might transform the linear system into one that is equivalent in the sense that it has the same solution, but that has more favorable spectral properties. A preconditioner is a matrix that effects such a transformation. A good preconditioner M should be

1. somehow a good approximation to A
2. not prohibitive to compute
3. easier to solve for $Mx = b$ than $Ax = b$

So the first step in Gmresm subroutine is to compute the preconditioner. The matrix A is split as $A = L_a + D_a + U_a$, where L_a is a strictly lower triangular, D_a is diagonal, and U_a is a strictly upper triangular. Then the preconditioner $M = L \times U = (D + L_a) \times D^{-1} \times (D + U_a)$ where $L = D + L_a$ and $U = I + D^{-1}U_a$. The subroutine would go through each line of the nij lines, find the pivots vector, D^{-1}, where $D = D_a - L_a D^{-1} U_a$ so that $M = A$. Due to the triangle properties of L_a and U_a, the D or D^{-1} could be calculated consequently which means the element D_i only depends on $D_1, D_2, \cdots, D_{i-1}$. The parallelization needs to pass each element of the pivots vector to specific process. The second one is the matrix vector multiplication. The algorithm

of such multiplication in serial version is as the definition of the multiplication, $b_i = \sum_j A_{i,j}x_j$. For parallel version, the calculation needs to be finished in N times where N is the number of processes. Assume $N = 10$ and $nij = 100$, in the mth round, where $0 \leq m < N$, and for the nth process, where $0 \leq n < N$, define $q = m + n$ if $m + n < N$ and $q = m + n - N$ if $m + n \geq N$, part of the array A from $10n - 9$ to $10n$ lines will multiply by part of the vector from $10q - 9$ to $10q$. This partial summation would be added for each round. The third one is the matrix solver which solves $My = x$. Since $M = LU$, then it becomes $LUy = x$. So $Uy = L^{-1}x$ and then $y = U^{-1}(L^{-1}x)$. So we need to solve a matrix equation for a upper triangular matrix and a lower triangular matrix. To solve such an equation is very straightforward. If the lower matrix L is a 3×3 matrix, i.e.

$$L = \begin{pmatrix} L_{11} & 0 & 0 \\ L_{21} & L_{22} & 0 \\ L_{31} & L_{32} & L_{33} \end{pmatrix} \tag{4.4}$$

and

$$b = \begin{pmatrix} b_1 \\ b_2 \\ b_3 \end{pmatrix} \tag{4.5}$$

then the solution is

$$\begin{aligned} x_1 &= \frac{b_1}{L_{11}} \\ x_2 &= \frac{b_2 - x_1 L_{21}}{L_{22}} \\ x_3 &= \frac{b_3 - x_1 L_{31} - x_2 L_{32}}{L_{33}} \end{aligned} \tag{4.6}$$

For a 3×3 upper matrix, i.e.

$$U = \begin{pmatrix} U_{11} & U_{12} & U_{13} \\ 0 & U_{22} & U_{23} \\ 0 & 0 & U_{33} \end{pmatrix} \tag{4.7}$$

and

$$b = \begin{pmatrix} b_1 \\ b_2 \\ b_3 \end{pmatrix} \tag{4.8}$$

then the solution is

$$\begin{aligned} x_3 &= \frac{b_3}{U_{33}} \\ x_2 &= \frac{b_2 - x_3 U_{23}}{U_{22}} \\ x_1 &= \frac{b_1 - x_3 U_{13} - x_2 U_{12}}{U_{11}} \end{aligned} \tag{4.9}$$

The method itself is very hard to parallelize. However, for the matrix in the RCM, in which the non-zero elements are regularly located, we could control the communications among processes. Nevertheless, this part is the real bottleneck of the whole parallelization.

A simple case of running MPI version of the RCM gives an overview of the speedup of the parallelization. This is a 1 minute simulation run. It needs about 50 seconds for 1 process to run. For 2 processes, the running time decreases to about 38 seconds. For 3 processes, the running time is about 36 seconds. For 4 processes, it reaches a minimum of about 32 seconds. But for 5 processes or more, it doesn't go down but up a little bit. It means the current algorithm of parallelization is not good enough. The maximum speed up is about 36%.

4.3 Web Interface

The CCMC is a multi-agency partnership to enable, support and perform the research and development for next-generation space science and space weather models. The CCMC is overseen by an interagency steering committee with rotating membership that provides strategic guidance to the CCMC operations. The CCMC is situated at NASA Goddard Space Flight Center (GSFC). The CCMC staff consists of NASA civil servants, contractors, postdoctoral fellows and visitors. It provides, to the scientific community, access to modern space research models (1) through an automated request system for model runs (2) through modern, online, visualization and analysis tools (3) through standard data formats for simulation data downloads. It could be used to test and evaluate models as an unbiased agent through event studies, and through real-time calculations. It is a great platform for space weather forecasters through model evaluations and the provisions of forecasting tools.

The RCM is an important part of magnetosphere model. However, the stand alone RCM doesn't have an interface in CCMC. Therefore, we want to build a CCMC type web page so that people would request a RCM run through the interface. The main page gives a brief introduction of the model, the inputs into the model and outputs from the model, basic contact information, and several references. In the first step, the user needs to provide basic information including first name, last name, and email address (Figure 4.2). A run number could be selected from 1 to 4 which means only 4 different runs are available for each day. You can overwrite a previous run number if you find out something is not properly input.

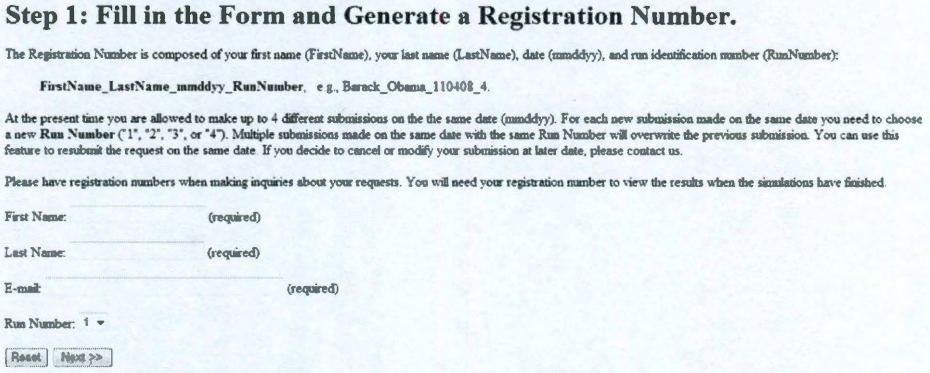

Figure 4.2 : Grid selection in the web interface.

The next step is to specify the interested time period form three methods (Figure 4.3). The first one is to select a major storm event from the drop list of 96 major storms since 1995 to 2008. The second is to select the beginning date and time as well as the ending date and time. The third way is to upload your own "inputs.dat" file.

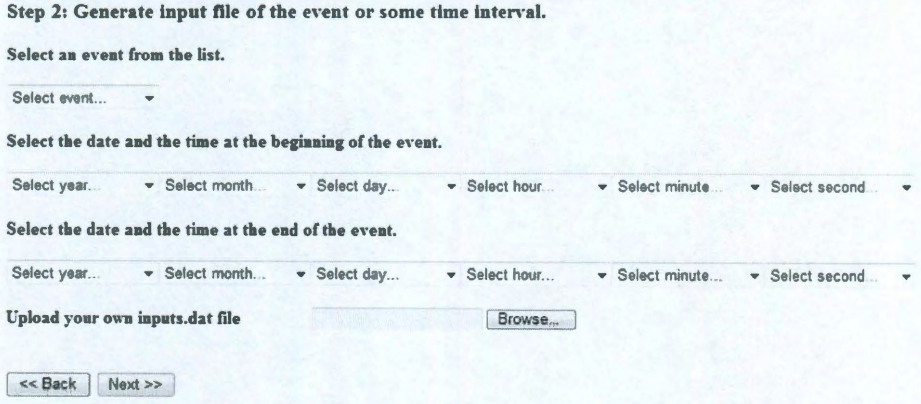

Figure 4.3 : Time period selection in the web interface.

The following step is to generate the "rcm.params" file. You should first select a grid resolution (Figure 4.4) from the list of 4 resolutions. You should also change

the five parameters of colatitude distribution if necessary. You could check the figure of colatitude spacing versus the colatitude. The grid needs to cover to about 80° colatitude.

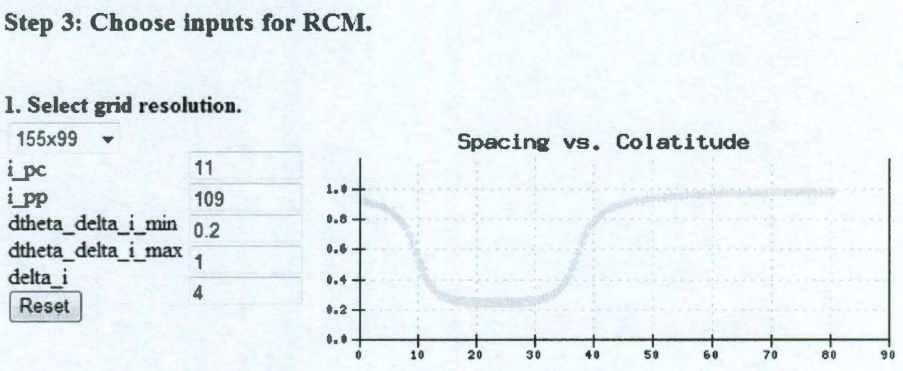

Figure 4.4 : Grid selection in the web interface.

You will also be asked about the magnetic field input, the number of energy channels for each of the three chemical species and energy level spacing, the ion and electron temperature ratio in the plasma sheet, the Kp index for ion composition calculation, the option of high latitude plasma sheet boundary condition, the kappa value of distribution function in the plasma sheet, and the initial distribution function (Figure 4.5).

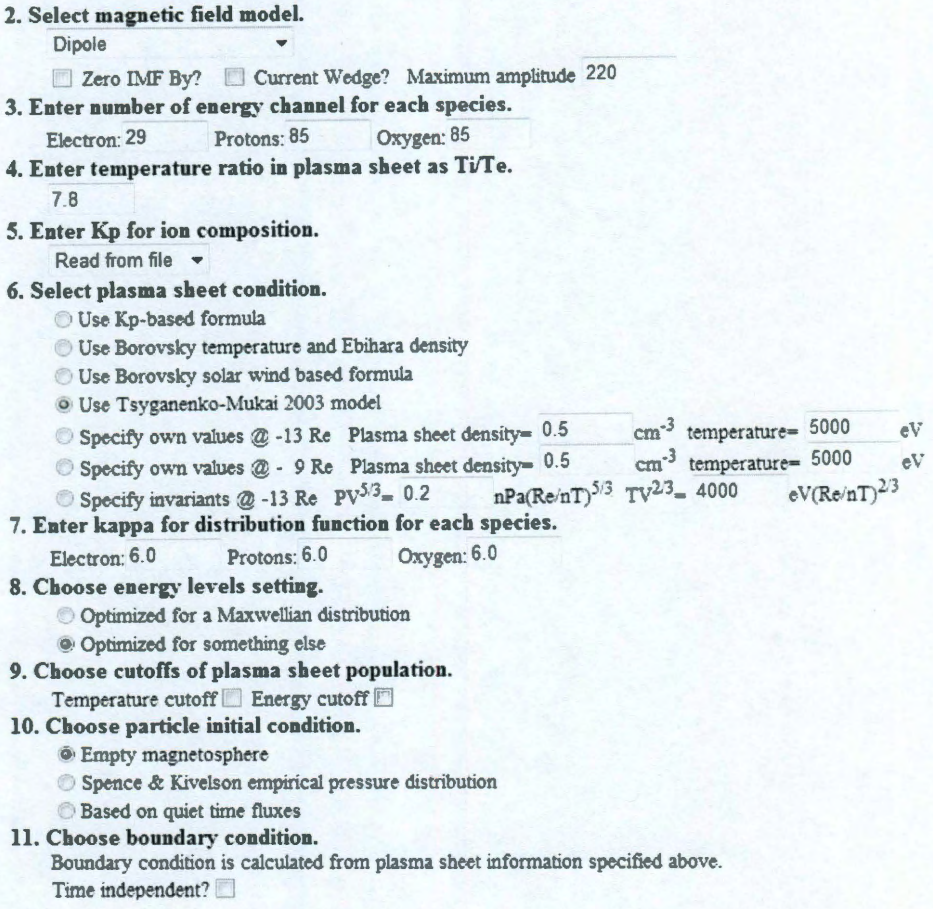

Figure 4.5 : Parameter selection in the web interface.

There are also modules of ionospheric conductances, electron and ion precipitation, charge exchange, thermospheric wind, field-aligned potential drop, ion outflow, polar cap potential (Figure 4.6).

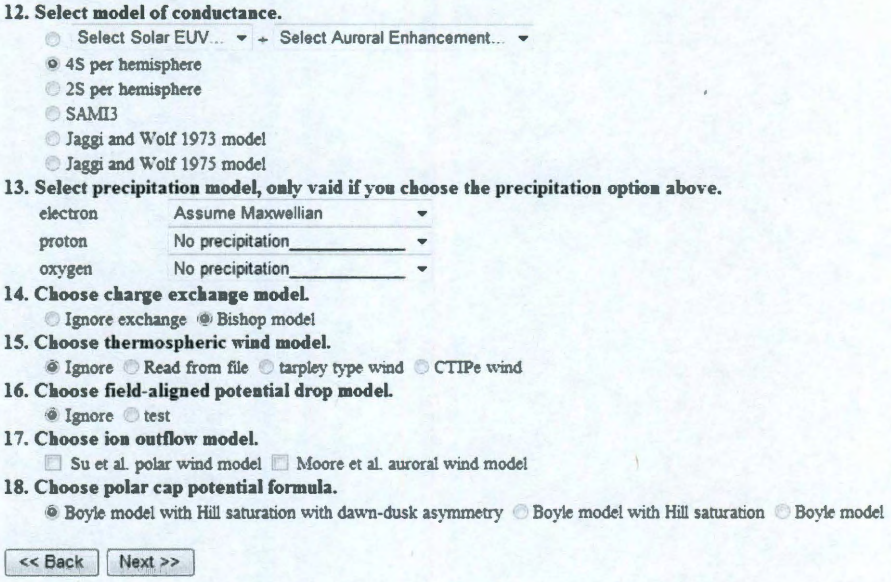

Figure 4.6 : Module selection in the web interface.

The fourth and the last step is to generate the "tecplot.params" file which is used in post processing. The file name is called tecplot because that is the main processing tool we used to analyze the RCM result. So we need to tell the tecplot converter what you need. A series of checkboxes are used to transform to logical parameters, such as axis information, magnetic field information, electric field and Birkeland current, ionospheric conductances, plasma properties, precipitating fluxes, conductance of species, plasma properties of species, q and r tests, quasi-3D plasma energy, quasi-3D claw velocity, and quasi-3D equatorial velocities (Figure 4.7).

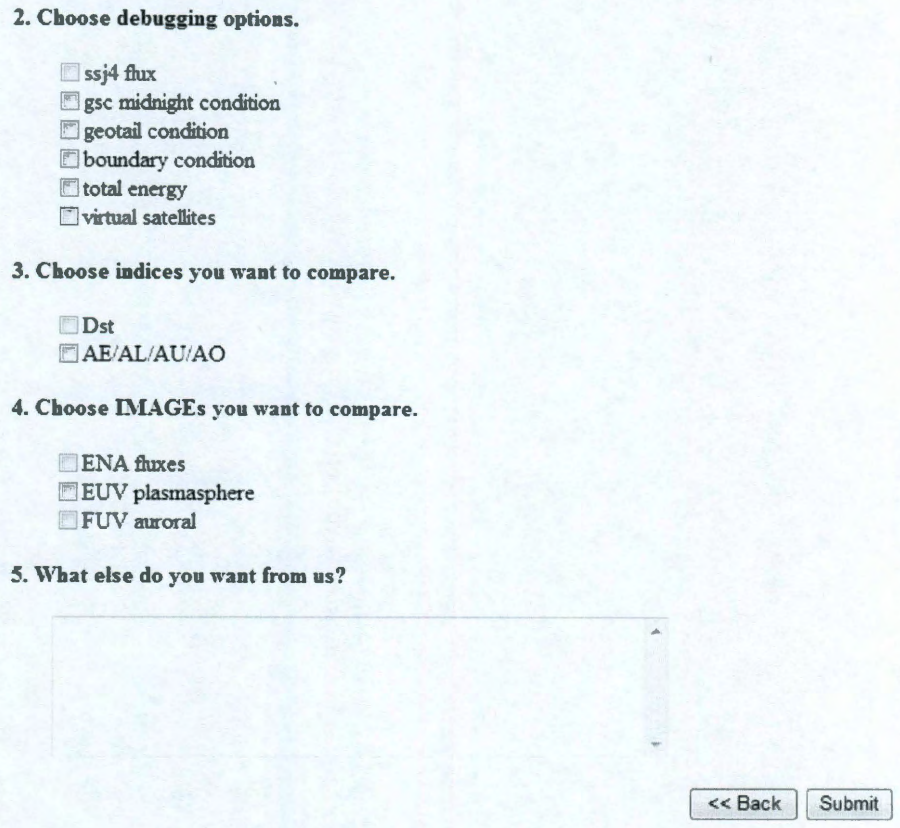

Figure 4.7 : Output selection in the web interface.

There are several debugging tools in the RCM to compare simulation results with observations. The precipitating flux could be compared with the DMSP ssj4 measurements. The DMSP satellites are in a sun-synchronous, low altitude polar orbit, as shown in Figure 4.8. The orbital period is 101 minutes and the nominal altitude is 830 km. The SSJ/4 is the Precipitating Electron and Ion Spectrometer. It provides a complete energy spectrum of the low energy particles that cause the aurora and other high latitude phenomena. The data set consists of electron and ion particle fluxes between 30 eV and 30 KeV recorded every second, satellite ephemeris and magnetic coordinates where the particles are likely to be absorbed by the atmosphere. The

detectors also record high energy ions that penetrate both the satellite and the instrument. This is most noticeable in the South Atlantic Anomaly and at the "horns" of the radiation belts. It consists of four electrostatic analyzers that record electrons and ions between 30 eV and 30 KeV as they flow past the spacecraft toward the Earth. The instruments "look" toward the satellite zenith. Electrons and ions of the selected energy are deflected toward the target by an imposed electric field applied across the two plates. The two low energy detectors consist of 10 channels centered at 34, 49, 71, 101, 150, 218, 320, 460, 670, and 960 eV. The high energy detector measures particles in 10 channels centered at 1.0, 1.4, 2.1, 3.0, 4.4, 6.5, 9.5, 14.0, 20.5 and 29.5 KeV. One of the main calculations in the RCM is the particle flux. By giving option of precipitating module, we could calculate the precipitating flux accordingly. However, the flux depends on the flux tube volume and thus the magnetic field mapping. Since it is a point measurement right above the ionosphere, the results could be quite different if the magnetic field model is not accurate enough.

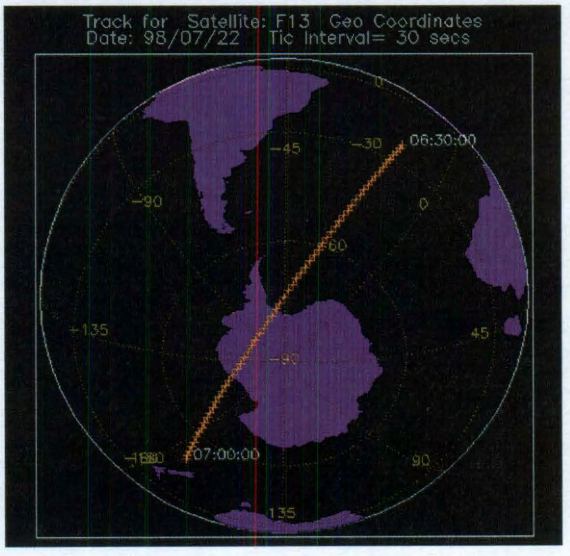

Figure 4.8 : F13 trajectories during 0630 UT and 0700 UT on July 22, 1998.

On the other hand, magnetospheric quantities are measured in the magnetotail region. We could estimate the flux at the nightside geosynchronous orbit, Geotail region, or high-latitude boundary. Virtual satellites could be constructed at all magnetic local time at either geosynchronous orbit or Geotail region as shown in Figure 4.9.

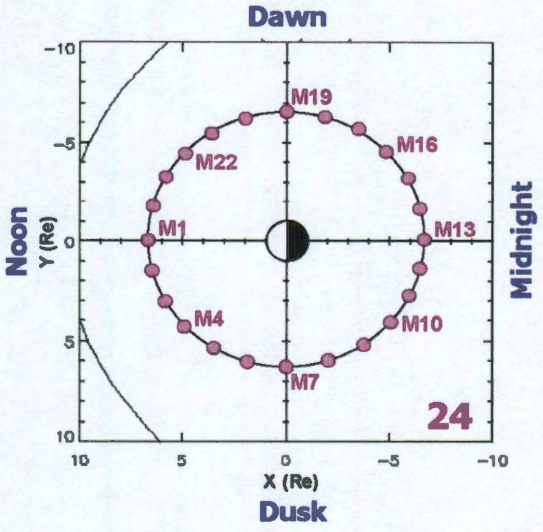

Figure 4.9 : The original idea of putting 24 virtual satellites at the geosynchronous orbit. Figure courtesy of Jichun Zhang.

We could also estimate the Dst change during a storm using the Dessler-Parker-Sckopke (DPS) relation by calculating the total energy within geosynchronous orbit. The DPS relation states that the ratio between the magnetic field perturbation and the magnetic field strength is proportional to the ratio between the total plasma kinetic energy and the total magnetic energy in a dipole field.

$$\frac{Dst}{B_0} = -\frac{2W_K}{3W_D} \tag{4.10}$$

The the Dst index should be proportional to the total ring current energy. However, since the magnetic field deviates from a dipole during magnetic disturbed conditions,

the DPS relation could at best predict the tendency of Dst change. A synthetic magnetogram calculation could be performed using the Biot-Savart law, an inverse-square law, and thus the relative influence of each current depends on its strength and is inversely proportional to the square of the distance from the observation point. There are over 200 ground-based magnetometers in constant operation to observe the magnetic field perturbations on Earth throughout the world. Much of this data is freely available for download and is available with one-minute and one-second resolution and with accuracy within one to a few nanotesla[17].

The Geographic Coordinate system (GEO) is defined so that its X-axis is in the Earths equatorial plane but is fixed with the rotation of the Earth so that it passes through the Greenwich meridian (0° longitude). Its Z-axis is parallel to the rotation axis of the Earth, and its Y-axis completes a right-handed orthogonal set. The Geomagnetic Coordinate system (MAG) is defined so that its Z-axis is parallel to the magnetic dipole axis. The Y-axis of this system is perpendicular to the geographic poles as $\mathbf{Y} = \mathbf{D} \times \mathbf{S}$ where $\mathbf{D}$ is the dipole position and $\mathbf{S}$ is the south pole. Finally, the X-axis completes a right-handed orthogonal set. The Geocentric Solar Magnetospheric System (GSM) has its X-axis in the Earth-Sun line. The Y-axis is defined to be perpendicular to the Earths magnetic dipole so that the X-Z plane contains the dipole axis. The positive Z-axis is chosen to be in the same sense as the northern magnetic pole. The RCM uses the GSM coordinate system.

Magnetic fields are comprised of a vector and thus the field must be described by three elements. The coordinate systems used for ground magnetic data are typically the HDZ, XYZ, and FDI, as shown in Figure 4.10. The declination (D) and inclination (I) are the elements needed to describe the field on the ground. By convention, D and I are measured in degrees. D is the angle between geographic north and the

horizontal vector, with east of north being positive, while I is the angle between the horizontal plane and the total geomagnetic field vector. The elements that describe field intensity are the total intensity (F), the horizontal component (H), the north (X) and east (Y) components of the horizontal intensity, and the vertical component with positive downward (Z) into the ground. The equations that relate the values of these coordinate elements are given by

$$\begin{aligned} F &= \sqrt{X^2 + Y^2 + Z^2} \\ F &= \sqrt{H^2 + Z^2} \\ H &= F\cos I \\ X &= H\cos D \\ Y &= H\sin D \\ Z &= F\sin I \end{aligned} \tag{4.11}$$

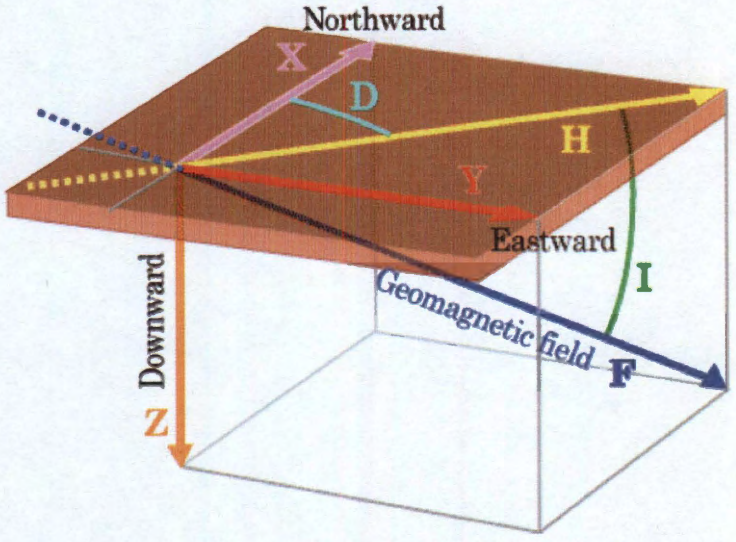

Figure 4.10 : The combinations of the three components frequently used in geomagnetism are HDZ, XYZ and FDI. Figure courtesy of World Data Center for Geomagnetism, Kyoto.

To avoid the confusion of XYZ magnetometer coordinate elements with other coordinate systems, it is helpful to think of the magnetometer field components as a variation of spherical coordinates given by

$$\begin{aligned} X &= -B_\theta \\ Y &= B_\phi \\ Z &= -B_r \end{aligned} \tag{4.12}$$

Since Dst measures the total depression of the horizontal component of the magnetic field, the baseline H must be found for each station to take into account secular variations. The annual mean values of H are calculated using a database of the five quietest days for each month. A second-order polynomial fit to the annual mean values is used to obtain the baseline values for each hour. This value is subtracted from the observation to get the field perturbation.

$$\Delta H(T) = H_{obs} - H_{base}(T) \tag{4.13}$$

where ΔH is the perturbation, H_{obs} is the observed field, and H_{base} is the computed baseline value. The effects of the solar quiet daily variation, a diurnal variation caused by currents in the ionosphere, is also subtracted from the recorded magnetic field using the five quietest days of each month.

$$D(T) = \Delta H(T) - S_q(T) \tag{4.14}$$

Finally, the perturbation D is averaged over the four stations (Honolulu, Kakioka or Alibag, Hermanus and San Juan) and normalized to the dipole equator to estimate the perturbation parallel to the dipole axis.

$$Dst(T) = \frac{\sum_{n=1}^{4} \frac{D_n(T)}{\cos \lambda_n}}{4} \tag{4.15}$$

To describe the geomagnetic disturbance fields in mid-latitudes, a longitudinally asymmetric (ASY) and a symmetric (SYM) disturbance index are introduced and derived for both horizontal (H) and orthogonal (D) components. The symmetric disturbance SYM-H is essentially the same as Dst index but with 1-minute time resolution. Their difference is less than 20 nT for intense storms[169]. The ASY-H is defined to be the range between the maximum and minimum deviation at each moment for the component parallel to the dipole axis[17]. There is a correlation between ASY-H index and AE index[170, 171], but there are essential difference between them.

The auroral electrojet (AE) indices are used to measure the ionospheric electrojet activity in the auroral zone. This set of indices uses a combination of 10 to 13 observatories along the auroral zone in the northern hemisphere to measure the variations in the horizontal component. At every minute in UT, out of all the available AE stations, the largest and smallest horizontal field perturbation is recorded. The AU (auroral upper) index is defined as the upper envelope of the largest recorded values, while the AL (auroral lower) index is defined as the lower envelope of the smallest recorded values. The AE index is defined as the difference between AU and AL (AU-AL). Another associated index is the AO index, and is computed as the average between AU and AL. The AU and AL indices can be interpreted as the effects due to the strongest eastward and westward auroral electrojet currents. The AE index therefore gives a measure of the overall electrojet activity[17].

The Bio-Savart law is defined as

$$\mathbf{B}(\mathbf{x}) = \frac{\mu_0}{4\pi} \int d^3x' \frac{\mathbf{j}(\mathbf{x}') \times (\mathbf{x} - \mathbf{x}')}{|\mathbf{x} - \mathbf{x}'|^3} \tag{4.16}$$

where $\mathbf{B}(\mathbf{x})$ is the magnetic field vector at the point $\mathbf{x}$, and $\mathbf{x}'$ is the location of the current source $\mathbf{j}(\mathbf{x}')$, and μ_0 is the permeability of free space. The total magnetic field is computed by integrating the entire current distribution and should be consistent

with Maxwell's equations of classical electromagnetism[17]. The effects of all current systems, magnetospheric, ionospheric, and geomagnetically induced currents (GIC), are accounted for ground magnetic field within the algorithm.

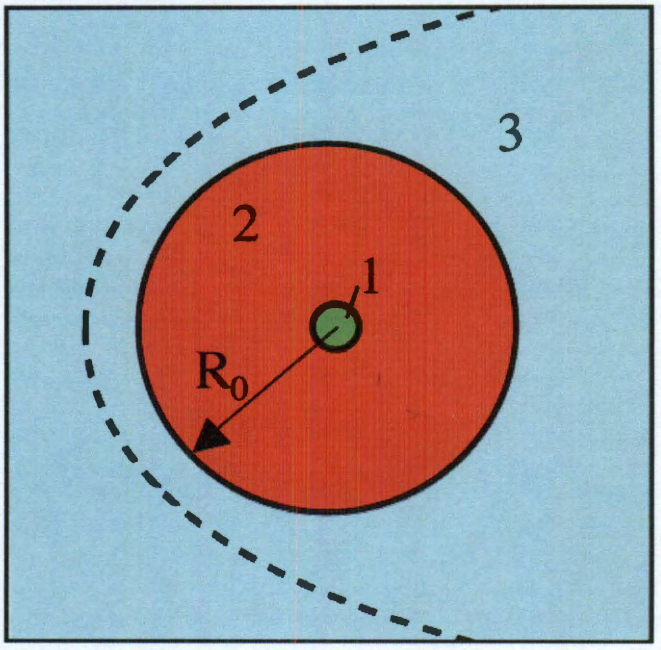

Figure 4.11 : Synthetic magnetogram computational domain. The dashed line represents the magnetopause boundary[17].

The calculation is divided into three concentric zones (Figure 4.11), the region below the Earth, the region from the ionosphere to a reference sphere of radius $R_0 \sim 8R_E$, and the region outside the reference sphere R_0. The contribution from zone 2, where the ionospheric and magnetospheric currents are computed by a magnetosphere-ionosphere coupling code, is from the numerical integration by the Biot-Savart law. The contributions from GICs (zone 1) and all currents outside the reference sphere R0 (zone 3) are computed by representing the magnetic effects due to those currents with scalar potentials.

The RCM also has the options of comparing its results with images, i.e. Imagers for Magnetopause-to-Aurora Global Exploration (IMAGE). This satellite was launched on March 25, 2000, and ceased its operation in December 2005. It has a highly elliptical polar orbit with initial geocentric apogee of 8.2 R_E and perigee altitude of 1000 km. It is the first spacecraft dedicated to observing and imaging the Earth's magnetosphere by identifying the dominant mechanisms for injecting plasma into the magnetosphere on substorm and geomagnetic storm time scales; determining the directly driven response of the magnetosphere to solar wind changes; discovering how and where magnetospheric plasmas are energized, transported, and lost during substorms and geomagnetic storms. It contains Neutral Atom Imagers (LENA, MENA, HENA), Far-ultraviolet (FUV) Imager, Extreme Ultraviolet (EUV) Imager, Radio Plasma Imager (RPI) which is aim to characterize plasma in the Earth's magnetosphere utilizing imaging in the radio frequency range. The RPI instrument is a low-power radar which operates in the radio frequency bands which contain the plasma resonance frequencies characteristic of the Earth's magnetosphere (3 kHz to 3 MHz). RPI can locate regions of various plasma densities by observing radar echoes from the plasma that are reflected where the radio frequency is equal to the plasma frequency. By stepping through various frequencies for the transmitted signal, features of various plasma densities can be observed and, by fitting contours and/or magnetospheric models to the features, a three dimensional specification of the shape of the magnetosphere can be created. Figure 4.12 shows some possible comparison between the RCM results and the images. After the form on the web page has been submitted, a PHP code would gather all the information there and put them into a file currently in csv form so that it could be modified in Microsoft Excel or other application softwares. Then we could run a Fortran program to retrieve those information

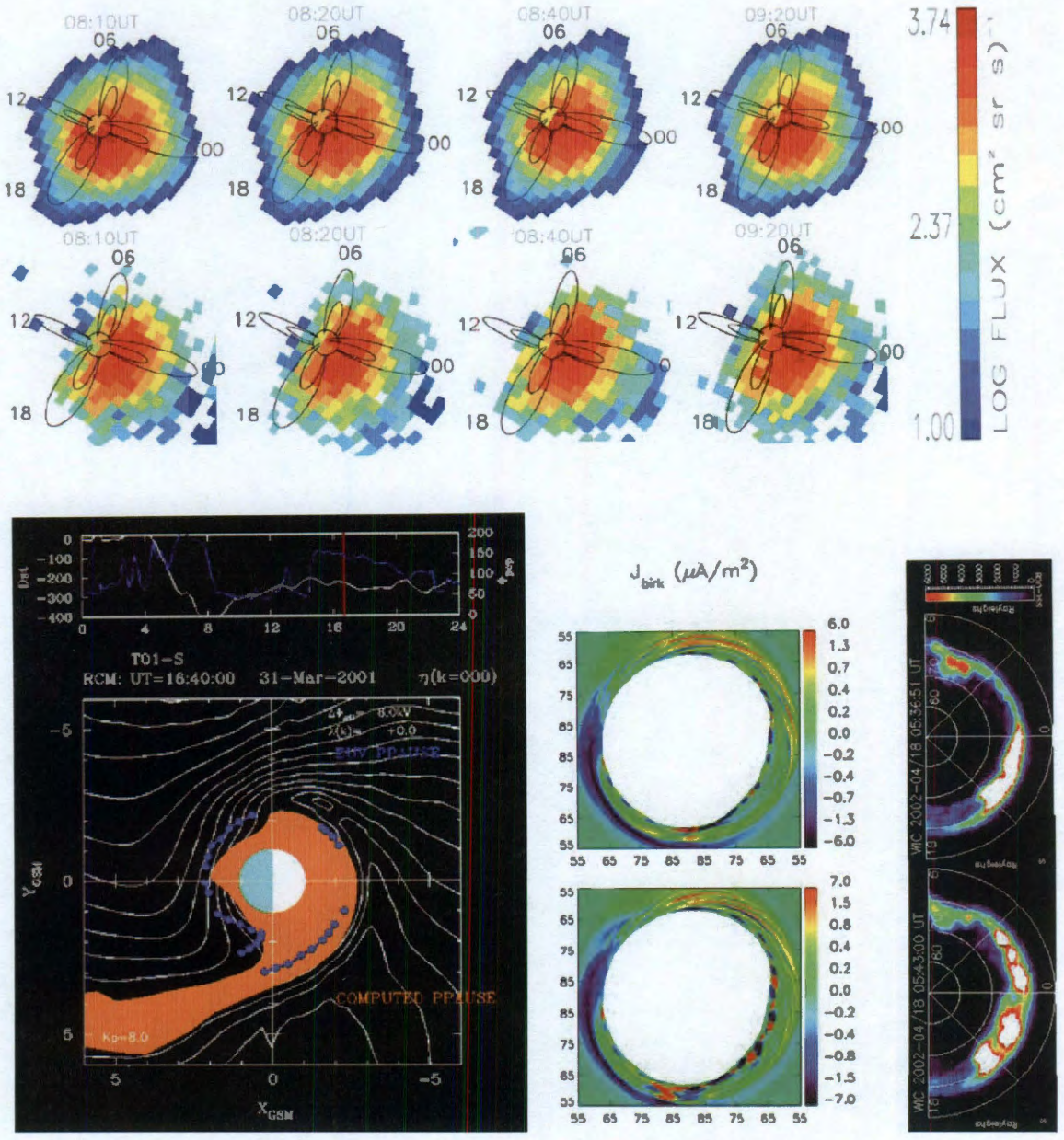

Figure 4.12 : Top: Energetic neutral atom flux of 10-60 keV hydrogen as measured by (second row) IMAGE/HENA compared with the corresponding synthetic flux from (first row) RCM simulation results of April 18, 2002 sawtooth event[18]. The images for times 0810, 0820, 0840, and 0920 UT are shown from left to right. The circle at the center of each image represents the Earth, and the curves are L = 4 and 8 dipole field lines at four local times. Bottom right: (left) the Birkeland current in the ionosphere, and (right) the IMAGE/FUV WIC images at times 0537 (top) and 0543 (bottom)[18]. The sun is to the left. The solid lines shown on the left are the electric potential lines every 8 kV. Bottom left: Comparison of computed plasmapause and observed EUV plasmapause of March 31, 2001 storm.

and generate the three files: "inputs.dat", "rcm.params", "tecplot.params" for each run. To do that, several files saving the history of inputs parameters are already downloaded. The F10.7 flux and the sunspot number could be obtained through

ftp://ftp.ngdc.noaa.gov/STP/SOLAR_DATA/SOLAR_RADIO/FLUX/

ftp://ftp.ngdc.noaa.gov/STP/SOLAR_DATA/SUNSPOT_NUMBERS/

The solar wind and IMF condition could be obtained from OMNI data at

ftp://nssdcftp.gsfc.nasa.gov/spacecraft_data/omni/high_res_omni/

The Dst index, or SYM-H could be achieved from OMNI as well, or read from where we get Kp index, the Geomagnetic Data Services in Kyoto University, Japan, through

http://wdc.kugi.kyoto-u.ac.jp/wdc/Sec3.html

Both yearly format or bimonthly format of ABI index is read from CEDAR database through

http://cedarweb.hao.ucar.edu/wiki/index.php/DMSP:ssj4_midnit

http://cedarweb.hao.ucar.edu/wiki/index.php/Instruments:eqb.

Chapter 5

Plasma Convection in Storm Event Simulation

The ultimate goal of numerical modeling in the magnetosphere is to predict space weather. A geomagnetic storm is a temporary disturbance of the Earth's magnetosphere caused by a reconnection in the nightside tail plasma sheet. Simulations of real time event is a big step for the RCM to be a module of the space weather prediction. Time dependent boundary condition must be used since the plasma sheet is very dynamic during the storms. Therefore, we can not use the average properties from statistical models in the plasma sheet as the boundary condition. Even under extreme solar wind pressure when the stand off distance is quite small, the RCM boundary is still further in the tail that the geosynchronous orbit. Those strong geomagnetic storms could last for days, so no spacecraft observation could be used throughout the event. Statistical plasma sheet properties varying with solar wind and interplanetary magnetic field conditions are proven to be useful in RCM simulation. This fact would help us evaluate the ring current injection during the main phase of geomagnetic storm. The role of these high latitude plasma boundary condition will also be discussed.

5.1 Storm Events

The magnetic storm that started early on March 31, 2001 was caused by a coronal mass ejection (Figure 5.1) and associated interplanetary shocks, leading to extreme

Figure 5.1 : An Earthbound coronal mass ejection associated with the large sun spot 9393 pushed into the Earth's magnetosphere on March 31, 2001.

solar wind conditions[172]. The solar wind dynamic pressure was high and the IMF exhibited intermittent periods of large southward B_Z, resulting in the dayside magnetopause being pushed inside geosynchronous orbit. The imposition of cross polar cap potential drops in excess of 200 kV resulted in the development of a strong ring current. At 0023UT, the solar wind monitoring satellite detected the arrival of a large high-speed solar wind shock front[173]. This large shock pushed in the dayside magnetosphere four or more earth radii and produced a wide spread, but short-duration geomagnetic field disturbance which was observed at approximately 0053 UT around the world. The region of highest-intensity would have been centered over the Pacific and at low latitudes.

Beginning around time 0200 UT, the solar wind magnetic field turned strongly southward beginning the growth of the main phase of the geomagnetic storm. These solar wind conditions persisted until approximately 0800 UT. The coupling caused by the solar wind began a process of building unstable magnetosphere structure that produced substorms and electrojet activity at high-latitude regions and the build up of the equatorial ring-current. The auroral activity is measured by POES satellite as Figure 5.2.

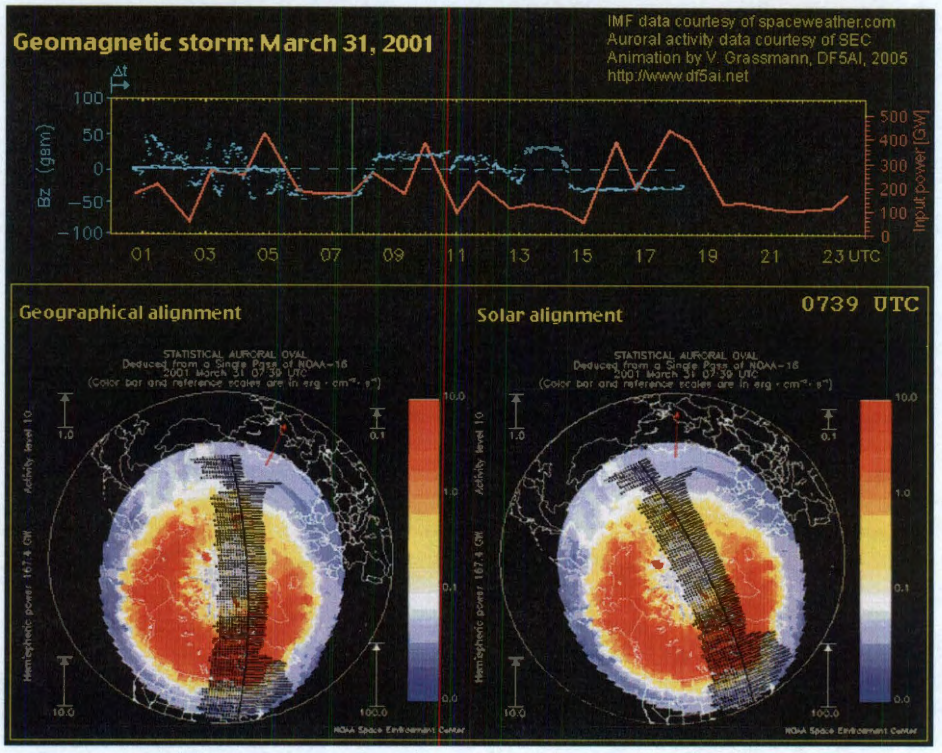

Figure 5.2 : Auroral activity about the minimum Dst on March 31, 2001 storm. The lower left polar plot displays the original POES data with the continents in fixed position. The actual position of the red arrow indicating the direction of the sun. The panel on the right shows the same data with fixing to the direction of the sun. The left and right panel therefore reflect an observer on Earth and an observer on the sun. The upper panel displays the variable Bz component (blue) of the interplanetary magnetic field (IMF) and the actual hemispheric input power (light red), respectively. The IMF data has been shifted by about 30 minutes to consider the solar wind's travel time from the ACE spacecraft to the Earth's magnetosphere. Figure from http://www.df5ai.net/ArticlesDL/Aurora_310301/A310301_aactivity.html

At 08UT, the solar wind polarity turned sharply northward and remained this way until 14UT, at which it turned southward once again until 22 UT. This prolonged southward orientation re-started another main phase of the geomagnetic storm, although it's too small that the injection of fresh ring current ions is balancing the decay of the ring current that was injected earlier. This began a process of substorm

activity and development and intensification of electrojet activity over broad regions.

At time 22UT, a second solar wind shock arrived, which would have again produced a small SSC. More importantly, its arrival heralded solar wind conditions that lead to the rapid decline of the storm, as interplanetary magnetic field strengths in the solar wind fell almost immediately to near zero.

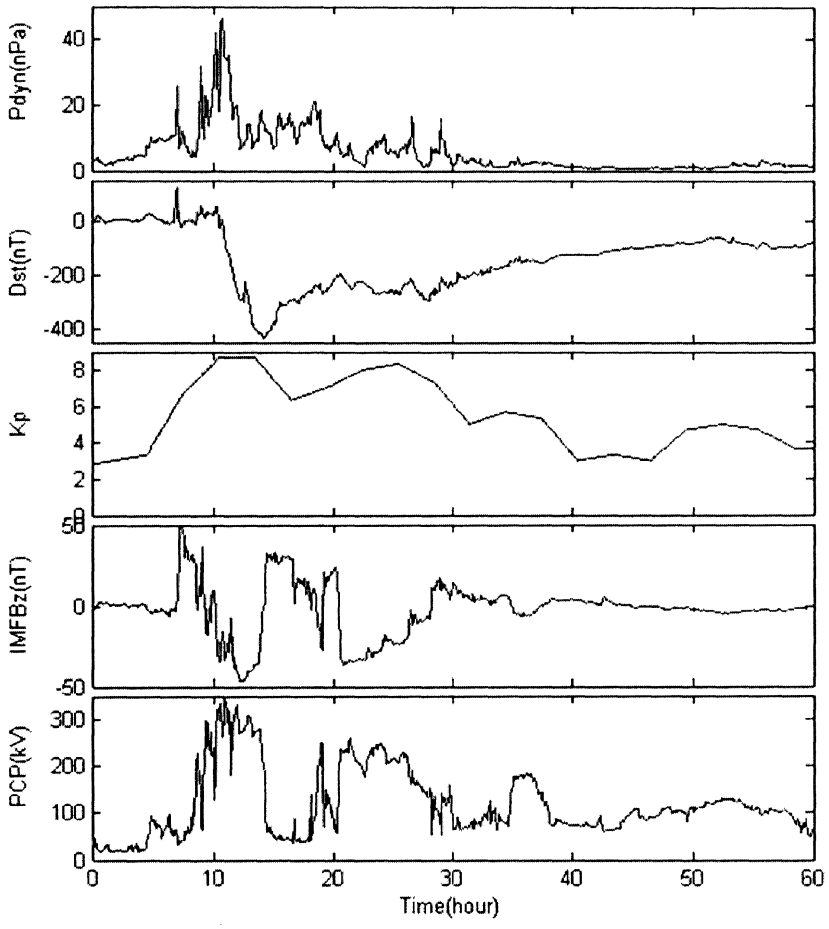

Figure 5.3 : The solar wind pressure, Dst index, Kp index, IMF B_Z, and the polar cap potential of March 31, 2001.

The solar wind pressure, Dst index, Kp index, IMF B_Z, and the polar cap potential

are shown in Figure 5.3. The simulation time 0 in the March 31, 2001 storm event starts at 18 UT of March 30, 2001 and ends at 06 UT of April 2, 2001, which has a 60 hours of simulation that covers the whole main phase and recovery phase. The IMF B_Z component triggers the magnetospheric convection. With the strong solar wind dynamic pressure coming in at at about 10 hours after the start of simulation, the southward IMF B_Z start the main phase in this event. The Dst starts to decrease and reach a minimum below -400 nT at about 14 hours. Then the IMF B_Z becomes northward after getting a minimum of -50 nT. The northward IMF B_Z last about 7 hours and turns to southward again. Because of lack of solar wind pressure, it doesn't create another main phase of a storm. However, it retards the Dst increase in the recovery phase. The polar cap potentials are strong when there are strong magnetospheric convection during southward IMF B_Z. Kp index gives a general idea of that the geomagnetic field is highly active between 7 hours and 30 hours which corresponding to the main phase and early recovery phase in this storm.

Figure 5.4 : Active Region 696 is summarized above from November 3-10, 2003 during its transit of the solar disk[19].

Another extreme strong event happened during November 7 to November 10, 2004. The time period from November 6 to November 9, 2004 have been very active days for solar and auroral events. A major sunspot group, Active Region (AR) 0696, as shown in Figure 5.4 with a complex magnetic field produced several Coronal Mass

Ejections and flares during this time. Only two X Class flares were observed: a X2 on November 7 and a X3 on November 10[19].

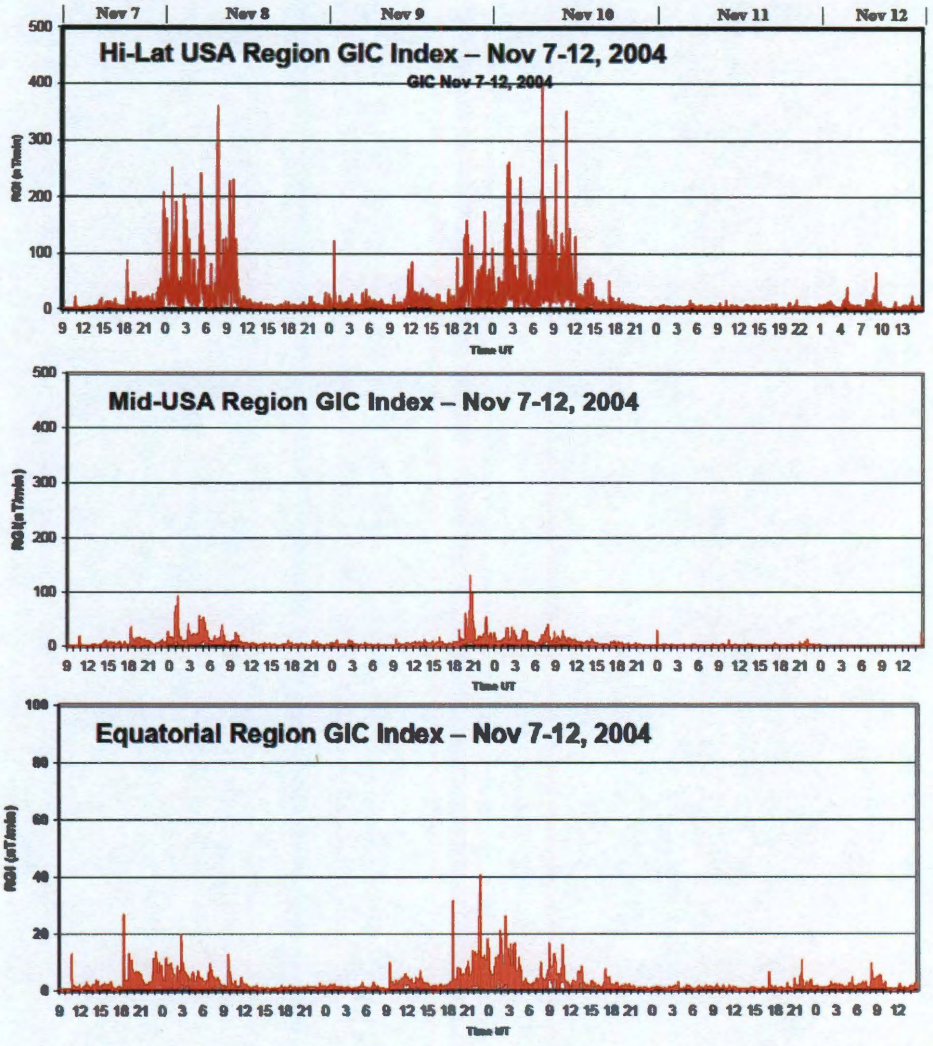

Figure 5.5 : Observed impulsive geomagnetic field disturbance conditions intensity for the high-latitude USA location (top), the mid-latitude USA location (center), and the equatorial region (bottom)[19].

Three separate CME passages occurred generated by flare activity from the above referenced sunspot activity. The first two CME passages generated long duration

geomagnetic storms, while the last one was minor with little geomagnetic storm activity. Figure 5.5 shows the geomagnetically induced currents during this period. It is clear that the most disturbed conditions are during November 7th to November 10th. Solar wind conditions produced energy transfers into the Earth's magnetosphere and this created optimal conditions for auroral precipitation and visible displays at mid-latitudes. That's why our simulation is in the 96-hour period from the 00 UT on November 7th to 24 UT on November 10th.

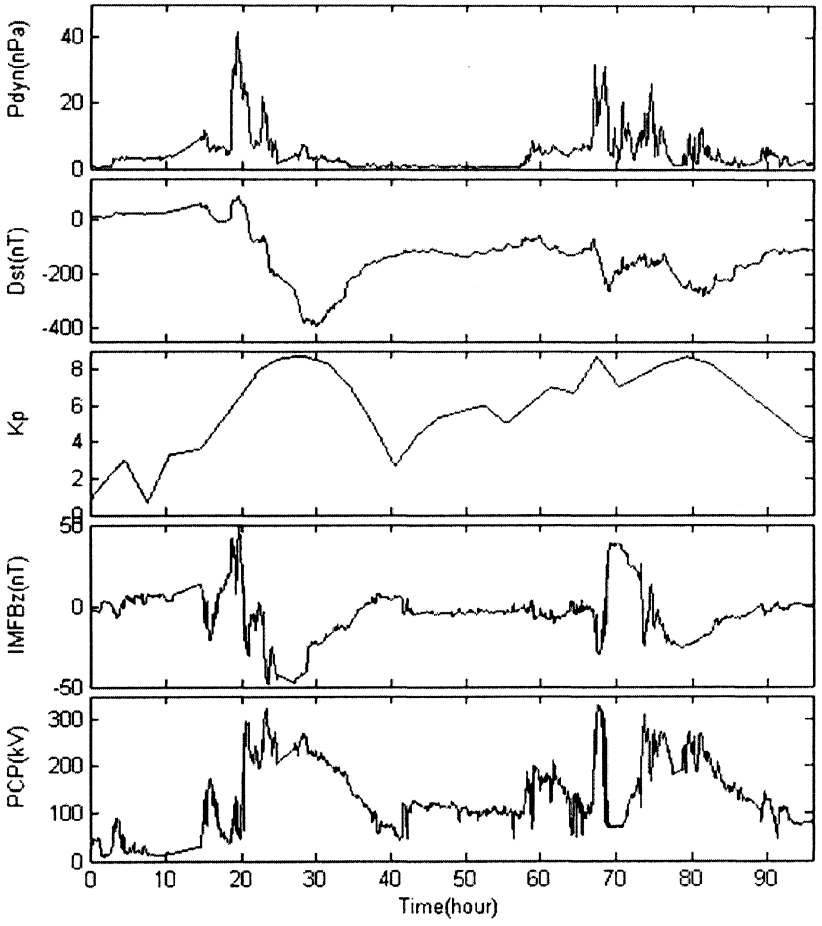

Figure 5.6 : The solar wind pressure, Dst index, Kp index, IMF B_Z, and the polar cap potential of November 7-10, 2004.

The solar wind pressure, Dst index, Kp index, IMF B_Z, and the polar cap potential are shown in Figure 5.6. It is obvious that there are 3 Dst minimum at about 30, 69, 82 hours, respectively. The first one at about 30 hours is the major one which has a minimum Dst of about -400 nT. The other two are close to each other. And the Kp index shows two strong active periods. This is also observed in the solar wind dynamic pressure. Again, the decrease of Dst is caused by the southward turning of IMF B_Z. It first turned southward at about 20 hours and reach the minimum about -50 nT at 27 hours. The IMF B_Z doesn't really turn to northward but keeps about zero for over 24 hours. A sudden drop happened at 68 hours. But it turns to northward quickly and then turns to southward again at about 75 hours. The polar cap potential drops are strong during southward IMF B_Z periods as indications of strong magnetospheric convection.

5.2 Comparison of Plasma Boundary Condition

To model these two storm events, we are using two magnetic field models. One if the Hilmer-Voigt magnetic field model. And the other one is T89 magnetic field model with T96 magnetopause. These two magnetic field models are developed in earlier time and really simple. Since the RCM fixed the grid points in the GSM coordinates and assumed north-south symmetry, so the IMF B_Y component is supposed to be negligible. Therefore, the T89 model depends only on the Kp index, which describes the degree of active in the magnetosphere. The magnetic field would not change if the Kp increases from 6- to above. And the Hilmer-Voigt magnetic field is a function of magnetopause standoff distance, the ring current strength measured by Dst index, and the auroral boundary index, which is the latitude of the equatorward edge of the auroral oval at midnight. The Dst dependence focuses on the direction

of ring current, or the sign of Dst index. But the magnetic field doesn't change too much for negative Dst index. Therefore, these two magnetic field models are not very sensitive to the magnetic field change and expected to be fine even for extreme strong storm. However, the real magnetic field was usually considerably more inflated than these simple models[174]. So the overestimating magnetic field might lead to underestimating flux-tube volume and overestimating particle energy or fluxes.

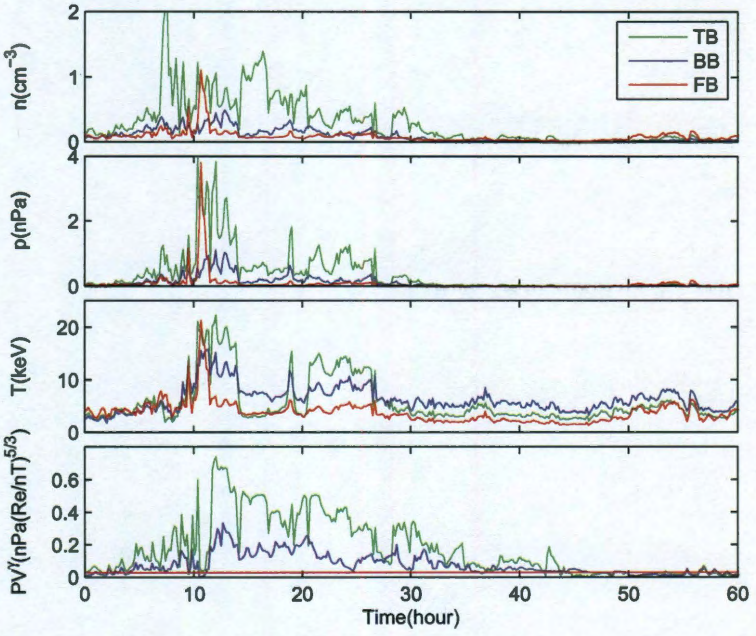

Figure 5.7 : The boundary conditions used in March 31, 2001 event simulation with Hilmer-Voigt magnetic field. The number density (in cm^{-3}), pressure (in nPa), temperature (in keV), and $pV^{5/3}$ (in $(R_E/nT)^{5/3}$) are plotted. The green lines correspond to Tsyganenko-Mukai boundary condition. The blue lines correspond to Borovsky's boundary condition. The red lines correspond to fixed boundary conditions.

In contrast to traditional ring current models, convection models like the Rice Convection Model (RCM)[63], Comprehensive Ring Current Model (CRCM)[116],

and self-consistent RAM model[117] calculate the inner magnetospheric potential electric field self-consistently, proceeding from a prescribed potential on the outer boundary. Convection models use particle boundary conditions that are similar to those of the traditional ring current models, except that most RCM runs place the tailward boundary further out in the tail.

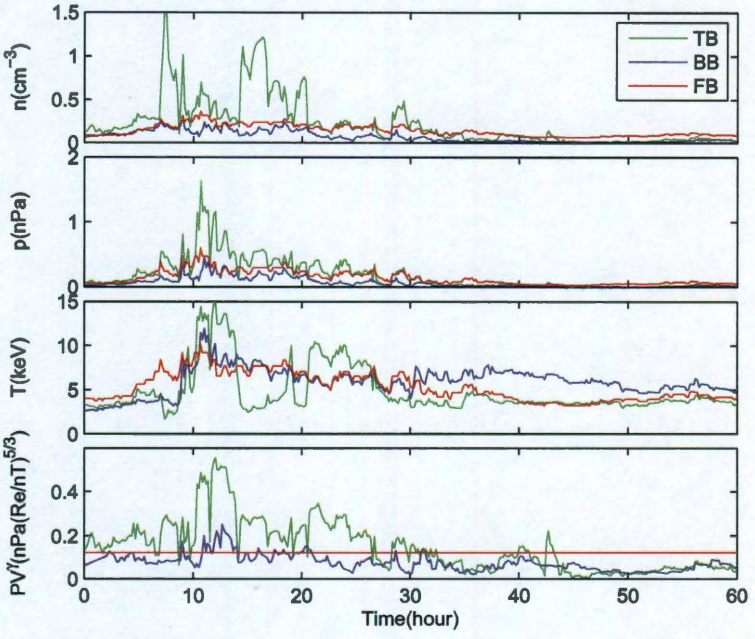

Figure 5.8 : The boundary conditions used in March 31, 2001 event simulation with T89 magnetic field. The number density (in cm^{-3}), pressure (in nPa), temperature (in keV), and $pV^{5/3}$ (in $(R_E/nT)^{5/3}$) are plotted. The green lines correspond to Tsyganenko-Mukai boundary condition. The blue lines correspond to Borovsky's boundary condition. The red lines correspond to fixed boundary conditions.

We are going to use three kinds of boundary conditions, two of which are time dependent boundary conditions. The two time dependent boundary condition are Tsyganenko-Mukai 2003 boundary conditions and Borovsky's boundary condition.

The Tsyganenko-Mukai boundary conditions are functions of solar wind density, velocity, and the IMF Bz components, while the Borovsky's boundary condition is not function of IMF condition but only a function of solar wind density and velocity. For the time independent boundary condition here, we used Tsyganenko-Mukai formula to calculate the plasma sheet density and temperature, and then the η on the boundary in the plasma sheet is kept constant.

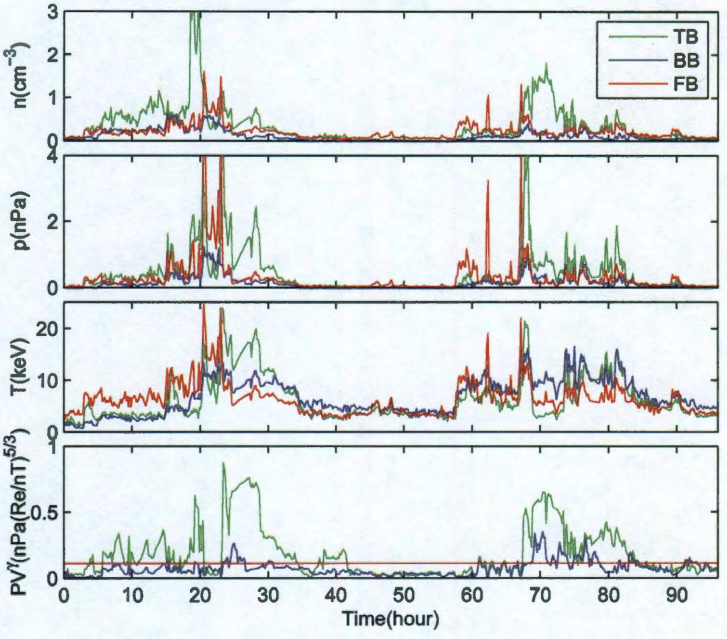

Figure 5.9 : The boundary conditions used in November 7-10, 2004 event simulation with Hilmer-Voigt magnetic field. The number density (in cm^{-3}), pressure (in nPa), temperature (in keV), and $pV^{5/3}$ (in $(R_E/nT)^{5/3}$) are plotted. The green lines correspond to Tsyganenko-Mukai boundary condition. The blue lines correspond to Borovsky's boundary condition. The red lines correspond to fixed boundary conditions.

In figures 5.7-5.10, I am showing the plasma properties at the midnight boundary of the RCM modeling region. The green lines correspond to Tsyganenko-Mukai

boundary condition. The blue lines correspond to Borovsky's boundary condition. The red lines correspond to fixed boundary conditions.

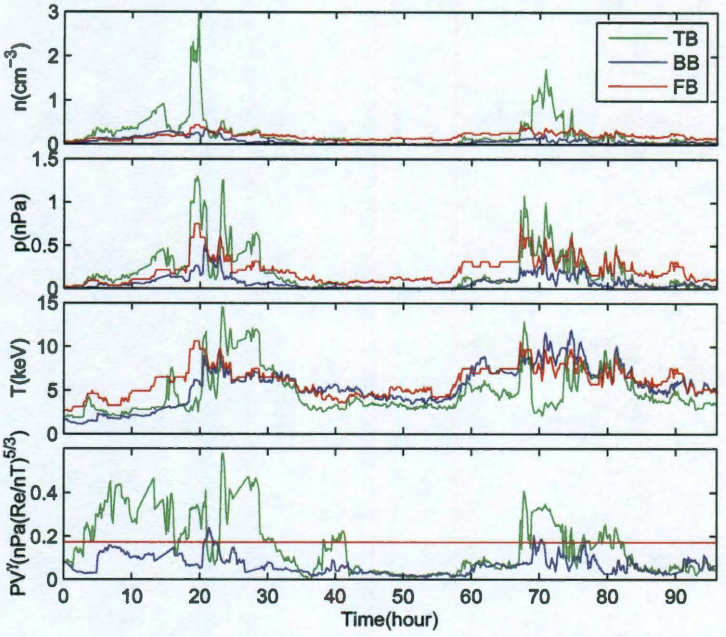

Figure 5.10 : The boundary conditions used in November 7-10, 2004 event simulation with T89 magnetic field. The number density (in cm^{-3}), pressure (in nPa), temperature (in keV), and $pV^{5/3}$ (in $(R_E/nT)^{5/3}$) are plotted. The green lines correspond to Tsyganenko-Mukai boundary condition. The blue lines correspond to Borovsky's boundary condition. The red lines correspond to fixed boundary conditions.

Since the quantity conserved in the time-independent plasma boundary condition is the plasma content in the flux tube volume η, considering the quantity $TV^{2/3}$ is proportional to the energy invariant $\lambda = KV^{2/3}$ by 3/2, the quantity $pV^{5/3}$ is also conserved on the plasma sheet boundary. That's why the entropy is constant for the fixed boundary condition in all four plots. Because of the change in the magnetic field, the flux tube volume is also changing with the time, the plasma sheet density, temperature, and pressure should not be constant for the fixed boundary condition. On

the other hand, the parameters coming from Tsyganenko-Mukai boundary conditions during active times always seem to be greater than the prediction from Borovsky's boundary condition. The huge difference implies that one of them is not very useful for estimating the boundary condition for major storms. The relation between the Tsyganenko-Mukai boundary conditions and fixed boundary condition highly depends on the initial solar wind conditions which is given as the input parameter to the fixed boundary condition.

5.3 Ring Current Injection

The main phase of geomagnetic storm is traditionally defined as a sustained decrease in the average horizontal field strength measured by low-latitude ground magnetometers, due to the growth of a westward ring current carried mainly by 1-200 keV ions that typically peak at L shell value at about 3 or 4. The storm main phase is associated with strong convection, driven by a sustained southward interplanetary magnetic field (IMF)[37].

The injection of the storm-time ring current has been represented quantitatively in terms of ring current models[112, 113, 114, 115] that assume a prescribed time-dependent convection electric field distribution and a prescribed magnetic field model. In these models, ion fluxes are specified at an outer boundary, usually set somewhere between 6.6 and 10 R_E. These models typically show inner plasma sheet ions from the outer boundary being injected to L value of 3 or 4 to form the storm-time ring current. Calculated flux levels are in reasonable agreement with observations. The RCM has been proved to be capable of calculating the plasma distribution and ionospheric electric field with the given magnetic field and magnetosphere-ionosphere coupling through the Birkeland currents. Garner et al. [2004] shows the simulation result of

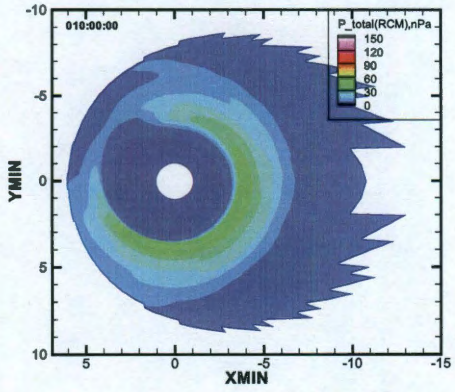
010:00:00
P_total(RCM),nPa
150
120
90
60
30
0
YMIN
XMIN

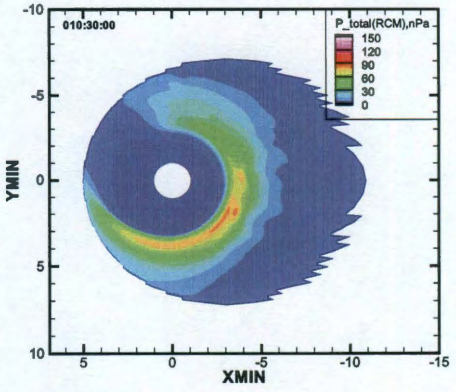
010:30:00
P_total(RCM),nPa
150
120
90
60
30
0
YMIN
XMIN

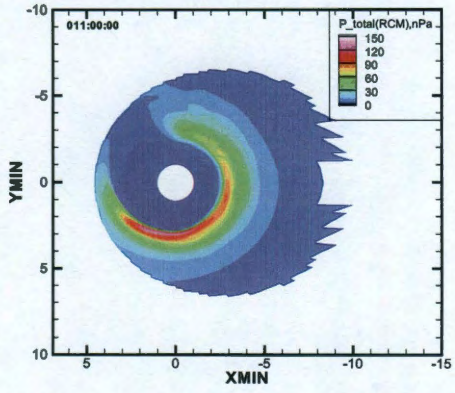
011:00:00
P_total(RCM),nPa
150
120
90
60
30
0
YMIN
XMIN

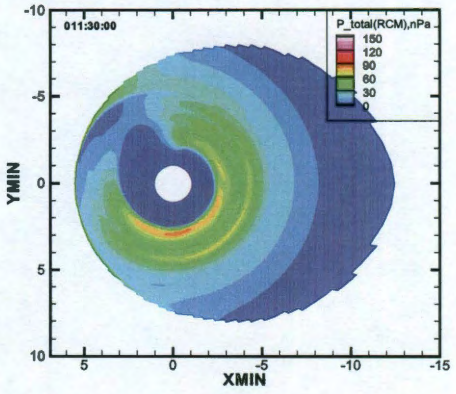
011:30:00
P_total(RCM),nPa
150
120
90
60
30
0
YMIN
XMIN

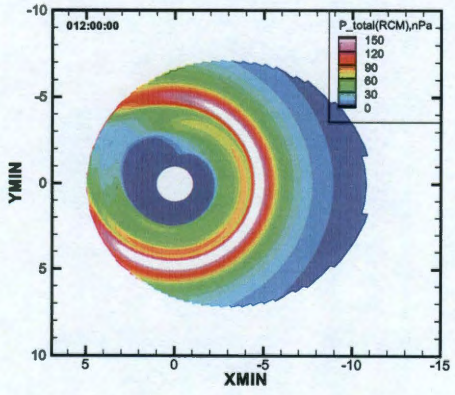
012:00:00
P_total(RCM),nPa
150
120
90
60
30
0
YMIN
XMIN

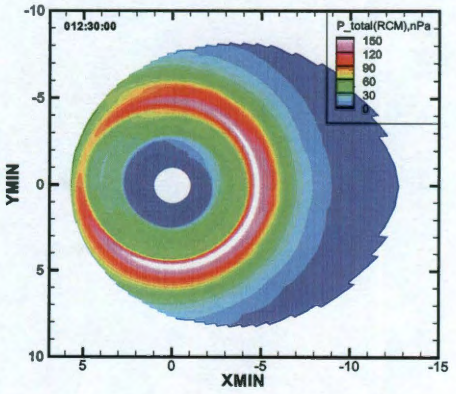
012:30:00
P_total(RCM),nPa
150
120
90
60
30
0
YMIN
XMIN

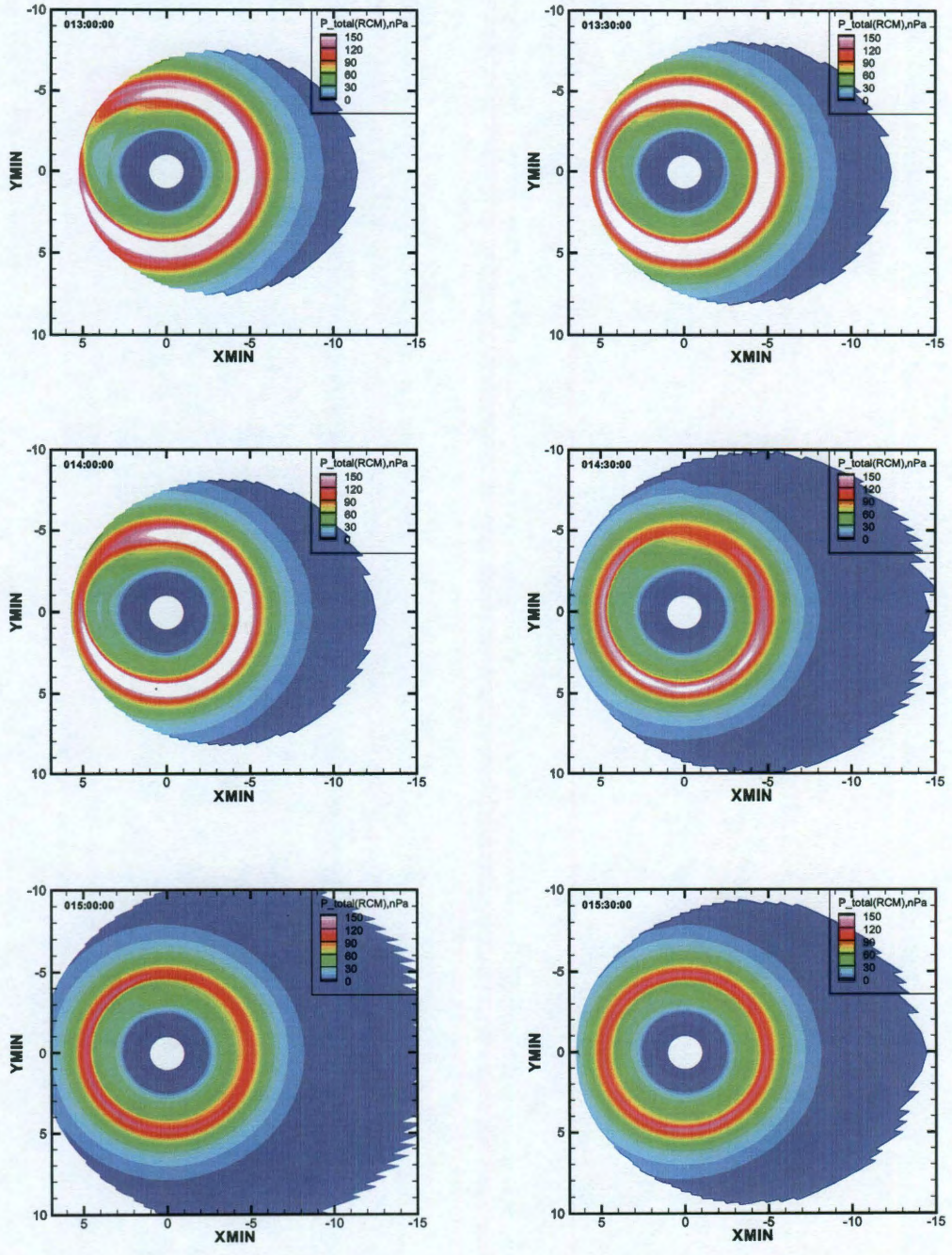

Figure 5.11 : Plasma injection during the main phase and early recovery phase of the March 31, 2001 storm, with Hilmer-Voigt magnetic field and Borovsky's boundary condition.

the well observed major magnetic storm June 4 to 5, 1991[174]. The results are reasonably compared with the Combined Release and Radiation Experiment (CRRES) satellite in the duskside inner magnetosphere and with three Defense Meterological Satellite Program (DMSP) spacecraft in the polar ionosphere[174]. However, the run used time-independent plasma boundary condition, reduced the pressure at the RCM boundary by a factor of 5 compared to empirical models to achieve comparable geosynchronous pressure, and neglected the contribution from oxygen ions. Therefore, the computed electric fields are sufficient to inject a storm-time ring current, but the RCM predicts much higher fluxes than observations. That's another reason we should use time-dependent plasma conditions based on statistical model.

Figure 5.11 shows the total plasma pressure in the March 31, 2001 storm, from 10 hours after the start of the simulation, when the main phase about to start, to 15.5 hours in the early recovery phase. At 10 hours, the pressure is peaked at about 5 R_E with a maximum about 55 nPa around the dusk. The particle haven't drifted to the prenoon sector leading to lower pressure in the there. In the main phase, the pressure goes up to over 250 nPa at about 14 hours, which is significantly higher than ordinary observations of 50 nPa[175]. Strong ring currents are build up and last from 12.5 to 14.5 hours. The maximum pressure decreases to about 120 nPa at 1 hour after the start of the recovery phase and the ring current is symmetric in azimuthal direction. The extremely high pressure shown in the simulation results is consistent with previous RCM runs to overestimate the ring current pressure[176]. If ions drift with no loss by charge exchange or precipitation, then the distribution function should be conserved along the drift path. Lossless adiabatic convection from the middle plasma sheet to inner plasma sheet gives higher high ion fluxes than are observed. Charge exchange loss does not seem capable of removing the discrepancy

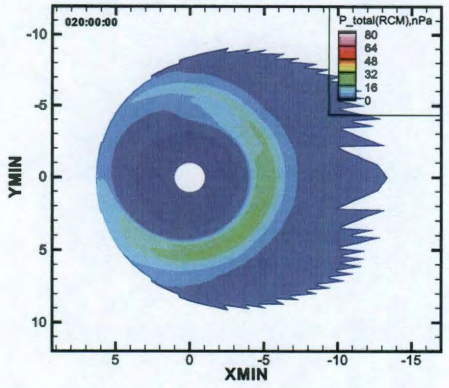
020:00:00
P_total(RCM),nPa
80
64
48
32
16
0
YMIN
XMIN

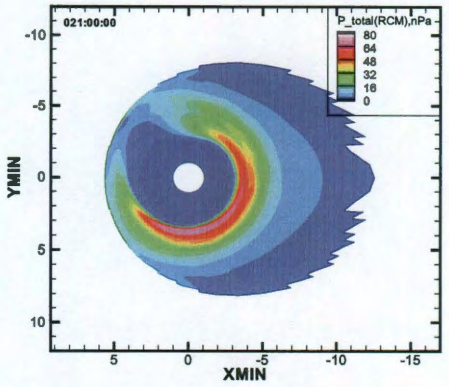
021:00:00
P_total(RCM),nPa
80
64
48
32
16
0
YMIN
XMIN

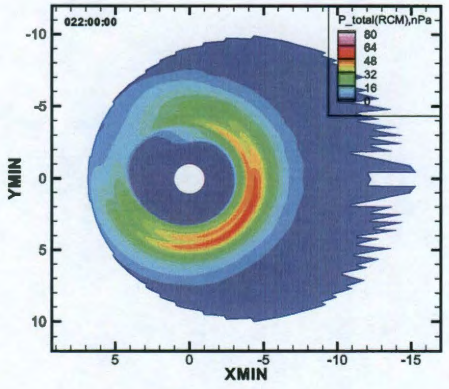
022:00:00
P_total(RCM),nPa
80
64
48
32
16
YMIN
XMIN

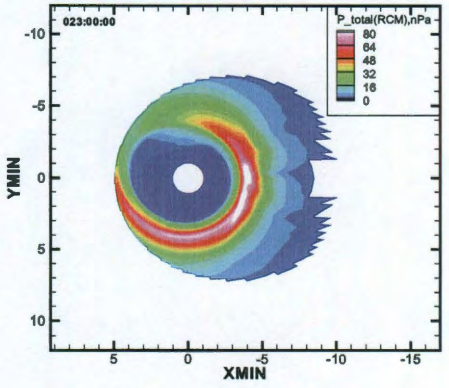
023:00:00
P_total(RCM),nPa
80
64
48
32
16
0
YMIN
XMIN

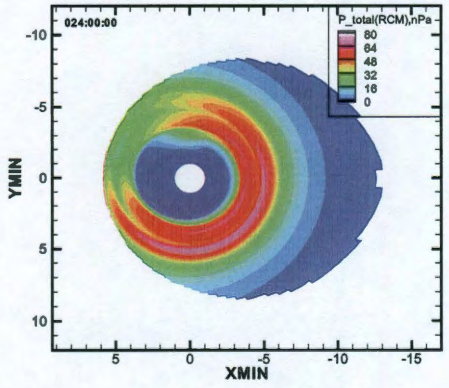
024:00:00
P_total(RCM),nPa
80
64
48
32
16
0
YMIN
XMIN

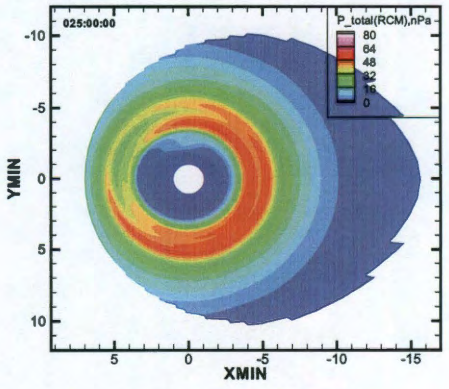
025:00:00
P_total(RCM),nPa
80
64
48
0
YMIN
XMIN

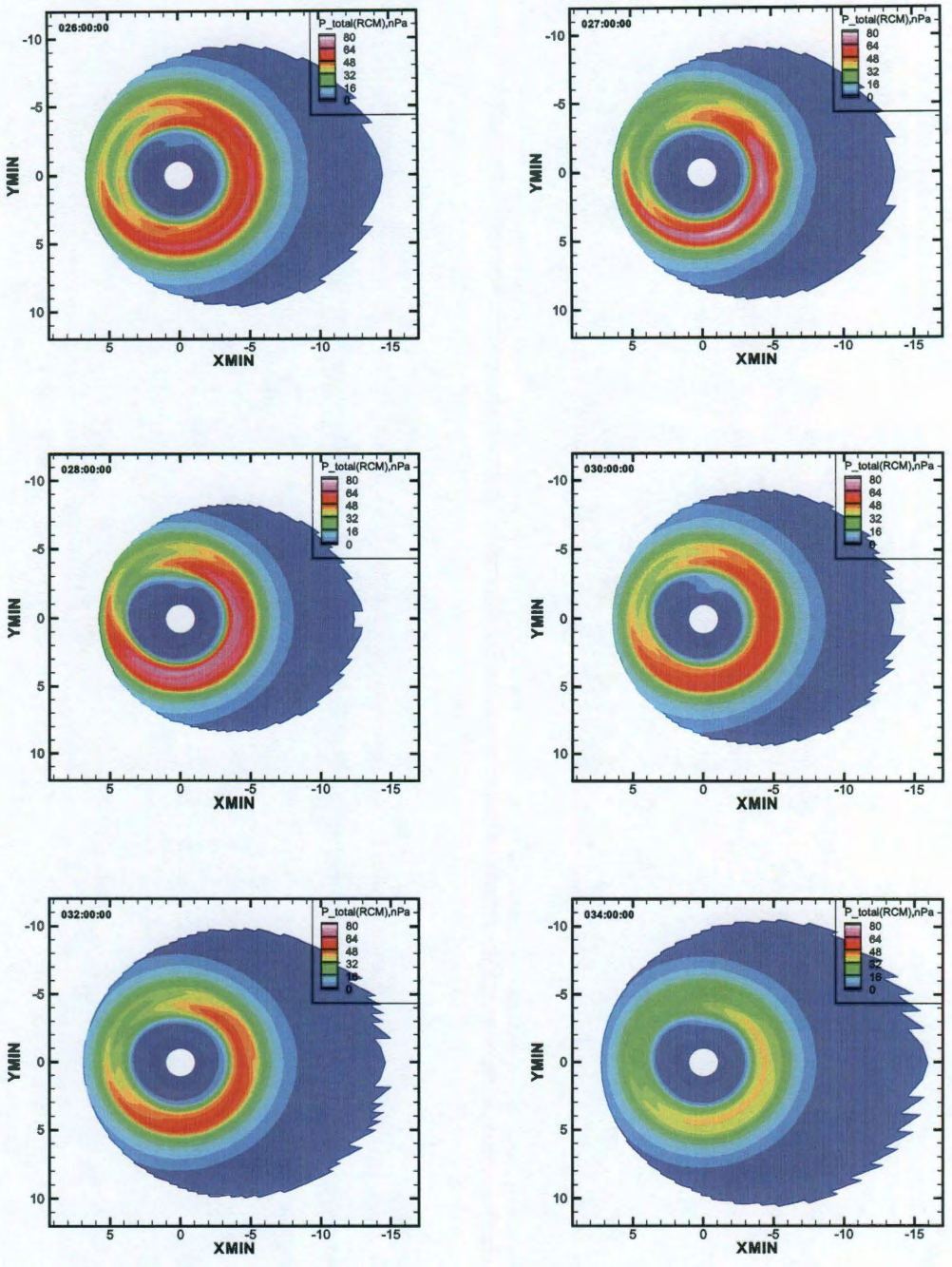

Figure 5.12 : Plasma injection during the main phase and early recovery phase of the first storm during November 7-10, 2004, with Hilmer-Voigt magnetic field and Borovsky's boundary condition.

since the lifetimes are very long. Therefore, ion precipitation must play an important role in order to get reasonable ring current pressure for large storms.

For the November 7-10, 2004 storms, Figure 5.12 shows the total plasma pressure from 20 hours, when the Dst starts to decrease in the main phase, to about 37 hours, in the recovery phase. At 20 hours, the pressure peaks around 5 R_E with a maximum of 22 nPa in the premidnight sector. It reaches a small peak at 2040 UT to above 80 nPa corresponding to the northward turning of IMF Bz. Another small peak is about 2310 UT to about 120 nPa corresponding to another northward turning of IMF B_Z. Double peaks of pressure appear after 2340 UT on November 7. They merge after 0300 UT on November 8. The pressure around the Dst minimum is only about 60 nPa but last for a few hours. The ring current pressure decrease to about 30 nPa after 1100 UT on November 8.

5.4 Interchange Instability

Although most important dynamic processes in the magnetotail are occurred in the plasma sheet, and people have taken efforts on the study of this area for many years, the complicated phenomena in the plasma sheet are still not understood well[15]. The interchange instability is one of the fundamental dynamics processes occurred in the plasma sheet.

Pressure-driven interchange instability for perfectly conducting plasma involves flux tubes with different plasma content measure by the entropy parameter $pV^{5/3}$. Consider two adjacent flux tubes with different flux tube volume V and entropy $pV^{5/3}$. Assume a sharp boundary exist between two flux tubes. A wave-like ripples on the boundary could generate a small field-aligned current in different directions on the two sides of the ripples. Then if the gradient of flux tube volume and the

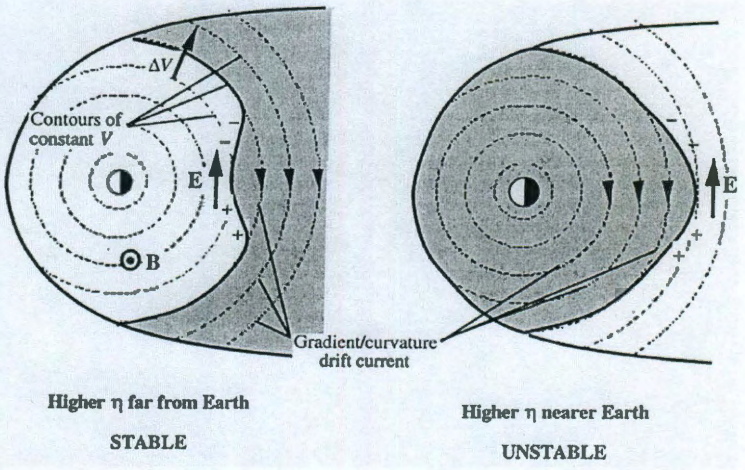

Figure 5.13 : The conditions for interchange instability in the magnetosphere[7].

gradient of entropy are parallel, the plasma in the ripple undergoes $\mathbf{E} \times \mathbf{B}$ drift in the direction of reducing amplitude, and the ripples will decay. If the gradient of flux tube volume and the gradient of entropy are antiparallel, then the ripples will grow. The plasma in one flux tube will penetrate into the other flux tube. No plasma content is lost to the surroundings. Each type of plasma occupies the new flux tube which is called "interchange"[177]. Figure 5.13 shows a general picture of interchange in the magnetosphere. The view is of the equatorial plane and from high above the north pole. So the magnetic field points out from the paper. The dashed circles are the contours of constant flux tube volume. The grey region has higher η than the white region. The left diagram shows the case in which higher entropy plasma occupies larger flux tubes and the right diagram is the opposite situation. If we make boundary of the two plasmas bulge outward from the high-entropy region, the negative charge accumulates on the east edge and positive on the west edge[15]. These extra charges are transported between the equatorial plane and the ionosphere by the field-aligned

current, which is closed by the eastward Pedersen current in the ionosphere. So the electric field in the bulge is eastward. The bulge is then drift to tailward by the $\mathbf{E} \times \mathbf{B}$ drift. In the left figure, the perturbation is stable. But in the right figure, the higher entropy plasma tends to move to higher volume location through the bulge, inducing the instability. Therefore, if the high $pV^{5/3}$ plasma occupies smaller volume tubes than the plasma of lower $pV^{5/3}$, interchange instability will occur. So the interchange instability happens when

$$\delta V \cdot \delta(pV^{5/3}) < 0 \tag{5.1}$$

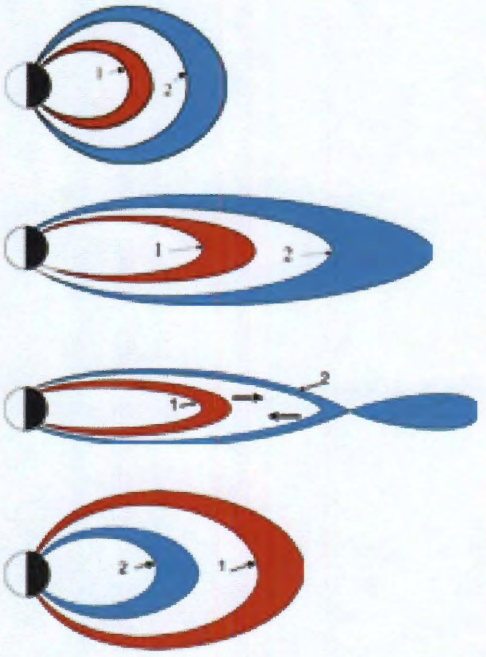

Figure 5.14 : The possible interchange motion of flux tubes in the magnetotail along with the magnetic reconnection. The two flux tubes are first under stable condition. After the magnetic field is stretched, the physical characteristic of the two tubes also change. If magnetic reconnection occurs, the plasma content and the flux tube volume change dramatically. Interchange motion will happen, the two tubes exchange their location and reach the new balance configuration. Adapted from Xing [2008][15].

Figure 5.14 illustrate two possible processes that can make interchange happen. Suppose two adjacent flux tubes 1 and 2 are under stable situation. Both the flux tube volume and the plasma content are larger in tube 2 than those in tube 1. When the solar wind conditions change, the physical parameters of the flux tubes would be strongly affected. The magnetic field configuration would change due to these solar wind condition changes as well. If the change of the volume of tube 2 is large enough to be smaller than that of the tube 1, the two tubes might become interchange unstable[15]. Even the stale requirements is still satisfied, as the tubes stretching out tailward, the magnetic field line in the northern and southern lobe meet at the neutral sheet and magnetic reconnection will happen. After the tube 2 breaks into two parts with one still connect to the Earth as a new tube with lower flux tube volume and plasma content and the other forms a plasmoid. The plasmoid is confined in the closed magnetic field lines and drift tailward quickly into the solar wind. The new tube 2 could have interchange with the tube 1.

The interchange instability has been advanced to explain bursty bulk flows (BBFs), which play an important role in plasma sheet plasma transport. This interchange motion is one way to transport plasma from the middle and far-tail X-line to the inner magnetotail, and thus transport particles and energy into the near Earth region. One example is the break ups of the aurora in the ionosphere through the acceleration of precipitating electrons in the upward Birkeland currents region.

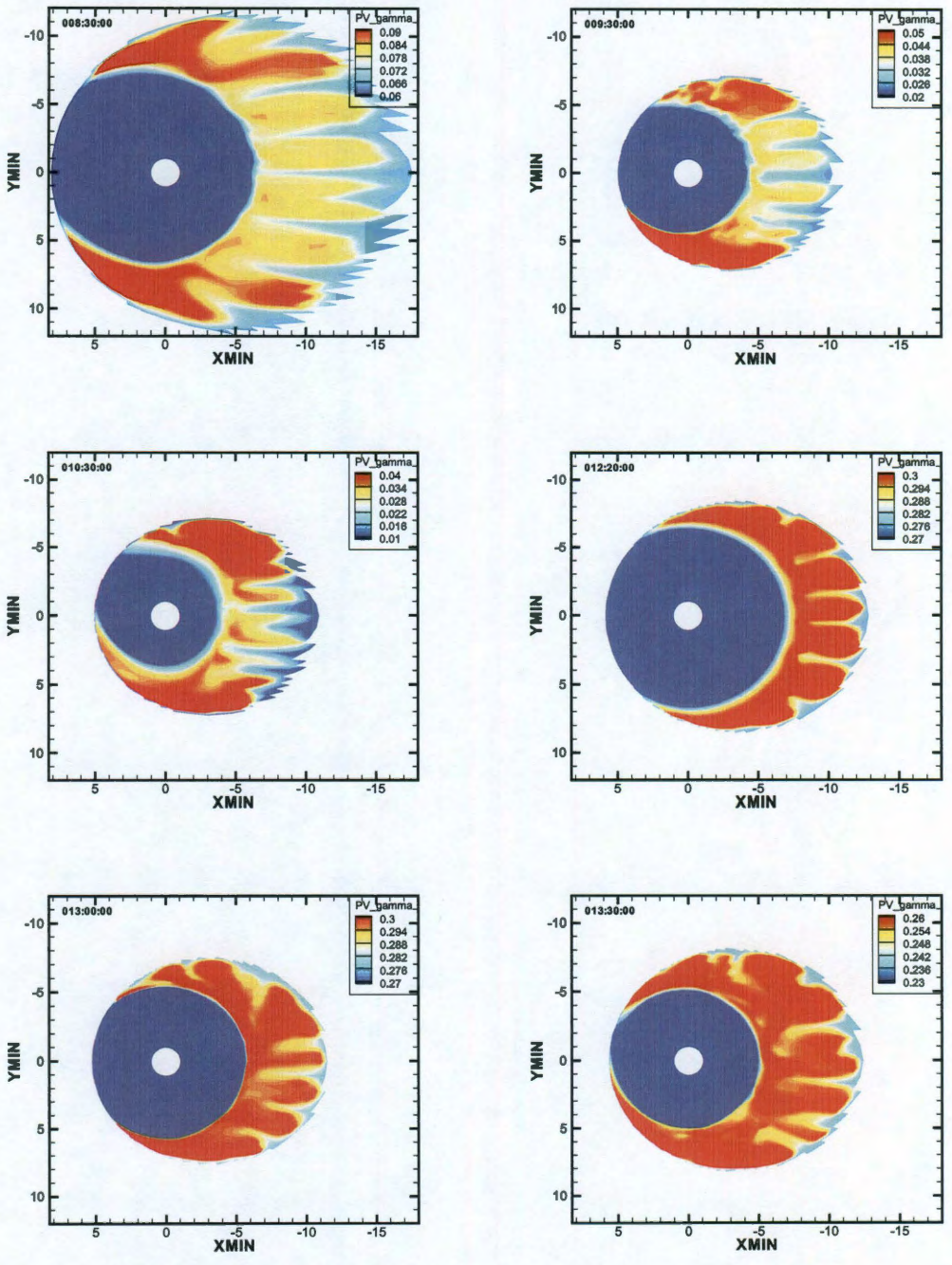

Figure 5.15 : Entropies of March 31, 2001 event with Hilmer-Voigt magnetic field and Brovosky's boundary condition in the main phase show that the magnetosphere is interchange unstable.

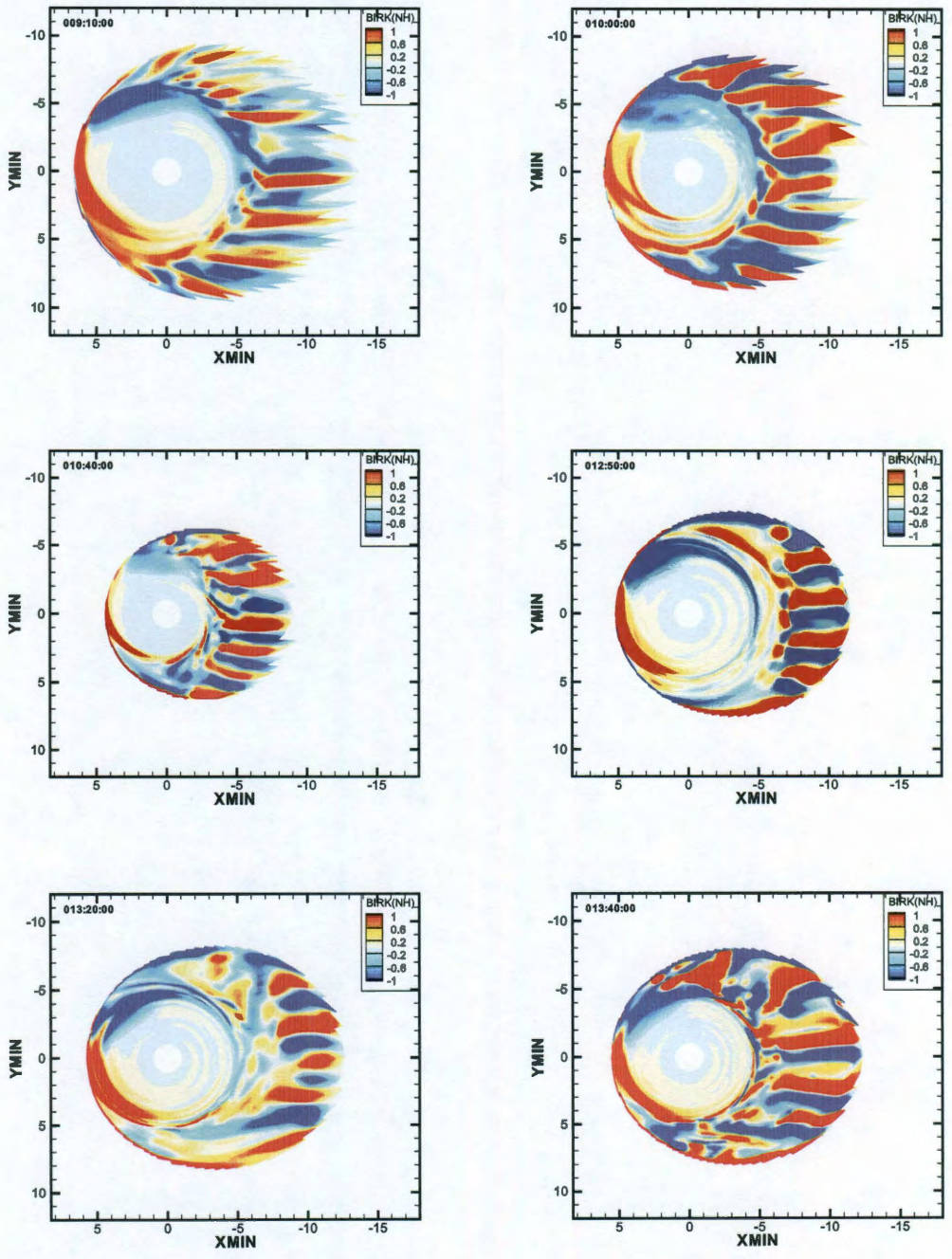

Figure 5.16 : Birkeland currents of March 31, 2001 event with Hilmer-Voigt magnetic field and Brovosky's boundary condition in the main phase show interchange type motion.

The interchange instability depends on the plasma boundary condition in the inner magnetosphere drift models. Since the flux tube volume is usually monotonically increase with the distance for current grid resolutions, if the entropy is lower far from the Earth, then the part of low entropy plasma could penetrate into the near Earth region. Figures 5.15 and 5.16 show the simulation results of March 31, 2001 event with strong interchange prior and during the main phase. There are 12 observed interchange motions from 8:30 to 13:40 which covers the entire main phase of the storm. 6 of them are shown by the entropy in the inner magnetosphere. Notice that the scales are different for each diagram. Since the entropy in the tail boundary is smaller than that closer to the Earth, interchange criteria would satisfy. For other 6 times, since the interchange behavior in the plasma sheet is mainly due to the electric field drift and the electric field is computed based on the field-aligned currents, the interchange motion is plotted by the field-aligned currents. The field-aligned currents are shown in the equatorial plane as mapping from the ionosphere. There have no field-aligned currents near the plasma sheet on average. So the field-aligned currents could be considered as an ionospheric quantity. To have a better idea throughout the interchange motion, we also plot the entropy on the RCM boundary, $pV^{5/3}$, in Figure 5.17. It could be seen that when the $pV^{5/3}$ drops suddenly, the interchange motion would appear several minutes later.

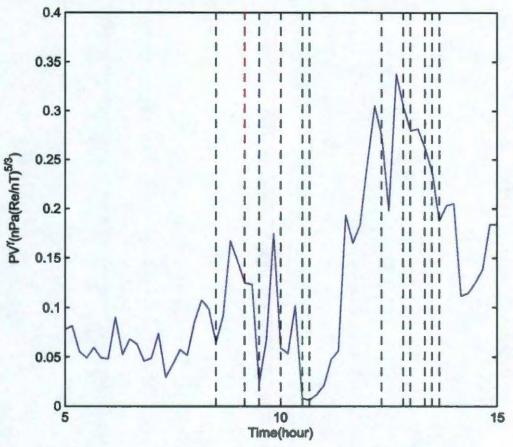

Figure 5.17 : Entropy at the midnight boundary of March 31, 2001 event with Hilmer-Voigt magnetic field and Brovosky's boundary condition in the main phase. The vertical dashed lines show the time for interchange type motion. The time resolution is 10 minutes.

5.5 Comparison of Ring Current Energy

The interchange is one type of plasma motion during disturbed type. The main feature of the storm is the ring current injection. Given different plasma boundary conditions, the plasma is injected to the inner magnetosphere with different amount and speed. The ring current strength is usually measured by the Dst index, which is some average of northward magnetic field perturbations due to westward ring current. The Dessler-Parker-Sckopke relation states that the ratio of this magnetic field perturbation and the field strength on the Earth in the equatorial plane should be proportional to the ratio of total plasma kinetic energy and the total magnetic energy

$$\frac{Dst}{B_0} = -\frac{2W_K}{3W_D} \tag{5.2}$$

Therefore, we could estimate the Dst index by

$$Dst_{DPS} = -\frac{U}{4 \times 10^{13} J} \tag{5.3}$$

where U is the total plasma kinetic energy within the ring current region. However, the DPS relation is only valid when the magnetic field is pure dipole. No easy conclusion could be made on whether the DPS relation could predict the value of Dst correctly for realistic magnetic field. But it seems like that the DPS relation has very similar results compared to Biot-Savart integral[146, 178, 179]. Although we could have more precise estimate through magnetogram calculation, we use this less time-consuming method to estimate whether these boundary conditions could lead to appropriate tendency of ring current energy. The two magnetic fields we used in these two storm simulations are quite simple and thus not too far away dipole field in the geosynchronous orbit. Figure 5.18 shows the comparisons between estimated Dst index and observations of the two storms with two different magnetic field models and three different plasma boundary conditions.

It is clear that Tsyganenko-Mukai boundary condition has very poor prediction of Dst index in the November 7-10, 2004 event. The fixed boundary condition gives bad prediction as well in the November 7-10, 2004 event with T89 magnetic field. It also doesn't recover well in the March 31, 2001 event in the recovery phase. In other cases, the ring current energy seems more or less to be proportional to the observed Dst index. The Borovsky prescription seems to be the most realistic, especially in the March 31, 2001 event with Hilmer-Voigt magnetic field. It still could be about 4 times smaller as in the November 7-10, 2004 event with T89 magnetic field. The Tsyganenko-Mukai boundary condition overestimate the injected plasma by providing too much plasma through the boundary. The statistical plasma sheet model is based on observations with IMF B_Z between about -10 nT to 10 nT and mostly concentrated in the region between -5 nT and 5 nT. The model doesn't really apply to extreme strong storms for which the IMF B_Z could reach as low as -50 nT.

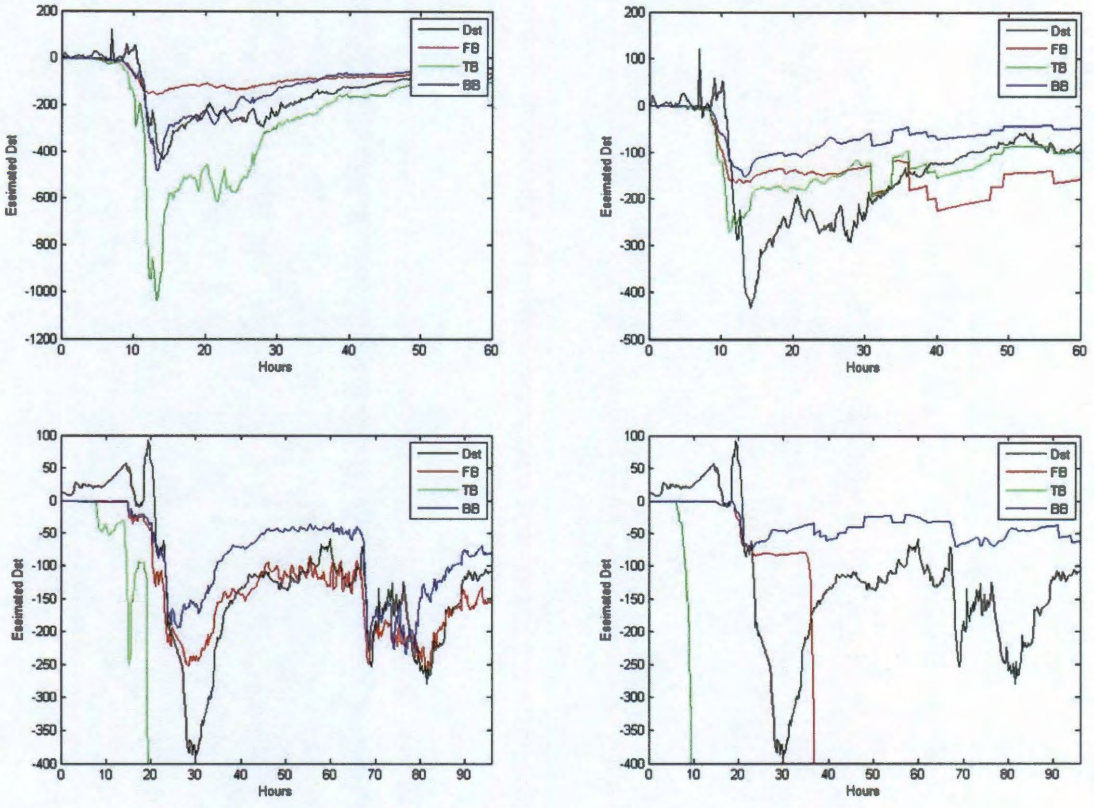

Figure 5.18 : The comparison among estimated Dst and observed Dst (black) in March 31, 2001 (top), and November 7-11, 2004 (bottom) events. The left column shows the results for Hilmer-Voigt magnetic field, the right column shows the results for T89 model. The green lines correspond to Tsyganenko-Mukai boundary condition. The blue lines correspond to Borovsky's boundary condition. The red lines correspond to fixed boundary conditions.

The choice of the empirical plasma sheet model in setting the tail-ward boundary condition in the ring current model makes a dramatic difference on the ring current injection. It necessary to use a prescribed plasma sheet model that varies with solar wind and IMF conditions. These models need to be used carefully to avoid extreme conditions that out of the range.

Chapter 6

Parallel electric field

Auroral zone in ionosphere is connected to the outer magnetosphere by means of field-aligned currents[180]. The auroral Birkeland currents, shown in Figure 6.1, generally occur as two sheet currents, extended in longitude but narrowly confined in latitude, although the current systems at noon and midnight are more complex in structure[181].

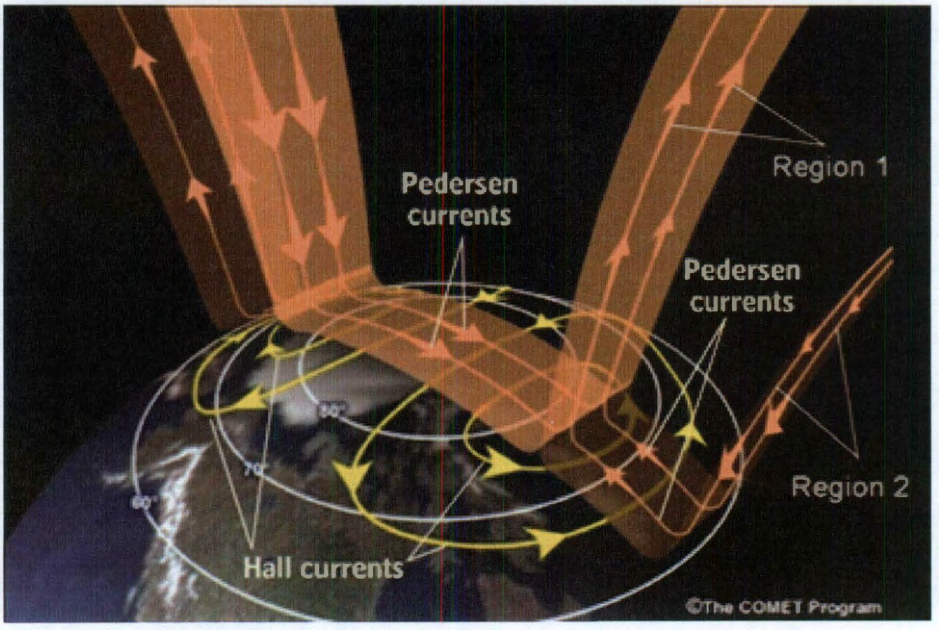

Figure 6.1 : Two sets of Birkeland currents. Figure courtesy to UCAR.

The existence of the auroral current systems requires that currents flow across magnetic field lines in the ionosphere, and also at some location in the outer magneto-

sphere. In the collisional ionosphere, the electromagnetic energy is dissipated. So the maintenance of the current system requires the presence of the generator somewhere in the outer magnetosphere. Thus the auroral current system represents tapping the kinetic or thermal energy of the magnetospheric plasma, and transporting it to the ionosphere where it is dissipated.

Since the ionosphere is very cold compared to thermalized plasma sheet, the thermoelectric effect and the interaction between Birkeland current carrier and the Earth's magnetic field results in electrostatic potential drop along the magnetic field line. A few thousand kilometers above the auroral arcs, the electron density is often below 1 per cube centimeter, but the parallel current density into discrete auroral region is often a few $\mu A/m^2$. To carry this current, the electrons must be accelerated to high energies for a low density plasma[181]. Parallel electric fields are now widely accepted as one (but not the only one) mechanism responsible for the acceleration of auroral particles. One of the major purposes of our work was to incorporate auroral conductance enhancements associated with upward field-aligned currents in the RCM. In other words, we would like to improve the realism of the RCM auroral model. The simplest approach is to include effects of field-aligned potential drops by assuming a form of the so-called current-voltage relationship. Although this neglects other mechanisms that are responsible for producing aurora (effects of wave-particle interactions, etc.), even this task has not been before, and in this work we present a first attempt at inclusion of auroral acceleration.

In this chapter, we present our approach to including field-aligned potential drops in the RCM. We derive a generalized form of the current-voltage relation and explain the reason for using that particular form, and then explain how this relation is implemented in the RCM. In a later chapter (chapter 9), we will present simulations

results that use this new implementation.

6.1 The Nature of Parallel Electric Fields

Field-aligned currents are an essential part of magnetosphere-ionosphere coupling. A strong correlation is found between upward Birkeland current systems and parallel potential drops. The Region-1 field-aligned currents are observed within the plasma sheet but most commonly at its outer edge[182] or at the poleward edge of the aurora[183, 184]. The Region-2 field-aligned currents flow at the inner edge of the plasma sheet. Parallel electric fields are demonstrated in the form of auroral precipitation peaked at low pitch angles near the poleward edge of the aurora. The statistical distributions of the field-aligned potential difference were determined from the energy spectra of electrons inverted "V" events for different conditions of geomagnetic activity indicated by the AE index[185]. It is narrow bands of electron precipitation in which the characteristic energy increases from a few hundred eV to a few keV and then decreases to a few hundred eV again, in an energy-time spectrogram measured by a polar-orbiting satellite.

In an ideal collisionless plasma, the conductivity parallel to the magnetic field is infinite and so there should be no parallel electric field. However, although the auroral zone plasma is collisionless above the ionosphere, ideal conditions break down due to the finite number of electrons available to carry current, especially in the upward current region where downward moving electrons must overcome the magnetic mirror forces in the Earth's dipole field in order to precipitate into the ionosphere and contribute to the net field-aligned current. The acceleration is observed between 3000 km and 7000 km above the Earth[186], as shown in Figure 6.2.

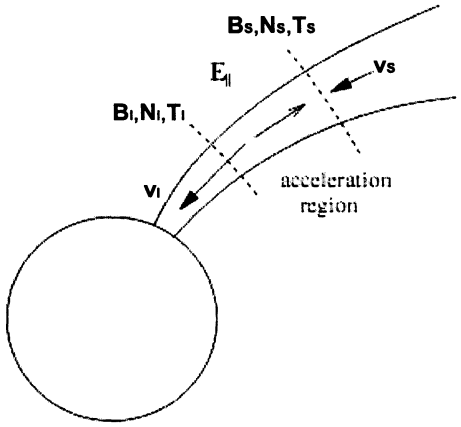

Figure 6.2 : Acceleration region along field lines.

Several mechanisms have been proposed to explain the formation of parallel potential drop. The principle concept is that parallel electric field exists to impede any process would produce charge separation along magnetic field lines so as to maintain quasi-neutrality in a magnetized collisionless plasma[185]. Approaches could be categorized into two types according to the way of describing momentum balance. The first type is that the momentum gained from electric field is essentially balanced by particle inertia. Particles gain kinetic energy from on place and lost it to another place depending on the distribution of electric field without local heating. The collective plasma motion along a magnetic field line is obtained by superposition of single particle motion in response to parallel electric field and magnetic field. This theory is supported by magnetic mirror effect[38, 187, 188, 189, 190, 191, 192, 193] and by double layers or electrostatic shocks[194, 195, 196, 197, 198, 199]. The second type is that the momentum is exchangeable among particles, waves and electrostatic fields. So the characteristics of the parallel electric field depend on plasma instability criteria and local plasma condition. The theories are based on anomalous resistivity[200, 201, 202, 203, 204, 205] or the thermoelectric effect[206, 207].

When a collisionless plasma moves in a inhomogeneous magnetic field, the charge carrier is affected by a magnetic mirror force $-\mu \cdot \nabla B$ along the magnetic field line. The total electrostatic potential drop is estimated to be proportional to the difference of magnetic field strength. When there are differential pitch angle anisotropies between electrons and ions in magnetic mirrors, parallel electric fields must be set up to compensate the charge separation caused by the magnetic mirror force to restore plasma quasi-neutrality equilibrium[208]. In a collisionless plasma, the maximum current density that can flow is limited to the random thermal current of the current carriers[185]. In a steady state condition, the local current density along any portion of the current path is controlled by the entire circuit to preserve current continuity and to prevent any point of the circuit from attaining an unreasonable charge accumulation. The best way to to increase the upward current density at low altitudes is by means of an upward parallel electric field to balance the repulsive magnetic mirror force. It does not require a differential pitch angle anisotropy between electrons and ions, but the electric field will generally produce differential anisotropies to maintain the parallel electric field[190].

A double layer is commonly identified as a surface with a potential jump across it. The quasi-neutrality is locally violated due to the existence of space charge layer. The total net space charge integrated over the double layer volume is very small so that the electric field is much weaker outside than inside. The thickness of the double layer should be much smaller than the collisional mean free path of the plasma[195]. The motions of the ions and electrons in the layer are mainly governed by the electrostatic and inertial forces. The development of a current-driven instability may be important for initiating the dynamics of double layer formation.

As a result of wave-particle interactions, the bulk motion of electrons may be

impeded by a resistivity that is much greater than classical resistivity due to particle-particle collisions[185]. This leads to a requirement for parallel electric field to balance the retarding force, so as to preserve current continuity. Charged particles experience the electro static force independent of particle energy throughout the anomalous resistance region. The frictional force decreases with increasing particle energy. Particles with velocity below a critical velocity are retarded by the dominant frictional force, but particles with higher velocity can be accelerated by the dominant electrostatic force. The anomalous resistivity contribution to the potential drop is very small because the process is far to dissipative to be powered by auroral particles[185]. Turbulence will cause anomalous resistivity and produce plasma heating to reduce the differential pitch angle anisotropy between ions and electrons. Thus it reduces the parallel potential drop along the current path as opposite to the effect of anomalous resistivity.

The basic cause of the production of a potential difference between plasmas of different temperatures is the existence of a higher flux of electrons from the hot plasma into the cold plasma than in the opposite direction. A net negative charge would then be built up in the cold plasma, which would produce an electrostatic field to prevent further charge separation. The potential drop grows to restrain the hot electrons until the electron fluxes in the two directions are equal.

In general, the potential drop is largest in the dusk to pre-midnight sector, smaller in the post-midnight to dawn sector, and smallest in the near noon sector during both quiet and disturbed geomagnetic conditions[185]. There is a steady asymmetry in the distribution. When the geomagnetic activity strengthened, the potential drop patterns extend to lower invariant latitude, and the magnitude increases significantly around dusk side.

The currents flowing in the auroral circuit must close in the ionosphere. The ionospheric currents consist of Pedersen currents parallel to the electric field in the ionosphere, and Hall currents which are perpendicular to both the electric and magnetic field. To a first approximation, the ionospheric conductivity can be considered to be constant, and in this case combining the ionospheric Ohm's Law with the linear current-voltage relation for parallel currents leads to an outer scale length, above which electric fields can map down to the ionosphere and below which parallel electric fields become important. The effects of particle precipitation make the picture more complex, leading to enhanced ionization in upward current regions and to the possibility of feedback interactions with the magnetosphere.

Whatever the source of the parallel electric field, the motion of charged particles under the combined effect of the electric field and the mirror field can give rise to a relationship between the potential drop, the mirror ratio between the source of the particles and the ionosphere, and the current density of the precipitating electrons. Under conditions that are easily satisfied in the auroral zone, this relationship is approximately linear.

Models of auroral current system generally fall into two classes. Kinetic models emphasize the adiabatic motions of particles originating in both the magnetosphere and ionosphere. The parallel potential drop is determined from the individual particle populations by means of quasi-neutrality. While these models have had success in describing the steady-state structure of the large-scale inverted-V regions, they are not easy to generalize to the time-dependent case[180]. While MHD models for a collisionless medium do not allow parallel electric fields. This deficiency can be remedied by assuming an effective resistivity in regions of strong field-aligned current.

A strictly one dimensional static formulation is possible only if there is no plasma

motion across the flux tube. This would be true in the absence of convection or when the current layer is moving with the convection speed[209]. In these models, the essential goal is to get the potential difference. But for a given potential difference between the two end points of a magnetic field line, there is not a unique distribution of electric potential between the end points[210]. Actually, the field-aligned potential distribution is not necessarily a monotonically decreasing function of altitude as is generally assumed in classical stationary kinetic models.

6.2 Knight's relation

We consider an electric field with the potential higher at the ionosphere than at the plasma sheet and monotonic between them. Then there are several distinct categories of electron trajectories. At any point on the field line each of these occupies a distinct region of velocity space. The equation of the loss cones at an arbitrary point are obtained from the equations of conservation of energy and of the first adiabatic invariant in terms of the local potential and those at the two bases.

Same results could be generated from a model based on integral flux relations shown in the next section. But a well known and earlier calculation from Knight[209] is based on Maxwellian distribution function. The current is calculated by integrate $-ev_{\|}\mathbf{f}(\mathbf{v})$ over all of velocity space.

$$j_{\|} = -e \int_{S_1} v_{\|}(f_S - f_E) d^3v \tag{6.1}$$

where

$$f_Y = N_Y \left(\frac{M}{2\pi k T_Y} \right)^{3/2} e^{-\frac{M}{2kT_Y}\left(v_\perp^2 + v_{\|}^2\right) + \frac{e}{kT_Y}(\phi - \phi_Y)} \tag{6.2}$$

the subscripts Y on the density N, the temperature T and the potential ϕ, refer to

values at the ionospheric, I or plasma sheet, S, bases, and S_1 is a trajectory connecting both plasma sheet and ionosphere. Applying mass of the electron, m, and mass of proton, M, and setting $\Delta = e(\phi_E - \phi_S)$, $t = T_S/T_E$, $n = N_S/N_E$, and $r = \Delta/T_E$, a dimensionless potential drop, we get

$$\frac{j_\parallel}{\frac{eB}{B_E}N_E\sqrt{\frac{kT_E}{M}}} = \sqrt{\frac{M}{2\pi m}}\left[\left(\frac{B_S - B_E}{B_E}e^{-\frac{rB_S}{B_E - B_S}} + \frac{B_E}{B_S}\right)e^{-r} - n\sqrt{t}\left(\frac{B_S - B_E}{B_S}e^{-\frac{r}{t}\frac{B_S}{B_E - B_S}} + \frac{B_E}{B_S}\right)\right] \tag{6.3}$$

Details will be shown in the Appendix B. Making assumptions $r \ll 10^3$, $t \gg 1$, $B_E \gg B_S$, we have $rB_S/B_E \ll 1$ and $(r/t)(B_S/B_E) \ll 1$, then the above equation could be written as

$$\begin{aligned}
\frac{j_\parallel}{\frac{eB}{B_E}N_E\sqrt{\frac{kT_E}{M}}} &\approx \sqrt{\frac{M}{2\pi m}}\left\{\left[\frac{B_S - B_E}{B_S}\left(1 - \frac{rB_S}{B_E - B_S} + \cdots\right) + \frac{B_E}{B_S}\right]e^{-r}\right. \\
&\quad \left. -n\sqrt{t}\left[\frac{B_S - B_E}{B_E}\left(1 - \frac{r}{t}\frac{B_S}{B_E - B_S} + \cdots\right) + \frac{B_E}{B_S}\right]\right\} \\
&\approx \sqrt{\frac{M}{2\pi m}}\left[(1+r)e^{-r} - n\sqrt{t}\left(1 + \frac{r}{t}\right)\right]
\end{aligned} \tag{6.4}$$

Since we evaluate the Birkeland current on the ionosphere, where $B = B_E$, we have

$$j_\parallel \approx eN_E\sqrt{\frac{kT_E}{2\pi m}}\left[(1+r)e^{-r} - n\sqrt{t}\left(1 + \frac{r}{t}\right)\right] \tag{6.5}$$

which gives a linearized version of Knight's relation. Because what we have in RCM is quantities in magnetosphere, this relation is equivalent to

$$j_\parallel \approx eN_S\sqrt{\frac{kT_S}{2\pi m}}\left[\frac{1 + r't}{n\sqrt{t}}e^{-r't} - (1 + r')\right] \tag{6.6}$$

where $r' = \Delta/T_S = r/t$ is another way to define the dimensionless potential drop. An example of the relation between the Birkeland currents and the field-aligned potential drop is shows in Figure 6.3. It shows one time snapshot from a substorm event

simulation in the expansion phase (discussed further in Chapter 9). Large field-aligned potential drop exist to accelerate plasma sheet electrons downward to the ionosphere to generate the upward field-aligned currents.

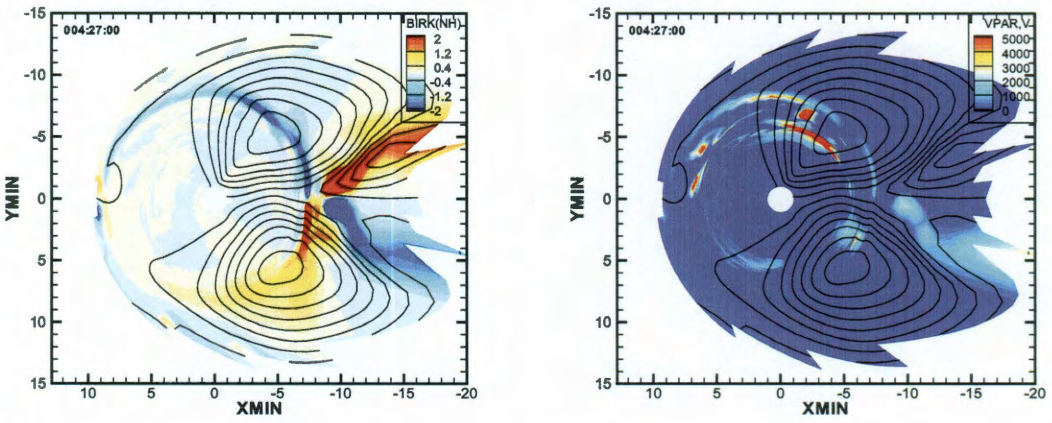

Figure 6.3 : Example of Birkeland currents and parallel potential drops in an RCM event simulation.

Noticing that the current is downward if the right hand side of the equation is positive and upward if it is negative, it is clear that the two components correspond to downward and upward currents. As r' goes up, the first term in the bracket decreases and the second term increases, which gives smaller value. Then the current is monotonic decreasing with increasing r'. Therefore, in the code, we could get a field-aligned potential drop, or r', from the field-aligned current calculated from Vasyliunas equation. When $r' = 0$, we could get maximum (downward) Birkeland current as $1/n\sqrt{t} - 1$. If n is in range of $10^{-4} \sim 10^{-2}$ and t is in range of $10^2 \sim 10^3$, then $n\sqrt{t}$ is in range of $10^{-3} \sim 10^{-0.5}$, so $1/n\sqrt{t}$ is greater than 1. The energy flux is

given by

$$\varepsilon_{\parallel} \approx N_S T_S \sqrt{\frac{T_S}{2\pi m}} \left[\left(2 + 2r' + r'^2\right) - \frac{1}{nt^{3/2}} e^{-r't} \left(2 + 2r't + r'^2 t^2\right) \right] \tag{6.7}$$

If we omit the term from ionosphere, there is a simpler linear relation

$$-j_{\parallel} \approx eN_S \sqrt{\frac{kT_S}{2\pi m}} (1 + r') \tag{6.8}$$

$$\varepsilon_{\parallel} \approx N_S k T_S \sqrt{\frac{kT_S}{2\pi m}} \left(2 + 2r' + r'^2\right) \tag{6.9}$$

which gives field-aligned potential drop only if the Birkeland current is upward. According to different n and t, the two solutions could be identical when the potential drop above about $10V$. But below this threshold, they are different and affect the system only a little bit through changing ionospheric conductances and electric field drift velocities.

In the RCM, Knight's formula can be implemented by inverting it. In other words, we first calculate the field-aligned currents by Vasyliunas equation, and the result must hold whether there are potential drops or not due to current conservation. Then, we use the Knight relation reversely to estimate the field-aligned potential drop. When we implemented is this way in the RCM, the code often fails to converge to a solution in the ionospheric potential solver due to excessively large values for parallel potential drops. This motivated us to generalize the original Knight relation as described in the rest of this chapter.

6.3 Adding a Cold Component

As we know, the particle distribution usually has high energy tail which forms a kappa like distribution instead of a Maxwellian distribution. But a single kappa distribution also underestimates the differential flux on the low energy side[211]. In

other words, the distribution lacks a cold component. We thus assume that the magnetospheric plasma has both a hot component and a cold component. The density ratio between the cold component and the hot component is 0.1586. The ratio of characteristic energy, for kappa distribution, is 40. These values were estimated from a survey of published particle data and are only a crude way of evaluating the effects of such composition. Here, we first examine a new case with isotropic bi-Maxwellian distribution which has an additional cold component originating in the ionosphere. Using the fact, for a kappa distribution

$$\kappa E_0 = \left(\kappa - \frac{3}{2}\right) kT \tag{6.10}$$

and $\kappa = 6$ and $\kappa = 3$ for hot and cold parts, we could estimate the temperature ratio to be 3/80. The cold component has subscript P except for using with the potential which should same as the hot component. There is no difference in the calculation between hot component and cold component except for their subscripts. Then the field-aligned current is

$$\begin{aligned}
j_{\parallel} &= -e\int_{S_1} v_{\parallel}(f_S + f_P - f_E)d^3v \\
&= -e\int_{S_1} v_{\parallel}\left[N_S\left(\frac{m}{2\pi kT_S}\right)^{3/2} e^{-\frac{m}{2kT_S}\left(v_\perp^2+v_\parallel^2\right)+\frac{e}{kT_S}(\phi-\phi_S)}\right. \\
&\quad N_P\left(\frac{m}{2\pi kT_P}\right)^{3/2} e^{-\frac{m}{2kT_P}\left(v_\perp^2+v_\parallel^2\right)+\frac{e}{kT_P}(\phi-\phi_S)} \\
&\quad \left.-N_E\left(\frac{m}{2\pi kT_E}\right)^{3/2} e^{-\frac{m}{2kT_E}\left(v_\perp^2+v_\parallel^2\right)+\frac{e}{kT_E}(\phi-\phi_E)}\right] d^3v \\
&= \frac{B}{B_E} eN_S\sqrt{\frac{kT_S}{2\pi m}}\left[\left(1+\frac{\Delta}{kT_E}\right)e^{-\frac{\Delta}{kT_E}}\frac{1}{n\sqrt{t}} - \left(1+\frac{\Delta}{kT_S}\right) - \frac{N_P}{N_S}\sqrt{\frac{T_P}{T_S}}\left(1+\frac{\Delta}{kT_P}\right)\right]
\end{aligned} \tag{6.11}$$

The biggest difference of including a cold component is to limit the field-aligned potential drop since the ratio of this field-aligned potential drop to the temperature

of cold component is much larger than the ratio to the temperature of hot component. Since the precipitating particle energy flux is only used in the ionospheric conductance calculation, and it doesn't use low energy particles, precipitating energy flux is:

$$\begin{aligned}\varepsilon_{\parallel} &= \int_{S_1} \frac{m}{2}\left(v_{\perp}^2 + v_{\parallel}^2\right) v_{\parallel}(f_S + f_P)d^3v \qquad (6.12)\\ &= N_S k T_S \sqrt{\frac{kT_S}{2\pi m}}\left[\left(2 + 2\frac{\Delta}{T_S} + \frac{\Delta^2}{T_S^2}\frac{B_E}{B_E - B_S}\right) + \frac{N_P}{N_S}\left(\frac{T_P}{T_S}\right)^{3/2}\left(2 + 2\frac{\Delta}{T_P} + \frac{\Delta^2}{T_P^2}\frac{B_E}{B_E - B_S}\right)\right]\end{aligned}$$

6.4 Changing Shape of Distribution Function

Preliminary results still show too large potential drop for a given upward field-aligned currents even with cold component from the plasma sheet. Therefore, we need to explore some other way to control the calculated field-aligned potential drop. We next assume that the particle distribution function has a kappa shape:

$$f = n\left(\frac{m}{2E_0}\right)^{3/2}\frac{\Gamma(\kappa+1)}{(\pi\kappa)^{3/2}\Gamma(\kappa-\frac{1}{2})}\frac{1}{\left(1+\frac{E}{\kappa E_0}\right)^{\kappa+1}} \qquad (6.13)$$

The Maxwellian distribution is an extreme of kappa distribution. Their relationship is illustrated in Figure 6.4.

Since the ionosphere is collisional, we could describe the thermal ionosphere plasma with a Maxwellian distribution. Only the plasma sheet component is considered for kappa distribution. If we only write out the component from the plasma sheet, then

$$\begin{aligned}j_{\parallel} &= -e\int_{S_1} v_{\parallel} f_S d^3v\\ &= -e\int_{S_1} v_{\parallel} N_S\left(\frac{m}{2E_{0S}}\right)^{3/2}\frac{\Gamma(\kappa_S+1)}{(\pi\kappa_S)^{3/2}\Gamma(\kappa_S-\frac{1}{2})}\frac{1}{\left(1+\frac{E}{\kappa_S E_{0S}}\right)^{\kappa_S+1}}d^3v\\ &\approx -eN_S\sqrt{\frac{kT_S}{2\pi m}}\frac{\sqrt{\kappa_S-\frac{3}{2}}\Gamma(\kappa_S-1)}{\Gamma(\kappa_S-\frac{1}{2})}\left[1+\frac{\kappa_S-1}{\kappa_S-\frac{3}{2}}\frac{e(\phi_E-\phi_S)}{kT_S}\right] \qquad (6.14)\end{aligned}$$

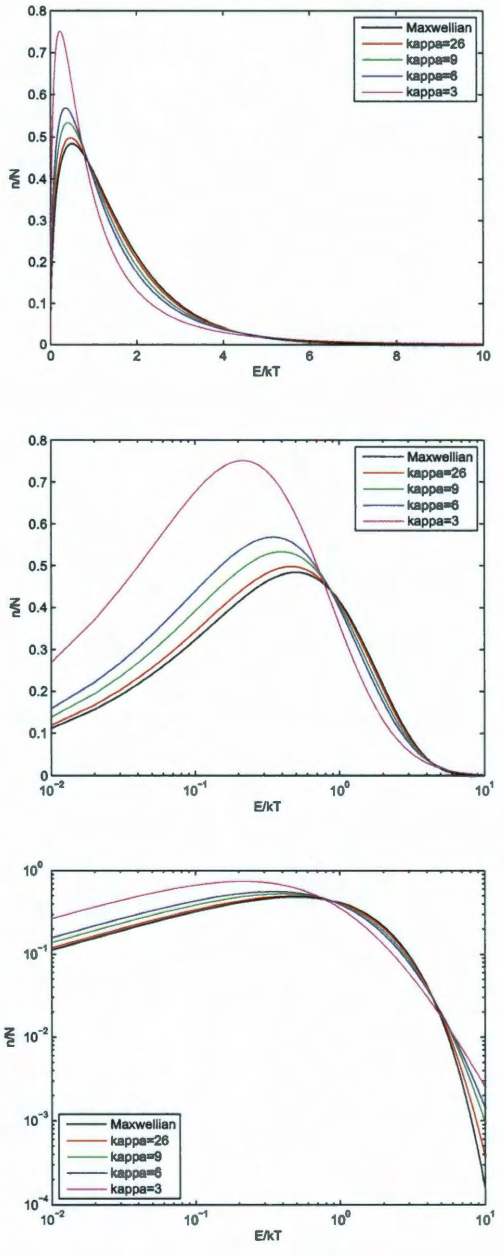

Figure 6.4 : The figures show normalized distribution function with vertical axes as fraction of total density and horizontal axis as a unitless energy. The step for the unitless energy is 0.01. The area under each distribution function calculated by the summation of product of fraction and energy step is 1. The top figure is in linear scale. The middle figure has energy axis in logarithm scale to have a better view of low energy distribution. The bottom figure is in logarithm scales for both axes to have a better view of high energy tail.

and the energy flux could be calculated as

$$\begin{aligned}
\varepsilon_{\parallel} &= \int_{S_1} \frac{m}{2}(v_\perp^2 + v_\parallel^2) v_\parallel f_S d^3v \\
&= \left(\frac{m}{2}\right)^{3/2} \int_{S_1} \frac{m}{2}(v_\perp^2 + v_\parallel^2) v_\parallel \frac{N_S}{E_{0S}^{3/2}} \frac{\Gamma(\kappa_S+1)}{(\pi\kappa_S)^{3/2}\Gamma(\kappa_S-\frac{1}{2})} \frac{1}{\left[1+\frac{\frac{m}{2}v_\perp^2+\frac{m}{2}v_\parallel^2-e(\phi-\phi_S)}{\kappa_S E_{0S}}\right]^{\kappa_S+1}} d^3v \\
&\approx N_S k T_S \sqrt{\frac{kT_S}{2\pi m}} \frac{\sqrt{\kappa_S-\frac{3}{2}}\Gamma(\kappa_S-2)}{\Gamma(\kappa_S-\frac{3}{2})} \\
&\quad \left[2 + 2\frac{\kappa_S-2}{\kappa_S-\frac{3}{2}} \frac{e(\phi_E-\phi_S)}{kT_S} + \frac{(\kappa_S-1)(\kappa_S-2)}{(\kappa_S-\frac{3}{2})^2} \frac{e^2(\phi_E-\phi_S)^2}{(kT_S)^2}\right] \qquad (6.15)
\end{aligned}$$

The details of integration are presented in Appendix C. If we compare the integration results of field-aligned currents using Maxwellian distribution as in the original Knight's relation and those using a kappa distribution shown above, the only differences are two constant factors. The major one is the slope of the function

$$\frac{\sqrt{\kappa_S-\frac{3}{2}}\Gamma(\kappa_S-1)}{\Gamma(\kappa_S-\frac{1}{2})} \frac{\kappa_S-1}{\kappa_S-\frac{3}{2}} \approx 1.0807 \qquad (6.16)$$

which gives smaller field-aligned potential drop. But only this factor is not enough. If we use bi-kappa distribution, at the distance of -13 R_E, the density of cold component is 0.1586 of the density of the hot component, and the hot component has 40 times larger E_0. The kappa value for the hot component is $\kappa_S = 6$ and the kappa value for the cold component is $\kappa_P = 3$. The field-aligned current and the energy flux of these two components are given by

$$\begin{aligned}
j_\parallel &= eN_E\sqrt{kT_E}2\pi m \left(1+\frac{\Delta}{kT_E}\right) e^{-\frac{\Delta}{kT_E}} \\
&\quad -eN_S\sqrt{\frac{kT_S}{2\pi m}} \frac{\sqrt{\kappa_S-\frac{3}{2}}\Gamma(\kappa_S-1)}{\Gamma(\kappa_S-\frac{1}{2})} \left(1+\frac{\kappa_S-1}{\kappa_S-\frac{3}{2}}\frac{\Delta}{kT_S}\right) \\
&\quad -eN_P\sqrt{\frac{kT_P}{2\pi m}} \frac{\sqrt{\kappa_P-\frac{3}{2}}\Gamma(\kappa_P-1)}{\Gamma(\kappa_P-\frac{1}{2})} \left(1+\frac{\kappa_P-1}{\kappa_P-\frac{3}{2}}\frac{\Delta}{kT_P}\right) \qquad (6.17)
\end{aligned}$$

$$
\begin{aligned}
\varepsilon_{\parallel} &= N_S k T_S \sqrt{\frac{kT_S}{2\pi m}} \frac{\sqrt{\kappa_S - \frac{3}{2}}\Gamma(\kappa_S - 2)}{\Gamma(\kappa_S - \frac{3}{2})} \\
&\left[2 + 2\frac{\kappa_S - 2}{\kappa_S - \frac{3}{2}}\frac{\Delta}{kT_S} + \frac{(\kappa_S - 1)(\kappa_S - 2)}{(\kappa_S - \frac{3}{2})^2}\frac{\Delta^2}{(kT_S)^2}\right] \\
&+ N_P k T_P \sqrt{\frac{kT_P}{2\pi m}} \frac{\sqrt{\kappa_P - \frac{3}{2}}\Gamma(\kappa_P - 2)}{\Gamma(\kappa_P - \frac{3}{2})} \\
&\left[2 + 2\frac{\kappa_P - 2}{\kappa_P - \frac{3}{2}}\frac{\Delta}{kT_P} + \frac{(\kappa_P - 1)(\kappa_P - 2)}{(\kappa_P - \frac{3}{2})^2}\frac{\Delta^2}{(kT_P)^2}\right] \qquad (6.18)
\end{aligned}
$$

The effect of adding the cold component and changing the distribution function is shown in Figure 6.5. For a given value of the field-aligned current, each line gives an estimated field-aligned potential drop. The blue line shows the result of assuming a Maxwellian distribution (original Knight's relation). The red line shows the result of a bi-Maxwellian distribution. The green line shows the result of assuming a kappa distribution. The black line shows the result of a bi-kappa distribution. The top figure is in logarithmic scale and the bottom figure is in linear scale. The ionospheric electron density and temperature are set to $10^3 cm^{-3}$ and 0.1 eV. The plasma sheet electron density and temperature are set to values $1 cm^{-3}$ and 1 keV for illustration purposes. The vertical axes show the magnitude of field-aligned currents in $\mu A/m^2$. The curves in the top figure have two branches. The left branches correspond to downward field-aligned currents, while the right branches correspond to upward field-aligned currents. The lines should be smooth if we plotted the value of the field-aligned currents instead of the magnitude. The bottom figure starts from 100 V of field-aligned potential drop so it doesn't show the downward field-aligned currents part. Adding cold component seems to have a major effect. Giving a $8\mu A/m^2$, the original Knight relation gives a field-aligned potential drop of 8511 V, but the generalized Knight relation using bi-kappa distribution only gives 4074 V. The total of changing distribution function in the plasma sheet makes the field-aligned potential drop about 2 times smaller.

This is the main result obtained in this section, and we will implement the derived relation in the RCM as described later in this Chapter.

6.5 A model based on integral flux relations

Since the algebra used to obtain the expression for the precipitation energy flux is quite tedius, we also used another way to derive this expression, with the purpose of making sure our result did not have algebraic errors. We present this derivation and reconciliation of the two results here. It is not necessary for the main work and the reader may choose to skip the following two sub-sections as they are provided mainly for completeness. Another model based on integral flux relation could be used to evaluate the precipitating number flux and energy flux[186]. For plasma with energy E, the contribution to the number flux is

$$2\pi \int_0^{\pi} j_a(E,\alpha)\cos(\alpha)\sin(\alpha)d\alpha$$

. The net downward integral number and energy fluxes, respectively, of the precipitating electrons close to the atmosphere can be calculated from the following relation [186]:

$$\phi_a = \pi \int_0^{\infty}\int_0^{\pi} j_a(E,\alpha)\sin(2\alpha)d\alpha dE \tag{6.19}$$

$$\theta_a = \pi \int_0^{\infty}\int_0^{\pi} E j_a(E,\alpha)\sin(2\alpha)d\alpha dE \tag{6.20}$$

where α is pitch angle.

Under the assumption that a parallel potential drop located at an altitude defined by B_a/B_i, the ratio between the earth magnetic field close to the atmosphere and at the acceleration region, accelerates an isotropic distribution of magnetospheric electrons downwards, where $j(E,\alpha) = j(E)$.

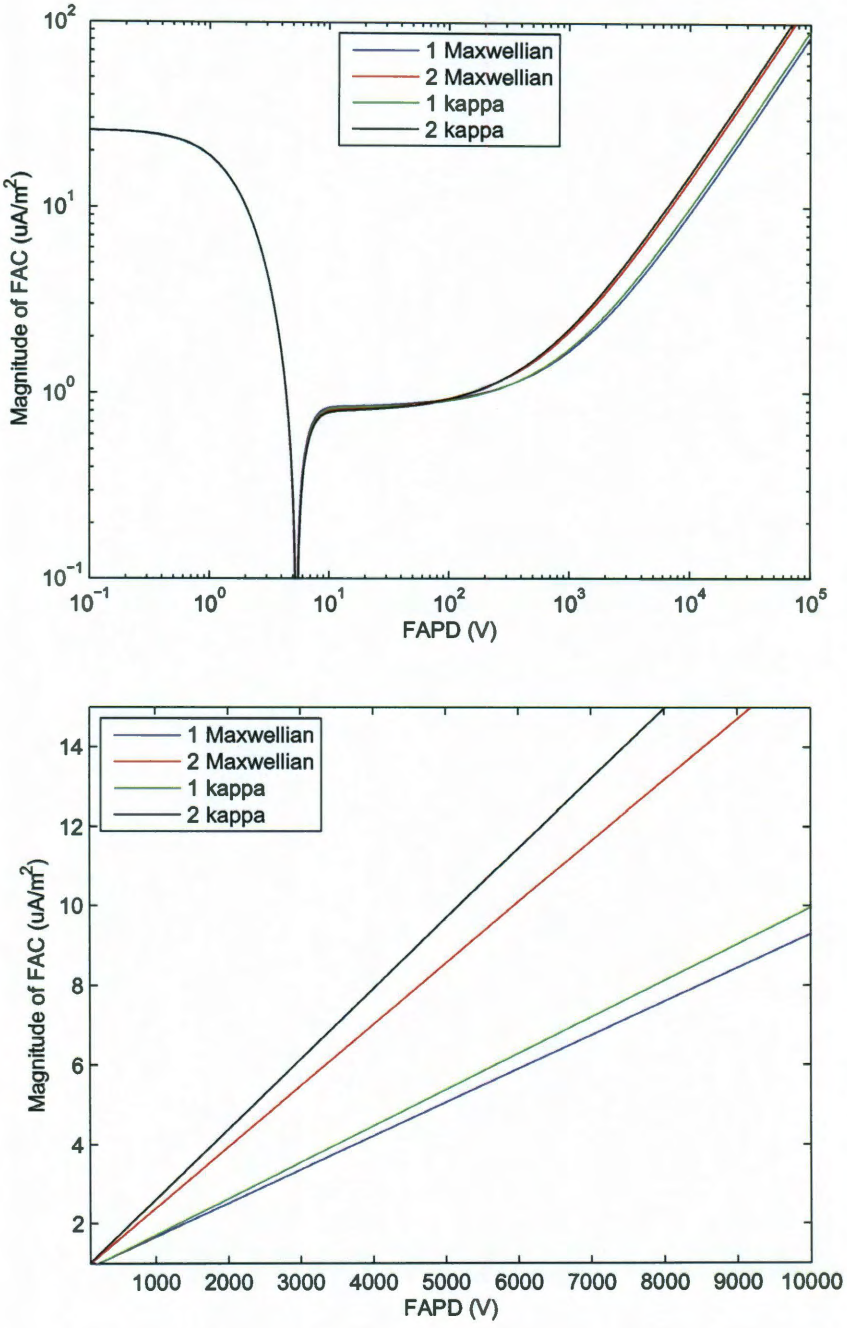

Figure 6.5 : The magnitude of field-aligned currents against the field-aligned potential drop in logarithm (top) and linear (bottom) scales.

Since low energy particles could penetrate into the atmosphere without mirroring back but high energy plasma has the chance of mirroring back, the number flux going into the atmosphere could be calculated as

$$\begin{aligned}
\phi_a &= \pi \int_0^{\infty} \int_0^{\pi/2} j_a(E,\alpha) \sin(2\alpha) d\alpha dE \\
&= \pi \frac{B_a}{B_i} \int_0^{E_b} \int_0^{\pi/2} j(E) \sin(2\alpha) d\alpha dE + \pi \frac{B_a}{B_i} \int_{E_b}^{\infty} \int_0^{\alpha_0} j(E) \sin(2\alpha) d\alpha dE \\
&= \pi \frac{B_a}{B_i} \int_0^{E_b} j(E) dE \int_0^{\pi/2} \sin(2\alpha) d\alpha + \pi \frac{B_a}{B_i} \int_{E_b}^{\infty} j(E) dE \int_0^{\alpha_0} \sin(2\alpha) d\alpha \\
&= \pi \frac{B_a}{B_i} \int_0^{E_b} j(E) dE \left(-\frac{1}{2}\right) \cos(2\alpha) \Big|_0^{\pi/2} + \pi \frac{B_a}{B_i} \int_{E_b}^{\infty} j(E) dE \left(-\frac{1}{2}\right) \cos(2\alpha) \Big|_0^{\alpha_0} \\
&= \pi \frac{B_a}{B_i} \int_0^{E_b} j(E) dE + \pi \frac{B_a}{2B_i} \int_{E_b}^{\infty} j(E) dE \sin^2 \alpha_0 \qquad (6.21)
\end{aligned}$$

where α_0 is the maximum pitch angle of particles in isotropic distribution to reach the atmosphere. Using the first adiabatic invariant, $E \sin^2 \alpha / B$ is constant, we get

$$\sin^2 \alpha_0 = \frac{B_i(E + eV)}{B_a E} \qquad (6.22)$$

then $\sin^2 \alpha_0 \leq 1$ gives

$$\begin{aligned}
E_b &\geq \frac{B_i eV}{B_a - B_i} \\
&= \frac{eV}{B_a/B_i - 1} \qquad (6.23)
\end{aligned}$$

so

$$\phi_a = \pi \frac{B_a}{B_i} \int_0^{E_b} j(E) dE + \pi \int_{E_b}^{\infty} \frac{E + eV}{E} j(E) dE \qquad (6.24)$$

All magnetospheric electrons entering the acceleration region are supposed to be accelerated freely in the potential drop, which means that the plasma energy at the atmosphere is $E + eV$. Then the energy flux is

$$\theta_a = \pi \frac{B_a}{B_i} \int_0^{E_b} (E + eV) j(E) dE + \pi \int_{E_b}^{\infty} \frac{(E + eV)^2}{E} j(E) dE \qquad (6.25)$$

Provided the electrons in the source plasma are isotropic and Maxwellian,

$$f(v) = n\left(\frac{m}{2\pi kT}\right)^{3/2} e^{-\frac{E}{kT}}$$

set $E_c = kT$, and

$$k(E_c, n) = \frac{n}{2\pi^{3/2}}\left(\frac{2}{m}\right)^{1/2}\frac{1}{E_c^{3/2}} \tag{6.26}$$

then the differential flux

$$\begin{aligned} j(E) &= f(p)p^2 \\ &= \frac{2mE}{m^3} n\left(\frac{m}{2\pi E_c}\right)^{3/2} e^{-\frac{E}{E_c}} \\ &= k(E_c, n) E e^{-\frac{E}{E_c}} \end{aligned} \tag{6.27}$$

so

$$\begin{aligned} \phi_a &= \pi\frac{B_a}{B_i}\int_0^{E_b} j(E)dE + \pi\int_{E_b}^{\infty}\frac{E+eV}{E}j(E)dE \\ &= \pi k(E_c,n)\left[\frac{B_a}{B_i}\int_0^{E_b} Ee^{-\frac{E}{E_c}}dE + \int_{E_b}^{\infty}(E+eV)e^{-\frac{E}{E_c}}dE\right] \\ &= \pi k(E_c,n)E_c\left[-\frac{B_a}{B_i}E\,e^{-\frac{E}{E_c}}\Big|_0^{E_b} + \frac{B_a}{B_i}\int_0^{E_b} e^{-\frac{E}{E_c}}dE\right. \\ &\quad \left. -E\,e^{-\frac{E}{E_c}}\Big|_{E_b}^{\infty} + \int_{E_b}^{\infty} e^{-\frac{E}{E_c}}dE - eV\,e^{-\frac{E}{E_c}}\Big|_{E_b}^{\infty}\right] \\ &= \pi k(E_c,n)E_c\left[-\frac{B_a}{B_i}E_b e^{-\frac{E_b}{E_c}} - \frac{B_a}{B_i}E_c\,e^{-\frac{E}{E_c}}\Big|_0^{E_b}\right. \\ &\quad \left. +E_b e^{-\frac{E_b}{E_c}} - E_c e^{-\frac{E}{E_c}}\Big|_{E_b}^{\infty} + eVe^{-\frac{E_b}{E_c}}\right] \\ &= \pi k(E_c,n)E_c\left[-\frac{B_a}{B_i}E_b e^{-\frac{E_b}{E_c}} - \frac{B_a}{B_i}E_c e^{-\frac{E_b}{E_c}} + \frac{B_a}{B_i}E_c + E_b e^{-\frac{E_b}{E_c}} + E_c e^{-\frac{E_b}{E_c}} + eVe^{-\frac{E_b}{E_c}}\right] \\ &= \pi k(E_c,n)E_c^2\left[\frac{B_a}{B_i} - e^{-\frac{E_b}{E_c}}\left(\frac{B_a E_b}{B_i E_c} + \frac{B_a}{B_i} - \frac{E_b}{E_c} - 1 - \frac{eV}{E_c}\right)\right] \\ &= \pi k(E_c,n)E_c^2\left[\frac{B_a}{B_i} - \left(\frac{B_a}{B_i} - 1\right)e^{-\frac{E_b}{E_c}}\right] \end{aligned} \tag{6.28}$$

and similarly, the energy flux is

$$\begin{aligned}
\theta_a &= \pi\frac{B_a}{B_i}\int_0^{E_b}(E+eV)j(E)dE + \pi\int_{E_b}^{\infty}\frac{(E+eV)^2}{E}j(E)dE \\
&= \pi k(E_c,n)\left[\frac{B_a}{B_i}\int_0^{E_b}E(E+eV)e^{-\frac{E}{E_c}}dE + \int_{E_b}^{\infty}(E+eV)^2e^{-\frac{E}{E_c}}dE\right] \\
&= \pi k(E_c,n)E_c\left[-\frac{B_a}{B_i}E(E+eV)\,e^{-\frac{E}{E_c}}\Big|_0^{E_b} + \frac{2B_a}{B_i}\int_0^{E_b}Ee^{-\frac{E}{E_c}}dE + \frac{B_a}{B_i}eV\int_0^{E_b}e^{-\frac{E}{E_c}}dE\right. \\
&\quad \left. -E(E+2eV)\,e^{-\frac{E}{E_c}}\Big|_{E_b}^{\infty} + 2\int_{E_b}^{\infty}Ee^{-\frac{E}{E_c}}dE + 2eV\int_{E_b}^{\infty}e^{-\frac{E}{E_c}}dE - (eV)^2\,e^{-\frac{E}{E_c}}\Big|_{E_b}^{\infty}\right] \\
&= \pi k(E_c,n)E_c\left[-\frac{B_a}{B_i}E_b(E_b+eV)e^{-\frac{E_b}{E_c}} - \frac{2B_a}{B_i}E_cE\,e^{-\frac{E}{E_c}}\Big|_0^{E_b} + \frac{2B_a}{B_i}E_c\int_0^{E_b}e^{-\frac{E}{E_c}}dE\right. \\
&\quad -\frac{B_a}{B_i}E_ceV\,e^{-\frac{E}{E_c}}\Big|_0^{E_b} + E_b(E_b+2eV)e^{-\frac{E_b}{E_c}} - 2E_cE\,e^{-\frac{E}{E_c}}\Big|_{E_b}^{\infty} + 2E_c\int_{E_b}^{\infty}e^{-\frac{E}{E_c}}dE \\
&\quad \left. -2E_ceV\,e^{-\frac{E}{E_c}}\Big|_{E_b}^{\infty} + (eV)^2e^{-\frac{E_b}{E_c}}\right] \\
&= \pi k(E_c,n)E_c\left[-\frac{B_a}{B_i}E_b(E_b+eV)e^{-\frac{E_b}{E_c}} - \frac{2B_a}{B_i}E_cE_be^{-\frac{E_b}{E_c}} - \frac{2B_a}{B_i}E_c^2\,e^{-\frac{E}{E_c}}\Big|_0^{E_b}\right. \\
&\quad -\frac{B_a}{B_i}E_ceVe^{-\frac{E_b}{E_c}} + \frac{B_a}{B_i}E_ceV + E_b(E_b+2eV)e^{-\frac{E_b}{E_c}} + 2E_cE_be^{-\frac{E_b}{E_c}} - 2E_c^2\,e^{-\frac{E}{E_c}}\Big|_{E_b}^{\infty} \\
&\quad \left. +2E_ceVe^{-\frac{E_b}{E_c}} + (eV)^2e^{-\frac{E_b}{E_c}}\right] \\
&= \pi k(E_c,n)E_c\left[-\frac{B_a}{B_i}E_b(E_b+eV)e^{-\frac{E_b}{E_c}} - \frac{2B_a}{B_i}E_cE_be^{-\frac{E_b}{E_c}} - \frac{2B_a}{B_i}E_c^2e^{-\frac{E_b}{E_c}} + \frac{2B_a}{B_i}E_c^2\right. \\
&\quad -\frac{B_a}{B_i}E_ceVe^{-\frac{E_b}{E_c}} + \frac{B_a}{B_i}E_ceV + E_b(E_b+2eV)e^{-\frac{E_b}{E_c}} + 2E_cE_be^{-\frac{E_b}{E_c}} + 2E_c^2e^{-\frac{E_b}{E_c}} \\
&\quad \left. +2E_ceVe^{-\frac{E_b}{E_c}} + (eV)^2e^{-\frac{E_b}{E_c}}\right] \\
&= \pi k(E_c,n)E_c\left\{\frac{B_a}{B_i}(2E_c^2+E_ceV) + e^{-\frac{E_b}{E_c}}\left[-\frac{B_a}{B_i}E_b(E_b+eV) + E_b(E_b+2eV) + (eV)^2\right.\right. \\
&\quad \left.\left. -\frac{2B_a}{B_i}E_cE_b + 2E_cE_b + 2E_ceV - \frac{2B_a}{B_i}E_c^2 - \frac{B_a}{B_i}E_ceV + 2E_c^2\right]\right\} \\
&= \pi k(E_c,n)E_c^2\left\{\frac{B_a}{B_i}(2E_c+eV) - \left[\frac{B_a}{B_i}eV + 2\left(\frac{B_a}{B_i}-1\right)E_c\right]e^{-\frac{E_b}{E_c}}\right\} \qquad (6.29)
\end{aligned}$$

It is interesting to notice that the energy flux increase, P, by the electrons after the acceleration is

$$P = eV\phi_a = \theta_a - \frac{B_a}{B_i}\theta_i \qquad (6.30)$$

where θ_i is the precipitating energy flux incident upon the potential drop. The net downward flux close to the atmosphere, ϕ_a, and above the potential drop, ϕ_i, is related by

$$\phi_a = \frac{B_a}{B_i}\phi_i \tag{6.31}$$

which is a consequence of the Liouville theorem. So if no other source or loss mechanism is present between the potential drop and the atmosphere, the upward current carried by energetic electrons is constant along the whole flux tube.

If the distribution is described by kappa function,

$$f(v) = n\left(\frac{m}{2E_0}\right)^{3/2} \frac{\Gamma(\kappa+1)}{(\pi\kappa)^{3/2}\Gamma(\kappa-\frac{1}{2})} \frac{1}{\left(1+\frac{E}{\kappa E_0}\right)^{\kappa+1}}$$

since

$$E^{\kappa}_{avg} = \frac{3}{2}E_0\frac{\kappa}{\kappa-\frac{3}{2}} \tag{6.32}$$

so

$$E_c = kT = E_0\frac{\kappa}{\kappa-\frac{3}{2}} \tag{6.33}$$

set

$$k(E_c, n) = \frac{n}{2\pi^{3/2}}\left(\frac{2}{m}\right)^{1/2} \frac{1}{E_c^{3/2}} \frac{\Gamma(\kappa+1)}{(\kappa-\frac{3}{2})^{3/2}\Gamma(\kappa-\frac{1}{2})} \tag{6.34}$$

then the differential flux

$$\begin{aligned} j(E) &= f(p)p^2 \\ &= \frac{2mE}{m^3} n\left(\frac{m}{2E_0}\right)^{3/2} \frac{\Gamma(\kappa+1)}{(\pi\kappa)^{3/2}\Gamma(\kappa-\frac{1}{2})} \frac{1}{\left(1+\frac{E}{\kappa E_0}\right)^{\kappa+1}} \\ &= \frac{n}{2\pi^{3/2}}\left(\frac{2}{m}\right)^{1/2} \frac{1}{E_c^{3/2}} \frac{\Gamma(\kappa+1)}{(\kappa-\frac{3}{2})^{3/2}\Gamma(\kappa-\frac{1}{2})} \frac{E}{\left(1+\frac{E}{\kappa E_0}\right)^{\kappa+1}} \\ &= k(E_c, n)\frac{E}{\left(1+\frac{E}{\kappa E_0}\right)^{\kappa+1}} \end{aligned} \tag{6.35}$$

To finish the integration, we could first derive

$$\int_{E_1}^{E_2} \frac{1}{\left(1+\frac{E}{\kappa E_0}\right)^{\kappa+1}} dE$$

$$= -E_0 \frac{1}{\left(1+\frac{E}{\kappa E_0}\right)^{\kappa}}\Bigg|_{E_1}^{E_2} \tag{6.36}$$

$$\int_{E_1}^{E_2} \frac{E}{\left(1+\frac{E}{\kappa E_0}\right)^{\kappa+1}} dE$$

$$= -E_0 \frac{E}{\left(1+\frac{E}{\kappa E_0}\right)^{\kappa}}\Bigg|_{E_1}^{E_2} + E_0 \int_{E_1}^{E_2} \frac{1}{\left(1+\frac{E}{\kappa E_0}\right)^{\kappa}} dE$$

$$= -E_0 \frac{E}{\left(1+\frac{E}{\kappa E_0}\right)^{\kappa}}\Bigg|_{E_1}^{E_2} + \frac{\kappa E_0^2}{1-\kappa} \frac{1}{\left(1+\frac{E}{\kappa E_0}\right)^{\kappa-1}}\Bigg|_{E_1}^{E_2} \tag{6.37}$$

$$\int_{E_1}^{E_2} \frac{E^2}{\left(1+\frac{E}{\kappa E_0}\right)^{\kappa+1}} dE$$

$$= -E_0 \frac{E^2}{\left(1+\frac{E}{\kappa E_0}\right)^{\kappa}}\Bigg|_{E_1}^{E_2} + 2E_0 \int_{E_1}^{E_2} \frac{E}{\left(1+\frac{E}{\kappa E_0}\right)^{\kappa}} dE$$

$$= -E_0 \frac{E^2}{\left(1+\frac{E}{\kappa E_0}\right)^{\kappa}}\Bigg|_{E_1}^{E_2} + \frac{2\kappa E_0^2}{1-\kappa} \frac{E}{\left(1+\frac{E}{\kappa E_0}\right)^{\kappa-1}}\Bigg|_{E_1}^{E_2} - \frac{2\kappa E_0^2}{1-\kappa} \int_{E_1}^{E_2} \frac{1}{\left(1+\frac{E}{\kappa E_0}\right)^{\kappa-1}} dE$$

$$= -E_0 \frac{E^2}{\left(1+\frac{E}{\kappa E_0}\right)^{\kappa}}\Bigg|_{E_1}^{E_2} + \frac{2\kappa E_0^2}{1-\kappa} \frac{E}{\left(1+\frac{E}{\kappa E_0}\right)^{\kappa-1}}\Bigg|_{E_1}^{E_2} - \frac{2\kappa^2 E_0^3}{(1-\kappa)(2-\kappa)} \frac{1}{\left(1+\frac{E}{\kappa E_0}\right)^{\kappa-2}}\Bigg|_{E_1}^{E_2} \tag{6.38}$$

where E_1 and E_2 are given energy lower and upper bounds. So

$$
\begin{aligned}
\phi_a =& \pi \frac{B_a}{B_i} \int_0^{E_b} j(E)dE + \pi \int_{E_b}^{\infty} \frac{E+eV}{E} j(E)dE \\
=& \pi k(E_c, n) \left[\frac{B_a}{B_i} \int_0^{E_b} \frac{E}{\left(1+\frac{E}{\kappa E_0}\right)^{\kappa+1}} dE + \int_{E_b}^{\infty} \frac{E+eV}{\left(1+\frac{E}{\kappa E_0}\right)^{\kappa+1}} dE \right] \\
=& -\pi k(E_c, n) E_0 \left[\frac{B_a}{B_i} \frac{E}{\left(1+\frac{E}{\kappa E_0}\right)^{\kappa}} \Bigg|_0^{E_b} - \frac{B_a}{B_i} \frac{\kappa E_0}{1-\kappa} \frac{1}{\left(1+\frac{E}{\kappa E_0}\right)^{\kappa-1}} \Bigg|_0^{E_b} \right. \\
& \left. + \frac{E}{\left(1+\frac{E}{\kappa E_0}\right)^{\kappa}} \Bigg|_{E_b}^{\infty} - \frac{\kappa E_0}{1-\kappa} \frac{1}{\left(1+\frac{E}{\kappa E_0}\right)^{\kappa-1}} \Bigg|_{E_b}^{\infty} + \frac{eV}{\left(1+\frac{E}{\kappa E_0}\right)^{\kappa}} \Bigg|_{E_b}^{\infty} \right] \\
=& -\pi k(E_c, n) E_0 \left[\frac{B_a}{B_i} \frac{E_b}{\left(1+\frac{E_b}{\kappa E_0}\right)^{\kappa}} - \frac{B_a}{B_i} \frac{\kappa E_0}{1-\kappa} \frac{1}{\left(1+\frac{E_b}{\kappa E_0}\right)^{\kappa-1}} + \frac{B_a}{B_i} \frac{\kappa E_0}{1-\kappa} \right. \\
& \left. - \frac{E_b}{\left(1+\frac{E_b}{\kappa E_0}\right)^{\kappa}} + \frac{\kappa E_0}{1-\kappa} \frac{1}{\left(1+\frac{E_b}{\kappa E_0}\right)^{\kappa-1}} - \frac{eV}{\left(1+\frac{E_b}{\kappa E_0}\right)^{\kappa}} \right] \\
=& -\pi k(E_c, n) \frac{\kappa E_0^2}{1-\kappa} \left[\frac{B_a}{B_i} + \left(1 - \frac{B_a}{B_i}\right) \frac{1}{\left(1+\frac{E_b}{\kappa E_0}\right)^{\kappa-1}} \right] \\
=& n \sqrt{\frac{kT}{2\pi m}} \frac{\sqrt{\kappa - \frac{3}{2}}\Gamma(\kappa-1)}{\Gamma(\kappa-\frac{1}{2})} \left[\frac{B_a}{B_i} + \left(1 - \frac{B_a}{B_i}\right) \frac{1}{\left(1+\frac{E_b}{\kappa E_0}\right)^{\kappa-1}} \right]
\end{aligned}
\tag{6.39}
$$

and the energy flux is

$$
\begin{aligned}
\theta_a =& \pi \frac{B_a}{B_i} \int_0^{E_b} (E+eV) j(E)dE + \pi \int_{E_b}^{\infty} \frac{(E+eV)^2}{E} j(E)dE \\
=& \pi k(E_c, n) \left[\frac{B_a}{B_i} \int_0^{E_b} \frac{E(E+eV)}{\left(1+\frac{E}{\kappa E_0}\right)^{\kappa+1}} dE + \int_{E_b}^{\infty} \frac{(E+eV)^2}{\left(1+\frac{E}{\kappa E_0}\right)^{\kappa+1}} dE \right]
\end{aligned}
$$

$$
\begin{aligned}
&= -\pi k(E_c,n)E_0\left[\frac{B_a}{B_i}\frac{E^2}{\left(1+\frac{E}{\kappa E_0}\right)^{\kappa}}\right|_0^{E_b} - \frac{B_a}{B_i}\frac{2\kappa E_0}{1-\kappa}\frac{E}{\left(1+\frac{E}{\kappa E_0}\right)^{\kappa-1}}\Bigg|_0^{E_b} \\
&\quad + \frac{B_a}{B_i}\frac{2\kappa^2E_0^2}{(1-\kappa)(2-\kappa)}\frac{1}{\left(1+\frac{E}{\kappa E_0}\right)^{\kappa-2}}\Bigg|_0^{E_b} + \frac{B_a}{B_i}eV\frac{E}{\left(1+\frac{E}{\kappa E_0}\right)^{\kappa}}\Bigg|_0^{E_b} - \frac{B_a}{B_i}eV\frac{\kappa E_0}{1-\kappa}\frac{1}{\left(1+\frac{E}{\kappa E_0}\right)^{\kappa-1}}\Bigg|_0^{E_b} \\
&\quad + \frac{E^2}{\left(1+\frac{E}{\kappa E_0}\right)^{\kappa}}\Bigg|_{E_b}^{\infty} - \frac{2\kappa E_0}{1-\kappa}\frac{E}{\left(1+\frac{E}{\kappa E_0}\right)^{\kappa-1}}\Bigg|_{E_b}^{\infty} + \frac{2\kappa^2E_0^2}{(1-\kappa)(2-\kappa)}\frac{1}{\left(1+\frac{E}{\kappa E_0}\right)^{\kappa-2}}\Bigg|_{E_b}^{\infty} \\
&\quad + 2eV\frac{E}{\left(1+\frac{E}{\kappa E_0}\right)^{\kappa}}\Bigg|_{E_b}^{\infty} - 2eV\frac{\kappa E_0}{1-\kappa}\frac{1}{\left(1+\frac{E}{\kappa E_0}\right)^{\kappa-1}}\Bigg|_{E_b}^{\infty} + e^2V^2\frac{1}{\left(1+\frac{E}{\kappa E_0}\right)^{\kappa}}\Bigg|_{E_b}^{\infty}\Bigg] \\
&= -\pi k(E_c,n)E_0\left[\frac{B_a}{B_i}\frac{E_b^2}{\left(1+\frac{E_b}{\kappa E_0}\right)^{\kappa}} - \frac{B_a}{B_i}\frac{2\kappa E_0}{1-\kappa}\frac{E_b}{\left(1+\frac{E_b}{\kappa E_0}\right)^{\kappa-1}} + \frac{B_a}{B_i}\frac{2\kappa^2E_0^2}{(1-\kappa)(2-\kappa)}\frac{1}{\left(1+\frac{E_b}{\kappa E_0}\right)^{\kappa-2}}\right. \\
&\quad - \frac{B_a}{B_i}\frac{2\kappa^2E_0^2}{(1-\kappa)(2-\kappa)} + \frac{B_a}{B_i}eV\frac{E_b}{\left(1+\frac{E_b}{\kappa E_0}\right)^{\kappa}} - \frac{B_a}{B_i}eV\frac{\kappa E_0}{1-\kappa}\frac{1}{\left(1+\frac{E_b}{\kappa E_0}\right)^{\kappa-1}} + \frac{B_a}{B_i}eV\frac{\kappa E_0}{1-\kappa} \\
&\quad - \frac{E_b^2}{\left(1+\frac{E_b}{\kappa E_0}\right)^{\kappa}} + \frac{2\kappa E_0}{1-\kappa}\frac{E_b}{\left(1+\frac{E_b}{\kappa E_0}\right)^{\kappa-1}} - \frac{2\kappa^2E_0^2}{(1-\kappa)(2-\kappa)}\frac{1}{\left(1+\frac{E_b}{\kappa E_0}\right)^{\kappa-2}} \\
&\quad \left. - 2eV\frac{E_b}{\left(1+\frac{E_b}{\kappa E_0}\right)^{\kappa}} + 2eV\frac{\kappa E_0}{1-\kappa}\frac{1}{\left(1+\frac{E_b}{\kappa E_0}\right)^{\kappa-1}} - e^2V^2\frac{1}{\left(1+\frac{E_b}{\kappa E_0}\right)^{\kappa}}\right] \\
&= -\pi k(E_c,n)E_0\left[-\frac{B_a}{B_i}\frac{2\kappa^2E_0^2}{(1-\kappa)(2-\kappa)} + \frac{B_a}{B_i}eV\frac{\kappa E_0}{1-\kappa}\right. \\
&\quad + \frac{B_a}{B_i}\frac{E_b(E_b+eV)}{\left(1+\frac{E_b}{\kappa E_0}\right)^{\kappa}} - \frac{E_b(E_b+2eV)}{\left(1+\frac{E_b}{\kappa E_0}\right)^{\kappa}} - (eV)^2\frac{1}{\left(1+\frac{E_b}{\kappa E_0}\right)^{\kappa}} \\
&\quad - \frac{B_a}{B_i}\frac{2\kappa E_0}{1-\kappa}\frac{E_b}{\left(1+\frac{E_b}{\kappa E_0}\right)^{\kappa-1}} - \frac{B_a}{B_i}eV\frac{\kappa E_0}{1-\kappa}\frac{1}{\left(1+\frac{E_b}{\kappa E_0}\right)^{\kappa-1}} \\
&\quad + \frac{2\kappa E_0}{1-\kappa}\frac{E_b}{\left(1+\frac{E_b}{\kappa E_0}\right)^{\kappa-1}} + eV\frac{2\kappa E_0}{1-\kappa}\frac{1}{\left(1+\frac{E_b}{\kappa E_0}\right)^{\kappa-1}} \\
&\quad \left. + \frac{B_a}{B_i}\frac{2\kappa^2E_0^2}{(1-\kappa)(2-\kappa)}\frac{1}{\left(1+\frac{E_b}{\kappa E_0}\right)^{\kappa-2}} - \frac{2\kappa^2E_0^2}{(1-\kappa)(2-\kappa)}\frac{1}{\left(1+\frac{E_b}{\kappa E_0}\right)^{\kappa-2}}\right]
\end{aligned}
$$

$$
\begin{aligned}
=&\pi k(E_c,n)\frac{\kappa E_0^2}{\kappa-1}\left[\frac{B_a}{B_i}\frac{2\kappa E_0}{\kappa-2}+\frac{B_a}{B_i}eV+\frac{-\frac{B_a}{B_i}eV+\frac{2\kappa E_0}{\kappa-2}\left(1-\frac{B_a}{B_i}\right)\left(1+\frac{E_b}{\kappa E_0}\right)}{\left(1+\frac{E_b}{\kappa E_0}\right)^{\kappa-1}}\right]\\
=&n\sqrt{\frac{kT}{2\pi m}}\frac{\left(\kappa-\frac{3}{2}\right)\Gamma(\kappa-1)}{\Gamma(\kappa-\frac{1}{2})}\left[\frac{B_a}{B_i}\frac{2\kappa E_0}{\kappa-2}+\frac{B_a}{B_i}eV+\frac{\left(1-\frac{B_a}{B_i}\right)\frac{2\kappa E_0}{\kappa-2}+\left(\frac{2}{2-\kappa}-\frac{B_a}{B_i}\right)eV}{\left(1+\frac{E_b}{\kappa E_0}\right)^{\kappa-1}}\right]
\end{aligned}
\tag{6.40}
$$

6.6 Equivalence of Two Methods

It could easily be shown that the result of this model is the same as the one we obtained in the previous section, so the integration from two methods are equivalent. The first integration is over parallel and perpendicular velocities. The second integration is over energy and pitch angle. If we evaluate the fluxes just above the ionosphere, then $eV=\Delta$, $D_E\to 0$, $C_E\to 0$, $D_S^2\to 2\Delta/m$, $C_S^2\to 1-B_S/B_E=1-B_i/B_a$, where

$$
\begin{aligned}
C_S^2 &= 1-\frac{B_S}{B}\\
D_S^2 &= \frac{2e}{m}(\phi-\phi_S)\\
C_E^2 &= \frac{B_E}{B}-1\\
D_E^2 &= \frac{2e}{m}(\phi_E-\phi)\\
V^2 &= \frac{C_E^2D_S^2-C_S^2D_E^2}{C_E^2+C_S^2}
\end{aligned}
\tag{6.41}
$$

As the cross point $V\to 0$, the limit set by C_E and D_E does not exist any more. Noticing the energy of particles has increased from E in the plasma sheet to $E'=E+\Delta$ in the ionosphere, also the pitch angle changed from α to α' related by

$$
\frac{E'\sin^2\alpha'}{B_a}=\frac{E\sin^2\alpha}{B_i}
\tag{6.42}
$$

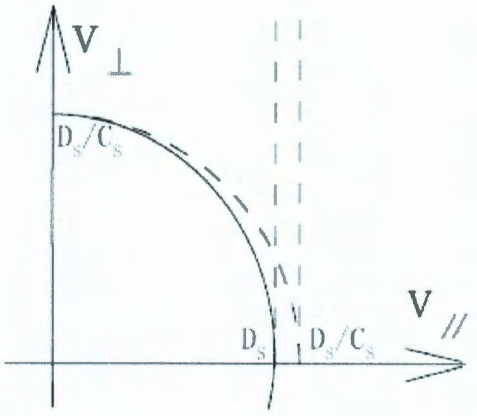

Figure 6.6 : Separating integration region.

According to the integration region separating as Figure 6.6, the integration for a function $g(E')$ is

$$\int_{S_1} f(E)g(E')v_{\parallel}d^3v$$

$$=2\pi\int_{D_S}^{\infty} v_{\parallel}dv_{\parallel}\int_0^{\frac{\sqrt{v_{\parallel}^2+D_E^2}}{C_E}} f(E)g(E')v_{\perp}dv_{\perp}+2\pi\int_V^{D_S} v_{\parallel}dv_{\parallel}\int_{\frac{\sqrt{D_S^2-v_{\parallel}^2}}{C_S}}^{\frac{\sqrt{v_{\parallel}^2+D_E^2}}{C_E}} f(E)g(E')v_{\perp}dv_{\perp}$$

$$=2\pi\int_{D_S}^{\infty} v_{\parallel}dv_{\parallel}\int_0^{\infty} f(E)g(E')v_{\perp}dv_{\perp}+2\pi\int_0^{D_S} v_{\parallel}dv_{\parallel}\int_{\sqrt{\frac{D_S^2-v_{\parallel}^2}{C_S^2}}}^{\infty} f(E)g(E')v_{\perp}dv_{\perp}$$

$$=2\pi\int_{D_S}^{\frac{D_S}{C_S}} v_{\parallel}dv_{\parallel}\int_0^{\sqrt{\frac{D_S^2}{C_S^2}-v_{\parallel}^2}} f(E)g(E')v_{\perp}dv_{\perp}+2\pi\int_{D_S}^{\frac{D_S}{C_S}} v_{\parallel}dv_{\parallel}\int_{\sqrt{\frac{D_S^2}{C_S^2}-v_{\parallel}^2}}^{\infty} f(E)g(E')v_{\perp}dv_{\perp}$$

$$+2\pi\int_{\frac{D_S}{C_S}}^{\infty} v_{\parallel}dv_{\parallel}\int_0^{\infty} f(E)g(E')v_{\perp}dv_{\perp}$$

$$+2\pi\int_0^{D_S} v_{\parallel}dv_{\parallel}\int_{\sqrt{\frac{D_S^2-v_{\parallel}^2}{C_S^2}}}^{\sqrt{\frac{D_S^2}{C_S^2}-v_{\parallel}^2}} f(E)g(E')v_{\perp}dv_{\perp}+2\pi\int_0^{D_S} v_{\parallel}dv_{\parallel}\int_{\sqrt{\frac{D_S^2}{C_S^2}-v_{\parallel}^2}}^{\infty} f(E)g(E')v_{\perp}dv_{\perp}$$

$$
\begin{aligned}
=&2\pi\int_{D_S}^{\frac{D_S}{C_S}} v_\parallel dv_\parallel \int_0^{\sqrt{\frac{D_S^2}{C_S^2}-v_\parallel^2}} f(E)g(E')v_\perp dv_\perp + 2\pi\int_0^{D_S} v_\parallel dv_\parallel \int_{\sqrt{\frac{D_S^2-v_\parallel^2}{C_S^2}}}^{\sqrt{\frac{D_S^2}{C_S^2}-v_\parallel^2}} f(E)g(E')v_\perp dv_\perp \\
&+2\pi\int_0^{\frac{D_S}{C_S}} v_\parallel dv_\parallel \int_{\sqrt{\frac{D_S^2}{C_S^2}-v_\parallel^2}}^{\infty} f(E)g(E')v_\perp dv_\perp + 2\pi\int_{\frac{D_S}{C_S}}^{\infty} v_\parallel dv_\parallel \int_0^{\infty} f(E)g(E')v_\perp dv_\perp \\
=&2\pi\int_{D_S}^{\frac{D_S}{C_S}} v^3 f(E)g(E')dv \int_0^{\arcsin\sqrt{\frac{1-\frac{D_S^2}{v^2}}{1-C_S^2}}} \sin\alpha'\cos\alpha' d(\alpha') \\
&+2\pi\int_{\frac{D_S}{C_S}}^{\infty} v^3 f(E)g(E')dv \int_0^{\pi/2} \sin\alpha'\cos\alpha' d(\alpha') \\
=&\frac{4\pi}{m^2}\int_{\Delta}^{\Delta+E_b} E' f(E)g(E')dE' \int_0^{\sqrt{\frac{1-\frac{D_S^2}{v^2}}{1-C_S^2}}} \sin\alpha' d(\sin\alpha') \\
&+\frac{4\pi}{m^2}\int_{\Delta+E_b}^{\infty} E' f(E)g(E')dE' \int_0^{\sqrt{\frac{B_i(E+\Delta)}{B_a E}}} \sin\alpha' d(\sin\alpha') \\
=&\frac{4\pi}{m^2}\int_0^{E_b} (E+\Delta) f(E)g(E')dE \int_0^1 \sin\alpha d(\sin\alpha)\frac{B_a E}{B_i(E+\Delta)} \\
&+\frac{4\pi}{m^2}\int_{E_b}^{\infty} (E+\Delta) f(E)g(E')dE \int_0^{\alpha_0} \sin\alpha d(\sin\alpha)\frac{B_a E}{B_i(E+\Delta)} \\
=&\frac{4\pi}{m^2}\frac{B_a}{B_i}\int_0^{E_b} E f(E)g(E')dE \int_0^{\pi/2} \sin\alpha\cos\alpha d\alpha \\
&+\frac{4\pi}{m^2}\frac{B_a}{B_i}\int_{E_b}^{\infty} E f(E)g(E')dE \int_0^{\alpha_0} \sin\alpha\cos\alpha d\alpha \qquad (6.43) \\
=&2\pi\frac{B_a}{B_i}\int_0^{E_b} g(E')j(E)dE \int_0^{\pi/2} \sin\alpha\cos\alpha d\alpha + 2\pi\frac{B_a}{B_i}\int_{E_b}^{\infty} g(E')j(E)dE \int_0^{\alpha_0} \sin\alpha\cos\alpha d\alpha
\end{aligned}
$$

where we used the fact that the solution of

$$C_S^2 v_\perp^2 + v_\parallel^2 = D_S^2 \qquad (6.44)$$

$$v_\perp^2 + v_\parallel^2 = v^2 \qquad (6.45)$$

is

$$v_\perp^2 = v^2\sin^2\alpha' = \frac{v^2 - D_S^2}{1 - C_S^2} \qquad (6.46)$$

6.7 Implementation in RCM

The Knight or a similar relation can be used to relate field-aligned currents and the precipitating number flux to the parallel potential drop. Since we do not have another way to estimate the field-aligned potential drop, but the field-aligned currents are estimated from the Vasyliunas equation, the way the generalized Knight relation is used in RCM is to first calculate the field-aligned currents by the Vasyliunas equation, and then evaluate the field-aligned potential drop by the Knight relation, as shown in the logical diagram in chapter 3. At the same time, we compute precipitation energy flux using the generalized formula.

As already mentioned in the beginning of this chapter, the original Knight relation implemented this way in the RCM results in too large field-aligned potential drops, and further leads to numerical instabilities and convergence problems in the ionospheric potential solver. Ignoring the neutral winds, the current conservation law gives

$$\nabla_h \cdot \left(-\overleftrightarrow{\Sigma} \cdot \nabla_h \Phi_i \right) = j_{\parallel} \sin(I) \tag{6.47}$$

the drift velocity is written as

$$v_D = \frac{\mathbf{B} \times \nabla H}{qB^2} \tag{6.48}$$

where $H = \Phi_M + K$ and Φ_i is the ionospheric electric potential, Φ_M is the magnetospheric electric potential. Their difference, besides the co-rotation term, is the field-aligned potential drop. When it is large, after solving for Φ_i which is a well-behaved solution in the ionosphere, Φ_M is too "noisy" across the boundary of large upward field-aligned currents region. The plasma will not convect systematically and will create structured pressure distribution. In addition, it comes out to have more complicated field-aligned currents which gives trouble in solving Φ_I for the next time

step. The code will typically not remain numerically stable for more than a few time steps.

We determined that by using the bi-kappa distributed plasma sheet plasma with Maxwellian distributed ionosphere plasma, field-aligned potential drops are smaller and thus greatly enhance the stability of the system, meaning that we were able to run even simulations. Therefore, we can evaluate the role of parallel electric field in magnetospheric substorms. We will show some simulation results in Chapter 9.

Finally, we need to comment on how our results in this chapter relate to the existing published literature on what might be called current-voltage relations. Since Knight's paper in 1973, there has been a very large number of studies that looked at different aspects of the problem. Indeed, a simple search for journal papers that mention Knight's formula in their title or abstract produces in excess of 400 results. Instead, Janhunen published a result that is most closely related to our derivation[212]. However, our result seems to be more general than theirs as we include a two component hot plasma and a cold ionospheric component, which makes a large difference. It is not possible for us here to review previously published theoretical work on deriving different forms of the current-voltage relationship in the aurora or testing those with observations[212, 213, 214, 215, 216, 217, 218, 219, 220, 221].

Chapter 7

Sources and Losses in the Inner Magnetosphere

Under RCM approximations, particles of certain types in the magnetosphere are conserved along their drift paths. However, in the system of magnetosphere ionosphere interaction, the plasma could have sources or sinks on time scales comparable to typical drift times. A major source of loss is precipitation into the atmosphere. A source of particles is ion outflows in the auroral zone along magnetic field lines. Previous versions of the RCM had a simple version of the electron precipitation (no ion precipitation) and no ion outflows module. However, both processes are affected by parallel electric fields, and in the case of ion outflows, having parallel drops is essential to energizing ionospheric ions to typical magnetospheric plasma energies. Since we now developed an algorithm for inclusion of parallel potential drops, as described in the previous chapter, we are now in a much better position to improve the precipitation algorithm for electrons, add ion precipitation in the RCM, and to introduce a module accounting for effects of direct auroral ion outflows. This chapter describes our work on improving particle precipitation, as well as adding Su's polar wind and Moore's auroral wind [222] models into the RCM. In addition to the charge exchange rate algorithm already implemented in the model, the RCM has the tools to deal with the change of plasma content during disturbed geomagnetic conditions. Due to complexity of this work, we do not present any simulations using these new or improved algorithms, in this thesis. Instead, this chapter serves as a reference on our code development efforts.

7.1 Particle Precipitation

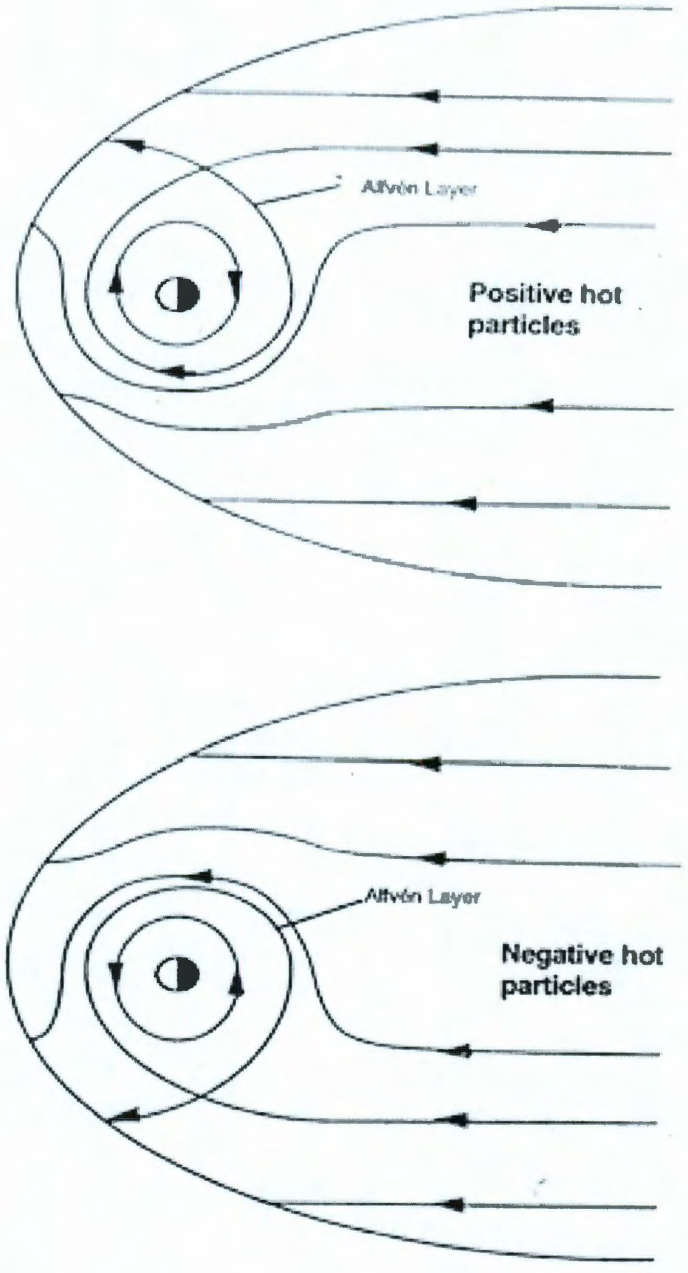

Figure 7.1 : Drift paths for positive and negative hot magnetospheric particles in the equatorial plane, with the Sun to the left. The separatrix between the trajectories that lead from the magnetotail to the dayside magnetopause and those that circle the Earth is called the "alfvén layer". Figure from [7].

For simplicity, let us presume that the motion of particles in the plasma sheet is controlled by a combination of two processes. The first is the action of the steady $\mathbf{E} \times \mathbf{B}$ convection together with gradient and curvature drifts[223, 224]. The second is abrupt injection of the plasma sheet particles into the inner magnetosphere associated with substorm activity. In a steady state configuration, $\mathbf{E} \times \mathbf{B}$ convection and gradient and curvature drifts will establish Alfvén energy layers near the Earth, shown in Figure 7.1, such that electrons with higher energy invariants are confined to increasingly larger radial distances.

Particle precipitation is an important factor in producing ionospheric conductances in the aurora. It also acts as a loss term in the RCM transport (advection) equation. The concept of ionospheric conductance is useful in studies of the electrodynamics of the high-latitude ionosphere. Because large parallel electrical conductivity along the nearly vertical geomagnetic field prevents the establishment of any significant vertical electric potential gradients, the horizontal electric field is nearly constant in altitude. Therefore, the height-integrated horizontal current density associated with the electric field can be directly computed from the conductance[149]. Both the energy flux and the incident energy of precipitating particles contribute to the ionospheric conductances[152, 149].

7.1.1 Electron Precipitation

The low-energy plasma sheet electrons are lost primarily through diffusion-induced precipitation along the magnetic field lines into the Earth's high-latitude regions[225].

As mentioned in the previous chapters, the RCM assumes isotropic pitch angle distribution along magnetic field lines. In general, conservation of the first and second adiabatic invariants will result in a distribution that is not isotropic. From the

calculation in previous chapter, a threshold energy E_b exist, if the energy of a particle is less than E_b, then it could precipitate into the ionosphere without mirroring. Usually, this energy is quite small. Here we assume it to be small enough, or at least less than the minimum energy of the lowest channel. The ratio of magnetic field strength at the atomspheric height over that at the location of the minimum magnetic field strength is given by

$$\frac{B_a}{B_i} = \frac{eV_\parallel}{E_b} + 1 \tag{7.1}$$

or

$$\sin^2 \alpha_0 = \frac{B_i}{B_a} \frac{E + eV_\parallel}{E} \tag{7.2}$$

where $V_\parallel$ is the parallel potential drop. With the assumption that the acceleration region is about 4000 km to 1 R_E above the ionosphere, the ratio between B_a and B_i could be assumed to be around 1.8. The threshold energy E_b is then a function of B_a/B_i and $V_\parallel$.

Thus, the loss rate for particles precipitating to the ionosphere is different for plasma with energy less or greater than the threshold energy E_b. For plasma with its kinetic energy less than E_b, or its velocity is less than v_{min} where $mv_{min}^2 = 2E_b$, all particles would precipitate into the atmosphere if they reach the acceleration area. For plasma with its kinetic energy greater than E_b, the loss rate is

$$\begin{aligned}
& \frac{\int_0^{\alpha_0} 2\pi v^2 dv \sin\alpha d\alpha}{\int_0^{\pi/2} 2\pi v^2 dv \sin\alpha d\alpha} \\
= & \frac{2\pi v^2 dv \,(1 - \cos\alpha_0)}{2\pi v^2 dv} \\
= & \; 1 - \cos\alpha_0 \\
= & \; 1 - \sqrt{1 - \frac{B_i(E + eV_\parallel)}{B_a E}} \\
= & \; 1 - \sqrt{1 - \frac{E_b}{E_b + eV_\parallel} \frac{E + eV_\parallel}{E}}
\end{aligned} \tag{7.3}$$

Since the energy E is assumed to be greater than E_b, then the term under the square root is always between 0 and 1. The lost rate is than somewhere between zero and one as expected. Figure 7.2 shows the results from the above the equation. The electron energy E is in the range between 100 eV and 20 keV. The five curves correspond to the formula with field-aligned potential drop equals to 1 V, 10 V, 100 V, 1 kV, 10 kV. These curves converge to 1/3. For a field-aligned potential drop of several kV, the loss rate is averaged to be somewhere between 1/2 and 1/3. The lifetime τ in the strong pitch angle diffusion limit can be expressed as[226]

$$\tau = \frac{\gamma m}{p} \frac{2VB_h}{1-\eta} \tag{7.4}$$

where p is the momentum, V is flux tube volume, B_h is the magnetic field strength at foot point, η is some backscatter coefficient.

The the loss rate in the strong pitch angle diffusion limit is

$$\lambda = \frac{1}{\tau} = \left(\frac{E}{2m}\right)^{1/2} \left(B_i \int \frac{ds}{B}\right)^{-1}$$

However, strong pitch angle diffusion is only a limiting idealization. Observations [225]and wave measurements[227, 228, 229, 230] suggest that pitch angle scattering may not always be strong throughout the plasma sheet. The computed precipitation lifetimes are found to be weakly dependent on magnetic activity[225]. The average lifetimes exceed those for the case of isotropy at all pitch angles by a factor between 2 and 3 for $Kp \leq 2$ and approximately 1.5 for $Kp > 2$. An estimation of 1/3 is defined as the "fudge" factor in the RCM.

Unfortunately, there are very few reported measurements of electron lifetimes in the plasma sheet. Many studies were done to estimate electron lifetimes[231, 232, 233, 234]. All of these empirical and theoretical estimates for electron lifetimes correspond to the limit of weak pitch angle diffusion, in which the particle lifetime is

directly proportional to an appropriately weighted sum of the wave spectral densities at the various resonance frequencies[235]. For the RCM we adopted the model of the scattering rate from Chen and Schulz et al.[235, 236]. They extrapolated the theoretical lifetimes of Albert [1994] both to lower energies and to higher L values, and then renormalized the results of Albert [1994] to "match" the empirical lifetimes compiled by Roberts [1969]. The scattering rate obtained is approximated by the expression

$$\lambda_0(E,L) = min\{0.08E^{-1.32}, 0.4 \times 10^{2L-6+0.4\log_2 E}\} day^{-1} \tag{7.5}$$

where energy E is measured in units of MeV as shown above. This scattering rate pertains only to wave-particle interactions without considering Coulomb scattering which might be dominant at sufficiently low L value. The first term depends on energy but not no L, which corresponds to the "flat" portion of any empirical lifetimes versus L plot. The second term corresponds to the "sloped" portion of the same lifetime versus L plot, and the "break" for specified E occurs at

$$L = L_b \approx 2.6505 - 0.3987 \log_2 E$$

To make a smooth transition between weak pitch angle diffusion ($\lambda\tau \ll 1$) and strong diffusion ($\lambda\tau \gg 1$), the loss rate is given by $\bar{\lambda} = \lambda/(1+\lambda\tau)$, where τ is the lifetime against strong pitch angle diffusion.

Taking into account that the wave activity is not uniformly distributed in MLT[229, 230], a modified MLT-dependent scattering rate was also used, so that

$$\lambda_{MLT} = \lambda_0 \left[1 + 0.8 \sin\left(\phi - \frac{\pi}{4}\right)\right] \tag{7.6}$$

where ϕ is the MLT coordinates. This formula is later corrected to[236]

$$\lambda(E,L,\phi) = \left[1 + 1.2 \sin\left(\phi + \frac{\pi}{6}\right) - 0.25 \cos\left(2\phi + \frac{\pi}{3}\right)\right] \lambda_0(E,L) \tag{7.7}$$

The number fluxes and energy fluxes could be calculated by integration as

$$\int \frac{1}{m^3}\pi(1-\eta)\bar{\lambda}\tau \left|\frac{B_r}{B}\right| p^2 f dE \tag{7.8}$$

$$\int \frac{1}{m^3}\pi(1-\eta)\bar{\lambda}\tau \left|\frac{B_r}{B}\right| (E+eV) p^2 f dE \tag{7.9}$$

7.1.2 Ion Precipitation

There is no loss of particles precipitating to the ionosphere for plasma sheet ions that have energy lower than the energy it needs to overcome the potential difference, eV; and for ions with energy is greater than eV, similar to those of electrons, the rate is

$$1-\sqrt{1-\frac{E_b}{E_b+eV}\frac{E-eV}{E}}$$

since the ions are decelerated by the parallel electric field. Figure 7.3 shows the loss rate of ions according to the above equation. The five curves correspond to a field-aligned potential drop of 1 V, 10 V, 100 V, 1 kV, and 10 kV. The energy range of ions is from 1 keV to 200 keV. For a field-aligned potential drop of several keV, the loss rate is varying between 0 and 0.2. An estimation of 1/10 is used as the loss rate as a fraction of strong pitch angle diffusion[33]. The number flux and energy flux of positive charged ions could be calculated from the integration of distribution functions.

$$\int \frac{1}{m^3}\pi(1-\eta)\bar{\lambda}\tau \left|\frac{B_r}{B}\right| p^2 f dE \tag{7.10}$$

$$\int \frac{1}{m^3}\pi(1-\eta)\bar{\lambda}\tau \left|\frac{B_r}{B}\right| (E-eV) p^2 f dE \tag{7.11}$$

This result is different due to the energy change through the potential drop region. We present the results for both Maxwellian and kappa distributions and also using two equivalent methods. From the energy conservation:

$$v_\perp'^2 + v_\parallel'^2 + \frac{2e}{m}\phi' = v_\perp^2 + v_\parallel^2 + \frac{2e}{m}\phi \tag{7.12}$$

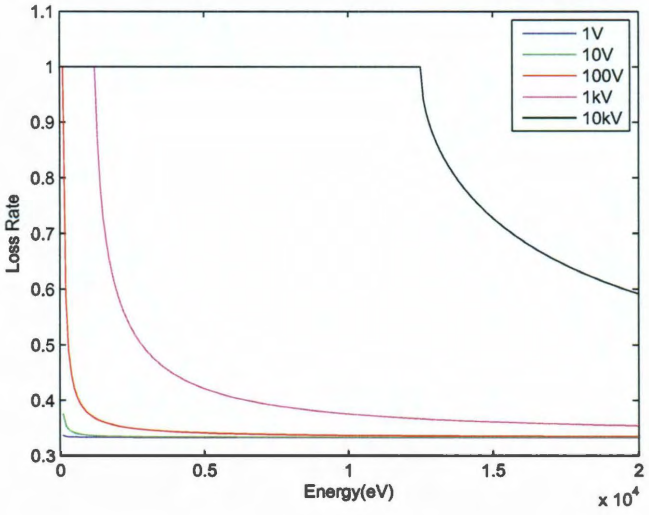

Figure 7.2 : The loss rate of electrons for different field-aligned potential drop.

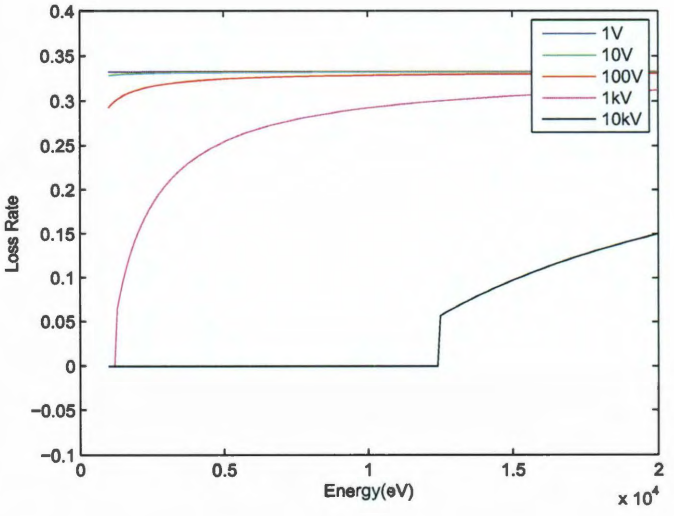

Figure 7.3 : The loss rate of ions for different field-aligned potential drops.

where the superscript $'$ means evaluating at the base. Using the first adiabatic invariant $v_\perp'^2 = v_\perp^2 B'/B$, we get

$$v_\parallel'^2 = \frac{2e}{m}(\phi - \phi') + v_\perp^2 \left(1 - \frac{B'}{B}\right) + v_\parallel^2 > 0 \tag{7.13}$$

Since $\phi > \phi_S$ and $B > B'$, the base S gives no restriction. But the base E gives

$$-C_E^2 v_\perp^2 + v_\parallel^2 > D_E^2 \tag{7.14}$$

where $C_E^2 = B_E/B - 1$, $D_E^2 = 2e(\phi_E - \phi)/m$. The region S_1 in the phase diagram is the space between the positive horizontal axis and the right branch of the hyperbola as shown in Figure 7.4.

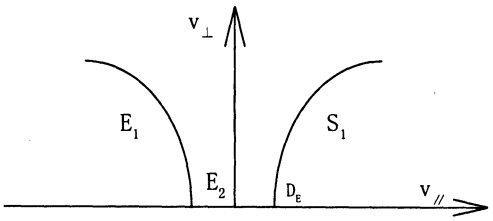

Figure 7.4 : Trajectories in phase space of ions.

Since we only care about the ions moving downward into the ionosphere, with intermediate parameters set to

$$\begin{aligned} A^2 &= \frac{m}{2kT_S} \\ x &= Av_\perp \\ y &= Av_\parallel \\ p &= x^2 \\ q &= y^2 \\ q' &= q + \frac{q}{C_E}^2 - \frac{A^2 D_E^2}{C_E^2} \end{aligned} \tag{7.15}$$

and $q' = q$ when $q' = A^2 D_E^2$. So the number flux is integrated as

$$
\begin{aligned}
\phi &= \int_{S_1} v_\parallel f_S d^3v \\
&= N_S e^{-\frac{e}{kT_S}(\phi-\phi_S)} \left(\frac{m}{2\pi k T_S}\right)^{3/2} \int_{S_1} v_\parallel e^{-\frac{m}{2kT_S}(v_\perp^2+v_\parallel^2)} d^3v \\
&= N_S e^{-\frac{e}{kT_S}(\phi-\phi_S)} \left(\frac{m}{2\pi k T_S}\right)^{3/2} 2\pi \iint v_\parallel v_\perp e^{-\frac{m}{2kT_S}(v_\perp^2+v_\parallel^2)} dv_\parallel dv_\perp \\
&= N_S e^{-\frac{e}{kT_S}(\phi-\phi_S)} \frac{A^3}{\pi^{3/2}} \frac{2\pi}{A^4} \iint yx e^{-x^2-y^2} dxdy \\
&= N_S e^{-\frac{e}{kT_S}(\phi-\phi_S)} \frac{2}{A\sqrt{\pi}} \int_{AD_E}^{\infty} y e^{-y^2} dy \int_0^{\frac{\sqrt{y^2-A^2E_E^2}}{C_E}} x e^{-x^2} dx \\
&= N_S e^{-\frac{e}{kT_S}(\phi-\phi_S)} \frac{1}{A\sqrt{\pi}} \int_{\infty}^{AD_E} y e^{-y^2} dy \left(e^{-\frac{y^2-A^2D_E^2}{C_E^2}} - 1\right) \\
&= N_S e^{-\frac{e}{kT_S}(\phi-\phi_S)} \frac{1}{A\sqrt{\pi}} \left(e^{\frac{A^2D_E^2}{C_E^2}} \int_{\infty}^{AD_E} y e^{-y^2-\frac{y^2}{C_E^2}} dy + \int_{AD_E}^{\infty} y e^{-y^2} dy\right) \\
&= N_S e^{-\frac{e}{kT_S}(\phi-\phi_S)} \frac{1}{2A\sqrt{\pi}} \left[e^{\frac{A^2D_E^2}{C_E^2}} \frac{1}{1+\frac{1}{C_E^2}} e^{-y^2\left(1+\frac{1}{C_E^2}\right)}\Big|_{AD_E}^{\infty} - e^{-y^2}\Big|_{AD_E}^{\infty}\right] \\
&= N_S e^{-\frac{e}{kT_S}(\phi-\phi_S)} \frac{1}{2A\sqrt{\pi}} \left[-e^{\frac{A^2D_E^2}{C_E^2}} \frac{1}{1+\frac{1}{C_E^2}} e^{-A^2D_E^2\left(1+\frac{1}{C_E^2}\right)} + e^{-A^2D_E^2}\right] \\
&= N_S e^{-\frac{e}{kT_S}(\phi-\phi_S)} \frac{1}{2A\sqrt{\pi}} e^{-A^2D_E^2} \left(1 - \frac{1}{1+\frac{1}{C_E^2}}\right) \\
&= N_S e^{-\frac{e}{kT_S}(\phi-\phi_S)} \frac{1}{2A\sqrt{\pi}} e^{-A^2D_E^2} \frac{1}{1+C_E^2} \\
&= N_S e^{-\frac{e}{kT_S}(\phi-\phi_S)} \sqrt{\frac{kT_S}{2\pi m}} e^{-\frac{m}{2kT_S}\frac{2e}{m}(\phi_E-\phi)} \frac{B}{B_E} \\
@E &= N_S \sqrt{\frac{kT_S}{2\pi m}} e^{-\frac{e}{kT_S}(\phi_E-\phi_S)}
\end{aligned}
\tag{7.16}
$$

and the energy flux is

$$
\begin{aligned}
\theta &= \int_{S_1} \frac{m}{2}\left(v_\perp^2+v_\parallel^2\right) v_\parallel f_S d^3v \\
&= N_S e^{-\frac{e}{kT_S}(\phi-\phi_S)}\left(\frac{m}{2\pi kT_S}\right)^{3/2}\frac{m}{2}\int_{S_1}\left(v_\perp^2+v_\parallel^2\right) v_\parallel e^{-\frac{m}{2kT_S}\left(v_\perp^2+v_\parallel^2\right)} d^3v \\
&= N_S e^{-\frac{e}{kT_S}(\phi-\phi_S)}\frac{A^3}{\pi^{3/2}}\frac{m}{2}2\pi\iint\left(v_\perp^2+v_\parallel^2\right) v_\parallel v_\perp e^{-A^2\left(v_\perp^2+v_\parallel^2\right)} dv_\parallel dv_\perp \\
&= N_S e^{-\frac{e}{kT_S}(\phi-\phi_S)}\frac{m}{4\sqrt{\pi}A^3}\iint (p+q)e^{-p-q}dpdq \\
&= \frac{mN_S e^{-\frac{e}{kT_S}(\phi-\phi_S)}}{4\sqrt{\pi}A^3}\left(\int_{A^2D_E^2}^{\infty} e^{-q}dq\int_0^{\frac{q-A^2D_E^2}{C_E^2}} pe^{-p}dp+\int_{A^2D_E^2}^{\infty} qe^{-q}dq\int_0^{\frac{q-A^2D_E^2}{C_E^2}} e^{-p}dp\right) \\
&= \frac{mN_S e^{-\frac{e}{kT_S}(\phi-\phi_S)}}{4\sqrt{\pi}A^3}\left[\int_{A^2D_E^2}^{\infty} e^{-q}dq\left(-pe^{-p}-e^{-p}\right)\Big|_0^{\frac{q-A^2D_E^2}{C_E^2}}+\int_{A^2D_E^2}^{\infty} qe^{-q}dq\left(-e^{-p}\right)\Big|_0^{\frac{q-A^2D_E^2}{C_E^2}}\right] \\
&= \frac{mN_S e^{-\frac{e}{kT_S}(\phi-\phi_S)}}{4\sqrt{\pi}A^3}\left[\int_{A^2D_E^2}^{\infty} e^{-q}dq\left(-\frac{q-A^2D_E^2+C_E^2}{C_E^2}e^{-\frac{q-A^2D_E^2}{C_E^2}}+1\right)\right. \\
&\quad \left.+\int_{A^2D_E^2}^{\infty} qe^{-q}dq\left(-e^{-\frac{q-A^2D_E^2}{C_E^2}}+1\right)\right] \\
&= \frac{mN_S e^{-\frac{e}{kT_S}(\phi-\phi_S)}}{4\sqrt{\pi}A^3}\int_{A^2D_E^2}^{\infty}\left[e^{-q}+qe^{-q}-e^{-q'}-q'e^{-q'}\right]dq \\
&= \frac{mN_S e^{-\frac{e}{kT_S}(\phi-\phi_S)}}{4\sqrt{\pi}A^3}\left[\left(e^{-q}-qe^{-q}-e^{-q}\right)-\frac{C_E^2}{C_E^2+1}\left(-e^{-q'}-q'e^{-q'}-e^{-q'}\right)\right]\Bigg|_{A^2D_E^2}^{\infty} \\
&= \frac{mN_S e^{-\frac{e}{kT_S}(\phi-\phi_S)}}{4\sqrt{\pi}A^3}\frac{A^2D_E^2+2}{C_E^2+1}e^{-A^2D_E^2} \\
&= N_S e^{-\frac{e}{kT_S}(\phi-\phi_S)}kT_S\sqrt{\frac{kT_S}{2\pi m}}\frac{B}{B_E}\left[\frac{m}{2kT_S}\frac{2e}{m}(\phi_E-\phi)+2\right]e^{-\frac{m}{2kT_S}\frac{2e}{m}(\phi_E-\phi)} \\
@E &= N_S kT_S\sqrt{\frac{kT_S}{2\pi m}}2e^{-\frac{e}{kT_S}(\phi_E-\phi_S)} \qquad (7.17)
\end{aligned}
$$

If the distribution is a kappa function, then the number flux is

$$
\begin{aligned}
\phi &= \int_{S_1} v_\parallel f_S d^3v \\
&= \left(\frac{m}{2E_{0S}}\right)^{3/2} \frac{N_S\Gamma(\kappa_S+1)}{(\pi\kappa_S)^{3/2}\Gamma(\kappa_S-\frac{1}{2})} \int_{S_1} \frac{2\pi v_\parallel v_\perp dv_\parallel dv_\perp}{\left[1+\frac{e(\phi-\phi_S)}{\kappa_S E_{0S}}+\frac{mv_\perp^2+mv_\parallel^2}{2\kappa_S E_{0S}}\right]^{\kappa_S+1}} \\
&= \sqrt{\frac{m}{2\pi\kappa_S E_{0S}}} \frac{N_S\Gamma(\kappa_S+1)}{\Gamma(\kappa_S-\frac{1}{2})} \int_{D_E}^{\infty} v_\parallel dv_\parallel \int_0^{v_\perp^2=\frac{v_\parallel^2-D_E^2}{C_E^2}} \frac{d\left(\frac{m}{2\kappa_S E_{0S}}v_\perp^2\right)}{\left[1+\frac{e(\phi-\phi_S)}{\kappa_S E_{0S}}+\frac{mv_\perp^2+mv_\parallel^2}{2\kappa_S E_{0S}}\right]^{\kappa_S+1}} \\
&= -\sqrt{\frac{m}{2\pi\kappa_S E_{0S}}} \frac{N_S\Gamma(\kappa_S)}{\Gamma(\kappa_S-\frac{1}{2})} \int_{D_E}^{\infty} v_\parallel dv_\parallel \left.\frac{1}{\left[1+\frac{e(\phi-\phi_S)}{\kappa_S E_{0S}}+\frac{mv_\perp^2+mv_\parallel^2}{2\kappa_S E_{0S}}\right]^{\kappa_S}}\right|_0^{\frac{v_\parallel^2-D_E^2}{C_E^2}} \\
&= \sqrt{\frac{m}{2\pi\kappa_S E_{0S}}} \frac{N_S\Gamma(\kappa_S)}{\Gamma(\kappa_S-\frac{1}{2})} \int_{D_E}^{\infty} v_\parallel dv_\parallel \\
&\quad \left\{ \frac{1}{\left[1+\frac{e(\phi-\phi_S)}{\kappa_S E_{0S}}+\frac{mv_\parallel^2}{2\kappa_S E_{0S}}\right]^{\kappa_S}} - \frac{1}{\left[1+\frac{e(\phi-\phi_S)}{\kappa_S E_{0S}}+\frac{m\frac{v_\parallel^2-D_E^2}{C_E^2}+mv_\parallel^2}{2\kappa_S E_{0S}}\right]^{\kappa_S}} \right\} \\
&= \sqrt{\frac{m}{2\pi\kappa_S E_{0S}}} \frac{N_S\Gamma(\kappa_S)}{\Gamma(\kappa_S-\frac{1}{2})} \frac{\kappa_S E_{0S}}{m} \left\{ \int_{v_\parallel=D_E}^{\infty} \frac{d\left(\frac{m}{2\kappa_S E_{0S}}v_\parallel^2\right)}{\left[1+\frac{e(\phi-\phi_S)}{\kappa_S E_{0S}}+\frac{mv_\parallel^2}{2\kappa_S E_{0S}}\right]^{\kappa_S}} \right. \\
&\quad \left. -\frac{C_E^2}{C_E^2+1} \int_{v_\parallel=D_E}^{\infty} \frac{d\left(\frac{C_E^2+1}{C_E^2}\frac{m}{2\kappa_S E_{0S}}v_\parallel^2\right)}{\left[1+\frac{e(\phi-\phi_S)}{\kappa_S E_{0S}}-\frac{mD_E^2}{2\kappa_S E_{0S}C_E^2}+\frac{C_E^2+1}{C_E^2}\frac{mv_\parallel^2}{2\kappa_S E_{0S}}\right]^{\kappa_S}} \right\} \\
&= \sqrt{\frac{\kappa_S E_{0S}}{2\pi m}} \frac{N_S\Gamma(\kappa_S-1)}{\Gamma(\kappa_S-\frac{1}{2})} \frac{1}{C_E^2+1} \frac{1}{\left[1+\frac{e(\phi-\phi_S)}{\kappa_S E_{0S}}+\frac{mD_E^2}{2\kappa_S E_{0S}}\right]^{\kappa_S-1}} \\
&= N_S\sqrt{\frac{\kappa_S E_{0S}}{2\pi m}} \frac{\Gamma(\kappa_S-1)}{\Gamma(\kappa_S-\frac{1}{2})} \frac{B}{B_E} \frac{1}{\left[1+\frac{e(\phi_E-\phi_S)}{\kappa_S E_{0S}}\right]^{\kappa_S-1}}
\end{aligned}
\tag{7.18}
$$

The integration of energy flux is much more complicated and is shown in Appendix

D. The expression looks like

$$\begin{aligned}
\theta &= \int_{S_1} \frac{m}{2}\left(v_\perp^2 + v_\parallel^2\right) v_\parallel f_S d^3v \\
&= \left(\frac{m}{2}\right)^{5/2} \frac{N_S}{E_{0S}^{3/2}} \frac{\Gamma(\kappa_S+1)}{(\pi\kappa_S)^{3/2}\Gamma(\kappa_S-\frac{1}{2})} \int_{S_1} \frac{\left(v_\perp^2+v_\parallel^2\right) 2\pi v_\parallel v_\perp dv_\parallel dv_\perp}{\left[1+\frac{e(\phi-\phi_S)}{\kappa_S E_{0S}}+\frac{mv_\perp^2+mv_\parallel^2}{2\kappa_S E_{0S}}\right]^{\kappa_S+1}} \\
&= \left(\frac{m\kappa_S E_{0S}}{2\pi}\right)^{1/2} \frac{N_S\Gamma(\kappa_S-1)}{2\Gamma(\kappa_S-\frac{1}{2})} \frac{\frac{B}{B_E}\frac{2e}{m}(\phi_E-\phi) - \frac{B}{B_E}\frac{4\kappa_S E_{0S}}{m(2-\kappa_S)}\left[1+\frac{e(\phi_E-\phi_S)}{\kappa_S E_{0S}}\right]}{\left[1+\frac{e(\phi_E-\phi_S)}{\kappa_S E_{0S}}\right]^{\kappa_S-1}} \\
@E &= N_S\sqrt{\frac{\kappa_S E_{0S}}{2\pi m}}\kappa_S E_{0S}\frac{\Gamma(\kappa_S-2)}{\Gamma(\kappa_S-\frac{1}{2})}\frac{2}{\left[1+\frac{e(\phi_E-\phi_S)}{\kappa_S E_{0S}}\right]^{\kappa_S-2}}
\end{aligned} \tag{7.19}$$

Since $B_i(E-eV) < B_a E$, for Maxwellian distribution, the number flux is also given by

$$\begin{aligned}
\phi &= \pi\int_0^\infty\int_0^{\pi/2} j_a(E,\alpha)\sin(2\alpha)d\alpha dE \\
&= \pi\frac{B_a}{B_i}\int_{eV}^\infty\int_0^{\alpha_0} j(E)\sin(2\alpha)d\alpha dE \\
&= \pi\frac{B_a}{B_i}\int_{eV}^\infty j(E)dE\sin^2\alpha_0 \\
&= \pi\int_{eV}^\infty \frac{E-eV}{E}f(p)p^2dE \\
&= \pi\int_{eV}^\infty \frac{E-eV}{E}\frac{2mE}{m^3}n\left(\frac{m}{2\pi kT}\right)^{3/2}e^{-\frac{E}{kT}}dE \\
&= \frac{2n\pi}{m^2}\left(\frac{m}{2\pi kT}\right)^{3/2}\int_{eV}^\infty (E-eV)e^{-\frac{E}{kT}}dE \\
&= -\frac{n}{\sqrt{2\pi kTm}}\left[(E-eV)\,e^{-\frac{E}{kT}}\Big|_{eV}^\infty - \int_{eV}^\infty e^{-\frac{E}{kT}}dE\right] \\
&= n\sqrt{\frac{kT}{2\pi m}}e^{-\frac{eV}{kT}}
\end{aligned} \tag{7.20}$$

and the energy flux is

$$\begin{aligned}
\theta &= \pi \int_{eV}^{\infty} \frac{(E-eV)^2}{E} j(E) dE \\
&= \pi \int_{eV}^{\infty} \frac{(E-eV)^2}{E} \frac{2mE}{m^3} n \left(\frac{m}{2\pi kT}\right)^{3/2} e^{-\frac{E}{kT}} dE \\
&= \frac{2n\pi}{m^2} \left(\frac{m}{2\pi kT}\right)^{3/2} 2kT \int_{eV}^{\infty} (E-eV) e^{-\frac{E}{kT}} dE \\
&= \frac{2n}{\sqrt{2\pi kTm}} kT \int_{eV}^{\infty} e^{-\frac{E}{kT}} dE \\
&= 2nkT \sqrt{\frac{kT}{2\pi m}} e^{-\frac{eV}{kT}} \qquad (7.21)
\end{aligned}$$

For a kappa distribution, the number flux is

$$\begin{aligned}
\phi &= \pi \int_{eV}^{\infty} \frac{E-eV}{E} j(E) dE \\
&= \pi \int_{eV}^{\infty} \frac{E-eV}{E} \frac{2mE}{m^3} n \left(\frac{m}{2E_0}\right)^{3/2} \frac{\Gamma(\kappa+1)}{(\pi\kappa)^{3/2}\Gamma\left(\kappa-\frac{1}{2}\right)} \frac{1}{\left(1+\frac{E}{\kappa E_0}\right)^{\kappa+1}} dE \\
&= \frac{2n\pi}{m^2} \left(\frac{m}{2E_0}\right)^{3/2} \frac{\Gamma(\kappa+1)}{(\pi\kappa)^{3/2}\Gamma\left(\kappa-\frac{1}{2}\right)} \int_{eV}^{\infty} \frac{(E-eV)dE}{\left(1+\frac{E}{\kappa E_0}\right)^{\kappa+1}} \\
&= \frac{2n\pi}{m^2} \left(\frac{m}{2E_0}\right)^{3/2} \frac{\Gamma(\kappa+1)}{(\pi\kappa)^{3/2}\Gamma\left(\kappa-\frac{1}{2}\right)} \\
&\quad \left[(-E_0) \frac{E}{\left(1+\frac{E}{\kappa E_0}\right)^{\kappa}} \Bigg|_{eV}^{\infty} + E_0 \int_{eV}^{\infty} \frac{dE}{\left(1+\frac{E}{\kappa E_0}\right)^{\kappa}} + eVE_0 \frac{1}{\left(1+\frac{E}{\kappa E_0}\right)^{\kappa}} \Bigg|_{eV}^{\infty} \right] \\
&= \frac{n\Gamma(\kappa)}{\sqrt{2\pi m\kappa E_0}\Gamma\left(\kappa-\frac{1}{2}\right)} \left[\frac{eV}{\left(1+\frac{eV}{\kappa E_0}\right)^{\kappa}} + \frac{\kappa E_0}{1-\kappa} \frac{1}{\left(1+\frac{E}{\kappa E_0}\right)^{\kappa-1}} \Bigg|_{eV}^{\infty} - \frac{eV}{\left(1+\frac{eV}{\kappa E_0}\right)^{\kappa}} \right] \\
&= n\sqrt{\frac{\kappa E_0}{2\pi m}} \frac{\Gamma(\kappa-1)}{\Gamma\left(\kappa-\frac{1}{2}\right)} \frac{1}{\left(1+\frac{eV}{\kappa E_0}\right)^{\kappa-1}} \qquad (7.22)
\end{aligned}$$

and the energy flux is

$$
\begin{aligned}
& \theta \\
= \; & \pi \int_{eV}^{\infty} \frac{(E-eV)^2}{E} j(E) dE \\
= \; & \frac{2n\pi}{m^2} \left(\frac{m}{2E_0} \right)^{3/2} \frac{\Gamma(\kappa+1)}{(\pi\kappa)^{3/2}\Gamma\left(\kappa-\frac{3}{2}\right)} \int_{eV}^{\infty} \frac{(E-eV)^2 dE}{\left(1+\frac{E}{\kappa E_0}\right)^{\kappa+1}} \\
= \; & \frac{2n\pi}{m^2} \left(\frac{m}{2E_0} \right)^{3/2} \frac{\Gamma(\kappa+1)}{(\pi\kappa)^{3/2}\Gamma\left(\kappa-\frac{3}{2}\right)} \\
& \left[\int_{eV}^{\infty} \frac{E^2 dE}{\left(1+\frac{E}{\kappa E_0}\right)^{\kappa+1}} - 2eV \int_{eV}^{\infty} \frac{E dE}{\left(1+\frac{E}{\kappa E_0}\right)^{\kappa+1}} + e^2V^2 \int_{eV}^{\infty} \frac{dE}{\left(1+\frac{E}{\kappa E_0}\right)^{\kappa+1}} \right] \\
= \; & \frac{2n\pi}{m^2} \left(\frac{m}{2E_0} \right)^{3/2} \frac{\Gamma(\kappa+1)(-E_0)}{(\pi\kappa)^{3/2}\Gamma\left(\kappa-\frac{3}{2}\right)} \left[\frac{E^2}{\left(1+\frac{E}{\kappa E_0}\right)^{\kappa}} \Bigg|_{eV}^{\infty} - 2 \int_{eV}^{\infty} \frac{E dE}{\left(1+\frac{E}{\kappa E_0}\right)^{\kappa}} \right. \\
& \left. -2eV \frac{E}{\left(1+\frac{E}{\kappa E_0}\right)^{\kappa}} \Bigg|_{eV}^{\infty} + 2eV \int_{eV}^{\infty} \frac{dE}{\left(1+\frac{E}{\kappa E_0}\right)^{\kappa}} + e^2V^2 \frac{1}{\left(1+\frac{E}{\kappa E_0}\right)^{\kappa}} \Bigg|_{eV}^{\infty} \right] \\
= \; & \frac{n\pi}{m} \left(\frac{m}{2E_0} \right)^{1/2} \frac{\Gamma(\kappa+1)}{(\pi\kappa)^{3/2}\Gamma\left(\kappa-\frac{3}{2}\right)} \left[\frac{e^2V^2}{\left(1+\frac{eV}{\kappa E_0}\right)^{\kappa}} + \frac{2\kappa E_0}{1-\kappa} \frac{E}{\left(1+\frac{E}{\kappa E_0}\right)^{\kappa-1}} \Bigg|_{eV}^{\infty} \right. \\
& \left. -\frac{2\kappa E_0}{1-\kappa} \int_{eV}^{\infty} \frac{dE}{\left(1+\frac{E}{\kappa E_0}\right)^{\kappa-1}} - \frac{2e^2V^2}{\left(1+\frac{eV}{\kappa E_0}\right)^{\kappa}} - \frac{2eV\kappa E_0}{1-\kappa} \frac{1}{\left(1+\frac{E}{\kappa E_0}\right)^{\kappa-1}} \Bigg|_{eV}^{\infty} + \frac{e^2V^2}{\left(1+\frac{eV}{\kappa E_0}\right)^{\kappa}} \right] \\
= \; & \frac{n}{m} \left(\frac{m}{2E_0} \right)^{1/2} \frac{\Gamma(\kappa)}{(\pi\kappa)^{1/2}\Gamma\left(\kappa-\frac{3}{2}\right)} \left[-\frac{2\kappa E_0}{1-\kappa} \frac{eV}{\left(1+\frac{eV}{\kappa E_0}\right)^{\kappa-1}} - \frac{2\kappa^2 E_0^2}{(1-\kappa)(2-\kappa)} \frac{1}{\left(1+\frac{E}{\kappa E_0}\right)^{\kappa-2}} \Bigg|_{eV}^{\infty} \right. \\
& \left. + \frac{2\kappa E_0 eV}{1-\kappa} \frac{1}{\left(1+\frac{eV}{\kappa E_0}\right)^{\kappa-1}} \right] \\
= \; & n\sqrt{\frac{\kappa E_0}{2\pi m}} \kappa E_0 \frac{\Gamma(\kappa-2)}{\Gamma\left(\kappa-\frac{1}{2}\right)} \frac{2}{\left(1+\frac{eV}{\kappa E_0}\right)^{\kappa-2}}
\end{aligned}
\tag{7.23}
$$

We can also show that these two methods are equivalent. When we evaluate the

quantities on the ionosphere in the first method, $D_E \to 0$, $C_E \to 0$, so

$$\begin{aligned}
&\int f(E)g(E')v_{\parallel}d^3v \\
&= 2\pi \int_{D_E}^{\infty} v_{\parallel}dv_{\parallel} \int_0^{\frac{\sqrt{v_{\parallel}^2 - D_E^2}}{C_E}} f(E)g(E')v_{\perp}dv_{\perp} \\
&= 2\pi \int_0^{\infty} v_{\parallel}dv_{\parallel} \int_0^{\infty} f(E)g(E')v_{\perp}dv_{\perp} \\
&= 2\pi \int_0^{\infty} v^3 f(E)g(E')dv \int_0^{\pi/2} \sin\alpha' \cos\alpha' d\alpha' \\
&= \frac{4\pi}{m^2} \int_0^{\infty} E' f(E)g(E')dE' \int_0^{1} \sin\alpha' d(\sin\alpha') \\
&= \frac{4\pi}{m^2} \int_0^{\infty} (E-\Delta) f(E)g(E')dE' \int_0^{\alpha_0} \sin\alpha d(\sin\alpha) \frac{EB_a}{B_i(E-\Delta)} \\
&= \frac{4\pi}{m^2}\frac{B_a}{B_i} \int_{\Delta}^{\infty} E f(E)g(E')dE \int_0^{\alpha_0} \sin\alpha\cos\alpha d\alpha \\
&= 2\pi\frac{B_a}{B_i} \int_{\Delta}^{\infty} g(E')j(E)dE \int_0^{\alpha_0} \sin\alpha\cos\alpha d\alpha
\end{aligned} \tag{7.24}$$

7.2 Charge Exchange

Another important lost term is the charge exchange. It has been confirmed to be one of the mechanisms accounting for the decay of the storm time ring current. Charge-exchange ionization is a gas phase reaction between an ion and an atom or molecule in which the charge of the ion is transferred to the neutral species:

$$A^+ + B \to A + B^+ \tag{7.25}$$

In charge exchange reactions, only a small amount (a few eV) of energy is transferred to the electron donor, so the newly created neutral retains most of the original energy of the ion. Since it no longer carries a charge, the energetic neutral atom (ENA) is not affected by electric and magnetic fields and travels along a straight path from the point where it was created. An imager on a spacecraft several hundreds or several

thousands of kilometers from a particular ENA source region, such as the Earth's ring current, can detect the ENA flux from that region, just as an optical telescope detects photons emitted from a distant astronomical object. The counts from the neutral atom detector can then be used to construct images of the ENA emission region. The number of ENA emitted from a given region of space depends on the energy and species of the energetic ion population in that region and on the density of the neutral gas with which the ions undergo charge exchange. In the case of the Earth's inner magnetosphere, most of the ENAs are produced through charge exchange with geocoronal neutral hydrogen, which is the primary process by which particles are lost from the ring current. The particles of the ring current have a finite lifetime before being lost to the Earth's atmosphere due to two processes: charge exchange and wave-particle interactions.

Once generated, ENAs passing through the inner magnetosphere can be reionized in several ways, in effect converting ENAs back into ring current ions but on new L shells[237]. ENA ionization constitutes a transport process acting independently of the more widely studied radial diffusion of trapped ions. Given that ENAs are unaffected by the geomagnetic field, ENA ionization offers a potentially effective process for sustaining a ring current population on inner L shells ($L \leq 3$) compared with radial diffusion.

Model developed by James Bishop estimates charge exchange rate, given the limitation that the RCM does not compute pitch angle distributions[237]. Given that (1) ion gyro periods are much shorter than bounce periods, (2) ion gyroradii are much smaller than typical scale lengths for variations in geocoronal and plasmaspheric densities, and (3) typical collisional depths along trapped ion gyropaths during a single bounce between conjugate mirror points are much smaller than unity, a bounce inte-

grated approach is both justified and convenient. He let the pitch-angle distributions relax under the action of charge exchange at given L, then fit the resulting net loss rate to find an effective overall loss lifetime.

7.3 Ion Outflows

The ionosphere is the ionized component of the Earth's upper atmosphere. Two different ionization processes are involved in its creation: photoionization, principally by solar extreme ultraviolet (EUV) and x-ray photons, and impact ionization by charged particles, including solar and galactic cosmic rays. During the daytime and at subauroral latitudes, photoionization is the dominant process, while at high latitudes and at night impact ionization by precipitating auroral electrons plays an important role in the production of ionospheric plasma.

The low-altitude ionosphere occupies approximately the same altitude range as the neutral mesosphere and thermosphere and, between 60 and 800 km, is vertically structured in three layers or regions that differ from one another in composition, density, ionization sources, degree of variability, chemistry, and dynamics: the D (60-90 km), E (90-150 km) and F (150-800 km) regions. The dominant ions in the D and E regions are NO^+ and O_2^+; in the F region, where the bulk of the ionospheric plasma resides, O^+ dominates. Above the F region is a region of exponentially decreasing density known as the "topside ionosphere". This region extends to an altitude of a few thousand kilometers and, at mid-latitudes, feeds into the plasmasphere, the region of cold, dense ionospheric plasma in the inner magnetosphere that is controlled by the Earth's co-rotating electric field.

Plasma densities in the ionosphere are characterized by strong day-night variability. The maximum ionospheric plasma density, approximately one million electrons

per cubic centimeter, occurs in the noon F region, at an altitude of 250-300 km. At night, ionospheric densities can drop by as much as two orders of magnitude, depending upon the region and altitude. The largest and most rapid decay occurs in the E and D regions, whose molecular ion constituents recombine with the ionospheric electrons much more rapidly than the F-region O^+ does. Ionospheric plasma densities also vary markedly with season, solar cycle, and level of geomagnetic activity.

The ionosphere and neutral atmosphere are strongly coupled, dynamically as well as chemically. At low and middle latitudes on the Earth's day side, for example, thermospheric neutral winds move the conducting plasma of the ionosphere across geomagnetic field lines, driving an atmospheric dynamo that generates the solar quiet current systems and the equatorial electrojet, a powerful eastward current that flows in the E region along the geomagnetic equator. In the polar regions, on the other hand, it is the ions drifting over the polar cap, in response to the imposed magnetospheric convection electric field, that "drag" the neutrals and thus generate neutral winds with speeds sometimes exceeding 3600 km per hour in the high-latitude F-region thermosphere.

The ionosphere also interacts strongly with the magnetosphere. A central aspect of this interaction is the electrodynamic coupling effected by electric currents flowing along the geomagnetic field lines that connect the ionosphere to the plasma sheet and the magnetospheric boundary layers. These "field-aligned" or "Birkeland" currents produce an electric field across the polar cap, which generates the horizontal currents in the polar ionosphere responsible for the convective ion flow referred to above. The field-aligned currents are carried both by auroral electrons precipitating downward along the field lines and by upward-flowing ionospheric electrons. The former deposits a substantial amount of energy into the upper atmosphere, with pro-

found effects on both the ionosphere and the neutral thermosphere. In addition to exciting auroral emissions, auroral electron precipitation enhances the plasma density and conductivity of the high-latitude ionosphere and supplies as much as a trillion watts of heat to the upper atmosphere, dramatically altering global thermospheric wind patterns at times of strong geomagnetic activity.

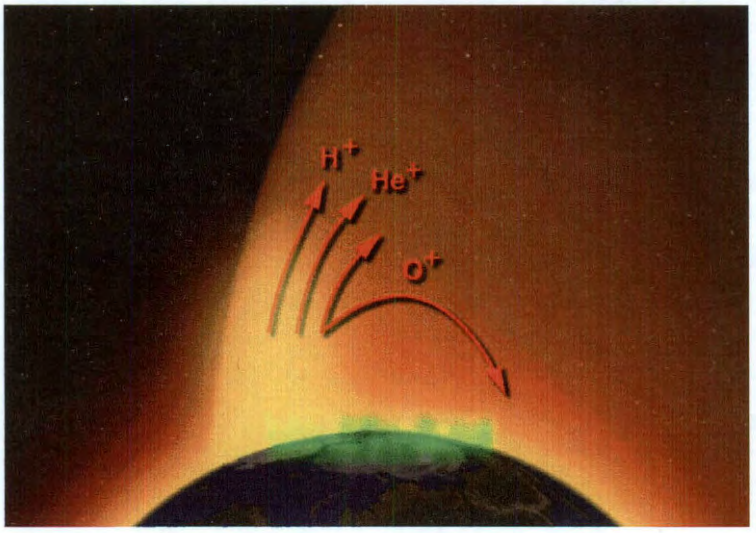

Figure 7.5 : Upflow of ions from ionosphere. Source: http://pluto.space.swri.edu/IMAGE/glossary/ionosphere3.html

Another important aspect of the ionosphere-magnetosphere interaction is the outflow of plasma from the ionosphere into the magnetosphere. It was suggested that light ionospheric ions (H^+ and He^+) might be able to escape along open magnetic field lines from the topside ionosphere into the tail regions of magnetosphere via an evaporative process[238, 239]. The sources of plasma sheet and ring current plasma are an important element in understanding the dynamics of the Earth's magnetosphere[240]. To distinguish these sources of plasma, one generally looks for O^+ as a proxy for an ionospheric source. When the composition is primarily H^+, it is assumed that the

source is the solar wind even though the ionosphere can be a major source of H^+.

The discovery of terrestrial O^+ and other heavy ions in magnetospheric hot plasmas, combined with the association of energetic ionospheric outflows with geomagnetic activity, led to the conclusion that increasing geomagnetic activity is responsible for filling the magnetosphere with ionospheric plasma[241]. It has been discovered that a major source of ionospheric heavy ion plasma outflow is responsive to the earliest impact of coronal mass ejecta upon the dayside ionosphere. Thus a large increase in ionospheric outflows begins promptly during the initial phase of geomagnetic storms, and is already present during the main phase development of such storms. The ion outflows were clearly driven by processes associated with the enhanced solar wind dynamic pressure and interplanetary magnetic field that followed the CME-driven interplanetary shock[20]. The fluctuations in solar wind dynamic pressure, rather than the enhanced dynamic pressure itself, would drive Alfvén waves from the magnetopause into the high-latitude ionosphere, heat ions in the topside ionosphere, thereby inducing outflows.

Figure 7.6 presents a flow chart showing the two principal pathways for generating ionospheric outflows[20]. The left hand side shows the flow of electromagnetic energy via Poynting flux. The right hand side shows the particle energy flow primarily through soft electron precipitation. The "causal" arrows indicate processes that are known to be causally related, while the "possibly causal" arrows indicate processes that could reasonably be causally related. The "correlated" shows processes that are correlated but do not have a direct causal relationship.

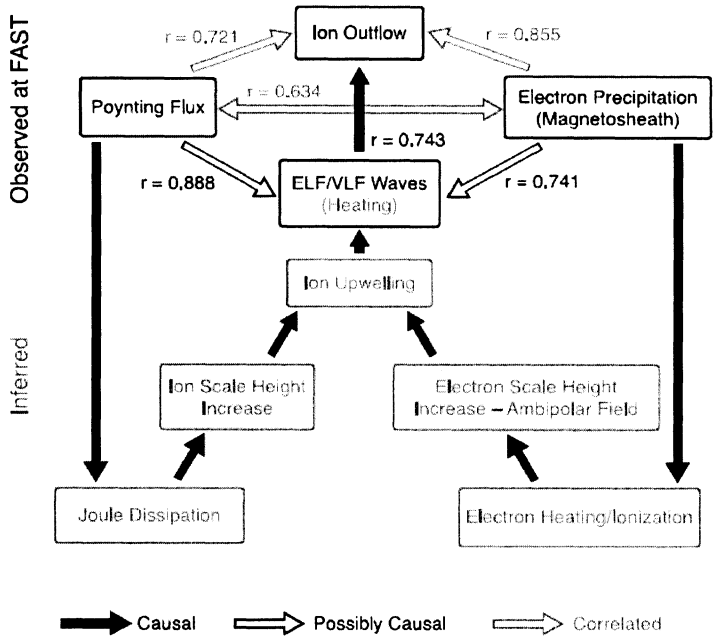

Figure 7.6 : Flow chart showing the relationship between energy inputs to the ionosphere and ion outflows. The upper half of the diagram corresponds to observations at FAST, while the lower half is the inferred pathway whereby Poynting flux or electron precipitation results in ion upwelling and subsequent outflows. The arrows connecting the various cells are labeled "causal", "possibly causal", and "correlated"[20].

This outflow is so substantial, 10^{26} ions per second[242] during magnetically disturbed periods near solar maximum, that the ionosphere could, in principle, fully populate the magnetosphere with plasma. The outflow of ions from the ionosphere takes a variety of forms: the supersonic polar wind, ion upwelling from the cleft ion fountain, polar cap outflows, and upward ion conics and beams from the auroral zone. In addition to these high-latitude sources, strong O^+ outflows from the mid-latitude ionosphere have been observed at times of intense geomagnetic activity. The strength and composition of the ionospheric plasma outflows vary with geomagnetic activity, season, solar cycle, local time, and altitude. For example, the ionospheric O^+ becomes a significant plasma pressure component in the inner plasma sheet and outer

ring current region, with a corresponding increase in the O^+ density of the plasma sheet, particularly when the solar wind is intense or its magnetic field is southward directed. The two primary sources of ionospheric outflow into the plasma sheet are the polar cusp and near midnight oval[240].

It has been recognized that the presence of suprathermal electrons, such as photoelectrons produced in the upper atmosphere during the ionization of neutral species by solar EUV radiation, can enhance the ambipolar electric fields that propel polar wind outflows[243]. Additional electric force due to the escaping photoelectrons could accelerate the ions to higher velocities if the photoelectron flux is larger than the escape flux of the thermal electrons in the polar wind[244]. Akebono observations have shown that the polar wind velocity was generally higher on the dayside than on the nightside and was strongly correlated with the ambient electron temperature[245]. Ionospheric photoelectrons are the source of both the upward suprathermal field-aligned electron fluxes obtained at high altitudes and the downward fluxes obtained at low altitudes as reflected by an upward electric field[246].

Ion upflow from the cusp region occurs outside the RCM modeling region, and its effects are included in the boundary condition. Faster drifting ion upflow which is accelerated by larger electric field on the relatively steep gradient of the plasma pressure can reach higher altitudes and constitute a significant component of the ion outflow. Only the outflow in the mid-latitude region should be considered as source term to the transport equation. No field-aligned current is considered due to these outflowing ionospheric ions. Strong correlations have been found between outflow fluxes and local electromagnetic energy flux, and also with the local precipitating electron density[222].

7.3.1 Proton Outflow

The plasmasphere is the end state of polar wind outflows on flux tubes that remain closed between the two hemispheres rather than circulating through the reconnection regions at high latitudes. Magnetospheric disturbances create sunward plasmaspheric plumes on flux tubes that are depleted as they reconnect with the solar wind field. When reconnected with their conjugate counterparts, they circulate into the inner, approximately co-rotating, magnetosphere, fill up and approach hydrostatic equilibrium [247]. The plasmasphere is properly thought of as a light ion extension of the ionosphere. The dynamics in the plasmasphere proper is usually ignored due to their low energies. The plasma in plasmasphere will be more readily tracked in fluid global circulation models that include ionospheric fluids, because of the low velocities of the protons involved. However, the plasmasphere contains little O^+, so it cannot contribute significantly to the pressure dominance O^+ observed during severe storms.

Outside the plasmasphere proper, polar wind light ion plasma flows continuously out of the ionosphere onto the circulating flux tubes that circulate throughout the auroral and polar magnetosphere, driven by high latitude reconnection at the magnetopause.

Polar wind protons were introduced at 1000 km altitude with initial conditions guided by observations from the Polar/TIDE survey[248] at all geomagnetic latitudes greater than 55^o ($L \sim 3$). The outflow flux depends on the solar zenith angle so that the variation of flux results from solar illumination of the ionosphere with substantially lower fluxes originating from darker regions[248]. If the solar zenith angle is below 90^o, then the flux at 1000 km altitude is

$$F = 2 \times 10^8 cm^{-2} s^{-1} \tag{7.26}$$

When the solar zenith angle is between 90^o and 110^o, then the flux is

$$F = 2 \times 10^{8-2.5\frac{SZA-90}{20}} \tag{7.27}$$

And if the solar zenith angle is between 110^o and 180^o, then the flux is

$$F = 2 \times 10^{5.5} \tag{7.28}$$

The flux is smooth both around 90° and 110°.

7.3.2 Oxygen Outflow

The amount of heavy ion outflow from the ionosphere through the magnetosphere is strongly dependent on the intensity and coupling strength of the solar wind. The growth of ring current in the terrestrial magnetosphere is produced through the expansion of heavy ion plasmas that originate in the Earth's ionosphere[241].

Like the polar wind protons, auroral wind oxygen ions were introduced at 1000 km altitude at all latitudes above 55^o. However, the oxygen initial conditions were locally specified in response to the boundary conditions imposed on the ionosphere, including the Poynting flux of electromagnetic energy into the ionosphere, the density of high altitude plasma precipitating into the ionosphere, as well as the current density being driven through the ionosphere by the magnetospheric circulation dynamics. The lowest energy oxygen ions were promptly returned to the atmosphere by gravity. A limiting local flux was imposed to avoid getting too much flux compared with the statistical database[249]. Since the precipitating electron density is closely related to diffuse auroral luminosity,a loss cone filling factor with a local time dependence from Chen and Schulz (2001) was used[235].

The outflow flux due to precipitation is

$$NV_{preci} = 2.8 \times 10^9 \times N^{2.2} cm^{-2} s^{-1} \tag{7.29}$$

where N is the number density in cm^{-3} and reduce by a loss cone filling factor with

$$FLC = 0.4\left[1 + 0.8\sin\left(2\pi\frac{MLT-3}{24}\right)\right] \tag{7.30}$$

The outflow flux due to the Poynting flux is

$$NV_{poynt} = 5.6 \times 10^7 \times (0.245 \times S_{120})^{1.26}(cm^{-2}s^{-1}) \tag{7.31}$$

where S_{120} is the Poynting flux in mWm^{-2} at 120 km altitude, the 0.245 factor maps if from 120 to 4000 km altitude. The total flux would be

$$NV = \sqrt{NV_{preci} \times NV_{poynt}} \tag{7.32}$$

with a local flux limit of $3 \times 10^9(cm^{-2}s^{-1})$.

The average auroral wind temperature is give by

$$T_{O^+} = 0.1 + 9.2 \times (0.24 \times S_{120})^{0.35}(eV) \tag{7.33}$$

The distribution is assumed to be Maxwellian before the acceleration by any parallel potential drop.

7.4 Implementation

The essential goal of the RCM is to provide particle distribution and electric field to either ionosphere and thermosphere modelers or global MHD modelers. The continuity equation is thus the major equation in the model. To complete the equation, we need to estimate the source and lost terms in the right hand side of the equation. The main processes involving the plasma content change in the coupled system of magnetosphere and ionosphere are particle precipitation, charge exchange, and ionospheric outflows.

The observation shows that the electron precipitation is less then strong pitch angle diffusion. We then have different ways to estimate the electron precipitation. A simple and straightforward way is to assume only a fraction of electrons would penetrate into the atmosphere. Some statistical ways, such as expressions from Chen and Schulz[235, 236] could be used as well. A self-consistent way is to estimate from loss cone effect as shown in the Appendix A. Electrons in the magnetosphere could penetrate into the atmosphere only when the magnetic field strength ratio at ionosphere foot point and plasma sheet satisfies certain requirements. The particle precipitation also appears in the ionospheric conductances calculation. For this purpose, the number flux and energy flux of the precipitating electrons could be calculated by integrating plasma moments properly. The parallel electric field would accelerate electrons into the atmosphere and thus increase both number flux and energy flux. On the other hand, the parallel electric field would decelerate ions along the field lines and prevent ions from penetrating into the atmosphere.

The charge exchange rate is a function of particle energy and location. Plasma with different energy and different would have different charge exchange rate as well as ionospheric outflow rate, which convert to particle loss rate before giving into CLAWPACK for plasma convection.

We don't show particular simulation results for these modules because those are corrections to the plasma convection pattern we are interested in. However, they might have huge impact for real time event simulations.

Chapter 8

Auroral Conductances in an Isolated Substorm

The ionospheric conductances relate the ionospheric convection electric field and ionospheric currents, which, together with the knowledge of field-aligned currents, are needed for computing the ionospheric electric potential self-consistently. Some basic knowledge of ionospheric conductances has been discussed in chapter 3. Estimates of the contribution from energetic particle precipitation can be obtained by using the precipitating energy flux and the average energy of these particles. We have several different ways to handle real time ionospheric conductances. Parallel electric fields are an important factor. However, we wait until the next chapter to add an even more uncertain element in the calculation, the effect of field-aligned potential drops. In this chapter, we will introduce two parameters that adjust calculated energy fluxes without the parallel electric field. An isolated substorm event is simulated by adding substorm current wedge in the magnetic field models and generating nonuniform high-latitude boundary condition to represent a localized bubble with reduced entropy. We present and discuss four simulations in an attempt to understand how auroral conductances and the uncertainties in calculating them affect substorm dynamics.

8.1 July 22, 1998 substorm event

The magnetospheric substorm is an important and not yet fully understood phenomenon in Earth's magnetosphere. To understand the magnetosphere-ionosphere

interactions is, together with the cause or trigger of the expansion phase, one of the remaining challenging questions in the study of substorms[250]. The substorms are triggered by the nightside magnetospheric reconfiguration. One of the main features of substorm is the rapid earthward transport (injection) of particles from the plasma sheet to the inner magnetosphere[251, 252]. Magnetic reconnection or current sheet disruption in the magnetotail are believed to be responsible for magnetic field reconfiguration and producing plasma bubbles, which consist of flux tubes that have lower entropy parameter $pV^{5/3}$ than their surrounding background plasma[253]. As the bubble moves into the inner magnetosphere, another set of Birkeland currents forms along its eastward and westward edges while strong westward electric field and earthward flow form inside of it. Current closure implies a westward electrojet in the ionosphere, usually indicated by an increase in the AE index. The bubble would drift westward due to gradient/curvature drift when it is closer to the Earth. The objective of simulation of bubble injection is to understand how the bubble evolves as it moves toward the inner magnetosphere and its effects on ionospheric and magnetospheric electric fields[254].

An inner magnetosphere physics model has to be able to simulate the injection of a bubble from magnetotail to the geosynchronous orbit. However, since the formation of plasma bubble is still under debate and might vary from case to case, we will present a simulation of the injection of a bubble into the inner magnetosphere without addressing the physics of bubble formation. A simple way to do this is to assume that the bubble is created tailward of our modeling region, so that the bubble is introduced into the RCM through the tailward boundary condition[253]. Then the process of bubble injection could be modeled by the plasma drift model. Previous results indicated that plasma-sheet flux tubes must experience entropy reduction in

order to be injected into the inner magnetosphere.

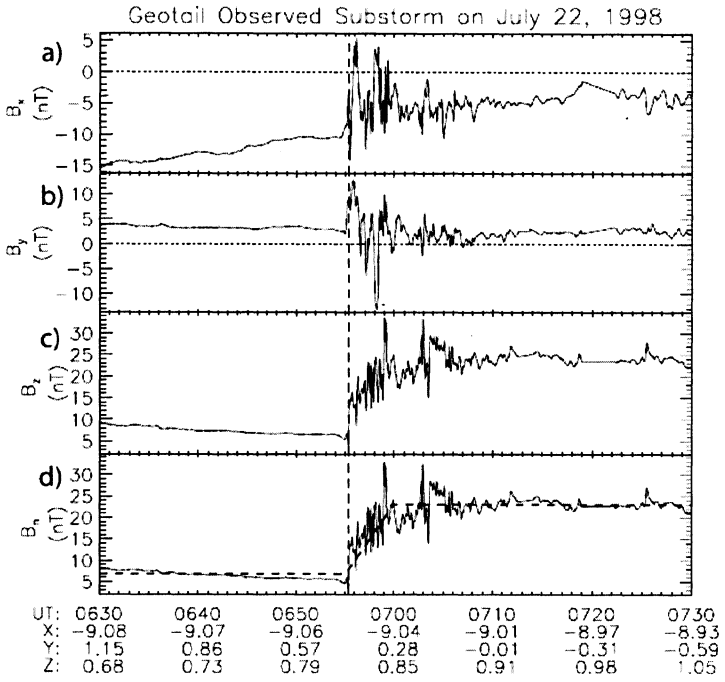

Figure 8.1 : Geotail magnetic field (a) x component (Bx), (b) y component (By), (c) z component (Bz), and (d) component normal to the current sheet (Bn) from 0630 to 0730 UT of July 22, 1998. In (d), the solid and dashed lines show, respectively, the 3-s data and the idealized form that we assumed in constructing our model. From [21].

In this chapter and the next chapter, we will discuss the simulation results of July 22, 1998 substorm event. During this substorm event, both the Geotail and GOES-10 spacecraft were positioned as to observe the substorm[255]. That is one reason why this event is widely studied[21, 254, 255]. In this chapter, we extend the results of [21, 254] by expanding, through simulations, on the effect of ionospheric conductances on the bubble injection. We follow closely the setup of simulations that earlier study, by using their inputs and setup, as well as the RCM code, with the following exceptions. First, the total conductance tensor is now calculated by taking

the root of the summation of the square of contributions from the solar EUV and precipitation, instead of adding up. Second, our electron precipitation model has been changed from assuming a Maxwellian distribution of precipitating particles to a kappa distribution, as mentioned in the previous chapter. Third, the present work also corrects an error of setting energy levels in the earlier papers[21, 254], the effect of which will be assessed in a separate study.

Following the work of [21, 254], Figure 8.1 shows the GSM magnetic field components Bx, By, and Bz measured by Geotail spacecraft near the center of the current sheet at approximately local midnight. The standard RCM does not accommodate dipole tilt. Therefore, we have to find an approximate way of mapping a tilted dipole magnetosphere onto an untilted magnetosphere. The critical method is to use the component normal to the realistic current sheet as the z component of the magnetic field instead of using the GSM B_Z component. To estimate the direction of the current sheet normal, we first convert to GSW (Geocentric Solar Wind) coordinates, then use the formulae of Tsyganenko and Fairfield [2004] to estimate the shape of the current sheet, for calculation of the normal. As observed increase of GSM B_Z from 5 nT to 25 nT, the magnetic field obviously dipolarizes between about 0655 and 0700 UT. During the substorm growth phase, Bn decreases from 8.3 nT at 0630 UT to 4.8 nT at 0655 UT. The dipolarization then increases Bn to an average of about 22.9 nT. The feature is also then evidenced by the substantial increase in Bn from 7 nT to 23 nT and the modest decrease in the magnitude of B_X component. The time 0655 UT is set as the substorm expansion phase onset.

8.2 Model Inputs

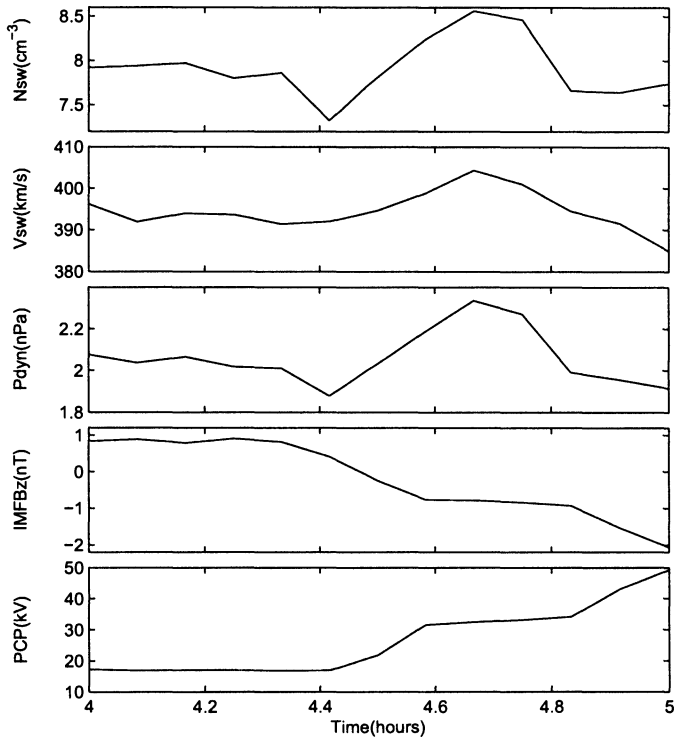

Figure 8.2 : Selected RCM input parameters of solar wind density, solar wind velocity, solar wind dynamic pressure, IMF normal component, polar cap potential drop, respectively from top to bottom.

Figure 8.2 shows selected RCM input parameters of solar wind density, solar wind velocity, solar wind dynamic pressure, IMF normal component, polar cap potential drop, respectively from top to bottom. The RCM was initialized by running the model with steady inputs for more than 4 hours prior to 0655 UT. The starting time of the simulation is 0230 UT. So the simulation time of 4 hour corresponds to 0630 UT. The figure shows the quantities from 4 hour to 5 hour as substorm growth phase and expansion phase. The expansion phase starts at 0655 UT, which is about 4.42 hour,

when the solar wind density and velocity increases and IMF B_Z turns southward. The polar cap potential drop is fairly low because the IMF B_Z is northward or weakly southward.

For completeness, here we describe how the inputs, particularly magnetic field, are specified for the RCM. We repeat in this section the procedure designed and first described by [21].For substorms, the RCM could used magnetic field models that are consistent with measurements from Geotail[21] or THEMIS[256] spacecraft, to trace the magnetic field lines from the ionosphere to the magnetosphere. The use of Tsyganenko statistical magnetic field models[100, 103, 107] can not reproduce a magnetic field component normal to the current sheet less than 10 nT at Geotail location with $x = -9R_E$ and $y = 0$ for observed solar wind and geomagnetic conditions. In order to simulate the substorm event of July 22, 1998, the magnetospheric magnetic field needs to match Geotail magnetic field observations. We use the same magnetic field, a force-balance argument in conjunction with in situ measurements of magnetic field and particle pressure, as described in Zhang[2009][21]. The 2-D flat space version of the Grad-Shafranov equation[257] is adapted to modify the T89 magnetic field model to represent the highly stretched magnetic field configuration in the growth phase of a substorm.

The low northward magnetic field in the current sheet is achieved by thinning and intensifying the existing current sheet in the critical region and also adding a new current sheet[258, 259, 260, 261]. However, this method leads to significant violations of the force-balance condition. To obtain a force-balanced magnetic field model, a new magnetic field is defined as the summation of T89 magnetic field and a correction term

$$\Delta\mathbf{B} = \nabla \times [h(\mathbf{A}_O - \mathbf{A}_T + \Delta\mathbf{A})] \tag{8.1}$$

where $h = 1$ near Geotail location and $h = 0$ far from the spacecraft location to localize this correction; $\mathbf{A}_0$ is the vector potential of a force-balanced analytic model of the magnetic field and particle pressure comparable to the magnetic field and particle pressure observed by Geotail, $\mathbf{A}_T$ is an analytic model that is consistent with the uncorrected T89 model near the spacecraft, and $\Delta\mathbf{A}$ is a constant vector potential. We consider magnetic field models with a vector potential is of the form $A(x,z)\hat{\mathbf{e}}_y$. Then the magnetic field is

$$\mathbf{B} = \mathbf{B}_T + \nabla \times \{\hat{\mathbf{e}}_y h(x,y,z)[A_0(x,z) - A_T(x,z) + \Delta A]\} \tag{8.2}$$

The analytic functions employed in $\mathbf{A}_0$ and $\mathbf{A}_T$ are solutions to the linear Grad-Shafranov equation ($\nabla^2 A = -\mu_0 dp/dA$). Since the 2-D Grad-Shafranov force-balance equation has the form

$$p = \frac{k^2 A^2}{2\mu_0} \tag{8.3}$$

$$(\nabla^2 + k^2)A = 0 \tag{8.4}$$

$$k^2 = \left\{ \begin{array}{cc} \left(\frac{\pi}{2\Delta}\right)^2 - \alpha^2 & for \quad |z| < \Delta \\ 0 & for \quad |z| \geq \Delta \end{array} \right\} \tag{8.5}$$

where the vector potentials for $|z| > \Delta$ represent pressure-free conditions with $\nabla^2 A = 0$. The two vector potentials look like

$$A_T(x,z) = b_T e^{\alpha_T x} \left\{ \begin{array}{cc} \cos\frac{\pi z}{2\Delta_T} & for \quad |z| < \Delta_T \\ \frac{\pi}{2\alpha_T \Delta_T}\sin[\alpha_T(\Delta_T - |z|)] & for \quad |z| \geq \Delta_T \end{array} \right\} \tag{8.6}$$

$$A_0(x,z) = b_0 e^{\alpha_0 x} \left\{ \begin{array}{cc} \cos\frac{\pi z}{2\Delta_0} & for \quad |z| < \Delta_0 \\ \frac{\pi}{2\alpha_0 \Delta_0}\sin[\alpha_0(\Delta_0 - |z|)] & for \quad |z| \geq \Delta_0 \end{array} \right\} \tag{8.7}$$

Then the parameters are defined from Geotail measurements of magnetic field and plasma pressure.

The function $h(x, y, z)$ is arbitrary. Since the critical adjustment is on the midnight along the x axis, we choose the form

$$h(x, y, z) = f(x)g(y, z) \tag{8.8}$$

with

$$g(y, z) = e^{-\frac{z^2}{\Delta_2^2} - \frac{y^2}{\Delta_3^2}} \tag{8.9}$$

to let the correction dies off far from the spacecraft. The x dependence is in the form of

$$f(x) = \begin{cases} e^{-k_2(x-x_x)^2} & x \geq x_2 \\ 1 & x_1 < x < x_2 \\ e^{-k_1(x-x_1)^2} & x \leq x_1 \end{cases} \tag{8.10}$$

where x_1 is the Geotail location. So tailward of the spacecraft, the B_z component is dominated by T89 model and drops off quickly. The values of k_2 and x_2 are chosen to make sure that the correction disappears on the dayside and B_z is approximately correct at geosynchronous orbit. The observations suggest that the Tsyganenko B_z value should be substantially reduced near Geotail but increased slightly at geosynchronous orbit[21].

To represent dipolarization of the magnetic field during the expansion phase, a substorm current wedge (SCW) is added to the growth-phase model[122]. The magnetic field of the SCW is represented by the vector potential due to a combination of two wire loops[12]. The code uses the following five adjustable parameters to describe the two fuzzy wire loops: total electric current amplitude coefficient A, initial wire radius R_0, stretch amplitude AL, stretch-scale ratio β, and wire inclination angle with respect to the equatorial plane γ ($< \pi/2$). In the growth phase, $A = 0$ and thus the SCW field is zero. Beginning at the end of the growth phase (0655 UT), A begins a linear increase from 0 to 220 in 5 min to represent rapid near-Earth field

dipolarization. After 0700 UT, A is held constant at 220. Note that $A = 100$ yields about $+10nT$ field disturbance inside the SCW[21]. Other parameters are held constant through the event: $R_0 = 6.0R_E$, $AL = 0.5$, $\beta = 0.5$, and $\gamma = 1.0rad$. These parameters were chosen to best fit the observed data from Geotail, GOES-8, and GOES-9.

Within the RCM modeling region, the modified T89 model with the addition of SCW, is able to reproduce both the highly stretched precollapse magnetic field configuration and the subsequent postcollapse dipolarized configuration. As shown in Figure 8.3, at 0655 UT, the field is highly stretched in the tail region. After the expansion phase onset, the field inside the current wedge becomes dipolarized, while outside the wedge, the field remains stretched and tail-like across the night side. To simulate a "bubble" in the RCM code, we reduce $pV^{5/3}$ by decreasing the number of particles per unit magnetic flux and enhance the tangential electric field on the tailward boundary near midnight[28]. The electric field potential distribution along the poleward boundary is given by

$$\Phi_{pb}(\phi, t) = \Phi_{drop}(t)\frac{F(\phi)}{\Delta F} \tag{8.11}$$

where

$$F(\phi) = -\frac{1}{2}\sin\phi + \xi\left(\frac{1}{2K(\phi_e - \phi_w)} ln\left\{\frac{cosh[K(\phi - \phi_w)]}{cosh[K(\phi - \phi_e)]}\right\} - \frac{\phi}{2\pi} + \frac{1}{2}\right) \tag{8.12}$$

in which the first term represents a standard dawn-dusk potential drop and the second term represents the effects of the plasma bubble on the boundary potential during the expansion phase, $\Phi_{drop}(t)$ is the total cross polar cap potential across the RCM boundary at time t, ϕ is the RCM local time angle counting from noon, ΔF is the difference between the maximum and minimum values of $F(\phi)$. The constants $\xi = 1$, $K = 10$, $\phi_e = 7\pi/6$, $\phi_w = 5\pi/6$.

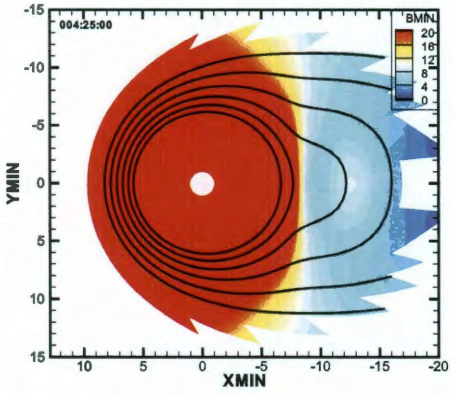
004:25:00
BMIN
20
16
12
8
4
0
YMIN
XMIN

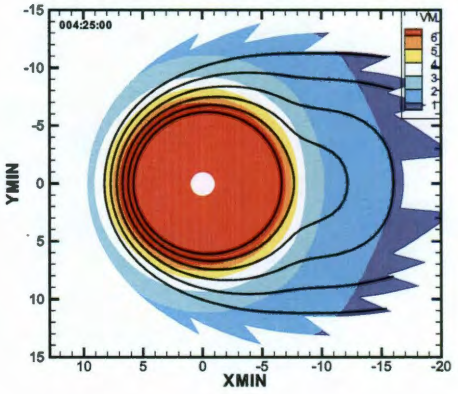
004:25:00
VM
YMIN
XMIN

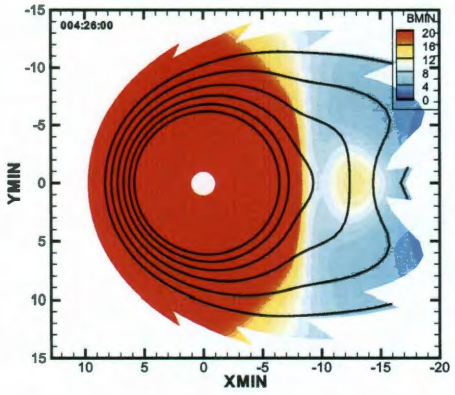
004:26:00
BMIN
20
16
12
8
4
0
YMIN
XMIN

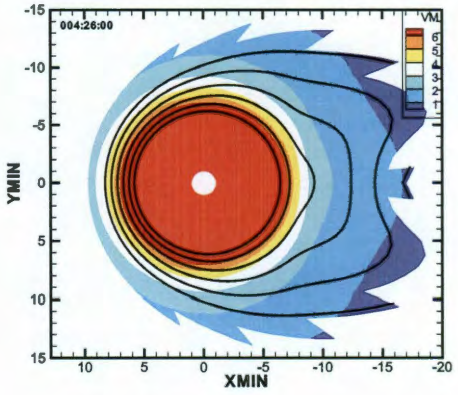
004:26:00
VM
YMIN
XMIN

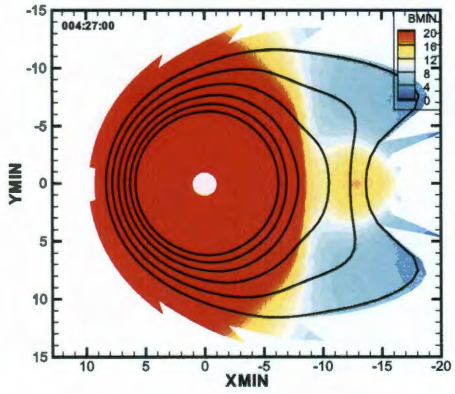
004:27:00
BMIN
20
16
12
8
4
0
YMIN
XMIN

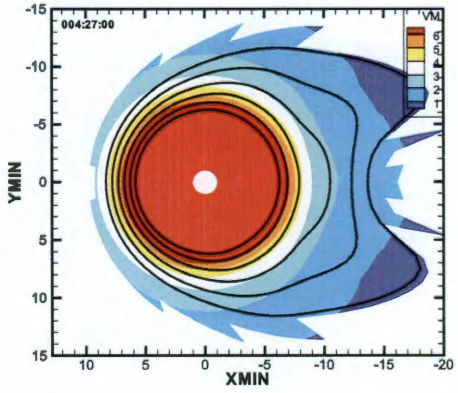
004:27:00
VM
YMIN
XMIN

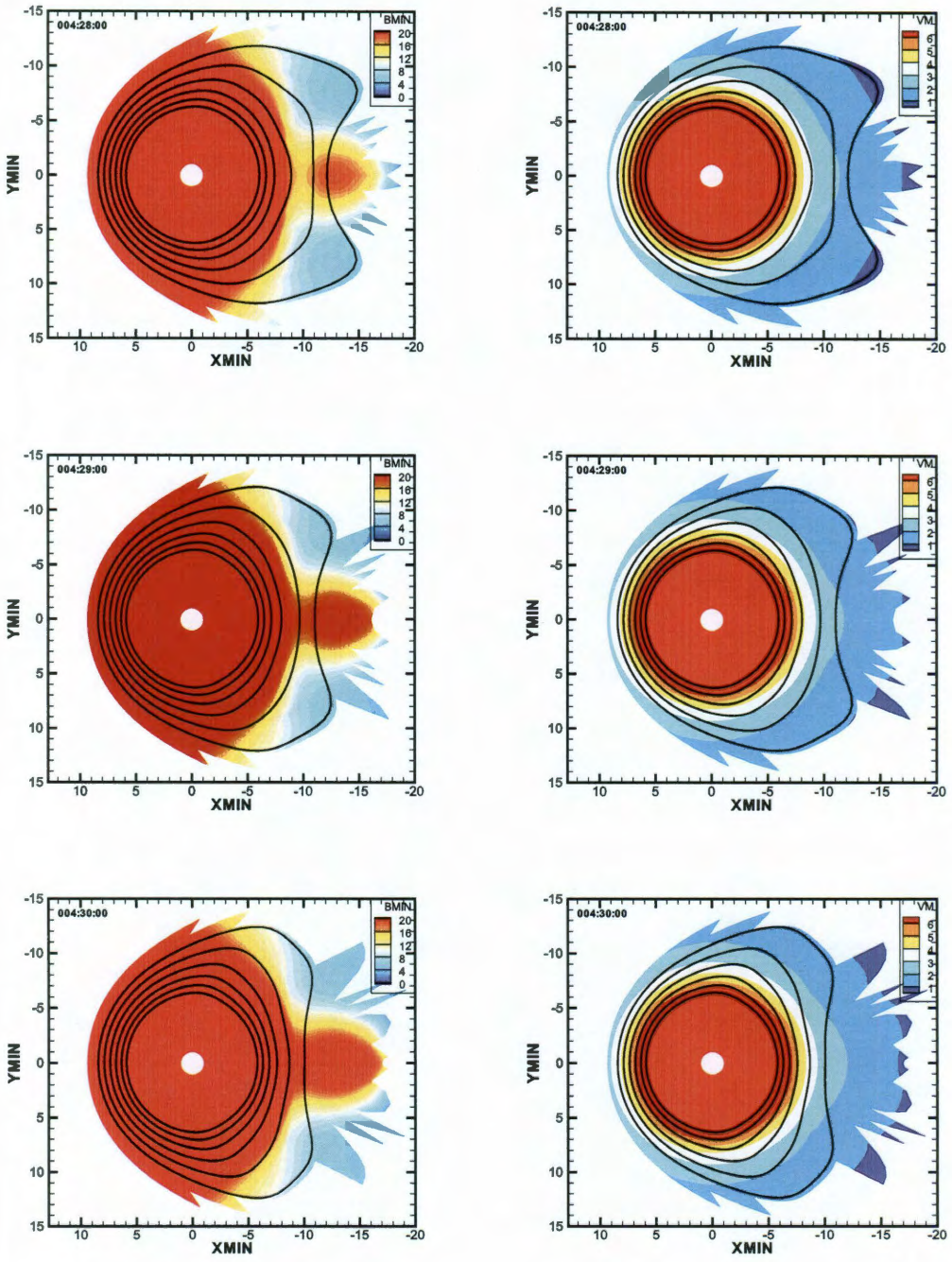

Figure 8.3 : Contours of constant magnetic field strength in the equatorial plane from 0655 UT to 0700 UT as in the substorm expansion phase, indicating changes in the magnetic field configuration. Blacks correspond to 65°, 66°, 67°, 68°, 69°, 70° latitudes.

A realistic quiet-time ring current is used[134] with an initial distribution function with $\kappa = 6$. The specified density, temperature, and pressure are approximately consistent with in situ observations from the Los Alamos Magnetospheric Plasma Analyzers (MPA). The plasma distribution at high-latitude boundary condition is conserved before 0630 UT and determined by comparing Geotail observations by 0630 UT. By giving the flux tube volume from the magnetic field model, the entropy, $pV^{5/3}$, keeps a value of $0.09nPa(R_E/nT)^{5/3}$ from 0630 UT to 0655 UT. During the expansion phase, the entropy is held at the same value outside the bubble. Inside the bubble, $pV^{5/3}$ decreases smoothly from the edge of the bubble to the midnight. The entropy near the Geotail location should be consistent with the observation. The entropy inside the bubble is a superposition of the satellite observation and the steady adiabatic convection value from the following equation[37]

$$\eta(\lambda, \phi) = F(\phi)\eta_o(\lambda) + (1 - F(\phi))\eta_c(\lambda, \phi) \tag{8.13}$$

where

$$F(\phi) = \frac{1}{2}\{tanh\left[K\left(\phi - \phi_w\right)\right] - tanh\left[K\left(\phi - \phi_e\right)\right]\} \tag{8.14}$$

The function η_o is set to have a constant η, $pV^{5/3}$, or $TV^{2/3}$ on the boundary. The values are determined to have proton density, temperature, and pressure to be consistent with Geotail observations approaching 0730 UT.

8.3 Simulation Results

The major feature of this substorm study is particle injection. This could be seen clearly in a set of figures of plasma entropy parameter in Figure 8.4.

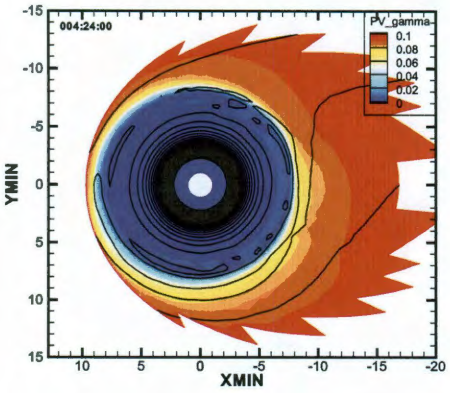
004:24:00
PV_gamma
0.1
0.08
0.06
0.04
0.02
0
YMIN
XMIN

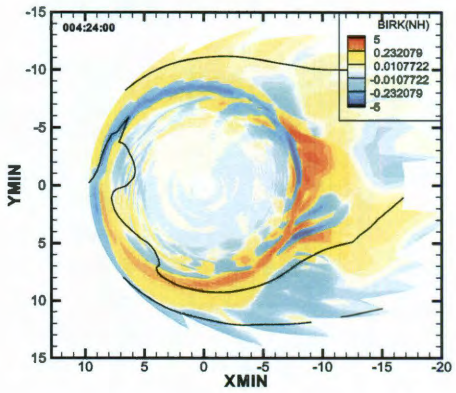
004:24:00
BIRK(NH)
5
0.232079
0.0107722
-0.0107722
-0.232079
-5
YMIN
XMIN

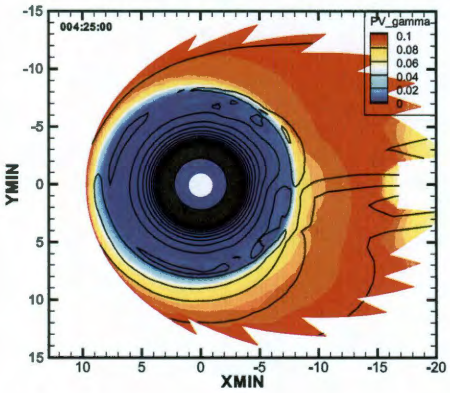
004:25:00
PV_gamma
0.1
0.08
0.06
0.04
0.02
0
YMIN
XMIN

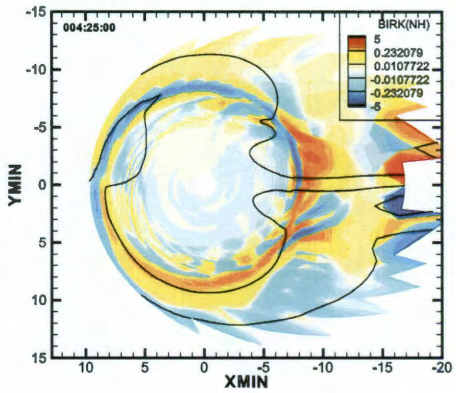
004:25:00
BIRK(NH)
5
0.232079
0.0107722
-0.0107722
-0.232079
-5
YMIN
XMIN

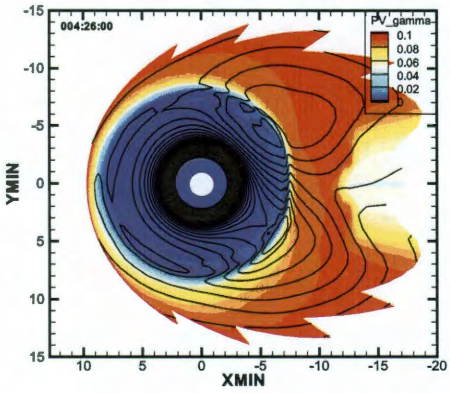
004:26:00
PV_gamma
0.1
0.08
0.06
0.04
0.02
0
YMIN
XMIN

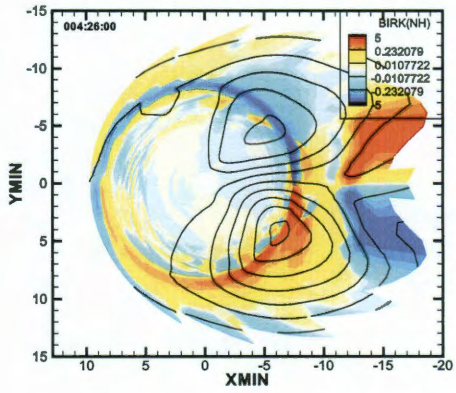
004:26:00
BIRK(NH)
5
0.232079
0.0107722
-0.0107722
-0.232079
-5
YMIN
XMIN

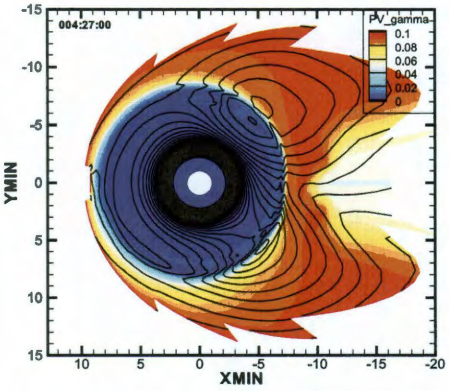
004:27:00
PV_gamma
0.1
0.08
0.06
0.04
0.02
0
YMIN
XMIN

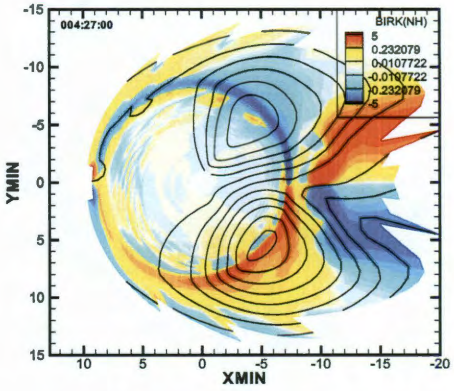
004:27:00
BIRK(NH)
5
0.232079
0.0107722
-0.0107722
-0.232079
-5
YMIN
XMIN

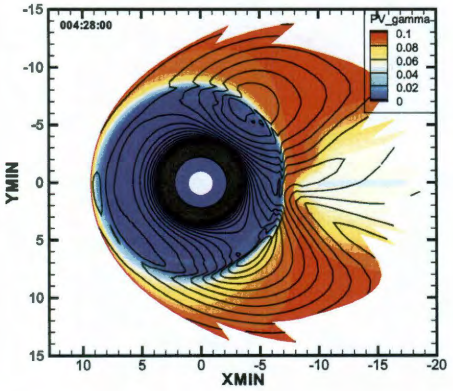
004:28:00
PV_gamma
0.1
0.08
0.06
0.04
0.02
0
YMIN
XMIN

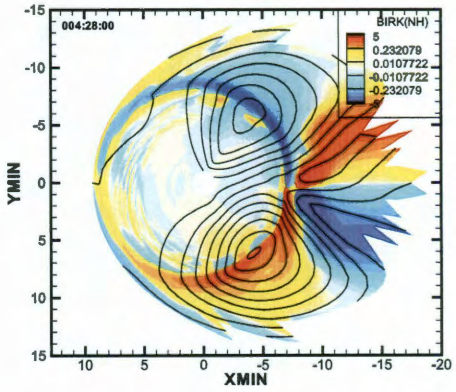
004:28:00
BIRK(NH)
5
0.232079
0.0107722
-0.0107722
-0.232079
YMIN
XMIN

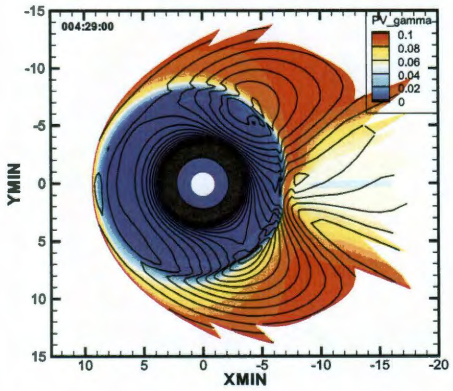
004:29:00
PV_gamma
0.1
0.08
0.06
0.04
0.02
0
YMIN
XMIN

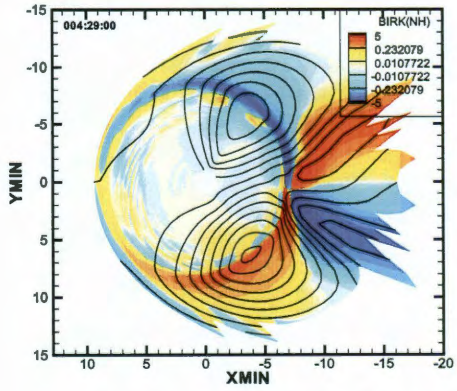
004:29:00
BIRK(NH)
5
0.232079
0.0107722
-0.0107722
-0.232079
-5
YMIN
XMIN

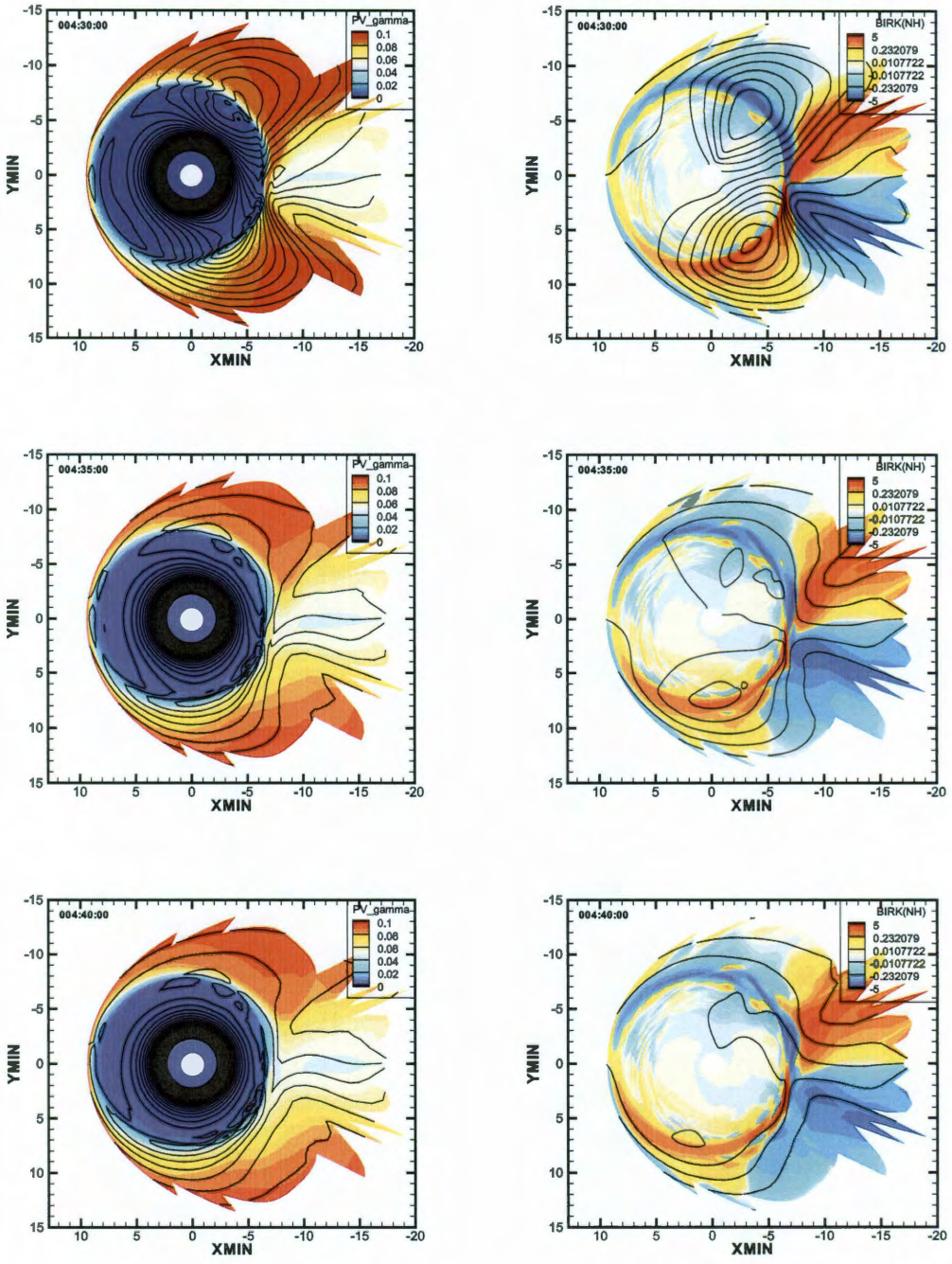

Figure 8.4 : Entropy and Birkeland currents in the simulation of July 22, 1998 substorm event at 12 times from 1 minute before the expansion onset to 10 minutes after the bubble was imposed.

The figures on the left are entropy $pV^{5/3}$ ranging from 0 to $0.1nPa(R_E/nT)^{5/3}$. The figures on the right are Birkeland current ranging from $-5\mu A/m^2$ to $5\mu A/m^2$. The black lines on the right figures are electrostatic equipotentials, while the black lines on the left figures are the average proton effective potential, given by

$$\langle \Phi_{eff} \rangle = \Phi_{ion} + \Phi_{cor} + \frac{\langle \lambda_i \rangle V^{-2/3}}{e} \tag{8.15}$$

where the term Φ_{ion} is the potential in the rest frame of the ionosphere, which rotates with the Earth, adding Φ_{cor} gives potential in the frame that does not rotate with the Earth, the last term comes from the kinetic energy of the ion. The spacing of the equipotentials are 5 kV. In the absence of an induction electric field, contours of constant $\langle \Phi_{eff} \rangle$ would represent instantaneous drift paths of particles of invariant energy $\langle \lambda_i \rangle = 3T_i V^{2/3}/2$.

As shown in this figure, a low entropy bubble is imposed at midnight on the tailward boundary at 0655 UT. The bubble drifts earthward and evolves into a depleted channel with lower entropy than postdusk and predawn regions. The shape of the channel is strongly affected by the energy dependent gradient/curvature drift as it drifts closer to the Earth. After reaching geosynchronous orbit in about 5 minutes, the channel turns to the west and spreads out in local time[254]. Birkeland currents beyond 8 RE form the substorm current wedge, with downward currents on the east side of the wedge and upward currents on the west side of the wedge. The strong westward convection (potential) electric field forms across the channel. Although not shown, the induction component of the electric field is also significant and westward across the channel. These results were obtained with the conductance model used in [254].

8.4 The Two Parameters

The RCM calculated the ionospheric conductances from solar radiation and particle precipitations. However, in the past, the RCM did not cover particle precipitations in region-1 field-aligned currents. The RCM should be able to place the electric field and precipitation boundaries in their correct physical spatial relationship to each other[23] without artificial blurring since the RCM computes the plasma sheet location, the precipitation pattern, and the electric field pattern self-consistently[23]. As shown in Figure 8.5, for the region poleward of the main RCM modeling region, the precipitation in the high-latitude part of the auroral zone could be associated with the electric field reversal region of the electric field model. We associate the equatorward edge of the region-1 currents with the equatorward edge of the electric field reversal region and the poleward boundary of the RCM modeling region[23]. The estimated fraction of the auroral energy flux precipitated poleward of the RCM modeling region is given by

$$f(\phi) = 0.5 + 0.3 \sin \phi \tag{8.16}$$

where ϕ is the local time angle starting at noon. The fraction f is thus assumed to range from a maximum of 0.8 at local dusk, where the inverted-V region and its associated strong electron precipitation lies in the region of intense upward Birkeland current poleward of modeling region, to a minimum of 0.2 at local dawn, where region-1 current is downward and associated precipitation is relatively weak. On the other hand, we could perform a Hardy normalization. The total energy flux is calculated from Hardy statistical conductance model. A fraction

$$f'(\phi) = 0.5 - 0.3 \sin \phi \tag{8.17}$$

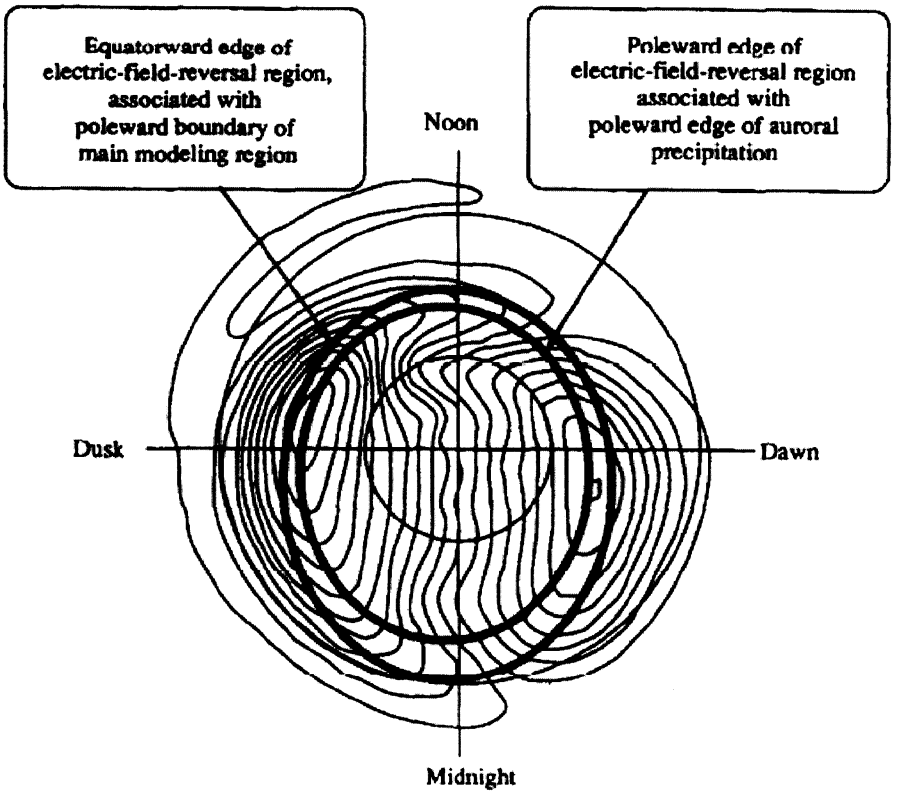

Figure 8.5 : Heppner and Maynard[22] empirical potential pattern with two ellipses bound the electric field reversal region. Figure from [23]. The two concentric circles represent 65° and 80° invariant latitude. The equatorward ellipse is scaled to coincide with the RCM calculation boundary.

of the total energy flux falls into the RCM modeling region. The distribution of these energy flux inside the RCM modeling region is proportional to the initial calculation of precipitation flux.

We obtained very low values for the region of the ionosphere that maps out to 20 or 30 R_E. The computed values of the precipitation rates could be three orders of magnitude below what is typicall measured in the region near the poleward boundary of the RCM. To avoid getting small conductances, a "floor" is placed under the precipitating energy flux. For each local time direction with grid index j, let $\Phi_{max}(j)$

be the peak energy flux value that probably occurs near the low-latitude edge of the diffuse aurora, we do not allow the energy flux poleward of that peak, but within the main RCM modeling region, to drop below $0.5\Phi_{max}(j)$. This floor has a practical reason to encourage the regions of sunward flow to be wider in latitude with a realistic factor. Both Pedersen conductances and Hall conductances are proportional to the square root of the energy flux. A factor of 2 change in energy flux between the peak of the diffuse auroral and the poleward boundary corresponds to only about a 30% change in conductance[23].

Therefore, we have two ways to adjust the energy flux including setting floor and Hardy normalization. We could choose to have either of them in the RCM setup file "rcm.params" with a logical switch. To illustrate the effect of these two parameters, we are showing the results of the substorm event with the four combinations from these two parameters.

8.5 Comparison of Entropy

First, we look at the comparison of bubble injection by presenting plots of plasma entropy in figures 8.6 to 8.8. The colors are entropy ranging from 0 to 0.1 $nPa(R_E/nT)^{5/3}$. The figures are showing the time right after the expansion onset, 2 minutes and 5 minutes after the expansion onset. The figure in the top left corner is the run with both floor and Hardy normalization. The figure in the top right corner is the run with floor but without Hardy normalization. The figure in the bottom left corner is the run with only the Hardy normalization. The figure in the bottom right corner is the run without any corrections. The black lines are equipotential contours with 5 kV spacing.

At the substorm onset, the entropy of the 4 runs are almost the same. The

electric fields are very similar inside 10 R_E. After 2 minutes of the bubble injection, the bubble could penetrate to about 8 R_E for the runs with both corrections, Hardy normalization only, and without both corrections. In the run on the top right, the injection of bubble is much slower. It only reaches 9 R_E after 2 minutes. The electric field inside the bubble of this run is much smaller compared to other 3 runs. The reason for it will become obvious from the conductance plots presented below. The run with both corrections seems to have the strongest electric field. The run with Hardy normalization has second large westward electric field. The run without both corrections has even smaller electric fields inside the bubble. For the 2 runs without energy flux floor, the bubble has a triangle shape. For the 2 runs with energy flux floor, the shape of the bubble looks like a bird heading to the Earth with the wing span as the edge of the bubble. Among these 2 runs, the one with both corrections seems to have a longer neck and touch the inner edge of the plasma sheet. After 5 minutes of bubble injection, the bubble in the run with only energy flux floor correction still hasn't reached the geosynchronous orbit. The bubble in the run without both corrections has just reached the inner edge of the plasma sheet. For the runs on the left, the depleted channel has been formed. For the with Hardy normalization, the with of the channel is wider at the front of the channel, and the bubble is directed more to the duskside, which is also seen in the run without both corrections. So only the run with both corrections, also the greatest electric field inside, the channel is nearly symmetric pre- and post-midnight.

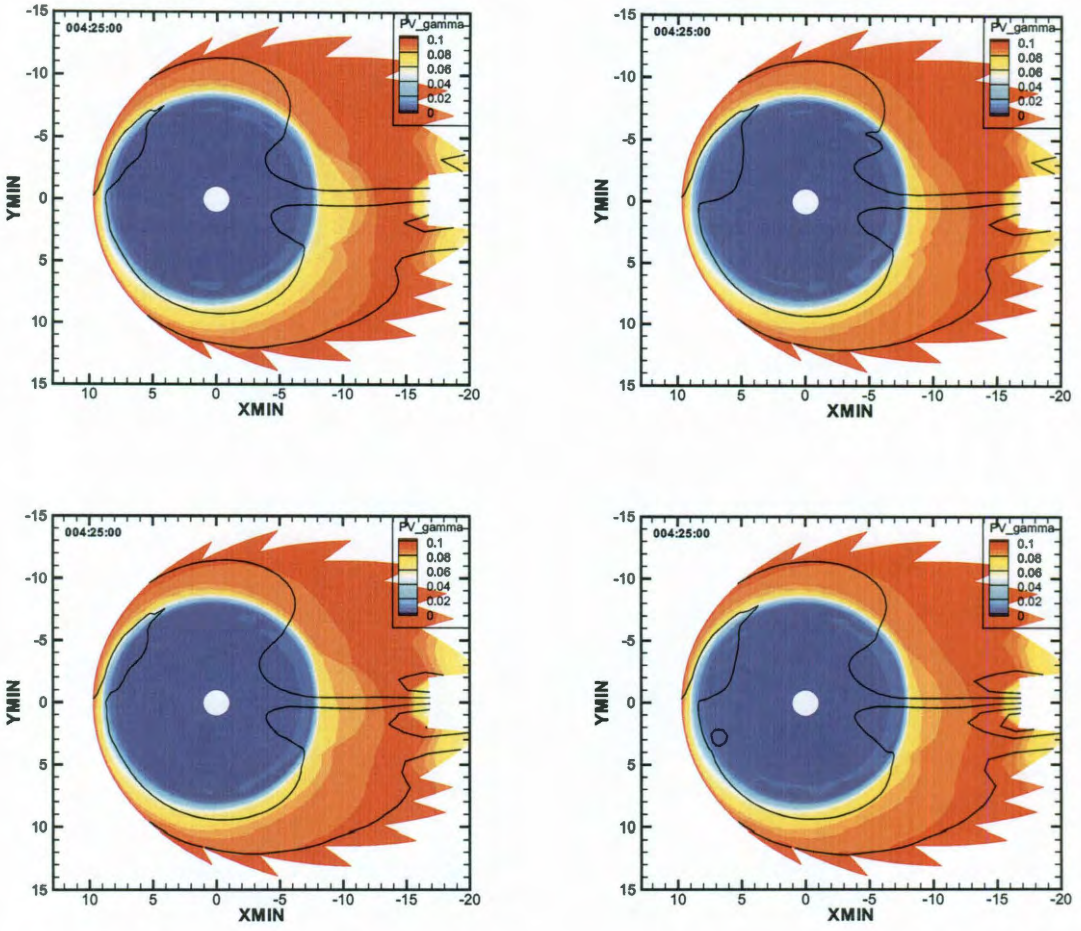

Figure 8.6 : Entropy right after expansion onset for the runs with both floor and Hardy normalization (top left), with floor only (top right), with Hardy normalization only (bottom left), without any corrections (bottom right). The black lines show ionospheric equipotential contours with 5 keV spacing.

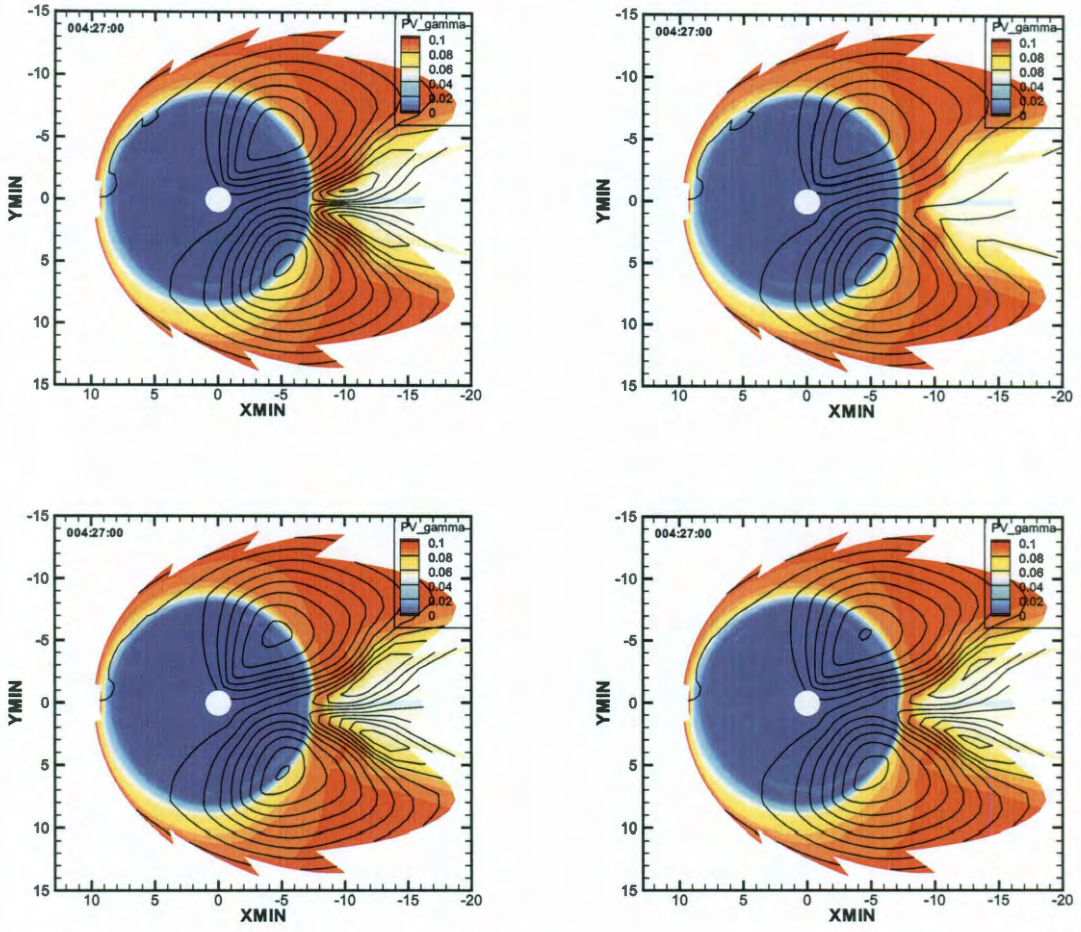

Figure 8.7 : Entropy at 2 minutes after expansion onset for the runs with both floor and Hardy normalization (top left), with floor only (top right), with Hardy normalization only (bottom left), without any corrections (bottom right). The black lines show ionospheric equipotential contours with 5 keV spacing.

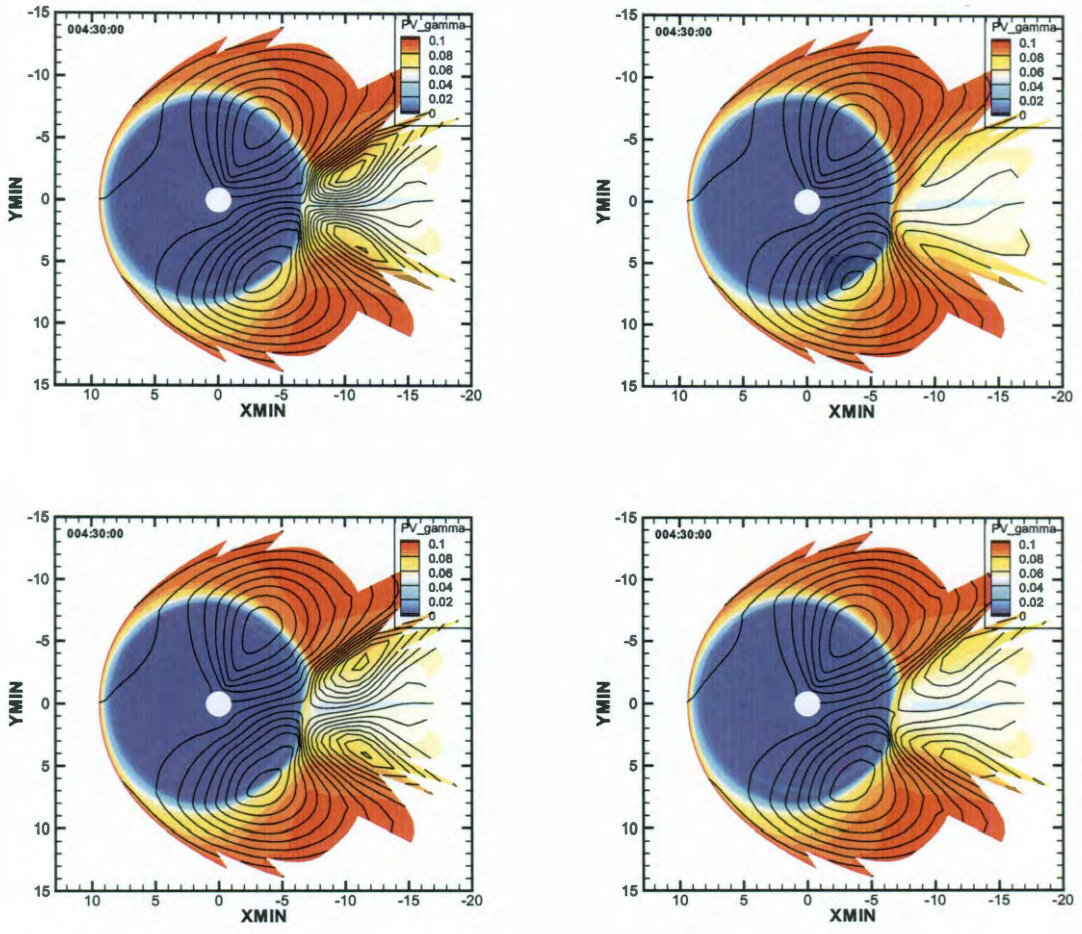

Figure 8.8 : Entropy at 5 minutes after expansion onset for the runs with both floor and Hardy normalization (top left), with floor only (top right), with Hardy normalization only (bottom left), without any corrections (bottom right). The black lines show ionospheric equipotential contours with 5 keV spacing.

8.6 Comparison of Field-Aligned Currents

Next, we present computed field-aligned currents in figures 8.9 to 8.12. The figures are showing the time 1 minute before the expansion onset, right after the expansion onset, 2 minutes and 5 minutes after the expansion onset. There is one set of field-aligned currents at about 7 to 8 R_E which is the region 2 field-aligned currents down to the ionosphere in dusk side and out of the ionosphere in dawn side. At the end of the growth phase, the difference of Birkeland currents is concentrated on the night-side. During the substorm expansion phase, there is a substorm current wedge, with downward field-aligned currents in the postmidnight sector and upward field-aligned currents in the premidnight sector. After the bubble injection, another set of field-aligned currents form on the edges of the bubble. The new sets of Birkeland currents are same for all the 4 runs. After 2 minutes, the new set of Birkeland currents are moving earthward and intersect with the region-2 field-aligned currents. The 2 runs without energy flux floor show very similar pattern of field-aligned currents. Since this set of Birkeland currents are formed on the edge of the bubble, the upward and downward Birkeland currents look like the sides of a triangle. For the runs with energy flux floor, the Birkeland currents look like the two wings of a bird. After 5 minutes of bubble injection, the run with floor but no Hardy normalization shows sharp and strong Birkeland currents at the front of the bubble.

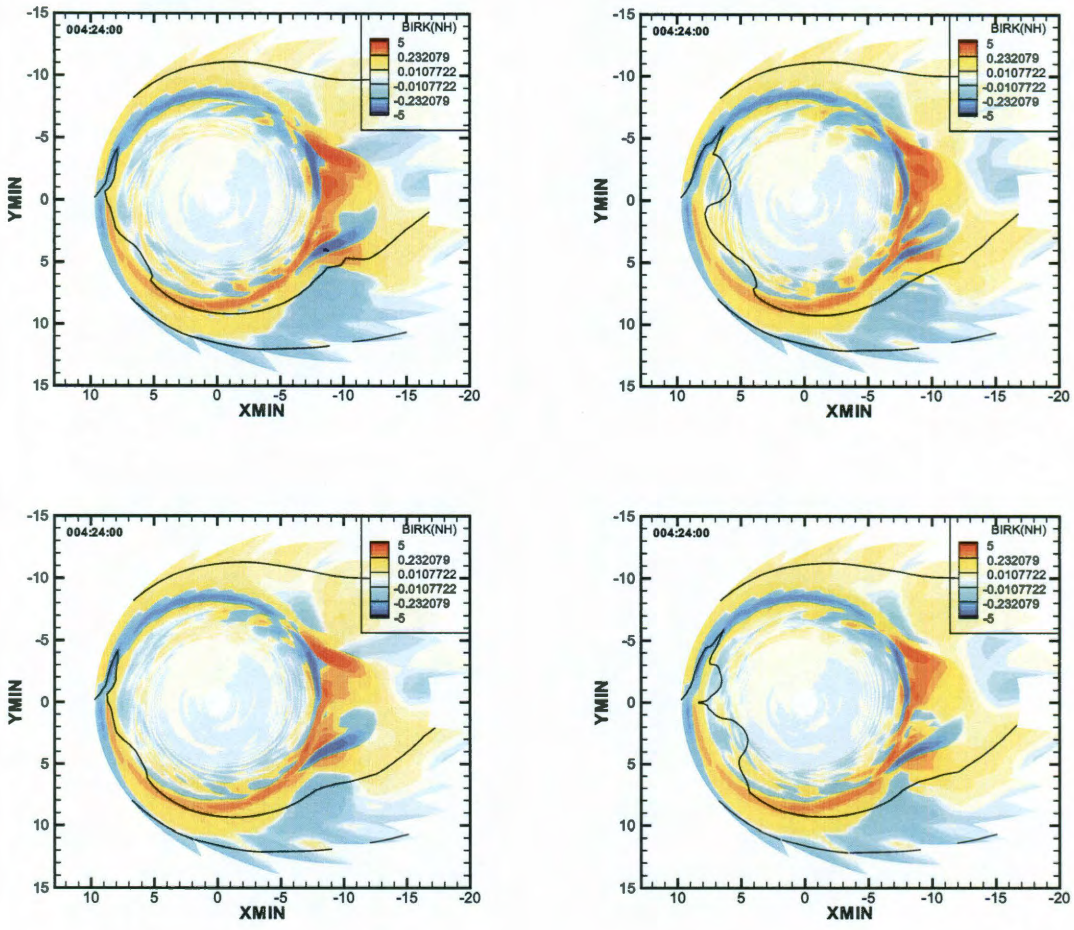

Figure 8.9 : Field-aligned currents at 1 minute before expansion onset for the runs with both floor and Hardy normalization (top left), with floor only (top right), with Hardy normalization only (bottom left), without any corrections (bottom right). The red region is downward field-aligned currents. The blue region is upward field-aligned currents. The black lines show ionospheric equipotential contours with 5 keV spacing.

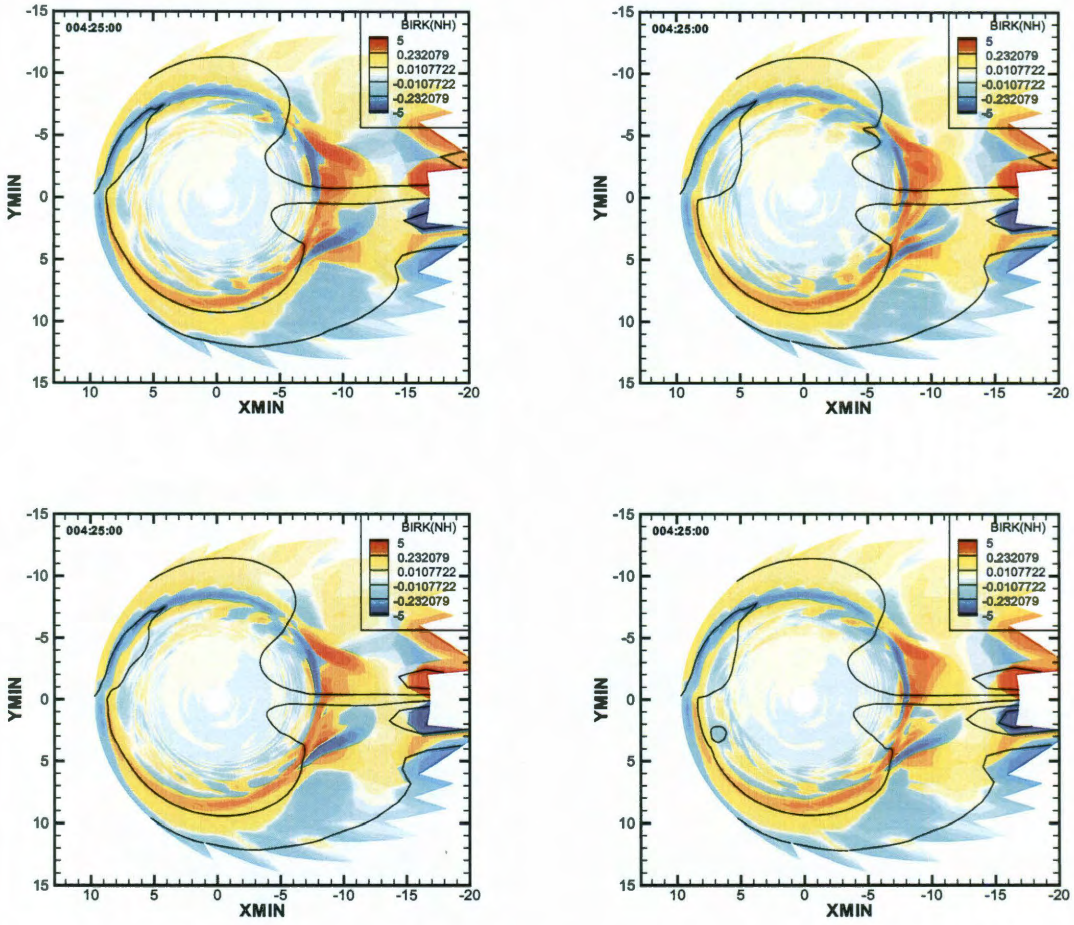

Figure 8.10 : Field-aligned currents right after expansion onset for the runs with both floor and Hardy normalization (top left), with floor only (top right), with Hardy normalization only (bottom left), without any corrections (bottom right). The red region is downward field-aligned currents. The blue region is upward field-aligned currents. The black lines show ionospheric equipotential contours with 5 keV spacing.

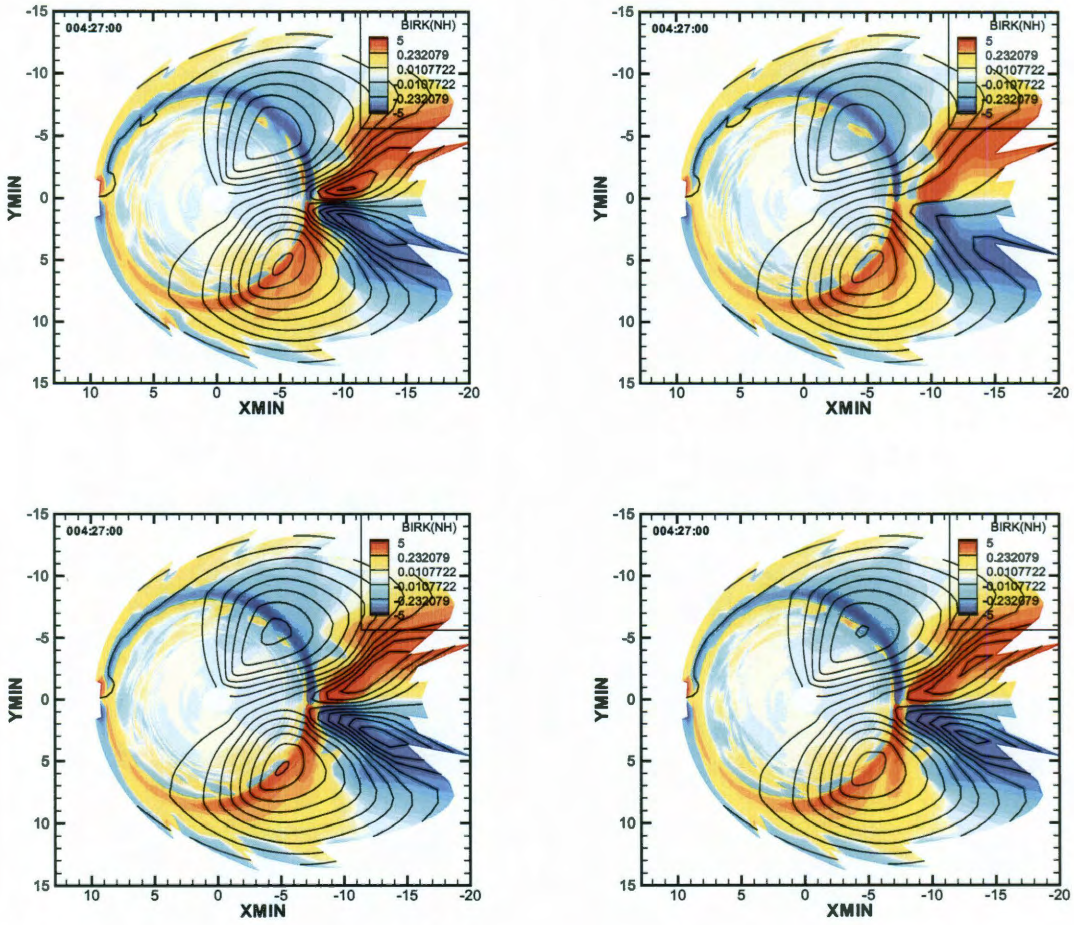

Figure 8.11 : Field-aligned currents at 2 minutes after expansion onset for the runs with both floor and Hardy normalization (top left), with floor only (top right), with Hardy normalization only (bottom left), without any corrections (bottom right). The red region is downward field-aligned currents. The blue region is upward field-aligned currents. The black lines show ionospheric equipotential contours with 5 keV spacing.

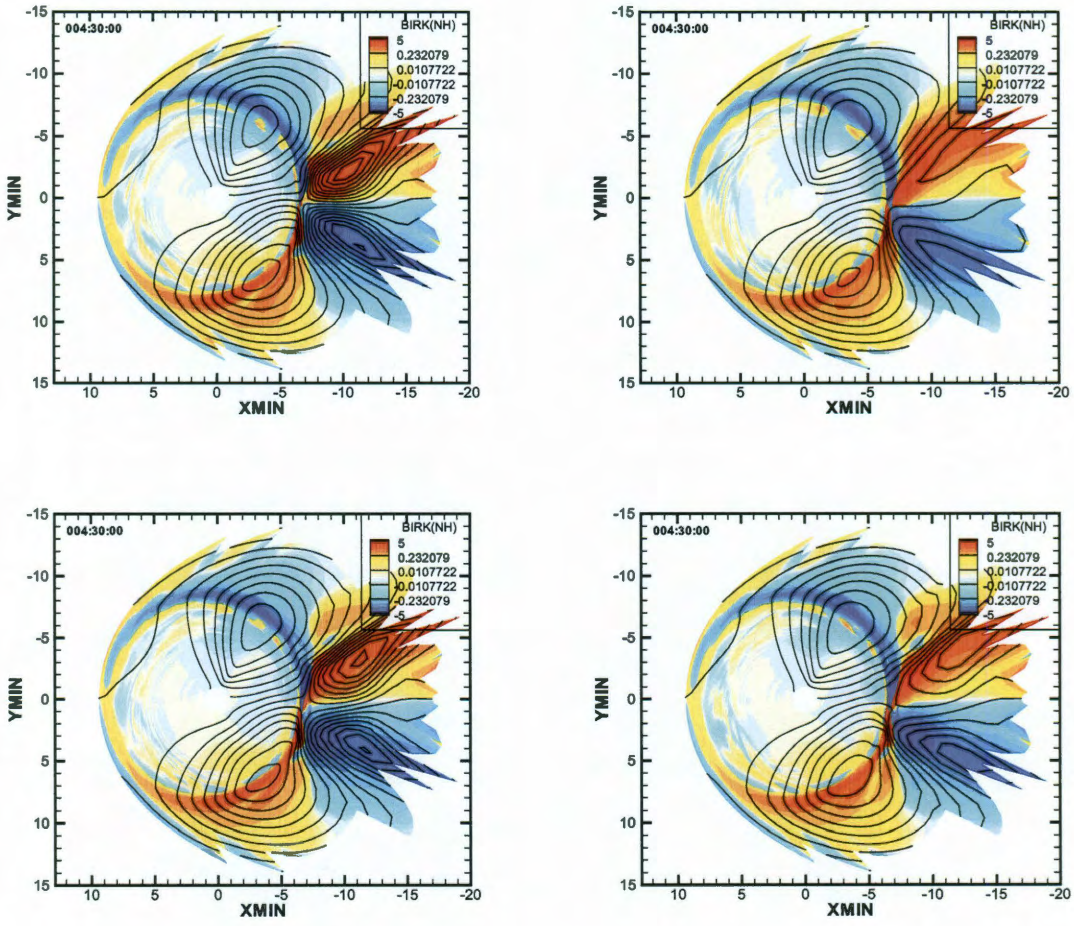

Figure 8.12 : Field-aligned currents at 5 minutes after expansion onset for the runs with both floor and Hardy normalization (top left), with floor only (top right), with Hardy normalization only (bottom left), without any corrections (bottom right). The red region is downward field-aligned currents. The blue region is upward field-aligned currents. The black lines show ionospheric equipotential contours with 5 keV spacing.

8.7 Comparison of Energy Flux and Average Energy

The precipitating electron energy flux is shown in figures 8.13 to 8.15, in the units of $[ergs/cm^{-2}/s]$. The figures are showing the time 1 minute before the expansion onset, 2 minutes and 5 minutes after the expansion onset. We could first look at the run without both corrections, the bottom right one, which gives the pure physics calculation. During the growth phase, the precipitation flux is relatively large between 7 R_E and 10 R_E. It's generally stronger in the dawnside due to the gradient/curvature drift. There is a peak at about 3 am. The precipitating flux gradually decreases with higher latitude. The difference between the top right one and the bottom right one shows how we introduce the energy flux floor. The precipitating energy flux would not go below one half of the peak value as the latitude increases along certain local time direction. The difference between the bottom left one and the bottom right one shows the effect of Hardy normalization. The energy flux decreases on the dayside and dusk side and increases on the nightside and dawn side. But the peaks remain in the post-midnight sector.

In the substorm growth phase, after 2 minutes of bubble injection, the run without both corrections shows increasing energy fluxes between 7 R_E and 10 R_E. The precipitation flux strengthens primarily at midnight forming a new peak at 7.5 R_E. It overlays the old peak at post-midnight. The difference between the top right one and the bottom right one is the energy flux floor as expected. The difference between the bottom left one and the bottom right one is the Hardy normalization. This time, the energy flux decreases from the post-noon sector to pre-dawn sector. The reason is that Hardy model is a statistical model and doesn't count the particle precipitation very well. So during the substorm expansion phase, when particles are injected into the inner magnetosphere, the Hardy normalization would decrease the energy flux

instead of increasing in the growth phase. We can not find a clear midnight peak of energy flux in the run with both corrections since we perform the energy flux floor before the Hardy normalization. In this way, the corrections make energy flux tailward of the midnight peak higher and lead to much stronger total flux which grinds the energy flux more along the azimuthal direction. After 5 minutes of bubble injection, similar patterns are observed except for a stronger but more earthward peak because more particles are pushing earthward by the low entropy plasma bubble.

The differences in the average precipitating electron energy are not significant at all both in growth phase (Figure 8.16) and expansion phase (Figure 8.17) due to limited differences in drift pattern. The average energy (units are keV) is determined by the distribution function of magnetospheric plasma. So the meaningful region of average energy is between 5 R_E and 10 R_E during the growth phase and further out to the tail during the expansion phase. The peak value for a given local time direction is located at about 8 R_E.

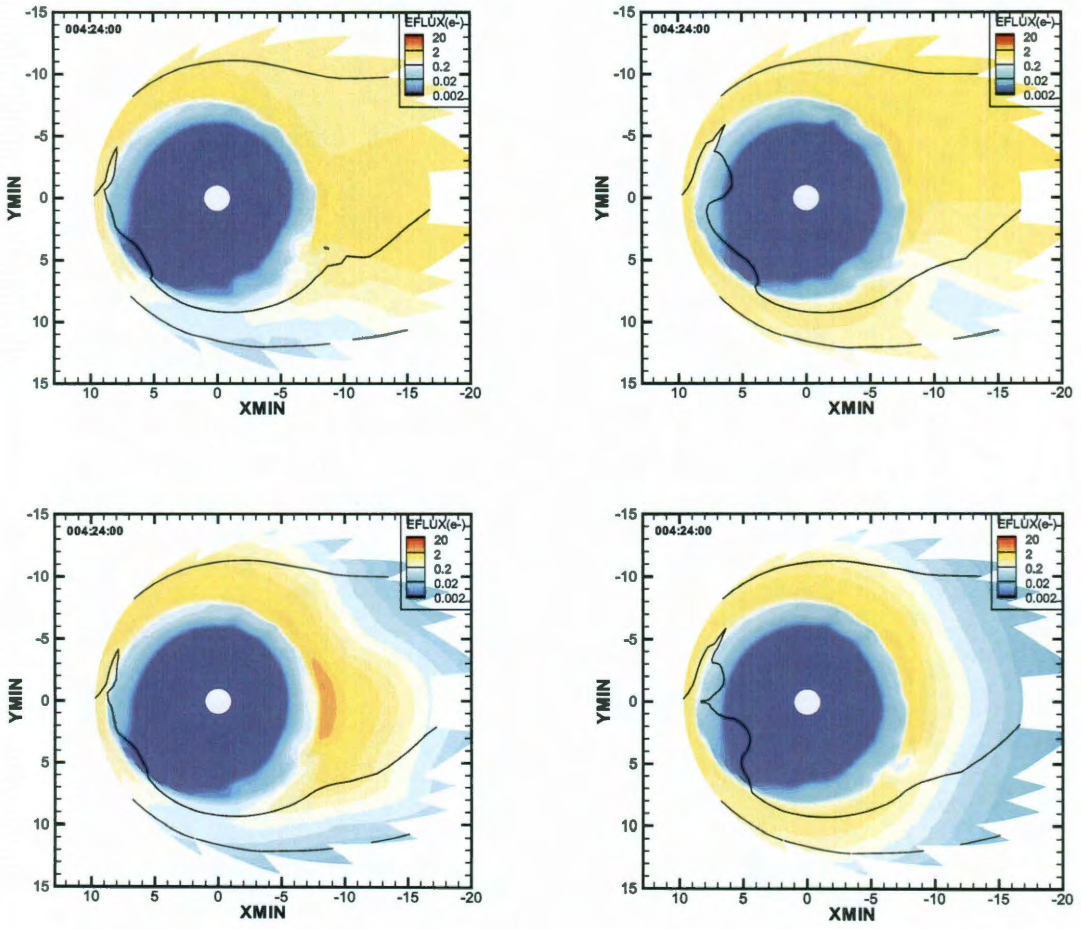

Figure 8.13 : Precipitating electron energy flux at 1 minute before expansion onset for the runs with both floor and Hardy normalization (top left), with floor only (top right), with Hardy normalization only (bottom left), without any corrections (bottom right). The red region is downward field-aligned currents. The blue region is upward field-aligned currents. The black lines show ionospheric equipotential contours with 5 keV spacing.

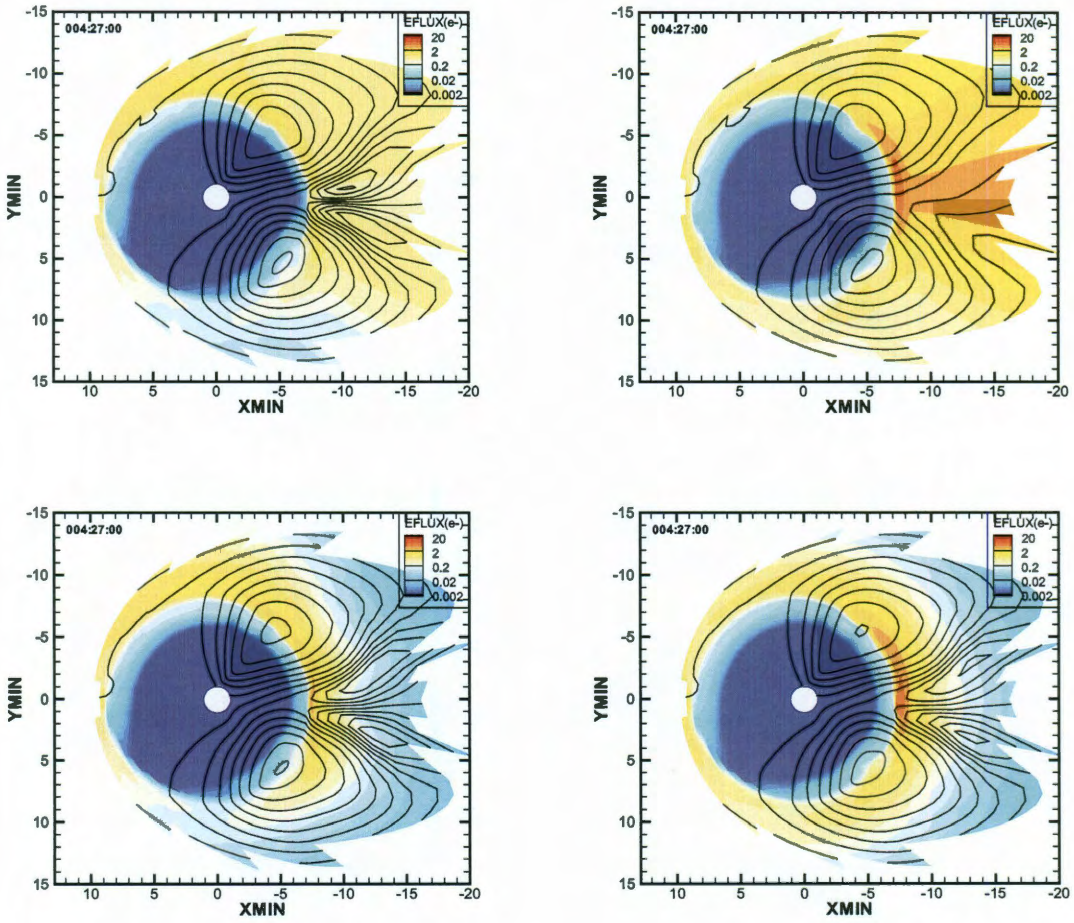

Figure 8.14 : Precipitating electron energy flux at 2 minutes after expansion onset for the runs with both floor and Hardy normalization (top left), with floor only (top right), with Hardy normalization only (bottom left), without any corrections (bottom right). The red region is downward field-aligned currents. The blue region is upward field-aligned currents. The black lines show ionospheric equipotential contours with 5 keV spacing.

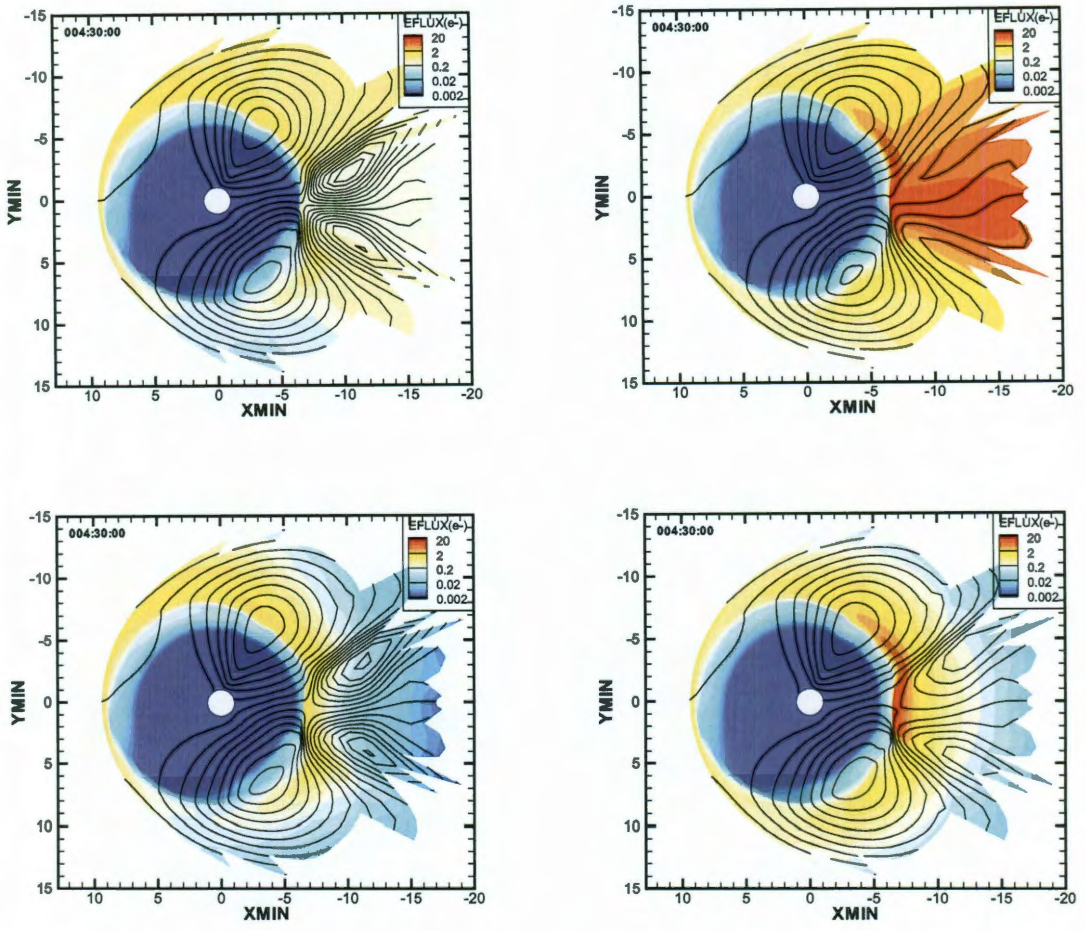

Figure 8.15 : Precipitating electron energy flux at 5 minutes after expansion onset for the runs with both floor and Hardy normalization (top left), with floor only (top right), with Hardy normalization only (bottom left), without any corrections (bottom right). The red region is downward field-aligned currents. The blue region is upward field-aligned currents. The black lines show ionospheric equipotential contours with 5 keV spacing.

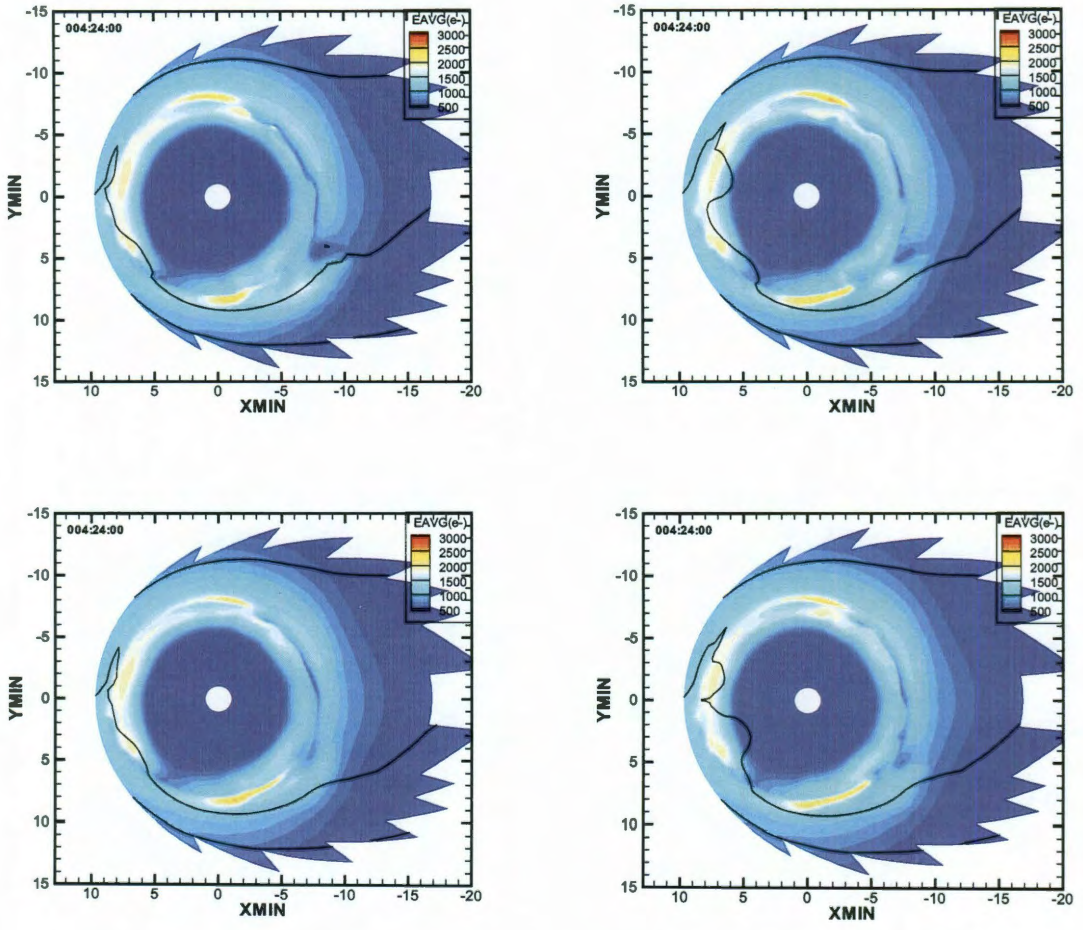

Figure 8.16 : Average energy of precipitating electron at 1 minute before expansion onset for the runs with both floor and Hardy normalization (top left), with floor only (top right), with Hardy normalization only (bottom left), without any corrections (bottom right). The red region is downward field-aligned currents. The blue region is upward field-aligned currents. The black lines show ionospheric equipotential contours with 5 keV spacing.

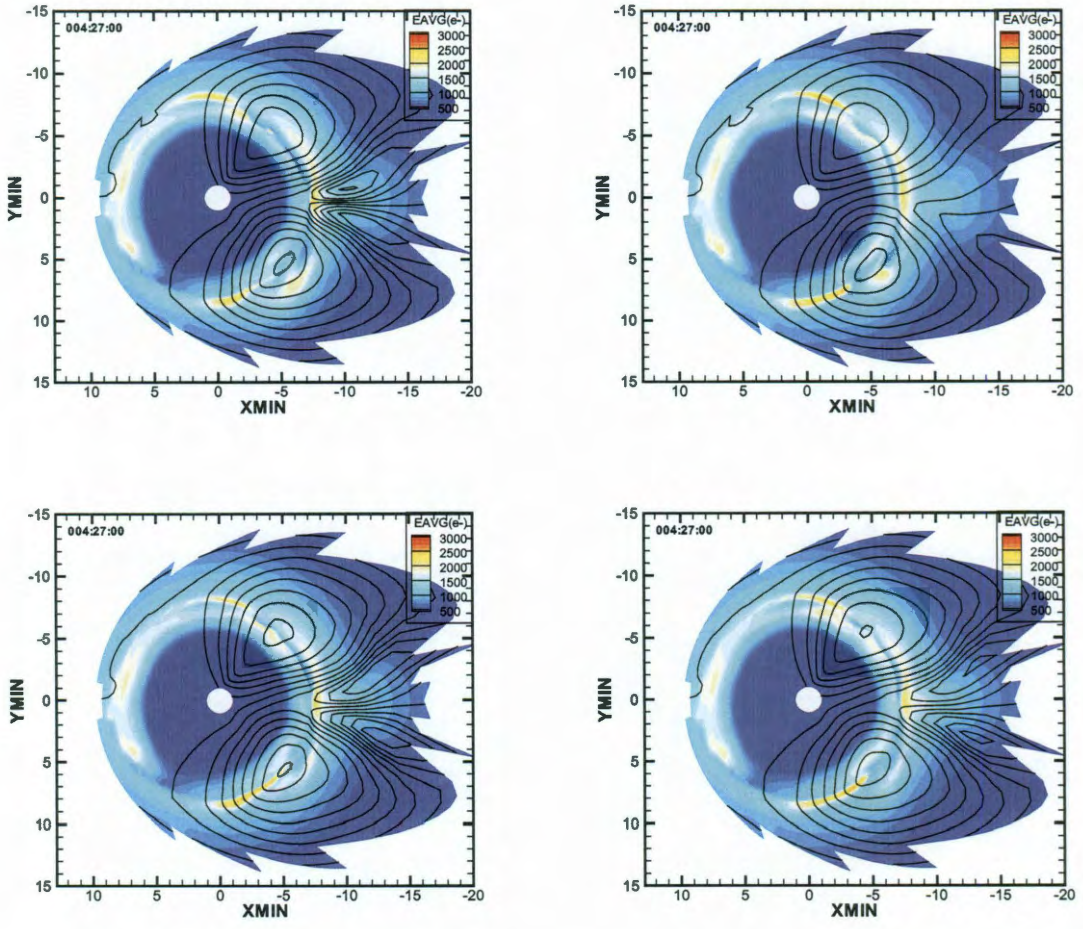

Figure 8.17 : Average energy of precipitating electron at 2 minutes after expansion onset for the runs with both floor and Hardy normalization (top left), with floor only (top right), with Hardy normalization only (bottom left), without any corrections (bottom right). The red region is downward field-aligned currents. The blue region is upward field-aligned currents. The black lines show ionospheric equipotential contours with 5 keV spacing.

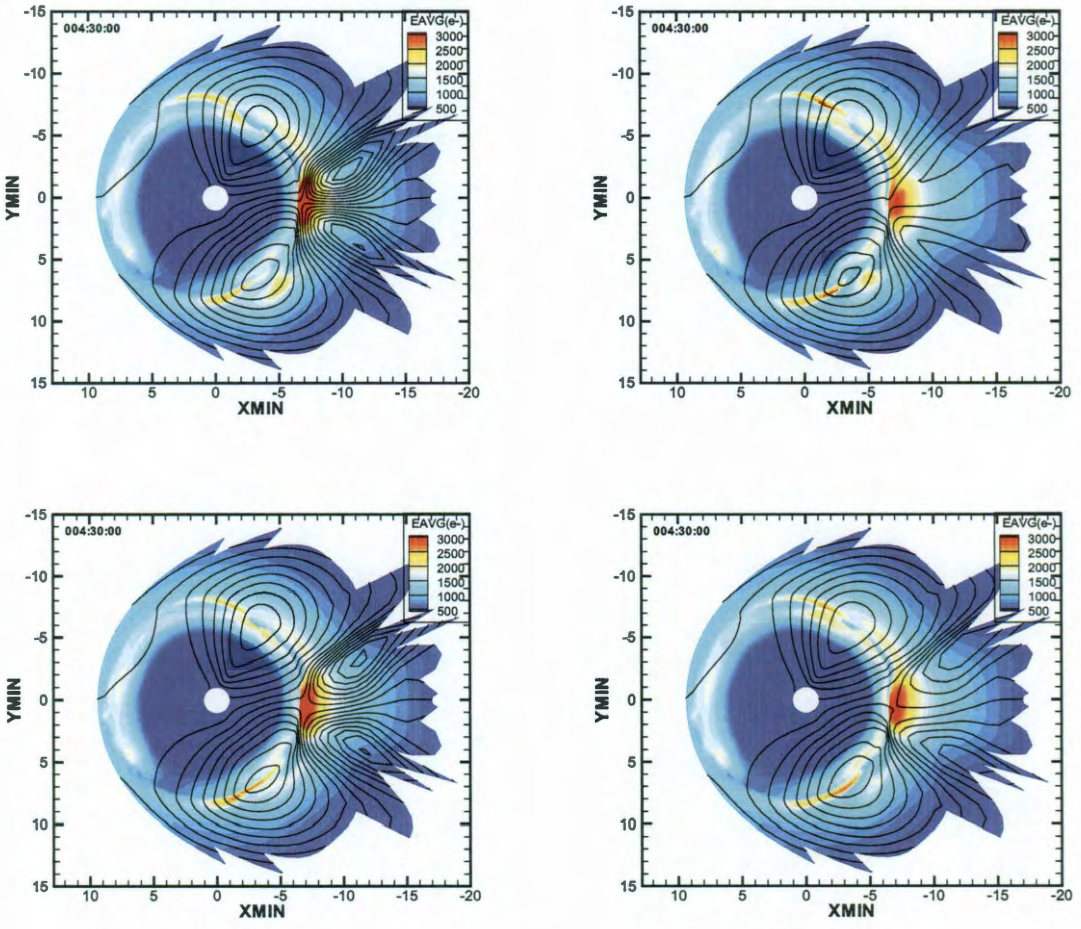

Figure 8.18 : Average energy of precipitating electron at 5 minutes after expansion onset for the runs with both floor and Hardy normalization (top left), with floor only (top right), with Hardy normalization only (bottom left), without any corrections (bottom right). The red region is downward field-aligned currents. The blue region is upward field-aligned currents. The black lines show ionospheric equipotential contours with 5 keV spacing.

8.8 Comparison of Ionospheric Conductances

The ionospheric conductances have contributions from solar radiation and particle precipitation. In these runs, we have neglected the proton precipitation. The conductances due to electron precipitation are calculated by precipitating energy flux and average energy. So the pattern of ionospheric conductances, either Pedersen conductances or Hall conductances, reflects structure in both energy flux and average energy. Conductance is dominated by the electron precipitating energy flux at nightside. Figure 8.19 to 8.21 are showing the time 1 minute before the expansion onset, right after the expansion onset, 2 minutes and 5 minutes after the expansion onset. The Hall conductance at nightside is mainly a half-circle at about 9 R_E. The strength of Hall conductances at midnight sector are different for the 4 runs. The one with only Hardy normalization gives stronger conductance around midnight due to the fake increase of energy flux. After 2 minutes of bubble injection, the run with floor only shows stronger conductance in the midnight tailward of 9 R_E. The high conductance usually leads smaller electric field and lower electric field drift. For the other 3 runs, the one without both corrections has a wider peak in the midnight around 8 R_E, the one with Hardy normalization gives a thinner peak, and the one with both corrections gives the thinnest peak there. Sin the bubble pushed in the plasma around Geotail location to the inner magnetosphere, the peak of nightside Hall conductance was pushing earthward as well. The circular peak about 9 R_E at midnight becomes a straight segment about 8 R_E.

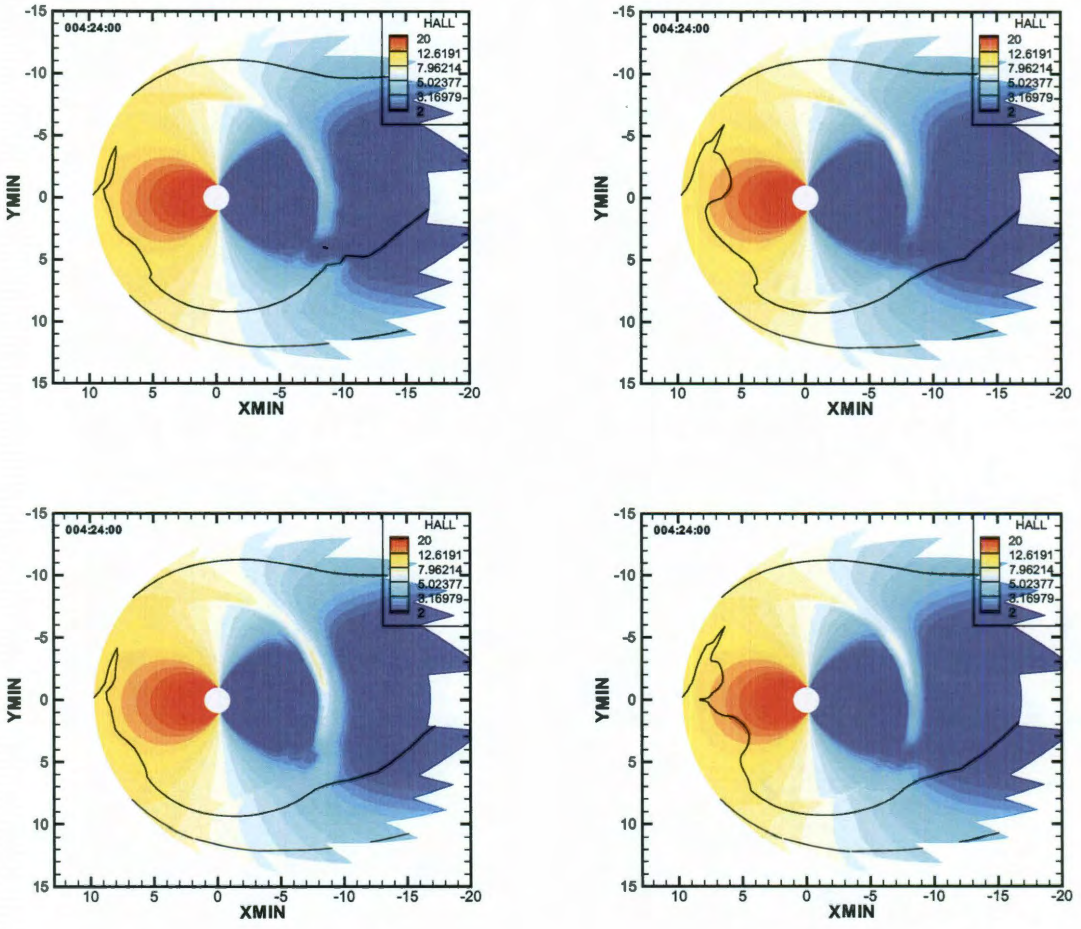

Figure 8.19 : Hall field-line integrated ionospheric conductances at 1 minute before expansion onset for the runs with both floor and Hardy normalization (top left), with floor only (top right), with Hardy normalization only (bottom left), without any corrections (bottom right). The red region is downward field-aligned currents. The blue region is upward field-aligned currents. The black lines show ionospheric equipotential contours with 5 keV spacing.

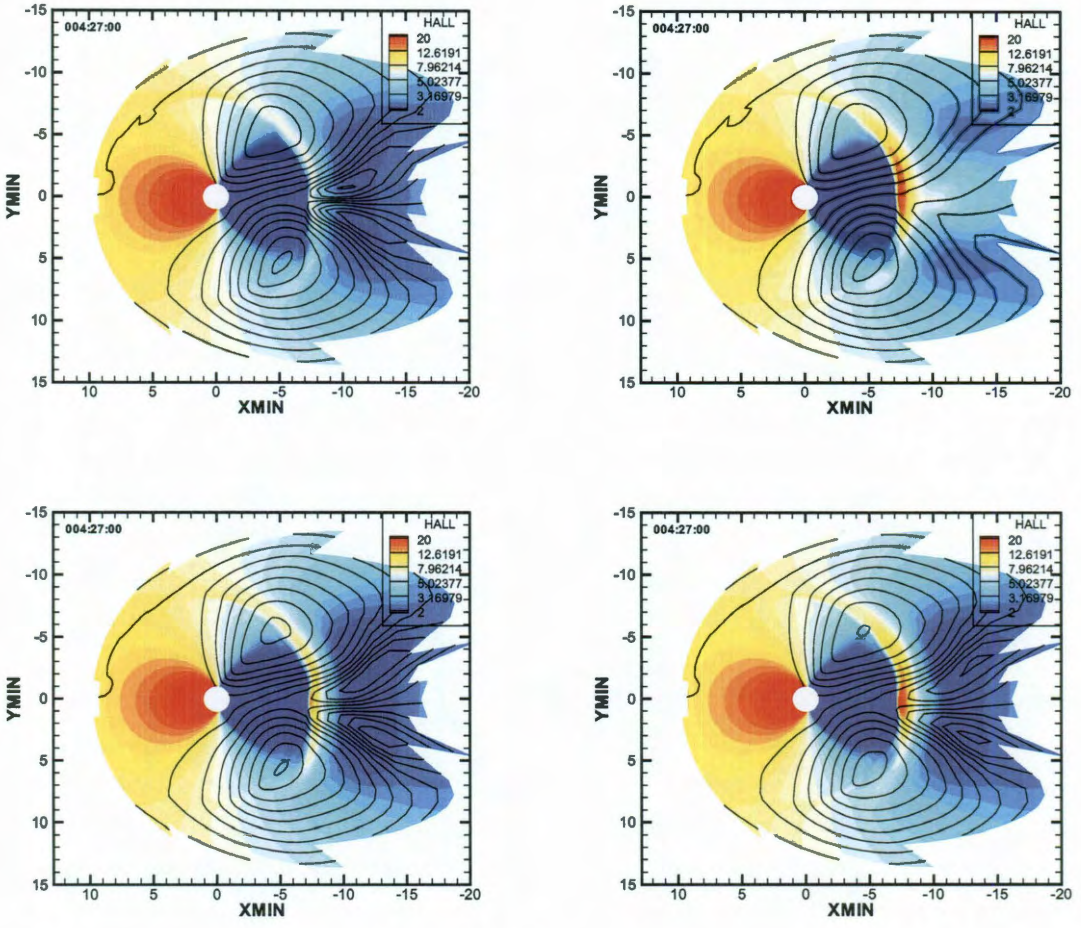

Figure 8.20 : Hall conductances right at 2 minutes after expansion onset for the runs with both floor and Hardy normalization (top left), with floor only (top right), with Hardy normalization only (bottom left), without any corrections (bottom right). The red region is downward field-aligned currents. The blue region is upward field-aligned currents. The black lines show ionospheric equipotential contours with 5 keV spacing.

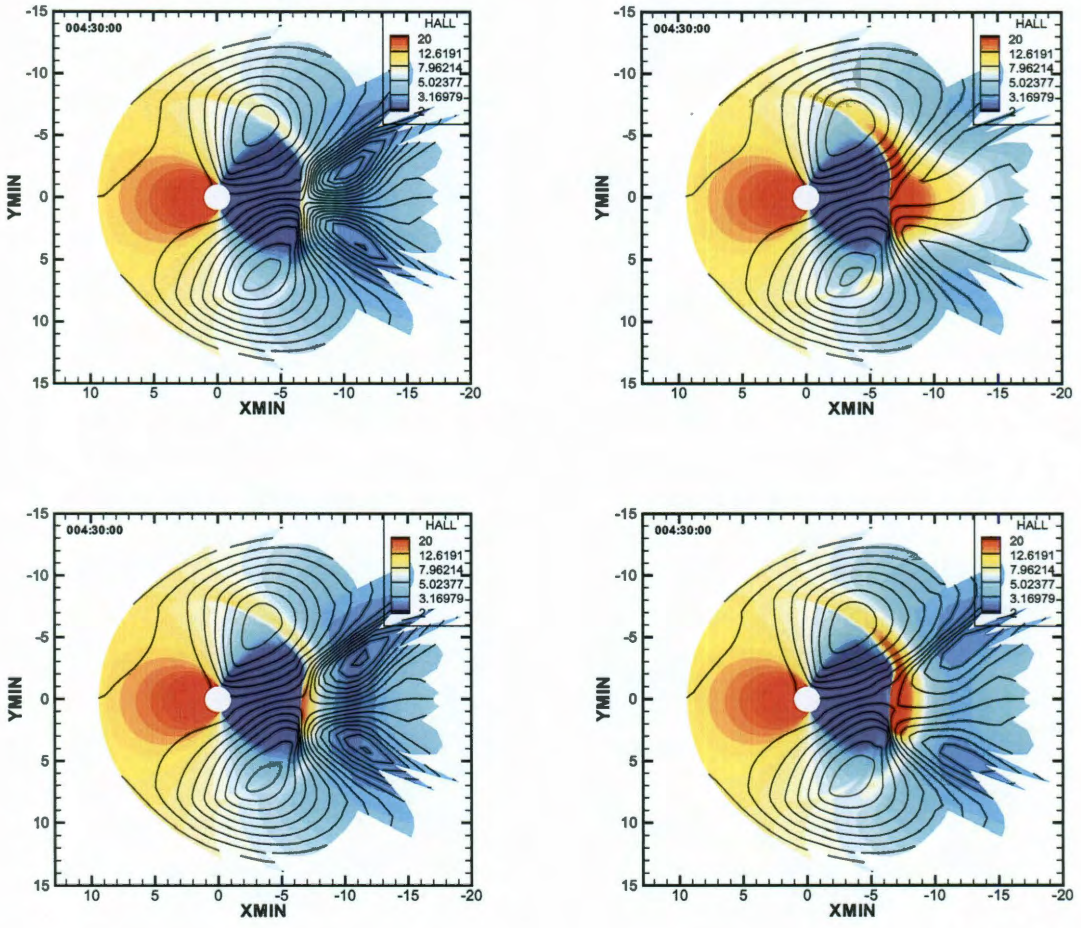

Figure 8.21 : Hall conductances at 5 minutes after expansion onset for the runs with both floor and Hardy normalization (top left), with floor only (top right), with Hardy normalization only (bottom left), without any corrections (bottom right). The red region is downward field-aligned currents. The blue region is upward field-aligned currents. The black lines show ionospheric equipotential contours with 5 keV spacing.

8.9 Discussion

8.9.1 Comparison of Two Parameters

The Vasyliunas equation used to calculate FACs from magnetospheric plasma pressure gradients assumes balance between the magnetic force and the pressure gradient with an assumption of slow flow compared to sound speed and Alfvén wave from the equatorial plane to the ionosphere[254]. The use of code could be not fully justified during the dipolarization between 0655 UT and 0700 UT especially down to the tail over 15 R_E. Although the code cannot describe the plasma evolution on time scales less than a minute, the RCM could still provide the essential process of substorm expansion. Smaller flow speed beyond 9 R_E, due to electric field inside the bubble, is helpful to the validity of applying the RCM to substorm simulations. Our results, if such, would then be theoretically more defensible than those of [254].

From four runs corresponding to the four combinations of floor setting and Hardy normalization, we could obtain quite different energy flux pattern. It leads to different ionospheric conductances and thus the electric field. The run with precipitating energy flux floor but no Hardy normalization shows the strongest energy flux and ionospheric conductances because it increases the energy flux inside the bubble. So it has the smallest electric field and the lowest drift velocity of the bubble. We will focus on the comparison between the run without both corrections and the run with energy flux floor since the former one gives pure physics calculation and the latter one gives smaller penetration electric fields. Figure 8.22 shows the difference of applying energy flux floor in affecting the convection electric field excluding the co-rotation. The time is 2 minutes after the expansion onset. The westward electric fields appear at dawn and dusk sides as well as midnight inside the bubble. The electric fields

inside the bubble are different by a factor of 2 as shown from the color scales. It must be emphasized that these conclusions are valid for the potential electric field only (induction electric fields are significant in the midnight region).

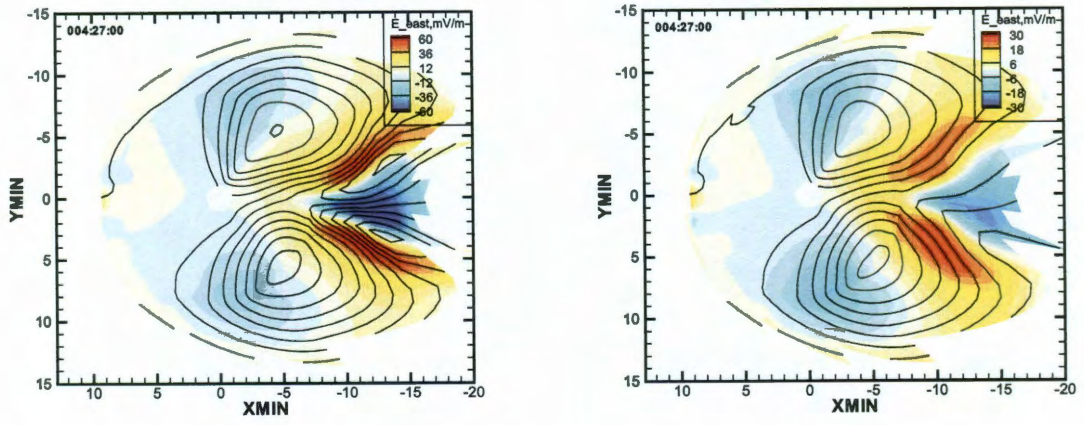

Figure 8.22 : Eastward electric field excluding the co-rotation at 2 minutes after expansion onset for the runs without any correction (left) and with floor only (right). The red region is eastward electric fields. The blue region is westward electric fields. The black lines show ionospheric equipotential contours with 5 keV spacing.

Figure 8.23 shows the computed Birkeland currents with electric equipotential contours in the nightside ionosphere from 1 minute before the expansion onset to 5 minutes after the expansion onset. With the given solar wind parameters, the location of RCM tailward boundary determined by the magnetic field model is fixed to about -20 R_E in the equatorial plane. As the magnetic field dipolarized during the expansion phase, the tailward boundary maps to high latitude which gives poleward expansion of the high-latitude boundary near local midnight. During the growth phase, the region-1 FACs locate poleward of the RCM modeling region, only the region-2 FACs are observed. The run with energy flux floor gives the region-2 FACs more equatorward. After bubble injection, region-1 sense FACs form on the western and eastern edges

of the bubble. The currents are almost the same for the two runs right after the bubble injection. A strong westward electric field exists inside the bubble. After 2 minutes of bubble injection, the region-2 FACs strengthen and move poleward leading to an eastward penetration electric fields at lower latitudes[254]. Then plasma has different motions at midnight in the auroral zone and in the subauroral region due to the electric field drift. The region-1 sense FACs also brighten and extend to higher latitude region. The peaks of region-1 and region-2 FACs are separate in the run with energy flux floor because of lower electric field strength.

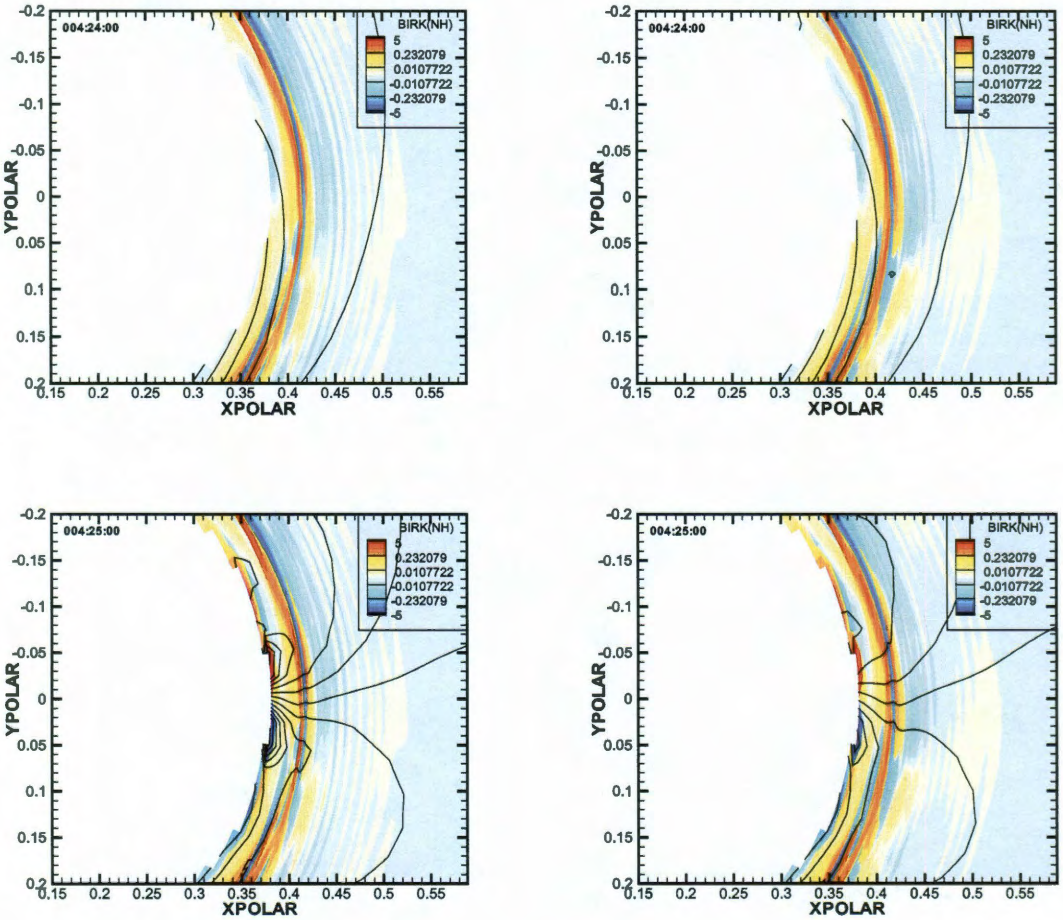

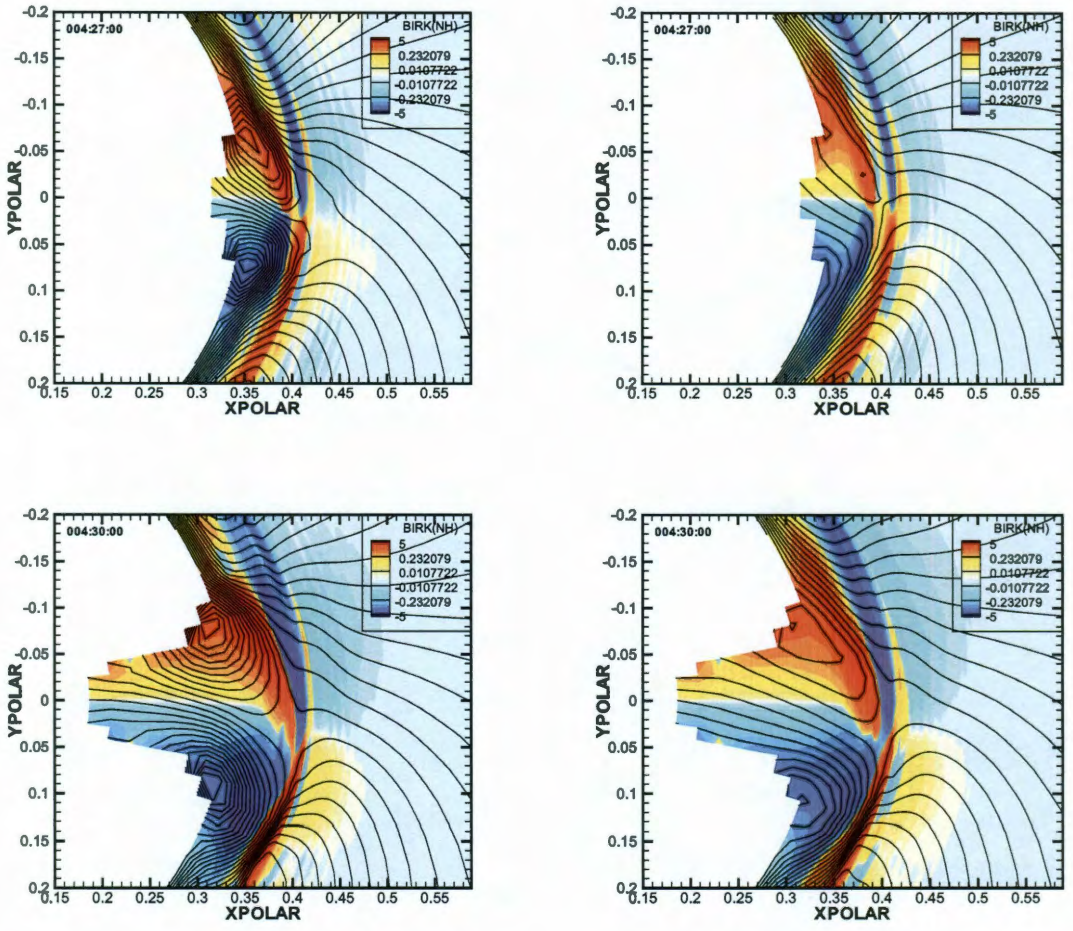

Figure 8.23 : Birkeland currents at 1 minute before expansion onset (first row), right after expansion onset (second row), 2 minutes after expansion onset (third row), 5 minutes after expansion onset (fourth row) for the runs without any correction (left) and with floor only (right). The red region is eastward electric fields. The blue region is westward electric fields. The black lines show ionospheric equipotential contours with 2 keV spacing.

Figure 8.24 shows the precipitating electron energy flux in the ionosphere from 1 minute before expansion onset to 5 minutes after expansion onset. There is limited electron energy flux at low-latitude region. The energy flux is localized in the region-2 field-aligned currents region in the run without any correction. The particles are

shielded from penetrating earthward and concentrated in the region. The run with energy flux floor shows more energy flux at high-latitude region. The peak of the precipitating energy flux represents the growth phase arc at the end of the growth phase. However, since we only calculate electron energy flux in these runs, the peak is in post-midnight sector which is usually not the case in observations. During the expansion phase, the peaks of the energy flux brighten and extend to higher latitude. The run with energy flux floor has its peak extending more dawnside in the azimuthal direction due to higher electron density there. Figure 8.25 shows the Hall conductances in the ionosphere from 1 minute before expansion onset to 5 minutes after expansion onset. Since we only show the nightside, the ionospheric conductances is determined by the precipitating energy flux. During the expansion phase, the run with energy flux floor shows higher conductances at high-latitude boundary near the midnight. The auroral region with high conductances moves poleward through the beginning of the expansion phase. The peak at equatorward boundary of the auroral region expands and also moves poleward which is the typical auroral signatures during a substorm.

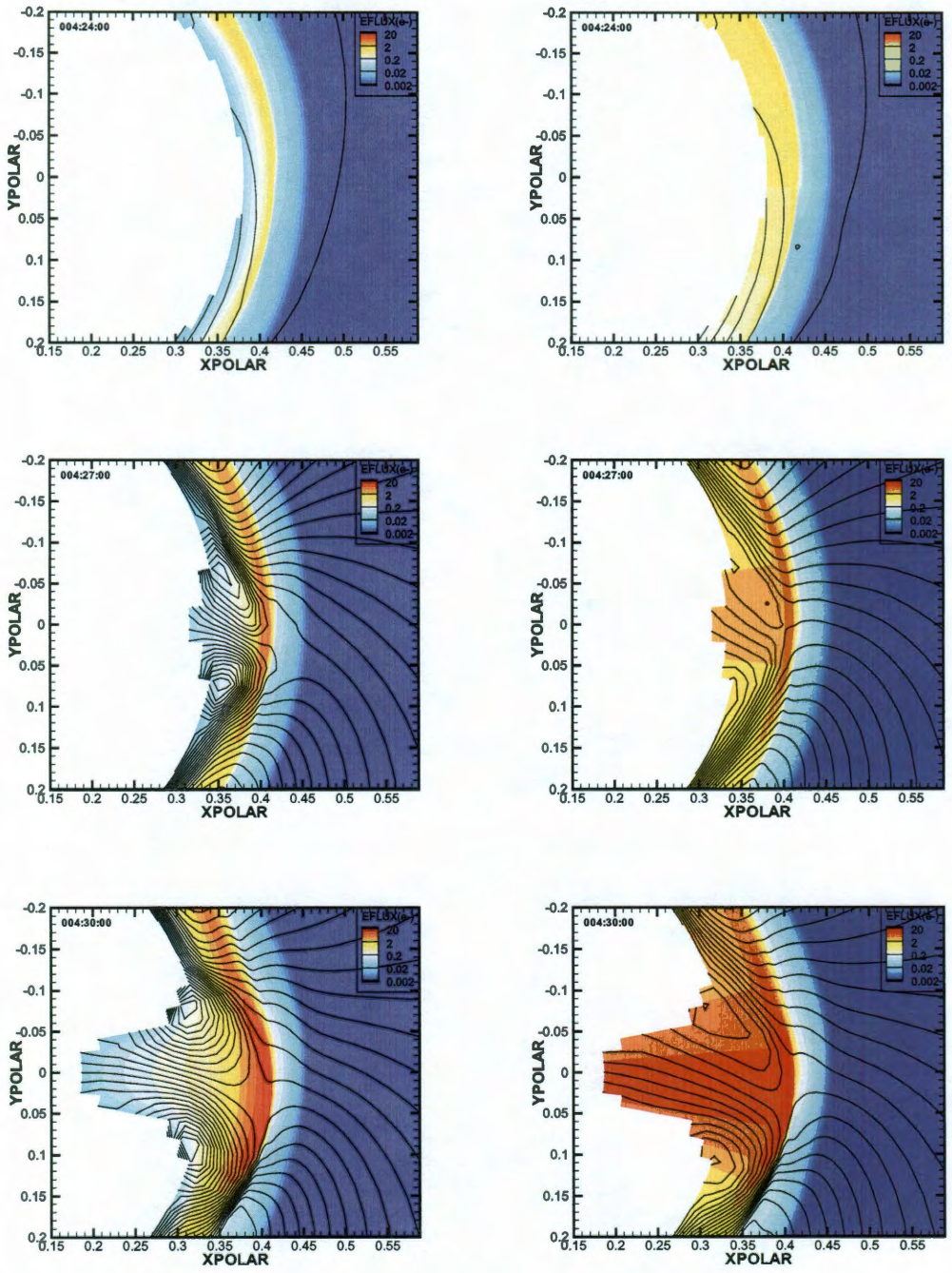

Figure 8.24 : Precipitating electron energy flux at 1 minute before expansion onset (top), 2 minutes after expansion onset (middle), 5 minutes after expansion onset (bottom) for the runs without any correction (left) and with floor only (right). The red region is eastward electric fields. The blue region is westward electric fields. The black lines show ionospheric equipotential contours with 2 keV spacing.

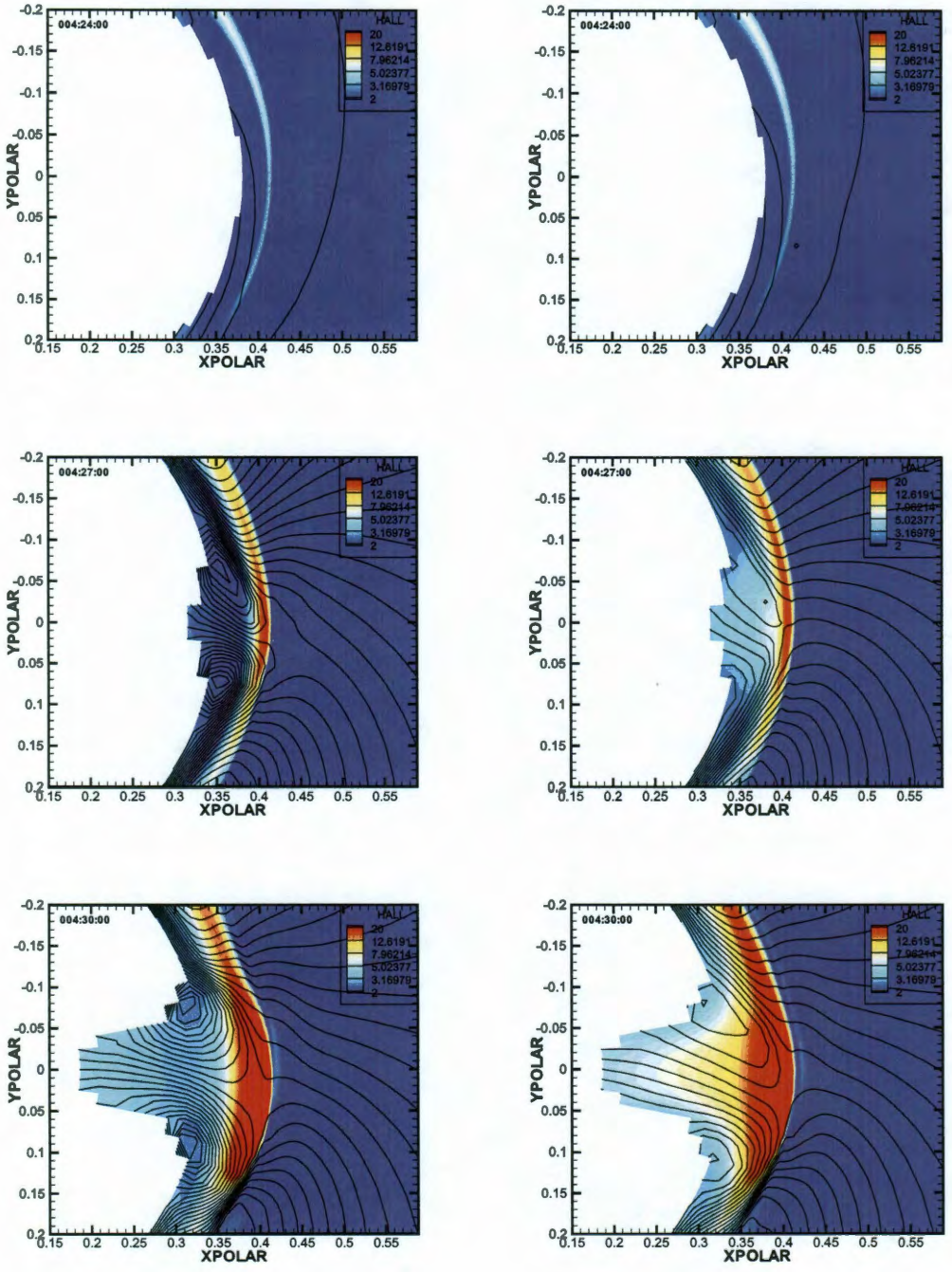

Figure 8.25 : Hall conductances at 1 minute before expansion onset (top), 2 minutes after expansion onset (middle), 5 minutes after expansion onset (bottom) for the runs without any correction (left) and with floor only (right). The red region is eastward electric fields. The blue region is westward electric fields. The black lines show ionospheric equipotential contours with 2 keV spacing.

8.9.2 Loss Rate

The loss rate used in the simulations was discussed in previous chapter. For the runs without parallel electric field, the loss rate for the electrons is 1/3 of the limit of strong pitch angle scattering and the loss rate for protons is neglected. The fraction 1/3 is consistent with the estimation between 1/2 and 1/3[225]. The next few graphs show the comparisons between the run with loss rate of 1/3 of strong pitch angle scattering and the run with full strong pitch angle scattering. Both of these runs are with energy flux floor but no Hardy normalization. Figure 8.26 shows the difference in precipitating energy flux. The energy flux is mainly determined by the density and temperature of magnetosphere electrons. For certain case with the same electron distributions, the energy fluxes are same for both runs. However, for the run which has more electrons loss to the ionosphere, the precipitating energy flux would be smaller due to less electrons in the magnetosphere. The peak of the energy flux in post-midnight sector is a result of more electrons drifting eastward around the Earth. The ionospheric conductances coming from the particle precipitation is proportional to the square root of the precipitating energy flux so that the conductances for the run with 1/3 strong pitch angle scattering has higher conductances at midnight and post-midnight than the run with full strong pitch angle scattering as shown in Figure 8.27. The bubble injection is shown in Figure 8.28. The main feature doesn't change much when we increase the lost rate. The entropy at dawn and dusk becomes smaller over 8 R_E. The electric field inside the channel is a little bit stronger at the time of 0657 UT for the run with full pitch angle scattering. Therefore, the bubble drift earthward a little bit more quickly. So at 0700 UT, the channel is formed between the inner magnetosphere and the tailward boundary.

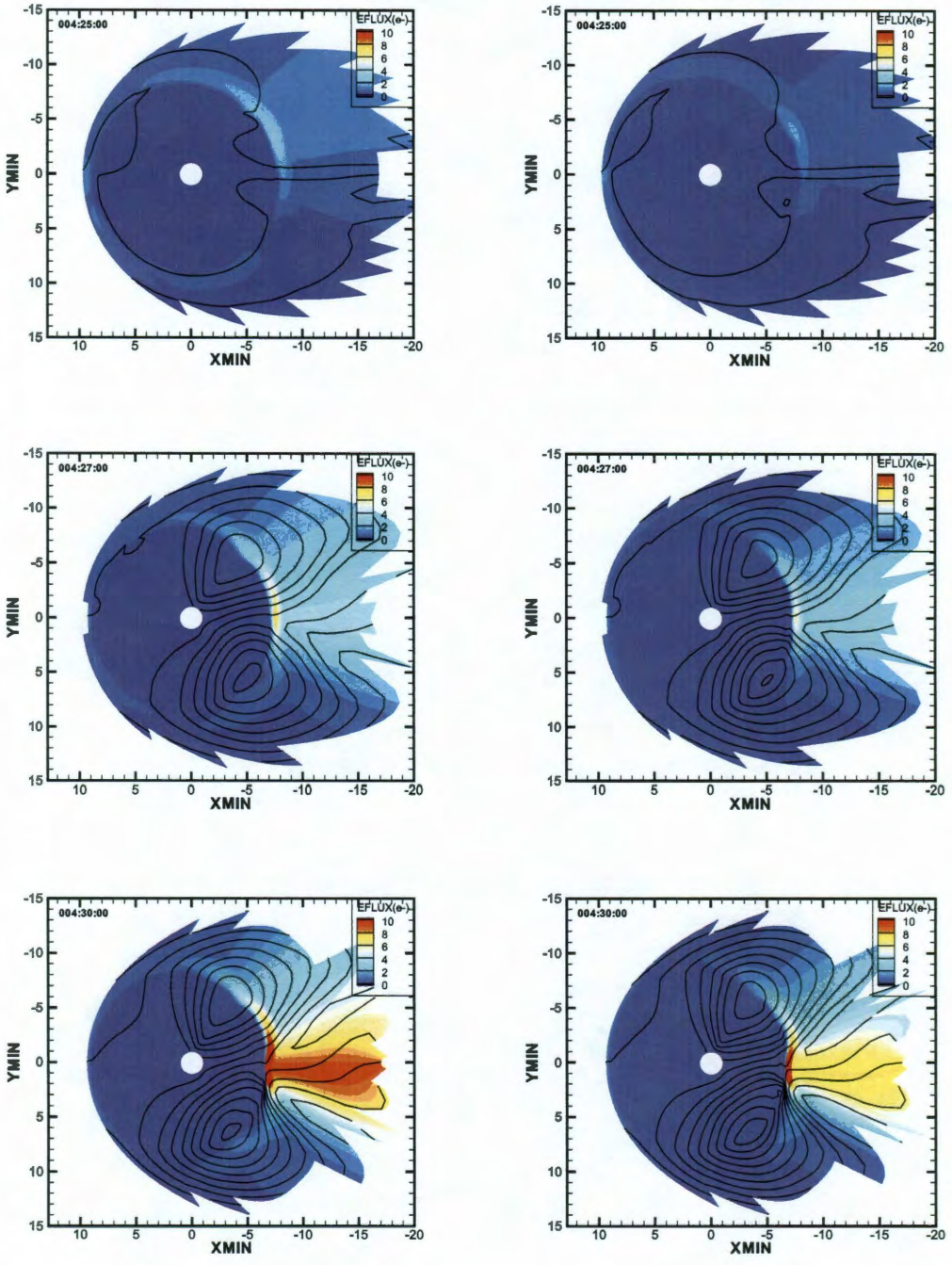

Figure 8.26 : Precipitating energy flux for the July 22, 1998 substorm event with a loss rate of 1/3(left) and 1(right) of strong pitch angle scattering at the expansion onset(top), 2 minutes(middle) and 5 minutes(bottom) after the expansion onset. The black lines are equipotential contours of ionospheric electric potential.

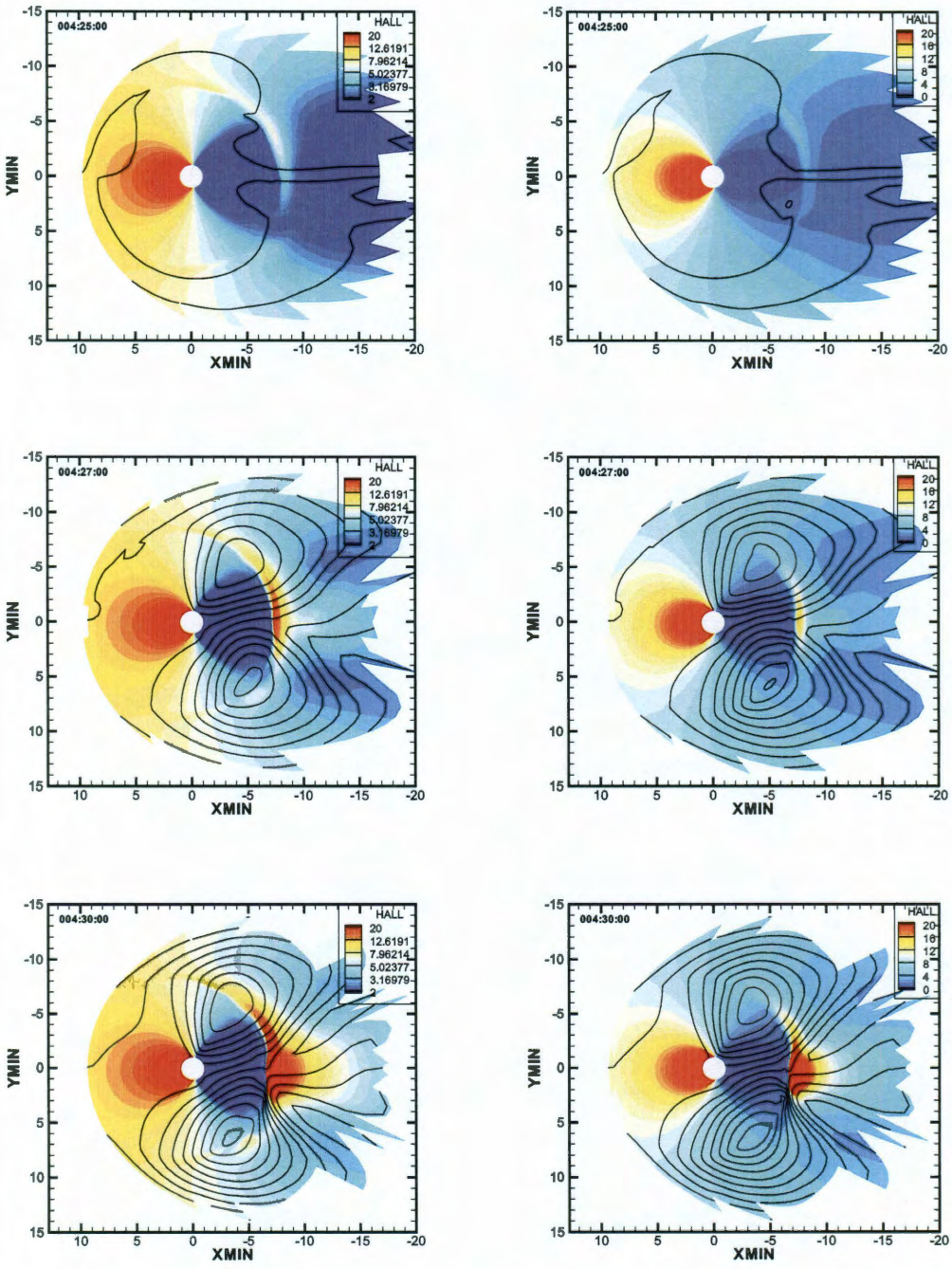

Figure 8.27 : Hall conductances for the July 22, 1998 substorm event with a loss rate of 1/3(left) and 1(right) of strong pitch angle scattering at the expansion onset(top), 2 minutes(middle) and 5 minutes(bottom) after the expansion onset. The black lines are equipotential contours of ionospheric electric potential.

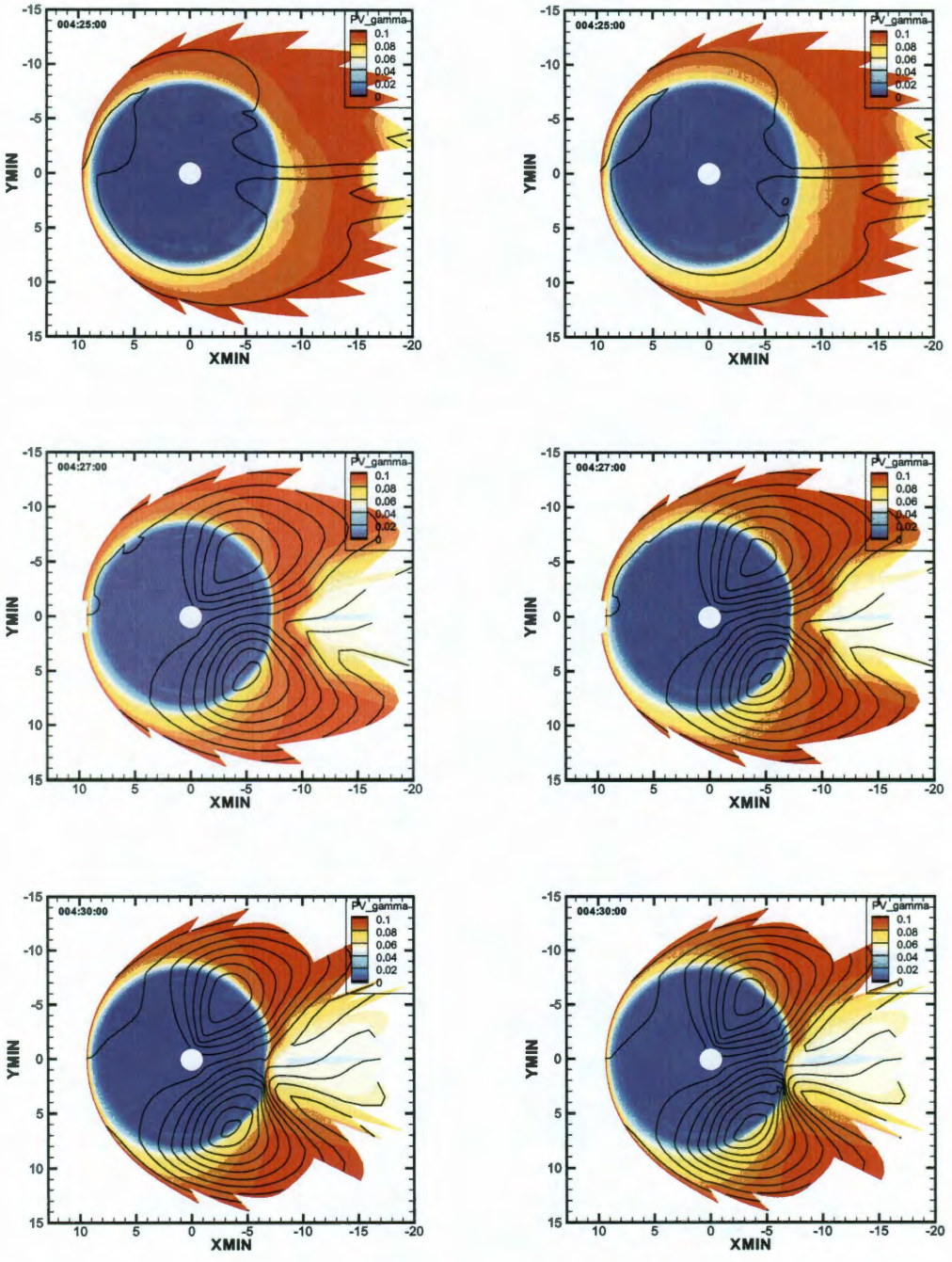

Figure 8.28 : Entropy for the July 22, 1998 substorm event with a loss rate of 1/3(left) and 1(right) of strong pitch angle scattering at the expansion onset(top), 2 minutes(middle) and 5 minutes(bottom) after the expansion onset. The black lines are equipotential contours of ionospheric electric potential.

Chapter 9

Parallel Electric Fields in an Isolated Substorm

The substorm current wedge is perhaps the most important recognizable feature in substorms. The ionospheric conductances produced by particle precipitation are, in the absence of calculation of optical emissions, the most direct indication of auroral structures and dynamics during the substorm expansion phase. Upward Birkeland currents in the wedge are carried mainly by downward magnetospheric electrons. These electrons are accelerated to overcome the magnetic mirror force and produce field-aligned currents. The auroral conductivity enhancement generated from the electric field acceleration is expected to be significant on the west edge of the substorm current wedge, where upward currents are observed as shown in the previous chapter. Taking into account parallel electric fields could potentially enhance the downward precipitating energy flux to the ionosphere. Including this effect in the RCM is thus important to reproduce the overall picture of an isolated substorm from the theoretical point of view, and also would eliminate the need for correction factors used and described in the previous chapter. Therefore, in this chapter we present our initial attempt at including effects of field-aligned potential drops in the RCM.

We are adding this important module into the RCM so that we could study substorm events with strong and localized upward field-aligned currents, something that the RCM was not able to do before. We are showing the simulations results by comparing a run with parallel electric fields and a run without them as already described in the previous chapter. Our main goal in this chapter is to present a

comprehensive overview of the results with this new module.

9.1 Run Setup

We are still going to discuss the simulation results of the July 22, 1998 substorm event. The magnetic field is modified from Tsyganenko T89 magnetic field model and mainly consistent with observation at Geotail location. The simulation starts at 0230 UT. The RCM was run with steady inputs for 4 hours from 0230 UT to 0630 UT, in order to bring the system to an approximate steady state[21]. The growth phase lasted from 0630 UT to 0655 UT. The substorm expansion started around 0655 UT. The magnetic field dipolarized between 0655 UT and 0700 UT. The electric field is computed self-consistently with the potential electric field calculated from the fundamental equation of magnetosphere-ionosphere coupling. For the runs with parallel electric fields, we turn the parallel electric field on after 4 hours of steady state convection. The Birkeland currents are calculated by the Vasyliunas equation through the magnetospheric pressure gradient. The generalized Knight relation derived and discussed earlier in Chapter 6 is used to convert the field-aligned currents to the field-aligned potential drops. The plasma sheet electron distribution is assumed to be bi-kappa. The precipitating electron energy flux is calculated by assuming bi-kappa distribution and given field-aligned potential drops. The average precipitating electron energy is computed by the ratio of energy flux and number flux. Robinson's formula is used to evaluate the precipitation part to the ionospheric conductances. The run without parallel electric fields has the energy flux floor but no Hardy normalization. The run with parallel electric field has no correction. The acceleration of electrons by the parallel electric fields should be able to produce high enough conductances at nightside further in the magnetotail. Parallel electric fields enter the

RCM calculation at two places. Besides the conductance enhancement, the parallel electric field is used to obtain plasma drifts in the inertial magnetospheric frame by subtracting parallel drops from the ionospheric potential in the rotating frame. Thus, we expect both ionospheric electric fields and magnetospheric particle dynamics to be affected by inclusion of parallel potential drops.

Figure 9.1 shows a time sequence of the plasma entropy parameter a few minutes in the growth phase after we turn on the calculation of parallel potential drops. At 10 seconds in the growth phase, the entropy doesn't change much. However, it changes dramatically after 10 more seconds. There is a significant decrease in the entropy between 00 UT and 02 UT. A small bump of low entropy region also appears at 22 UT. At 30 seconds in the growth phase, the peak of low entropy region at midnight has separated into two peaks. So three peaks of low entropy regions, with blue color in the center and yellow color around, stand at 22 UT, 00 UT, and 02 UT. In the next 2 minute, this three branches are azimuthally wavy and radially flexible. More plasma penetrate into low entropy area. The peaks then shrink back to geosynchronous orbit. The peak at 02 UT is the first one to disappear. One and a half minute later, the two peaks left begin to combine together. They become single low entropy area in pre-midnight sector after 7 minutes in the growth phase. This area further shrinks due to penetration from more plasma. This picture indicates that even before the expansion phase, parallel electric fields affect the solutions in such a way as to prevent a steady-state unstructured solution from persisting. To what extent this is physical and how much the numerics affect the solution is difficult to tell at this point.

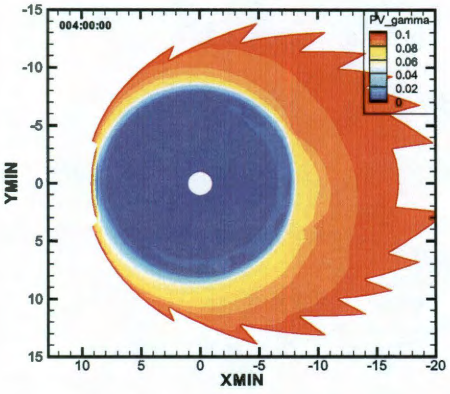
004:00:00
PV_gamma
0.1
0.08
0.06
0.04
0.02
0
YMIN
XMIN

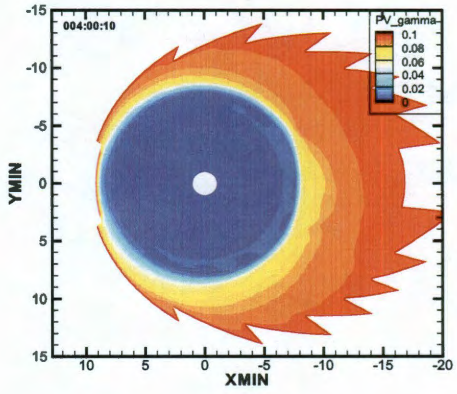
004:00:10
PV_gamma
0.1
0.08
0.06
0.04
0.02
0
YMIN
XMIN

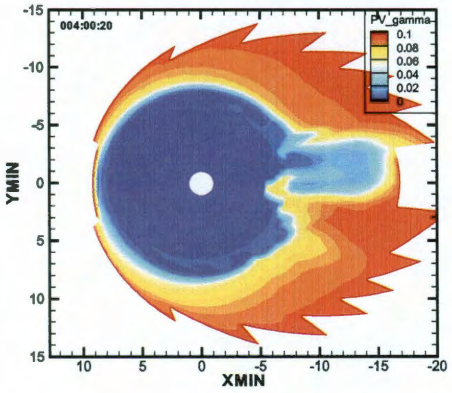
004:00:20
PV_gamma
0.1
0.08
0.06
0.04
0.02
0
YMIN
XMIN

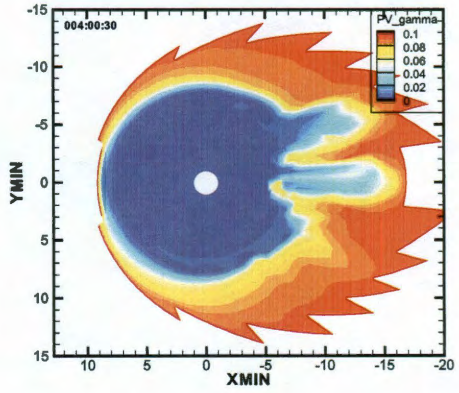
004:00:30
PV_gamma
0.1
0.08
0.06
0.04
0.02
0
YMIN
XMIN

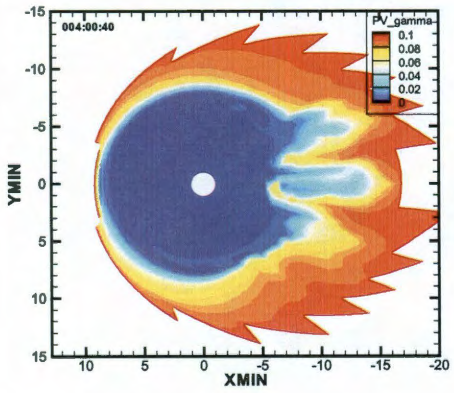
004:00:40
PV_gamma
0.1
0.08
0.06
0.04
0.02
0
YMIN
XMIN

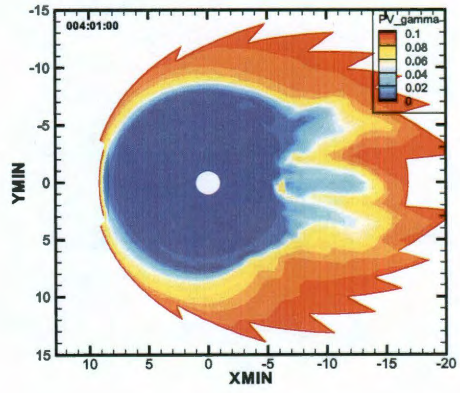
004:01:00
PV_gamma
0.1
0.08
0.06
0.04
0.02
0
YMIN
XMIN

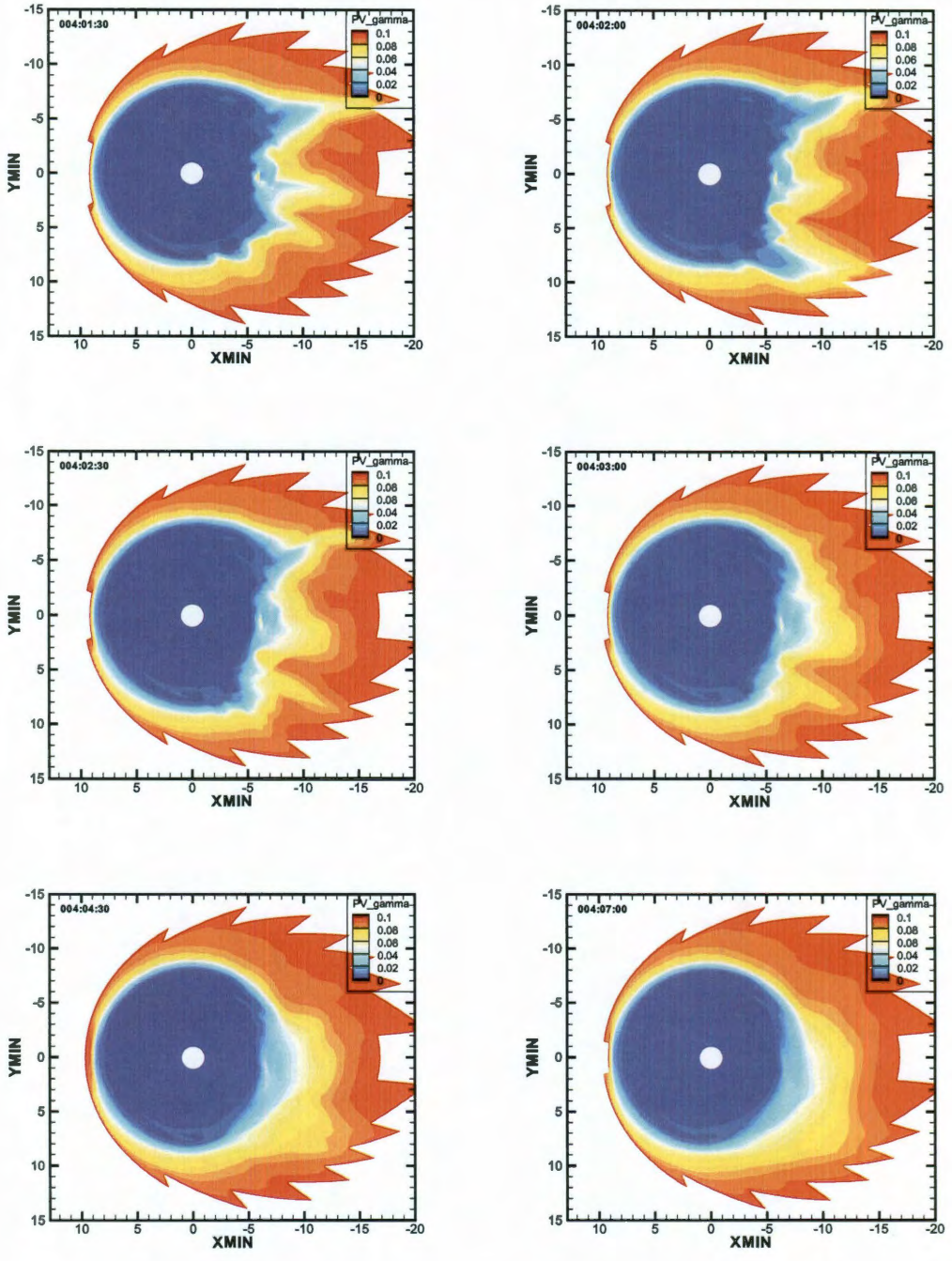

Figure 9.1 : Entropy of substorm run with parallel electric field at the beginning of growth phase, 10 seconds, 20 seconds, 30 seconds, 40 seconds, 1.0 minute, 1.5 minutes, 2.0 minutes, 2.5 minutes, 3 minutes, 4.5 minutes, 7 minutes in the growth phase.

9.2 Comparison of Entropy

The most important feature is still the bubble injection. We will keep examining the difference of plasma entropy, as shown in Figure 9.2, without and with the parallel electric fields. At the expansion onset, the bubble with low entropy is coming in from the tailward boundary. The spatial structures of entropy at about 8 R_E are quite similar in these two runs. However, for the run with parallel electric field, the plasma are more spread out as discussed in previous section. There is less plasma in post-dusk and pre-midnight sectors between 8 R_E and 10 R_E. Some particles in this region have penetrated to the geosynchronous orbit. This is caused by large and structured electric fields causing motion of plasma due to the difference between ionospheric electric potential and magnetospheric electric potential. In the expansion phase, the bubble still is injected into the inner magnetosphere. However, the ionospheric electric field at the west edge of the bubble is smaller for the run with parallel electric fields. The electric field is greater at the east edge of the bubble. So the east edge of the bubble is more flat than the west edge. In addition, the entropy in the dawn side is still lower in the run with parallel electric fields than the run without. Injection is a little bit quicker so that the channel with low entropy is connected with the extreme low entropy region within 7 R_E.

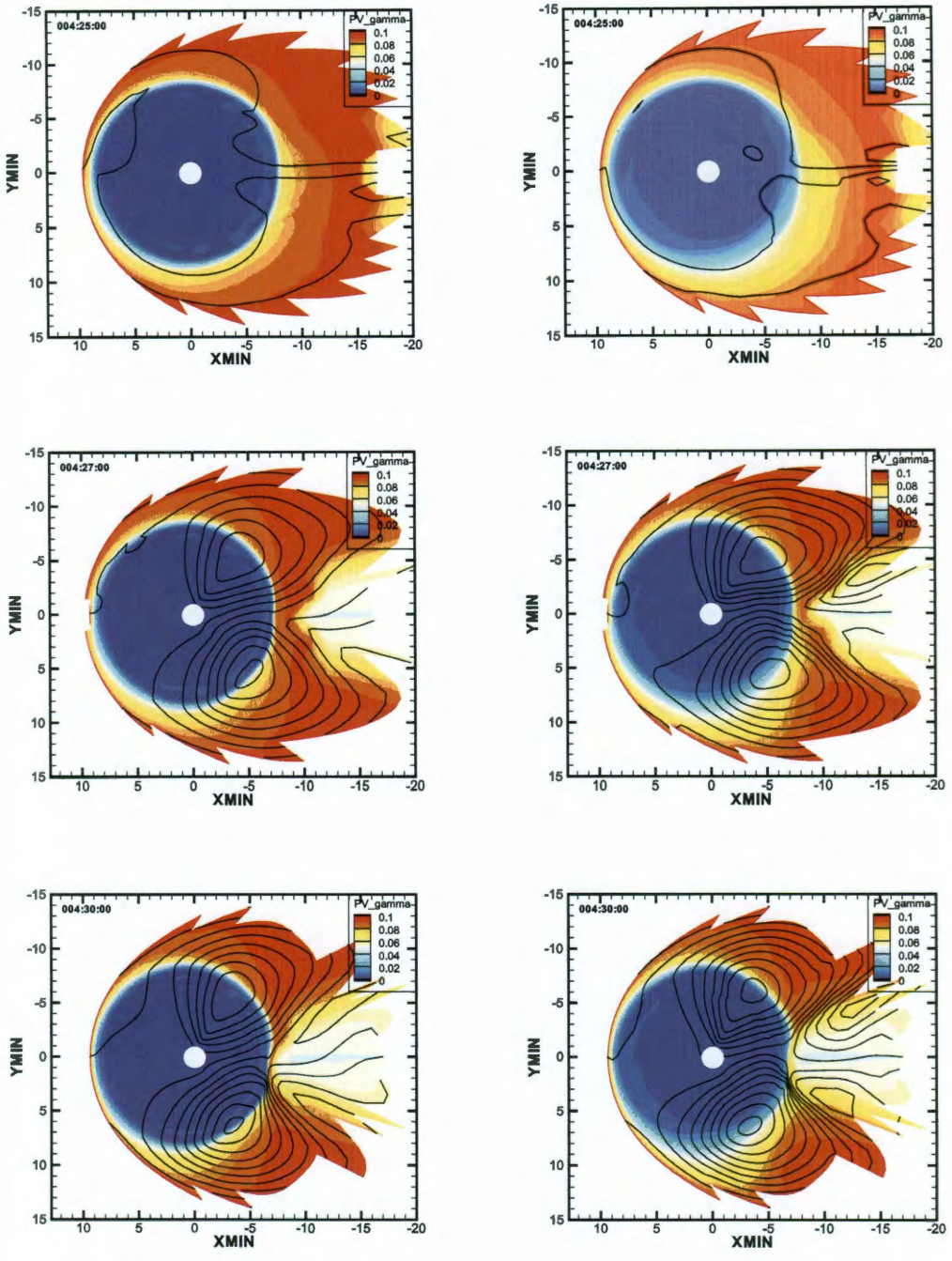

Figure 9.2 : Entropy right after expansion onset (top), 2 minutes after expansion onset (middle), 5 minutes after expansion onset (bottom) for the runs without (left) and with (right) parallel electric fields. The black lines show ionospheric equipotential contours with 5 keV spacing.

9.3 Comparison of Birkeland Currents

Next, we turn our attention to the current wedge. The downward field-aligned currents on the east edge of the wedge and the upward field-aligned currents on the west edge of the wedge are essential in forming westward electric field inside the bubble and its earthward motion. Figure 9.3 shows the Birkeland currents at the end of growth phase, the beginning of the expansion phase, 2 minutes and 5 minutes in the expansion phase. The Birkeland currents in the growth phase are pretty much the same at the end of the growth phase. The region-2 field-aligned currents in the run without field-aligned potential drop are more localized and stronger. The Birkeland currents outside 7 R_E are stronger in the run with parallel electric field especially in the dawn side and nightside. The second difference is at the region about 9 R_E at 03 UT. The run without parallel electric fields show upward field-aligned currents while the run with parallel electric fields show downward field-aligned current. The third difference is a stripe in the dawnside also about 9 R_E. The downward Birkeland currents changed to upward Birkeland currents in the with parallel electric fields. At the expansion onset, the substorm current wedge appears at the tailward boundary. In the expansion phase, the run with parallel electric fields seems to have quicker drift velocity of the bubble.

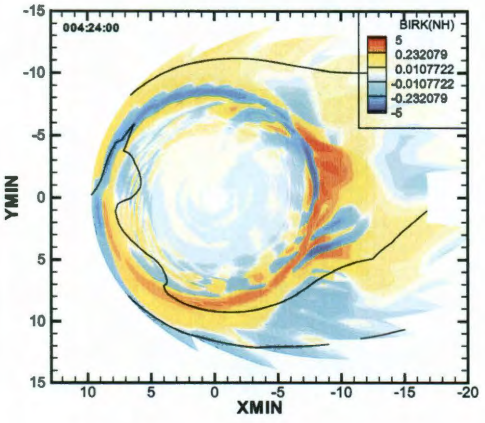
004:24:00
BIRK(NH)
5
0.232079
0.0107722
-0.0107722
-0.232079
-5
YMIN
XMIN

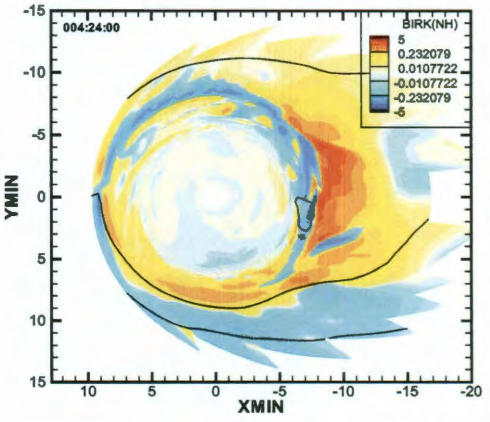
004:24:00
BIRK(NH)
5
0.232079
0.0107722
-0.0107722
-0.232079
-5
YMIN
XMIN

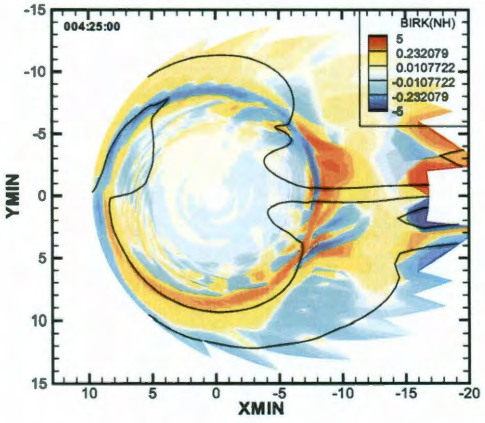
004:25:00
BIRK(NH)
5
0.232079
0.0107722
-0.0107722
-0.232079
-5
YMIN
XMIN

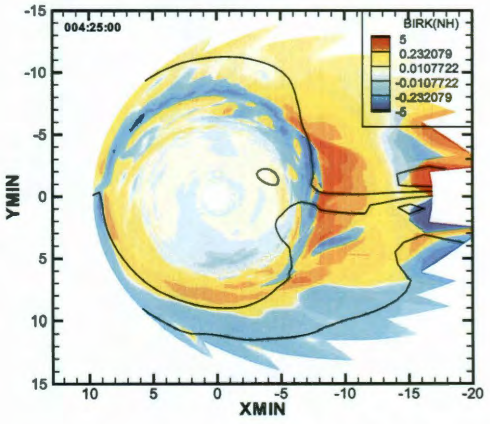
004:25:00
BIRK(NH)
5
0.232079
0.0107722
-0.0107722
-0.232079
-5
YMIN
XMIN

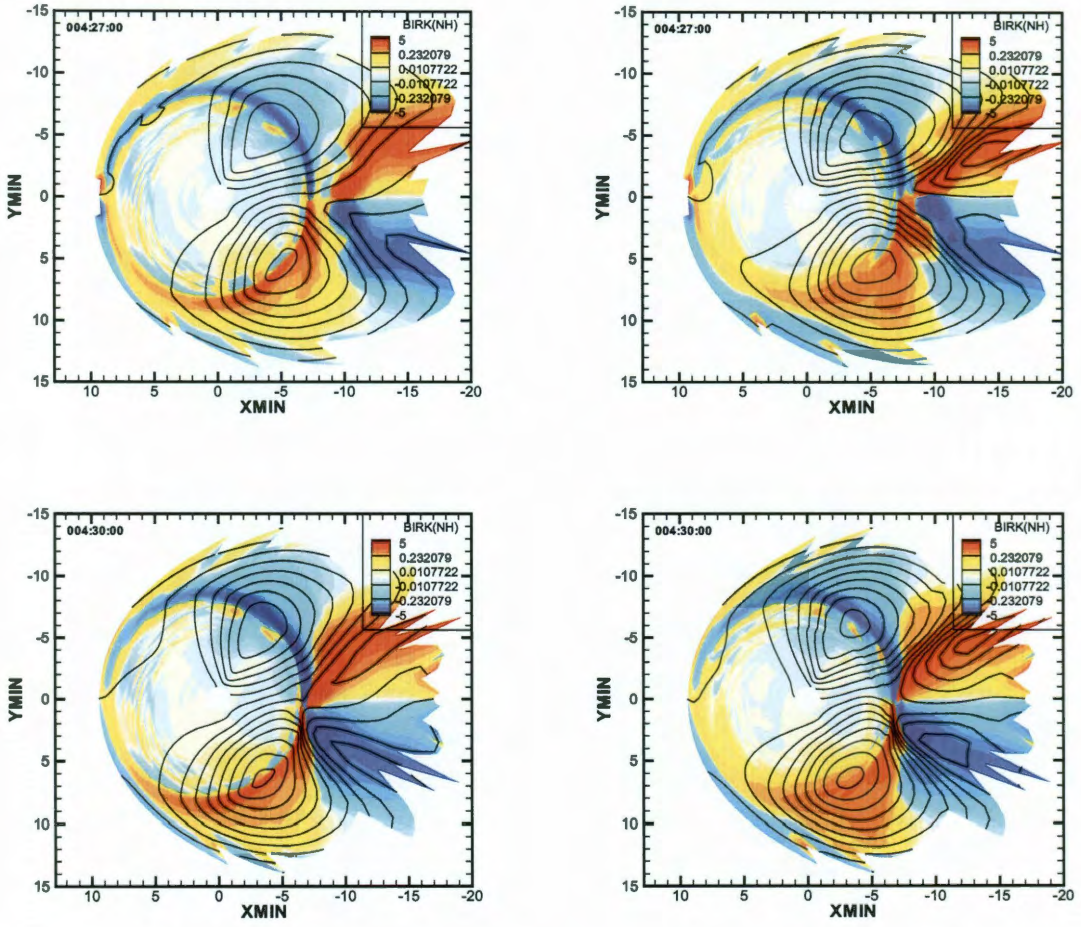

Figure 9.3 : Entropy at the end of growth phase(first row), right after expansion onset (second row), 2 minutes after expansion onset (third row), 5 minutes after expansion onset (forth row) for the runs without (left) and with (right) parallel electric fields. The black lines show ionospheric equipotential contours with 5 keV spacing.

9.4 Comparison of Precipitating Energy Fluxes

As mentioned earlier, the run without parallel electric fields uses the energy flux floor so that the precipitating energy flux tailward of the peak at certain local times could not be lower than half of the peak value. In the run with parallel electric field, the

energy flux has a great contribution from the acceleration of the parallel electric fields, therefore, we removed the energy floor and Hardy normalization. Figure 9.4 presents a comparison of the two cases. In the growth phase, there is an azimuthal band between 5 R_E and 7 R_E with energy flux between 0.1 and 1 per square centimeter per second per sterradian in the run without parallel electric fields. This ring is mainly symmetric except for the local time around 15 UT. It is because that electrons undergo more dynamics motion and reluctant to penetrate into geosynchronous orbit. Also, the acceleration of parallel electric field increases the electron loss rate especially in the dawnside with upward field-aligned currents, so there is less plasma in the band region. In the substorm expansion phase, a strong peak stands in the night side about 7.5 R_E since the bubble pushed in some plasma in the night side earthward. The run without parallel electric field gives much higher energy flux in the night side where the plasma bubble comes in. So the energy flux inside the bubble could be much higher than values of the edges of the bubble. On the other hand, for the run with parallel electric fields, the enhancement of particle precipitation appears only on the west edge of the bubble where upward field-aligned currents exist.

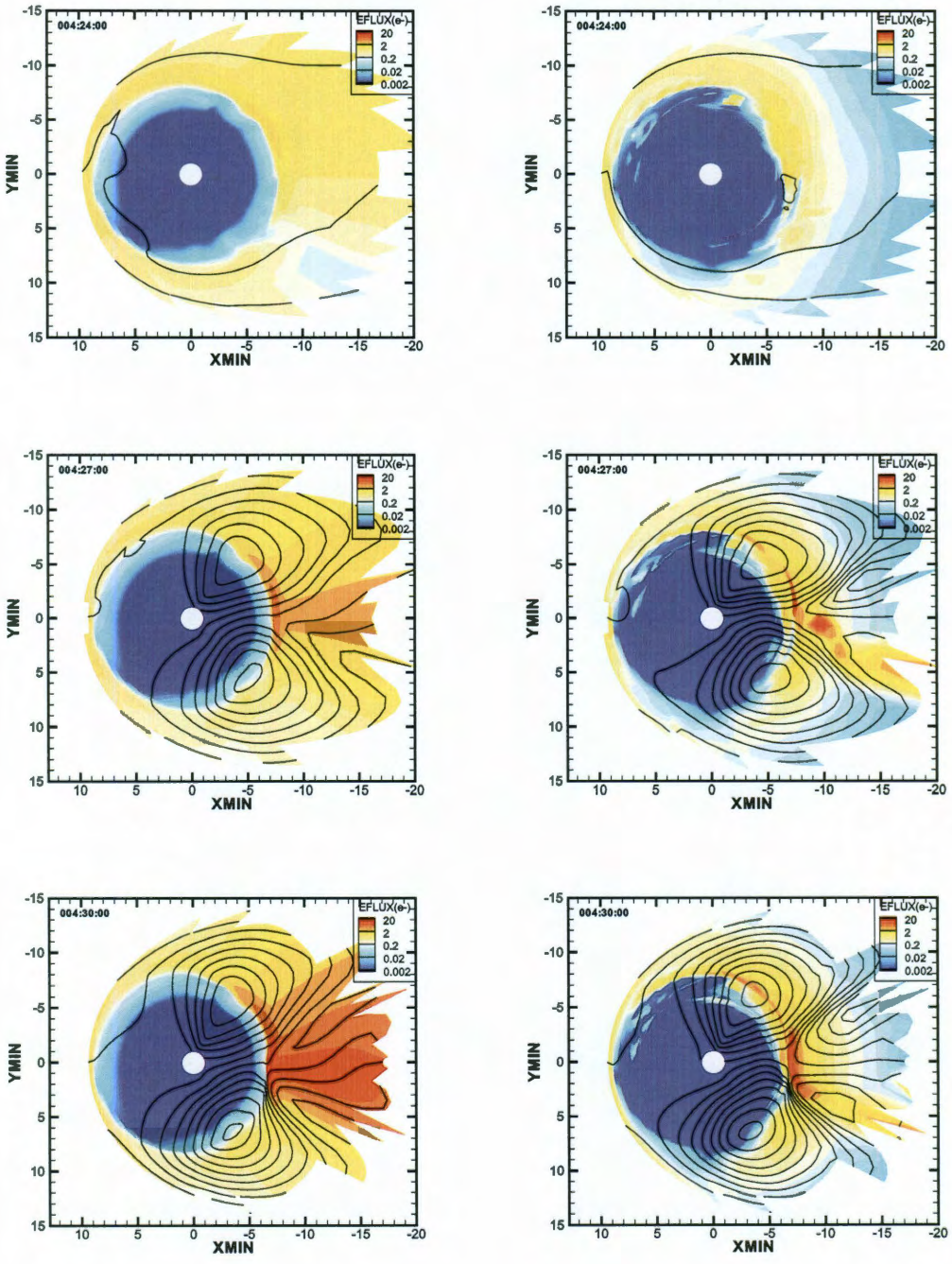

Figure 9.4 : Precipitating electron energy flux at the end of growth phase(top), 2 minutes after expansion onset (middle), 5 minutes after expansion onset (bottom) for the runs without (left) and with (right) parallel electric fields. The black lines show ionospheric equipotential contours with 5 keV spacing.

9.5 Comparison of Ionospheric Conductances

We again use the Hall conductances to illustrate the difference between the two runs as Figure 9.5. The ionospheric conductances are calculated by taking the square root of the sum of the squares of solar radiation and particle precipitation. The dayside ionospheric conductances are dominated by the solar EVU contribution. The nightside ionospheric conductances are dominated by the contribution from energetic particle precipitation. In the growth phase, the Hall conductances in the run without parallel electric fields show a symmetric pattern except for a band between midnight and dawnside about 8 R_E. This is because plasma sheet electrons drift eastward due to the gradient/curvature drifts around the Earth. The Hall conductances for the run with parallel electric fields show some enhancement due to higher energy fluxes. During the expansion phase, the ionospheric conductances are higher inside the bubble on the left figures, while strengthened mainly on the west edge of the bubble on the right figures. It means we cannot get westward electrojet during substorm simulation with parallel electric field. Since the ionospheric conductances are calculated from statistical formula based on precipitating flux and energy, it is necessary to introduce a new way of calculation for either more precipitating particles or stronger conductances for the same flux. Since lower ionospheric conductances tend to result in stronger convection electric fields (and vice versa), the run with parallel electric field tends to have stronger potential electric fields on the east edge of the bubble and also weaker electric field on the west edge of the bubble.

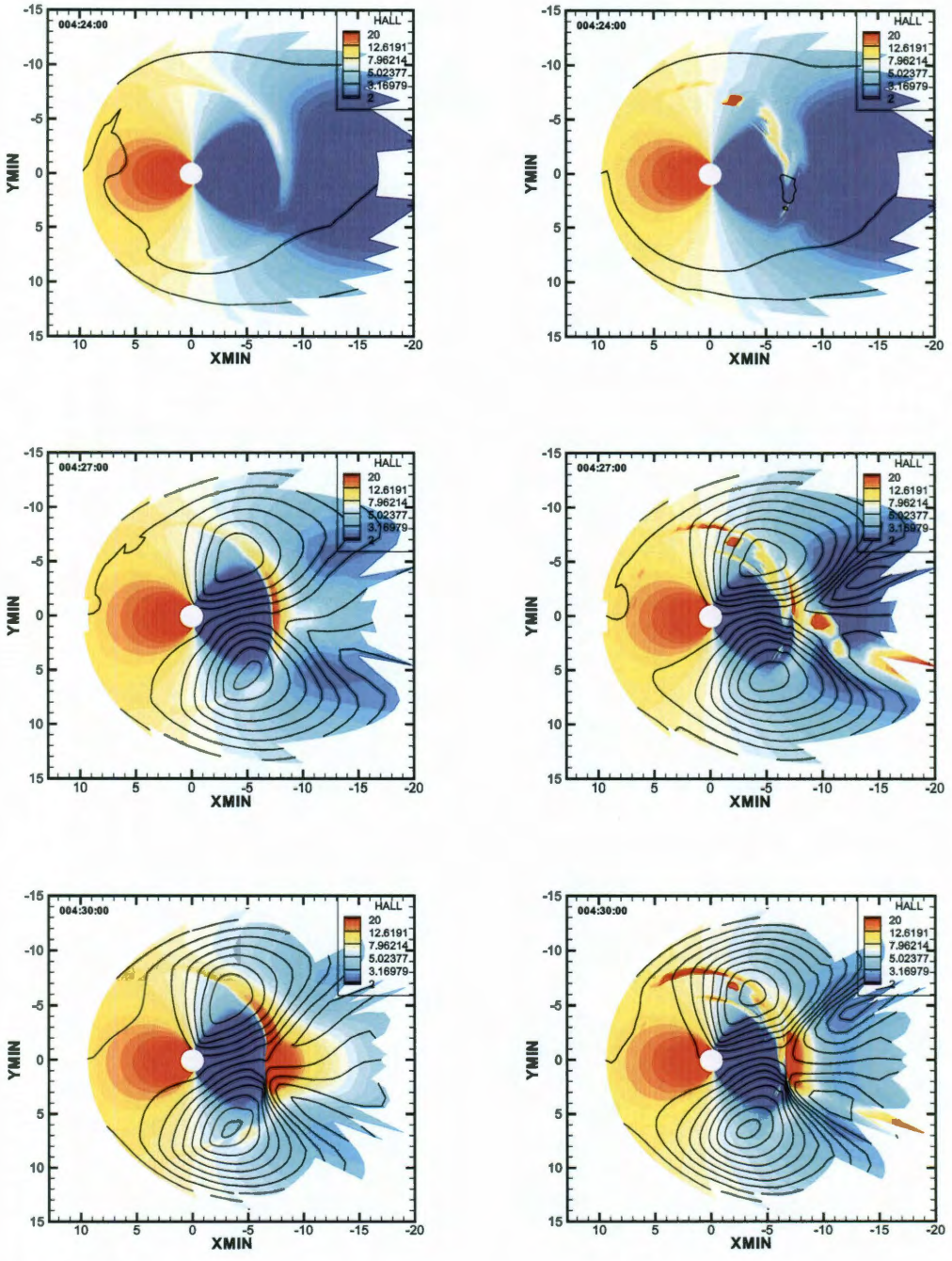

Figure 9.5 : Precipitating electron energy flux at the end of growth phase(top), 2 minutes after expansion onset (middle), 5 minutes after expansion onset (bottom) for the runs without (left) and with (right) parallel electric fields. The black lines show ionospheric equipotential contours with 5 keV spacing.

9.6 Discussions

In this chapter, we presented the simulation results of July 22, 1998 isolated substorm event both without and with parallel electric field. The plasma bubble with lower plasma content penetrates into the inner magnetosphere from the tailward boundary. The parallel electric field is strong in the upward field-aligned currents region. It also enhanced the electron precipitation and thus ionospheric conductances. The addition of parallel potential drops turns out to complicate the physical picture of the substorm injection more than one might expect based on simple theoretical considerations.

9.6.1 Parallel Electric Fields

We examined the role of parallel electric fields in the run of substorm event. Figure 9.6 shows the relation between Birkeland currents and parallel potential drops. One result of our simulation is existence of parallel potential drops almost everywhere throughout the simulation domain, with large values being present in the region of upward Birkeland currents. This result is not unexpected, as some sort of parallel potential drops ought to be present in the diffuse aurora where currents are upward. However, noticeable parallel potential drops in regions around the inner edge of the electron plasma sheet (where electron fluxes are low) are most likely to be an artifact of our algorithm and should be considered unphysical. In the expansion phase, the parallel electric fields appear in the west edge of the bubble with the upward field-aligned currents, and these are probably physical.

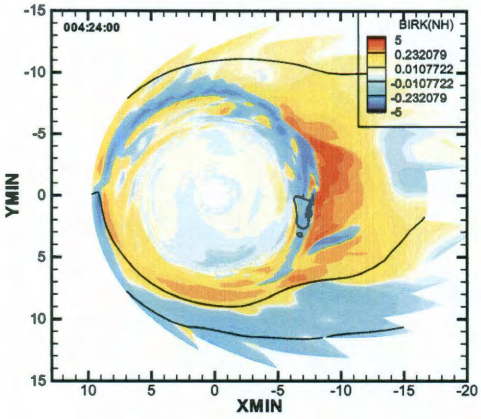
004:24:00
BIRK(NH)
5
0.232079
0.0107722
-0.0107722
-0.232079
-5
YMIN
XMIN

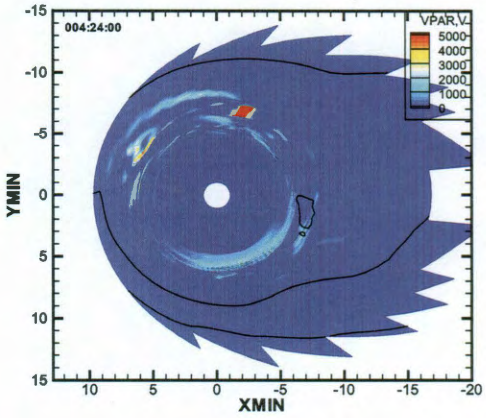
004:24:00
VPAR,V
5000
4000
3000
2000
1000
0
YMIN
XMIN

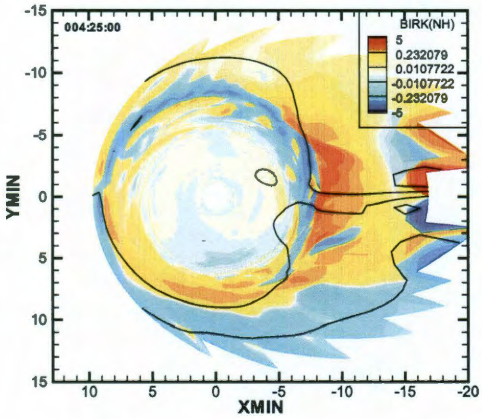
004:25:00
BIRK(NH)
5
0.232079
0.0107722
-0.0107722
-0.232079
-5
YMIN
XMIN

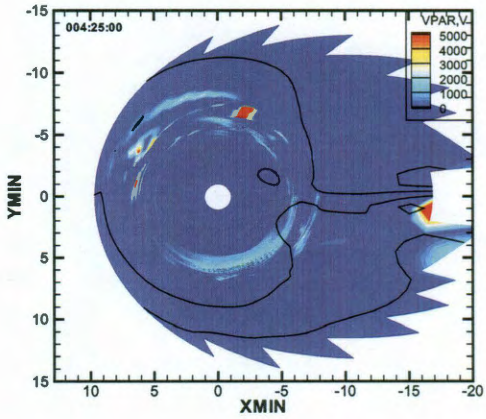
004:25:00
VPAR,V
5000
4000
3000
2000
1000
0
YMIN
XMIN

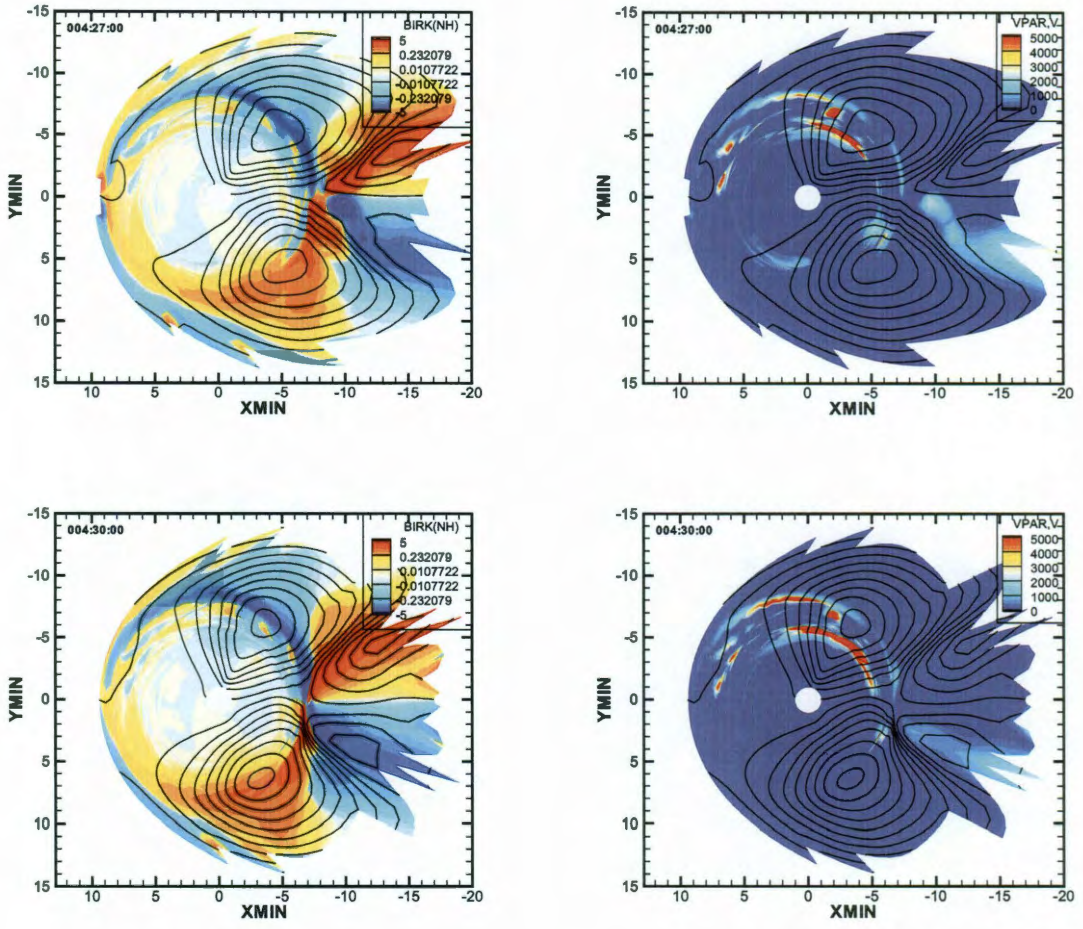

Figure 9.6 : Birkeland currents (left) and parallel potential drop (right) at the end of growth phase(first row), right after expansion onset (second row), 2 minutes after expansion onset (third row), 5 minutes after expansion onset (forth row). The black lines show ionospheric equipotential contours with 5 keV spacing.

9.6.2 Auroral Signatures

Some comparisons have been shown in the equatorial plane, but it is still helpful to be compared in the ionosphere. Figure 9.7 shows a comparison of Birkeland currents on the ionosphere. In general, the run with parallel electric fields has more structures

due to disturbed motion of plasma in the magnetosphere. In the growth phase, the upward field-aligned currents are much thicker in the run with parallel electric fields. There is also an arc of downward field-aligned currents nearly parallel to the upward region-2 field-aligned currents but more equatorward. At the expansion onset, the substorm onset is mapped to the high-latitude boundary of the RCM modeling region. The downward field-aligned currents form on the post-midnight sector. The upward field-aligned currents form on the pre-midnight sector. The downward Birkeland currents between the substorm current wedge and the region-2 field-aligned currents are stronger in the run with parallel electric fields. After 2 minutes, the substorm current wedge moves equatorward. It intersects with the region-2 field-aligned currents in the run with parallel electric fields. There are still several arcs in the equatorward side of the region-2 field-aligned currents. After 5 minutes after expansion onset, the substorm current wedge pushes the region-2 field-aligned currents equatorward. In the run without parallel electric fields, the region-2 Birkeland currents are also dragged a little bit to the dawn side due to strong asymmetric westward electric fields inside the bubble. Again, we must conclude that the run with parallel potential drops does produce a stronger enhancement on the westward edge of the bubble, but the overall auroral pattern is too structured and is probably influenced by numerical artifacts.

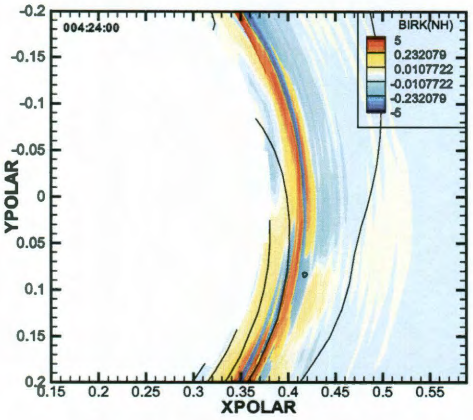
004:24:00
BIRK(NH)
5
0.232079
0.0107722
-0.0107722
-0.232079
-5
YPOLAR
XPOLAR

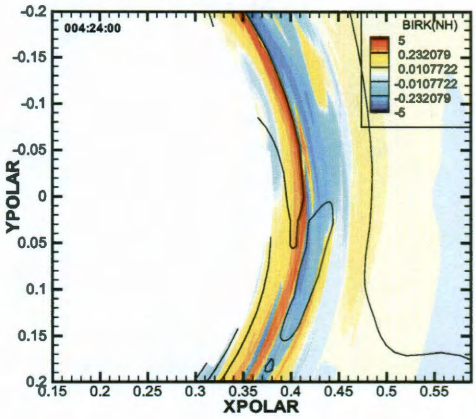
004:24:00
BIRK(NH)
5
0.232079
0.0107722
-0.0107722
-0.232079
-5
YPOLAR
XPOLAR

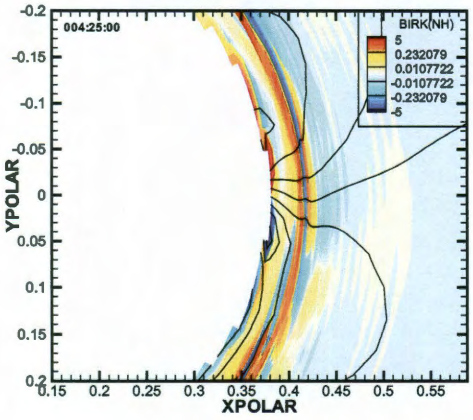
004:25:00
BIRK(NH)
5
0.232079
0.0107722
-0.0107722
-0.232079
-5
YPOLAR
XPOLAR

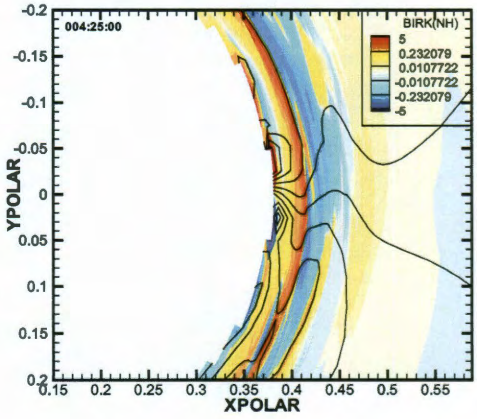
004:25:00
BIRK(NH)
5
0.232079
0.0107722
-0.0107722
-0.232079
-5
YPOLAR
XPOLAR

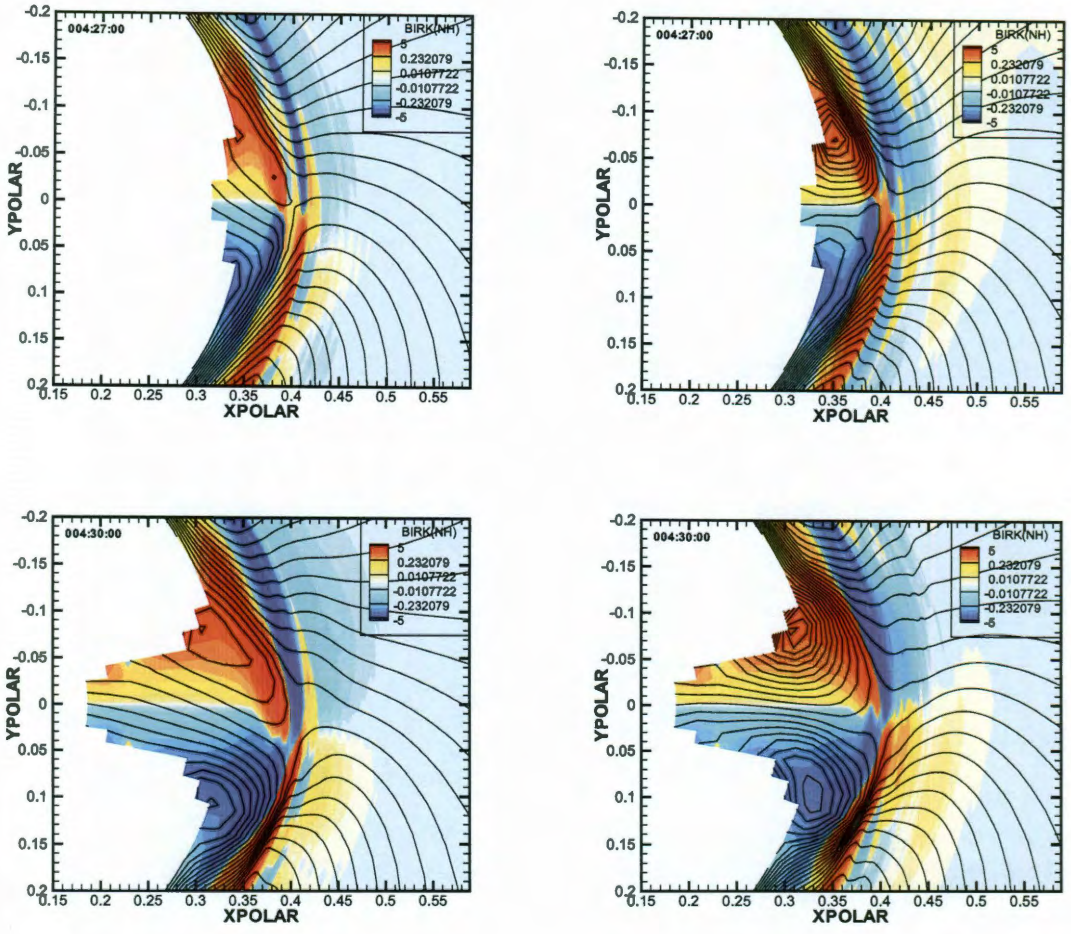

Figure 9.7 : Birkeland currents at 1 minute before expansion onset (first row), right after expansion onset (second row), 2 minutes after expansion onset (third row), 5 minutes after expansion onset (fourth row) for the runs without parallel electric fields (left) and with parallel electric fields (right). The red region is eastward electric fields. The blue region is westward electric fields. The black lines show ionospheric equipotential contours with 2 keV spacing.

For the precipitating energy flux shown in Figure 9.8, there are two bands in the run without parallel electric fields in the growth phase. The poleward band tends to have stronger energy flux than the equatorward one. However, there are three bands in the run with parallel electric fields. The poleward band and the

equatorward band have lower energy flux, while the middle one has higher energy flux. The most poleward band is a direct consequence of not setting the energy flux floor. The brightening arc is a little equatorward but closer to midnight sector instead of post-midnight sector. In the expansion phase, the modeling region moves poleward. Because of the energy flux floor in the run without parallel electric fields, the energy flux poleward of the peak for each local time is at least half of the peak value. In the run with parallel electric fields, the peak is poleward to the one already exists since the growth phase and only in the dawn side. Furthermore, more flux are precipitating only in the dusk side edge of the bubble. There is a lower energy flux band equatorward of the flux peak for both runs but highly structured in the run with parallel electric fields.

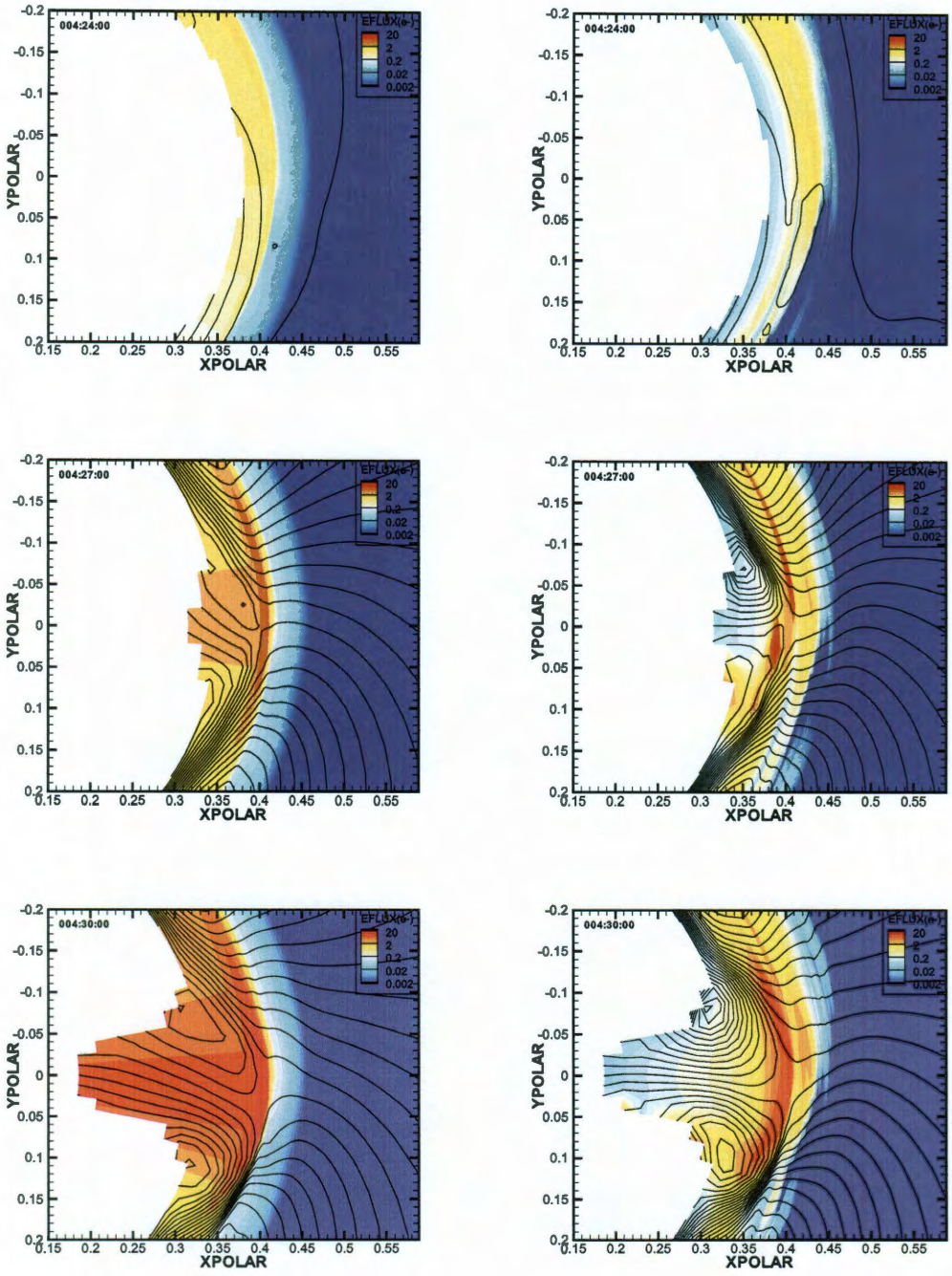

Figure 9.8 : Precipitating electron energy flux at 1 minute before expansion onset (top), 2 minutes after expansion onset (middle), 5 minutes after expansion onset (bottom) for the runs without parallel electric fields (left) and with parallel electric fields (right). The red region is eastward electric fields. The blue region is westward electric fields. The black lines show ionospheric equipotential contours with 2 keV spacing.

The nighside Hall conductance is related to the square root of the precipitating energy flux. Figure 9.9 shows the Hall conductances in the night side, which has a better view than the precipitating energy flux. Both runs have a band structure, but the band in the run with parallel electric fields is wider and maximum value is also larger. There is a relatively low conductance region about 22 UT because of the lack of electrons drifting to there. During the expansion phase, the conductance enhanced by the particle precipitation is very clear and poleward to the existing peak for the run with parallel electric fields. The conductance in the bubble is lower so that the westward electric field is stronger.

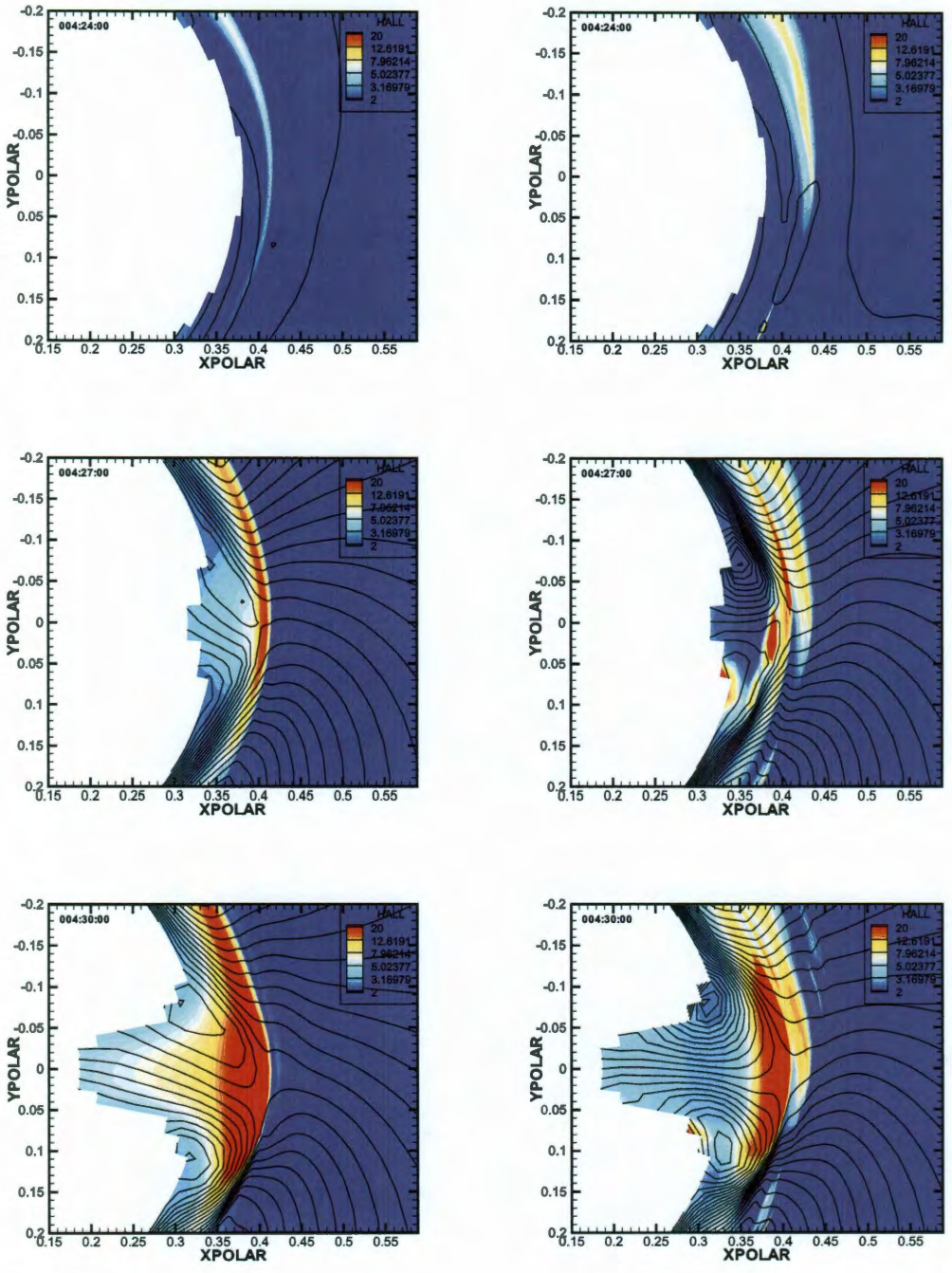

Figure 9.9 : Hall conductances at 1 minute before expansion onset (top), 2 minutes after expansion onset (middle), 5 minutes after expansion onset (bottom) for the runs without parallel electric fields (left) and with parallel electric fields (right). The red region is eastward electric fields. The blue region is westward electric fields. The black lines show ionospheric equipotential contours with 2 keV spacing.

9.6.3 Transport of Magnetic Flux

Similar to using the integral of the ionospheric electric fields as a polar cap potential drop to indicate the strength of convection, we could use the integral of magnetospheric electric fields to represent the rate of transport of magnetic flux earthward in the tail. Figure 9.10 shows some comparisons between computed parameters and values deducted form Geotail observations for the run without parallel electric fields, including magnetic field normal to the current sheet, the x component of plasma velocity, the y component of electric fields at Geotail location, and magnetic flux transport as computed by the integration $\int E_y dt$. The observed B_n is an approximation of the published result[21]. The results of drift velocity and electric fields indicate that the inductive electric fields dominate when Geotail observed fast earthward flow[21]. The RCM is unable to represent the wavy structures as the effects of waves bouncing back and forth. To represent the bubble injection during the substorm, the RCM needs to recover the total magnetic flux in the bubble and the entropy inside the bubble. This magnetic flux is pretty good in the first 5 minutes of the expansion phase, which is expected as the run was set up in part to obtain a good agreement.

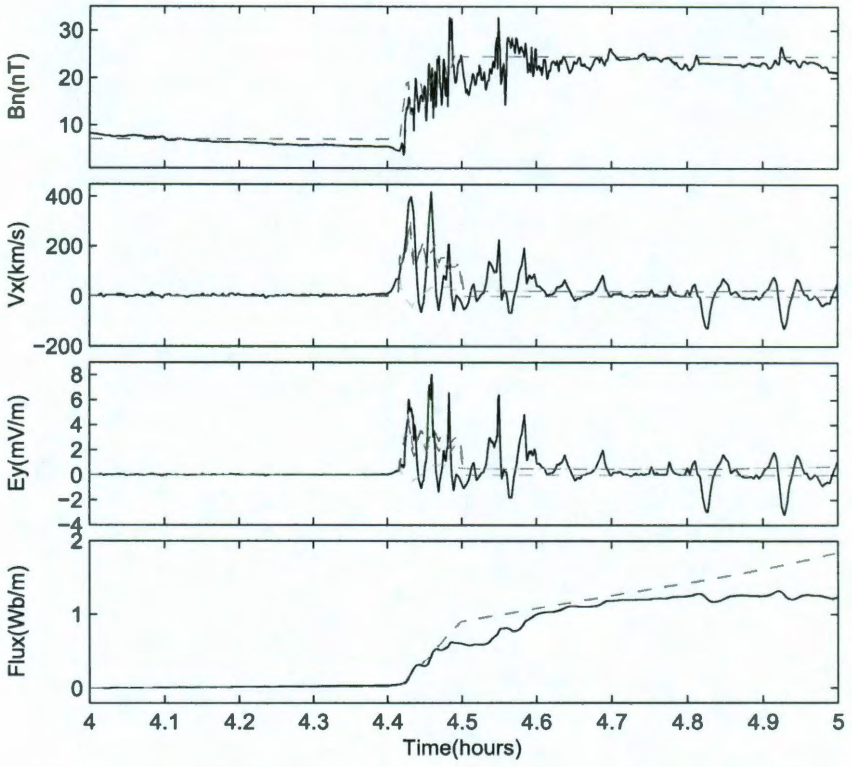

Figure 9.10 : Geotail data (black) and their comparison with the RCM simulation results for the run without parallel electric fields (red) from 0630 UT to 0730 UT during the July 22, 1998 substorm event. Four figures from top to bottom are magnetic field component normal to the current sheet, plasma velocity x component, electric field y component, magnetic flux transport. The blue and green curves represent induction and potential electric field effects.

The same quantities are shown for the run with parallel electric fields in Figure 9.11. For the first 5 minutes in the growth phase, both the drift velocity and the electric field have a wavy structure due the addition of parallel electric fields. Some spikes appear later in the run which could be in the same order or even large than the wavy structure in the observations. These effects are indicative of the chaotic motion the plasma could undergo in the simulation and that we attribute, at least in part, to numerical artifacts. Unlike the result in the run without parallel electric

field, the magnetic flux here shows good agreement with observation after 5 minutes in the expansion phase.

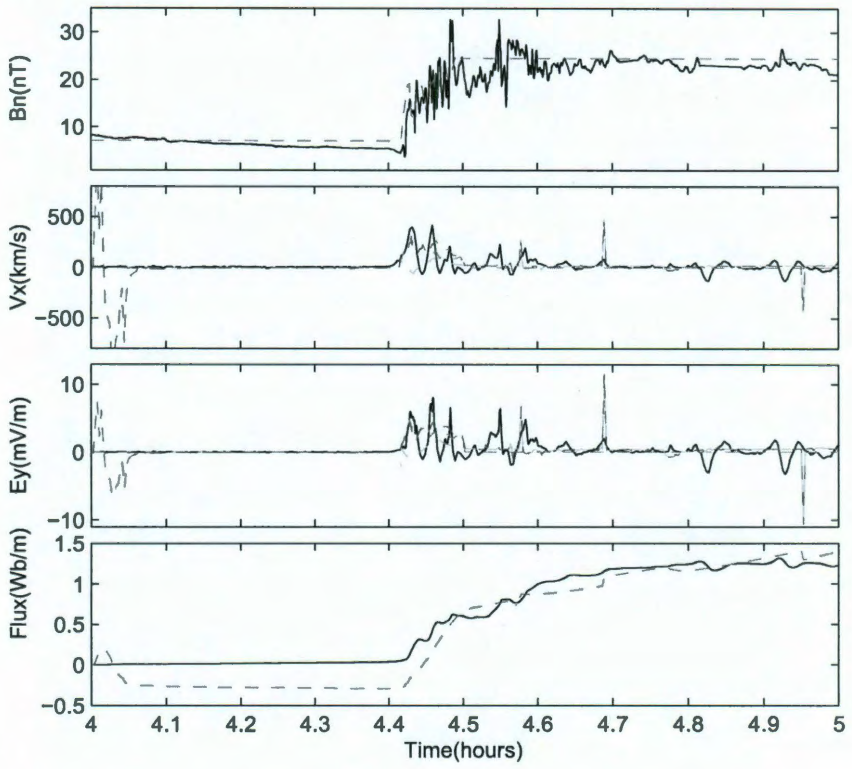

Figure 9.11 : Geotail data (black) and their comparison with the RCM simulation results for the run with parallel electric fields (red) from 0630 UT to 0730 UT during the July 22, 1998 substorm event. Four figures from top to bottom are magnetic field component normal to the current sheet, plasma velocity x component, electric field y component, magnetic flux transport. The blue and green curves represent induction and potential electric field effects.

The figures shown above use the calculation at -9 R_E in the midnight. However, the Geotail satellite moves slower than the Earth. The position of the satellite is always changing. On the other hand, we have simplified the problem in z direction in the RCM by adjusting the magnetic field relative to the current sheet. In the y

direction, the RCM ignores the change of IMF B_Y and assumes dawn-dusk symmetric of the magnetic field. The effect of this simplification and the moving satellite questions the validity of fixing the virtual satellite to the coordinate of (-9,0,0). Figure 9.12 shows the magnetic transport flux at 9 locations from -0.5 R_E to 0.5 R_E in y direction. The 9 curves show a clear tendency that the virtual satellite moving from dawn to dusk the flux is increasing. The main difference is for the part after 5 minutes in expansion phase although it is still noticeable during the first 5 minutes in the expansion phase.

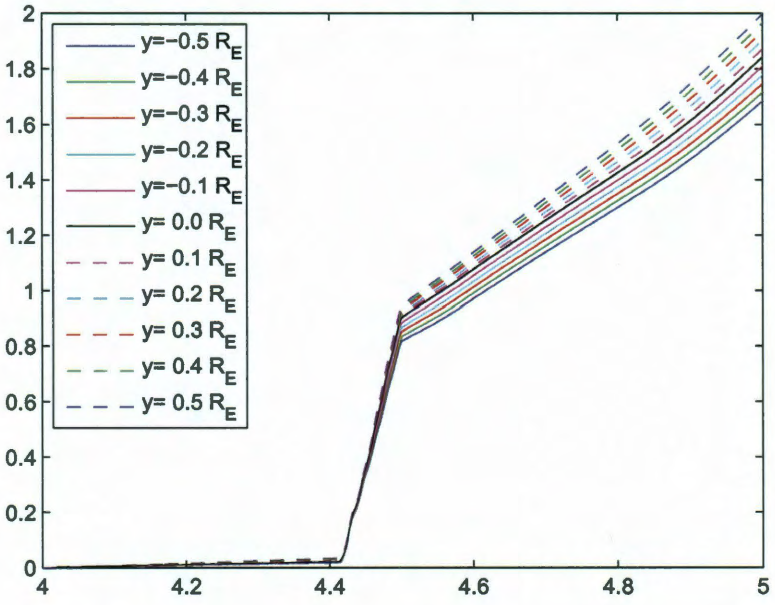

Figure 9.12 : Computed magnetic flux transport at 9 different locations with x fixed to -9 R_E and y ranging from -0.5 R_E to 0.5 R_E.

9.6.4 Plasma Injection

In our simulations, we carefully chose the boundary conditions to let the proton density, temperature, and pressure at (-9R_E,0,0) to be consistent with Geotail observations after 4 hours of initial run. The depleted level is also adjusted to let above quantities be comparable to Geotail values. In Figure 9.13, the right panel is at the Geotail location (-9R_E,0,0) and the left panel is at the geosynchronous orbit (-6.6R_E,0,0). Since the pressures are quite different between the grid point earthward and tailward of the Geotail location, the plasma parameters are calculated by the linear interpolation from the two grid points tailward of the Geotail location. During the dipolarization between 0655 UT and 0700 UT, the flux tube volume is oscillating because of the different mapping from the ionosphere grid points to the equatorial plane. Right after the expansion onset, the bubble is injected from the tailward boundary and pushes the plasma in the night side earthward. Several peaks can be seen in the figures of proton density, pressure, and also entropy. There is no significant peak in proton temperature. In the left figure, the dipolarization is very clear from 0655 UT to 0700 UT. The peaks of density, pressure, and entropy appear at 0700 UT. They start to increase about 2 minutes earlier instead of 0655 UT as in the right figure. The temperature has a peak about 2 minutes earlier, as a result of pushing in ring current plasma which stays about 7 R_E in the growth phase. These plasma keep drifting around the Earth and reduces the peak in temperature.

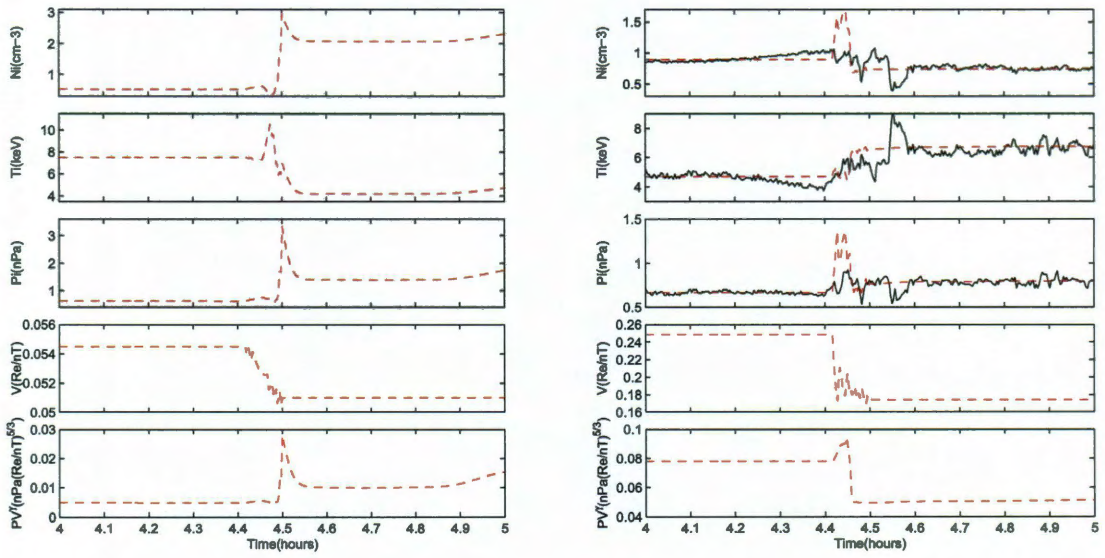

Figure 9.13 : Proton density, temperature, pressure, flux tube volume, and entropy during substorm growth phase and expansion phase at geosynchronous orbit (-6.6R_E,0,0) and Geotail position (-9R_E,0,0), black for Geotail observations and red for RCM results.

Figure 9.14 shows the same content but for the run with parallel electric field. A huge disturbance at 20 seconds in the growth phase could be seen in both figures. Some particles are drifting from 8 to 15 R_E earthward to the geosynchronous orbit. This results in a sudden decrease of proton density, temperature, pressure, and entropy in the Geotail location and a sudden increase in the geosynchronous orbit. These quantities almost recover to values in the run without parallel electric fields at the end of the growth phase. So the same peaks are found during the first 5 minutes in the expansion phase. At 10 minutes after expansion onset, the parameters show another set of peaks in the geosynchronous orbit due to some disturbance in pre-midnight sector. The peaks have nearly the same magnitude compared to the peaks created by bubble injection. It indicates the effect of introducing the correct

magnitude of parallel electric fields.

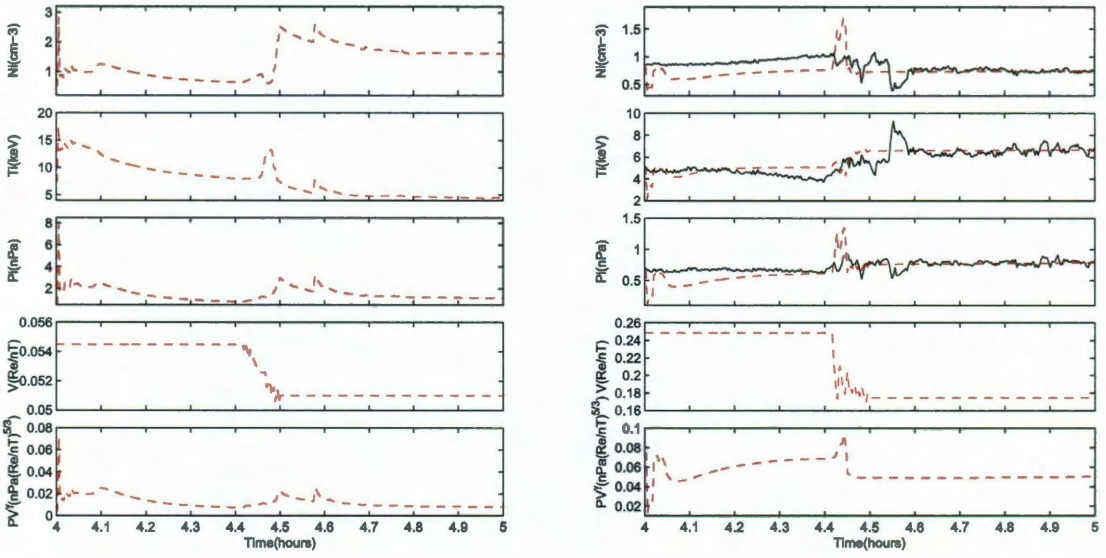

Figure 9.14 : Proton density, temperature, pressure, flux tube volume, and entropy during substorm growth phase and expansion phase at geosynchronous orbit (-6.6R_E,0,0) and Geotail position (-9R_E,0,0), black for Geotail observations and red for RCM results.

Figure 9.15 shows the same thing for a run with parallel electric fields but the density ratio between cold component and hot component is 1.0 but not 0.1586. The parallel electric fields are then smaller than the previous run. The initial perturbation during the growth phase is smaller. No second peaks appear in the expansion phase because of weaker perturbation in the west edge of plasma bubble.

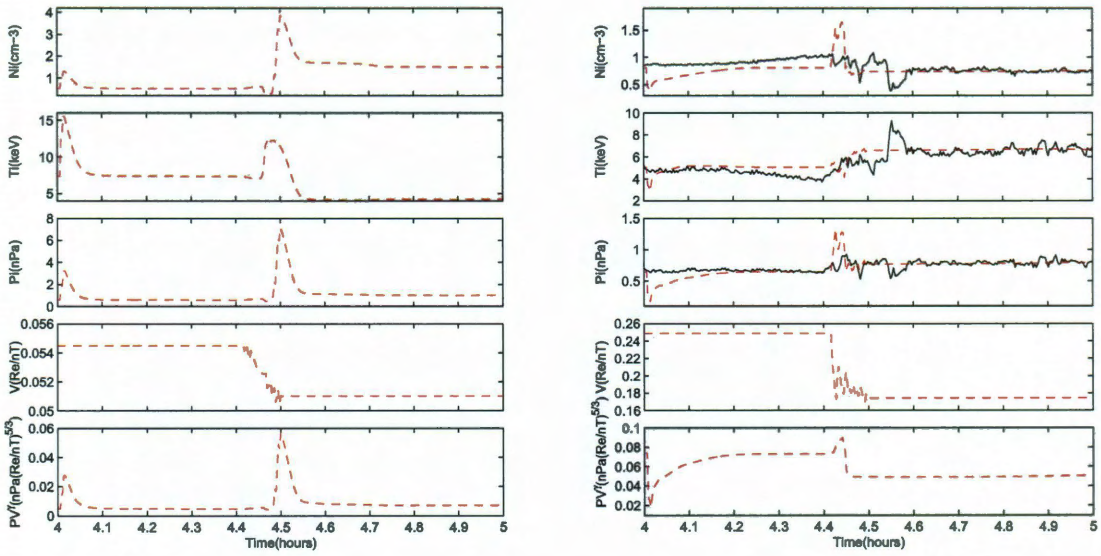

Figure 9.15 : Proton density, temperature, pressure, flux tube volume, and entropy during substorm growth phase and expansion phase at geosynchronous orbit (-6.6R_E,0,0) and Geotail position (-9R_E,0,0), black for Geotail observations and red for RCM results.

Chapter 10

Summary

The Rice Convection Model is a theoretical tool to explore some of the essential physics in the inner magnetosphere. The gradient and curvature drifts make this area different from other regions of geospace. It plays a critical role in the interactive system of solar wind-terrestrial coupling. The RCM uses two dimensional ionospheric calculation instead of three dimensional magnetospheric calculation to compute the plasma distribution, field-aligned currents, and ionospheric electric potential self-consistently. Our motivation in this work was to further develop, improve, and test the model as a space weather model that can be used for routine event simulations. In the past, running RCM for specific events required manual and painstaking collection and setting up of inputs and boundary conditions, and as a result, over many years only very few real events have been simulated with the RCM. Furthermore, several major global MHD codes have been coupled with the RCM to give self-consistent magnetic field model and tail-ward boundary conditions. Some ionosphere or thermosphere models aimed to work together with the RCM as well. They provide more physics in the complex situation of magnetosphere-ionosphere coupling.

To further facilitate the use of the code, we made major improvements to the code that we described in this work. Our technical developments, detailed in Chapter 4, include:

1. Re-writing of the code to eliminate arcane and obsolete features.
2. Designing a web interface for users to specify their RCM runs without touching

the code itself (the files necessary to run the RCM code could be generated from filling in the forms on the web). The form contains all the parameters and choices of modules of the code. The webpage has basic self-check function. Therefore, users will not wait for a run but get a notice from the code developer to tell them some parameters are incorrect or several parameters can not be used together. The users will also have a better chance to select the options they really want especially if they are not familiar with the code very much. To request a run from the web interface is convenient both for specific real events or some artificial test runs when you only have limited solar wind information for few times. The developer has saved the necessary files of observation data in order to generate the RCM inputs file. You could upload your own inputs file as well.

3. Implementing use of several empirical magnetic field models in the RCM which can be run with knowledge of common geomagnetic indices and geophysical parameters routinely available.

4. Implementing use of several data-based models for the outer tailward boundary condition on plasma fluxes in the RCM that are controlled by indices and/or solar wind and IMF conditions.

5. Writing a parallel version of the RCM using the MPI library to be used in the future for simulations that require significant computing resources (e.g., using highly resolved spatial grids, etc.)

Although the RCM is a well established large scale numerical model, more detailed physics and models are necessary to be included to further understand the inner magnetosphere plasma convection. In this work, we added several new physics modules to the RCM. The major concern is the magnetosphere and ionosphere coupling. The ionosphere is far more complicated than just a conducting shell. But the ionospheric

conductances are still the major part in our calculation, especially in the studies of magnetospheric substorms. The electron and proton precipitation is critical to the system. Strong pitch angle diffusion is not a good description in the consideration of precipitation. A fraction of strong pitch angle diffusion is a simple modification to this. It could have a good agreement with observation on average. However, the plasma loss rate should depend on their energy and location, so several different models are implemented into the code. Chen and Schulz gave example of formulas for electron pitch angle diffusion less than everywhere strong, in which it approaches to strong pitch angle diffusion at high energy end, but has much less scattering rate at low energy end. We could also use the first adiabatic invariant to determine the loss rate along magnetic field lines. We could assume the particle is isotropic in the plasma sheet. In Chapter 7, we described our code developments in this area.

Another important issue related to ionospheric conductances is the field-aligned potential drop. It accelerates the electrons into the ionosphere to create large upward field-aligned currents which mainly concentrated in regions of dawnside region-2 field-aligned currents and duskside region-1 field-aligned currents. To do that, we need the current density of the field-aligned current which is calculated from Vasyliunas equation or global MHD code. The Knight relation gives a way to compute field-aligned currents or field-aligned potential drop from one another. The field-aligned potential drop calculated is generally too high due to the goal of accelerating electrons to compensate the magnetospheric pressure gradient for both ions and electrons. The high field-aligned potential drop not only increases the current density or the number flux, but also increase the energy flux a lot. The high energy flux could lead to much higher conductances in the nightside. On the other hand, the strong field-aligned potential drop makes the potential solver harder to converge for the calculation of ionospheric

electric potential, and the plasma undergoing chaotic motion in the magnetosphere due to large difference between the magnetospheric electric fields and the ionospheric electric fields. Chapter 6 described our derivation of the generalized current-voltage relation and its implementation in the RCM, by changing the magnetospheric plasma distribution from a Maxwellian to bi-kappa distributions as the combination of a hot component and a cold component. The change makes the code working for the sub-storm run without crashing due to divergence in the potential solver. Although it won't change the convection pattern very much, it could generate a lot of detailed structures due to the unpredictable motion of the plasma.

The precipitation and the large field-aligned potential drop could also contribute in ion outflow, which is the other source of plasma besides coming from the magnetotail X line through the high latitude boundary condition. That is a major source of O^+ of storm time ring current. The particle precipitation, ion outflow, and estimated charge exchange rate complete the full continuity equation. We added a new model for ion outflow effects in the RCM, as described in Chapter 7.

In Chapter 5, We examined the ring current injection using the simulations of two extremely strong geomagnetic storms with the new version of the RCM. The role of tailward boundary condition on ring current particle injection was analyzed. We found that using empirical magnetic field models and empirical plasma sheet models for setting the RCM tailward boundary condition, interchange instability appears when the plasma entropy, $pV^{5/3}$, has a sudden drop so that the flux tube more tailward has smaller entropy. Since it is nearly impossible to use satellite observations as tail-ward boundary conditions of the RCM, time-dependent statistical plasma sheet models should be used for real time event simulations. We found that in these two extremely strong storm, the Tsyganenko-Mukai boundary condition results in the

RCM overestimating ring current injection. Using the Borovsky's boundary condition produced results closer matching observations.

In Chapter 8, we presented simulations of an isolated substorm that occured on July 22, 1998. We varied two adjustable parameters used to constrain the auroral precipitation model in the RCM. An energy flux floor is used to avoid very small conductance and thus very strong electric field. Hardy normalization of energy flux is applied since the RCM modeling region excludes the contribution from region-1 field-aligned currents. In the isolated substorm event simulations, we found that the run with only energy flux floor shows the highest conductances and the lowest electric field inside the injection channel. In general, varying auroral conductance model has significant effect on results, emphasizing the importance of replacing adjustable parameters with something better.

Another method to resolve theoretical difficulties in estimating energy flux is to include the parallel electric field. Our initial attempt was presented in Chapter 9. We found that in general, after acceleration by the field-aligned potential drop, the energy flux is enhanced where field-aligned potential drops are large in the region of strong upward field-aligned currents. However, we also found profound effects of inclusion of the parallel potential drop on particle drift paths in the magnetosphere that may not be realistic, calling for further work in this area.

Despite a large of volume of results presented in this thesis, there is plenty of future work needed. Further analysis of the run with parallel electric fields in Chapter 9 would require comparison of model predictions with observations of auroral precipitation by low-altitude spacecraft such as DMSP, to decide how realistic our model of precipitation in the RCM. Calculation of ground-based magnetic perturbations and magnetic indices such as AE and AL for the runs in Chapter 8 would also provide

a much-needed connection to reality, in deciding which adjustable parameters in the auroral precipitation model are best suited for event simulations. Testing of effects of ion outflows and proton precipitation are two major undertakings that we hope will increase the physics sophistication of the RCM and will keep it at the cutting edge of magnetospheric research.

Appendix A

Space Physics Coordinate Transformations

A.1 General Remarks

The need for more than one coordinate system arises from the fact that often various physical processes are more understood, experimental data more ordered, or calculations more easily performed in one or another of the various systems. Frequently, it is necessary to transform from one to another of these systems. It is possible to derive the transformation from one coordinate system to another in terms of trigonometric relations between angles measured in each system by means of the formulas of spherical trigonometry[262].

However, the use of this technique can be very tricky and can result in rather complex relationships. Another technique is to find the required Euler rotation angles and construct the associated rotation matrices[262]. Then these rotation matrices can be multiplied to give a single transformation matrix. The vector-matrix formalism is attractive not only because it permits a shorthand representation of the transformation, but also because it permits multiple transformations to be performed readily by matrix multiplication and the inverse transformation to be derived readily. The heliocentric coordinate systems and their transformations are described by Hapgood [1992][263]. The geocentric systems are also described by Russell [1971][262]. Therefore, only selected geocentric systems are relisted in this chapter as a reference.

In general, you need two quantities to define a coordinate system: the direction of

one of the axes and the orientation of the other two axes in the plane perpendicular to this direction. This latter orientation is often specified by requiring one of the two remaining axes to be perpendicular to some direction. A fortunate feature of rotation matrices, the matrix that transforms a vector from one system to another, is that the inverse is simply its transpose. Thus, if the matrix A transforms the vector V^a measured in system a to V^b measured in system b, then the matrix that transforms V^b into V^a is A^t. Thus we may write

$$\begin{aligned} A \cdot \mathbf{V}^a &= \mathbf{V}^b \\ A^t \cdot \mathbf{V}^b &= \mathbf{V}^a \end{aligned} \tag{A.1}$$

The simplest way to obtain the transformation matrix A is to find the directions of the three new coordinate axes for system b in the old system a. If the direction cosines of the new X-direction expressed in the old system are (X_1,X_2,X_3), of the new Y-direction are (Y_1,Y_2,Y_3) and the new Z-direction are (Z_1,Z_2,Z_3). When two of these three directions are know, the third one completes a right-handed orthogonal set, $\mathbf{Z} = \mathbf{X} \times \mathbf{Y}$, $\mathbf{X} = \mathbf{Y} \times \mathbf{Z}$, $\mathbf{Y} = \mathbf{Z} \times \mathbf{X}$). The rotation matrix is formed by these three vectors as rows:

$$\begin{pmatrix} X_1 & X_2 & X_3 \\ Y_1 & Y_2 & Y_3 \\ Z_1 & Z_2 & Z_3 \end{pmatrix} \cdot \begin{pmatrix} V_x^a \\ V_y^a \\ V_z^a \end{pmatrix} = \begin{pmatrix} V_x^b \\ V_y^b \\ V_z^b \end{pmatrix} \tag{A.2}$$

Similarly the transformation from system b to a is

$$\begin{pmatrix} X_1 & Y_1 & Z_1 \\ X_2 & Y_2 & Z_2 \\ X_3 & Y_3 & Z_3 \end{pmatrix} \cdot \begin{pmatrix} V_x^b \\ V_y^b \\ V_z^b \end{pmatrix} = \begin{pmatrix} V_x^a \\ V_y^a \\ V_z^a \end{pmatrix} \tag{A.3}$$

Since the three axes are perpendicular to each other, so the transpose a matrix is equivalent to its inverse matrix

$$\begin{pmatrix} X_1 & X_2 & X_3 \\ Y_1 & Y_2 & Y_3 \\ Z_1 & Z_2 & Z_3 \end{pmatrix} \cdot \begin{pmatrix} X_1 & Y_1 & Z_1 \\ X_2 & Y_2 & Z_2 \\ X_3 & Y_3 & Z_3 \end{pmatrix} = \begin{pmatrix} 1 & 0 & 0 \\ 0 & 1 & 0 \\ 0 & 0 & 1 \end{pmatrix} \tag{A.4}$$

A.2 Geocentric Equatorial Inertial System

The Geocentric Equatorial Inertial System (GEI) has its X-axis pointing from the Earth towards the first point of Aries, the position of the Sun at the vernal equinox. This direction is the intersection of the Earth's equatorial plane and the ecliptic plane and thus the X-axis lies in both planes. The Z-axis is parallel to the rotation axis of the Earth and Y completes the right-handed orthogonal set ($\mathbf{Y} = \mathbf{Z} \times \mathbf{X}$). This is the system commonly used in astronomy and satellite orbit calculations. If (V_x,V_y,V_z) is a vector in GEI with magnitude V, then its right ascension, $\alpha = \arctan(V_y/V_x)$, $0° \leq \alpha \leq 180°$ if $V_y \geq 0$, $180° \leq \alpha \leq 360°$ if $V_y \leq 0$. Its declination, $\theta = \arcsin(V_z/V)$, $-90° \leq \theta \leq 90°$.

A.3 Geographic Coordinates

The geographic coordinate system (GEO) is defined so that its X-axis is in the Earth's equatorial plane but is fixed with the rotation of the Earth so that it passes through the Greenwich meridian (0° longitude). Its Z-axis is parallel to the rotation axis of the Earth. This system is used for defining the positions of ground observatories and transmitting and receiving stations. The longitude and latitude are defined as right ascension and declination in GEI.

Since the GEO and GEI coordinate systems have their Z-axes in common, if we

let Greenwich Mean Sidereal Time θ, the angle between the Greenwich meridian and the first point of Aries measured eastwards from the first point of Aries in the Earth's equator, which is a function of the time of day and the time of year, then the first point of Aries is at ($\cos\theta$, $-\sin\theta$,0) in GEO coordinates and the transformation is

$$\begin{pmatrix} \cos\theta & -\sin\theta & 0 \\ \sin\theta & \cos\theta & 0 \\ 0 & 0 & 1 \end{pmatrix} \cdot \begin{pmatrix} V_x \\ V_y \\ V_z \end{pmatrix}_{GEO} = \begin{pmatrix} V_x \\ V_y \\ V_z \end{pmatrix}_{GEI} \tag{A.5}$$

and the inverse transformation is

$$\begin{pmatrix} \cos\theta & \sin\theta & 0 \\ -\sin\theta & \cos\theta & 0 \\ 0 & 0 & 1 \end{pmatrix} \cdot \begin{pmatrix} V_x \\ V_y \\ V_z \end{pmatrix}_{GEI} = \begin{pmatrix} V_x \\ V_y \\ V_z \end{pmatrix}_{GEO} \tag{A.6}$$

where the matrix are defined as T_1 and T_1^t.

A.4 Geomagnetic Coordinates

The geomagnetic coordinate system (MAG) is defined so that its Z-axis is parallel to the magnetic dipole axis. The geographic coordinates of the dipole axis from the International Geomagnetic Reference Field 1965.0 (IGRF 1965.0) are 11.435° colatitude and 69.761° east longitude. Thus the Z-axis is (0.06859,-0.18602,0.98015) in GEO coordinates. The Y-axis of this system is perpendicular to the geographic poles such that if $\mathbf{D}$ is the dipole position and $\mathbf{S}$ is the south pole then $\mathbf{Y} = \mathbf{D} \times \mathbf{S}$. This system is often used for defining the position of magnetic observatories and tracing field lines. The magnetic longitude is measured eastwards from the X-axis and magnetic latitude is measured from the equator in magnetic meridians, positive northward and negative southwards. Thus, if (V_x,V_y,V_z) is a vector in the MAG

with magnitude V then its magnetic longitude, $\lambda = \arctan(V_y/V_x)$, $0° \leq \lambda \leq 180°$ if $V_y \geq 0$, $180° \leq \lambda \leq 360°$ if $V_y \leq 0°$. Its magnetic latitude, $\theta = \arcsin(V_z/V)$, $-90° \leq \theta \leq 90°$.

Except near the poles, magnetic longitude will generally be about 69.8° greater than geographic longitude. A simple cartesian representation of the dipole magnetic field exists in this system[38]. This system is fixed in the rotating Earth and thus the transformation from GEO to MAG is constant.

$$\begin{pmatrix} 0.33907 & -0.91964 & -0.19826 \\ 0.93826 & 0.34594 & 0 \\ 0.06859 & -0.18602 & 0.98015 \end{pmatrix} \cdot \begin{pmatrix} V_x \\ V_y \\ V_z \end{pmatrix}_{GEO} = \begin{pmatrix} V_x \\ V_y \\ V_z \end{pmatrix}_{MAG} \tag{A.7}$$

where the matrix is defined as T_5.

A.5 Geocentric Solar Ecliptic System

The geocentric solar ecliptic system (GSE) has its X-axis pointing from the Earth towards the Sun, its Y-axis is chosen to be in the ecliptic plane pointing towards dusk and its Z-axis is parallel to the ecliptic pole. Relative to an inertial system this system has a yearly rotation. This system has been used to display satellite trajectories, interplanetary magnetic field observations, and solar wind velocity data. Longitude is measured in the X-Y plane from the X-axis toward the Y-axis and latitude is the angle out of the X-Y plane, positive for positive Z components.

The most common required transformation into the GSE system of those discussed so far is from the GEI system. The direction of the ecliptic pole (0,-0.398,0.917) is constant in the GEI system. If the direction of the X-axis is (S_1,S_2,S_3), then the

Y-axis in GEI (Y_1,Y_2,Y_3) is $(0, -0.398, 0.917) \times (S_1, S_2, S_3)$ and the transformation is

$$\begin{pmatrix} S_1 & S_2 & S_3 \\ Y_1 & Y_2 & Y_3 \\ 0 & -0.398 & 0.917 \end{pmatrix} \cdot \begin{pmatrix} V_x \\ V_y \\ V_z \end{pmatrix}_{GEI} = \begin{pmatrix} V_x \\ V_y \\ V_z \end{pmatrix}_{GSE} \tag{A.8}$$

where the matrix is defined as T_2.

A.6 Geocentric Solar Equatorial System

The geocentric solar equatorial system (GSEQ) as with the GSE system has its X-axis pointing towards the Sun from the Earth. However, instead of having its Y-axis in the ecliptic plane, the GSEQ Y-axis is parallel to the Sun's equatorial plane which is inclined to the ecliptic. The Sun's axis of rotation might not be in the Z direction, but has to lie in the X-Z plane. The Z-axis is chosen to be in the same sense as the ecliptic pole. This system is useful for ordering data controlled by the Sun and therefore is an improvement over the use of the GSE system for studying the interplanetary magnetic field and the solar wind.

The rotation axis of the Sun, **R**, has a right ascension of $-74.0°$ and a declination of 63.8°. Thus **R** is (0.122,-0.424,0.899) in GEI. To transform from GEI to GSEQ, we must know the position of the Sun (S_1,S_2,S_3) in GEI. Then the Y-axis in GEI (Y_1,Y_2,Y_3) is parallel to $\mathbf{R} \times \mathbf{S}$. Since the cross product of two unit vectors is not a unit vector unless they are perpendicular to each other, this cross product must be normalized. Finally the Z-axis in GEI $(Z_1, Z_2, Z_3) = \mathbf{S} \times \mathbf{Y}$. Then

$$\begin{pmatrix} S_1 & S_2 & S_3 \\ Y_1 & Y_2 & Y_3 \\ Z_1 & Z_2 & Z_3 \end{pmatrix} \cdot \begin{pmatrix} V_x \\ V_y \\ V_z \end{pmatrix}_{GEI} = \begin{pmatrix} V_x \\ V_y \\ V_z \end{pmatrix}_{GSEQ} \tag{A.9}$$

Since both GSE and GSEQ coordinate systems have their X-axes directed towards the Sun, they differ only by a rotation about the X-axis. Thus the transformation matrix from GSE to GSEQ must be of the form

$$\begin{pmatrix} 1 & 0 & 0 \\ 0 & \cos\theta & -\sin\theta \\ 0 & \sin\theta & \cos\theta \end{pmatrix} \cdot \begin{pmatrix} V_x \\ V_y \\ V_z \end{pmatrix}_{GSE} = \begin{pmatrix} V_x \\ V_y \\ V_z \end{pmatrix}_{GSEQ} \tag{A.10}$$

where the matrix is defined as T_6. If the transformations from GEI to GSE and GEI to GSEQ are both known, then the angle may be determined by examining the angle between the Y-axes in the two systems or the Z-axes. If these transformation matrices are not available, it may be calculated from the following formula

$$\sin\theta = \frac{\mathbf{S} \cdot (0.031, -0.112, -0.049)}{|(0.122, -0.424, 0.899) \times \mathbf{S}|} \tag{A.11}$$

where $\mathbf{S}$ is the position of the Sun in GEI. The Sun's spin axis is inclined 7.25° to the ecliptic. When the Sun's spin axis is directed most towards the Earth, the Earth reaches its most northerly heliographic latitude and get $\theta = 0$.

A.7 Geocentric Solar Magnetospheric System

The geocentric solar magnetospheric system (GSM), as with both the GSE and GSEQ systems, has its X-axis from the Earth to the Sun. The Y-axis is defined to be perpendicular to the Earth's magnetic dipole so that the X-Z plane contains the dipole axis and the Y-axis is always in the magnetic equator and in the dawn-dusk meridian. The positive Z-axis is chosen to be in the same sense as the northern magnetic pole. The difference between the GSM system and the GSE and GSEQ is simply a rotation about the X-axis. This system is useful for displaying magnetopause and shock boundary positions, magnetosheath and magnetotail magnetic fields and

magnetosheath solar wind velocities. The angle of the north magnetic pole to the GSM Z-axis is called the dipole tilt angle and is positive when the north magnetic pole is tilted towards the Sun. GSM longitude is measured in the X-Y plane from X towards Y and latitude is the angle northward from the X-Y plane.

To transform from GEI to GSM we need to know both the position of the Sun in GEI and the position of the Earth's dipole axis. In geographic coordinates, the dipole is at 11.435° colatitude and 69.761° east longitude (IGRF 1965.0). Thus, the dipole $\mathbf{D}$ in GEO coordinates is (0.06859,-0.18602,0.98015). If $\mathbf{D}'$ is $\mathbf{D}$ transformed into GEI, the Y-axis is

$$\frac{\mathbf{D}' \times \mathbf{S}}{|\mathbf{D}' \times \mathbf{S}|} \tag{A.12}$$

The normalizing factor occurs because $\mathbf{D}'$ and $\mathbf{S}$ are not necessarily perpendicular. $Z = \mathbf{S} \times \mathbf{Y}$ and the transformation becomes

$$\begin{pmatrix} S_1 & S_2 & S_3 \\ Y_1 & Y_2 & Y_3 \\ Z_1 & Z_2 & Z_3 \end{pmatrix} \cdot \begin{pmatrix} V_x \\ V_y \\ V_z \end{pmatrix}_{GEI} = \begin{pmatrix} V_x \\ V_y \\ V_z \end{pmatrix}_{GSM} \tag{A.13}$$

The transformation matrix from GSE to GSM has the same form as from GSE to GSEQ

$$\begin{pmatrix} 1 & 0 & 0 \\ 0 & \cos\theta & -\sin\theta \\ 0 & \sin\theta & \cos\theta \end{pmatrix} \cdot \begin{pmatrix} V_x \\ V_y \\ V_z \end{pmatrix}_{GSE} = \begin{pmatrix} V_x \\ V_y \\ V_z \end{pmatrix}_{GSM} \tag{A.14}$$

where the matrix from GSE to GSM is defined as T_3. Then the transformation from GSM to GSEQ is $T_3^t T_6$.

A.8 Solar Magnetic Coordinates

In solar magnetic coordinates (SM) the Z-axis is chosen parallel to the north magnetic pole and the Y-axis perpendicular to the Earth-Sun line towards dusk. The difference between this system and the GSM system is a rotation about the Y-axis by the dipole tilt angle. The X-axis does not point directly at the Sun. The system is useful for ordering data controlled more strongly by the Earth's dipole field than by the solar wind. It has been used for magnetopause cross sections and magnetospheric magnetic fields.

As for GSM, the transformation from GEI to SM requires a knowledge of the Earth Sun direction $\mathbf{S}$, and the dipole direction $\mathbf{D}$ in GEI, so

$$Y = \frac{\mathbf{D} \times \mathbf{S}}{|\mathbf{D} \times \mathbf{S}|} \tag{A.15}$$

and $\mathbf{X} = \mathbf{Y} \times \mathbf{D}$. Then the transformation becomes

$$\begin{pmatrix} X_1 & X_2 & X_3 \\ Y_1 & Y_2 & Y_3 \\ D_1 & D_2 & D_3 \end{pmatrix} \cdot \begin{pmatrix} V_x \\ V_y \\ V_z \end{pmatrix}_{GEI} = \begin{pmatrix} V_x \\ V_y \\ V_z \end{pmatrix}_{SM} \tag{A.16}$$

The transformation from GSM to SM is simply a rotation about the Y-axis by the dipole tilt angle μ. Thus

$$\begin{pmatrix} \cos\mu & 0 & -\sin\mu \\ 0 & 1 & 0 \\ \sin\mu & 0 & \cos\mu \end{pmatrix} \cdot \begin{pmatrix} V_x \\ V_y \\ V_z \end{pmatrix}_{GSM} = \begin{pmatrix} V_x \\ V_y \\ V_z \end{pmatrix}_{SM} \tag{A.17}$$

where the matrix is defined as T_4. All the coordinate systems described so far have been geocentric. The table shows the transformation among these systems.

Table A.1 : Transformation matrices between the coordinate systems

To	From						
	GEI	GEO	MAG	GSE	GSEQ	GSM	SM
GEI	1	T_1^t	$T_1^t T_5^t$	T_2^t	$T_2^t T_6^t$	$T_2^t T_3^t$	$T_2^t T_3^t T_4^t$
GEO	T_1	1	T_5^t	$T_1 T_2^t$	$T_1 T_2^t T_6^t$	$T_1 T_2^t T_3^t$	$T_1 T_2^t T_3^t T_4^t$
MAG	$T_5 T_1$	T_5	1	$T_5 T_1 T_2^t$	$T_5 T_1 T_2^t T_6^t$	$T_5 T_1 T_2^t T_3^t$	$T_5 T_1 T_2^t T_3^t T_4^t$
GSE	T_2	$T_2 T_1^t$	$T_2 T_1^t T_5^t$	1	T_6^t	T_3^t	$T_3^t T_4^t$
GSEQ	$T_6 T_2$	$T_6 T_2 T_1^t$	$T_6 T_2 T_1^t T_5^t$	T_6	1	$T_6 T_3^t$	$T_6 T_3^t T_4^t$
GSM	$T_3 T_2$	$T_3 T_2 T_1^t$	$T_3 T_2 T_1^t T_5^t$	T_3	$T_3 T_6^t$	1	T_4^t
SM	$T_4 T_3 T_2$	$T_4 T_3 T_2 T_1^t$	$T_4 T_3 T_2 T_1^t T_5^t$	$T_4 T_3$	$T_4 T_3 T_6^t$	T_4	1

A.9 Other Geocentric Systems

There is another class of cartesian coordinate systems that can be used: those based on a local measurement. For example, one may wish to define a coordinate system in which the solar wind flow is parallel to one of the coordinate axes. This could be done in coordinate systems such as GSE, GSEQ and GSM by replacing the position of the Sun by the vector antiparallel to the observed solar wind flow. The second condition for choosing the coordinate system would be that the Y-axis is perpendicular to the solar wind and the ecliptic pole (for GSE) and the Sun's rotation axis (for GSEQ) and the Earth's dipole (for GSM).

Geocentric Solar Wind coordinate system (GSW) replaces the X-axis antiparallel to the currently observed solar wind flow vector, rather than aligned with the Earth-Sun line. The orientation of axes in the GSW system can be uniquely defined by specifying three components (V_x,V_y,V_z) of the solar wind velocity, and in the case of a strictly radial anti-sunward flow ($V_y = V_z = 0$), the GSW system becomes identical to the standard GSM.

Appendix B

Integrations of Field-Aligned Currents and Electron Energy Flux for Maxwellian Distribution

The conservation of energy gives

$$v_\perp'^2 + v_\parallel'^2 - \frac{2e}{m}\phi' = v_\perp^2 + v_\parallel^2 - \frac{2e}{m}\phi \tag{B.1}$$

The first adiabatic invariant gives

$$\frac{v_\perp'^2}{B'} = \frac{v_\perp^2}{B} \tag{B.2}$$

where primes denote values at a base, either on the ionosphere or in the plasma sheet, unprimed quantities at an arbitrary point on the field line. For a trajectory to pass through the appropriate base we need $v_\parallel'^2 > 0$ which gives

$$\frac{2e}{m}(\phi' - \phi) + v_\perp^2\left(1 - \frac{B'}{B}\right) + v_\parallel^2 > 0 \tag{B.3}$$

So trajectories passing through the ionosphere base must occupy a region A of velocity space satisfying this equation for ϕ_E and B_E and those through the plasma sheet base a region B for ϕ_S and B_S. Since $\phi_E > \phi > \phi_S$ and $B_E > B > B_S$, the region A lies between the hyperbola $C_E^2 v_\perp^2 - v_\parallel^2 = D_E^2$ and the $v_\perp = 0$ axis and the region B lies outside the ellipse $C_S^2 v_\perp^2 + v_\parallel^2 = D_S^2$, where

$$\begin{aligned} C_S^2 &= 1 - \frac{B_S}{B} \\ D_S^2 &= \frac{2e}{m}(\phi - \phi_S) \\ C_E^2 &= \frac{B_E}{B} - 1 \\ D_E^2 &= \frac{2e}{m}(\phi_E - \phi) \end{aligned} \tag{B.4}$$

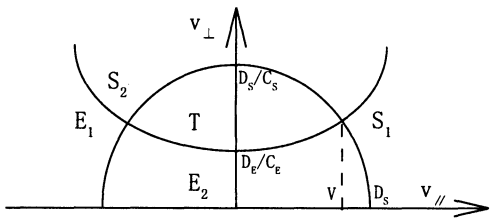

Figure B.1 : Trajectories in phase space.

In the case of a monotonic potential, there are five disjoint regions. The straight through trajectories are from one end to the other, named as E_1 and S_1. There also trajectories from ionosphere not reaching sheet or from sheet not reaching ionosphere, named as E_2 and S_2. The trapped trajectories which could not go to either end is noted as T.

$$\begin{aligned} E_1, S_1 &\subseteq A \cap B \\ T &\subseteq \bar{A} \cap \bar{B} \\ E_2 &\subseteq A \cap \bar{B} \\ S_2 &\subseteq \bar{A} \cap B \end{aligned} \tag{B.5}$$

And here V is the parallel velocity where two curves intersect with each other.

$$V^2 = \frac{C_E^2 D_S^2 - C_S^2 D_E^2}{C_E^2 + C_S^2} \tag{B.6}$$

For simplicity, we define

$$\begin{aligned} A^2 &= \frac{m}{2kT} \\ x &= A v_\perp \\ y &= A v_\parallel \\ \Delta &= e(\phi_E - \phi_S) \end{aligned}$$

then the current could be calculated by integration as

$$\begin{aligned}
j_{\parallel} &= -e\int_{S_1} v_{\parallel}(f_S - f_E)d^3v \\
&= -e\int_{S_1} v_{\parallel}\left[N_S\left(\frac{m}{2\pi kT_S}\right)^{3/2} e^{-\frac{m}{2kT_S}\left(v_\perp^2+v_{\parallel}^2\right)+\frac{e}{kT_S}(\phi-\phi_S)}\right. \\
&\quad \left. -N_E\left(\frac{m}{2\pi kT_E}\right)^{3/2} e^{-\frac{m}{2kT_E}\left(v_\perp^2+v_{\parallel}^2\right)+\frac{e}{kT_E}(\phi-\phi_E)}\right]d^3v \\
&= -e\int_{S_1}\left[N_S e^{\frac{e}{kT_S}(\phi-\phi_S)}\left(\frac{m}{2\pi kT_S}\right)^{3/2} v_{\parallel}e^{-\frac{m}{2kT_S}\left(v_\perp^2+v_{\parallel}^2\right)}\right. \\
&\quad \left. -N_E e^{\frac{e}{kT_E}(\phi-\phi_E)}\left(\frac{m}{2\pi kT_E}\right)^{3/2} v_{\parallel}e^{-\frac{m}{2kT_E}\left(v_\perp^2+v_{\parallel}^2\right)}\right]d^3v \\
&= -e\left[N_S e^{\frac{e}{kT_S}(\phi-\phi_S)}I(T_S) - N_E e^{\frac{e}{kT_E}(\phi-\phi_E)}I(T_E)\right] \qquad \text{(B.7)}
\end{aligned}$$

where

$$\begin{aligned}
I(T) &= \left(\frac{m}{2\pi kT}\right)^{3/2}\int_{S_1} v_{\parallel}e^{-\frac{m}{2kT}\left(v_\perp^2+v_{\parallel}^2\right)}d^3v \\
&= \left(\frac{m}{2\pi kT}\right)^{3/2} 2\pi\iint_{S_1} v_{\parallel}v_\perp e^{-\frac{mv^2}{2kT}}dv_{\parallel}dv_\perp \\
&= \frac{A^3}{\pi^{3/2}}\frac{2\pi}{A^4}\iint_{S_1} yxe^{-(x^2+y^2)}dxdy \\
&= \frac{2}{A\sqrt{\pi}}\left(\int_{AD_S}^{\infty} ye^{-y^2}dy\int_0^{\frac{\sqrt{y^2+A^2D_E^2}}{C_E}} xe^{-x^2}dx + \int_{AV}^{AD_S} ye^{-y^2}dy\int_{\frac{\sqrt{A^2D_S^2-y^2}}{C_S}}^{\frac{\sqrt{y^2+A^2D_E^2}}{C_E}} xe^{-x^2}dx\right) \\
&= \frac{2}{A\sqrt{\pi}}\left[\int_{AD_S}^{\infty} ye^{-y^2}dy\left(-\frac{1}{2}\right)e^{-x^2}\Big|_0^{\frac{y^2+A^2D_E^2}{C_E}} + \int_{AV}^{AD_S} ye^{-y^2}dy\left(-\frac{1}{2}\right)e^{-x^2}\Big|_{\frac{\sqrt{A^2D_S^2-y^2}}{C_S}}^{\frac{\sqrt{y^2+A^2D_E^2}}{C_E}}\right] \\
&= \frac{1}{A\sqrt{\pi}}\left[\int_{\infty}^{AD_S} ye^{-y^2}\left(e^{-\frac{y^2+A^2D_E^2}{C_E^2}}-1\right)dy + \int_{AD_S}^{AV} ye^{-y^2}\left(e^{-\frac{y^2+A^2D_E^2}{C_E^2}} - e^{-\frac{A^2D_S^2-y^2}{C_S^2}}\right)dy\right] \\
&= \frac{1}{2A\sqrt{\pi}}\left[\int_{y=AD_S}^{y=\infty} e^{-y^2-\frac{y^2+A^2D_E^2}{C_E^2}}d(-y^2) - \int_{y=AD_S}^{y=\infty} e^{-y^2}d(-y^2)\right. \\
&\quad \left. + \int_{y=AV}^{y=AD_S} e^{-y^2-\frac{y^2+A^2D_E^2}{C_E^2}}d(-y^2) - \int_{y=AV}^{y=AD_S} e^{-y^2-\frac{A^2D_S^2-y^2}{C_S^2}}d(-y^2)\right]
\end{aligned}$$

$$
\begin{aligned}
&= \frac{1}{2A\sqrt{\pi}} \left[\frac{1}{1+\frac{1}{C_E^2}} e^{-\frac{A^2 D_E^2}{C_E^2}} e^{-\frac{y^2(C_E^2+1)}{C_E^2}} \Big|_{AV}^{\infty} - e^{-y^2} \Big|_{AD_S}^{\infty} - \frac{1}{1-\frac{1}{C_S^2}} e^{-\frac{A^2 D_S^2}{C_S^2}} e^{-\frac{y^2(C_S^2-1)}{C_S^2}} \Big|_{AV}^{AD_S} \right] \\
&= \frac{1}{2A\sqrt{\pi}} \left[-\frac{e^{-\frac{A^2 D_E^2}{C_E^2}}}{1+\frac{1}{C_E^2}} e^{-\frac{A^2 V^2 (C_E^2+1)}{C_E^2}} + e^{-A^2 D_S^2} \left(1 - \frac{1}{1-\frac{1}{C_S^2}} \right) + \frac{e^{-\frac{A^2 D_S^2}{C_S^2}}}{1-\frac{1}{C_S^2}} e^{-\frac{A^2 V^2 (C_S^2-1)}{C_S^2}} \right] \\
&= \frac{1}{2A\sqrt{\pi}} \left\{ -\frac{1}{1+\frac{1}{\frac{B_E}{B}-1}} e^{-\frac{A^2}{C_E^2}\left[D_E^2 + \frac{C_E^2 D_S^2 - C_S^2 D_E^2}{C_E^2+C_S^2}(C_E^2+1) \right]} + e^{-A^2 D_S^2} \frac{1}{1-C_S^2} \right. \\
&\quad \left. + \frac{1}{1-\frac{1}{1-\frac{B_S}{B}}} e^{-\frac{A^2}{C_S^2}\left[D_S^2 + \frac{C_E^2 D_S^2 - C_S^2 D_E^2}{C_E^2+C_S^2}(C_S^2-1) \right]} \right\} \\
&= \frac{1}{2A\sqrt{\pi}} \left[\left(\frac{B}{B_E} - 1 \right) e^{-A^2 \frac{(C_E^2+1)D_S^2 + (1-C_S^2)D_E^2}{C_E^2+C_S^2}} + \frac{B}{B_S} e^{-A^2 D_S^2} \right. \\
&\quad \left. + \left(1 - \frac{B}{B_S} \right) e^{-A^2 \frac{(1-C_S^2)D_E^2 + (C_E^2+1)D_S^2}{C_E^2+C_S^2}} \right] \\
&= \sqrt{\frac{kT}{2\pi m}} \left[\left(\frac{B}{B_E} - \frac{B}{B_S} \right) e^{-\frac{m}{2kT} \frac{B_E \frac{2e}{m}(\phi-\phi_S) + B_S \frac{2e}{m}(\phi_E-\phi)}{B_E - B_S}} + \frac{B}{B_S} e^{-\frac{m}{2kT}\frac{2e}{m}(\phi-\phi_S)} \right] \\
&= \sqrt{\frac{kT}{2\pi m}} B e^{\frac{e(\phi_E-\phi)}{kT}} \left[\frac{1}{B_S} e^{\frac{e(\phi_S-\phi_E)}{kT}} + \left(\frac{1}{B_E} - \frac{1}{B_S} \right) e^{\frac{eB_E(\phi_S-\phi_E)}{kT(B_E-B_S)}} \right] \\
&= \sqrt{\frac{kT}{2\pi m}} B e^{\frac{e(\phi_E-\phi)}{kT}} \frac{1}{B_S} e^{-\frac{\Delta}{kT}} \left[1 - \frac{B_E - B_S}{B_E} e^{-\frac{\Delta}{kT\left(\frac{B_E}{B_S}-1\right)}} \right] \\
&\equiv \sqrt{\frac{kT}{2\pi m}} B e^{\frac{e(\phi_E-\phi)}{kT}} g(\Delta, T)
\end{aligned}
\tag{B.8}
$$

So if we evaluate at ionosphere, where $\phi = \phi_E$, then the current is

$$
\begin{aligned}
j_{\parallel} &= -eB_E \left[e^{\frac{\Delta}{kT_S}} N_S \sqrt{\frac{kT_S}{2\pi m}} g(\Delta, T_S) - N_E \sqrt{\frac{kT_E}{2\pi m}} g(\Delta, T_E) \right] \\
&= eN_E \sqrt{\frac{kT_E}{M}} \sqrt{\frac{M}{2\pi m}} \left\{ -B_E e^{\frac{\Delta}{kT_S}} \frac{N_S}{N_E} \sqrt{\frac{T_S}{T_E}} \frac{1}{B_S} e^{-\frac{\Delta}{kT_S}} \left[1 - \frac{B_E - B_S}{B_E} e^{-\frac{\Delta}{kT_S\left(\frac{B_E}{B_S}-1\right)}} \right] \right. \\
&\quad \left. + B_E \frac{1}{B_S} e^{-\frac{\Delta}{kT_E}} \left[1 - \frac{B_E - B_S}{B_E} e^{-\frac{\Delta}{kT_E\left(\frac{B_E}{B_S}-1\right)}} \right] \right\} \\
&= eN_E \sqrt{\frac{kT_E}{2\pi m}} \left[\left(\frac{B_S - B_E}{B_S} e^{-\frac{rB_S}{B_E - B_S}} + \frac{B_E}{B_S} \right) e^{-r} - n\sqrt{t} \left(\frac{B_S - B_E}{B_S} e^{-\frac{r}{t}\frac{B_S}{B_E - B_S}} + \frac{B_E}{B_S} \right) \right]
\end{aligned}
$$

$$
\begin{aligned}
\approx & eN_E\sqrt{\frac{kT_E}{2\pi m}}\left\{\left[\frac{B_S-B_E}{B_S}\left(1-\frac{rB_S}{B_E-B_S}+\cdots\right)+\frac{B_E}{B_S}\right]e^{-r}\right. \\
& \left.-n\sqrt{t}\left[\frac{B_S-B_E}{B_S}\left(1-\frac{r}{t}\frac{B_S}{B_E-B_S}+\cdots\right)+\frac{B_E}{B_S}\right]\right\} \\
\approx & eN_E\sqrt{\frac{kT_E}{2\pi m}}\left[(1+r)e^{-r}-n\sqrt{t}\left(1+\frac{r}{t}\right)\right] \\
= & eN_S\sqrt{\frac{kT_S}{2\pi m}}\left[(1+r't)e^{-r't}\frac{1}{n\sqrt{t}}-(1+r')\right]
\end{aligned}
\tag{B.9}
$$

where the ratios are set as $t = T_S/T_E$, $n = N_S/N_E$, $r = \Delta/kT_E$, and $r' = \Delta/kT_S$, with assumptions $rB_S/B_E \ll 1$ and $rB_S/tB_E \ll 1$.

We could do similar integration for energy flux. Before doing that, we set

$$
\begin{aligned}
p &= x^2 \\
q &= y^2 \\
q' &= \frac{C_E^2+1}{C_E^2}q \\
q'' &= \frac{1-C_S^2}{C_S^2}q
\end{aligned}
\tag{B.10}
$$

This time, let's calculate the function $I'(T)$ first.

$$
\begin{aligned}
I'(T) = & \left(\frac{m}{2\pi kT}\right)^{3/2}\frac{m}{2}\int_{S_1}\left(v_\perp^2+v_\parallel^2\right)v_\parallel e^{-\frac{m}{2kT}\left(v_\perp^2+v_\parallel^2\right)}d^3v \\
= & \frac{A^3}{\pi^{3/2}}\frac{m}{2}2\pi\iint_{S_1}\left(v_\perp^2+v_\parallel^2\right)v_\parallel v_\perp e^{-A^2\left(v_\perp^2+v_\parallel^2\right)}dv_\parallel dv_\perp \\
= & \frac{m}{\sqrt{\pi}A^3}\iint_{S_1}\left(x^2+y^2\right)xye^{-x^2-y^2}dxdy \\
= & \frac{m}{4\sqrt{\pi}A^3}\iint_{S_1}\left(x^2+y^2\right)e^{-x^2-y^2}d(x^2)d(y^2) \\
= & \frac{m}{4\sqrt{\pi}A^3}\iint_{S_1}(p+q)e^{-p-q}dpdq
\end{aligned}
$$

$$
\begin{aligned}
=&\frac{m}{4\sqrt{\pi}A^3}\left(\int_{A^2D_S^2}^{\infty}e^{-q}dq\int_0^{\frac{q+A^2D_E^2}{C_E^2}}pe^{-p}dp+\int_{A^2V^2}^{A^2D_S^2}e^{-q}dq\int_{\frac{A^2D_S^2-q}{C_S^2}}^{\frac{q+A^2D_E^2}{C_E^2}}pe^{-p}dp\right.\\
&\left.+\int_{A^2D_S^2}^{\infty}qe^{-q}dq\int_0^{\frac{q+A^2D_E^2}{C_E^2}}e^{-p}dp+\int_{A^2V^2}^{A^2D_S^2}qe^{-q}dq\int_{\frac{A^2D_S^2-q}{C_S^2}}^{\frac{q+A^2D_E^2}{C_E^2}}e^{-p}dp\right)\\
=&\frac{m}{4\sqrt{\pi}A^3}\left[\int_{A^2D_S^2}^{\infty}e^{-q}dq\left(-pe^{-p}-e^{-p}\right)\Big|_0^{\frac{q+A^2D_E^2}{C_E^2}}+\int_{A^2V^2}^{A^2D_S^2}e^{-q}dq\left(-pe^{-p}-e^{-p}\right)\Big|_{\frac{A^2D_S^2-q}{C_S^2}}^{\frac{q+A^2D_E^2}{C_E^2}}\right.\\
&\left.+\int_{A^2D_S^2}^{\infty}qe^{-q}dq\left(-e^{-p}\right)\Big|_0^{\frac{q+A^2D_E^2}{C_E^2}}+\int_{A^2V^2}^{A^2D_S^2}e^{-q}dq\left(-e^{-p}\right)\Big|_{\frac{A^2D_S^2-q}{C_S^2}}^{\frac{q+A^2D_E^2}{C_E^2}}\right]\\
=&\frac{m}{4\sqrt{\pi}A^3}\left[\int_{A^2D_S^2}^{\infty}e^{-q}dq\left(-\frac{q+A^2D_E^2+C_E^2}{C_E^2}e^{-\frac{q+A^2D_E^2}{C_E^2}}+1\right)\right.\\
&+\int_{A^2V^2}^{A^2D_S^2}e^{-q}dq\left(-\frac{q+A^2D_E^2+C_E^2}{C_E^2}e^{-\frac{q+A^2D_E^2}{C_E^2}}+\frac{A^2D_S^2+C_S^2-q}{C_S^2}e^{-\frac{A^2D_S^2-q}{C_S^2}}\right)\\
&\left.+\int_{A^2D_S^2}^{\infty}qe^{-q}dq\left(-e^{-\frac{q+A^2D_E^2}{C_E^2}}+1\right)+\int_{A^2V^2}^{A^2D_S^2}qe^{-q}dq\left(-e^{-\frac{q+A^2D_E^2}{C_E^2}}+e^{-\frac{A^2D_S^2-q}{C_S^2}}\right)\right]\\
=&\frac{m}{4\sqrt{\pi}A^3}\left[\int_{A^2D_S^2}^{\infty}e^{-q}dq+\int_{A^2D_S^2}^{\infty}qe^{-q}dq\right.\\
&-\frac{A^2D_E^2+C_E^2}{C_E^2}\int_{A^2V^2}^{\infty}e^{-\frac{\left(C_E^2+1\right)q+A^2D_E^2}{C_E^2}}dq+\frac{A^2D_S^2+C_S^2}{C_S^2}\int_{A^2V^2}^{A^2D_S^2}e^{-\frac{\left(C_S^2-1\right)q+A^2D_S^2}{C_S^2}}dq\\
&\left.-\left(1+\frac{1}{C_E^2}\right)\int_{A^2V^2}^{\infty}qe^{-\frac{\left(C_E^2+1\right)q+A^2D_E^2}{C_E^2}}dq+\left(1+\frac{1}{C_S^2}\right)\int_{A^2V^2}^{A^2D_S^2}qe^{-\frac{\left(C_S^2-1\right)q+A^2D_S^2}{C_S^2}}dq\right]\\
=&\frac{m}{4\sqrt{\pi}A^3}\left[-(q+2)\,e^{-q}\Big|_{A^2D_S^2}^{\infty}-\frac{A^2D_E^2+C_E^2}{C_E^2}e^{-\frac{A^2D_E^2}{C_E^2}}\left(\frac{C_E^2}{C_E^2+1}\right)\int_{A^2V^2\frac{C_E^2+1}{C_E^2}}^{\infty}e^{-q'}dq'\right.\\
&+\frac{A^2D_S^2+C_S^2}{C_S^2}e^{-\frac{A^2D_S^2}{C_S^2}}\left(\frac{C_S^2}{1-C_S^2}\right)\int_{A^2V^2\frac{1-C_S^2}{C_S^2}}^{A^2D_S^2\frac{1-C_S^2}{C_S^2}}e^{q''}dq''\\
&-\left(\frac{C_E^2+1}{C_E^2}\right)e^{-\frac{A^2D_E^2}{C_E^2}}\left(\frac{C_E^2}{C_E^2+1}\right)^2\int_{A^2V^2\frac{C_E^2+1}{C_E^2}}^{\infty}q'e^{-q'}dq'\\
&\left.+\left(\frac{C_S^2-1}{C_S^2}\right)e^{-\frac{A^2D_S^2}{C_S^2}}\left(\frac{C_S^2}{1-C_S^2}\right)^2\int_{A^2V^2\frac{1-C_S^2}{C_S^2}}^{A^2D_S^2\frac{1-C_S^2}{C_S^2}}q''e^{q''}dq''\right]
\end{aligned}
$$

$$
\begin{aligned}
=&\frac{m}{4\sqrt{\pi}A^3}\left[\left(A^2D_S^2+2\right)e^{-A^2D_S^2}+\frac{A^2D_E^2+C_E^2+C_E^2(q'+1)}{C_E^2+1}e^{-\frac{A^2D_E^2}{C_E^2}}\ e^{-q'}\Big|_{A^2V^2\frac{C_E^2+1}{C_E^2}}^{\infty}+\right.\\
&\left.+\frac{A^2D_S^2+C_S^2-C_S^2(q''-1)}{1-C_S^2}e^{-\frac{A^2D_S^2}{C_S^2}}\ e^{q''}\Big|_{A^2V^2\frac{1-C_S^2}{C_S^2}}^{A^2D_S^2\frac{1-C_S^2}{C_S^2}}\right]\\
=&\frac{m}{4\sqrt{\pi}A^3}\left[\left(A^2D_S^2+2\right)e^{-A^2D_S^2}-\left(A^2V^2+\frac{A^2D_E^2+2C_E^2}{C_E^2+1}\right)e^{-A^2\frac{D_E^2+V^2\left(C_E^2+1\right)}{C_E^2}}\right.\\
&\left.\left(\frac{A^2D_S^2+2C_S^2}{1-C_S^2}-A^2D_S^2\right)e^{-A^2D_S^2}-\left(\frac{A^2D_S^2+2C_S^2}{1-C_S^2}-A^2V^2\right)e^{-A^2\frac{D_S^2-V^2\left(1-C_S^2\right)}{C_S^2}}\right]\\
=&\frac{m}{4\sqrt{\pi}A^3}\left[\frac{A^2D_S^2+2}{1-C_S^2}e^{-A^2D_S^2}-\left(\frac{A^2D_E^2+2C_E^2}{C_E^2+1}+\frac{A^2D_S^2+2C_S^2}{1-C_S^2}\right)e^{-A^2\frac{\left(C_E^2+1\right)D_S^2+\left(1-C_S^2\right)D_E^2}{C_E^2+C_S^2}}\right]\\
=&kT\sqrt{\frac{kT}{2\pi m}}\left\{\frac{B}{B_S}\left[\frac{m}{2kT}\frac{2e}{m}(\phi-\phi_S)+2\right]e^{-\frac{m}{2kT}\frac{2e}{m}(\phi-\phi_S)}-\left[\frac{B}{B_E}\frac{m}{2kT}\frac{2e}{m}(\phi_E-\phi)\right.\right.\\
&\left.\left.+2\left(1-\frac{B}{B_E}\right)+\frac{B}{B_S}\frac{m}{2kT}\frac{2e}{m}(\phi-\phi_S)+2\left(\frac{B}{B_S}-1\right)\right]e^{-\frac{m}{2kT}\frac{B_E\frac{2e}{m}(\phi-\phi_S)+B_S\frac{2e}{m}(\phi_E-\phi)}{B_E-B_S}}\right\}\\
=&kT\sqrt{\frac{kT}{2\pi m}}\left\{\frac{B}{B_S}\left[\frac{e(\phi-\phi_S)}{2kT}+2\right]e^{-\frac{e(\phi-\phi_S)}{kT}}\right.\\
&-\frac{B}{B_E}\left[\frac{e(\phi_E-\phi)}{kT}-2\right]e^{-\frac{e}{kT}\frac{B_E(\phi-\phi_S)+B_S(\phi_E-\phi)}{B_E-B_S}}\\
&\left.-\frac{B}{B_S}\left[\frac{e(\phi-\phi_S)}{kT}+2\right]e^{-\frac{e}{kT}\frac{B_E(\phi-\phi_S)+B_S(\phi_E-\phi)}{B_E-B_S}}\right\}\\
=&kT\sqrt{\frac{kT}{2\pi m}}B\left\{\frac{1}{B_S}\left[\frac{e(\phi-\phi_S)}{2kT}+2\right]e^{-\frac{e(\phi-\phi_S)}{kT}}\right.\\
&-\frac{1}{B_E}\left[\frac{e(\phi_E-\phi)}{kT}-2\right]e^{-\frac{e(\phi-\phi_S)}{kT}\frac{B_E}{B_E-B_S}-\frac{e(\phi_E-\phi)}{kT}\frac{B_S}{B_E-B_S}}\\
&\left.-\frac{1}{B_S}\left[\frac{e(\phi-\phi_S)}{kT}+2\right]e^{-\frac{e(\phi-\phi_S)}{kT}\frac{B_E}{B_E-B_S}-\frac{e(\phi_E-\phi)}{kT}\frac{B_S}{B_E-B_S}}\right\}\\
=&kT\sqrt{\frac{kT}{2\pi m}}Be^{\frac{e(\phi_E-\phi)}{kT}}\left\{\frac{1}{B_S}\left[\frac{e(\phi-\phi_S)}{2kT}+2\right]e^{-\frac{e(\phi_E-\phi_S)}{kT}}\right.\\
&\left.-\frac{1}{B_E}\left[\frac{e(\phi_E-\phi)}{kT}-2\right]e^{-\frac{e(\phi_E-\phi_S)}{kT}\frac{B_E}{B_E-B_S}}-\frac{1}{B_S}\left[\frac{e(\phi-\phi_S)}{kT}+2\right]e^{-\frac{e(\phi_E-\phi_S)}{kT}\frac{B_E}{B_E-B_S}}\right\}
\end{aligned}
\tag{B.11}
$$

So the energy flux is given by

$$
\begin{aligned}
\varepsilon_{\parallel} &= \int_{S_1} \frac{m}{2}\left(v_{\perp}^2+v_{\parallel}^2\right) v_{\parallel}\left(f_S-f_E\right) d^3v \\
&= \int_{S_1}\left[N_S e^{\frac{e(\phi-\phi_S)}{kT_S}}\left(\frac{m}{2\pi kT_S}\right)^{3/2}\frac{m}{2}\left(v_{\perp}^2+v_{\parallel}^2\right) v_{\parallel} e^{-\frac{m}{2kT_S}\left(v_{\perp}^2+v_{\parallel}^2\right)}\right. \\
&\quad \left. N_E e^{\frac{e(\phi-\phi_E)}{kT_E}}\left(\frac{m}{2\pi kT_E}\right)^{3/2}\frac{m}{2}\left(v_{\perp}^2+v_{\parallel}^2\right) v_{\parallel} e^{-\frac{m}{2kT_E}\left(v_{\perp}^2+v_{\parallel}^2\right)}\right] d^3v \\
&= N_S e^{\frac{e(\phi-\phi_S)}{kT_S}} I'(T_S) - N_E e^{\frac{e(\phi-\phi_E)}{kT_E}} I'(T_E) \\
&= \frac{B}{B_E} N_E kT_E \sqrt{\frac{kT_E}{2\pi m}} B_E \left\langle e^{\frac{\Delta}{kT_S}} nt^{3/2}\left\{\frac{1}{B_S}\left[\frac{e(\phi-\phi_S)}{kT_S}+2\right] e^{-\frac{\Delta}{kT_S}}\left[1-e^{-\frac{\Delta B_S}{kT_S(B_E-B_S)}}\right]\right.\right. \\
&\quad \left. -\frac{1}{B_E}\left[\frac{e(\phi_E-\phi)}{kT_S}-2\right] e^{-\frac{\Delta}{kT_S}} e^{-\frac{\Delta B_S}{kT_S(B_E-B_S)}}\right\} \\
&\quad -\left\{\frac{1}{B_S}\left[\frac{e(\phi-\phi_S)}{kT_E}+2\right] e^{-\frac{\Delta}{kT_E}}\left[1-e^{-\frac{\Delta B_S}{kT_E(B_E-B_S)}}\right]\right. \\
&\quad \left. \left. -\frac{1}{B_E}\left[\frac{e(\phi_E-\phi)}{kT_E}-2\right] e^{-\frac{\Delta}{kT_E}} e^{-\frac{\Delta B_S}{kT_E(B_E-B_S)}}\right\}\right\rangle \\
&= \frac{B}{B_E} N_E kT_E \sqrt{\frac{kT_E}{2\pi m}}\left[nt^{3/2}\left\langle \frac{B_E}{B_S}\left[\frac{e(\phi-\phi_S)}{kT_S}+2\right]-\left\{\frac{B_E}{B_S}\left[\frac{e(\phi-\phi_S)}{kT_S}+2\right]\right.\right.\right. \\
&\quad \left. \left. +\left[\frac{e(\phi_E-\phi)}{kT_S}+2\right]\right\} e^{-\frac{\Delta B_S}{kT_S(B_E-B_S)}}\right\rangle - e^{-\frac{\Delta}{kT_E}}\left\langle \frac{B_E}{B_S}\left[\frac{e(\phi-\phi_S)}{kT_E}+2\right]\right. \\
&\quad \left. \left. -\left\{\frac{B_E}{B_S}\left[\frac{e(\phi-\phi_S)}{kT_E}+2\right]+\left[\frac{e(\phi_E-\phi)}{kT_E}-2\right]\right\} e^{-\frac{\Delta B_S}{kT_E(B_E-B_S)}}\right\rangle\right] \\
@E &= N_E kT_E \sqrt{\frac{kT_E}{2\pi m}}\left\langle nt^{3/2}\left\{\frac{B_E}{B_S}\left(\frac{\Delta}{kT_S}+2\right)-\left[\frac{B_E}{B_S}\left(\frac{\Delta}{kT_S}+2\right)-2\right] e^{-\frac{\Delta B_S}{kT_S(B_E-B_S)}}\right\}\right. \\
&\quad \left. -e^{-\frac{\Delta}{kT_E}}\left\{\frac{B_E}{B_S}\left(\frac{\Delta}{kT_E}+2\right)-\left[\frac{B_E}{B_S}\left(\frac{\Delta}{kT_E}+2\right)-2\right] e^{-\frac{\Delta B_S}{kT_E(B_E-B_S)}}\right\}\right\rangle \\
&\approx N_E kT_E \sqrt{\frac{kT_E}{2\pi m}}\left\langle nt^{3/2}\left\{\frac{B_E}{B_S}\left(\frac{r}{t}+2\right)-\left[\frac{B_E}{B_S}\left(\frac{r}{t}+2\right)-2\right]\left(1-\frac{r}{t}\frac{B_S}{B_E-B_S}\right)\right\}\right. \\
&\quad \left. -e^{-x}\left\{\frac{B_E}{B_S}(r+2)-\left[\frac{B_E}{B_S}(r+2)-2\right]\left(1-\frac{rB_S}{B_E-B_S}\right)\right\}\right\rangle \\
&= N_E kT_E \sqrt{\frac{kT_E}{2\pi m}}\left\{nt^{3/2}\left[2+2\frac{r}{t}+\frac{r^2 B_E}{t^2(B_E-B_S)}\right]-e^{-r}\left(2+2r+\frac{r^2 B_E}{B_E-B_S}\right)\right\} \\
&= N_S kT_S \sqrt{\frac{kT_S}{2\pi m}}\left[\left(2+2r'+\frac{r'^2 B_E}{B_E-B_S}\right)-\frac{1}{nt^{3/2}} e^{-r't}\left(2+2r't+\frac{r'^2 t^2 B_E}{B_E-B_S}\right)\right] \\
&\approx N_S kT_S \sqrt{\frac{kT_S}{2\pi m}}\left[\left(2+2r'+\frac{r'^2 B_E}{B_E-B_S}\right)-\frac{1}{nt^{3/2}} e^{-r't}\left(2+2r't+r'^2 t^2\right)\right] \qquad \text{(B.12)}
\end{aligned}
$$

Appendix C

Integrations of Field-Aligned Currents and Electron Energy Flux for kappa Distribution

We have shown the following definitions

$$\begin{aligned} C_S^2 &= 1 - \frac{B_S}{B} \\ D_S^2 &= \frac{2e}{m}(\phi - \phi_S) \\ C_E^2 &= \frac{B_E}{B} - 1 \\ D_E^2 &= \frac{2e}{m}(\phi_E - \phi) \\ V^2 &= \frac{C_E^2 D_S^2 - C_S^2 D_E^2}{C_E^2 + C_S^2} \end{aligned} \tag{C.1}$$

The integration path S_1 is the straight through trajectory from plasma sheet to the ionosphere. So the field-aligned currents could be integrated as

$$
\begin{aligned}
j_{\parallel} &= -e\int_{S_1} v_{\parallel} f_S d^3v \\
&= -e\int_{S_1} v_{\parallel} N_S \left(\frac{m}{2E_{0S}}\right)^{3/2} \frac{\Gamma(\kappa_S+1)}{(\pi\kappa_S)^{3/2}\Gamma(\kappa_S-\frac{1}{2})} \frac{1}{\left(1+\frac{E}{\kappa_S E_{0S}}\right)^{\kappa_S+1}} d^3v \\
&= -e\left(\frac{m}{2}\right)^{3/2} \int_{S_1} v_{\parallel} \frac{N_S}{E_{0S}^{3/2}} \frac{\Gamma(\kappa_S+1)}{(\pi\kappa_S)^{3/2}\Gamma(\kappa_S-\frac{1}{2})} \frac{1}{\left[1+\frac{\frac{1}{2}mv_{\perp}^2+\frac{1}{2}mv_{\parallel}^2-e(\phi-\phi_S)}{\kappa_S E_{0S}}\right]^{\kappa_S+1}} d^3v \\
&= -e\left(\frac{m}{2}\right)^{3/2} \frac{N_S}{E_{0S}^{3/2}} \frac{\Gamma(\kappa_S+1)}{(\pi\kappa_S)^{3/2}\Gamma(\kappa_S-\frac{1}{2})} \int_{S_1} \frac{v_{\parallel} 2\pi v_{\perp} dv_{\parallel} dv_{\perp}}{\left[1-\frac{e(\phi-\phi_S)}{\kappa_S E_{0S}}+\frac{mv_{\perp}^2+mv_{\parallel}^2}{2\kappa_S E_{0S}}\right]^{\kappa_S+1}} \\
&= -e\left(\frac{m}{2}\right)^{3/2} \frac{N_S}{E_{0S}^{3/2}} \frac{\Gamma(\kappa_S+1)}{(\pi\kappa_S)^{3/2}\Gamma(\kappa_S-\frac{1}{2})} \frac{2\pi\kappa_S E_{0S}}{m} \\
&\quad \left\{ \int_{D_S}^{\infty} v_{\parallel} dv_{\parallel} \int_0^{v_{\perp}^2=\frac{v_{\parallel}^2+D_E^2}{C_E^2}} \frac{d\left(\frac{m}{2\kappa_S E_{0S}} v_{\perp}^2\right)}{\left[1-\frac{e(\phi-\phi_S)}{\kappa_S E_{0S}}+\frac{mv_{\perp}^2+mv_{\parallel}^2}{2\kappa_S E_{0S}}\right]^{\kappa_S+1}} \right. \\
&\quad \left. + \int_V^{D_S} v_{\parallel} dv_{\parallel} \int_{v_{\perp}^2=\frac{D_S^2-v_{\parallel}^2}{C_S^2}}^{v_{\perp}^2=\frac{v_{\parallel}^2+D_E^2}{C_E^2}} \frac{d\left(\frac{m}{2\kappa_S E_{0S}} v_{\perp}^2\right)}{\left[1-\frac{e(\phi-\phi_S)}{\kappa_S E_{0S}}+\frac{mv_{\perp}^2+mv_{\parallel}^2}{2\kappa_S E_{0S}}\right]^{\kappa_S+1}} \right\} \\
&= e\left(\frac{m}{2\pi}\right)^{1/2} \frac{N_S}{E_{0S}^{1/2}} \frac{\Gamma(\kappa_S+1)}{\kappa_S^{3/2}\Gamma(\kappa_S-\frac{1}{2})} \left\{ \int_{D_S}^{\infty} v_{\parallel} dv_{\parallel} \frac{1}{\left[1-\frac{e(\phi-\phi_S)}{\kappa_S E_{0S}}+\frac{mv_{\perp}^2+mv_{\parallel}^2}{2\kappa_S E_{0S}}\right]^{\kappa_S}} \right|_0^{v_{\perp}^2=\frac{v_{\parallel}^2+D_E^2}{C_E^2}} \\
&\quad \left. + \int_V^{D_S} v_{\parallel} dv_{\parallel} \frac{1}{\left[1-\frac{e(\phi-\phi_S)}{\kappa_S E_{0S}}+\frac{mv_{\perp}^2+mv_{\parallel}^2}{2\kappa_S E_{0S}}\right]^{\kappa_S}} \right|_{v_{\perp}^2=\frac{D_S^2-v_{\parallel}^2}{C_S^2}}^{v_{\perp}^2=\frac{v_{\parallel}^2+D_E^2}{C_E^2}} \right\}
\end{aligned}
$$

$$=e\left(\frac{m}{2\pi}\right)^{1/2}\frac{N_S}{E_{0S}^{1/2}}\frac{\Gamma(\kappa_S+1)}{\kappa_S^{3/2}\Gamma(\kappa_S-\frac{1}{2})}$$

$$\left\langle\int_{D_S}^{\infty}v_\parallel dv_\parallel\left\{\frac{1}{\left[1-\frac{e(\phi-\phi_S)}{\kappa_S E_{0S}}+\frac{m\frac{v_\parallel^2+D_E^2}{C_E^2}+mv_\parallel^2}{2\kappa_S E_{0S}}\right]^{\kappa_S}}-\frac{1}{\left[1-\frac{e(\phi-\phi_S)}{\kappa_S E_{0S}}+\frac{v_\parallel^2}{2\kappa_S E_{0S}}\right]^{\kappa_S}}\right\}\right.$$

$$\left.\int_{V}^{D_S}v_\parallel dv_\parallel\left\{\frac{1}{\left[1-\frac{e(\phi-\phi_S)}{\kappa_S E_{0S}}+\frac{m\frac{v_\parallel^2+D_E^2}{C_E^2}+v_\parallel^2}{2\kappa_S E_{0S}}\right]^{\kappa_S}}-\frac{1}{\left[1-\frac{e(\phi-\phi_S)}{\kappa_S E_{0S}}+\frac{m\frac{D_S^2-v_\parallel^2}{C_S^2}+mv_\parallel^2}{2\kappa_S E_{0S}}\right]^{\kappa_S}}\right\}\right\rangle$$

$$=e\left(\frac{m}{2\pi}\right)^{1/2}\frac{N_S}{E_{0S}^{1/2}}\frac{\Gamma(\kappa_S+1)}{\kappa_S^{3/2}\Gamma(\kappa_S-\frac{1}{2})}\frac{\kappa_S E_{0S}}{m}$$

$$\left\{\frac{B_E-B}{B_E}\int_{D_S}^{\infty}\frac{d\left(\frac{B_E}{B_E-B}\frac{mv_\parallel^2}{2\kappa_S E_{0S}}\right)}{[1-\frac{e(\phi-\phi_S)}{\kappa_S E_{0S}}+\frac{mD_E^2}{2\kappa_S E_{0S}C_E^2}+\frac{B_E}{B_E-B}\frac{mv_\parallel^2}{2\kappa_S E_{0S}}]^{\kappa_S}}-\int_{D_S}^{\infty}\frac{d\left(\frac{mv_\parallel^2}{2\kappa_S E_{0S}}\right)}{[1-\frac{e(\phi-\phi_S)}{\kappa_S E_{0S}}+\frac{mv_\parallel^2}{2\kappa_S E_{0S}}]^{\kappa_S}}\right.$$

$$+\frac{B_E-B}{B_E}\int_{V}^{D_S}\frac{d\left(\frac{B_E}{B_E-B}\frac{mv_\parallel^2}{2\kappa_S E_{0S}}\right)}{[1-\frac{e(\phi-\phi_S)}{\kappa_S E_{0S}}+\frac{mD_E^2}{2\kappa_S E_{0S}C_E^2}+\frac{B_E}{B_E-B}\frac{mv_\parallel^2}{2\kappa_S E_{0S}}]^{\kappa_S}}$$

$$\left.-\frac{B_S-B}{B_S}\int_{D_S}^{\infty}\frac{d\left(\frac{B_S}{B_S-B}\frac{mv_\parallel^2}{2\kappa_S E_{0S}}\right)}{[1-\frac{e(\phi-\phi_S)}{\kappa_S E_{0S}}+\frac{mD_S^2}{2\kappa_S E_{0S}C_S^2}+\frac{B_E}{B_E-B}\frac{mv_\parallel^2}{2\kappa_S E_{0S}}]^{\kappa_S}}\right\}$$

$$=e\left(\frac{1}{2\pi m}\right)^{1/2}N_S\frac{E_{0S}^{1/2}\Gamma(\kappa_S+1)}{\kappa_S^{1/2}\Gamma(\kappa_S-\frac{1}{2})(1-\kappa_S)}$$

$$\left\{\frac{B_E-B}{B_E}\frac{1}{[1-\frac{e(\phi-\phi_S)}{\kappa_S E_{0S}}+\frac{mD_E^2}{2\kappa_S E_{0S}C_E^2}+\frac{B_E}{B_E-B}\frac{mv_\parallel^2}{2\kappa_S E_{0S}}]^{\kappa_S-1}}\right|_{D_S}^{\infty}$$

$$-\frac{1}{[1-\frac{e(\phi-\phi_S)}{\kappa_S E_{0S}}+\frac{mv_\parallel^2}{2\kappa_S E_{0S}}]^{\kappa_S-1}}\Bigg|_{D_S}^{\infty}+\frac{1}{[1-\frac{e(\phi-\phi_S)}{\kappa_S E_{0S}}+\frac{mD_E^2}{2\kappa_S E_{0S}C_E^2}+\frac{B_E}{B_E-B}\frac{mv_\parallel^2}{2\kappa_S E_{0S}}]^{\kappa_S-1}}\Bigg|_{V}^{D_S}$$

$$\left.-\frac{B_S-B}{B_S}\frac{1}{[1-\frac{e(\phi-\phi_S)}{\kappa_S E_{0S}}+\frac{mD_S^2}{2\kappa_S E_{0S}C_S^2}+\frac{B_S}{B_S-B}\frac{mv_\parallel^2}{2\kappa_S E_{0S}}]^{\kappa_S-1}}\right|_{V}^{D_S}\right\}$$

$$
\begin{aligned}
=& e\left(\frac{1}{2\pi m}\right)^{1/2} N_S \frac{E_{0S}^{1/2}\Gamma(\kappa_S+1)}{\kappa_S^{1/2}\Gamma(\kappa_S-\frac{1}{2})(1-\kappa_S)} \left\{ \frac{1}{[1-\frac{e(\phi-\phi_S)}{\kappa_S E_{0S}}+\frac{mD_S^2}{2\kappa_S E_{0S}}]^{\kappa_S-1}} \right. \\
& -\frac{B_E-B}{B_E}\frac{1}{[1-\frac{e(\phi-\phi_S)}{\kappa_S E_{0S}}+\frac{mD_E^2}{2\kappa_S E_{0S}C_E^2}+\frac{B_E}{B_E-B}\frac{mV^2}{2\kappa_S E_{0S}}]^{\kappa_S-1}} \\
& -\frac{B_S-B}{B_S}\frac{1}{[1-\frac{e(\phi-\phi_S)}{\kappa_S E_{0S}}+\frac{mD_S^2}{2\kappa_S E_{0S}C_S^2}+\frac{B_S}{B_S-B}\frac{mD_S^2}{2\kappa_S E_{0S}}]^{\kappa_S-1}} \\
& \left. +\frac{B_S-B}{B_S}\frac{1}{[1-\frac{e(\phi-\phi_S)}{\kappa_S E_{0S}}+\frac{mD_S^2}{2\kappa_S E_{0S}C_S^2}+\frac{B_S}{B_S-B}\frac{mV^2}{2\kappa_S E_{0S}}]^{\kappa_S-1}} \right\} \\
=& e\left(\frac{1}{2\pi m}\right)^{1/2} N_S \frac{E_{0S}^{1/2}\Gamma(\kappa_S+1)}{\kappa_S^{1/2}\Gamma(\kappa_S-\frac{1}{2})(1-\kappa_S)} \left\{ 1-\frac{B_E-B}{B_E}\frac{1}{[1+\frac{B_S}{B_E-B_S}\frac{e(\phi_E-\phi_S)}{\kappa_S E_{0S}}]^{\kappa_S-1}} \right. \\
& \left. -\frac{B_S-B}{B_S}+\frac{B_S-B}{B_S}\frac{1}{[1+\frac{B_S}{B_E-B_S}\frac{e(\phi_E-\phi_S)}{\kappa_S E_{0S}}]^{\kappa_S-1}} \right\} \\
=& -e\left(\frac{1}{2\pi m}\right)^{1/2} N_S \frac{E_{0S}^{1/2}\kappa_S^{1/2}\Gamma(\kappa_S-1)}{\Gamma(\kappa_S-\frac{1}{2})} \left\{ \frac{B}{B_S}+\left(\frac{B}{B_E}-\frac{B}{B_S}\right)\frac{1}{[1+\frac{B_S}{B_E-B_S}\frac{e(\phi_E-\phi_S)}{\kappa_S E_{0S}}]^{\kappa_S-1}} \right\} \\
@E =& -e\left(\frac{1}{2\pi m}\right)^{1/2} N_S \frac{E_{0S}^{1/2}\kappa_S^{1/2}\Gamma(\kappa_S-1)}{\Gamma(\kappa_S-\frac{1}{2})} \left\{ \frac{B_E}{B_S}+\left(1-\frac{B_E}{B_S}\right)\frac{1}{[1+\frac{B_S}{B_E-B_S}\frac{e(\phi_E-\phi_S)}{\kappa_S E_{0S}}]^{\kappa_S-1}} \right\} \\
\approx& -eN_S\sqrt{\frac{E_{0S}\kappa_S}{2\pi m}}\frac{\Gamma(\kappa_S-1)}{\Gamma(\kappa_S-\frac{1}{2})} \left\{ \frac{B_E}{B_S}+\left(1-\frac{B_E}{B_S}\right)\left[1-(\kappa_S-1)\frac{B_S}{B_E-B_S}\frac{e(\phi_E-\phi_S)}{\kappa_S E_{0S}}\right] \right\} \\
=& -eN_S\sqrt{\frac{kT_S}{2\pi m}}\frac{\sqrt{\kappa_S-\frac{3}{2}}\Gamma(\kappa_S-1)}{\Gamma(\kappa_S-\frac{1}{2})}\left[1+(\kappa_S-1)\frac{e(\phi_E-\phi_S)}{\kappa_S E_{0S}}\right] \\
=& -eN_S\sqrt{\frac{kT_S}{2\pi m}}\frac{\sqrt{\kappa_S-\frac{3}{2}}\Gamma(\kappa_S-1)}{\Gamma(\kappa_S-\frac{1}{2})}\left[1+\frac{\kappa_S-1}{\kappa_S-\frac{3}{2}}\frac{e(\phi_E-\phi_S)}{kT_S}\right] \qquad \text{(C.2)}
\end{aligned}
$$

and the energy flux could be calculated as

$$
\begin{aligned}
&\varepsilon_{\parallel} \\
&= \int_{S_1} \frac{m}{2}(v_\perp^2 + v_\parallel^2) v_\parallel f_S d^3v \\
&= \left(\frac{m}{2}\right)^{3/2} \int_{S_1} \frac{m}{2}(v_\perp^2 + v_\parallel^2) v_\parallel \frac{N_S}{E_{0S}^{3/2}} \frac{\Gamma(\kappa_S+1)}{(\pi\kappa_S)^{3/2}\Gamma(\kappa_S-\frac{1}{2})} \frac{1}{\left[1+\frac{\frac{m}{2}v_\perp^2+\frac{m}{2}v_\parallel^2-e(\phi-\phi_S)}{\kappa_S E_{0S}}\right]^{\kappa_S+1}} d^3v \\
&= \left(\frac{m}{2}\right)^{5/2} \frac{N_S}{E_{0S}^{3/2}} \frac{\Gamma(\kappa_S+1)}{(\pi\kappa_S)^{3/2}\Gamma(\kappa_S-\frac{1}{2})} \int_{S_1} \frac{(v_\perp^2+v_\parallel^2) v_\parallel 2\pi v_\perp dv_\parallel dv_\perp}{\left[1-\frac{e(\phi-\phi_S)}{\kappa_S E_{0S}}+\frac{mv_\perp^2+mv_\parallel^2}{2\kappa_S E_{0S}}\right]^{\kappa_S+1}} \\
&= 2\pi \left(\frac{m}{2}\right)^{5/2} \frac{N_S}{E_{0S}^{3/2}} \frac{\Gamma(\kappa_S+1)}{(\pi\kappa_S)^{3/2}\Gamma(\kappa_S-\frac{1}{2})} \\
&\quad \left\{ \int_{S_1} v_\parallel dv_\parallel \frac{v_\perp^3 dv_\perp}{\left[1-\frac{e(\phi-\phi_S)}{\kappa_S E_{0S}}+\frac{mv_\perp^2+mv_\parallel^2}{2\kappa_S E_{0S}}\right]^{\kappa_S+1}} + \int_{S_1} v_\parallel^3 dv_\parallel \frac{v_\perp dv_\perp}{\left[1-\frac{e(\phi-\phi_S)}{\kappa_S E_{0S}}+\frac{mv_\perp^2+mv_\parallel^2}{2\kappa_S E_{0S}}\right]^{\kappa_S+1}} \right\} \\
&= \pi \left(\frac{m}{2}\right)^{3/2} \frac{N_S}{E_{0S}^{1/2}} \frac{\kappa_S\Gamma(\kappa_S+1)}{(\pi\kappa_S)^{3/2}\Gamma(\kappa_S-\frac{1}{2})} \left\{ \int_{D_S}^{\infty} v_\parallel dv_\parallel \int_0^{v_\perp^2=\frac{v_\parallel^2+D_E^2}{C_E^2}} \frac{v_\perp^2 d\left(\frac{m}{2\kappa_S E_{0S}} v_\perp^2\right)}{\left[1-\frac{e(\phi-\phi_S)}{\kappa_S E_{0S}}+\frac{mv_\perp^2+mv_\parallel^2}{2\kappa_S E_{0S}}\right]^{\kappa_S+1}} \right. \\
&\quad + \int_V^{D_S} v_\parallel dv_\parallel \int_{v_\perp^2=\frac{D_S^2-v_\parallel^2}{C_S^2}}^{v_\perp^2=\frac{v_\parallel^2+D_E^2}{C_E^2}} \frac{v_\perp^2 d\left(\frac{m}{2\kappa_S E_{0S}} v_\perp^2\right)}{\left[1-\frac{e(\phi-\phi_S)}{\kappa_S E_{0S}}+\frac{mv_\perp^2+mv_\parallel^2}{2\kappa_S E_{0S}}\right]^{\kappa_S+1}} \\
&\quad + \int_{D_S}^{\infty} v_\parallel^3 dv_\parallel \int_0^{v_\perp^2=\frac{v_\parallel^2+D_E^2}{C_E^2}} \frac{d\left(\frac{m}{2\kappa_S E_{0S}} v_\perp^2\right)}{\left[1-\frac{e(\phi-\phi_S)}{\kappa_S E_{0S}}+\frac{mv_\perp^2+mv_\parallel^2}{2\kappa_S E_{0S}}\right]^{\kappa_S+1}} \\
&\quad \left. + \int_V^{D_S} v_\parallel^3 dv_\parallel \int_{v_\perp^2=\frac{D_S^2-v_\parallel^2}{C_S^2}}^{v_\perp^2=\frac{v_\parallel^2+D_E^2}{C_E^2}} \frac{d\left(\frac{m}{2\kappa_S E_{0S}} v_\perp^2\right)}{\left[1-\frac{e(\phi-\phi_S)}{\kappa_S E_{0S}}+\frac{mv_\perp^2+mv_\parallel^2}{2\kappa_S E_{0S}}\right]^{\kappa_S+1}} \right\}
\end{aligned}
$$

$$= -\pi\left(\frac{m}{2}\right)^{3/2}\frac{N_S}{E_{0S}^{1/2}}\frac{\Gamma(\kappa_S+1)}{(\pi\kappa_S)^{3/2}\Gamma(\kappa_S-\frac{1}{2})}\left\langle\int_{D_S}^{\infty}v_\parallel dv_\parallel\left\{\frac{v_\perp^2}{\left[1-\frac{e(\phi-\phi_S)}{\kappa_S E_{0S}}+\frac{mv_\perp^2+mv_\parallel^2}{2\kappa_S E_{0S}}\right]^{\kappa_S}}\right|_0^{\frac{v_\parallel^2+D_E^2}{C_E^2}}\right.$$

$$\left.-\int_0^{\frac{v_\parallel^2+D_E^2}{C_E^2}}\frac{d(v_\perp^2)}{\left[1-\frac{e(\phi-\phi_S)}{\kappa_S E_{0S}}+\frac{mv_\perp^2+mv_\parallel^2}{2\kappa_S E_{0S}}\right]^{\kappa_S}}\right\}$$

$$+\int_V^{D_S}v_\parallel dv_\parallel\left\{\frac{v_\perp^2}{\left[1-\frac{e(\phi-\phi_S)}{\kappa_S E_{0S}}+\frac{mv_\perp^2+mv_\parallel^2}{2\kappa_S E_{0S}}\right]^{\kappa_S}}\right|_{\frac{D_S^2-v_\parallel^2}{C_S^2}}^{\frac{v_\parallel^2+D_E^2}{C_E^2}}$$

$$\left.-\int_{\frac{D_S^2-v_\parallel^2}{C_S^2}}^{\frac{v_\parallel^2+D_E^2}{C_E^2}}\frac{d(v_\perp^2)}{\left[1-\frac{e(\phi-\phi_S)}{\kappa_S E_{0S}}+\frac{mv_\perp^2+mv_\parallel^2}{2\kappa_S E_{0S}}\right]^{\kappa_S}}\right\}+\int_{D_S}^{\infty}v_\parallel^3 dv_\parallel\left.\frac{1}{\left[1-\frac{e(\phi-\phi_S)}{\kappa_S E_{0S}}+\frac{mv_\perp^2+mv_\parallel^2}{2\kappa_S E_{0S}}\right]^{\kappa_S}}\right|_0^{\frac{v_\parallel^2+D_E^2}{C_E^2}}$$

$$\left.+\int_V^{D_S}v_\parallel^3 dv_\parallel\left.\frac{1}{\left[1-\frac{e(\phi-\phi_S)}{\kappa_S E_{0S}}+\frac{mv_\perp^2+mv_\parallel^2}{2\kappa_S E_{0S}}\right]^{\kappa_S}}\right|_{\frac{D_S^2-v_\parallel^2}{C_S^2}}^{\frac{v_\parallel^2+D_E^2}{C_E^2}}\right\rangle$$

$$
\begin{aligned}
= & -\pi\left(\frac{m}{2}\right)^{3/2}\frac{N_S}{E_{0S}^{1/2}}\frac{\Gamma(\kappa_S+1)}{(\pi\kappa_S)^{3/2}\Gamma(\kappa_S-\frac{1}{2})}\left\langle\int_{D_S}^{\infty}v_\parallel dv_\parallel\left\{\frac{\frac{v_\parallel^2+D_E^2}{C_E^2}}{\left[1-\frac{e(\phi-\phi_S)}{\kappa_S E_{0S}}+\frac{m\frac{v_\parallel^2+D_E^2}{C_E^2}+mv_\parallel^2}{2\kappa_S E_{0S}}\right]^{\kappa_S}}\right.\right. \\
& \left.\left.-\frac{2\kappa_S E_{0S}}{m(1-\kappa_S)}\frac{1}{\left[1-\frac{e(\phi-\phi_S)}{\kappa_S E_{0S}}+\frac{mv_\perp^2+mv_\parallel^2}{2\kappa_S E_{0S}}\right]^{\kappa_S-1}}\right|_0^{\frac{v_\parallel^2+D_E^2}{C_E^2}}\right\} \\
& +\int_V^{D_S}v_\parallel dv_\parallel\left\{\frac{\frac{v_\parallel^2+D_E^2}{C_E^2}}{\left[1-\frac{e(\phi-\phi_S)}{\kappa_S E_{0S}}+\frac{m\frac{v_\parallel^2+D_E^2}{C_E^2}+mv_\parallel^2}{2\kappa_S E_{0S}}\right]^{\kappa_S}}-\frac{\frac{D_S^2-v_\parallel^2}{C_S^2}}{\left[1-\frac{e(\phi-\phi_S)}{\kappa_S E_{0S}}+\frac{m\frac{D_S^2-v_\parallel^2}{C_S^2}+mv_\parallel^2}{2\kappa_S E_{0S}}\right]^{\kappa_S}}\right. \\
& \left.-\frac{2\kappa_S E_{0S}}{m(1-\kappa_S)}\frac{1}{\left[1-\frac{e(\phi-\phi_S)}{\kappa_S E_{0S}}+\frac{mv_\perp^2+mv_\parallel^2}{2\kappa_S E_{0S}}\right]^{\kappa_S-1}}\right|_{\frac{D_S^2-v_\parallel^2}{C_S^2}}^{\frac{v_\parallel^2+D_E^2}{C_E^2}}\Bigg\} \\
& +\int_{D_S}^{\infty}v_\parallel^3 dv_\parallel\left\{\frac{1}{\left[1-\frac{e(\phi-\phi_S)}{\kappa_S E_{0S}}+\frac{m\frac{v_\parallel^2+D_E^2}{C_E^2}+mv_\parallel^2}{2\kappa_S E_{0S}}\right]^{\kappa_S}}-\frac{1}{\left[1-\frac{e(\phi-\phi_S)}{\kappa_S E_{0S}}+\frac{mv_\parallel^2}{2\kappa_S E_{0S}}\right]^{\kappa_S}}\right\} \\
& +\int_V^{D_S}v_\parallel^3 dv_\parallel\left\{\frac{1}{\left[1-\frac{e(\phi-\phi_S)}{\kappa_S E_{0S}}+\frac{m\frac{v_\parallel^2+D_E^2}{C_E^2}+mv_\parallel^2}{2\kappa_S E_{0S}}\right]^{\kappa_S}}-\frac{1}{\left[1-\frac{e(\phi-\phi_S)}{\kappa_S E_{0S}}+\frac{m\frac{D_S^2-v_\parallel^2}{C_S^2}+mv_\parallel^2}{2\kappa_S E_{0S}}\right]^{\kappa_S}}\right\}\Bigg\rangle
\end{aligned}
$$

$$
\begin{aligned}
&= -\pi\left(\frac{m}{2}\right)^{3/2}\frac{N_S}{E_{0S}^{1/2}}\frac{\Gamma(\kappa_S+1)}{(\pi\kappa_S)^{3/2}\Gamma(\kappa_S-\frac{1}{2})}\\
&\left\langle\int_{D_S}^{\infty}v_\parallel dv_\parallel\left\{\frac{\frac{v_\parallel^2+D_E^2}{C_E^2}}{\left[1-\frac{e(\phi-\phi_S)}{\kappa_S E_{0S}}+\frac{mD_E^2}{2\kappa_S E_{0S}C_E^2}+\frac{B_E}{B_E-B}\frac{mv_\parallel^2}{2\kappa_S E_{0S}}\right]^{\kappa_S}}\right.\right.\\
&\left.-\frac{2\kappa_S E_{0S}}{m(1-\kappa_S)}\frac{1}{\left[1-\frac{e(\phi-\phi_S)}{\kappa_S E_{0S}}+\frac{m\frac{v_\parallel^2+D_E^2}{C_E^2}+mv_\parallel^2}{2\kappa_S E_{0S}}\right]^{\kappa_S-1}}+\frac{2\kappa_S E_{0S}}{m(1-\kappa_S)}\frac{1}{\left[1-\frac{e(\phi-\phi_S)}{\kappa_S E_{0S}}+\frac{mv_\parallel^2}{2\kappa_S E_{0S}}\right]^{\kappa_S-1}}\right\}\\
&+\int_V^{D_S}v_\parallel dv_\parallel\left\{\frac{\frac{v_\parallel^2+D_E^2}{C_E^2}}{\left[1-\frac{e(\phi-\phi_S)}{\kappa_S E_{0S}}+\frac{mD_E^2}{2\kappa_S E_{0S}C_E^2}+\frac{B_E}{B_E-B}\frac{mv_\parallel^2}{2\kappa_S E_{0S}}\right]^{\kappa_S}}\right.\\
&-\frac{\frac{D_S^2-v_\parallel^2}{C_S^2}}{\left[1-\frac{e(\phi-\phi_S)}{\kappa_S E_{0S}}+\frac{mD_S^2}{2\kappa_S E_{0S}C_S^2}+\frac{B_S}{B_S-B}\frac{mv_\parallel^2}{2\kappa_S E_{0S}}\right]^{\kappa_S}}\\
&\left.-\frac{2\kappa_S E_{0S}}{m(1-\kappa_S)}\frac{1}{\left[1-\frac{e(\phi-\phi_S)}{\kappa_S E_{0S}}+\frac{m\frac{v_\parallel^2+D_E^2}{C_E^2}+mv_\parallel^2}{2\kappa_S E_{0S}}\right]^{\kappa_S-1}}+\frac{2\kappa_S E_{0S}}{m(1-\kappa_S)}\frac{1}{\left[1-\frac{e(\phi-\phi_S)}{\kappa_S E_{0S}}+\frac{m\frac{D_S^2-v_\parallel^2}{C_S^2}+mv_\parallel^2}{2\kappa_S E_{0S}}\right]^{\kappa_S-1}}\right\}\\
&+\int_{D_S}^{\infty}v_\parallel^3 dv_\parallel\left\{\frac{1}{\left[1-\frac{e(\phi-\phi_S)}{\kappa_S E_{0S}}+\frac{mD_E^2}{2\kappa_S E_{0S}C_E^2}+\frac{B_E}{B_E-B}\frac{mv_\parallel^2}{2\kappa_S E_{0S}}\right]^{\kappa_S}}-\frac{1}{\left[1-\frac{e(\phi-\phi_S)}{\kappa_S E_{0S}}+\frac{mv_\parallel^2}{2\kappa_S E_{0S}}\right]^{\kappa_S}}\right\}\\
&+\int_V^{D_S}v_\parallel^3 dv_\parallel\left\{\frac{1}{\left[1-\frac{e(\phi-\phi_S)}{\kappa_S E_{0S}}+\frac{mD_E^2}{2\kappa_S E_{0S}C_E^2}+\frac{B_E}{B_E-B}\frac{mv_\parallel^2}{2\kappa_S E_{0S}}\right]^{\kappa_S}}\right.\\
&\left.\left.-\frac{1}{\left[1-\frac{e(\phi-\phi_S)}{\kappa_S E_{0S}}+\frac{mD_S^2}{2\kappa_S E_{0S}C_S^2}+\frac{B_S}{B_S-B}\frac{mv_\parallel^2}{2\kappa_S E_{0S}}\right]^{\kappa_S}}\right\}\right\rangle
\end{aligned}
$$

$$
\begin{aligned}
&= -\pi\left(\frac{m}{2}\right)^{3/2}\frac{N_S}{E_{0S}^{1/2}}\frac{\Gamma(\kappa_S+1)}{(\pi\kappa_S)^{3/2}\Gamma(\kappa_S-\frac{1}{2})} \\
&\left\{\frac{B_E}{B_E-B}\int_V^{\infty} v_\parallel^3 dv_\parallel \frac{1}{\left[1-\frac{e(\phi-\phi_S)}{\kappa_S E_{0S}}+\frac{mD_E^2}{2\kappa_S E_{0S}C_E^2}+\frac{B_E}{B_E-B}\frac{mv_\parallel^2}{2\kappa_S E_{0S}}\right]^{\kappa_S}}\right. \\
&+\frac{B_S}{B-B_S}\int_V^{Ds} v_\parallel^3 dv_\parallel \frac{1}{\left[1-\frac{e(\phi-\phi_S)}{\kappa_S E_{0S}}+\frac{mD_S^2}{2\kappa_S E_{0S}C_S^2}+\frac{B_S}{B_S-B}\frac{mv_\parallel^2}{2\kappa_S E_{0S}}\right]^{\kappa_S}} \\
&-\int_{Ds}^{\infty} v_\parallel^3 dv_\parallel \frac{1}{\left[1-\frac{e(\phi-\phi_S)}{\kappa_S E_{0S}}+\frac{mv_\parallel^2}{2\kappa_S E_{0S}}\right]^{\kappa_S}} \\
&-\frac{2\kappa_S E_{0S}}{m(1-\kappa_S)}\int_V^{\infty} v_\parallel dv_\parallel \frac{1}{\left[1-\frac{e(\phi-\phi_S)}{\kappa_S E_{0S}}+\frac{mD_E^2}{2\kappa_S E_{0S}C_E^2}+\frac{B_E}{B_E-B}\frac{mv_\parallel^2}{2\kappa_S E_{0S}}\right]^{\kappa_S-1}} \\
&+\frac{2\kappa_S E_{0S}}{m(1-\kappa_S)}\int_{Ds}^{\infty} v_\parallel dv_\parallel \frac{1}{\left[1-\frac{e(\phi-\phi_S)}{\kappa_S E_{0S}}+\frac{mv_\parallel^2}{2\kappa_S E_{0S}}\right]^{\kappa_S-1}} \\
&+\frac{2\kappa_S E_{0S}}{m(1-\kappa_S)}\int_V^{Ds} v_\parallel dv_\parallel \frac{1}{\left[1-\frac{e(\phi-\phi_S)}{\kappa_S E_{0S}}+\frac{mD_S^2}{2\kappa_S E_{0S}C_S^2}+\frac{B_S}{B_S-B}\frac{mv_\parallel^2}{2\kappa_S E_{0S}}\right]^{\kappa_S-1}} \\
&+\frac{B}{B_E-B}\frac{2e(\phi_E-\phi)}{m}\int_V^{\infty} v_\parallel dv_\parallel \frac{1}{\left[1-\frac{e(\phi-\phi_S)}{\kappa_S E_{0S}}+\frac{mD_E^2}{2\kappa_S E_{0S}C_E^2}+\frac{B_E}{B_E-B}\frac{mv_\parallel^2}{2\kappa_S E_{0S}}\right]^{\kappa_S}} \\
&\left.-\frac{B}{B-B_S}\frac{2e(\phi-\phi_S)}{m}\int_V^{Ds} v_\parallel dv_\parallel \frac{1}{\left[1-\frac{e(\phi-\phi_S)}{\kappa_S E_{0S}}+\frac{mD_S^2}{2\kappa_S E_{0S}C_S^2}+\frac{B_S}{B_S-B}\frac{mv_\parallel^2}{2\kappa_S E_{0S}}\right]^{\kappa_S}}\right\}
\end{aligned}
$$

$$
\begin{aligned}
= &- \sqrt{\frac{m}{8\pi}} N_S \frac{E_{0S}^{1/2}\Gamma(\kappa_S+1)}{\kappa_S^{1/2}\Gamma(\kappa_S-\frac{1}{2})} \left\{ \int_{v_\parallel=V}^{\infty} \frac{v_\parallel^2 d\left(\frac{B_E}{B_E-B}\frac{mv_\parallel^2}{2\kappa_S E_{0S}}\right)}{\left[1-\frac{e(\phi-\phi_S)}{\kappa_S E_{0S}}+\frac{mD_E^2}{2\kappa_S E_{0S}C_E^2}+\frac{B_E}{B_E-B}\frac{mv_\parallel^2}{2\kappa_S E_{0S}}\right]^{\kappa_S}} \right. \\
&- \int_{v_\parallel=V}^{v_\parallel=D_S} \frac{v_\parallel^2 d\left(\frac{B_S}{B_S-B}\frac{mv_\parallel^2}{2\kappa_S E_{0S}}\right)}{\left[1-\frac{e(\phi-\phi_S)}{\kappa_S E_{0S}}+\frac{mD_S^2}{2\kappa_S E_{0S}C_S^2}+\frac{B_S}{B_S-B}\frac{mv_\parallel^2}{2\kappa_S E_{0S}}\right]^{\kappa_S}} - \int_{v_\parallel=D_S}^{\infty} \frac{v_\parallel^2 d\left(\frac{mv_\parallel^2}{2\kappa_S E_{0S}}\right)}{\left[1-\frac{e(\phi-\phi_S)}{\kappa_S E_{0S}}+\frac{mv_\parallel^2}{2\kappa_S E_{0S}}\right]^{\kappa_S}} \\
&- \frac{B_E-B}{B_E}\frac{2\kappa_S E_{0S}}{m(1-\kappa_S)(2-\kappa_S)} \frac{1}{\left[1-\frac{e(\phi-\phi_S)}{\kappa_S E_{0S}}+\frac{mD_E^2}{2\kappa_S E_{0S}C_E^2}+\frac{B_E}{B_E-B}\frac{mv_\parallel^2}{2\kappa_S E_{0S}}\right]^{\kappa_S-2}}\Bigg|_V^{\infty} \\
&+ \frac{2\kappa_S E_{0S}}{m(1-\kappa_S)(2-\kappa_S)} \frac{1}{\left[1-\frac{e(\phi-\phi_S)}{\kappa_S E_{0S}}+\frac{mv_\parallel^2}{2\kappa_S E_{0S}}\right]^{\kappa_S-2}}\Bigg|_{D_S}^{\infty} \\
&+ \frac{B_S-B}{B_S}\frac{2\kappa_S E_{0S}}{m(1-\kappa_S)(2-\kappa_S)} \frac{1}{\left[1-\frac{e(\phi-\phi_S)}{\kappa_S E_{0S}}+\frac{mD_S^2}{2\kappa_S E_{0S}C_S^2}+\frac{B_S}{B_S-B}\frac{mv_\parallel^2}{2\kappa_S E_{0S}}\right]^{\kappa_S-2}}\Bigg|_V^{D_S} \\
&+ \frac{B}{B_E}\frac{2e(\phi_E-\phi)}{m}\frac{1}{1-\kappa_S}\int_V^{\infty} \frac{1}{\left[1-\frac{e(\phi-\phi_S)}{\kappa_S E_{0S}}+\frac{mD_E^2}{2\kappa_S E_{0S}C_E^2}+\frac{B_E}{B_E-B}\frac{mv_\parallel^2}{2\kappa_S E_{0S}}\right]^{\kappa_S-1}}\Bigg|_V^{\infty} \\
&+ \left. \frac{B}{B_S}\frac{2e(\phi-\phi_S)}{m}\frac{1}{1-\kappa_S}\int_V^{D_S} \frac{1}{\left[1-\frac{e(\phi-\phi_S)}{\kappa_S E_{0S}}+\frac{mD_S^2}{2\kappa_S E_{0S}C_S^2}+\frac{B_S}{B_S-B}\frac{mv_\parallel^2}{2\kappa_S E_{0S}}\right]^{\kappa_S-1}}\Bigg|_V^{D_S} \right\}
\end{aligned}
$$

$$
\begin{aligned}
=&\sqrt{\frac{m}{8\pi}}N_S\frac{E_{0S}^{1/2}\Gamma(\kappa_S+1)}{\kappa_S^{1/2}(\kappa_S-1)\Gamma(\kappa_S-\frac{1}{2})}\left\{\left.\frac{v_\parallel^2}{\left[1-\frac{e(\phi-\phi_S)}{\kappa_S E_{0S}}+\frac{mD_E^2}{2\kappa_S E_{0S}C_E^2}+\frac{B_E}{B_E-B}\frac{mv_\parallel^2}{2\kappa_S E_{0S}}\right]^{\kappa_S-1}}\right|_V^\infty\right.\\
&-\int_{V^2}^{\infty}\frac{d(v_\parallel^2)}{\left[1-\frac{e(\phi-\phi_S)}{\kappa_S E_{0S}}+\frac{mD_E^2}{2\kappa_S E_{0S}C_E^2}+\frac{B_E}{B_E-B}\frac{mv_\parallel^2}{2\kappa_S E_{0S}}\right]^{\kappa_S-1}}\\
&\left.-\left.\frac{v_\parallel^2}{\left[1-\frac{e(\phi-\phi_S)}{\kappa_S E_{0S}}+\frac{mD_S^2}{2\kappa_S E_{0S}C_S^2}+\frac{B_S}{B_S-B}\frac{mv_\parallel^2}{2\kappa_S E_{0S}}\right]^{\kappa_S-1}}\right|_V^{D_S}\right.\\
&+\int_{V^2}^{D_S^2}\frac{d(v_\parallel^2)}{\left[1-\frac{e(\phi-\phi_S)}{\kappa_S E_{0S}}+\frac{mD_S^2}{2\kappa_S E_{0S}C_S^2}+\frac{B_S}{B_S-B}\frac{mv_\parallel^2}{2\kappa_S E_{0S}}\right]^{\kappa_S-1}}\\
&\left.-\left.\frac{v_\parallel^2}{\left[1-\frac{e(\phi-\phi_S)}{\kappa_S E_{0S}}+\frac{mv_\parallel^2}{2\kappa_S E_{0S}}\right]^{\kappa_S-1}}\right|_{D_S}^{\infty}+\int_{D_S^2}^{\infty}\frac{d(v_\parallel^2)}{\left[1-\frac{e(\phi-\phi_S)}{\kappa_S E_{0S}}+\frac{mv_\parallel^2}{2\kappa_S E_{0S}}\right]^{\kappa_S-1}}\right.\\
&+\frac{B_E-B}{B_E}\frac{2\kappa_S E_{0S}}{m(2-\kappa_S)}\frac{1}{\left[1-\frac{e(\phi-\phi_S)}{\kappa_S E_{0S}}+\frac{mD_E^2}{2\kappa_S E_{0S}C_E^2}+\frac{B_E}{B_E-B}\frac{mv_\parallel^2}{2\kappa_S E_{0S}}\right]^{\kappa_S-2}}\\
&-\frac{2\kappa_S E_{0S}}{m(2-\kappa_S)}\frac{1}{\left[1-\frac{e(\phi-\phi_S)}{\kappa_S E_{0S}}+\frac{mD_S^2}{2\kappa_S E_{0S}}\right]^{\kappa_S-2}}\\
&+\frac{B_S-B}{B_S}\frac{2\kappa_S E_{0S}}{m(2-\kappa_S)}\frac{1}{\left[1-\frac{e(\phi-\phi_S)}{\kappa_S E_{0S}}+\frac{mD_S^2}{2\kappa_S E_{0S}C_S^2}+\frac{B_S}{B_S-B}\frac{mD_S^2}{2\kappa_S E_{0S}}\right]^{\kappa_S-2}}\\
&-\frac{B_S-B}{B_S}\frac{2\kappa_S E_{0S}}{m(2-\kappa_S)}\frac{1}{\left[1-\frac{e(\phi-\phi_S)}{\kappa_S E_{0S}}+\frac{mD_S^2}{2\kappa_S E_{0S}C_S^2}+\frac{B_E}{B_E-B}\frac{mV^2}{2\kappa_S E_{0S}}\right]^{\kappa_S-2}}\\
&-\frac{B}{B_E}\frac{2e(\phi_E-\phi)}{m}\frac{1}{\left[1-\frac{e(\phi-\phi_S)}{\kappa_S E_{0S}}+\frac{mD_E^2}{2\kappa_S E_{0S}C_E^2}+\frac{B_E}{B_E-B}\frac{mV^2}{2\kappa_S E_{0S}}\right]^{\kappa_S-1}}\\
&+\frac{B}{B_S}\frac{2e(\phi-\phi_S)}{m}\frac{1}{\left[1-\frac{e(\phi-\phi_S)}{\kappa_S E_{0S}}+\frac{mD_S^2}{2\kappa_S E_{0S}C_S^2}+\frac{B_E}{B_E-B}\frac{mV^2}{2\kappa_S E_{0S}}\right]^{\kappa_S-1}}\\
&\left.-\frac{B}{B_S}\frac{2e(\phi-\phi_S)}{m}\frac{1}{\left[1-\frac{e(\phi-\phi_S)}{\kappa_S E_{0S}}+\frac{mD_E^2}{2\kappa_S E_{0S}C_E^2}+\frac{B_E}{B_E-B}\frac{mv_\parallel^2}{2\kappa_S E_{0S}}\right]^{\kappa_S-2}}\right\}
\end{aligned}
$$

$$
\begin{aligned}
=&\sqrt{\frac{m}{8\pi}}N_S\frac{E_{0S}^{1/2}\kappa_S^{1/2}\Gamma(\kappa_S-1)}{\Gamma(\kappa_S-\frac{1}{2})}\left\{\frac{V^2-\frac{B}{B_E}\frac{2e(\phi_E-\phi)}{m}}{\left[1-\frac{e(\phi-\phi_S)}{\kappa_S E_{0S}}+\frac{mD_E^2}{2\kappa_S E_{0S}C_E^2}+\frac{B_E}{B_E-B}\frac{mv_\parallel^2}{2\kappa_S E_{0S}}\right]^{\kappa_S-1}}\right.\\
&-\frac{B_E-B}{B_E}\frac{2\kappa_S E_{0S}}{m(2-\kappa_S)}\frac{1}{\left[1-\frac{e(\phi-\phi_S)}{\kappa_S E_{0S}}+\frac{mD_E^2}{2\kappa_S E_{0S}C_E^2}+\frac{B_E}{B_E-B}\frac{mv_\parallel^2}{2\kappa_S E_{0S}}\right]^{\kappa_S-2}}\Bigg|_V^\infty\\
&+\frac{-D_S^2+\frac{B}{B_S}\frac{2e(\phi-\phi_S)}{m}}{\left[1-\frac{e(\phi-\phi_S)}{\kappa_S E_{0S}}+\frac{mD_S^2}{2\kappa_S E_{0S}C_S^2}+\frac{B_S}{B_S-B}\frac{mD_S^2}{2\kappa_S E_{0S}}\right]^{\kappa_S-1}}\\
&+\frac{V^2-\frac{B}{B_S}\frac{2e(\phi-\phi_S)}{m}}{\left[1-\frac{e(\phi-\phi_S)}{\kappa_S E_{0S}}+\frac{mD_S^2}{2\kappa_S E_{0S}C_S^2}+\frac{B_S}{B_S-B}\frac{mV^2}{2\kappa_S E_{0S}}\right]^{\kappa_S-1}}\\
&+\frac{B_S-B}{B_S}\frac{2\kappa_S E_{0S}}{m(2-\kappa_S)}\frac{1}{\left[1-\frac{e(\phi-\phi_S)}{\kappa_S E_{0S}}+\frac{mD_S^2}{2\kappa_S E_{0S}C_S^2}+\frac{B_S}{B_S-B}\frac{mv_\parallel^2}{2\kappa_S E_{0S}}\right]^{\kappa_S-2}}\Bigg|_V^{D_S}\\
&+\frac{D_S^2)}{\left[1-\frac{e(\phi-\phi_S)}{\kappa_S E_{0S}}+\frac{mD_S^2}{2\kappa_S E_{0S}}\right]^{\kappa_S-1}}+\frac{2\kappa_S E_{0S}}{m(2-\kappa_S)}\frac{1}{\left[1-\frac{e(\phi-\phi_S)}{\kappa_S E_{0S}}+\frac{mv_\parallel^2}{2\kappa_S E_{0S}}\right]^{\kappa_S-2}}\Bigg|_{D_S}^\infty\\
&+\frac{B_E-B}{B_E}\frac{2\kappa_S E_{0S}}{m(2-\kappa_S)}\frac{1}{\left[1-\frac{e(\phi-\phi_S)}{\kappa_S E_{0S}}+\frac{mD_E^2}{2\kappa_S E_{0S}C_E^2}+\frac{B_E}{B_E-B}\frac{mV^2}{2\kappa_S E_{0S}}\right]^{\kappa_S-2}}\\
&-\frac{2\kappa_S E_{0S}}{m(2-\kappa_S)}\frac{1}{\left[1-\frac{e(\phi-\phi_S)}{\kappa_S E_{0S}}+\frac{mD_S^2}{2\kappa_S E_{0S}}\right]^{\kappa_S-2}}\\
&+\frac{B_S-B}{B_S}\frac{2\kappa_S E_{0S}}{m(2-\kappa_S)}\frac{1}{\left[1-\frac{e(\phi-\phi_S)}{\kappa_S E_{0S}}+\frac{mD_S^2}{2\kappa_S E_{0S}C_S^2}+\frac{B_S}{B_S-B}\frac{mD_S^2}{2\kappa_S E_{0S}}\right]^{\kappa_S-2}}\\
&\left.-\frac{B_S-B}{B_S}\frac{2\kappa_S E_{0S}}{m(2-\kappa_S)}\frac{1}{\left[1-\frac{e(\phi-\phi_S)}{\kappa_S E_{0S}}+\frac{mD_S^2}{2\kappa_S E_{0S}C_S^2}+\frac{B_E}{B_E-B}\frac{mV^2}{2\kappa_S E_{0S}}\right]^{\kappa_S-2}}\right\}
\end{aligned}
$$

$$
\begin{aligned}
&=\sqrt{\frac{m}{8\pi}}N_S\frac{E_{0S}^{1/2}\kappa_S^{1/2}\Gamma(\kappa_S-1)}{\Gamma(\kappa_S-\frac{1}{2})}\\
&\left\{\frac{\frac{B_E-B}{B_E}\frac{4\kappa_S E_{0S}}{m(2-\kappa_S)}+\frac{B_E-B}{B_E-B_S}\left(\frac{2}{2-\kappa_S}\frac{B_S}{B_E}-1\right)\frac{2e(\phi-\phi_S)}{m}+\frac{B_E-B}{B_E-B_S}\frac{B_S}{B_E}\frac{\kappa_S}{2-\kappa_S}\frac{2e(\phi_E-\phi)}{m}}{\left[1+\frac{B_S}{B_E-B_S}\frac{e(\phi_E-\phi_S)}{\kappa_S E_{0S}}\right]^{\kappa_S-1}}\right.\\
&+\frac{\frac{B_S-B}{B_S}\frac{4\kappa_S E_{0S}}{m(2-\kappa_S)}+\frac{B-B_S}{B_S}\frac{2e(\phi-\phi_S)}{m}}{1^{\kappa_S-1}}\\
&+\frac{\frac{B-B_S}{B_S}\frac{4\kappa_S E_{0S}}{m(2-\kappa_S)}+\frac{B-B_S}{B_E-B_S}\left(\frac{2}{2-\kappa_S}-\frac{B_E}{B_S}\right)\frac{2e(\phi-\phi_S)}{m}+\frac{B_S-B}{B_E-B_S}\frac{\kappa_S}{\kappa_S-2}\frac{2e(\phi_E-\phi)}{m}}{\left[1+\frac{B_S}{B_E-B_S}\frac{e(\phi_E-\phi_S)}{\kappa_S E_{0S}}\right]^{\kappa_S-1}}\\
&\left.+\frac{-\frac{4\kappa_S E_{0S}}{m(2-\kappa_S)}+\frac{2e(\phi-\phi_S)}{m}}{1^{\kappa_S-1}}\right\}\\
&=\sqrt{\frac{1}{2\pi m}}N_S\frac{E_{0S}^{1/2}\kappa_S^{1/2}\Gamma(\kappa_S-1)}{\Gamma(\kappa_S-\frac{1}{2})}\left\{\frac{B}{B_S}\frac{2\kappa_S E_{0S}}{\kappa_S-2}+\frac{B}{B_S}e(\phi-\phi_S)\right.\\
&\left.+\frac{\left(\frac{B}{B_E}-\frac{B}{B_S}\right)\frac{2\kappa_S E_{0S}}{\kappa_S-2}+\left(\frac{2}{2-\kappa_S}\frac{B}{B_E}-\frac{B}{B_S}\right)e(\phi-\phi_S)+\frac{\kappa_S}{2-\kappa_S}\frac{B}{B_E}e(\phi_E-\phi)}{\left[1+\frac{B_S}{B_E-B_S}\frac{e(\phi_E-\phi_S)}{\kappa_S E_{0S}}\right]^{\kappa_S-1}}\right\}
\end{aligned}
$$

$$
\begin{aligned}
@E =&N_S\sqrt{\frac{E_{0S}\kappa_S}{2\pi m}}\frac{\Gamma(\kappa_S-1)}{\Gamma(\kappa_S-\frac{1}{2})}\\
&\left\{\frac{B_E}{B_S}\frac{2\kappa_S E_{0S}}{\kappa_S-2}+\frac{B_E}{B_S}e(\phi-\phi_S)+\frac{\left(1-\frac{B_E}{B_S}\right)\frac{2\kappa_S E_{0S}}{\kappa_S-2}+\left(\frac{2}{2-\kappa_S}-\frac{B_E}{B_S}\right)e(\phi_E-\phi_S)}{\left[1+\frac{B_S}{B_E-B_S}\frac{e(\phi_E-\phi_S)}{\kappa_S E_{0S}}\right]^{\kappa_S-1}}\right\}\\
&\approx N_S\sqrt{\frac{kT_S}{2\pi m}}\frac{\sqrt{\kappa_S-\frac{3}{2}}\Gamma(\kappa_S-1)}{\Gamma(\kappa_S-\frac{1}{2})}\left\{\frac{B_E}{B_S}\frac{2\kappa_S E_{0S}}{\kappa_S-2}+\frac{B_E}{B_S}e(\phi_E-\phi_S)+\right.\\
&\left.\left[\left(1-\frac{B_E}{B_S}\right)\frac{2\kappa_S E_{0S}}{\kappa_S-2}+\left(\frac{2}{2-\kappa_S}-\frac{B_E}{B_S}\right)e(\phi_E-\phi_S)\right]\left[1-\frac{(\kappa_S-1)B_S}{B_E-B_S}\frac{e(\phi_E-\phi_S)}{\kappa_S E_{0S}}\right]\right\}\\
&=N_S\sqrt{\frac{kT_S}{2\pi m}}\frac{\sqrt{\kappa_S-\frac{3}{2}}\Gamma(\kappa_S-1)}{\Gamma(\kappa_S-\frac{1}{2})}\left[\frac{2\kappa_S E_{0S}}{\kappa_S-2}+\frac{2}{2-\kappa_S}e(\phi_E-\phi_S)+2\frac{\kappa_S-1}{\kappa_S-2}e(\phi_E-\phi_S)+\right.\\
&\left.\frac{2B_S}{B_E-B_S}\frac{\kappa_S-1}{\kappa_S-2}\frac{e^2(\phi_E-\phi_S)^2}{\kappa_S E_{0S}}+\frac{B_E}{B_E-B_S}(\kappa_S-1)\frac{e^2(\phi_E-\phi_S)^2}{\kappa_S E_{0S}}\right]\\
&\approx N_S kT_S\sqrt{\frac{kT_S}{2\pi m}}\frac{\sqrt{\kappa_S-\frac{3}{2}}\Gamma(\kappa_S-2)}{\Gamma(\kappa_S-\frac{3}{2})}\\
&\left[2+2\frac{\kappa_S-2}{\kappa_S-\frac{3}{2}}\frac{e(\phi_E-\phi_S)}{kT_S}+\frac{(\kappa_S-1)(\kappa_S-2)}{(\kappa_S-\frac{3}{2})^2}\frac{e^2(\phi_E-\phi_S)^2}{(kT_S)^2}\right] \qquad \text{(C.3)}
\end{aligned}
$$

Appendix D

Integration of Ion Energy Flux for kappa Distribution

We have shown the following definitions

$$\begin{aligned} C_E^2 &= \frac{B_E}{B} - 1 \\ D_E^2 &= \frac{2e}{m}(\phi_E - \phi) \end{aligned} \tag{D.1}$$

The integration path S_1 is the straight through trajectory from plasma sheet to the ionosphere. So the energy flux is given by

$$\theta$$

$$= \int_{S_1} \frac{m}{2} \left(v_\perp^2 + v_\parallel^2\right) v_\parallel f_S d^3v$$

$$= \left(\frac{m}{2}\right)^{5/2} \frac{N_S}{E_{0S}^{3/2}} \frac{\Gamma(\kappa_S+1)}{(\pi\kappa_S)^{3/2}\Gamma(\kappa_S-\frac{1}{2})} \int_{S_1} \frac{\left(v_\perp^2+v_\parallel^2\right) 2\pi v_\parallel v_\perp dv_\parallel dv_\perp}{\left[1+\frac{e(\phi-\phi_S)}{\kappa_S E_{0S}}+\frac{mv_\perp^2+mv_\parallel^2}{2\kappa_S E_{0S}}\right]^{\kappa_S+1}}$$

$$= \left(\frac{m}{2}\right)^{5/2} \frac{N_S}{E_{0S}^{3/2}} \frac{\pi\Gamma(\kappa_S+1)}{(\pi\kappa_S)^{3/2}\Gamma(\kappa_S-\frac{1}{2})}$$

$$\left\{ \int_{S_1} v_\parallel dv_\parallel \frac{v_\perp^2 2v_\perp dv_\perp}{\left[1+\frac{e(\phi-\phi_S)}{\kappa_S E_{0S}}+\frac{mv_\perp^2+mv_\parallel^2}{2\kappa_S E_{0S}}\right]^{\kappa_S+1}} + \int_{S_1} v_\parallel^3 dv_\parallel \frac{2v_\perp dv_\perp}{\left[1+\frac{e(\phi-\phi_S)}{\kappa_S E_{0S}}+\frac{mv_\perp^2+mv_\parallel^2}{2\kappa_S E_{0S}}\right]^{\kappa_S+1}} \right\}$$

$$= \left(\frac{m}{2}\right)^{3/2} \frac{N_S\Gamma(\kappa_S+1)}{(\pi\kappa_S E_{0S})^{1/2}\Gamma(\kappa_S-\frac{1}{2})} \left\{ \int_{D_E}^{\infty} v_\parallel dv_\parallel \int_0^{v_\perp^2=\frac{v_\parallel^2-D_E^2}{C_E^2}} \frac{v_\perp^2 d\left(\frac{m}{2\kappa_S E_{0S}} v_\perp^2\right)}{\left[1+\frac{e(\phi-\phi_S)}{\kappa_S E_{0S}}+\frac{mv_\perp^2+mv_\parallel^2}{2\kappa_S E_{0S}}\right]^{\kappa_S+1}} \right.$$

$$\left. + \int_{D_E}^{\infty} v_\parallel^3 dv_\parallel \int_0^{v_\perp^2=\frac{v_\parallel^2-D_E^2}{C_E^2}} \frac{d\left(\frac{m}{2\kappa_S E_{0S}} v_\perp^2\right)}{\left[1+\frac{e(\phi-\phi_S)}{\kappa_S E_{0S}}+\frac{mv_\perp^2+mv_\parallel^2}{2\kappa_S E_{0S}}\right]^{\kappa_S+1}} \right\}$$

$$= -\left(\frac{m}{2}\right)^{3/2} \frac{N_S\Gamma(\kappa_S)}{(\pi\kappa_S E_{0S})^{1/2}\Gamma(\kappa_S-\frac{1}{2})} \left\langle \int_{D_E}^{\infty} v_\parallel dv_\parallel \left\{ \frac{v_\perp^2}{\left[1+\frac{e(\phi-\phi_S)}{\kappa_S E_{0S}}+\frac{mv_\perp^2+mv_\parallel^2}{2\kappa_S E_{0S}}\right]^{\kappa_S}} \right|_0^{\frac{v_\parallel^2-D_E^2}{C_E^2}} \right.$$

$$\left. - \int_0^{v_\perp^2=\frac{v_\parallel^2-D_E^2}{C_E^2}} \frac{dv_\perp^2}{\left[1+\frac{e(\phi-\phi_S)}{\kappa_S E_{0S}}+\frac{mv_\perp^2+mv_\parallel^2}{2\kappa_S E_{0S}}\right]^{\kappa_S}} \right\}$$

$$\left. + \int_{D_E}^{\infty} v_\parallel^3 dv_\parallel \frac{1}{\left[1+\frac{e(\phi-\phi_S)}{\kappa_S E_{0S}}+\frac{mv_\perp^2+mv_\parallel^2}{2\kappa_S E_{0S}}\right]^{\kappa_S}} \right|_0^{\frac{v_\parallel^2-D_E^2}{C_E^2}} \Bigg\rangle$$

$$= -\left(\frac{m}{2}\right)^{3/2} \frac{N_S\Gamma(\kappa_S)}{(\pi\kappa_S E_{0S})^{1/2}\Gamma(\kappa_S-\frac{1}{2})} \left\langle \int_{D_E}^{\infty} v_\parallel dv_\parallel \left\{ \frac{\frac{v_\parallel^2-D_E^2}{C_E^2}}{\left[1+\frac{e(\phi-\phi_S)}{\kappa_S E_{0S}}+\frac{m\frac{v_\parallel^2-D_E^2}{C_E^2}+mv_\perp^2}{2\kappa_S E_{0S}}\right]^{\kappa_S}} \right.\right.$$

$$\left. -\frac{2\kappa_S E_{0S}}{m(1-\kappa_S)} \frac{1}{\left[1+\frac{e(\phi-\phi_S)}{\kappa_S E_{0S}}+\frac{mv_\perp^2+mv_\parallel^2}{2\kappa_S E_{0S}}\right]^{\kappa_S-1}} \right|_0^{\frac{v_\parallel^2-D_E^2}{C_E^2}} \Bigg\}$$

$$\left. + \int_{D_E}^{\infty} v_\parallel^3 dv_\parallel \left\{ \frac{1}{\left[1+\frac{e(\phi-\phi_S)}{\kappa_S E_{0S}}+\frac{m\frac{v_\parallel^2-D_E^2}{C_E^2}+mv_\parallel^2}{2\kappa_S E_{0S}}\right]^{\kappa_S}} - \frac{1}{\left[1+\frac{e(\phi-\phi_S)}{\kappa_S E_{0S}}+\frac{mv_\parallel^2}{2\kappa_S E_{0S}}\right]^{\kappa_S}} \right\} \right\rangle$$

$$= -\left(\frac{m}{2}\right)^{3/2} \frac{N_S\Gamma(\kappa_S)}{(\pi\kappa_S E_{0S})^{1/2}\Gamma(\kappa_S-\frac{1}{2})} \left\{ \frac{C_E^2+1}{C_E^2} \int_{D_E}^{\infty} \frac{v_\parallel^3 dv_\parallel}{\left[1+\frac{e(\phi-\phi_S)}{\kappa_S E_{0S}}-\frac{mD_E^2}{2\kappa_S E_{0S}}+\frac{mv_\parallel^2\frac{C_E^2+1}{C_E^2}}{2\kappa_S E_{0S}}\right]^{\kappa_S}} \right.$$

$$-\frac{D_E^2}{C_E^2} \int_{D_E}^{\infty} \frac{v_\parallel dv_\parallel}{\left[1+\frac{e(\phi-\phi_S)}{\kappa_S E_{0S}}-\frac{mD_E^2}{2\kappa_S E_{0S}}+\frac{mv_\parallel^2\frac{C_E^2+1}{C_E^2}}{2\kappa_S E_{0S}}\right]^{\kappa_S}}$$

$$-\frac{2\kappa_S E_{0S}}{m(1-\kappa_S)} \int_{D_E}^{\infty} \frac{v_\parallel dv_\parallel}{\left[1+\frac{e(\phi-\phi_S)}{\kappa_S E_{0S}}-\frac{mD_E^2}{2\kappa_S E_{0S}}+\frac{mv_\parallel^2\frac{C_E^2+1}{C_E^2}}{2\kappa_S E_{0S}}\right]^{\kappa_S-1}}$$

$$\left. -\int_{D_E}^{\infty} \frac{v_\parallel^3 dv_\parallel}{\left[1+\frac{e(\phi-\phi_S)}{\kappa_S E_{0S}}+\frac{mv_\parallel^2}{2\kappa_S E_{0S}}\right]^{\kappa_S}} + \frac{2\kappa_S E_{0S}}{m(1-\kappa_S)} \int_{D_E}^{\infty} \frac{v_\parallel dv_\parallel}{\left[1+\frac{e(\phi-\phi_S)}{\kappa_S E_{0S}}+\frac{mv_\parallel^2}{2\kappa_S E_{0S}}\right]^{\kappa_S-1}} \right\}$$

$$= -\left(\frac{m}{2}\right)^{3/2} \frac{N_S \Gamma(\kappa_S)}{(\pi \kappa_S E_{0S})^{1/2} \Gamma(\kappa_S - \frac{1}{2})}$$

$$\left\{ \frac{\kappa_S E_{0S}}{m(1-\kappa_S)} \frac{v_\parallel^2}{\left[1 + \frac{e(\phi-\phi_S)}{\kappa_S E_{0S}} - \frac{mD_E^2}{2\kappa_S E_{0S}} + \frac{mv_\parallel^2 \frac{C_E^2+1}{C_E^2}}{2\kappa_S E_{0S}}\right]^{\kappa_S - 1}} \right|_{D_E}^{\infty}$$

$$- \frac{\kappa_S E_{0S}}{m(1-\kappa_S)} \int_{D_E^2}^{\infty} \frac{dv_\parallel^2}{\left[1 + \frac{e(\phi-\phi_S)}{\kappa_S E_{0S}} - \frac{mD_E^2}{2\kappa_S E_{0S}} + \frac{mv_\parallel^2 \frac{C_E^2+1}{C_E^2}}{2\kappa_S E_{0S}}\right]^{\kappa_S - 1}}$$

$$- \frac{D_E^2}{C_E^2} \frac{C_E^2}{C_E^2+1} \frac{\kappa_S E_{0S}}{m(1-\kappa_S)} \frac{1}{\left[1 + \frac{e(\phi-\phi_S)}{\kappa_S E_{0S}} - \frac{mD_E^2}{2\kappa_S E_{0S}} + \frac{mv_\parallel^2 \frac{C_E^2+1}{C_E^2}}{2\kappa_S E_{0S}}\right]^{\kappa_S - 1}} \Bigg|_{D_E}^{\infty}$$

$$- \frac{2\kappa_S E_{0S}}{m(1-\kappa_S)} \frac{C_E^2}{C_E^2+1} \frac{\kappa_S E_{0S}}{m(2-\kappa_S)} \frac{1}{\left[1 + \frac{e(\phi-\phi_S)}{\kappa_S E_{0S}} - \frac{mD_E^2}{2\kappa_S E_{0S}} + \frac{mv_\parallel^2 \frac{C_E^2+1}{C_E^2}}{2\kappa_S E_{0S}}\right]^{\kappa_S - 2}} \Bigg|_{D_E}^{\infty}$$

$$- \frac{\kappa_S E_{0S}}{m(1-\kappa_S)} \frac{v_\parallel^2}{\left[1 + \frac{e(\phi-\phi_S)}{\kappa_S E_{0S}} + \frac{mv_\parallel^2}{2\kappa_S E_{0S}}\right]^{\kappa_S - 1}} \Bigg|_{D_E}^{\infty}$$

$$+ \frac{\kappa_S E_{0S}}{m(1-\kappa_S)} \int_{D_E^2}^{\infty} \frac{dv_\parallel^2}{\left[1 + \frac{e(\phi-\phi_S)}{\kappa_S E_{0S}} + \frac{mv_\parallel^2}{2\kappa_S E_{0S}}\right]^{\kappa_S - 1}}$$

$$+ \frac{2\kappa_S E_{0S}}{m(1-\kappa_S)} \frac{\kappa_S E_{0S}}{m(2-\kappa_S)} \frac{1}{\left[1 + \frac{e(\phi-\phi_S)}{\kappa_S E_{0S}} + \frac{mv_\parallel^2}{2\kappa_S E_{0S}}\right]^{\kappa_S - 2}} \Bigg|_{D_E}^{\infty} \Bigg\}$$

$$
\begin{aligned}
&= \left(\frac{m\kappa_S E_{0S}}{2\pi}\right)^{1/2} \frac{N_S \Gamma(\kappa_S - 1)}{2\Gamma(\kappa_S - \frac{1}{2})} \Bigg\{ -\frac{D_E^2}{\left[1 + \frac{e(\phi-\phi_S)}{\kappa_S E_{0S}} - \frac{mD_E^2}{2\kappa_S E_{0S}} + \frac{mD_E^2 \frac{C_E^2+1}{C_E^2}}{2\kappa_S E_{0S}}\right]^{\kappa_S - 1}} \\
&\quad - \frac{2\kappa_S E_{0S}}{m(2-\kappa_S)} \frac{C_E^2}{C_E^2+1} \frac{1}{\left[1 + \frac{e(\phi-\phi_S)}{\kappa_S E_{0S}} - \frac{mD_E^2}{2\kappa_S E_{0S}} + \frac{mv_\parallel^2 \frac{C_E^2+1}{C_E^2}}{2\kappa_S E_{0S}}\right]^{\kappa_S - 2}} \Bigg|_{D_E}^{\infty} \\
&\quad + \frac{D_E^2}{1+C_E^2} \frac{1}{\left[1 + \frac{e(\phi-\phi_S)}{\kappa_S E_{0S}} - \frac{mD_E^2}{2\kappa_S E_{0S}} + \frac{mv_\parallel^2 \frac{C_E^2+1}{C_E^2}}{2\kappa_S E_{0S}}\right]^{\kappa_S - 1}} \\
&\quad + \frac{2\kappa_S E_{0S}}{m(2-\kappa_S)} \frac{C_E^2}{C_E^2+1} \frac{1}{\left[1 + \frac{e(\phi-\phi_S)}{\kappa_S E_{0S}} - \frac{mD_E^2}{2\kappa_S E_{0S}} + \frac{mv_\parallel^2 \frac{C_E^2+1}{C_E^2}}{2\kappa_S E_{0S}}\right]^{\kappa_S - 2}} \\
&\quad + \frac{D_E^2}{\left[1 + \frac{e(\phi-\phi_S)}{\kappa_S E_{0S}} + \frac{mv_\parallel^2}{2\kappa_S E_{0S}}\right]^{\kappa_S - 1}} + \frac{2\kappa_S E_{0S}}{m(2-\kappa_S)} \frac{1}{\left[1 + \frac{e(\phi-\phi_S)}{\kappa_S E_{0S}} + \frac{mv_\parallel^2}{2\kappa_S E_{0S}}\right]^{\kappa_S - 2}} \Bigg|_{D_E}^{\infty} \\
&\quad - \frac{2\kappa_S E_{0S}}{m(2-\kappa_S)} \frac{1}{\left[1 + \frac{e(\phi-\phi_S)}{\kappa_S E_{0S}} + \frac{mD_E^2}{2\kappa_S E_{0S}}\right]^{\kappa_S - 2}} \Bigg\} \\
&= \left(\frac{m\kappa_S E_{0S}}{2\pi}\right)^{1/2} \frac{N_S \Gamma(\kappa_S - 1)}{2\Gamma(\kappa_S - \frac{1}{2})} \Bigg\{ \frac{\frac{B}{B_E}\frac{2e}{m}(\phi_E - \phi)}{\left[1 + \frac{e(\phi-\phi_S)}{\kappa_S E_{0S}} + \frac{m\frac{2e}{m}(\phi_E-\phi)}{2\kappa_S E_{0S}}\right]^{\kappa_S - 1}} \\
&\quad + \frac{4\kappa_S E_{0S}}{m(2-\kappa_S)} \left(-1 + \frac{1}{1+\frac{1}{C_E^2}}\right) \frac{1}{\left[1 + \frac{e(\phi-\phi_S)}{\kappa_S E_{0S}} + \frac{m\frac{2e}{m}(\phi_E-\phi)}{2\kappa_S E_{0S}}\right]^{\kappa_S - 2}} \Bigg\} \\
&= \left(\frac{m\kappa_S E_{0S}}{2\pi}\right)^{1/2} \frac{N_S \Gamma(\kappa_S - 1)}{2\Gamma(\kappa_S - \frac{1}{2})} \frac{\frac{B}{B_E}\frac{2e}{m}(\phi_E - \phi) - \frac{B}{B_E}\frac{4\kappa_S E_{0S}}{m(2-\kappa_S)}\left[1 + \frac{e(\phi_E-\phi_S)}{\kappa_S E_{0S}}\right]}{\left[1 + \frac{e(\phi_E-\phi_S)}{\kappa_S E_{0S}}\right]^{\kappa_S - 1}} \\
@E &= N_S \sqrt{\frac{\kappa_S E_{0S}}{2\pi m}} \kappa_S E_{0S} \frac{\Gamma(\kappa_S - 2)}{\Gamma(\kappa_S - \frac{1}{2})} \frac{2}{\left[1 + \frac{e(\phi_E-\phi_S)}{\kappa_S E_{0S}}\right]^{\kappa_S - 2}} \qquad \text{(D.2)}
\end{aligned}
$$

Bibliography

[1] L. Svalgaard, "The solar radio microwave flux." http://www.leif.org/research/Solar Radio Flux.pdf, 2009.

[2] H. W. Brandhorst Jr., *Technologies*, vol. 2 of *NASA SP-509*. 1992.

[3] C. T. Russell, *A brief history of solar-terrestrial physics*, ch. 1, pp. 1–26. Cambridge University Press, 1995.

[4] M. G. Kivelson, *Physics of Space Plasmas*, ch. 2, pp. 27–53. Cambridge University Press, 1995.

[5] W. N. Spjeldvik and P. L. Rothwell, *The Radiation Belts*, ch. 5. Air Force Geophysics Laboratory, 1985.

[6] T. W. Hill, *Solar-wind magnetosphere coupling*, pp. 261–302. Norwell, MA: D. Reidel Publishing Company, 1983.

[7] R. A. Wolf, "Physics of the magnetosphere." 1995.

[8] L. J. Lanzerotti, "Space weather effects on technologies," in *Space Weather* (P. Song, H. J. Singer, and G. L. Sisco, eds.), no. 125 in Geophysical monograph, pp. 11–22, 2000 Florida Avenue, N. W., Washington, DC 20009: American Geophysical Union, 2001.

[9] V. M. Vasyliunas, *Fundamentals of planetary magnetospheres.*

[10] Y. Song, S. Sazykin, and R. A. Wolf, "On the relationship between kinetic and fluid formalisms for convection in the inner magnetosphere," *J. Geophys. Res.*, vol. 113, p. A08216, 2008.

[11] T. W. Hill, "Magnetic merging in a collisionless plasma," *J. Geophys. Res.*, vol. 80, pp. 4689–4699, 1975.

[12] N. A. Tsyganenko, "An empirical model of the substorm current wedge," *J. Geophys. Res.*, vol. 102, no. A9, pp. 19935–19941, 1997.

[13] N. A. Tsyganenko, "Modeling the earth's magnetospheric magnetic field confined within a realistic magnetopause," *J. Geophys. Res.*, vol. 100, no. A4, pp. 5599–5612, 1995.

[14] N. A. Tsyganenko and T. Mukai, "Tail plasma sheet models derived from geotail particle data," *J. Geophys. Res.*, vol. 108, no. A3, p. 1136, 2003.

[15] X. Xing, *Criterion for interchange instability in the plasma sheet.* PhD thesis, Rice University, 2008.

[16] T. Iijima and T. A. Potemra, "Field-aligned currents in the dayside cusp observed by triad," *J. Geophys. Res.*, vol. 81, pp. 5971–5979, 1976.

[17] P. A. Ontiveros, *Synthetic magnetogram calculations from magnetosphere-ionosphere coupling models.* PhD thesis, Rice University, 2008.

[18] J. Yang, F. R. Toffoletto, R. A. Wolf, S. Sazykin, R. W. Spiro, P. C. Brandt, M. G. Henderson, and H. U. Frey, "Rice convection model simulation of the 18 april 2002 sawtooth event and evidence for interchange instability," *J. Geophys. Res.*, vol. 113, p. A11214, 2008.

[19] M. A. P. S. Division, "Overview of solar and geomagnetic storm conditions and impacts november 7-12, 2004." http://www.metatech-aps.com/Summary/2004/GeomagneticStormSummary11_7_to_12_2004.pdf, 2004.

[20] R. J. Strangeway, R. E. Ergun, Y.-J. Su, C. W. Carlson, and R. C. Elphic, "Factors controlling ionosppheric outflow as oobserved at intermediate altitudes," *J. Geophys. Res.*, vol. 110, p. A03221, 2005.

[21] J.-C. Zhang, R. A. Wolf, G. M. Erickson, R. W. Spiro, F. R. Toffoletto, and J. Yang, "Rice convection model simulation of the substorm-associated injection of an observed bubble into the inner magnetosphere: 1. magnetic field and other inputs," *J. Geophys. Res.*, vol. 114, p. A08218, 2009.

[22] J. P. Heppner and N. C. Maynard, "Empirical high-latitude electric field models," *J. Geophys. Res.*, vol. 92, p. 4467, 1987.

[23] R. A. Wolf, R. W. Spiro, and F. J. Rich, "Extension of convection modeling into the high-latitude ionosphere: some theoretical difficulties," *J. Atmos. and Terr. Phys.*, 1991.

[24] N. S. W. Program, "Strategic plan," Tech. Rep. FCM-P30-95, Washington, D.C., 1995.

[25] C. T. Russell, "Solar wind and interplanetary magnetic field: a tutorial," in *Space Weather* (P. Song, H. J. Singer, and G. L. Sisco, eds.), no. 125 in Geophysical monograph, pp. 73–89, 2000 Florida Avenue, N. W., Washington, DC 20009: American Geophysical Union, 2001.

[26] E. N. Parker, "Space weather and the changing sun," in *Space Weather* (P. Song, H. J. Singer, and G. L. Sisco, eds.), no. 125 in Geophysical monograph, pp. 91–99, 2000 Florida Avenue, N. W., Washington, DC 20009: American Geophysical Union, 2001.

[27] P. M. Bellan, *Fundamentals of Plasma Physics.* The Edinburgh Building, Cambridge, UK: Cambridge, 2006.

[28] C. Lemon, R. A. Wolf, T. W. Hill, S. Sazykin, R. W. Spiro, F. R. Toffoletto, J. Birn, and M. Hesse, "Magnetic storm ring current injection modeled with rice convection model and a self-consistent magnetic field," *Geophys. Res. Lett.*, vol. 31, p. L21801, 2004.

[29] J. A. V. Allen, G. H. Ludwig, E. C. Ray, and C. E. McIlwain, "Observations of high intensity radiation by satellites 1958 alpha and gamma," *Jet Propul*, vol. 28, pp. 588–592, 1958.

[30] J. A. Van Allen and L. A. Frank, "Radiation around the earth to a radial distance of 107,400 km," *Nature*, vol. 183, p. 430, 1959.

[31] J. Berchem and C. T. Russell, "The thickness of the magnetopause current layer: Isee 1 and 2 observations," *J. Geophys. Res.*, vol. 87, pp. 2108–2114, 1982.

[32] W. Baumjohann, G. Paschmann, and C. A. Cattell, "Average plasma properties in the central plasma sheet," *J. Geophys. Res.*, vol. 94, p. 6597, 1989.

[33] J. E. Borovsky, M. F. Thomsen, and R. C. Elphic, "The driving of plasma sheet by the solar wind," *J. Geophys. Res.*, vol. 103, no. A8, pp. 17617–17639, 1998.

[34] T. Kunkel, W. Baumjohann, J. Untiedt, and R. Greenwald, "Electric fields and currents at the harang discontinuity: A case study," *J. Geophys. Res.*, vol. 59, p. 73, 1986.

[35] G. M. Erickson, R. W. Spiro, and R. A. Wolf, "The physics of harang discontinuity," *J. Geophys. Res.*, vol. 96, no. A2, pp. 1633–1645, 1991.

[36] A. S. Rodger, S. W. H. Cowley, M. J. Brown, M. Pinnock, and D. A. Simmons, "Dawn-dusk (y) of the interplanetary magnetic field and local time of the harang discontinuity," *Planet. Space Sci.*, vol. 32, p. 1021, 1984.

[37] C. L. Lemon, *Simulating the driven magnetosphere.* PhD thesis, Rice University, 2005.

[38] H. Alfvén and C.-G. Fälthammar, *Cosmical Electrodynamics: Fundamental Principles.* International series of monographs on physics, Oxford, Clarendon, 2 ed., 1963.

[39] G. L. Siscoe, *Solar system magnetohydrodynamics*, pp. 11–100. Norwell, MA: D. Reidel Publishing Company, 1983.

[40] R. A. Wolf, *The quasi-static (slow-flow) region of the magnetosphere*, pp. 303–368. Norwell, MA: D. Reidel Publishing Company, 1983.

[41] W. I. Axford, "The interaction between the solar wind and the earth's magnetosphere," *J. Geophys. Res.*, vol. 67, pp. 3791–3796, 1962.

[42] W. I. Axford and C. O. Hines, "A unifying theory of high-latitude geophysical phenomena and geomagnetic storms," *Canadian J. Phys.*, vol. 39, pp. 1433–1464, 1961.

[43] J. L. Burch and R. A. Heelis, "Imf changes and polar-cap electric fields and currents," in *Dynamics of the Magnetosphere* (S.-I. Akasofu, ed.), (Boston), pp. 47–62, D. Reidel Publishing Co., 1979.

[44] J. W. Dungey, "Interplanetary magneitc field and the auroral zones," vol. 6, p. 47, 1961.

[45] F. R. Toffoletto, S. Sazykin, R. W. Spiro, R. A. Wolf, and J. G. Lyon, "Rcm meets lfm: Initial results of one-way coupling," *J. Atmos. Solar-Terr. Phys.*, vol. 66, p. 1361, 2004.

[46] V. M. Vasyliunas, *Large-scale morphology of the magnetosphere*, p. 243. Norwell, MA: D. Reidel Publishing Company, 1983.

[47] L. C. Lee, R. K. Albano, and J. R. Kan, "Kelvin-helmholtz instability in the magnetopause boundary layer region," *J. Geophys. Res.*, vol. 86, no. A1, p. 54, 1981.

[48] F. R. Toffoletto, *Model of solar-wind magnetosphere coupling.* PhD thesis, Rice University, 1987.

[49] P. H. Reiff, R. W. Spiro, and T. W. Hill, "Dependence of polar cap potential drop on interplanetary parameters," *J. Geophys. Res.*, vol. 86, p. 7639, 1981.

[50] S. Chapman and J. Bartels, vol. 1, ch. 9. Oxford: Clarendon Press, 1940.

[51] D. F. Webb, N. U. Crooker, S. P. Plunkett, and O. C. S. Cyr, "The solar sources of geoeffective structures," in *Space Weather* (P. Song, H. J. Singer, and G. L. Sisco, eds.), no. 125 in Geophysical monograph, pp. 123–141, 2000

Florida Avenue, N. W., Washington, DC 20009: American Geophysical Union, 2001.

[52] J. E. Borovsky and M. H. Denton, "Differences between cme-driven storms and cir-driven storms," *J. Geophys. Res.*, vol. 111, p. A07S08, 2006.

[53] W. D. Gonzales, J. A. Joselyn, Y. Kamide, H. W. Kroehl, G. Rostoker, B. T. Tsurutani, and V. M. Vasyliunas, "What is a geomagnetic storm?," *J. Geophys. Res.*, vol. 99, no. A4, pp. 5771–5792, 1994.

[54] J. Yang, *Inner Magnetospheric Modeling During Geomagnetic Active Times.* PhD thesis, Rice University, 2009.

[55] J. E. Borovsky, M. F. Thomsen, and D. J. McComas, "The superdense plasma sheet: Plasmaspheric origin, solar wind origin, or ionospheric origin?," *J. Geophys. Res.*, vol. 102, pp. 22089–22097, 1997.

[56] L. R. Lyons and M. Schulz, "Access of energetic particles to storm time ring current through enhanced radial diffusion," *J. Geophys. Res.*, vol. 94, p. 5491, 1989.

[57] R. M. Robinson and R. A. Behnke, "The u.s. national space weather program: A retrospective," in *Space Weather* (P. Song, H. J. Singer, and G. L. Sisco, eds.), no. 125 in Geophysical monograph, pp. 1–10, 2000 Florida Avenue, N. W., Washington, DC 20009: American Geophysical Union, 2001.

[58] R. L. Lambour, *Calibration of the Rice Magnetospheric Specification and Forecast Model for the inner magnetosphere.* PhD thesis, Rice University, 1994.

[59] R. A. Wolf, "Effects of ionospheric conductivity on convective flow of plasma in the magnetosphere," *J. Geophys. Res.*, vol. 75, pp. 4677–4698, 1970.

[60] R. K. Jaggi and R. A. Wolf, "Self-consistent calculation of the motion of a sheet of ions in the magnetosphere," *J. Geophys. Res.*, vol. 78, pp. 2852–2866, 1973.

[61] M. Harel, R. A. Wolf, P. H. Reiff, R. W. Spiro, W. J. Burke, F. J. Rich, and M. Smiddy, "Quantitative simulation of a magnetospheric substorm 1, model logic and overview," *J. Geophys. Res.*, vol. 86, no. A4, pp. 2217–2241, 1981.

[62] R. W. Spiro, R. A. Wolf, and B. G. Fejer, "Penetration of high-latitude electric-field effects to low latitudes during sundial 1984," *Ann. Geophys.*, vol. 6, p. 211, 1988.

[63] F. R. Toffoletto, S. Sazykin, R. W. Spiro, and R. A. Wolf, "Inner magnetospheric modeling with the rice convection model," *Space Science Reviews*, vol. 107, pp. 175–196, 2003.

[64] H. J. Singer, G. R. Heckman, and J. W. Hirman, "Space weather forcasting: A grand challenge," in *Space Weather* (P. Song, H. J. Singer, and G. L. Sisco, eds.), no. 125 in Geophysical monograph, pp. 23–29, 2000 Florida Avenue, N. W., Washington, DC 20009: American Geophysical Union, 2001.

[65] G. L. Withbroe, "Living with a star," in *Space Weather* (P. Song, H. J. Singer, and G. L. Sisco, eds.), no. 125 in Geophysical monograph, pp. 45–51, 2000 Florida Avenue, N. W., Washington, DC 20009: American Geophysical Union, 2001.

[66] K. G. Powell, P. L. Roe, T. J. Linde, T. I. Gombosi, and D. L. D. Zeeuw, "A

solution-adaptive upwind scheme for ideal magnetohydrodynamics," *J. Comput. Phys.*, vol. 154, no. 2, p. 284, 1999.

[67] C. P. T. Groth, D. L. De Zeeuw, T. I. Gombosi, and K. G. Powell, "A parallel adaptive 3d mhd scheme for modeling coronal and solar wind plasma flows," *Space Science Reviews*, vol. 87, pp. 193–198, 1999.

[68] D. L. De Zeeuw, T. I. Gombosi, C. P. T. Groth, K. G. Powell, and Q. F. Stout, "An adaptive mhd method for global space weather simulations," *IEEE TRANSACTIONS ON PLASMA SCIENCE*, vol. 28, no. 6, pp. 1956–1965, 2000.

[69] V. M. Vasyliunas, *Mathematical models of magnetospheric convection and its coupling to the ionosphere, in Particles and Fields in the Magnetosphere*, pp. 60–71. Norwell, MA: D. Reidel Publishing Company, 1970.

[70] M. Heinemann and R. A. Wolf, "Relationships of models of the inner magnetosphere to the rice convection model," *J. Geophys. Res.*, vol. 106, no. 8, pp. 15545–15554, 2001.

[71] J. G. Lyon, J. Fedder, and J. Huba, "The effect of different resistivity models on magnetotail dynamics," *J. Geophys. Res.*, vol. 91, pp. 8057–8064, 1986.

[72] J. Raeder, R. J. Walker, and M. Ashour-Abdalla, "The structure of the distant geomagnetic tail during long periods of northward imf," *Geophys. Res. Lett.*, vol. 22, pp. 349–352, 1995.

[73] D. Fontaine and M. Blanc, "A theoretical approach to the morphology and the dynamics of diffuse auroral zones," *J. Geophys. Res.*, vol. 88, pp. 7171–7184, 1983.

[74] D. Fontaine, M. Blanc, L. Reinhart, and R. Glowinski, "Numerical simulations of the magnetospheric convection including the effects of electron precipitation," *J. Geophys. Res.*, vol. 90, pp. 8343–8360, 1985.

[75] C. Peymirat and D. Fontaine, "Numerical simulation of magnetospheric convection including the effect of field-aligned currents and electron precipitation," *J. Geophys. Res.*, vol. 99, p. 11155, 1994.

[76] M. Heinemann, "Role of collisionless heat flux in magnetospheric convection," *J. Geophys. Res.*, vol. 104, p. 28397, 1999.

[77] S. I. Braginskii, "Transport processes in a plasma," *Rev. Plasma Phys.*, vol. 1, p. 205, 1965.

[78] W. W. Liu, "Heat flux in magnetospheric convection: A calculation based on adiabatic drift theory," *Geophys. Res. Lett.*, vol. 33, p. L19104, 2006.

[79] D. L. De Zeeuw, S. Sazykin, R. A. Wolf, T. I. Gombosi, A. J. Ridley, and G. Töth, "Coupling of a global mhd code and an inner magnetospheric model: Initial results," *J. Geophys. Res.*, vol. 109, p. A12219, 2004.

[80] B. Hu, F. R. Toffoletto, R. A. Wolf, S. Sazykin, J. Raeder, D. Larson, and A. Vapirev, "One-way coupled openggcm/rcm simulation of the march 23rd 2007 substorm event," *J. Geophys. Res.*, 2010.

[81] C.-L. Huang, H. E. Spence, J. G. Lyon, F. R. Toffoletto, H. J. Singer, and S. Sazykin, "Storm-time configuration of the inner magnetosphere: Lyon-fedder-mobarry mhd code, tsyganenko model, and goes observations," *J. Geophys. Res.*, vol. 111, p. A11S16, 2006.

[82] V. M. Vasyliunas, *The interrelationship of magnetospheric processes.*

[83] J. Büchner and L. M. Zelenyi, "Regular and chaotic charged particle motion in magnetotaillike field reversals, 1. basic theory of trapped motion," *J. Geophys. Res.*, vol. 94, pp. 11821–11842, 1989.

[84] A. Usadi, R. A. Wolf, M. Heinemann, and W. Horton, "Does chaos alter the ensemble averaged drift equations?," *J. Geophys. Res.*, vol. 101, p. 15491, 1996.

[85] P. B. Snyder, G. W. Hammett, and W. Dorland, "Landau fluid models of collisionless magnetohydrodynamics," *Phys. Plasmas*, vol. 4, p. 3974, 1997.

[86] R. W. Schunk, "Mathematical structure of transport equations for multispecies flows," *Rev. Geophys.*, vol. 15, p. 429, 1977.

[87] D. T. Young, H. Balsiger, and J. Geiss, "Correlations of magnetospheric ion composition with geomagnetic and solar activity," *J. Geophys. Res.*, vol. 87, no. A11, pp. 9077–9096, 1982.

[88] T. W. Hill, A. J. Dessler, and R. A. Wolf, "Mercury and mars: The role of ionospheric conductivity in the acceleration of magnetospheric particles," *Geophys. Res. Lett.*, vol. 3, p. 429, 1976.

[89] G. L. Siscoe, G. M. Erickson, B. U. O. Sonnerup, N. C. Maynard, J. A. Schoendorf, K. D. Siebert, D. R. Weimer, W. W. White, and G. R. Wilson, "Hill model of transpolar potential saturation: Comparisons with mhd simulations," *J. Geophys. Res.*, vol. 107, no. A6, 2002.

[90] C. B. Boyle, P. H. Reiff, and M. R. Hairston, "Empirical polar cap potentials," *J. Geophys. Res.*, vol. 102, no. A1, pp. 111–125, 1997.

[91] T. W. Hill, "Magnetic coupling between solar wind and magnetosphere: Regulated by ionospheric conductance?," *Eos Trans.*, vol. 65, p. 1047, 1984.

[92] T. G. Northrop and E. Teller, "Stability of the adiabatic motion of charged particles in the earths field," *Phys. Rev.*, vol. 117, pp. 215–225, 1960.

[93] D. P. Stern, "Euler potentials," vol. 38, pp. 494–501, 1970.

[94] D. P. Stern, "The art of mapping the magnetosphere," *J. Geophys. Res.*, vol. 99, no. A9, pp. 17169–17198, 1994.

[95] R. V. Hilmer and G.-H. Voigt, "A magnetospheric magnetic field model with flexible current systems driven by independent physical parameters," *J. Geophys. Res.*, vol. 100, no. A4, pp. 5613–5626, 1995.

[96] N. A. Tsyganenko, "Empirical magnetic field models for the space weather program," in *Space Weather* (P. Song, H. J. Singer, and G. L. Sisco, eds.), no. 125 in Geophysical monograph, pp. 273–280, 2000 Florida Avenue, N. W., Washington, DC 20009: American Geophysical Union, 2001.

[97] R. A. Wolf, "Physics of the magnetosphere." Prepublication draft for use in PHYS 510, 2003.

[98] N. A. Tsyganenko and A. V. Usmanov, "Determination of the mangetospheric current system parameters and development of experimental geomagnetic field models based on data from imp and heos satellites," *Planet. Space Sci.*, vol. 30, p. 985, 1982.

[99] N. A. Tsyganenko, "Global quantitative models of the geomagnetic field in the cislunar magnetosphere for different disturbance levels," *Planet. Space Sci.*,

vol. 35, p. 1347, 1987.

[100] N. A. Tsyganenko, "A magnetospheric magnetic field model with a warped tail current sheet," *Planet. Space Sci.*, vol. 37, pp. 5–20, 1989.

[101] N. A. Tsyganenko and M. Peredo, "Analytical models of the magnetic field of disk-shaped current sheets," *J. Geophys. Res.*, vol. 99, no. A1, pp. 199–205, 1994.

[102] A. T. Y. Lui, R. W. McEntire, and S. M. Krimigis, "Evolution of the ring current during two geomagnetic storms," *J. Geophys. Res.*, vol. 92, p. 7459, 1987.

[103] N. A. Tsyganenko and D. P. Stern, "Modeling the global magnetic field of the large-scale birkeland current systems," *J. Geophys. Res.*, vol. 101, no. A12, pp. 27187–27198, 1996.

[104] N. A. Tsyganenko, "A model of the near magnetosphere with a dawn-dusk asymmetry. 1. mathematical structure," *J. Geophys. Res.*, vol. 107, no. A8, p. SMP12, 2002.

[105] N. A. Tsyganenko, "A model of the near magnetosphere with a dawn-dusk asymmetry. 2. parameterization and fitting to observations," *J. Geophys. Res.*, vol. 107, no. A8, p. SMP10, 2002.

[106] N. A. Tsyganenko, H. J. Singer, and J. C. Kasper, "Storm-time distortion of the inner magnetosphere: How severe can it get?," *J. Geophys. Res.*, vol. 108, no. A5, p. 1209, 2003.

[107] N. A. Tsyganenko and M. I. Sitnov, "Modeling the dynamics of the inner magnetosphere during strong geomagnetic storms," *J. Geophys. Res.*, vol. 110, p. A03208, 2005.

[108] N. A. Tsyganenko and M. I. Sitnov, "Magnetospheric configurations from a high-resolution data-based magnetic field model," *J. Geophys. Res.*, vol. 112, p. A06225, 2007.

[109] G.-H. Voigt, "A three dimensional, analytical magnetospheric model with defined magnetopause," *Z. Geophys.*, vol. 38, pp. 319–346, 1972.

[110] G.-H. Voigt, "A mathematical magnetospheric field model with independent physical parameters," *Planet. Space Sci.*, vol. 29, pp. 1–20, 1981.

[111] C. Ding, *Analytical and numerical modeling of the electromagnetic structure of geospace.* PhD thesis, Rice University, 1995.

[112] M.-C. Fok and T. E. Moore, "Ring current modeling in a realistic magnetic field configuration," *Geophys. Res. Lett.*, vol. 24, no. 14, pp. 1775–1778, 1997.

[113] J. U. Kozyra, M. W. Liemohn, C. R. Clauer, A. J. Ridley, M. F. Thomsen, J. E. Borovsky, J. L. Roeder, V. K. Jordanova, and W. D. Gonzalez, "Multistep dst development and ring current composition changes during the 4-6 june 1991 magnetic storm," *J. Geophys. Res.*, vol. 107, no. A8, 2002.

[114] V. K. Jordanova, A. Boonsiriseth, R. M. Thorne, and Y. Dotan, "Ring current asymmetry from global simulations using a high-resolution electric field model," *J. Geophys. Res.*, vol. 108, no. A12, p. 1443, 2003.

[115] M. W. Chen, M. Shulz, G. Lu, and L. R. Lyons, "Quasi-steady drift paths in a model magnetosphere with amie electric field: Implications for ring current formation," *J. Geophys. Res.*, vol. 108, no. A5, p. 1180, 2003.

[116] M.-C. Fok, R. A. Wolf, R. W. Spiro, and T. E. Moore, "Comprehensive computational model of earth's ring current," *J. Geophys. Res.*, vol. 106, no. A5, pp. 8417–8424, 2001.

[117] A. J. Ridley and M. W. Liemohn, "A model-derived storm time asymmetric ring current driven electric field description," *J. Geophys. Res.*, vol. 107, no. A8, p. 1151, 2002.

[118] G. L. Siscoe, "70 years of magnetospheric modeling," in *Space Weather* (P. Song, H. J. Singer, and G. L. Sisco, eds.), no. 125 in Geophysical monograph, pp. 211–227, 2000 Florida Avenue, N. W., Washington, DC 20009: American Geophysical Union, 2001.

[119] T. I. Gombosi, D. L. De Zeeuw, K. G. Powell, A. J. Ridley, I. V. Sololov, Q. F. Stout, and G. Tóth, "Adaptive mesh refinement for global magnetohydrodynamic simulation," in *Space Plasma Simulation* (J. Büchner, C. T. Dum, and M. Scholer, eds.), pp. 247–274, Springer, 2003.

[120] M. Hesse and J. Birn, "Three-dimensional magnetotail equilibria by numerical relaxation techniques," *J. Geophys. Res.*, vol. 98, p. 3973, 1993.

[121] F. R. Toffoletto, R. W. Spiro, R. A. Wolf, J. Birn, and M. Hesse, "Modeling inner magnetospheric electrodynamics," in *Space Weather* (P. Song, H. J. Singer, and G. L. Sisco, eds.), no. 125 in Geophysical monograph, pp. 265–272, 2000

Florida Avenue, N. W., Washington, DC 20009: American Geophysical Union, 2001.

[122] R. L. McPherron, C. T. Russell, and M. P. Aubry, "Satellite studies of magnetospheric substorms on august 15, 1968. 9. phenomenological model for substorms," *J. Geophys. Res.*, vol. 78, no. 16, pp. 3131–3149, 1973.

[123] A. T. Y. Lui, R. E. Lopez, B. J. Anderson, K. Takahashi, L. J. Zanetti, R. W. McEntire, T. A. Potemra, D. M. Klumpar, E. M. Greene, and R. Strangeway, "Current disruptions in the near-earth neutral sheet region," *J. Geophys. Res.*, vol. 97, no. A2, pp. 1461–1480, 1992.

[124] S. Sazykin, R. A. Wolf, R. W. Spiro, T. I. Gombosi, D. L. De Zeeuw, and M. F. Thomsen, "Interchange instability in the inner magnetosphere associated with geosynchronous particle flux decreases," *Geophys. Res. Lett.*, vol. 29, no. 10, p. 88, 2002.

[125] G. M. Erickson and R. A. Wolf, "Is steady convection possible in the earth's magnetotail," *Geophys. Res. Lett.*, vol. 7, no. 11, pp. 897–900, 1980.

[126] K. Schindler and J. Birn, "Self-consistent theory of time-dependent convection in the earth's magnetotail," *J. Geophys. Res.*, vol. 187, pp. 2263–2275, 1982.

[127] M. G. Kivelson and H. E. Spence, "On the possibility of quasi-static convection in the quiet magnetotail," *Geophys. Res. Lett.*, vol. 15, no. 13, pp. 1541–1544, 1988.

[128] T. W. Garner, R. A. Wolf, R. W. Spiro, M. F. Thomsen, and H. Korth, "Pressure balance inconcsistency exhibited in a statistical model of magnetospheric plasma," *J. Geophys. Res.*, vol. 108, no. A8, p. 1331, 2003.

[129] R. L. Kaufmann, W. R. Paterson, and L. A. Frank, "Presure, volume, density relationships in the plasma sheet," *J. Geophys. Res.*, vol. 109, p. A08204, 2004.

[130] X. Xing and R. A. Wolf, "Criterion for interchange instability in a plasma connected to a conducting ionosphere," *J. Geophys. Res.*, vol. 112, p. A12209, 2007.

[131] C.-P. Wang, L. R. Lyons, R. A. Wolf, R. Nagai, T. Weygand, and M. Lui, "Plasma sheet $pv^{5/3}$ and nv and associated plasma and energy transport for different convection strengths and *ae* levels," *J. Geophys. Res.*, vol. 114, p. A00D02, 2009.

[132] R. A. Wolf, Y. Wan, X. Xing, J.-C. Zhang, and S. Sazykin, "Entropy and plasma sheet transport," *J. Geophys. Res.*, vol. 114, p. A00D05, 2009.

[133] H. E. Spence and M. G. Kivelson, "The variation of the plasma sheet polytropic index along the midnight meridian in a finite width magnetotail," *Geophys. Res. Lett.*, vol. 17, pp. 591–594, 1990.

[134] H. E. Spence and M. G. Kivelson, "Contributions of the low-latitude boundary layer to the finite width magnetotail," *J. Geophys. Res.*, vol. 98, no. A9, pp. 15487–15496, 1993.

[135] C.-P. Wang, L. R. Lyons, M. W. Chen, and R. A. Wolf, "Modeling the quiet time inner plasma sheet protons," *J. Geophys. Res.*, vol. 106, no. A4, pp. 6161–6178, 2001.

[136] C.-P. Wang, L. R. Lyons, M. W. Chan, and F. R. Toffoletto, "Modeling the transition of the inner plasma sheet from weak to enhanced convection," *J. Geophys. Res.*, vol. 109, p. A12202, 2004.

[137] D. H. Pontius Jr and R. A. Wolf, "Transient flux tubes in the terrestrial magnetosphere," *Geophys. Res. Lett.*, vol. 17, no. 1, pp. 49–52, 1990.

[138] C. X. Chen and R. A. Wolf, "Interpretation of high speed flows in the plasma sheet," *J. Geophys. Res.*, vol. 98, pp. 21409–21419, 1993.

[139] C. X. Chen and R. A. Wolf, "Theory of thin-filament motion in earth's magnetotail and its application to bursty bulk flows," *J. Geophys. Res.*, vol. 104, no. A7, pp. 14613–14626, 1990.

[140] V. A. Sergeev and W. Lennartsson, "Plasma sheet at x $\approx -20r_e$ during steady magnetospheric convection," *Planet. Space Sci.*, vol. 36, no. 4, pp. 353–370, 1988.

[141] W. Baumjohann, G. Paschmann, and H. Luehr, "Characteristics of high-speed ion flows in the plasma sheet," *J. Geophys. Res.*, vol. 95, pp. 3801–3809, 1990.

[142] V. Angelopoulos, W. Baumjohann, C. F. Kennel, F. V. Coroniti, M. G. Kivelson, R. Pellat, R. J. Walker, H. Luehr, and G. Paxchmann, "Bursty bulk flows in the inner central plasma sheet," *J. Geophys. Res.*, vol. 97, pp. 4027–4039, 1992.

[143] V. Angelopoulos, C. F. Kennel, F. V. Coroniti, R. Pellat, H. E. Spence, M. G. Kivelson, R. J. Walker, W. Baumjohann, W. C. Feldman, and J. T. Gosling, "Characteristics of ion flow in the quiet state of the inner plasma sheet," *Geophys. Res. Lett.*, vol. 20, pp. 1711–1714, 1993.

[144] C.-P. Wang, L. R. Lyons, M. W. Chen, and R. A. Wolf, "Two-dimensional quiet time equilibrium for the inner plasma sheet protons and magnetic field," *Geophys. Res. Lett.*, vol. 29, no. 24, p. 2186, 2002.

[145] J. E. Borovsky, M. F. Thomsen, R. C. Elphic, T. E. Cayton, and D. J. McComas, "The transport of plasma sheet material from the distant tail to geosynchronous orbit," *J. Geophys. Res.*, vol. 103, no. A9, pp. 20297–20331, 1998.

[146] Y. Ebihara and M. Ejiri, "Simulation study on fundamental properties of the storm-time ring current," *J. Geophys. Res.*, vol. 105, no. A7, pp. 15843–15859, 2000.

[147] D. A. Hardy, M. S. Gussenhoven, and D. Brautigam, "A statistical model of auroral ion precipitation," *J. Geophys. Res.*, vol. 94, no. A1, pp. 370–392, 1989.

[148] D. D. Wallis and E. E. Budzinsky, "Empirical models of height integrated conductivities," *J. Geophys. Res.*, vol. 86, pp. 125–137, 1981.

[149] M. Galand and A. D. Richmond, "Ionospheric electrical conductances produced by auroal proton precipitation," *J. Geophys. Res.*, vol. 106, no. A1, pp. 117–125, 2001.

[150] D. A. Hardy and M. S. Gussenhoven, "A statistical model of auroral electron precipitation," *J. Geophys. Res.*, vol. 90, no. A5, pp. 4229–4248, 1985.

[151] D. H. Brautigam, M. S. Gussenhoven, and D. A. Hardy, "A statistical study on the effects of imf bz and solar wind speed on auroral ion and electron precipitation," *J. Geophys. Res.*, vol. 96, no. A4, pp. 5525–5538, 1991.

[152] R. M. Robinson, R. R. Vondrak, K. Miller, T. Dabbs, and D. Hardy, "On calculating ionospheric conductances from the flux and energy of precipiating electrons," *J. Geophys. Res.*, vol. 92, no. A3, pp. 2565–2569, 1987.

[153] J. D. Huba, G. Joyce, S. Sazykin, R. A. Wolf, and R. W. Spiro, "Simulation study of penetration electric field effects on the low- to mid-latitude ionosphere," *Geophys. Res. Lett.*, vol. 32, p. L23101, 2005.

[154] J. D. Huba, G. Joyce, and J. A. Fedder, "Sami2 is another model of the ionosphere (sami2): A new low-latitude ionosphere model," *J. Geophys. Res.*, vol. 105, pp. 23035–23054, 2000.

[155] J. D. Huba, G. Joyce, and J. A. Fedder, "Simulation study of mid-latitude ionosphere fluctuations observed at millstone hill," *Geophys. Res. Lett.*, vol. 30, no. 18, p. 1943, 2003.

[156] A. E. Hedin, "Extension of the msis thermospheric model into the middle and lower atmosphere," *J. Geophys. Res.*, vol. 96, p. 1159, 1991.

[157] K. Labitzke, J. J. Barnett, and B. Edwards, "Handbook map 16." SCOSTEP, University of Illinois, Urbana, 1985.

[158] A. E. Hedin, M. J. Buonsanto, M. Codrescu, M.-L. Duboin, C. G. Fesen, M. E. Hagan, K. L. Miller, and D. P. Sipler, "Solar activity variations in the midlatitude thermospheric meridional winds," *J. Geophys. Res.*, vol. 99, pp. 17601–17608, 1994.

[159] A. E. Hedin, E. L. Fleming, A. H. Manson, F. J. Schmidlin, S. K. Avery, R. R. Clark, S. J. Franke, G. J. Fraser, T. Tsuda, F. Vial, and R. Vincent, "Empirical wind model for the upper, middle and lower atmosphere," *J. Atmos. and Terr. Phys.*, vol. 58, pp. 1421–1447, 1996.

[160] A. E. Hedin, N. W. Spencer, and T. L. Killeen, "Empirical global model of

upper thermosphere winds based on atmosphere and dynamics explorer satellite data," *J. Geophys. Res.*, vol. 93, pp. 9959–9978, 1988.

[161] A. E. Hedin, M. A. Biondi, R. G. Burnside, G. Hernandez, R. M. Johnson, T. L. Killeen, C. Mazaudier, J. W. Meriwether, J. E. Salah, R. J. Sica, R. W. Smith, N. W. Spencer, V. B. Wickwar, and T. S. Virdi, "Revised global model of thermosphere winds using satellite and ground-based observations," *J. Geophys. Res.*, vol. 96, pp. 7657–7688, 1991.

[162] L. Scherliess and B. G. Fejer, "Radar and satellite global equatorial f region vertical drift model," *J. Geophys. Res.*, vol. 104, pp. 6829–6842, 1999.

[163] T. J. Fuller-Rowell and D. Rees, "A three-dimensional, time-dependent, global model of the thermosphere," *Journal of Atmospheric Science*, vol. 37, p. 2545, 1980.

[164] T. J. Fuller-Rowell and D. Rees, "Derivation of a conservation equation for mean molecular weight for a two constituent gas within a three-dimensional, time-dependent, model of the thermosphere," *Planet. Space Sci.*, vol. 31, p. 1209, 1983.

[165] S. Quegan, G. J. Bailey, R. J. Moffett, R. A. Heelis, T. J. Fuller-Rowell, D. Rees, and R. W. Spiro, "A theoretical study of the distribution of ionization in the high-latitude ionosphere and plasmasphere: first results on the mid-latitude trough and the light ion trough," *J. Atmos. and Terr. Phys.*, vol. 44, p. 619, 1982.

[166] G. H. Millward, R. J. Moffett, S. Quegan, and T. J. Fuller-Rowell, *A coupled thermosphere-ionosphere-plasmasphere model (CTIP).* 1996.

[167] T. J. Fuller-Rowell, D. Rees, S. Quegan, R. J. Moffett, M. V. Codrescu, and G. H. Millward, *A coupled thermosphere ionosphere model (CTIM).* 1996.

[168] R. J. Leveque, "Wave propogation algorithms for multidimensional hyperbolic systems," *J. Comput. Phys.*, vol. 131, pp. 327–353, 1997.

[169] J. A. Wanliss and K. M. Showalter, "High-resolution global storm index: Dst versus sym-h," *J. Geophys. Res.*, vol. 111, p. A02202, 2006.

[170] N. U. Crooker, "High-time resolution of the low-latitude asymmetric disturbance in the geomagnetic field," *J. Geophys. Res.*, vol. 77, no. 4, pp. 773–775, 1972.

[171] C. R. Clauer and R. L. McPherron, "The relative importance of the interplanetary electric field and magnetospheric substorms on the partial ring current development," *J. Geophys. Res.*, vol. 85, pp. 6747–6759, 1980.

[172] N. Maryama, S. Sazykin, R. W. Spiro, D. Anderson, A. Anghel, R. A. Wolf, F. R. Toffoletto, T. J. Fuller-Rowell, M. V. Codrescu, A. D. Richmond, and G. H. Millward, "Modeling storm-time electrodynamics of the low-latitude ionosphere-thermosphere system: Can long lasting disturbance electric fields be accounted for?," *J. Atmos. and Terr. Phys.*, vol. 69, pp. 1181–1199, 2007.

[173] M. A. P. S. Division, "Review of march 31, 2001 geomagnetic storm activity." http://www.metatech-aps.com/Summary/2001/GeomagneticStormSummary03_31.pdf, 2001.

[174] T. W. Garner, R. A. Wolf, R. W. Spiro, W. J. Burke, B. G. Fejer, S. Sazykin, J. L. Roeder, and M. R. Hairston, "Magnetospheric electric fields and plasma

sheet injection to low l-shells during the 4-5 june 1991 magnetic storm: Comparison between the rice convection model and observations," *J. Geophys. Res.*, vol. 109, p. A02214, 2004.

[175] D. Hamilton, G. Gloeckler, F. Ipavich, W. Stüdemann, B. Wilken, and G. Kremser, "Ring current development during the great geomagnetic storm of february 1986," *J. Geophys. Res.*, vol. 93, pp. 14343–14355, 1998.

[176] R. A. Wolf, F. R. Toffoletto, R. W. Spiro, M. Hesse, and J. Birn, *Magnetospheric substorms: An inner-magnetospheric modeling perspective*, pp. 221–229. Amsterdam: Pergamon Press, 2002.

[177] R. A. Wolf, *Magnetisphric configuration*, pp. 288–329. Cambridge, England: Cambridge University Press, 1995.

[178] V. M. Vasyliunas, "Comment on "simulation study on fundamental properties of the storm-time ring current" by y. ebihara and m. ejiri," *J. Geophys. Res.*, vol. 106, no. A4, pp. 6321–6322, 2001.

[179] Y. Ebihara and M. Ejiri, "Reply," *J. Geophys. Res.*, vol. 106, no. A4, pp. 6323–6324, 2001.

[180] R. Lysak, "Electrodynamic coupling of the magnetosphere and ionosphere," *Space Science Reviews*, vol. 52, pp. 33–87, 1988.

[181] K. Rönnmark, "Electron acceleration in the auroral current circuit," *Geophys. Res. Lett.*, vol. 26, pp. 983–986, 1999.

[182] M. P. Aubry, M. G. Kivelson, R. L. McPherron, C. T. Russell, and D. S. Colburn, "A study of the outer magnetosphere near midnight at quiet and

disturbed times," *J. Geophys. Res.*, vol. 77, p. 5487, 1972.

[183] R. J. Park and P. A. Cloutier, "Rocket-based measurements of birkeland currents related to an auroral arc and electrojet," *J. Geophys. Res.*, vol. 76, p. 7714, 1971.

[184] L. W. Choy, R. L. Arnoldy, W. Potter, P. Kintner, and L. J. Cahill Jr, "Field aligned currents near an auroral arc," *J. Geophys. Res.*, vol. 76, p. 8279, 1971.

[185] H.-C. B. Yeh, *Parallel electric field on auroral magnetic field lines.* PhD thesis, Rice University, 1982.

[186] R. Lundin and I. Sandahl, "Some characterisitcs of the parallel electric field acceleration of electrons over discrete auroral arcs as observed rom two rocket flights," in *European sounding-rocket, balloon and related*, p. 125, 1978.

[187] H. Persson, "Electric field parallel to the magnetic field in a low density plasma," *Phys. Fluids*, vol. 9, p. 1090, 1966.

[188] W. Lennartsson, "On the magnetic mirroring as the basic cause of parallel electric fields," *J. Geophys. Res.*, vol. 81, p. 5583, 1976.

[189] W. Lennartsson, "On the role of magnetic mirroring in the auroral phenomena," *Astrophys. Space Sci.*, vol. 51, p. 461, 1977.

[190] W. Lennartsson, "On the consequences of the interaction between the auroral plasma and the geomagnetic field," *Planet. Space Sci.*, vol. 28, p. 135, 1980.

[191] T. Y. Chiu and M. Schulz, "Self-consistent particle and parallel electrostatic field distributions in the magnetospheric-ionospheric auroral region," *J. Geophys. Res.*, vol. 83, p. 629, 1978.

[192] L. R. Lyons, "Generation of large-scale regions of auroral currents, electric potentials, and precipitation by the divergence of the convection electric field," *J. Geophys. Res.*, vol. 85, no. A1, pp. 17–24, 1980.

[193] L. R. Lyons, "Discrete aurora as the direct result of an inferred, high-altitude generating potential distribution," *J. Geophys. Res.*, vol. 86, p. 1, 1981.

[194] L. P. Block, "Potential double payers in the ionosphere," *Cosmic Electrodynamics*, vol. 3, p. 349, 1972.

[195] L. P. Block, "A double layers review," *Astrophys. Space Sci.*, vol. 55, no. 1, pp. 59–83, 1978.

[196] L. P. Block, "Double layers in the laboratory and above the aurora," in *Physics of Auroral Arc Formation* (S.-I. Akasofu and J. R. Kan, eds.), vol. 25 of *Geophysical Monograph*, p. 218, AGU series, 1981.

[197] C. K. Goertz and G. Joyce, "Numerical simulation of the plasma double layer," *Astrophys. Space Sci.*, vol. 32, p. 165, 1975.

[198] J. R. Kan and L. C. Lee, "On the auroral double layer criterion," *J. Geophys. Res.*, vol. 85, p. 788, 1980.

[199] J. R. Kan and L. C. Lee, "Double-layer criterion on the altitude of the auroral acceleration region," *Geophys. Res. Lett.*, vol. 7, p. 429, 1980.

[200] C. T. Dum and T. D. Dupree, "Non-linear stabilization of high frequency instabilities in a magnetic field," *Phys. Fluids*, vol. 13, p. 2064, 1970.

[201] J. M. Kindel and C. F. Kennel, "Topside current instabilities," *J. Geophys. Res.*, vol. 76, p. 3055, 1971.

[202] T. Tange and S. Ichimaru, "Theory of anomalous resistivity and turbulent heating in plasma," *J. Phys. Soc. Jap.*, vol. 36, p. 1437, 1974.

[203] K. Papadopoulos and T. Coffey, "Anomalous resistivity of the auroral plasma," *J. Geophys. Res.*, vol. 79, p. 1558, 1974.

[204] K. Papadopoulos, "A review of anomalous resistivity for the ionosphere," *Rev. Geophys. Space Phys.*, vol. 15, p. 113, 1977.

[205] H. L. Rowland, P. J. Palmadesso, and K. Papadopoulos, "Anomalous resistivity on auroral field lines," *Geophys. Res. Lett.*, vol. 8, p. 1257, 1981.

[206] B. Hultqvist, "On the production of a magnetic-field-aligned electric field by the interaction between the hot magnetospheric plasma and cold ionosphere," *Planet. Space Sci.*, vol. 17, p. 749, 1971.

[207] L. P. Block and C.-G. Fälthammar, "Mechanism that may support magnetic-field-aligned electric fields in the magnetosphere," *Ann. Geophys.*, vol. 32, p. 161, 1976.

[208] H. Persson, "Electric field along a magnetic field lines of force in a low density plasma," *Phys. Fluids*, vol. 6, p. 1756, 1963.

[209] S. Knight, "Parallel electric fields," *Planet. Space Sci.*, vol. 21, pp. 741–750, 1973.

[210] M. Fridman and J. Lemaire, "Relationship between auroral electrons fluxes and field aligned electric potential difference," *J. Geophys. Res.*, vol. 85, no. A2, pp. 664–670, 1980.

[211] S. Christon, D. Williams, D. Mitchell, C. Huang, and L. Frank, "Spectral characteristics of plasma sheet ion and electron populations during disturbed geomagnetic conditions," *J. Geophys. Res.*, vol. 96, no. A1, pp. 1–22, 1991.

[212] P. Janhunen and A. Olsson, "The current-voltage relationship revisited: exact and approximate formulas with almost general validity for hot magnetospheric electrons for bi-maxwellian and kappa distributions," *Annales Geophysicae-Atmospheres Hydrospheres and Space Sciences*, vol. 16, no. 3, pp. 292–297, 1998.

[213] R. E. Ergun, C. W. Carlson, J. P. McFadden, F. S. Mozer, and R. J. Strangeway, "Parallel electric fields in discrete arcs," *Geophys. Res. Lett.*, vol. 27, no. 24, pp. 4053–4056, 2000.

[214] G. V. Khazanov, M. W. Liemohn, E. N. Krivorutsky, and T. E. Moore, "Generalized kinetic description of a plasma in an arbitrary field-aligned potential energy structure," *J. Geophys. Res.*, vol. 103, no. A4, pp. 6871–6889, 1998.

[215] G. Lu, P. H. Reiff, J. L. Burch, and J. D. Winnningham, "On the auroral current-voltage relationship," *J. Geophys. Res.*, vol. 96, no. A3, pp. 3523–3531, 1991.

[216] A. Olsson, A. I. Eriksson, and P. Janhunen, "On the current-voltage relationship in auroral breakups and westwards-travelling surges," *Ann. Geophys.*, vol. 14, no. 12, pp. 1265–1273, 1996.

[217] A. Olsson, L. Andersson, A. L. Eriksson, J. Clemmons, R. E. Erlandsson, G. Reeves, T. Huges, and J. S. Murphee, "Freja studies of the current-voltage re-

lation in substorm-related events," *J. Geophys. Res.*, vol. 103, no. A3, pp. 4285–4301, 1998.

[218] A. Olsson and P. Janhunen, "A statistical study of nightside inverted-v events using freja electron data: implications for the current-voltage relationship," *J. Atmos. Solar-Terr. Phys.*, vol. 62, no. 2, pp. 81–92, 2000.

[219] V. Pierrard, "New model of magnetospheric current-voltage relationship," *J. Geophys. Res.*, vol. 101, no. A2, pp. 2669–2675, 1996.

[220] V. Pierrard, G. V. Khazanov, and J. F. Lemaire, "Current-voltage relationship," *J. Atmos. Solar-Terr. Phys.*, vol. 69, no. 16, pp. 2048–2057, 2007.

[221] K. Rönnmark, "Auroral current-voltage relation," *J. Geophys. Res.*, vol. 107, no. A12, p. 1430, 2002.

[222] T. E. Moore, M.-C. Fok, D. C. Delcourt, S. P. Slinker, and J. A. Fedder, "Global aspects of solar wind-ionosphere interactions," *J. Atmos. Solar-Terr. Phys.*, vol. 69, pp. 265–278, 2007.

[223] M. G. Kivelson, S. M. Kaye, and D. J. Southwood, *The physics of plasma injection events*, p. 385. Hingham, Massachusetts: D. Reidel, 1979.

[224] M. S. Gussenhoven, D. A. Hardy, and N. Heinemann

[225] T. L. Schumaker, M. S. Gussenhovan, D. A. Hardy, and R. L. Carovillano, "The relationship between diffuse auroral and plasma sheet electron distribution near local midnight," *J. Geophys. Res.*, vol. 94, no. A8, pp. 10061–10078, 1989.

[226] M. Schulz, "Particle lifetimes in strong diffusion," *Astrophys. Space Sci.*, vol. 31, pp. 37–42, 1974.

[227] M. P. Gough, P. J. Christiansen, G. Martelli, and E. J. Gershuny, "Interaction of electrostatic waves with warm electrons at the geomagnetic equator," *Nature*, vol. 279, p. 515, 1979.

[228] G. Belmont, D. Fontaine, and P. Canu, "Are equatorial electron cyclotron waves responsible for diffuse auroral electron precipitation?," *J. Geophys. Res.*, vol. 88, pp. 9163–9170, 1983.

[229] J. L. Roeder and H. C. Koons, "A survey of electron cyclotron waves in the magnetosphere and the diffuse auroral electron precipitation," *J. Geophys. Res.*, vol. 94, pp. 2529–2541, 1989.

[230] H. C. Koons and J. L. Roeder, "A survey of equatorial magnetospheric wave activity between 5 and 8 r_e," *Planet. Space Sci.*, vol. 38, pp. 1335–1341, 1990.

[231] C. S. Roberts, "Pitch angle diffusion of electrons in the magnetosphere," *Rev. Geophys.*, vol. 7, pp. 305–337, 1969.

[232] J. A. Van Allen, "Charged particles in the magnetosphere," *Rev. Geophys.*, vol. 7, pp. 233–255, 1969.

[233] L. R. Lyons, R. M. Thorne, and C. F. Kennel, "Pitch angle diffusion of radiation belt electrons within the plasmasphere," *J. Geophys. Res.*, vol. 77, pp. 3455–3474, 1972.

[234] J. M. Albert, "Quasi-linear pitch angle diffusion coefficients: Retaining high harmonics," *J. Geophys. Res.*, vol. 99, pp. 23741–23745, 1994.

[235] M. W. Chen and M. Shulz, "Simulations of diffuse aurora with plasma sheet electrons in pitch angle diffusion less than everywhere strong," *J. Geophys. Res.*,

vol. 106, no. A12, pp. 1–18, 2001.

[236] M. W. Chen, M. Shulz, P. C. Anderson, G. Lu, G. Germany, and M. Wüest, "Storm time distributions of diffuse auroral electron energy and x-ray flux: Comparison of drift-loss simulations with observations," *J. Geophys. Res.*, vol. 110, p. A03210, 2005.

[237] J. Bishop, "Multiple charge exchange and ionization collisions within the ring current-geocorona-plasmasphere system: Generation of a secondary ring current on inner l shells," *J. Geophys. Res.*, vol. 101, no. A8, pp. 17325–17336, 1996.

[238] S. J. Bauer, *The structure of the topside ionosphere*, pp. 387–397. New York: North-Holland, 1966.

[239] A. J. Dessler and F. C. Michel, "Plasma in geomagnetic tail," *J. Geophys. Res.*, vol. 71, p. 1421, 1966.

[240] J. P. McFadden, Y. K. Tung, C. W. Carlson, R. J. Strangeway, E. Moebius, and L. M. Kistler, "Fast observations of ion outflow associated with magnetic storms," in *Space Weather* (P. Song, H. J. Singer, and G. L. Sisco, eds.), no. 125 in Geophysical monograph, pp. 413–421, 2000 Florida Avenue, N. W., Washington, DC 20009: American Geophysical Union, 2001.

[241] T. Moore, M. O. Chandler, M.-C. Fok, B. L. Giles, D. C. Delcourt, J. L. Horwitz, and C. J. Pollock, "Ring currents and internal plasma sources," *Space Science Reviews*, vol. 95, pp. 555–568, 2001.

[242] E. Engwall, A. I. Eriksson, C. M. Cully, M. André, R. Torbert, and H. Vaith, "Earth's ionospheric outflow dominated by hidden cold plasma," *Nature Geoscience*, vol. 2, pp. 24–27, 2009.

[243] W. I. Axford, "The polar wind and the terrestrial helium budge," *J. Geophys. Res.*, vol. 73, p. 6855, 1968.

[244] J. Lemaire, "Effect of escaping photoelectrons in a polar exospheric model," vol. 12, p. 1413, 1972.

[245] T. Abe, B. A. Whalen, A. W. Yau, S. Watanable, E. Sagawa, and K. I. Oyama, "Altitude profile of the polar wind velocity and its relationship to ionospheric conditions," *Geophys. Res. Lett.*, vol. 20, p. 2825, 1993.

[246] F. Yasseen, J. M. Retterer, T. Chang, and J. D. Winningham, "Monte-carlo modeling of polar wind photoelectron distributions with anomalous heat flux," *Geophys. Res. Lett.*, vol. 16, p. 1023, 1989.

[247] T. E. Moore, R. Lundin, D. Alcayde, M. Andréand, S. Ganguli, M. Temerin, and A. Yau, "Source processes in the high latitude ionosphere," *Space Science Reviews*, vol. 88, no. 1-2, p. 7, 1999.

[248] Y.-J. Su, J. L. Horwitz, T. E. Moore, B. L. Giles, M. O. Chandler, P. D. Craven, M. Hirahara, and C. J. Pollock, "Polar wind survey with the thermal ion dynamics experiment/plasma source instrument suite aboard polar," *J. Geophys. Res.*, vol. 103, no. A12, pp. 29305–39337, 1998.

[249] A. W. Yau, W. K. Peterson, and E. G. Shelley, "Quantitative parameterization of energetic ionospheric ion outflow," in *Modeling magnetospheric plasmas*, vol. 44 of *Geophysical Monograph Series*, (Washington, D. C.), pp. 211–217, American Geophysical Union, 1988.

[250] D. M. Ober, N. C. Maynard, W. J. Burke, W. K. Peterson, J. B. Sigwarth, L. A. Frank, J. D. Scudder, W. J. Hughes, and C. T. Russel, "Electrodynamics

of the poleward auroral border observed by polar during a substorm on april 22, 1998," *J. Geophys. Res.*, vol. 106, no. A4, pp. 5927–5943, 2001.

[251] T. E. Moore, R. L. Arnoldy, J. Feynmann, and D. A. Hardy, "Propagating substorm injection fronts," *J. Geophys. Res.*, vol. 86, pp. 6713–6726, 1981.

[252] V. A. Sergeev, M. A. Schukhtina, R. Rasinkangas, A. Korth, G. D. Reeves, H. J. Singer, M. F. Thomsen, and L. I. Vagina, "Event study of deep energetic particle injections during substorm," *J. Geophys. Res.*, vol. 103, no. A5, pp. 9217–9234, 1998.

[253] J.-C. Zhang, R. A. Wolf, S. Sazykin, and F. R. Toffoletto, "Injection of a bubble into the inner magnetosphere," *Geophys. Res. Lett.*, vol. 35, p. L02110, 2008.

[254] J.-C. Zhang, R. A. Wolf, R. W. Spiro, G. M. Erickson, S. Sazykin, F. R. Toffoletto, and J. Yang, "Rice convection model simulation of the substorm-associated injection of an observed bubble into the inner magnetosphere: 2. simulation results," *J. Geophys. Res.*, vol. 114, p. A08219, 2009.

[255] P. J. Chi, C. T. Russell, and S. Ohtani, "Substorm onset timing via traveltime magnetoseismology," *Geophys. Res. Lett.*, vol. 36, p. L08107, 2009.

[256] V. A. Sergeev, T. A. Kornilova, I. A. Kornilov, V. Angelopoulos, M. V. Kubyshkina, M. Fillingim, R. Nakamura, J. P. McFadden, and D. Larson, "Auroral signatures of the plasma injection and dipolarization in the inner mangetosphere," *J. Geophys. Res.*, vol. 115, p. A02202, 2010.

[257] G.-H. Voigt and R. A. Wolf, "Quasi-static magnetospheric mhd processes and the "ground sta" of the magnetosphere," *Rev. Geophys.*, vol. 26, pp. 823–843, 1988.

[258] T. I. Pulkkinen, D. N. Baker, D. H. Fairfield, R. J. Pellinen, J. S. Murphree, R. D. Elphinstone, R. L. McPherron, J. F. Fennell, R. E. Lopez, and T. Nagai, "Modeling the growth phase of a substorm using the tsyganenko model and multi-spacecraft observations: Cdaw-9," *Geophys. Res. Lett.*, vol. 18, no. 11, pp. 1963–1966, 1991.

[259] T. I. Pulkkinen, H. E. J. Koskinen, and R. J. Pellinen, "Mapping of auroral arcs during substorm growth phase," *J. Geophys. Res.*, vol. 96, no. A12, pp. 21087–21094, 1991.

[260] T. I. Pulkkinen, D. N. Baker, R. J. Pellinen, J. Büchnner, H. E. J. Koskinen, R. E. Lopez, R. L. Dyson, and L. A. Frank, "Particle scattering and current sheet stability in the geomagnetic tail during the substorm growth phase," *J. Geophys. Res.*, vol. 97, no. A12, pp. 19283–19297, 1992.

[261] T. I. Pulkkinen, D. N. Baker, D. G. Mitchell, R. L. McPerron, C. Y. Huang, and L. A. Frank, "Thin current sheets in the magnetotail during substorm: Cdaw 6 revisited," *J. Geophys. Res.*, vol. 99, no. A4, pp. 5793–5803, 1994.

[262] C. T. Russell, "Geophysical coordinate transformations," *Cosmic Electrodynamics*, vol. 2, pp. 184–196, 1971.

[263] M. A. Hapgood, "Space physics coordinate transformations: a user guide," *Planet. Space Sci.*, vol. 40, no. 5, pp. 711–717, 1992.